T 42/v. 3

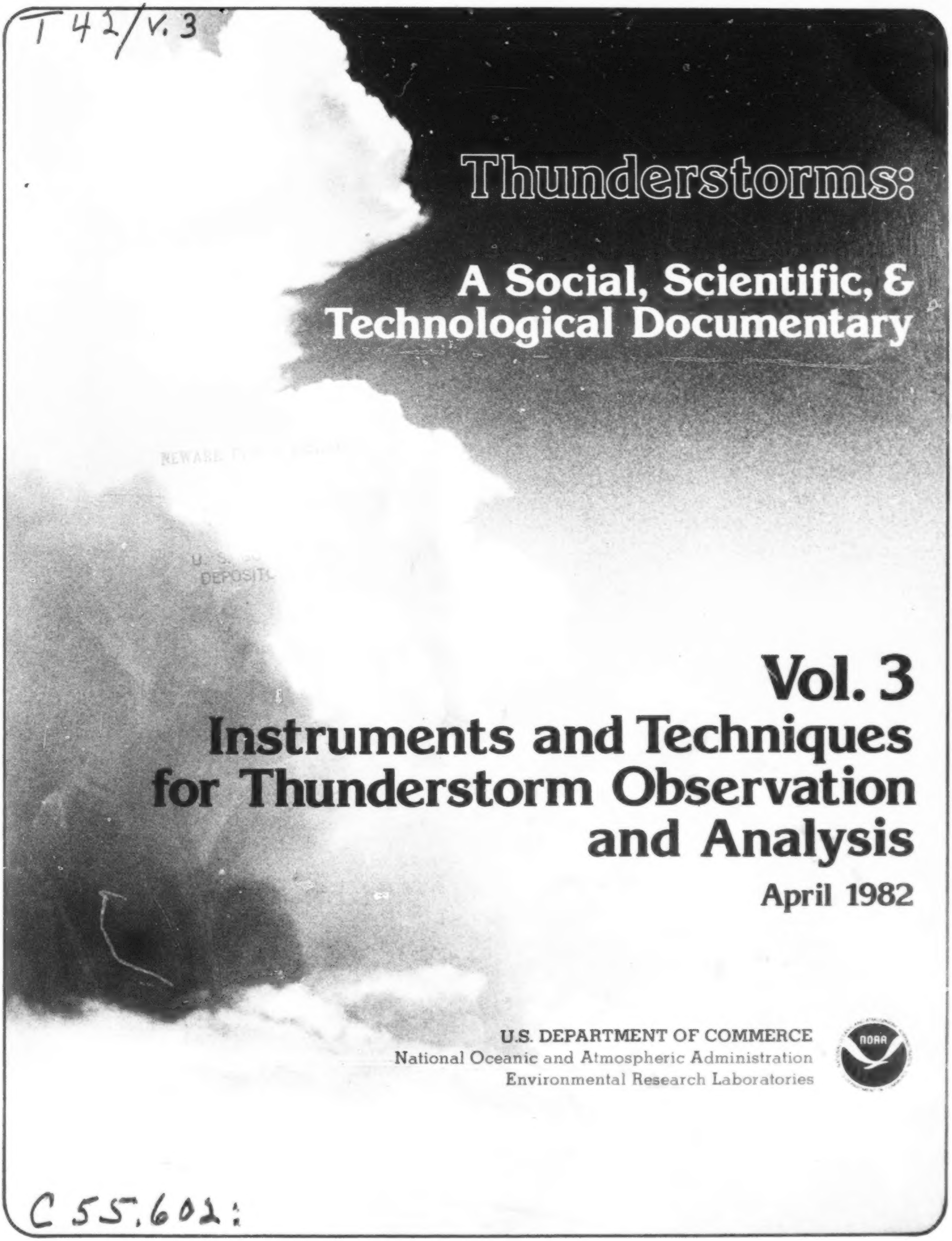

Thunderstorms:

A Social, Scientific, & Technological Documentary

NEWARK

U S
DEPOSIT

Vol. 3

Instruments and Techniques for Thunderstorm Observation and Analysis

April 1982

U.S. DEPARTMENT OF COMMERCE
National Oceanic and Atmospheric Administration
Environmental Research Laboratories

C 55.602:

11

NEWARK PUBLIC LIBRARY

OCT 28 [illegible]

U. S. GOVT. PUBS.
DEPOSITORY 376

Instruments and Techniques for Thunderstorm Observation and Analysis

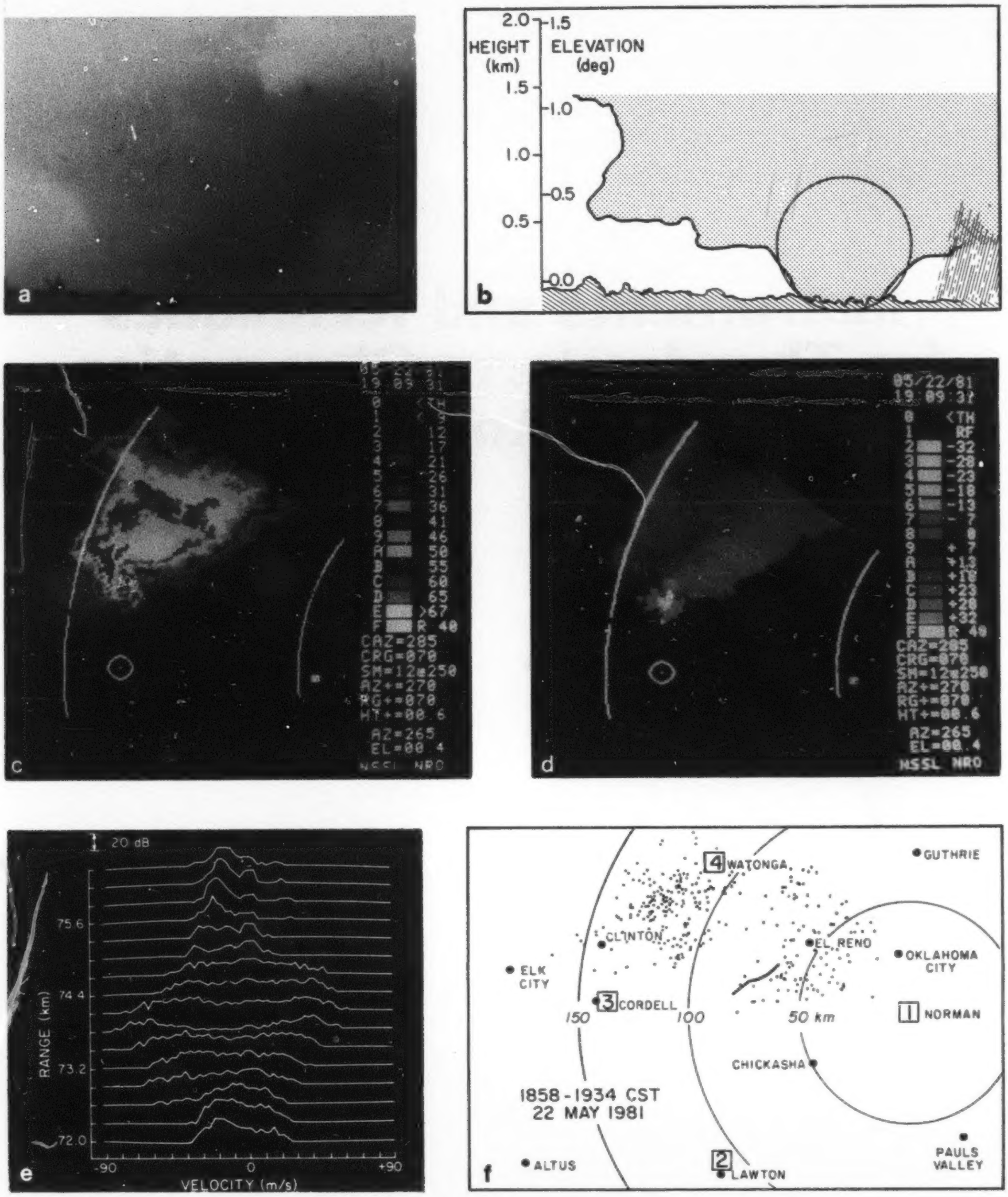

Frontispiece: (a) A major tornado near Binger, Okla., 22 May 1981, was photographed by a Storm Intercept team 5 km from the funnel cloud. (b) Circle shows how the Doppler radar at Norman illuminated the funnel 75 km away. (c) Plan distribution of reflectivity factor includes some values >60 dBZ, and shows a shape characteristic of tornadic storms. (d) Plan distribution of radial velocities--reds denote motion away from the radar; the tornado lies in the strong color change region. (e) Velocity spectra along beam as in (b) show speeds from -85 to +80 m s^{-1} within the 1.3-km beamwidth. (f) Ground strike points of lightning show no clustering along the tornado ground path. See also Chapters II, IV, VII, IX, and X.

Thunderstorms: A Social, Scientific, &
Technological Documentary

Vol. 3

Instruments and Techniques for Thunderstorm Observation and Analysis

Edwin Kessler, Editor

April 1982

U.S. DEPARTMENT OF COMMERCE
National Oceanic and Atmospheric Administration
Environmental Research Laboratories

NOTICE

Mention of a commercial company or product does not constitute an endorsement by NOAA Environmental Research Laboratories. Use for publicity or advertising purposes of information from this publication concerning proprietary products or the tests of such products is not authorized.

For sale by the Superintendent of Documents, U.S. Government Printing Office, Washington, D.C. 20402

READEX FICHE

best copy available

PREFACE

This third and last volume of a comprehensive documentation of thunderstorms presents tools and techniques for acquisition and analysis of data on thunderstorms.

The authors have been cooperative and gracious during a process that began in 1976. They have my heartfelt thanks. Reviewers have also contributed substantially. Reviewers of this volume include Sigmund Fritz, Thomas H. Georges, Roland List, Don R. MacGorman, Roddy R. Rogers, W. David Rust, William L. Taylor, and Charles Warner. I particularly thank the staff of the Environmental Research Laboratories, Publication Services Division, Boulder, Colo., for arduous editorial work expertly accomplished. My secretary, Barbara R. Franklin, and my wife, Lottie Menger Kessler, have also been indispensable to completion of this work.

Edwin Kessler
Norman, Oklahoma
January 1982

blank page

CONTENTS

Page

I. STATION NETWORKS FOR STORM OBSERVATION . . . 1
K. E. Wilk and S. L. Barnes

1. INTRODUCTION. . . . 1
2. EARLY MESOMETEOROLOGICAL NETWORKS FOR SEVERE-STORM RESEARCH (1946-1966) 1
3. SEVERE-STORM NETWORKS AFTER 1970. . . . 6
4. COOPERATIVE OBSERVERS AND NESTED NETWORKS 8
5. INSTRUMENTS FOR MESOSCALE METEOROLOGICAL NETWORKS 9
6. MODERN DIGITAL PROCESSING AND RECORDING TECHNIQUES. . . . 13
7. OBJECTIVE ANALYSIS OF SPATIALLY DISTRIBUTED TIME SERIES OBSERVATIONS. . . . 16
   a. General description. . . . 16
   b. Mathematical properties. . . . 18
   c. Examples of analysis based on real observations. . . . 23
   d. Concluding remarks on objective analysis 28
REFERENCES 28

II. TORNADO INTERCEPTION WITH MOBILE TEAMS. . . . 33
Robert P. Davies-Jones

1. INTRODUCTION. . . . 33
2. TIP GOALS 34
3. PERSONNEL AND EQUIPMENT 34
4. TIP STRATEGY. . . . 35
5. THE CHANCE OF INTERCEPTION. . . . 38
6. PROJECT ACCOMPLISHMENTS 39
7. PROJECT APPRAISAL 44
REFERENCES 44

III. OBSERVATIONS FROM INSTRUMENTED AIRCRAFT 47
John McCarthy and Donald L. Veal

1. INTRODUCTION. . . . 47
2. COMPARISON OF AIRBORNE AND GROUND-BASED THUNDERSTORM PROBES 51
3. MEASUREMENTS BY AIRBORNE SENSORS. . . . 52
   a. State of the atmosphere. . . . 52
   b. State of the aircraft. . . . 56
   c. Measurement of air velocities. . . . 58
4. MICROPHYSICAL MEASUREMENT TECHNIQUES. . . . 61
   a. Cloud droplet size and concentration 62
   b. Liquid water content 62
   c. Raindrop size and concentration. . . . 64
   d. Ice particle size and concentration. . . . 65
5. AIRBORNE RADAR. . . . 68
6. AIRBORNE COMMUNICATIONS AND DATA SYSTEMS. . . . 69
7. SPECIAL USES OF AIRCRAFT IN THUNDERSTORM RESEARCH 71
   a. Chaff as an air motion sensor. . . . 71
   b. Lightning suppression experiments. . . . 71
8. SYNTHESIS OF AIRBORNE DATA. . . . 71
REFERENCES 74

IV. PHOTOGRAMMETRY OF THUNDERSTORMS 77
Ronald L. Holle

- 1. INTRODUCTION. 77
- 2. BASIC EQUATIONS FOR PHOTOGRAMMETRIC ANALYSIS. 78
- 3. PHOTOGRAMMETRY OF GROUND-BASED PICTURES 79
  - a. Handheld-camera pictures 79
  - b. Single time-lapse camera pictures. 81
  - c. Panoramic photographs. 83
  - d. Multiple time-lapse camera photographs 83
  - e. Stereoscopic photographs 85
  - f. Photos of tornadoes and severe weather 86
  - g. Summary. 86
- 4. PHOTOGRAMMETRY OF AIRCRAFT-BASED PICTURES 88
  - a. Special considerations 88
  - b. Handheld-camera pictures 89
  - c. Stereoscopic views 90
  - d. Time-lapse photographs 90
  - e. Mapping of clouds. 92
  - f. Measuring widths and heights of clouds 93
  - g. Pictures from downward-looking cameras 94
- 5. CONCLUDING REMARKS. 94
- Acknowledgments. 96
- REFERENCES 96

V. STORM ACOUSTICS 99
Roy T. Arnold

- 1. INTRODUCTION. 99
- 2. PROPAGATION EFFECTS 99
- 3. THUNDER 102
  - a. Sounds of thunder. 102
  - b. Measurements and theory. 104
- 4. TORNADO ACOUSTICS 109
  - a. Tornadic sounds. 109
  - b. Temporal evolution of tornadic sounds. 111
- 5. WIND NOISE. 113
- 6. CONCLUSION. 113
- Acknowledgments. 113
- REFERENCES 113

VI. INFRASOUND FROM THUNDERSTORMS 117
T. M. Georges

- 1. INTRODUCTION. 117
- 2. HISTORICAL PERSPECTIVE. 117
- 3. INSTRUMENTATION AND SOME REPRESENTATIVE OBSERVATIONS. 118
  - a. Surface pressure 118
  - b. Ionospheric waves. 119
- 4. A CASE ILLUSTRATION: INFRASOUND FROM A NEARBY TORNADIC STORM. 122
- 5. A POSSIBLE SOURCE MECHANISM 125
- 6. IS IT USEFUL FOR STORM WARNING? 127

7. CONCLUSION . . . 129
Acknowledgments . . . 129
REFERENCES . . . 129

VII. SFERICS AND OTHER ELECTRICAL TECHNIQUES FOR STORM INVESTIGATIONS . . . 135
E. T. Pierce

1. INTRODUCTION . . . 135
2. LONG-DISTANCE TECHNIQUES . . . 135
  a. Introduction . . . 135
  b. Single-station methods . . . 136
  c. Multistation techniques . . . 139
3. INTERMEDIATE DISTANCES . . . 140
4. CLOSE DISTANCES . . . 141
  a. Lightning mapping . . . 141
  b. Warning techniques . . . 144
  c. Studies of electrical fields and field changes . . . 145
REFERENCES . . . 147

VIII. OBSERVATION AND MEASUREMENT OF HAILFALL . . . 149
Griffith M. Morgan, Jr.

1. INTRODUCTION . . . 149
2. HAIL OBSERVATION BY CONVENTIONAL WEATHER STATION NETWORKS . . . 149
3. HAILFALL AND CROP DAMAGE . . . 150
  a. Hailfall inferred from kinetic energy . . . 151
  b. Hailfall inferred from insurance records . . . 152
  c. Hailfall inferred from aerial photography of crop damage . . . 154
4. HAIL DATA FROM OBSERVERS' REPORTS . . . 154
5. HAILFALL MEASUREMENT INSTRUMENTS . . . 156
  a. Integrating sensors . . . 157
  b. Recording instruments . . . 160
  c. Remote-sensing techniques . . . 161
  d. Limits to accuracy of point hailfall measurements with instruments . . . 163
6. COLLECTION OF HAIL FOR SCIENTIFIC ANALYSIS . . . 165
7. DESIGN OF NETWORKS FOR HAILFALL OBSERVATION . . . 166
  a. An example of the effect of sampling density on estimates of areal extent of damaging hail . . . 167
  b. An example of degradation of hailfall pattern with decreasing network density . . . 167
  c. An illustration of the evaluation of network sampling performance . . . 169
  d. Network size and shape . . . 173
8. CONCLUSION . . . 174
Acknowledgments . . . 175
REFERENCES . . . 175

IX. WEATHER RADAR . . . 181
Richard J. Doviak, Dale Sirmans, and Dusan Zrnic'

- 1. INTRODUCTION . . . 181
- 2. PRINCIPLES OF RADAR . . . 182
  - a. Electromagnetic waves . . . 182
  - b. Doppler radar transmitting aspects . . . 184
  - c. The target . . . 189
  - d. Attenuation . . . 190
  - e. Doppler radar receiving aspects . . . 192
  - f. Radar measurement limitations . . . 195
- 3. WEATHER ECHO SIGNALS . . . 199
  - a. The echo sample . . . 199
  - b. The weather radar equation . . . 201
  - c. Signal-to-noise ratio for weather targets . . . 205
- 4. DOPPLER SPECTRA OF WEATHER ECHOES . . . 206
  - a. Estimating Doppler power spectra . . . 208
  - b. Velocity spectrum width, shear, and turbulence . . . 210
- 5. OBSERVATION OF WEATHER . . . 212
  - a. Dual Doppler radar . . . 213
  - b. Single Doppler radar . . . 216
  - c. Pulsed Doppler observation of clear-air wind fields . . . 227
- 6. CONCLUSIONS . . . 231
- Acknowledgments . . . 233
- REFERENCES . . . 233

X. MEASURING STORM RAINFALL BY RADAR AND RAIN GAGE . . . 241
E. A. Brandes and J. W. Wilson

- 1. INTRODUCTION . . . 241
- 2. GAGE MEASUREMENT OF RAINFALL . . . 242
  - a. Instrument error . . . 243
  - b. Areal estimate error . . . 243
- 3. RADAR MEASUREMENT OF RAINFALL . . . 244
  - a. Radar equation and calculation of rainfall rate . . . 244
  - b. Sources of error . . . 246
- 4. RADAR-GAGE COMPARISONS . . . 253
- 5. ADJUSTMENT OF RADAR-DERIVED RAINFALL ESTIMATES . . . 261
  - a. Changing the Z-R relationship . . . 261
  - b. Calibration with rain gages . . . 261
- 6. CLOSING REMARKS . . . 265
- REFERENCES . . . 266

Appendix: ADJUSTMENTS TO THE RADAR MEASUREMENT . . . 273
E. A. Brandes and D. Sirmans

- A.1. ATTENUATION BY RAINFALL . . . 273
- A.2. ATTENUATION BY CLOUDS . . . 274
- A.3. ABSORPTION BY ATMOSPHERIC GASES . . . 275
- A.4. RANGE-AVERAGING BIAS FOR LOGARITHMIC RECEIVERS . . . 276
- A.5. CONCLUDING REMARKS . . . 277

XI. ON THE USE OF SATELLITE OBSERVATIONS. 279
R. A. Maddox and T. H. VonderHaar

1. INTRODUCTION. 279
2. SATELLITE TECHNOLOGY. 279
   a. Vertical-temperature profile radiometer (VTPR) 280
   b. Visible and infrared spin scan radiometer (VISSR). 280
3. ANALYSIS AND INTERPRETATION OF THUNDERSTORM IMAGES. 282
   a. Determination of convective rainfall 282
   b. Monitoring movement and intensity of thunderstorm gust fronts. 283
   c. Severe-thunderstorm/jetstream relationship 285
   d. Thunderstorm boundaries and intersections. 287
   e. Cloudtop tornadic signatures 288
   f. Mesoscale convective weather systems 288
4. THUNDERSTORM RESEARCH TECHNIQUES. 292
   a. Cloudtop temperature fields. 293
   b. Cloud motions and wind fields. 294
   c. Thunderstorm microphysics. 298
5. REMOTE SOUNDING OF THE THUNDERSTORM ENVIRONMENT 301
6. SUMMARY 304
Acknowledgments. 304
REFERENCES 304

BIOGRAPHIES OF AUTHORS. 309

Owing to limitations of the equipment used in preparing this volume, negative exponentiation appears in the following manner: $5.0\ \mathrm{m}^{-2}\ \mathrm{s}^{-1}$.

Please note that the Greek letter nu appears as V.

I. STATION NETWORKS FOR STORM OBSERVATION

K. E. Wilk and S. L. Barnes

1. INTRODUCTION

The National Weather Service and its predecessor organizations have always maintained and operated a network of meteorological stations (see Vol. 1, Ch. VII). Measurements taken at these stations allow meteorologists to monitor large-scale weather systems and gather climatological records on smaller scale events, including showers and thunderstorms.

Since individual severe thunderstorms are only 15-30 km across, observations are needed at many points within this narrow region to describe accurately the distributions of storm-associated parameters. Observations by radar, electric field sensors, and weather satellites are sufficiently detailed, but an adequate thermodynamic description of individual local storms also requires observations of the kind provided by the regular network of weather-observing stations. Thus, direct measurements of wind velocity, temperature, and moisture, which are essential for storm research, are provided by a few local mesoscale networks of in situ sensors. This chapter reviews the development of mesometeorological research networks and their instrumentation, and outlines some modern methods for data acquisition and analysis.

2. EARLY MESOMETEOROLOGICAL NETWORKS FOR SEVERE-STORM RESEARCH (1946-1966)

Since World War II, several mesoscale-observing experiments have provided better definition of patterns of pressure, temperature, wind, and moisture associated with severe local storms. The Thunderstorm Project was the first major national effort to gain comprehensive knowledge of severe thunderstorms (Byers and Braham, 1949). Collection of storm data was undertaken in 1946-1947, as a joint project of the University of Chicago, the U.S. Weather Bureau, the National Advisory Committee for Aeronautics, and the U.S. military agencies. The project set a pattern in the use of research stations for observations at the Earth's surface and in the upper air that would continue for two decades.

Table 1 lists project instrumentation at 55 network sites, placed first in Florida and later moved to Ohio. The network in Ohio was expanded to cover the somewhat larger scale of thunderstorms and related meteorological fields in the Midwest as compared with those observed in Florida (compare Figs. 1a,b). Note also the sites for radar and surrounding rawinsondes, which for the first time played a role in observing local storms and their environment. (The development of upper-air sounding capability has been detailed by Middleton [1969], and the early history of U.S. aerology has been summarized by Ferguson [1933].) During the summers of 1946 and 1947, the networks operated fewer than 300 days yet recorded useful data during 180 rain periods, most of which involved thunderstorms. The composite data set included 1,327 wind soundings and many individual storm traverses by instrumented aircraft. By comprehensive analysis, case-by-case, Byers and his associates (Byers and Braham, 1948; Byers and Rodebush, 1948; Braham, 1952; Bleeker and Andre, 1950) produced the first definitive study of meteorological features accompanying thunderstorms in the United States. Using averages from Weather Bureau stations surrounding the network to determine the large-scale patterns of pressure and wind (which

Table 1.--Meteorological instrumentation* in the Thunderstorm Project, 1946-47

Parameter	Florida	Ohio
Wind direction	Vane with 4 contacts and double-register recorder for 8-point (45°) resolution	Vane with continuous output provided by variable resistor connected to strip chart recorder
Windspeed	3-cup sensor with internal recording of miles of air-flow	3-cup sensor with AC generator providing continuous output from 0 to 75 kn, on strip chart
Temperature/humidity	Bendix hygrothermograph using Bourdon tube for temperature and hair hygrometer for measuring relative humidity	Same
Rainfall	Weighing-bucket rain gage with 20-in-diameter collector	Same
Pressure	Microbarograph using double Sylphon bellows (checked weekly with aneroid barometer)	Same

*Drive gears on most recorders provided charts that could be read to a resolution of 1 minute.

were then subtracted from the dense-network data), project meteorologists were able to analyze and track the mesoscale perturbations associated with developing thunderstorms. The high- and low-pressure cells so revealed were on the same scale as the major storm elements and were attributed to vertical motions in the organizing convective-cloud systems. New questions arose with these measurements, with speculation on the origins and implications of gust fronts and local pressure and temperature anomalies. For example, Tepper (1950) suggested that pressure jumps, sometimes observed before squall line occurrence, might be a basis for advanced warning of tornadoes.

In 1955, the U.S. Army Signal Corps sponsored a reanalysis of the Thunderstorm Project data by staff at the Illinois State Water Survey, searching for repetitive patterns that might improve short-range forecasting. Both organizations then developed local research networks. The Army facility at Fort Huachuca, Ariz., operated a 12-station network for military applications. The Illinois State Water Survey operated several mesoscale rain gage networks to define thunderstorm rainfall characteristics, and later developed the first urban networks designed to improve water resources management (Changnon and Semonin, 1971). During that same period, Williams (1953) and Fujita et al.

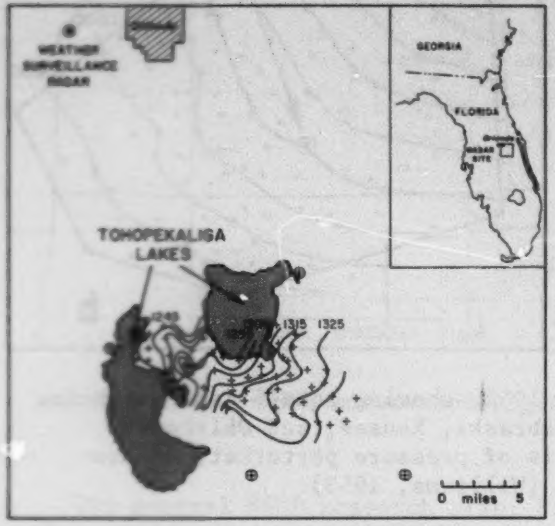
WEATHER SURVEILLANCE RADAR
GEORGIA
FLORIDA
RADAR SITE
TOHOPEKALIGA LAKES
1315
1325
0 miles 5

Figure 1a.--Isochrones of "first gust" 9 July 1946 in the Florida network of the Thunderstorm Project. Such analyses disclosed that new storms often form on the intersection of outflow boundaries from existing storms (Byers and Braham, 1948).

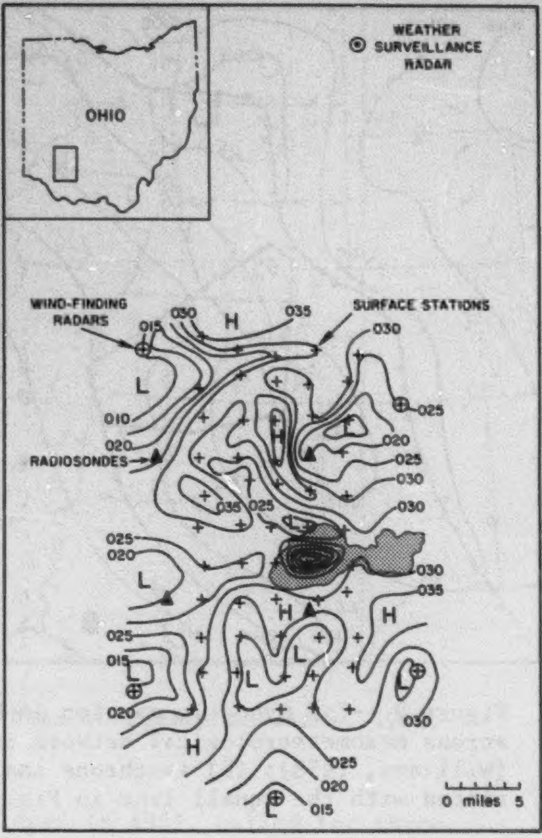
WEATHER SURVEILLANCE RADAR
OHIO
WIND-FINDING RADARS
SURFACE STATIONS
RADIOSONDES
H
L
015
020
025
030
035
010
0 miles 5

Figure 1b.--Perturbation pressure at 1430 CST, 25 August 1947, in the Ohio network of the Thunderstorm Project. Shaded area shows radar echo from cumulonimbus cloud producing rain and localized area of high pressure (Bleeker and Andre, 1950).

(1956) developed analysis techniques with data collected from a much larger network in Nebraska, Kansas, and Oklahoma (Figs. 2a,b). Such data were used to produce the first views of smaller scale pressure, wind, and temperature structure in combination with the detailed view of convective precipitation given by weather radar. New terminology, e.g., "wake depression" and "thunderstorm high," described patterns that appeared commonly with severe thunderstorms.

Increases in fatalities from aircraft accidents in thunderstorms and increases in property destruction from tornadoes during the 1950's renewed interest in gathering and analyzing storm data, and the National Severe Storms Project (NSSP), with headquarters in Kansas City, Mo., was created within the U.S. Weather Bureau. The project established a field office in Oklahoma City and designed three networks to collect pressure and rainfall data from squall lines over a three-state area.

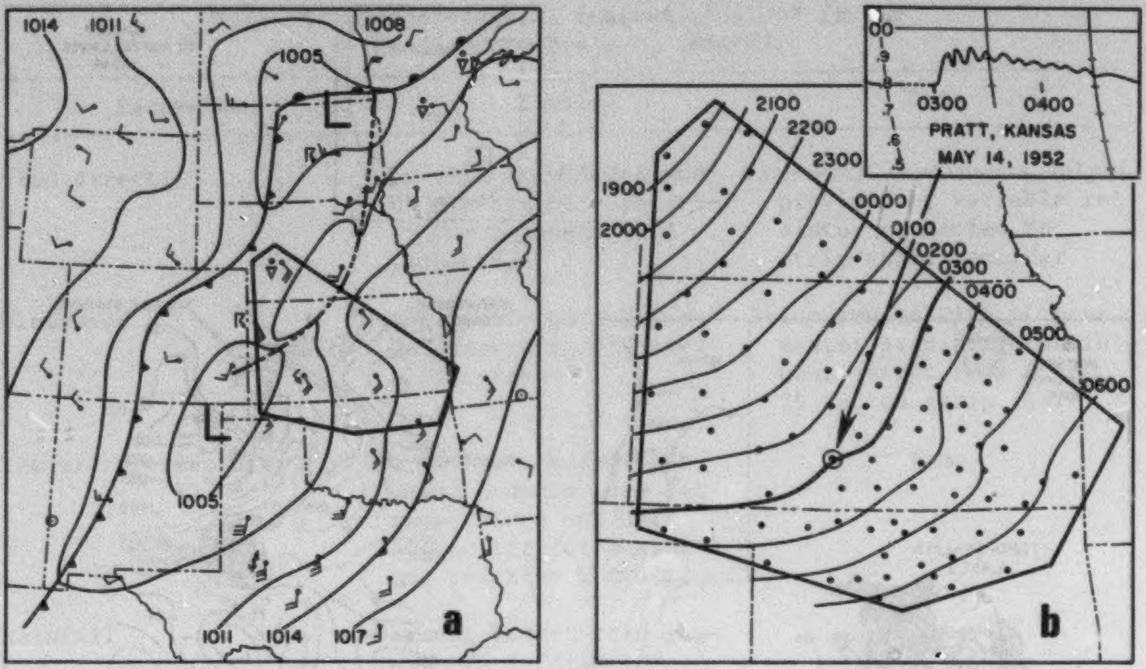
1014
1011
1008
1005
1005
1011
1014
1017
a
2100
2200
2300
1900
2000
0000
0100
0200
0300
0400
0500
0600
1.00
.9
.8
.7
.6
.5
0300
0400
PRATT, KANSAS
MAY 14, 1952
b

Figure 2.--(a) Synoptic map for 14 May 1952, showing squall line advancing across mesometeorological network in Nebraska, Kansas, and Oklahoma. (Williams, 1953); (b) isochrone analysis of pressure perturbation associated with the squall line in Fig. 2a (Williams, 1953).

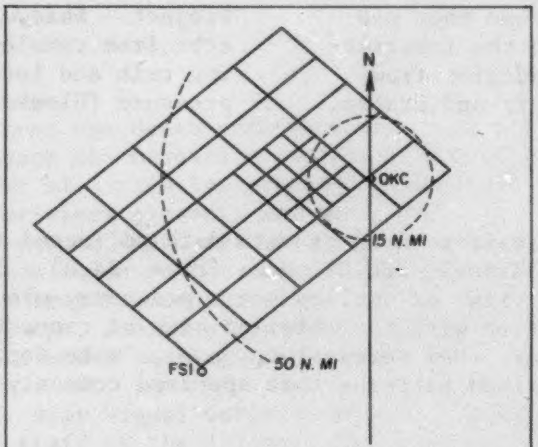
N
OKC
15 N. MI
FSI
50 N. MI
ADM
SPS
0
10
20
30
40
50

Figure 3.--Schematic plan for NSSP mesometeorological networks, 1961.

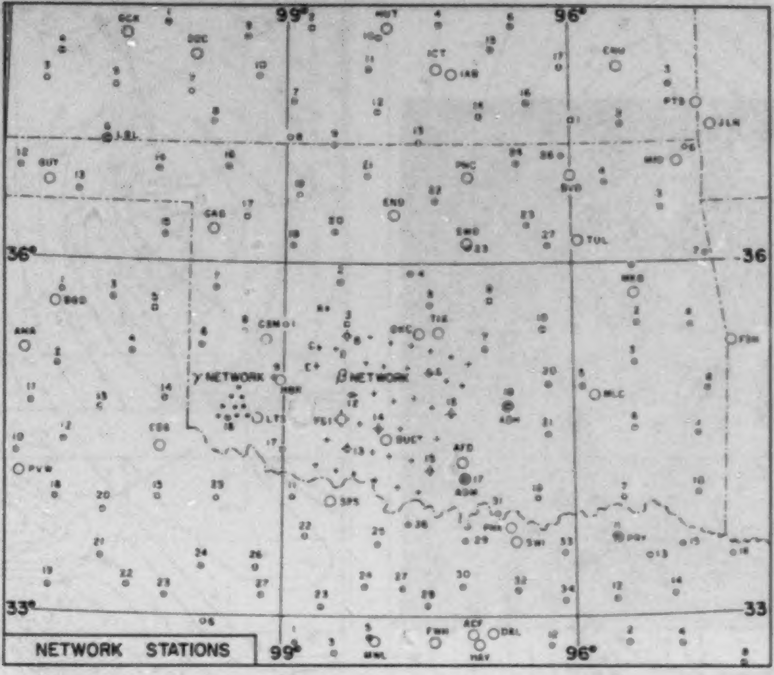

Figure 4.--NSSP mesometeorological beta and gamma networks, 1963.

The general NSSP research plan, developed in 1961, called for three scales of investigation (NSSP Staff, 1961) using nested networks, shown schematically in Fig. 3. The NSSP nested networks (Fig. 4) used hygrothermographs, microbarographs, and rain gages extensively--but with stations relatively far apart and over a much larger area than that covered by the Thunderstorm Project. Fujita and Stuhmer (1963) prepared the first extensive mesosynoptic analysis using data from the NSSP interlaced networks, newly installed in 1962 (Fig. 5).

As the NSSP program progressed, increased emphasis was placed on the smaller scale (2 to 20 km) to supplement the fine-scale measurements provided by improved radar and aircraft instrumentation. This new mesoscale network (Fujita, 1962) was established in Oklahoma to study surface characteristics of individual severe thunderstorms. Emphasis on storm scale events has continued to the present, both at NSSL and at new field projects of the National Center for Atmospheric Research (NCAR), where hailstorm characteristics have been studied (Foote and Knight, 1977).

During 1960-1965, the Air Force Air Weather Service and the Weather Bureau expanded their jointly operated Severe Local Storms Forecast Center at Kansas City to search for better techniques to anticipate squall line development, and the Federal Aviation Administration's research group (National Aviation Facilities Experiment Center, NAFEC) at Atlantic City, N.J., developed a reporting mesonetwork in the expectation that terminal forecasting might be greatly improved by use of local information in real time. However, the NAFEC data indicated that there was not yet sufficient knowledge of the behavior of mesoscale weather systems to develop a dependable short-range forecasting system, even with detailed real-time measurements.

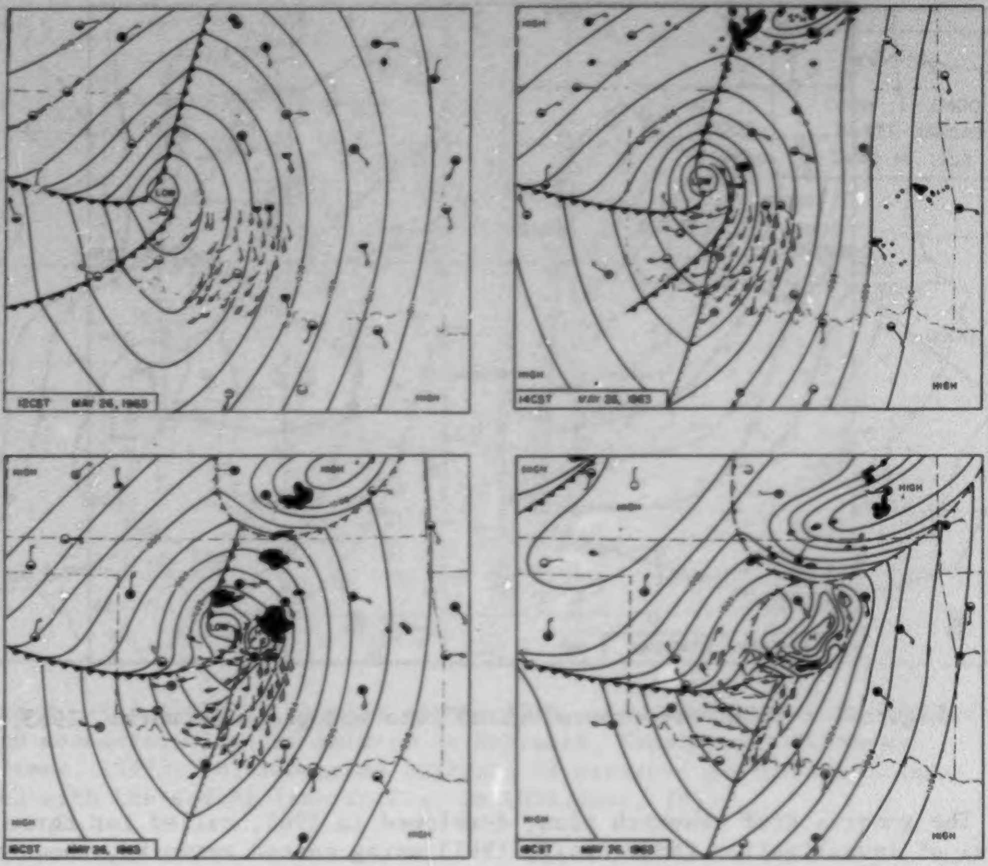

Figure 5.--A mesosynoptic analysis of tornado cyclone case of 26 May 1963.

In late 1963, the nucleus of the NSSP was moved to Norman, Okla., and reorganized in 1964 as the National Severe Storms Laboratory (NSSL) to become a national focus of observations on severe local storms (Kessler, 1965; 1977). Both NSSP and NSSL gave considerable emphasis to development of weather radar. Radarscope photographs of thunderstorms became commonplace after 1965, as several research groups sought better prediction techniques to anticipate storm formation, movement, and severity.

3. SEVERE-STORM NETWORKS AFTER 1970

The rapid improvement in research radars in the mid-1960s (Lhermitte and Kessler, 1965) pointed the way to continuous, quantitative observations of storm development. Newton (1963) and Browning and Donaldson (1963) had developed qualitative models of large convective storms; these affirmed a need for three-dimensional mesoscale data to be obtained by combining radar, rawinsonde, and surface network observations. Kreitzberg and Brown (1970) further stressed the value of including serial soundings from special rawinsonde networks by constructing cross sections of wind, temperature, and moisture, and tracing the vertical displacement of the air surrounding severe storms.

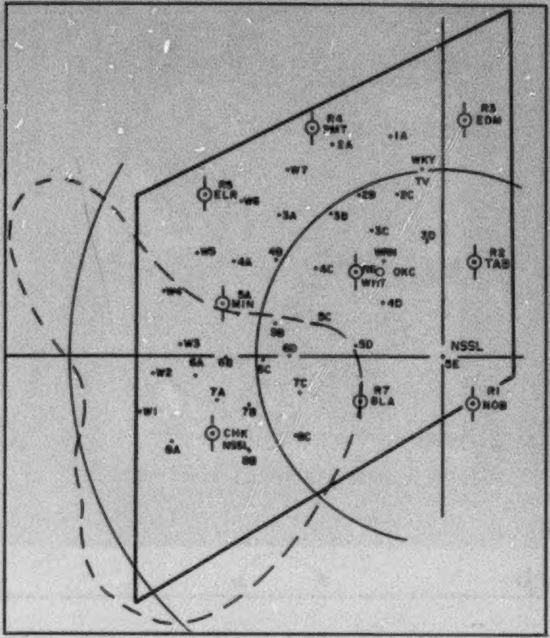

Figure 6a.--NSSL surface, upper-air, and mesonetwork stations, 1970. Soundings were obtained at approximately 60-min intervals to 400 mb during selected periods, at stations marked by circles with vertical bars. The dashed line marks the boundary of the dense rain gage network maintained by the Agricultural Research Service. A 20-nmi-range circle intersects the tall, instrumented WKY tower at azimuth 356°.

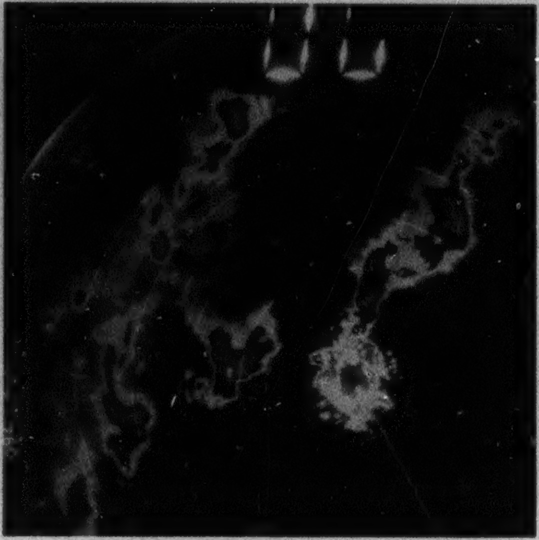

Figure 6b.--WSR-57 radar display of thunderstorms crossing central Oklahoma on 29 April 1970. The storm 40 miles west of the radar site (second range mark) is also visible in Fig. 7a.

In 1970, Barnes et al. (1971) led the design and analysis of a major observational program at NSSL to "trap" a tornado-producing thunderstorm within dense, interlaced surface and upper-air networks (Fig. 6a). On 29 April 1970, a series of severe storms moved across central Oklahoma (Fig. 6b), and after 12 exhausting hours of probing and waiting, the efforts of the 40 scientists and technicians were rewarded with a very detailed data set. (At midnight, the classic tornado-bearing superstorm [Figs. 7a and b] was monitored clearly by radar and the surface network as it moved through the Oklahoma City area, causing widespread destruction.) Detailed analyses of these data (Barnes, 1978a,b; Barnes and Nelson, 1978) provided a new perspective of the wind, temperature, and moisture fields measured at all levels from the surface to the tropopause in a severe storm's environment. The studies relating the surface events to the radar echoes were especially valuable in providing clear evidence that the mesocyclone (i.e., the tornado cyclone of Brooks [1949, 1951]) is the parent circulation of tornadoes (Fig. 7b). The analyses showed that spacing and recording intervals of the 1970 mesonetwork stations were effective in resolving scales of about 10 kilometers and 5 minutes.

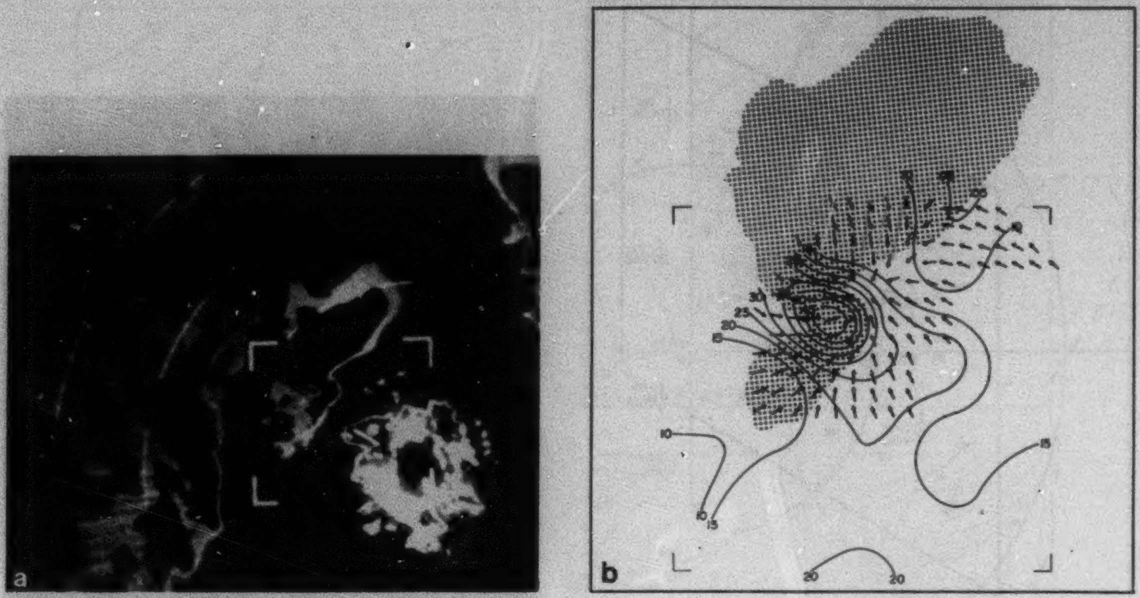

Figure 7.--(a) WSR-57 radar display of tornado-bearing thunderstorm; (b) surface patterns of windspeed (solid lines) and direction (arrows) as the storm crosses the NSSL mesonetwork, 29 April 1970.

4. COOPERATIVE OBSERVERS AND NESTED NETWORKS

In the first networks installed by the National Severe Storms Project, sites were secured by contracts with landowners, who also assisted in changing recorder charts, winding instrument clocks, and safeguarding the equipment. With this help, a few technicians could oversee many tens of network sites. Such operations required careful procedures for checking records and weekly contacts with observers to help correct malfunctions. As in any volunteer program, observer performance varied greatly and control of quality to a high level was difficult. Later, when the areal coverage of the network was reduced for concentrated study of individual storms, each site was visited frequently to make comparative measurements and properly annotate and replace charts.

Although recent programs place much emphasis on the thunderstorm scale, there has been a continuing need to relate detailed observations to the synoptic scale. At NSSL, this link has been forged by "subsynoptic" stations placed between existing NWS and FAA observing facilities. The subsynoptic concept provided a background network, having 100-km station spacing, that surrounds the mesoscale network having 10-km spacing. Sites for the subsynoptic network in Oklahoma were selected from more than 200 potential locations, which included municipal fire stations, airports, and junior colleges. Staff at many of these facilities needed weather observations for their own operations or research projects and were delighted to share responsibility for locating and operating research weather stations. Laboratory technicians visited the sites monthly or at the request of the station manager. Since commercial power was available at most subsynoptic stations, multiple-channel strip chart recorders were installed at several locations to record eight

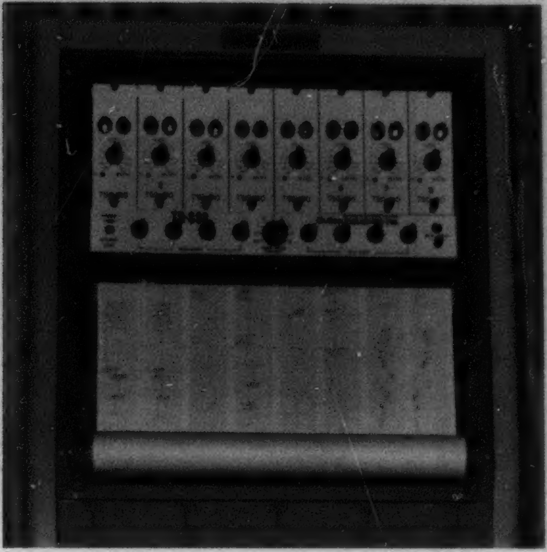

Figure 8.--Linear, eight-channel strip chart recorder used in NSSL's subsynoptic network, 1972-1973.

channels of information simultaneously (Fig. 8). The recording-pen travel was more accurate than the older strip chart records, and the linearity allowed semiautomated data retrieval with x-y readers.

In 1973, the combination of observations from these stations with data from more finely spaced mesoscale sites was a valuable aid to reconstruction of meteorological patterns associated with the first major tornado observed with the NSSL Doppler radar (Brown, 1976). Analysis of wind trajectories located mesocyclogenesis and gust fronts, which have been shown to precede tornado development (Brandes, 1977).

The series of successful field experiments at NSSL and NCAR in the 1970's, with proof of advantages in Doppler radars, led to the design and operation of a national field project in 1979. The SESAME (Severe Environmental Storms and Mesoscale Experiment) observational program was the largest program directed toward severe local storms ever undertaken (Alberty et al., 1979). The SESAME networks (Fig. 9) recorded synoptic, subsynoptic, and mesoscale weather patterns using advanced digital recording and Doppler radar systems.

5. INSTRUMENTS FOR MESOSCALE METEOROLOGICAL NETWORKS

Until 1979, a typical field station in the NSSL mesometeorological networks (Fig. 10) consisted of a fenced grassy plot of about 100 square meters, isolated from buildings and trees. Wind-sensing equipment was installed on towers 5 to 10 meters high; instruments recording on strip charts were housed in standard wooden shelters used by the Weather Bureau. The hygrothermographs, microbarographs, and rain gages contained precision spring-driven clocks that powered rotating drums (Fig. 11). Examples of recordings made by these instruments during severe thunderstorms are shown in Fig. 12.

The accuracy of these systems, which are still in occasional use today, depends greatly on precalibrations and adjustments made prior to field instal-

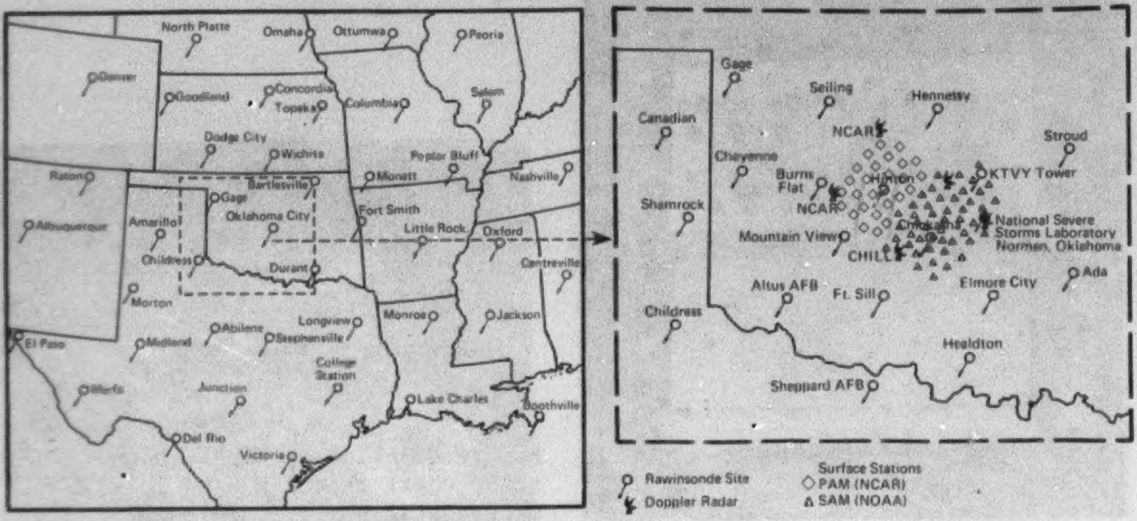
North Platte
Omaha
Ottumwa
Peoria
Denver
Goodland
Concordia
Topeka
Columbia
Salem
Dodge City
Wichita
Poplar Bluff
Raton
Gage
Bartlesville
Monett
Nashville
Albuquerque
Amarillo
Oklahoma City
Fort Smith
Little Rock
Oxford
Childress
Durant
Centreville
Morton
Abilene
Longview
Stephenville
Monroe
Jackson
El Paso
Midland
College Station
Marfa
Junction
Lake Charles
Boothville
Del Rio
Victoria
Gage
Canadian
Seiling
Hennessy
NCAR
Stroud
Cheyenne
Burns Flat
Hinton
KTVY Tower
Shamrock
NCAR
Chickasha
National Severe Storms Laboratory Norman, Oklahoma
Mountain View
CHILL
Altus AFB
Ft. Sill
Elmore City
Ada
Childress
Healdton
Sheppard AFB
Rawinsonde Site
Doppler Radar
Surface Stations
◇ PAM (NCAR)
△ SAM (NOAA)

Figure 9.--Project SESAME observational networks, 1979: left, regional scale domain; right, storm scale domain.

lation. Such procedures are followed carefully by meteorological technicians to ensure that all instruments have similar responses and that their values correspond to preestablished standards, i.e., those set by the calibrated mercurial barometer and aspirated psychrometer.

Initially, the instruments are cleaned carefully and mechanical linkages adjusted according to manufacturers' specifications. A few days before field installation, all instruments are placed in a calibration room, and adjustments on the clocks and linkage are fine tuned to ensure agreement among all

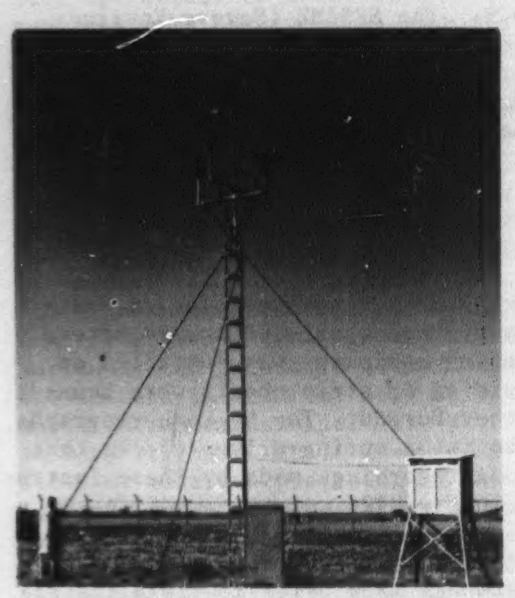

Figure 10.--A typical site in the NSSL mesonetwork.

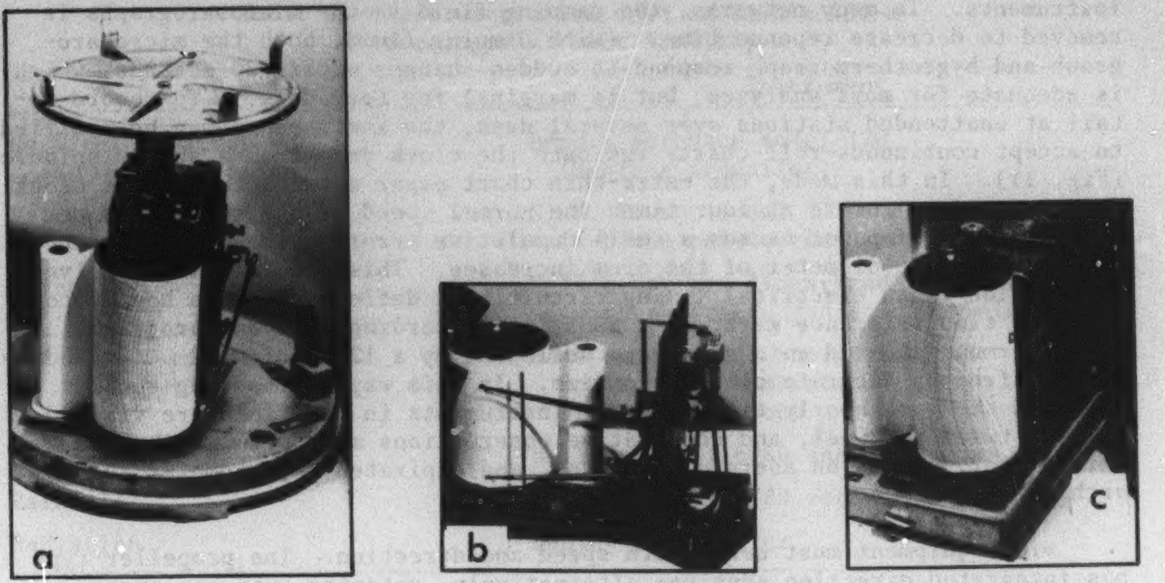

Figure 11.--Modified (a) rain gage, (b) hygrothermograph, (c) microbarograph used in the NSSL mesonetwork from 1965 to 1978. Paper transport mechanisms have been added to the basic instruments to facilitate continuous recording for up to a week without overwriting.

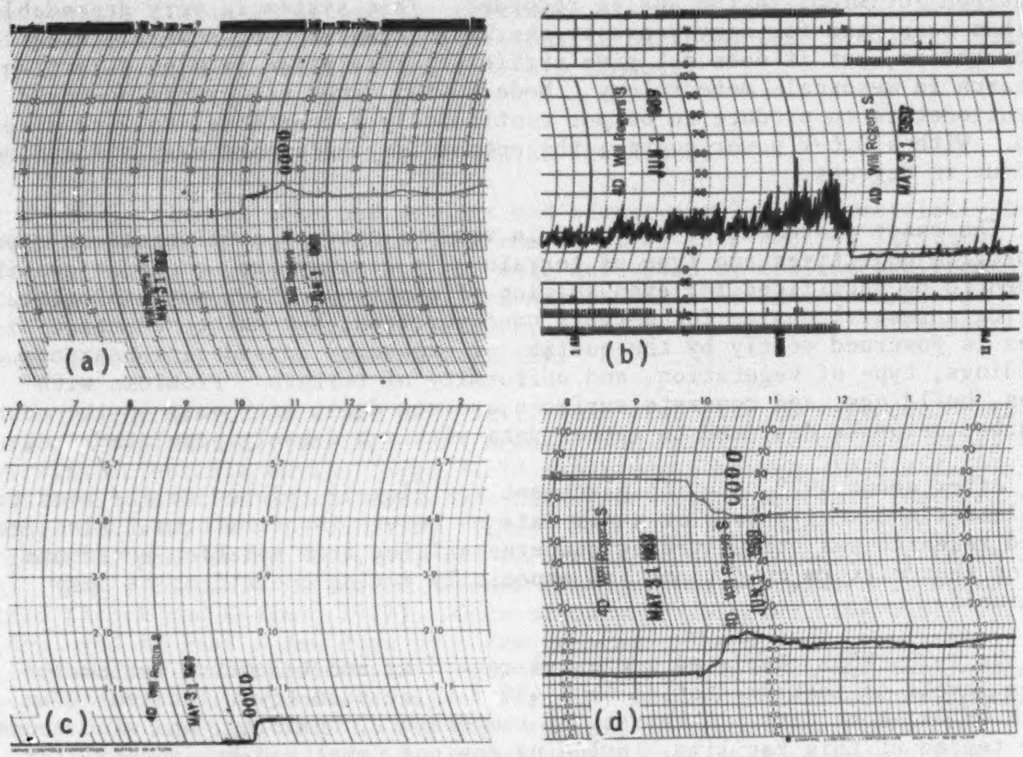

Figure 12.--Examples of network data: (a) pressure, (b) wind, (c) precipitation, and (d) temperature-humidity.

instruments. In many networks, the damping fluid in the microbarographs is removed to decrease reponse time. (With damping fluid, both the microbarograph and hygrothermograph respond to sudden changes within 20 seconds, which is adequate for most analyses, but is marginal for tornadoes.) To record detail at unattended stations over several days, the instruments may be modified to accept continuous-roll charts fed onto the clock drum from a supply spindle (Fig. 11). In this mode, the extra-thin chart paper accumulates on the clock drum, geared to rotate at four times the normal speed of one revolution per day. Buildup of paper causes a small cumulative error in the time reference as the effective diameter of the drum increases. This problem can be solved by addition of an electrical timing circuit that deflects the pen hourly to create a time reference mark. (At NSSL, the recording pens on barograph, hygrothermograph, and rain gage were deflected by a 12-V solenoid activated by a pulse from an accurate clock mechanism. In this way, all analog records included the same hourly time marks.) Instruments in the field are visited once or twice per week, and comparative observations made with calibrated chronometer, precision aneroid barometer, and aspirated psychrometer are archived.

Wind equipment must sense both speed and direction. The propeller type has integrated direction sensing; alternatively, rotating cups can sense speed and a separate vane is used for direction sensing. Propeller devices adapt easily for digital conversion and storage, since the speed and direction outputs are continuous. The cups can also drive a DC generator and produce an output linearly proportional to windspeed. However, early versions of direction-sensing vanes accompanying cup anemometers produced a coded output from 16 multiple-point contacts located in the sensor, and connected to 8 event-pen locations in the analog recorder. This system is very dependable and has been used for many years by the Weather Bureau and several research laboratories, but it does not give sufficient resolution in wind direction for research in mesoscale meteorology. Modern wind vanes use precision-wound potentiometers to produce an output continuously proportional to wind direction. With a 3.6-V power source, the output is conditioned easily for direct readout in degrees.

The exact placement of stations in various network configurations depends on program objectives and type of terrain. In early years, exposure quality tended to be sacrificed for even spacing of stations. Now, meteorologists provide a general design for network configuration, but exact selection of sites is governed mostly by the quality of exposure, considering nearness of buildings, type of vegetation, and uniformity of terrain. Problems with trees, buildings, and concrete surfaces are now dealt with only in the context of urban networks designed to gather data within a densely populated area.

After about 1973, station placement was closely related to the need to complement and verify Doppler radar data on severe thunderstorms. Also, renewed research was stimulated by concerns arising from aviation accidents during thunderstorm conditions and especially during operations at busy terminals.

In 1973, NSSL completed a digital recording and telemetry system for seven levels of instrumentation on a 450-m television tower located 10 km north of Oklahoma City. A variety of temperature, humidity, and wind sensors were tested at this facility, including devices developed by industry for environmental monitoring. Other tests included acoustical and optical radars (Danielson, 1975), sonic anemometers (Sahashi, 1972), and tetroons (Angell et

Table 2.--Instrumentation used on NSSL's 450-m meteorological tower facility

Parameter	Instrument
Horizontal windspeed and wind direction	Bendix aerovane model 120 (3-blade propeller)
Vertical velocity	R. M. Young, model 27100 anemometer (4-blade polystyrene propeller)
Dry-bulb temperature	Yellow Springs linearized thermistor (with aspirated radiation shield)
Wet-bulb temperature	Same as dry-bulb thermistor, but modified with moistened muslin wick attached to probe and water reservoir
Pressure	Belfort model 6080 aneroid barometer
Rainfall	Belfort model 5780 recording rain gage
Radiation	Eppley pyranometer

al., 1973). The tower instrumentation was stabilized in 1976 with devices to measure temperature (dry bulb and wet bulb), horizontal windspeed and direction, and vertical air motion (at intervals of 1 to 10 minutes). Surface rainfall, pressure, and solar radiation were recorded at the base of the tower. These sensors (Table 2) became the reference standard for the NSSL mesonetwork, and by 1974, several surface stations in Oklahoma were similarly equipped with aspirated-temperature and wet-bulb sensors.

6. MODERN DIGITAL PROCESSING AND RECORDING TECHNIQUES

By 1975, several low-cost devices had become available commercially to provide telemetry of analog data from remote sites to a central facility. To reduce telephone costs, these systems were activated by calling the remote unit, which answered automatically, scanned channels of information, and transmitted the data by encoded frequency tone, for display by teletypewriter or analog recorder at the central facility.

The early devices did not have sufficient stability to reproduce data accurately and reliably for research needs. The experience of NCAR staff and university scientists during large field experiments between 1970 and 1975 led to development of an automatic digital system with desirable features of economy, accuracy, and reliability. Thus, Brock (1974) demonstrated at NCAR the control, processing, display, and recording of meteorological data in real time. NCAR's Portable Automated Mesonet (PAM) system was placed in operation in 1976 (Brock and Govind, 1977). Once sites were selected, the whole system was deployed in just a few days by a few persons. The system consisted of a trailer-mounted base station and a network of 40 remote stations for logging mesoscale data. Each remote station (Fig. 13) sampled local sensors synchronously and transmitted data to the base station by means of a radio link. Through antennas mounted on a 50-m tower at the base station and on 12-m towers at remote stations, the communication link could extend approximately 80 km.

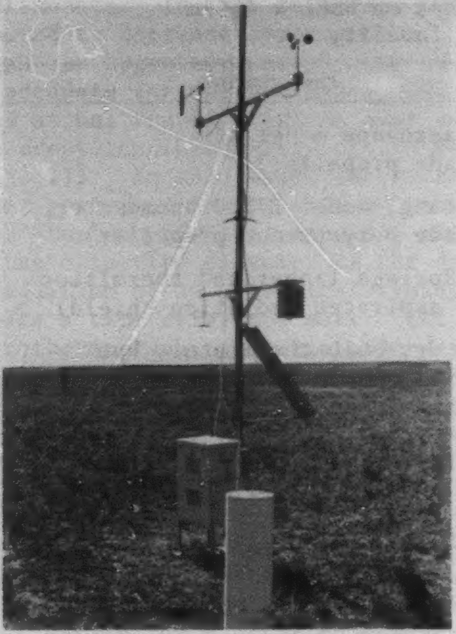

Figure 13.--Digital recording station in NCAR's Portable Automated Mesonetwork (PAM), September 1980.

The PAM base station has a minicomputer for the automation of data logging, for real-time data quality checks, and for real-time data analysis and display. The data are immediately available in physical units, allowing experimenters a "quick look" at the data soon after it is recorded.

The PAM system has proved very useful for study of thunderstorms and several other phenomena, and it has provided a ground reference for testing new remote sensors. Usual station spacing ranges from 1 to 10 km, and the basic sampling rate of the PAM system is one sample per minute.

A somewhat similar automated network, but without remote callup capabilities for continuous monitoring, was developed at NSSL and deployed for the first time (jointly with NCAR's PAM system) during SESAME in spring of 1979 (see Fig. 9). It was designed to provide accurate measurements of temperature, pressure, wind, humidity, and precipitation having high temporal resolution and requiring a minimum of human intervention. The data are recorded on cassette recorders, which are collected weekly and processed for quick look with a desk computer. The tabulated record of a squall line passage over a station near Criner, Okla., is shown in Fig. 14a, with some strip chart records (Fig. 14b) of the same event for comparison.

It may be noted that continuous relay of data in the PAM system facilitates archiving of the data in a synoptic format, i.e., in a chronological sequence. In the NSSL system, on the other hand, the reformatting of multiple cassette tapes into series from many stations presented a formidable problem for computer operators and programers, which was solved at NSSL about two years after initial installation of the electronic mesonetwork.

By 1981, semiautomatic and automatic archiving and retrieval of meteorological data sensed at surface stations had become a standard practice, and

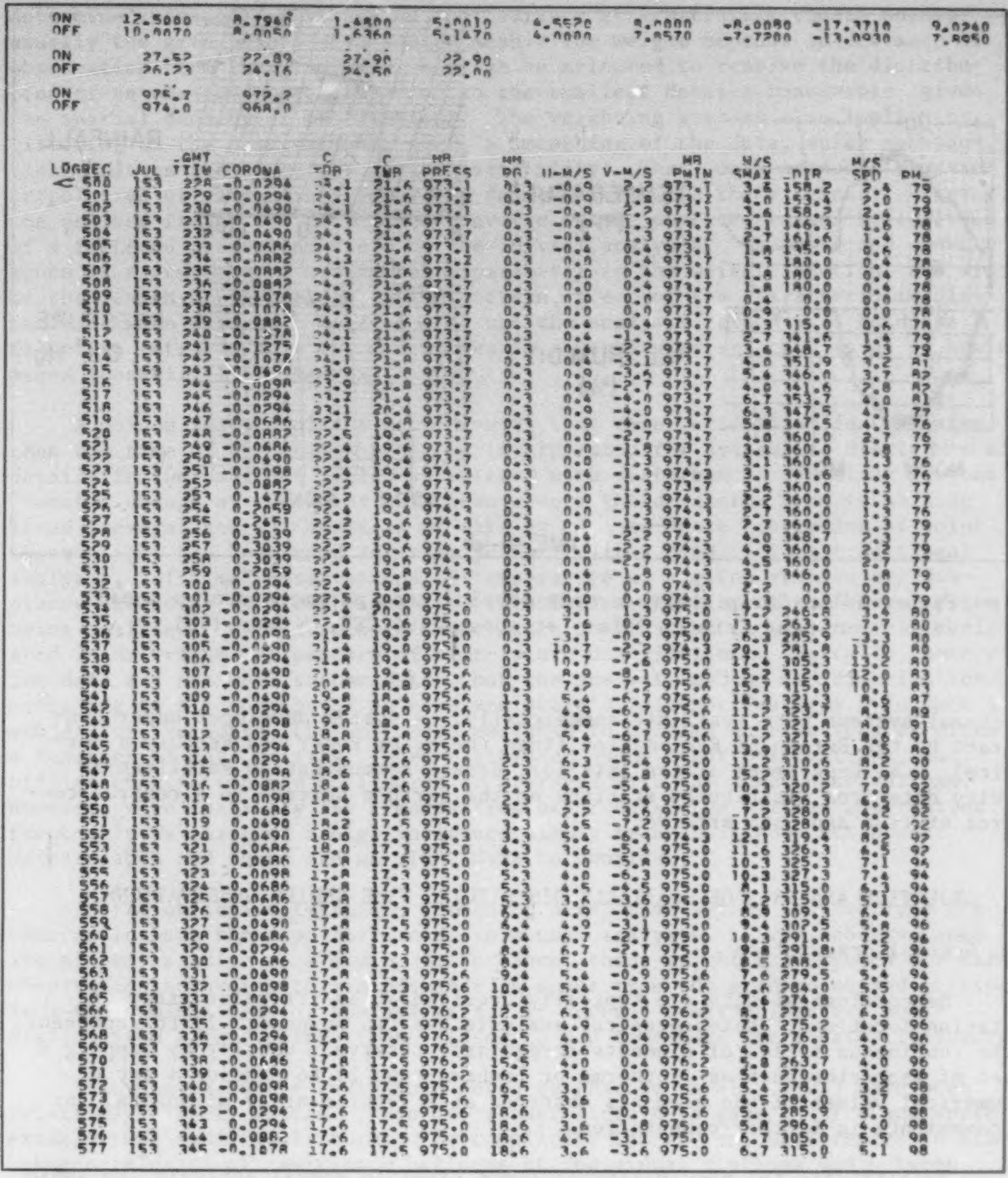

```
ON     12.5000    8.7968    1.4800    5.0010    4.5520    8.0000   -8.0080  -17.3710     9.0240
OFF    10.0070    8.0050    1.6360    5.1470    4.0000    7.8570   -7.7200  -13.0930     7.8950

ON       27.52     22.89     27.90     22.90
OFF      26.23     24.16     24.50     22.00

ON       975.7     972.2
OFF      974.0     968.0

             _GMT              C     C     MB     MM                  MB    M/S          M/S
LOGREC  JUL  TIIM  CORONA     TDB   TWB  PRESS   RG  U-M/S V-M/S  PMIN   SMAX  _DIR   SPD  RH_
<  500  153  228 -0.0294     24.1  21.6  973.1  0.3  -0.9   2.7  973.1   3.6  158.2   2.4  79
   501  153  229 -0.0294     24.1  21.6  973.2  0.3  -0.9   1.8  973.2   4.0  153.4   2.0  79
   502  153  230 -0.0690     24.1  21.6  973.1  0.3  -0.9   2.2  973.1   3.6  158.2   2.4  79
   503  153  231 -0.0690     24.3  21.6  973.7  0.3  -0.9   1.3  973.7   3.1  146.3   1.6  78
   504  153  232 -0.0490     24.3  21.6  973.7  0.3  -0.4   1.3  973.7   2.7  161.6   1.4  78
   505  153  233 -0.0686     24.3  21.6  973.1  0.3  -0.4   0.4  973.1   1.8  135.0   0.6  78
   506  153  234 -0.0882     24.3  21.6  973.2  0.3   0.0   0.4  973.7   1.3  180.0   0.4  78
   507  153  235 -0.0882     24.1  21.6  973.1  0.3   0.0   0.4  973.1   1.8  180.0   0.4  79
   508  153  236 -0.0882     24.3  21.6  973.7  0.3   0.0   0.4  973.7   1.8  180.0   0.4  78
   509  153  237 -0.1078     24.3  21.6  973.7  0.3   0.0   0.0  973.7   0.4    0.0   0.0  78
   510  153  238 -0.1078     24.3  21.6  973.7  0.3   0.0   0.0  973.7   0.9    0.0   0.0  78
   511  153  239 -0.0882     24.3  21.6  973.7  0.3   0.4  -0.4  973.7   1.3  315.0   0.6  78
   512  153  240 -0.1278     24.1  21.6  973.7  0.3   0.4  -1.3  973.7   2.7  341.6   1.4  79
   513  153  241 -0.1275     24.1  21.6  973.7  0.3   0.4  -2.2  973.7   3.6  348.7   2.3  79
   514  153  242 -0.1078     24.1  21.8  973.7  0.3   0.4  -3.1  973.7   4.0  351.9   3.2  81
   515  153  243 -0.0490     23.9  21.8  973.7  0.3   0.9  -3.6  973.7   5.4  346.0   3.7  82
   516  153  244 -0.0098     23.9  21.8  973.7  0.3   0.9  -2.7  973.7   4.0  341.6   2.8  82
   517  153  245 -0.0294     23.2  21.4  973.7  0.3   0.4  -4.0  973.7   6.7  353.7   4.0  81
   518  153  246 -0.0294     23.1  20.4  973.7  0.3   0.9  -4.0  973.7   6.3  347.5   4.1  77
   519  153  247 -0.0686     22.7  19.8  973.7  0.3   0.9  -4.0  973.7   5.8  347.5   4.1  76
   520  153  248 -0.0882     22.5  19.6  973.7  0.3   0.0  -2.7  973.7   4.0  360.0   2.7  76
   521  153  249 -0.0686     22.4  19.6  973.7  0.3   0.0  -1.8  973.7   3.1  360.0   1.8  77
   522  153  250 -0.0490     22.4  19.6  973.7  0.3   0.0  -1.3  973.7   3.1  360.0   1.3  76
   523  153  251 -0.0098     22.4  19.6  974.3  0.3   0.4  -1.3  974.3   3.1  341.6   1.4  76
   524  153  252  0.0882     22.2  19.4  973.7  0.3   0.0  -1.3  973.7   3.6  360.0   1.3  77
   525  153  253  0.1471     22.2  19.6  974.3  0.3   0.0  -1.3  974.3   2.2  360.0   1.3  77
   526  153  254  0.2059     22.4  19.4  974.3  0.3   0.0  -1.3  974.3   2.7  360.0   1.3  76
   527  153  255  0.2651     22.2  19.6  974.3  0.3   0.0  -1.3  974.3   2.7  360.0   1.3  79
   528  153  256  0.3039     22.2  19.4  974.3  0.3   0.4  -2.2  974.3   4.0  348.7   2.3  77
   529  153  257  0.3039     22.2  19.6  974.3  0.3   0.0  -2.2  974.3   4.9  360.0   2.2  79
   530  153  258  0.3039     22.4  19.6  974.3  0.3   0.0  -2.7  974.3   4.5  360.0   2.7  77
   531  153  259  0.2059     22.4  19.8  974.3  0.3   0.4  -1.8  974.3   3.1  346.0   1.8  79
   532  153  300  0.0294     22.4  19.8  974.3  0.3   0.0   0.0  974.3   2.2    0.0   0.0  79
   533  153  301 -0.0294     22.5  20.0  974.3  0.3   0.0   0.0  974.3   1.3    0.0   0.0  79
   534  153  302 -0.0294     22.4  20.0  975.0  0.3   3.1   1.3  975.0   7.2  246.8   3.4  80
   535  153  303 -0.0294     22.0  19.6  975.0  0.3   7.6   0.9  975.0  13.4  263.3   7.7  80
   536  153  304 -0.0098     21.6  19.2  975.0  0.3   3.1  -0.9  975.0   6.3  285.9   3.3  80
   537  153  305 -0.0490     21.4  19.0  975.0  0.3  10.7  -2.2  974.3  20.1  281.8  11.0  80
   538  153  306 -0.0294     21.8  19.6  975.0  0.3  10.7  -7.6  975.0  17.4  305.3  13.2  80
   539  153  307 -0.0490     21.4  19.4  975.6  0.3   8.9  -8.1  975.6  15.2  312.0  12.0  83
   540  153  308 -0.0294     20.8  18.8  975.6  0.3   7.2  -7.2  975.6  15.7  315.0  10.1  83
   541  153  309 -0.0490     19.8  18.4  975.6  1.3   5.4  -6.7  975.6  10.3  321.3   8.6  87
   542  153  310 -0.0294     19.2  18.0  975.6  1.3   4.9  -6.7  975.6  11.2  323.7   8.3  89
   543  153  311  0.0098     19.0  18.0  975.6  1.3   4.9  -6.3  975.6  11.2  321.8   8.0  91
   544  153  312  0.0294     18.8  17.8  975.6  1.3   5.4  -6.7  975.6  11.2  321.3   8.6  91
   545  153  313 -0.0294     18.8  17.6  975.0  1.3   6.7  -8.1  975.0  13.9  320.2  10.5  89
   546  153  314 -0.0294     18.6  17.6  975.0  2.3   6.3  -5.4  975.0  11.2  310.6   8.2  90
   547  153  315  0.0098     18.6  17.6  975.0  2.3   5.4  -5.8  975.0  15.2  317.3   7.9  90
   548  153  316 -0.0882     18.4  17.6  975.0  2.3   4.5  -5.4  975.0  10.3  320.2   7.0  92
   549  153  317 -0.0098     18.4  17.6  975.0  2.3   3.6  -5.4  975.0   9.4  326.3   6.5  92
   550  153  318  0.0686     18.4  17.6  975.0  3.3   2.2  -3.6  975.0   7.2  328.0   4.2  92
   551  153  319  0.0490     18.2  17.5  975.0  3.3   4.5  -7.2  975.0  13.9  328.0   8.4  92
   552  153  320  0.0490     18.0  17.3  974.3  3.3   5.4  -6.3  974.3  12.1  319.4   8.2  92
   553  153  321  0.0686     18.0  17.3  975.0  4.3   3.6  -5.4  975.0  11.6  326.3   6.5  92
   554  153  322  0.0686     17.8  17.5  975.0  4.3   4.0  -5.8  975.0  10.3  325.3   7.1  96
   555  153  323  0.0098     17.8  17.3  975.0  5.3   4.0  -6.3  975.0  10.3  327.3   7.4  94
   556  153  324 -0.0686     17.8  17.3  975.0  5.3   4.5  -4.5  975.0   8.1  315.0   6.3  94
   557  153  325 -0.0686     17.8  17.3  975.0  5.3   3.6  -3.6  975.0   7.2  315.0   5.1  94
   558  153  326 -0.0490     17.8  17.3  975.0  6.4   4.9  -4.0  975.0   8.9  309.3   6.4  94
   559  153  327 -0.0490     17.8  17.5  975.0  6.4   4.9  -3.1  975.0   9.4  302.5   5.8  96
   560  153  328 -0.0686     17.8  17.5  975.0  7.4   6.7  -2.7  975.0  10.3  291.8   7.2  96
   561  153  329 -0.0294     17.8  17.3  975.0  8.4   6.7  -2.7  975.0   9.8  291.8   7.2  94
   562  153  330 -0.0686     17.8  17.3  975.0  8.4   5.4  -1.8  975.0   8.5  288.4   5.7  94
   563  153  331 -0.0490     17.8  17.3  975.6  9.4   5.4  -0.9  975.6   7.6  279.5   5.4  94
   564  153  332  0.0098     17.6  17.3  975.6 10.4   5.4  -1.3  975.6   7.6  284.0   5.5  96
   565  153  333 -0.0490     17.8  17.5  976.2 11.4   5.4  -0.4  976.2   7.6  274.8   5.4  96
   566  153  334 -0.0294     17.8  17.5  976.2 12.5   6.3   0.0  976.2   8.1  270.0   6.3  96
   567  153  335 -0.0490     17.8  17.5  976.2 13.5   4.9  -0.4  976.2   7.6  275.2   4.9  96
   568  153  336 -0.0294     17.8  17.5  976.2 14.5   4.0  -0.4  976.2   5.8  276.3   4.0  96
   569  153  337 -0.0098     17.8  17.5  976.8 14.5   3.6   0.0  976.2   4.9  270.0   3.6  96
   570  153  338 -0.0686     17.8  17.5  976.2 15.5   4.0   0.4  976.2   5.8  263.7   4.0  96
   571  153  339 -0.0490     17.8  17.5  976.2 16.5   3.6   0.0  976.2   5.4  270.0   3.6  96
   572  153  340 -0.0098     17.6  17.5  975.6 16.5   3.1  -0.4  975.6   5.4  278.1   3.2  98
   573  153  341 -0.0098     17.6  17.5  975.6 17.5   3.6  -0.9  975.6   4.5  284.0   3.7  98
   574  153  342 -0.0294     17.6  17.5  975.6 18.6   3.1  -0.9  975.6   5.4  285.9   3.3  98
   575  153  343  0.0294     17.6  17.5  975.0 18.6   3.6  -1.8  975.0   5.8  296.6   4.0  98
   576  153  344 -0.0882     17.6  17.5  975.0 18.6   4.5  -3.1  975.0   6.7  305.0   5.5  98
   577  153  345 -0.1078     17.6  17.5  975.0 18.6   3.6  -3.6  975.0   6.7  315.0   5.1  98
```

Figure 14a.--0300 GMT, 2 June 1981 digital record for a small portion of the period shown in (b). Successive columns indicate record number, Julian date, Greenwich time in hours and minutes, an indication of corona current, dry- and wet-bulb temperatures, pressure in millibars, accumulated rainfall in millimeters, minute averages of u and v wind components, minimum pressure during the preceding minute, maximum of 60 wind measurements during the preceding minute, average wind direction, average speed, and relative humidity deduced from dry and wet bulb.

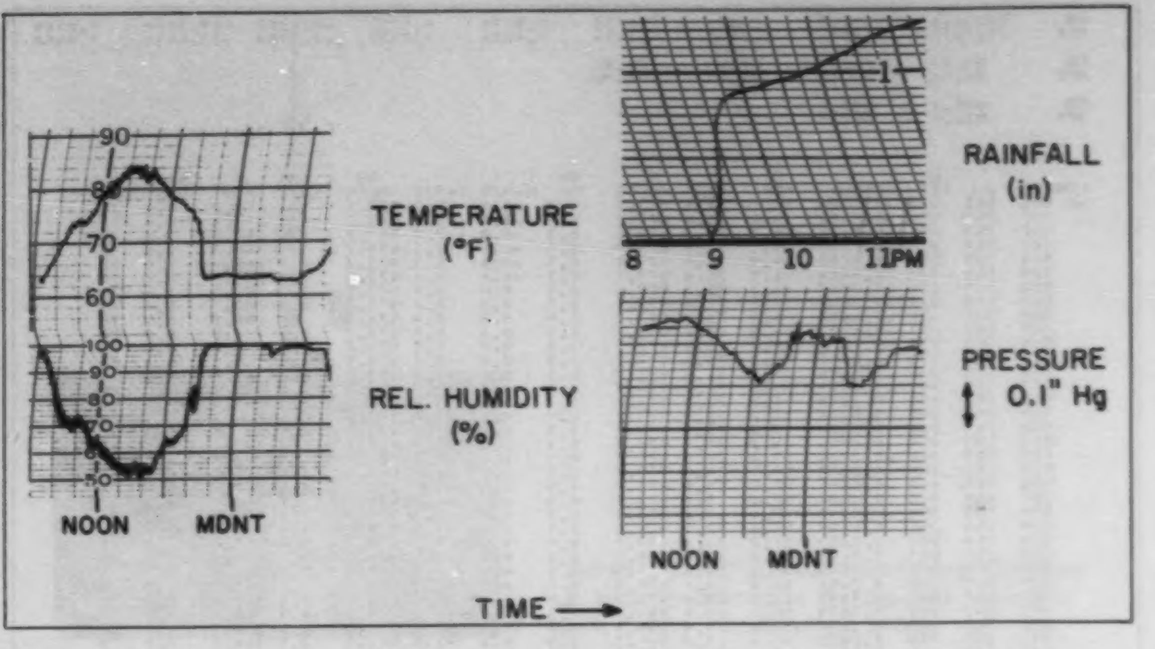

Figure 14b.--Strip chart records showing some parameters of a squall line event near Criner, Okla., at about 2100 CST, 1 June 1981.

several systems were available commercially. A system developed under contract by the Bureau of Reclamation (then the Water Power and Resources Service), U.S. Department of the Interior, uses a communication satellite to relay data from distributed stations on the Earth's surface to a central control station and data archive.

7. OBJECTIVE ANALYSIS OF SPATIALLY DISTRIBUTED TIME SERIES OBSERVATIONS

a. General description

Meteorological data are typically acquired at an irregular array of station locations. Meteorological analysis has two purposes: 1) to represent the continuous fields of elements irregularly observed, usually by mapping a set of isopleths such as isotherms or isobars; and 2) to provide a set of numerical values of the elements observed at a regular array of points, for convenience in further computations.

To eliminate the possibility of human error in manual analysis, to avoid the tedium of massive manual analysis, and to provide a speed in real-time operations that manual analysis cannot achieve, analysis is often performed by computer calculation. This method is called "objective" analysis, although many of the decisions necessary to implement it are no less arbitrary than those required by the presumably "subjective" manual technique.

The objective map analysis method treated here has been developed from an earlier technique (Barnes, 1964), which was based upon a suggestion by Sasaki (1960). The scheme uses weighted averages of observations on a surface to determine interpolated values on that surface at arbitrarily chosen points, usually the grid points of a square mesh. The weight depends on distance of observation from the grid point and can be selected to resolve the distribution of an observed parameter down to the smallest details resolvable, given the spatial density of observations. The weighting process also implies a filtering of the observations, i.e., a smoothing of the data, which substantially alters the structure of its variability. Thus, data produced by reinterpolation of grid points generally do not agree with the original. However, the derived fields can be made to converge to the observed values by addition of a filtered correction field to the initial analysis. The attained convergence is a function of a selectable parameter in the weight function, and also of the length of variations in the pattern, i.e., of the characteristic distance between extrema. One can also use the analysis method as a bandpass filter to retrieve only those features in a particular selected range of scale sizes (Doswell, 1977; Maddox, 1980).

A unique feature of the procedure is that observations earlier or later than the time of the analysis can be incorporated for systematic disclosure of details in the analyzed fields associated with disturbances traveling without dramatic change of character. Because severe thunderstorms tend to be long lived (several hours), analysis of data by time-to-space conversion of point observations has been used for many years (Fujita, 1963). In a traditional analysis, "offtime" observations of temperature at a given station are displaced according to a representative translation velocity of the storm system being analyzed. Each displaced temperature observation is subjectively evaluated to determine the pattern of temperature distribution. Typically, some of the data are not well accommodated, but the analyst smooths the distribution according to his concept of an observed storm's relevant features. In such a subjective procedure, the influence assigned to offtime observations is often a function of data density. When positioned among other observations, an offtime observation may be ignored or averaged with the other observations. However, when spatially far removed from other data, the offtime observation frequently is assigned a high influence simply because it does not appear unreasonable and there are no other data to consider.

In the objective technique presented here, time series observations are treated in much the same fashion as in manual analysis. First, observations are placed relative to a moving disturbance; then, weight is computed for each observation according to its distance in space from the grid point and in time from the nominal time of the analysis. If several observations are equidistant from a grid point, those closer to map time have the greater influence.

Stations in NSSL's rawinsonde networks (Barnes et al., 1971) have been relatively closely spaced. Even so, rather large data gaps in time and space exist around individual storms. To complicate the matter, differences in time between releases of rawinsonde balloons at individual stations and between release and arrival at a given elevation, as well as horizontal differences in space between release position and balloon position aloft, are important in analysis of individual storms. Analysis techniques should accommodate these effects.

Below, we first indicate filtering properties implicit in the analysis scheme, and then illustrate practical application, including the manner in which offtime observations are incorporated. We also illustrate use of the method with both dense surface observations and sparse upper-air data.

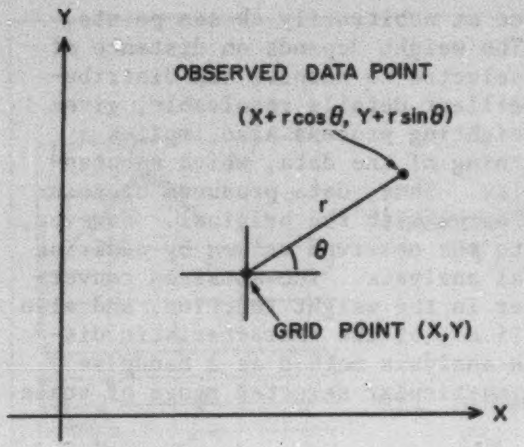

Figure 15.--Coordinate system used in objective analysis expressed by Eq. 1. (x,y) is conveniently chosen as a grid point of a square mesh; (x + r cos θ, y + r sin θ) represents one point where information is observed.

b. Mathematical properties

(1) Filtering properties of the interpolation scheme

Consider an atmospheric variable distributed as f(x,y). We can filter (weigh) this function according to distance from an arbitrary point (x,y).

$$g(x,y) \equiv \int_0^{2\pi} \int_0^{\infty} f(x + r\cos\theta,\ y + r\sin\theta)\ w(r,k)\ r\ dr\ d\theta \ , \qquad (1)$$

where r is the distance between the grid point and the observation point (in Fig. 15), and the normalized weight function is Gaussian:

$$w(r,k) = \frac{1}{4\pi k}\ [\exp(-r^2/4k)] \ . \qquad (2)$$

The parameter k determines the relative weights associated with the value of the function at various distances from (x,y); i.e., it determines w's filtering properties. It can be shown that the relationship between the value f and weighted value g at point (x,y) is of the form

$$g(x,y) = D(a,k)\ f(x,y) \ , \qquad (3)$$

where D(a,k) is a response function dependent on the characteristic wavelengths or scale sizes contained in f, a is wave number (2π/λ), and λ is the wavelength. Holloway (1958) shows, for example, that for f(x,y) = A sin(ax),

$$D(a,k) = \exp(-a^2k) \ . \qquad (4)$$

Note that the effect of the filtering does not alter the phase of f, but acts only to damp its amplitude. Figure 16 indicates the effect of D(a,k) as a function of wavelength λ and for various choices of parameter k. In general, response is nearly zero for very short fluctuations and approaches unity for very long variations. For bandpass filtering such as that done by Maddox

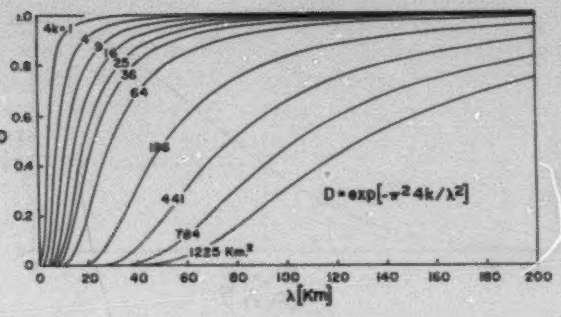

Figure 16.--Relationship of response function D (Eq. 4) to wavelength λ for various choices of parameter k. These responses correspond to one pass through the data with filter (Eq. 2).

(1980), conceptually, two analyses of the same data set are made using different values for k, and then one of the resultant analyses is subtracted from the other. Since both analyses retain long waves with nearly equal amplitudes and neither retains very short waves, the residual of the manipulation is only those features whose wavelengths lie in a midscale range.

In practice, of course, one does not know the continuous function, f(x,y), but has only observations of it at an irregular array of points. Then, in a practical analysis scheme, the integrals are replaced by summations of observed values multiplied by the weighting function, as shown in Eq. 14. Derived grid point values represent the incompletely specified natural distribution with systematic alteration of the harmonic content implied by the observations.

(2) Retrieving amplitude lost through filtering

After filtering, it is often desirable to match the interpolated function g to the original observations within arbitrarily small differences at selected points. An adjustment field can be obtained through application of the filter w to residual differences between f and g, where the value of g is defined by linear interpolation from the grid points to the data points where f is observed. For this retrieval process, it is important to reduce the value of k from the value used during the original process, thus increasing the convergence rate of the iterative technique.

We rewrite Eq. 3 as

$$g_o(x,y) = D_o\ f(x,y)\ . \qquad (5)$$

Subscript zero denotes the first-pass result with weight function $\eta_o = \exp(-\pi^2/4k_o)$. (The normalizing coefficient in Eq. 2 drops out in the actual computations; see Eq. 14.) The second pass yields smoothed values of the residual differences between f and g, which are added to the first-pass field:

$$g_1(x,y) = g_o(x,y) + [f(x,y) - g_o(x,y)]D_1\ , \qquad (6)$$

where D_1 is the response resulting from the application of

$$\eta_1 = \exp(-r^2/4k_1);\ k_1 = \gamma k_o \text{ for } 0 < \gamma < 1\ . \qquad (7)$$

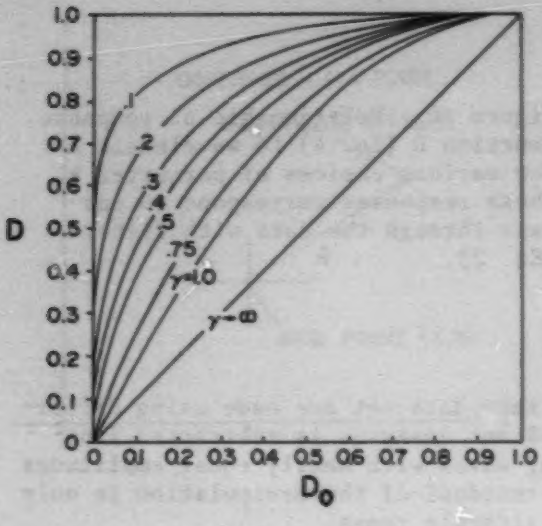

Figure 17.--Response D after one correction pass as a function of initial response D_o and parameter γ (see Eq. 10).

Thus,

$$D_1 = \exp(-a^2k_1) = \exp(-a^2\gamma k_o) = D_o{}^{\gamma} , \qquad (8)$$

and we have, from Eqs. 5 and 6,

$$g_1(x,y) = f(x,y)\ D_o[1 + D_o^{\gamma-1} - D_o{}^{\gamma}] . \qquad (9)$$

The resulting response function,

$$D = D_o(1 + D_o^{\gamma-1} - D_o^{\gamma}) , \qquad (10)$$

is now also a function of γ. Figure 17 shows the relationship of D to D_o and γ. The improved amplitude response is demonstrated by the following. Suppose, for a given wavelength feature in the observed field, the response to the initial filtering pass yields only 0.3 of the true amplitude (the actual response depends not only on our choice of k_o but also on the distribution of observations in the vicinity of this feature). Then for γ = 0.2, say, the response after the second pass (first correction pass, e.g., Eq. 6) would be 0.85. Theoretically, one could choose γ very small and achieve nearly perfect amplitude response to such a feature, but experimental results (Barnes, 1973) indicate that γ should be chosen within the range 0.2 to 0.4.

(3) Time series data

Generally, weather disturbances move from one place to another while their overall structure varies somewhat regularly. When only a few simultaneous observations are available for reconstructing the spatial distribution of a given meteorological variable, it becomes necessary to use the atmosphere's

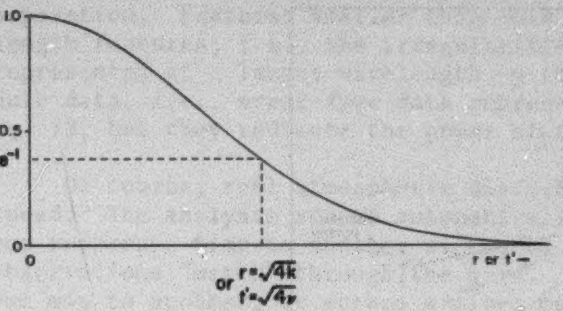

Figure 18.--Exponential weight function for space and time analysis (Eq. 12 with the coefficient suppressed). Abscissa is either the radial distance from observation to grid point (see Fig. 15) or the time difference from reference map time.

persistence to enhance the available information. However, the manner in which temporal information is entered into analysis is critical. If observations are averaged in time before being analyzed spatially, significant features may be strongly damped. On the other hand, time-to-space conversion yields results with enhanced details, a consequence of an effective increase in observation density.

Consider now the functional representation of a moving disturbance:

$$g(x,y,t) = \int_{\infty}^{\infty}\int_{0}^{2\pi}\int_{0}^{\infty} f[x + r\cos\theta - c(t + t')(y + r\sin\theta)]$$

$$\times\ w(r,t',k,v)\, r\, dr\, d\theta\, dt', \qquad (11)$$

where x increases in the direction of motion, c is its phase speed, t is an arbitrary reference time, and t' is time difference from reference time, either positive or negative. The weight function used to interpolate and filter discrete observations on this distribution must reflect the characteristic time scale of spatial development, which depends upon the nature of the phenomenon and its size. With this in mind, a suitable normalized weight function can be defined as

$$w(r,t',k,v) = w(r,k)\, w(t',v) = \frac{1}{4\pi k}\exp(-r^2/4k)\,\frac{1}{2\pi^{\frac{1}{2}}v^{\frac{1}{2}}}\exp(-t'^2/4v)$$

$$= \frac{1}{8\pi^{3/2}kv^{\frac{1}{2}}}\exp(-r^2/4k - t'^2/4v)\ , \qquad (12)$$

where v is to be related to the disturbance's characteristic decay time, as k (in Eq. 2) was related to its spatial scale. Parameter v has this significance: large v is chosen when slowly changing disturbances are to be analyzed (all data apply with nearly equal weight, regardless of when observed); small v is properly assigned when the phenomenon is changing rapidly relative to the time interval between observations. Figure 18 indicates the weight function shape as it relates to k and v.

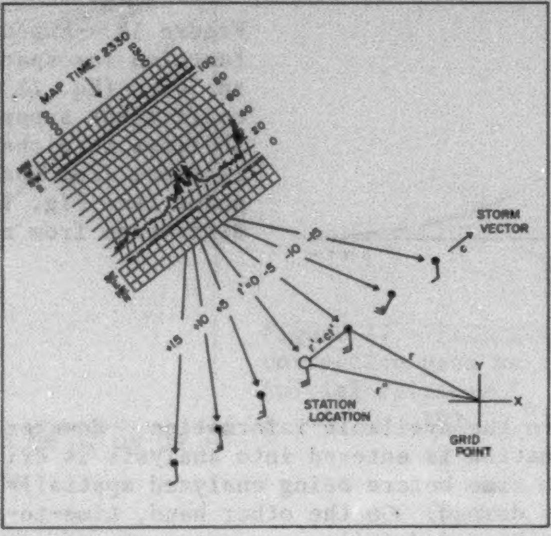

Figure 19.--Schematic of time-to-space analysis technique illustrated for surface wind observations at 5-min intervals. Station has fixed location, r", relative to the example grid point at (x,y). Map time observation is positioned at the station and influences interpolated value at grid point in proportion to r''^2. The time series observations are displaced along the storm's translation vector, c, by an amount r' = ct' and influence grid point value in proportion to r^2 and t'^2.

In an analysis scheme involving observations at discrete points in space and time, the implications of t' can be explained as follows. First, t' determines the position of each observation relative to the moving disturbance, such that r' = ct', where c is an appropriate translation velocity and r' is the position vector from the station to the displaced observation (Fig. 19). Thus r' and r", the position vector from a grid point to the station, add to give r for the offtime observation that will determine the weight it carries because of its spatial position (compare Figs. 19 and 15). Second, t' determines the weight (as Fig. 18) assigned to the observation according to its age relative to the chosen map time.

The analytical form of the response function for this time-space analysis scheme cannot be derived as was Eq. 4. Even for a simple translating wave such as

$$f(x,y,t) = A \sin [a(x - ct')] , \qquad (13)$$

if either A or c varies with time or space, Eq. 11 becomes mathematically intractable. If A and c are both constant, however, it can be shown that the analysis yields an undamped response with proper phase for waves whose length is sufficiently long (roughly, four times the average station separation) that they can be resolved by the basic station array. Smaller scale features are depicted less accurately, but empirical results indicate that the analysis scheme retrieves details as small as a theoretical limit of twice the station separation. Features smaller than this are always aliased into longer wavelength features; i.e., the irregularities manifested by the short waves are represented at a longer wavelength by the analysis. These results relate to pure data, i.e., error-free data representing a simple wave of the form of Eq. 13, but they indicate the power of this analysis tool.

Of course, real atmospheric disturbances do change in amplitude and phase speed. The analysis scheme automatically incorporates amplitude changes from one reference time to another since, as reference time changes, different observations "march" through the grid. Small changes in phase velocity from one map to another, or across a given map, do not influence the results very much, since they appear as small displacement "errors" for the offtime observations. These errors become fictitious, very short wavelength perturbations that are not passed through the filtering process. If phase velocity changes significantly (a judgment), there is no reason not to incorporate this change into the analyses as a function of reference time. More complicated is a case in which different parts of the system move with different velocities. Although this too can be incorporated into the scheme, assigning values of c as a function of space, it requires a careful preliminary consideration of just what it is the system is doing and how one might best incorporate the information to yield a useful analysis. In the examples to follow, only temporal change in phase velocity has been incorporated. Spatial variation in c is not considered.

c. Examples of analysis based on real observations

(1) Surface observations

The objective time-to-space analysis procedure described above was applied for the first time to data obtained by the National Severe Storms Laboratory from severe-thunderstorm events in central Oklahoma during 29-30 April 1970 (Barnes, 1978a,b; Barnes and Nelson, 1978). In 1970, NSSL operated a 44-station network of surface recording stations, including 9 upper-air sounding sites. Figure 20 shows the locations of these stations relative to NSSL and the 3.175-km mesh over which the surface data were analyzed. The increased density of observations due to the time-to-space technique is obvious in Fig. 21, in which 7 wind observations from each of the 44 stations are plotted in the manner of Fig. 19. The analysis of these data resulted in the streamline and isotach pattern presented as Fig. 22. Note that the smallest distance between relative extrema (half wavelength) in the isotach pattern (dashed) is about the same as the station separation, which indicates again the technique's capability to resolve wavelengths near the theoretical limit of twice the station separation. A supercell thunderstorm was traversing the northwestern corner of the network at a speed of 21.4 m s^{-1} from 233°. The sink in the streamline pattern marks the location of the updraft's roots in the surface layer of air and also the mesocyclone center. The storm's cold air outflow boundary lies along the confluence zone south and southwest of the sink.

(2) Upper-air observations

Because of the normally large distances between National Weather Service upper-air stations and a principal concern with large-scale atmospheric systems, routine synoptic analyses of radiosonde data treat the data as though simultaneously observed vertically above the station. As mentioned above, however, it is imperative that the actual positions of the observations in

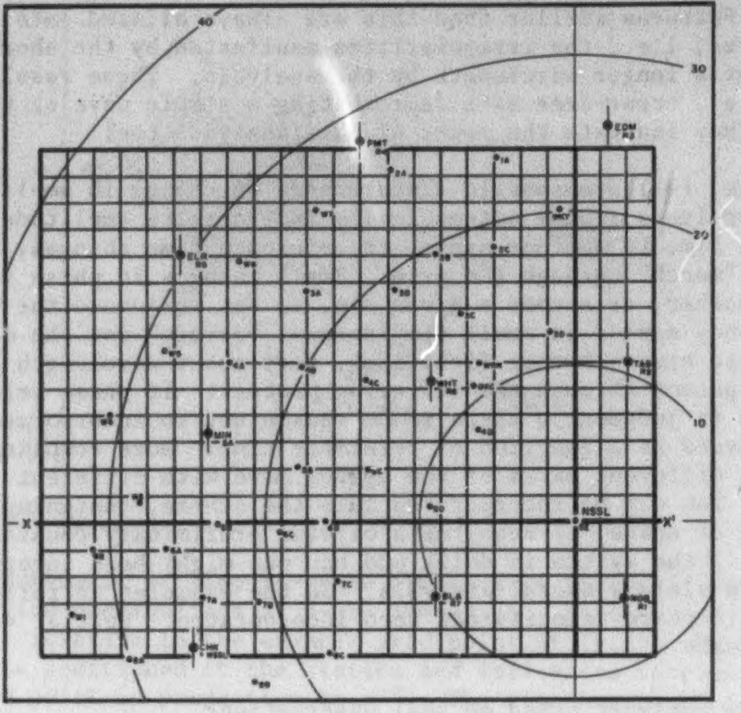

Figure 20.--Forty-four-station NSSL mesonetwork for 1970. Dots are surface station locations; circles denote rawinsonde sites. Grid has mesh size of 3.175 km. Average distance between surface stations is about 10 km.

time and space be considered for depicting features on the scale of an individual thunderstorm or thunderstorm system. Fankhauser (1969) successfully developed a partly objective technique for accomplishing this in an analysis of a squall line. Data were first plotted on time-height sections for each station, then linearly interpolated to common times. The results were then transferred to actual balloon positions on maps for manual analysis of the spatial distributions.

As with the surface data analysis described above, the upper-air analysis technique places observations in space relative to a moving storm, taking into account not only the actual time of the observation but also the balloon drift. Then, observations are interpolated to grid points by applying the normalized, discrete formula.

$$g(r,\theta,t) = \frac{\Sigma\eta(r,t',k,v)\ f(r,\theta,t+t')}{\Sigma\eta(r,t',k,v)}, \qquad (14)$$

where $\eta(r,t',k,v) = \exp(-r^2/4k - t'^2/4v)$, summed over all observations, or at least over those that lie within a suitably large radius of the grid point. Such a radius leaves the influence of data beyond that radius as a small fraction of the total, e.g., less than 1%.

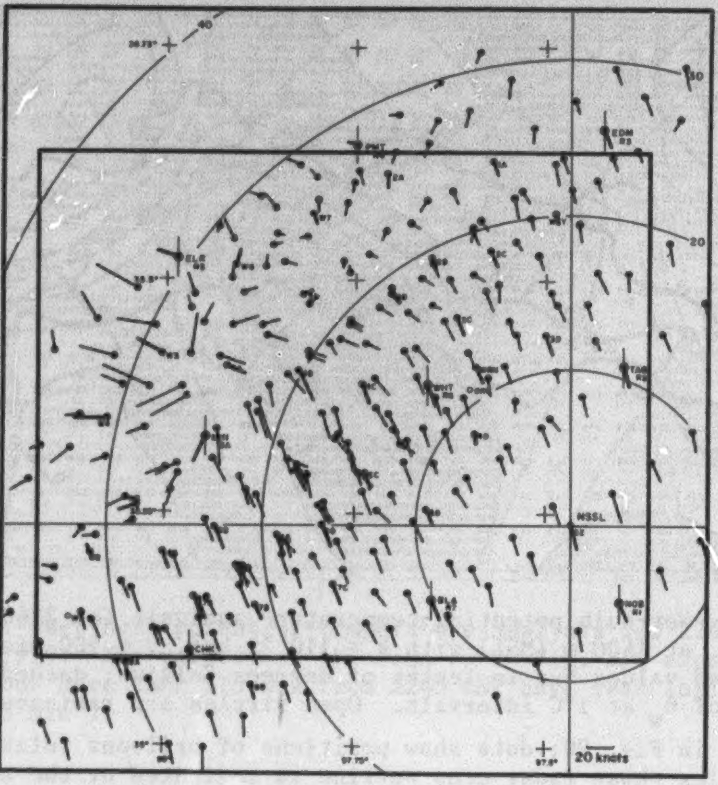

60
30
EDM R3
FMT
ELR R5
20
NSSL
20 knots

Figure 21.--Distribution of surface wind observations averaged over 5-min intervals for ±15 min of map time 0030 CST, 30 April 1979. Vectors project in direction from which wind is blowing. Offtime observations are plotted as in Fig. 19. A large, severe thunderstorm was present at this time in the northwest corner of the network, moving at 21 m s^{-1} from 233°.

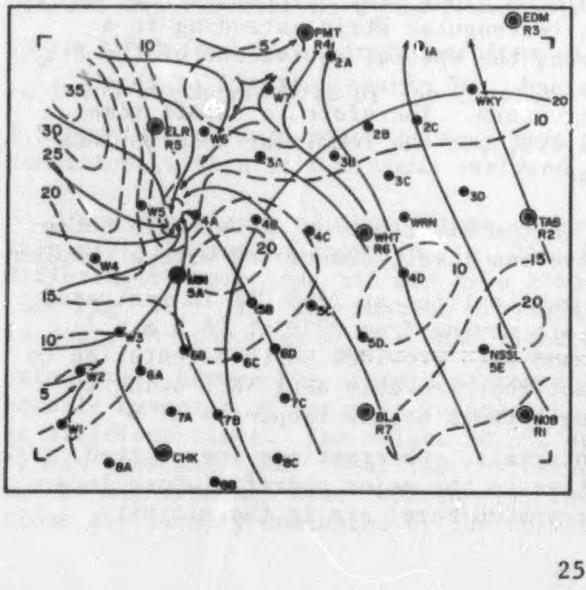

10
5
FMT R4
EDM R3
1A
2A
W7
WKY
20
10
35
30
25
ELR R5
W6
2B
2C
3A
3B
3C
3D
20
W5
4A
4B
4C
WHT R6
WRN
TAB R2
W4
20
-15
MIN 5A
10
4D
15
5B
5C
-20
10
W3
5D
6B
6C
6D
NSSL 5E
W2
6A
5
7A
7B
7C
BLA R7
NOB R1
W1
CHK
8A
8C
9B

Figure 22.--Surface wind analysis for 0030 CST, 30 April 1970, based on observations shown in Fig. 21. Streamlines are solid curved arrows; isotachs are dashed and labeled in knots. Parameters in Eq. 14 were chosen to be $k = 16\ km^2$, $\nu = 32\ min^2$; $\gamma = 0.5$ (eq. 7).

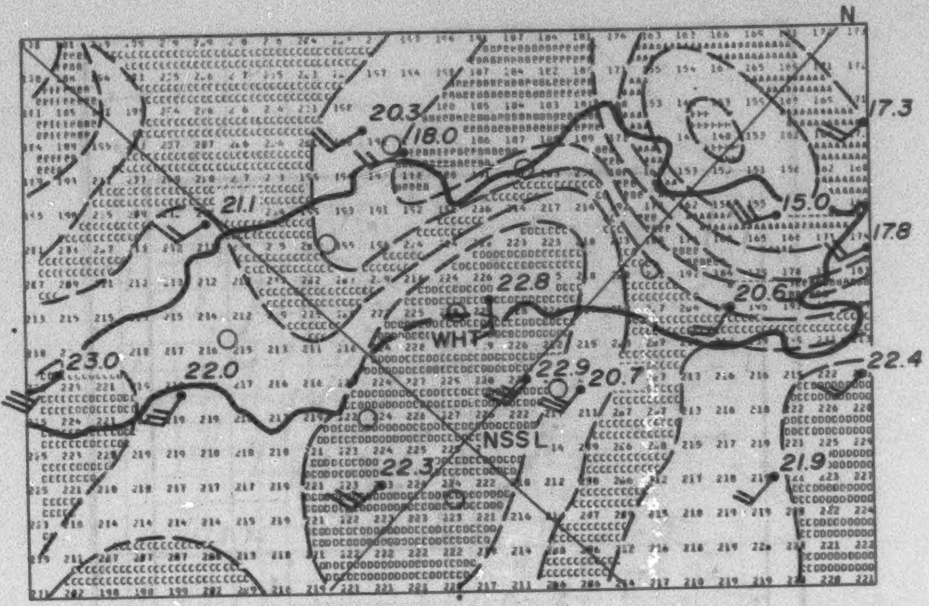

Figure 23.--Wet-bulb potential-temperature analysis for 2240 CST, 29 April 1970, at 1500 m (MSL) with k = 110.25 km^2, ν = 900 min^2, γ = 0.34. Interpolated values are in tenths of degrees Celsius; dashed lines are isotherms of θ_w at 1°C intervals. Open circles are rawinsonde stations identified in Fig. 20; dots show positions of balloons relative to the storm complex whose radar echo outline is indicated by the heavy line. One full barb represents a windspeed of 10 m s^{-1}.

The upper-air analyses for the 29-30 April 1970 case study are displayed over a 25 × 17 grid with mesh size of 6.35 km. The center of the grid is placed at Wheatland, Okla. (WHT in Fig. 23), which is the central rawinsonde site of the nine-station network (circles). The long axis of the grid is placed parallel to the direction of storm travel in order to encompass off-time observations, which have been displaced along that direction. One may visualize the observational domain as a rectangular strip extending in a southwest-northeast direction and covering the spatial equivalent of the 8-h period during which soundings were obtained. Of course, not all of that information is pertinent to a particular storm. Therefore, a cutoff time (distance) was incorporated in the analysis, and the remaining observations were given weight according to their age.

The illustrated pattern (Fig. 23) is the distribution of wet-bulb potential temperature θ_w at 1,500 meters above sea level, associated with a complex of two large thunderstorms whose radar echo outline at 2240 CST is indicated by the heavy solid line. These storms are moving from 227° at 24.5 m s^{-1}. The large cross locates the NSSL radar and also provides north orientation to the figure (the radar's storm echo is not representable near NSSL owing to ground clutter). The artificial shading between dashed isopleths of θ_w highlights the analyzed field at 1°C intervals. Observations are plotted at balloon positions (solid dots) relative to the major updrafts whose locations (based on independent data not presented here) are in the vicinity

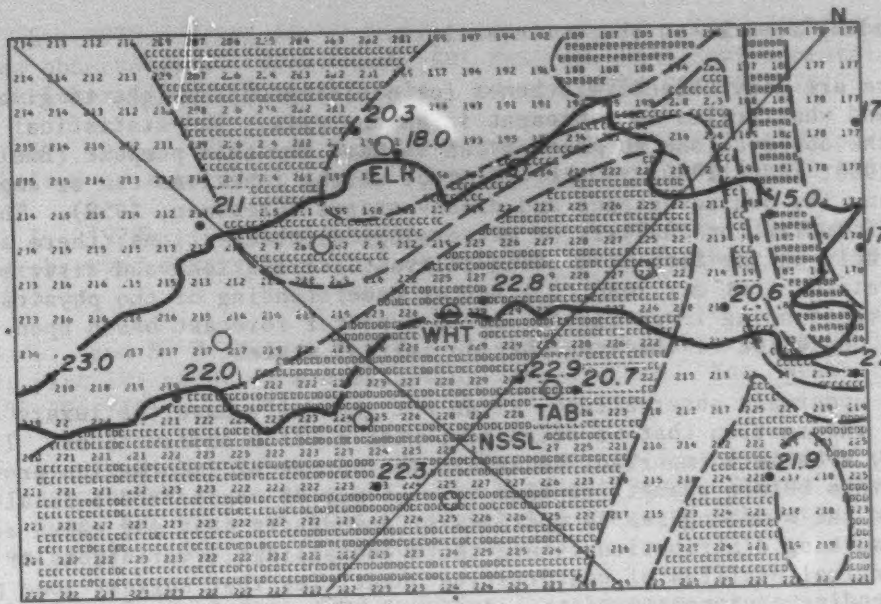

Figure 24.--Wet-bulb potential-temperature analysis for 2240 CST, 29 April 1970. The values are the same as in Fig. 23, except that observations more than ±15 min from 2240 CST have less influence ($v = 56.25\ \text{min}^2$).

of WHT and at the southwest echo tip. Winds relative to Earth are indicated by the convention that one full barb equals 10 m s^{-1}. Interpolated values are printed to tenths of degrees Celsius, and the bottom of each rightmost digit locates a grid point.

Although the analyzed θ_w pattern within the radar echo boundary cannot be taken literally because observations therein are influenced by convective motions (i.e., they induce some degree of temporal and spatial aliasing), the general distribution of θ_w is reasonable. Two tongues of moist, warm air ($\theta_w > 22^\circ$C) feed the updraft portions of the storms, while drier, cooler air is found north and west of the complex. The 15°C minimum for θ_w noted here at 1,500 meters is indicative of downdraft air descended from above, and it is consistent with a 16°C minimum analyzed at the surface just west of WHT.

The importance of the offtime observations in providing the details of this distribution is shown in Fig. 24. Here, the influences of observations differing by more than ±15 min from 2240 CST are diminished to less than 1/e (see Fig. 18). The information provided by the 15°C observation (at 2145 CST) is lost, and the high θ_w air associated with the updraft near WHT appears to extend well beyond the storm's northwest boundary. Also in Fig. 24 are two notable examples of analysis response to closely spaced observations obtained at different times. The values 20.3°C and 18.0°C near ELR were observed 4 and 17 min from map time. Near TAB the values 22.9°C and 20.7°C were observed 5 and 26 min from map time. Obviously, the analyzed values near those two stations are largely dominated by the observations closer to map time.

d. Concluding remarks on objective analysis

There are many objective schemes for deciding what weight to give observations and what scales to represent in an analysis. The statistical properties of the observations themselves can be used for this purpose (Buell, 1960; Gandin, 1963; Eddy, 1964). Other forms of weight functions can be employed, each having its own advantages and disadvantages (Cressman, 1959). There are no magic formulas for analysis of meteorological observations; there are only tools to help in the task of finding relevant correlations and distributions in observations that may lead to a better understanding of the physics driving the phenomenon being investigated, or to a better forecast based upon a representative depiction of the atmosphere's initial state.

With upper-air observations, we do not generally have the luxury of redundant information that we often have with surface observations. It is, therefore, even more important to assess the nature of information provided by the soundings before submitting them to what may be considered a final analysis. Did the sounding sample updrafts or downdrafts that may cause aliasing in the resulting distributions? Are there unexplainable variations or biases in the vertical profiles of conservative quantities that suggest some problem in the sounding equipment or data reduction? Where, relative to a storm system, were the observations obtained? These questions are pertinent not only to special data from mesoscale networks but also to the analysis of larger scale synoptic data. Unfortunately, in an operational mode, one does not usually have time (or facilities) for viewing individual profiles of soundings forming the data base. Cursory checks for consistency can be (and are) made automatically, but they are not always sufficient to detect problem data. During research, it is appropriate to review the observations thoroughly prior to an analysis such as that described in Sec. 7c.

Finally, are the analyzed distributions reasonable when compared with the observations? A good, objective analysis scheme produces results similar to those presented by careful manual analysis of the observations, but it does so with ease, consistency, and impartiality. If it does not produce expected results, the user should find the reasons. The thinking human is still the most important link in analysis.

REFERENCES

Alberty, R. L., D. W. Burgess, C. E. Hane, and J. F. Weaver, 1979. Project Severe Environmental Storms and Mesoscale Experiment (SESAME). SESAME 1979 Operations Summary, NOAA Environmental Research Laboratories, Boulder, Colo.

Angell, J. K., W. H. Hoecker, C. R. Dickson, and D. H. Pack, 1973. Urban influence on a strong daytime airflow as determined from tetroon flights. J. Appl. Meteorol. 12:924-936.

Barnes, S. L., 1964. A technique for maximizing details in numerical weather map analysis. J. Appl. Meteorol. 3:396-409.

Barnes, S. L., 1973. Mesoscale objective map analysis using weighted time-series observations. Tech. Memo. ERL NSSL-62, NOAA Environmental Research Laboratories, Boulder, Colo., 60 pp. (NTIS COM-73-10781).

Barnes, S. L., 1978a. Oklahoma thunderstorms on 29-30 April 1970; part I: morphology of a tornadic storm. Mon. Weather Rev. 106(5):673-684.

Barnes, S. L., 1978b. Oklahoma thunderstorms on 29-30 April 1970; part II: radar-observed merger of twin hook echoes. Mon. Weather Rev. 106(5): 685-696.

Barnes, S. L., and S. P. Nelson, 1978. Oklahoma thunderstorms on 29-30 April 1970; part IV: study of a dissipating severe storm. Mon. Weather Rev. 106(5):704-712.

Barnes, S. L., J. H. Henderson, and R. J. Ketchum, 1971. Rawinsonde observation and processing techniques at the National Severe Storms Laboratory. Tech. Memo. ERL NSSL-53, NOAA Environmental Research Laboratories, Boulder, Colo., 246 pp. (NTIS COM-71-00707).

Bleeker, W., and M. J. Andre, 1950. Convective phenomena in the atmosphere. J. Meteorol. 7:195-209.

Braham, R. R., Jr., 1952. The water and energy budgets of the thunderstorm and their relation to thunderstorm development. J. Meteorol. 9:227-242.

Brandes, E. A., 1977. Gust front evolution and tornado genesis as viewed by Doppler radar. J. Appl. Meteorol. 16:333-338.

Brock, F. V., 1974. Portable Automated Mesonet. Atmos. Tech. 6:21-25.

Brock, F. V., and P. K. Govind, 1977. Portable Automated Mesonet in operation. J. Appl. Meteorol. 16:299-310.

Brooks, E. M., 1949. The tornado cyclone. Weatherwise 2:32-33.

Brooks, E. M., 1951. Tornadoes and related phenomena. In Compendium of Meteorology, T. F. Malone (ed.), American Meteorological Society, Boston, Mass., 673-680.

Brown, R. A., (ed.), 1976. The Union City, Oklahoma, tornado of 24 May 1973. Tech. Memo. ERL NSSL-80, NOAA Environmental Research Laboratories, Boulder, Colo., 235 pp.

Browning, K. A., and R. J. Donaldson, Jr., 1963. Airflow and structure of a tornadic storm. J. Atmos. Sci. 20:533-545.

Buell, C. E., 1960. The structure of two-point wind correlations in the atmosphere. J. Geophys. Res. 65:3353-3366.

Byers, H. R., and R. R. Braham, Jr., 1948. Thunderstorm structure and circulation. J. Meteorol. 5:71-86.

Byers, H. R., and R. R. Braham, Jr., 1949. The Thunderstorm. U.S. Weather Bureau, Washington, D.C., 287 pp.

Byers, H. R., and H. R. Rodebush, 1948. Causes of thunderstorms of the Florida peninsula. *J. Meteorol.* 5:275-280.

Changnon, S. A., and R. G. Semonin, 1971. Metromex: an investigation of inadvertent weather modification. *Bull. Am. Meteorol. Soc.* 52:958-967.

Cressman, G. P., 1959. An operational objective analysis system. *Mon. Weather Rev.* 87:367-374.

Danielson, E., 1975. Predicting and modifying severe weather. In *NCAR Annual Report*, National Center for Atmospheric Research, Boulder, Colo., 89-95.

Doswell, C. A., III, 1977. Obtaining meteorologically significant surface divergence fields through the filtering property of objective analysis. *Mon. Weather Rev.* 105:885-892.

Eddy, A., 1964. The objective analysis of horizontal wind divergence fields. *Q. J. R. Meteorol. Soc.* 90:424-440.

Fankhauser, J. C., 1969. Convective processes resolved by a mesoscale rawinsonde network. *J. Appl. Meteorol.* 8:778-798.

Ferguson, S. P., 1933. The early history of aerology in the United States. *Bull. Am. Meteorol. Soc.* 14:252-256.

Foote, G. B., and C. A. Knight, 1977. *Hail: A Review of Hail Science and Hail Suppression*. Meteorol. Monogr. 16(38), American Meteorological Society, Boston, Mass., 277 pp.

Fujita, T. T., 1962. Index to the NSSP surface network. National Severe Storms Project Report No. 6, U.S. Weather Bureau, Washington, D. C., 32 pp.

Fujita, T. T., 1963. Analytical mesometeorology: a review. In *Severe Local Storms*, Meteorol. Monogr. 5(27), American Meteorological Society, Boston, Mass., 77-125.

Fujita, T. T., and R. Stuhmer, 1963. Proposed mechanism of hook echo formation, with a preliminary mesosynoptic analysis of tornado cyclone case of 26 May 1963. Research Paper No. 27, Mesometeorology Project, Department of the Geophysical Sciences, University of Chicago, 35 pp.

Fujita, T. T., H. Newstein, and M. Tepper, 1956. Mesoanalysis, an important scale in the analysis of weather data. Res. Paper No. 39, U.S. Weather Bureau, Washington, D.C., 39 pp.

Gandin, L. S., 1963. *Objective Analysis of Meteorological Fields*. Translated by Israel Program for Scientific Translations (National Technical Information Service, Springfield, Va., TT-65-50007), 242 pp.

Holloway, J. L., Jr., 1958. Smoothing and filtering of time series and space fields. In *Advances in Geophysics*, Vol. 4, Academic Press, N.Y., 351-389.

Kessler, E., 1965. Purposes and program of the U.S. Weather Bureau National Severe Storms Laboratory, Norman, Okla. Trans. Am. Geophys. Union 46(2):389-397.

Kessler, E., 1977. National Severe Storms Laboratory: history and 1976 program. NSSL Special Report, NOAA Environmental Research Laboratories, Boulder, Colo., 71 pp.

Kreitzberg, C. W., and H. A. Brown, 1970. Weather systems within an occlusion. J. Appl. Meteorol. 9:417-432.

Lhermitte, R. M., and Kessler, E., 1965. A weather radar signal integrator. Preprints, International Conference on Cloud Physics, Tokyo and Sapporo, Japan, May 24-June 1, 302-308.

Maddox, R. A., 1980. An objective technique for separating macroscale and mesoscale features in meteorological data. Mon. Weather Rev. 108: 1108-1121.

Middleton, W. E. K., 1969. Invention of the Meteorological Instruments. Johns Hopkins Press, Baltimore, Md., 362 pp.

Newton, C. W., 1963. Dynamics of severe convective storms. In Severe Local Storms, Meteorol. Monogr. 5(27), American Meteorological Society, Boston, Mass., 33-57.

NSSP (National Severe Storms Project) Staff, 1961. Objectives and basic design. National Severe Storms Project Report No. 1, U.S. Weather Bureau, Washington, D.C., 16 pp.

Sahashi, K., 1972. Preliminary report on the feasibility study of mesomicrometeorological interaction with sonic anemometer--thermometers installed at the WKY-TV tower. Report to Environmental Research Laboratories on NOAA grant N22-47-72(G), 8 pp.

Sasaki, Y., 1960. An objective analysis for determining initial conditions for the primitive equations. Tech. Report (Ref. 60-16T), Department of Oceanography and Meteorology, Texas A & M University, College Station, 22 pp.

Tepper, M., 1950. A proposed mechanism of squall lines: the pressure jump line. J. Meteorol. 7:21-29.

Williams, D. T., 1953. Pressure wave observations in the central Midwest, 1952. Mon. Weather Rev. 81:278-298.

blank page

II. TORNADO INTERCEPTION WITH MOBILE TEAMS

Robert P. Davies-Jones

1. INTRODUCTION

Tornadoes, because of their infrequency, small size, and destructivity, are not easily observed and measured. Eyewitnesses are seldom trained meteorologists and consequently pay scant attention to attendant cloud structures or to the sequence of events preceding the tornado. They also do not move with the storm, so their observation time is limited. Tornadoes are too small to be resolved by radars and mesonetworks, although these sensors provide important data on the parent storms. Anemometers directly in the path of the storm are frequently damaged, and microbarographs respond too sluggishly to the rapidly passing vortex. Almost all data on the tornado scale have been gathered from visual and photographic records and damage surveys. Lack of observational data and hence of clear physical knowledge of the phenomenon has hindered the construction of sound tornado theories and models (Lilly, 1965; Morton, 1966), and has led Lilly (1975) to name the tornado as "perhaps the last frontier in tropospheric meteorology--the only intense and easily identifiable phenomenon whose internal structure and dynamics remain highly speculative." Although chance eyewitnesses have occasionally taken revealing tornado movies, much knowledge has also been gained from visual observations made by trained meteorologists in pursuit of tornadoes.

Ward (1961) and Donaldson and Lamkin (1963) were among the first to document successful ground intercepts (i.e., close-range approaches), and Bates (1962, 1963) had similar successes from the air. These investigators went into the field only occasionally and did not obtain high-quality photography, although they made skillful observations. Rossow's (1970) and Golden's (1974) field experiments revealed many interesting properties of waterspouts.

The Tornado Intercept Project (TIP), a cooperative effort between the National Severe Storms Laboratory (NSSL) and Oklahoma University (OU), began in the spring of 1972 (Golden and Morgan, 1972). TIP is based in Norman, Okla. Its formation represented an unprecedented commitment to severe-storm intercepts and an attempt to combine close-range visual observations with data from other sensors such as radar. Tornado "chasing" quickly became a favorite pastime for a few meteorology students, fascinated by the sublime appearance and coherent structure of rotational storms. The skills developed and the observations made by many a self-funded impromptu intercept team, relying heavily on its own visual observations for guidance, have greatly supplemented the knowledge gained on official intercepts (e.g., Moller et al., 1974; Smith, 1974; Burgess, 1976).

This chapter discusses TIP's goals, the intercept techniques developed during the course of the field program, the chances for success, and the knowledge gained so far.

2. TIP GOALS

The original goal of approaching within close range of tornadoes with conventional automobiles has been achieved many times since 1972. The continuing goals of the Tornado Intercept Project are these:

(1) To obtain accurate times and locations of tornadoes and to document changes in vortex size, shape, and tilt for use in Doppler radar analysis and other studies. Precision times and locations allow the tornado to be placed accurately relative to the radar echo and permit relations between the tornado and parent storm to be investigated.

(2) To obtain high-quality movies of tornado debris clouds so that tornado winds can be measured photogrammetrically.

(3) To observe and document photographically the evolution of storms with the ultimate intent of constructing descriptive models of tornadic storms based on visual and radar appearances.

(4) To obtain visual and photographic records of tornadoes and their parent clouds, of changes in cloud structure, and of sequences of events spanning tornadoes. Such qualitative observations provide an important real-world starting point for tornado models.

(5) To measure the wind, thermodynamic, and electrical fields near tornadoes.

3. PERSONNEL AND EQUIPMENT

Each TIP team consists of a team leader and three other members. The team leader has the final word on all in-vehicle decisions and is responsible for his team's safety and performance. He also chooses the intercept route, based on the availability of roads, visual storm observations, and information received from base. Team members are assigned driving, documentary, photographic, and navigational duties. Emphasis is placed on accurate entries of time, location, and records of photography and visual observations in a log (usually a tape recording). A large van with windows on all sides is the best type of vehicle because it offers good visibility, ample space, and easy accessibility to equipment. Items carried into the field include maps, tape recorders, an insulated chest containing dry ice (for hail collection if the opportunity arises), 16-mm movie cameras, 35-mm slide cameras, intervalometers, and other photographic accessories and supplies. Each van is equipped with FM radio and a radio telephone. FM communications with base (NSSL) are routed through a repeater located at the 440-m level on a tall television tower 40 km north of NSSL. Beyond the FM system's range (115 km from the repeater), the radio telephone is used when an operator is within range and the channels are not busy; otherwise a public telephone has to be found whenever updated information is needed. Direct, short-range, intervehicle communications, provided by a second FM radio channel, enable teams to exchange information during intercepts of storms that lie beyond the repeater's range.

The nowcaster is the NSSL-based person who communicates with the team leaders. His duties include preparing a 0- to 9-h forecast by 1000 CST and monitoring the weather throughout the day when the potential for severe-storm development exists. His aids are the NAFAX weather maps (both analyses and prognoses), the standard teletype data reports, half-hourly satellite photographs, visual observations from the intercept teams, and NSSL radar and rawinsonde observations. By keeping abreast of the latest developments, the nowcaster seeks understanding of the current state and tendency of the atmosphere. He relays the latest nowcast and radar information to the field team members, obtains their opinions and current visual observations, and directs the vehicles to the most strategic locations. Usually, the team leader and nowcaster agree on strategy; however, if they fail to do so, the nowcaster makes the final decision. The nowcaster is also the link between the intercept teams and other participants in NSSL's Spring Observational Program. Field reports of tornadoes are relayed to the Doppler radar meteorologists (and also to the local National Weather Service Office for public alerts) while information concerning echo position, motions, characteristics, and signatures of mesocyclones and tornado vortices (see Vol. 2, Ch. X) flows out to the field.

At times during the last few years the nowcaster has served six teams simultaneously. NSSL and Oklahoma University have fielded four photographic teams (two long range and two restricted to the area of best radar coverage) with goals as outlined in Sec. 2. The primary goals of the other teams were to collect hail (National Center for Atmospheric Research) and to record electrical parameters and tornado acoustics (University of Mississippi/NSSL).

4. TIP STRATEGY

To maximize intercept chances, teams enter the field well before severe weather develops and often even before the formation of echoes on NSSL's WSR-57 radar scope. Immediately after the 1000 CST forecast (or even before if conditions warrant), the initial status of each team is resolved. The choices are these: (a) dismiss the teams, (b) place them on standby at NSSL, (c) dispatch them to a designated standby location in the field, or (d) vector them toward a target storm. Since the initial decision may prove to be a vital one, much depends on the forecaster's ability to assess the probability of severe storms during the day and the prime time and location for development. On potential or actual severe-storm days, the status of each team is updated frequently until the mission is called off, either because of darkness or because of lack of suitable target storms within range.

After storms have developed, the intercept strategy chosen is based on vehicle positions in relation to storm locations and movements, and expected developments. Unless a decision is made to forgo existing storms in favor of ones anticipated in a different region, a target storm is chosen for each vehicle based on the storm's accessibility and its tornadic potential. As a field team approaches a storm, it maneuvers around the precipitation core and takes up a tracking position on the storm's right rear flank. Driving through the core is avoided whenever possible because bad driving conditions force the vehicle to slow down; large hail and strong winds may be encountered and the team may drive "blindly" out of the precipitation core into the path of a tornado. (Incidentally, lightning, flash floods, and traffic accidents probably are greater hazards to field personnel than the tornado.)

As target distance decreases, the intercept crew's own visual observations become increasingly important and their reliance on relayed radar information diminishes, which is fortunate since communication channels are

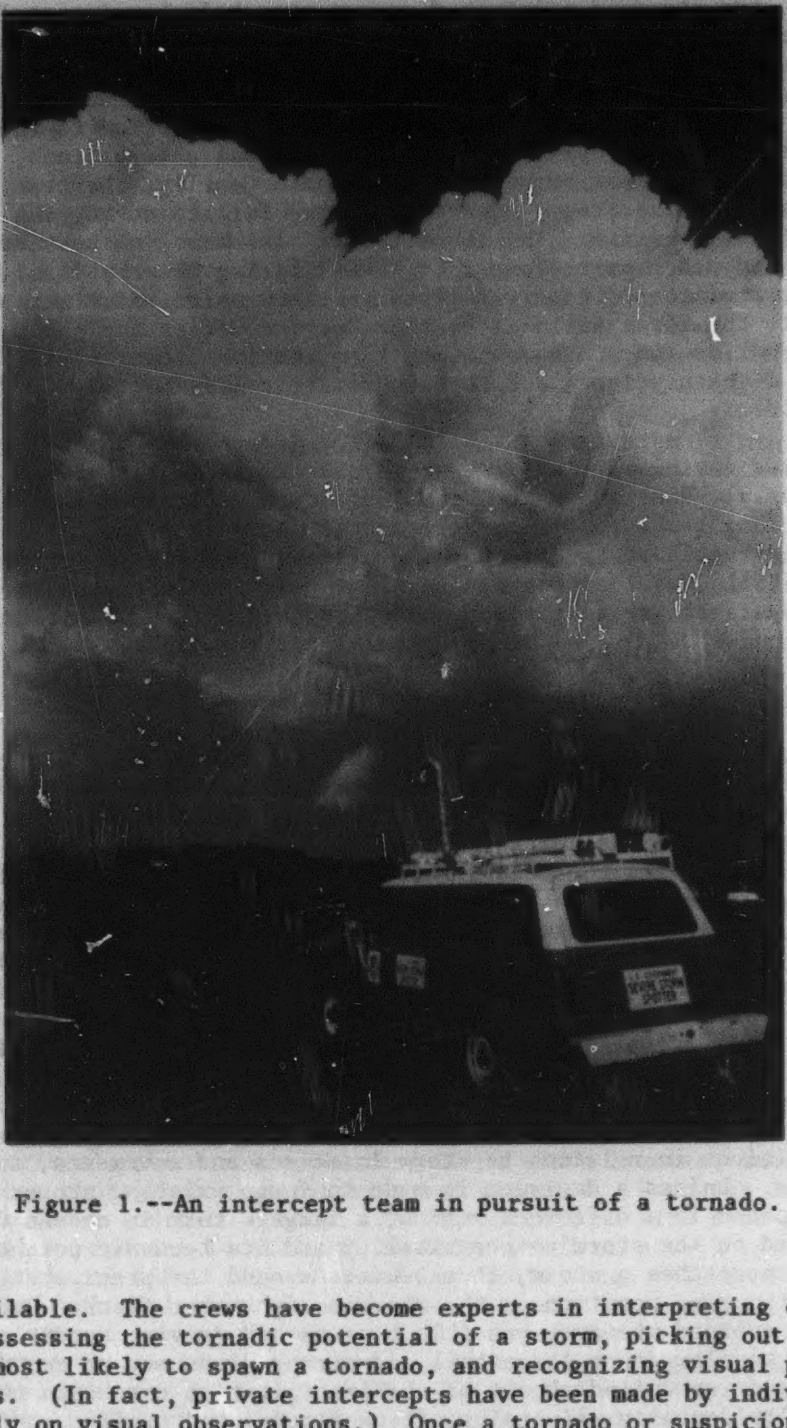

Figure 1.--An intercept team in pursuit of a tornado.

often unavailable. The crews have become experts in interpreting cloud features, assessing the tornadic potential of a storm, picking out the part of a storm most likely to spawn a tornado, and recognizing visual precursors of tornadoes. (In fact, private intercepts have been made by individuals acting solely on visual observations.) Once a tornado or suspicious cloud feature has been spotted (Fig. 1), the team positions itself ahead and to the right of the extrapolated track. This vantage point generally offers the best visibility because the tornado is silhouetted against a light background and there is less likelihood of intervening precipitation (Fig. 2). Teams that have pursued tornadoes from behind have experienced poor photographic

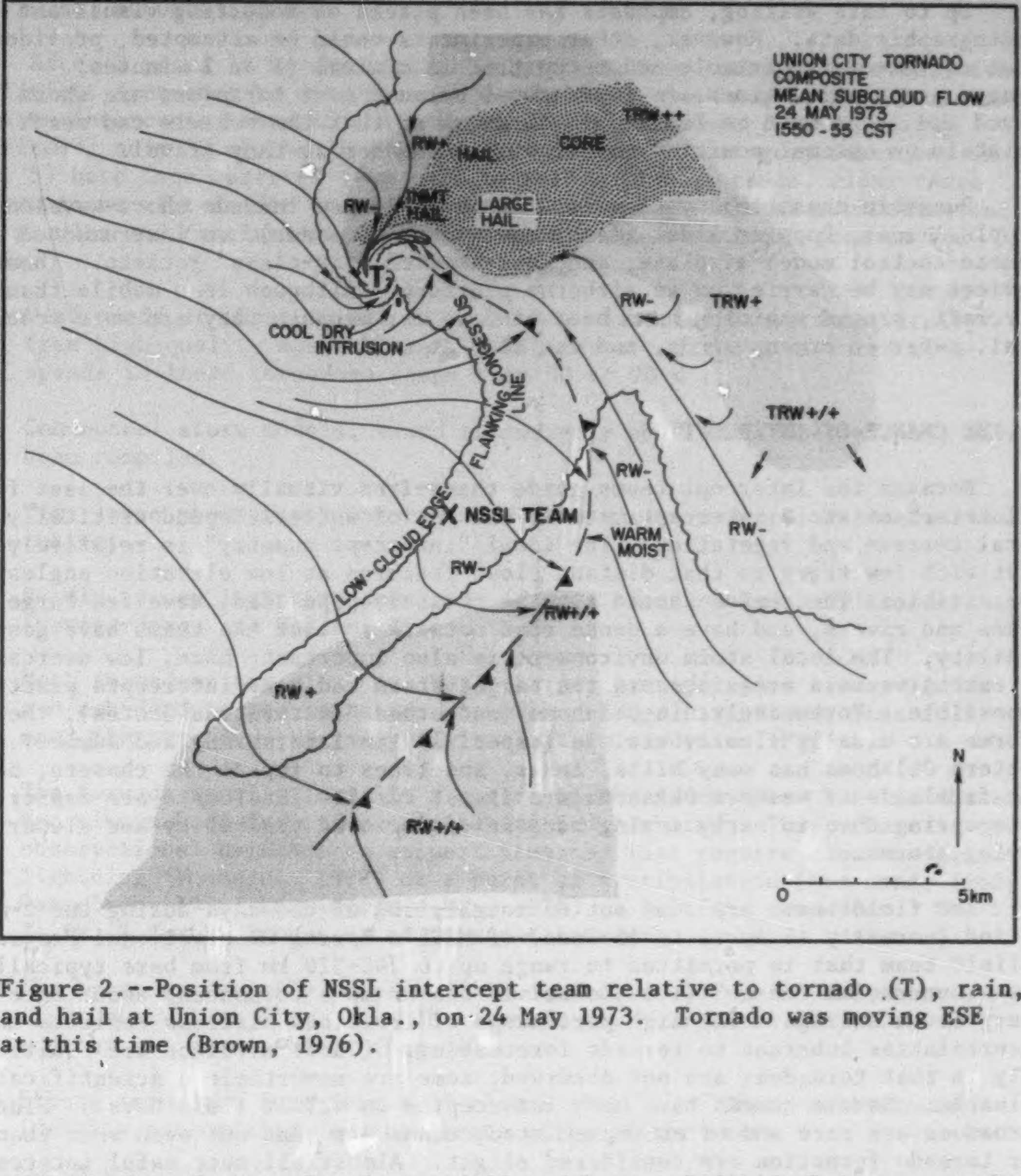
UNION CITY TORNADO
COMPOSITE
MEAN SUBCLOUD FLOW
24 MAY 1973
1550 - 55 CST
TRW++
RW+
HAIL
CORE
RW-
HAIL
LARGE HAIL
T
RW-
TRW+
COOL DRY INTRUSION
FLANKING CONGESTUS LINE
TRW+/+
RW-
LOW-CLOUD EDGE
X NSSL TEAM
WARM MOIST
RW-
RW-
RW+/+
RW+
N
RW+/+
0
5km

Figure 2.--Position of NSSL intercept team relative to tornado (T), rain, and hail at Union City, Okla., on 24 May 1973. Tornado was moving ESE at this time (Brown, 1976).

contrast and road obstacles due to fallen debris. Individual intercepts have been described by Brown (1976), Moller et al. (1974), Smith (1974), and Gannon (1973).

Even though most of Oklahoma is covered by a network of section roads 1 mile apart and oriented N-S and E-W, these roads are avoided except as a last resort. Because they are unpaved, they become treacherous when wet. Also, they often end at creeks and rivers. Thus, the intercept vehicles stay on major highways practically all the time.

One dilemma faced by the intercept teams is when to leave one storm for another. Sometimes a storm with a deteriorating visual appearance will produce a tornado after an intercept team has abandoned it.

Up to this writing, emphasis has been placed on acquiring visual and photographic data. However, other experiments could be attempted, provided that equipment is portable and setup time is minimal (1 or 2 minutes). Longer preparation times are impractical because most tornadoes are short lived and stops must be limited in duration so that the vehicle can reach and maintain an optimal position for viewing tornadoes as they travel.

Possible measuring systems for future field use include short-wavelength Doppler radar, Doppler lidar (laser equivalent of radar), an instrumented remote-control model airplane, and instrumented "toy-class" rockets. These devices may be carried on an airborne platform. Although less mobile than aircraft, ground vehicles have been used so far because they are more economical, safer in strong winds, and can stop at will.

5. THE CHANCE OF INTERCEPTION

Because the intercept teams guide themselves visually over the last few kilometers of storm intercepts, their chances of success depend critically on local terrain and vegetation. The ideal "intercept country" is relatively flat with few trees so that distant cloud features at low elevation angles are visible. The region should also be sparsely populated, have few large lakes and rivers, and have a dense road network so that the teams have good mobility. The local storm environment is also important; haze, low overcast, or extensive rain areas obscure the target storm and make intercepts practically impossible. Fortunately, in Oklahoma (and other Great Plains States), the storms are usually clearly visible (especially in late spring and summer). Eastern Oklahoma has many hills, lakes, and trees to impede the chasers, but the farmlands of western Oklahoma are almost ideal. Intercepts are easier in late spring than in early spring because of improved visibility and slower moving storms.

The field teams are sent out on roughly 30% of the days during the 2-mo period (normally 15 April to 15 June) of NSSL's Spring Observational Program. A field team that is permitted to range up to 240-320 km from base typically has a successful "chase" (i.e., observes one or more tornadoes) about once in every seven outings. The high percentage of fruitless missions reflects the uncertainties inherent to tornado forecasting. (These missions are fruitless only in that tornadoes are not observed; some are nevertheless scientifically valuable. Severe storms have been intercepted on 42% of field days.) Since tornadoes are rare and often unpredicted, teams are sent out even when chances for tornado formation are considered slight. Almost all successful intercepts have been made in the western half of Oklahoma or in the Texas Panhandle.

Because of the time consumed in making a morning forecast, deciding upon initial strategy, and traveling to the area where severe storms are anticipated, the teams are often not in position to make intercepts before 1300 CST. Fortunately, only 7% of Oklahoma tornadoes occur during the first half of the day (0700-1300 CST). After 1900 CST, lighting rapidly becomes too low for photography. Thus, we define those tornadoes that occur between 1300 and 1900 CST (50% of the total) within 240 km of Norman as pursuable. Central Oklahoma experiences in an average 2-mo severe-storm season about 18 pursuable tornadoes and 7 pursuable-tornado days. Twenty-three percent of pursuable tornadoes have been sighted by field teams (both official and private) during an 8-yr period (1972-9).

6. PROJECT ACCOMPLISHMENTS

After 2 years it became apparent that tornadoes could be observed with sufficient frequency to make pursuit worthwhile. Counting both official and private intercepts, more than 130 Great Plains tornadoes (76 officially confirmed; only 30 of the 76 fall in the "pursuable" category described in Sec. 5) have been observed from 1972 to 1979. In most cases, close-range observations of tornadic storms began well before actual tornado formation. The results and conclusions of TIP's extensive observational program are these:

(1) Windspeeds of three tornadoes have been measured photogrammetrically from high-quality movies taken by TIP teams. Maximum measured windspeeds in these tornadoes range from 60 to 90 $m\ s^{-1}$.

(2) Conceptual storm models, based extensively on visual observations, have been compiled.

(3) Time-lapse photography has revealed that entire convective towers rotate.

(4) Rarely is any lightning seen near (closer than 2-3 km) or within tornadoes (Davies-Jones and Golden, 1975).

(5) Most tornadoes are close to, but outside, precipitation areas. A few are embedded in precipitation, however. Large hailstones often fall near the tornado, generally on its left forward side (Fig. 2).

(6) The tornado usually forms in a region of the storm where the cloudbase has always been free of precipitation and lighting. Thus, there is no observational evidence to support theories that require cloud-to-ground lightning (Vonnegut, 1960) or a burst of precipitation (Rossmann, 1960; Danielsen, 1975; Eskridge and Das, 1976) to initiate tornadoes. See Vol. 2, Ch. X for a discussion of tornado theories.

(7) The tornado generally develops from convective towers on the storm's right rear flank (Fig. 3). The tornado may be located very near the edge of its parent cloud (Fig. 4).

(8) Strong tornadoes form from wall clouds (Fig. 5). Thus, wall clouds identify potentially very dangerous parts of the storm.

(9) Gradual evaporation of cloud is often observed in the wall cloud, first to the rear of the tornado and then slowly propagating around its right side (Lemon and Doswell, 1979). This observation apparently indicates the presence of a developing unsaturated rear flank downdraft. Intense upward motions seen ahead and to the left of the tornado indicate that the tornado is located near an updraft-downdraft interface.

(10) Relatively isolated storms are the best tornado producers (Fig. 6), presumably because they are not competing with neighbors for available warm, moist inflow air.

(11) In some cases, surface weather features pinpoint small areas of maximum tornado threat. Tegtmeier (1974) showed that favored locations for

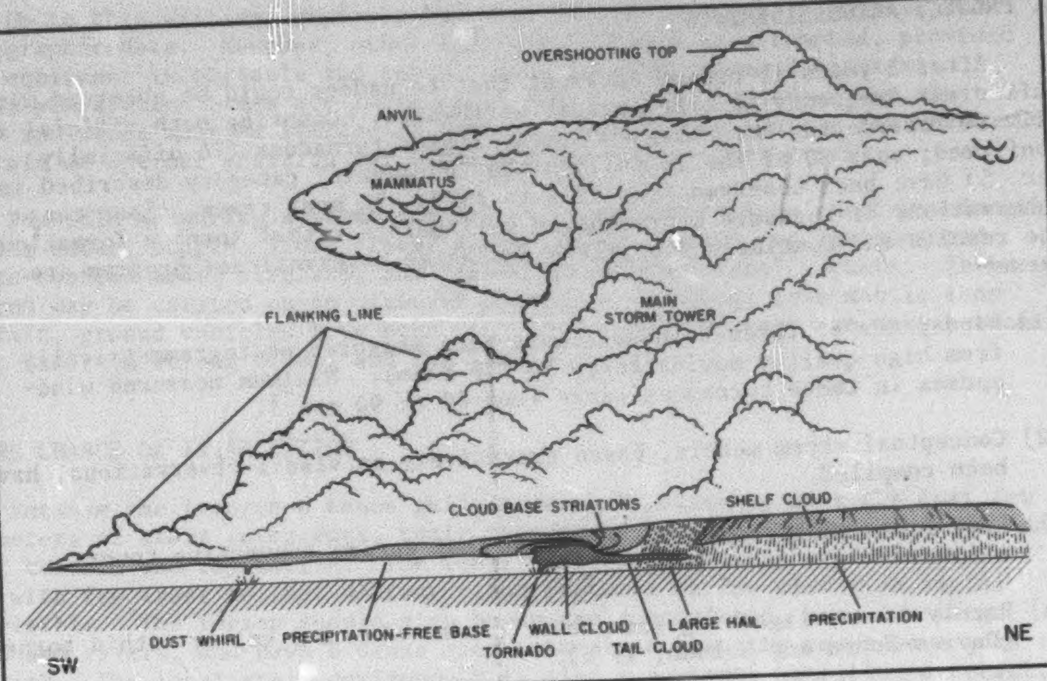
OVERSHOOTING TOP
ANVIL
MAMMATUS
FLANKING LINE
MAIN STORM TOWER
CLOUD BASE STRIATIONS
SHELF CLOUD
DUST WHIRL
PRECIPITATION-FREE BASE
WALL CLOUD
TORNADO
TAIL CLOUD
LARGE HAIL
PRECIPITATION
SW
NE

Figure 3.--Composite view of a typical tornado-producing cumulonimbus as seen from a southeasterly direction. Horizontal scale is compressed. The features shown cannot all be seen simultaneously from a single location (diagram by C. Doswell).

tornadoes are the northeast sides of developing small-scale lows and the moist sides of bulges in the dryline (Fig. 7).

(12) Anticyclonic tornadoes definitely exist (Fig. 8) (Burgess, 1976).

(13) TIP storm observations and photography have been incorporated in a training movie (NOAA, 1977) and slide collection (NOAA, 1980) for tornado spotters (Moller, 1978).

(14) A new type of severe storm, which fails to fit the classic model, has been identified (Davies-Jones et al., 1976; Burgess and Davies-Jones, 1979).

(15) TIP has provided vital information to Doppler radar meteorologists involved both in operational projects and in the analysis of research data. For example, well-documented TIP tornado observations verified 11 out of 34 experimental tornado warnings issued solely on the basis of Doppler radar observations during 1977 (Burgess et al., 1978).

The most successful intercept so far has been the Union City, Okla., tornado of 24 May 1973 (Brown et al., 1976), because movies that were photogrammetrically analyzable for tornadic windspeeds were obtained and because

Figure 4.--Tornado near edge of cloud at Quail, Tex., 16 May 1977.

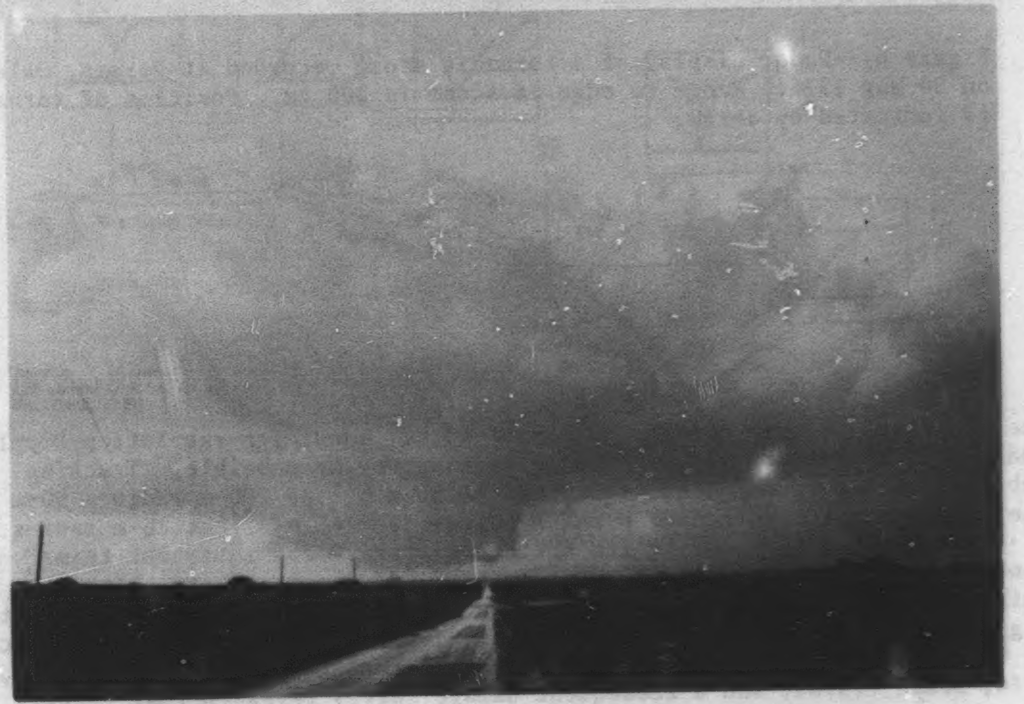

Figure 5.--Wall cloud (discrete lowering of cloudbase).

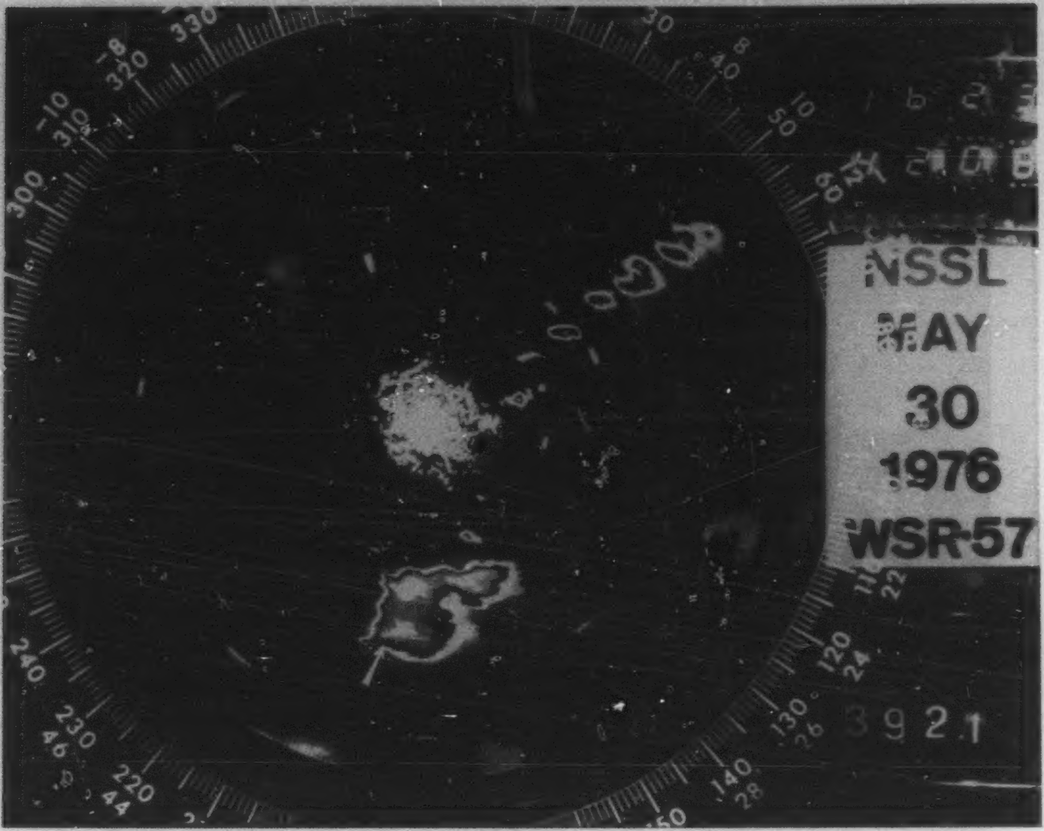

Figure 6.--Radar display of a tornadic storm recorded at Norman, Okla., on 30 May 1976. Range to edge of scope is 200 km. Position of tornado is indicated by arrow.

the closeness of this tornado to NSSL (~40 km) made high-resolution Doppler radar data collection and detailed damage surveying possible. Tracking debris in the movie yielded windspeeds to 80 m s^{-1} at 200-m radius, 90-m elevation during the tornado's mature stage, and 65 m s^{-1} at 25-m radius, 50- to 80-m elevation during its shrinking stage. The intercept teams' documentation of the tornado's position in time and space and its tilt with height helped establish the significance of Doppler radar's tornadic vortex signature, first discovered in the Union City storm. The complete life cycle of the Union City tornado was observed and filmed (Fig. 9; Moller et al., 1974; Brown, 1976), and a subsequent damage survey revealed that changes in tornado structure were accompanied by corresponding changes in damage intensity and debris configuration (Vol. 2, Ch. X, Sec. 3).

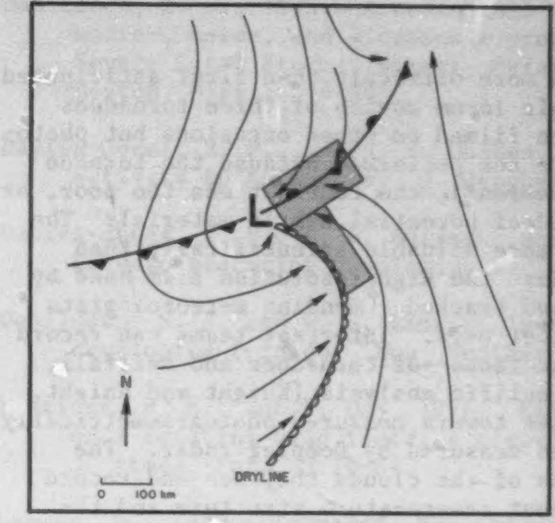
L
N
DRYLINE
0 100 km

Figure 7.--Schematic of surface flow features for a case where small-scale low and dryline bulge are present simultaneously. Stippling indicates maximum threat areas.

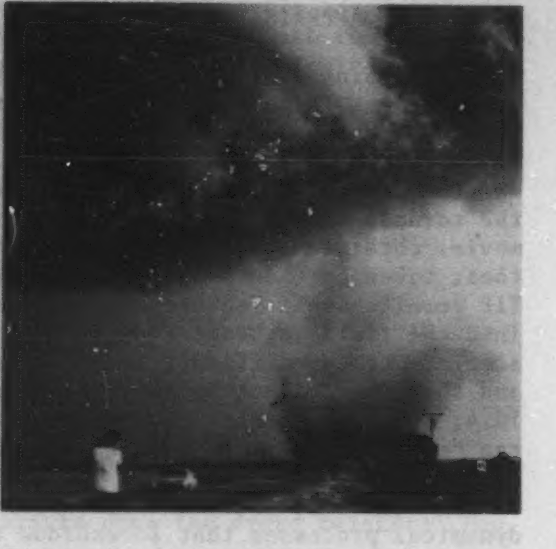

Figure 8.--Anticyclonic tornado near Alva, Okla., 6 June 1975. Note condensation funnel at top center (photo courtesy of J. Leonard and E. Sims).

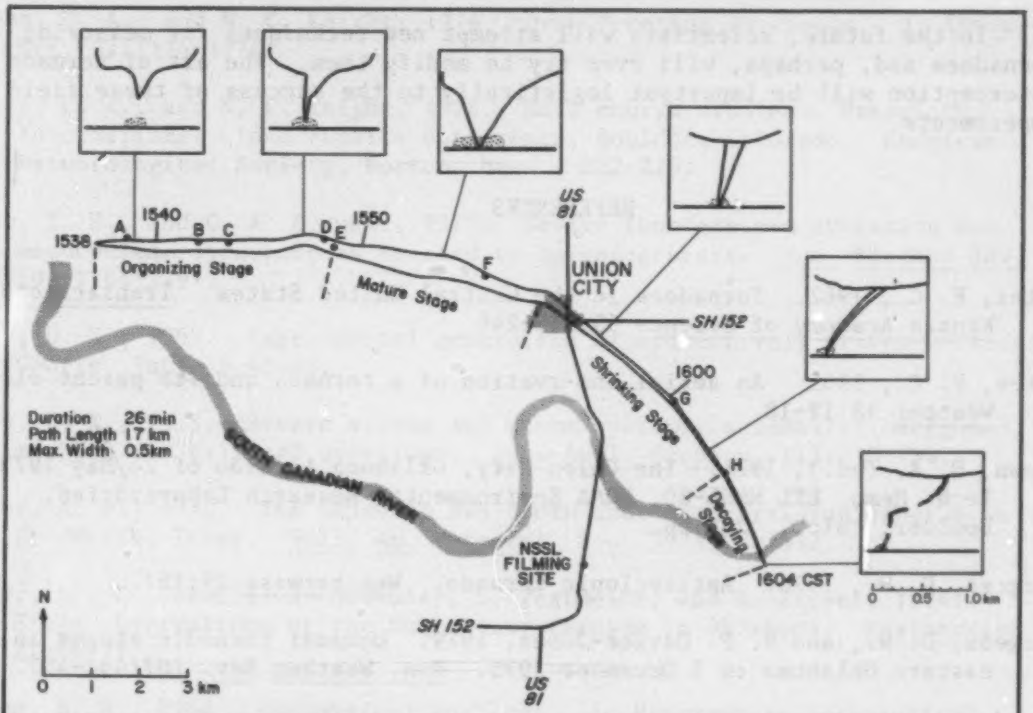
US 81
1538
A
1540
B
C
D
E
1550
F
Organizing Stage
Mature Stage
UNION CITY
SH 152
Shrinking Stage
1600
G
H
Decaying Stage
1604 CST
Duration 26 min
Path Length 17 km
Max. Width 0.5km
SOUTH CANADIAN RIVER
NSSL FILMING SITE
SH 152
US 81
N
0 1 2 3 km
0 0.5 1.0 km

Figure 9.--Damage path of the 24 May 1973 Union City, Okla., tornado with sketches of the funnel at different life cycle stages (Brown, 1976).

7. PROJECT APPRAISAL

Obtaining debris movies has proved more difficult than first anticipated. Nevertheless, high-resolution, analyzable 16-mm movies of three tornadoes have been obtained. Tornadoes have been filmed on other occasions but photogrammetric analyses of these movies were not performed because the tornado was too distant (or too near on one occasion!), the contrast was too poor, or the tornado traveled over terrain devoid of potential debris material. The movies obtained by intercept crews are more valuable scientifically than those taken by chance eyewitnesses because the high-resolution film used by TIP permits small features to be seen and tracked. Sending meteorologists into the field is beneficial in many other ways. Intercept teams can record accurate times--difficult to obtain post facto--of tornadoes and hailfall, and they can collect hailstones for scientific analysis (Knight and Knight, 1974; 1976). The rise rate of convective towers measured photogrammetrically can be compared with vertical velocities measured by Doppler radar. The everchanging visual outlines and motions of the clouds they see and record on film contain valuable information about severe-storm structure and the dynamical processes that foreshadow tornadoes. Many fruitless tornado theories would never have been conceived if the instigators had witnessed tornadogenesis firsthand. The field crews also may make fortuitous discoveries of great research value, such as the first proven anticyclonic tornado (Burgess, 1976). Occasionally, they may see severe storms that are so unadorned and have such elementary structure that their internal dynamics can be deduced from their visual appearance alone (e.g., Davies-Jones et al., 1976).

In the future, scientists will attempt new techniques for measuring tornadoes and, perhaps, will even try to modify them. The art of tornado interception will be important logistically to the success of these field experiments.

REFERENCES

Bates, F. C., 1962. Tornadoes in the Central United States. Transactions Kansas Academy of Science 65:215-246.

Bates, F. C., 1963. An aerial observation of a tornado and its parent cloud. Weather 18:12-18.

Brown, R. A. (ed.), 1976. The Union City, Oklahoma tornado of 24 May 1973. Tech. Memo. ERL NSSL-80, NOAA Environmental Research Laboratories, Boulder, Colo., 235 pp.

Burgess, D. W., 1976. Anticyclonic tornado. Weatherwise 29:167.

Burgess, D. W., and R. P. Davies-Jones, 1979. Unusual tornadic storms in eastern Oklahoma on 5 December 1975. Mon. Weather Rev. 107:451-457.

Burgess, D. W., J. D. Bonewitz, and D. R. Devore, 1978. Operational Doppler radar experiments: results year 1. Preprints, Eighteenth Conference on Radar Meteorology, Atlanta, Georgia. American Meteorological Society, Boston, Mass., 442-448.

Danielsen, E. F., 1975. A conceptual theory of tornadogenesis based on macro-, meso-, and microscale processes. Preprints, Ninth Conference on Severe Local Storms, Norman, Oklahoma. American Meteorological Society, Boston, Mass., 376-383.

Davies-Jones, R. P., and J. H. Golden, 1975. On the relation of electrical activity to tornadoes. J. Geophys. Res. 80:1614-1616.

Davies-Jones, R. P., D. W. Burgess, and L. R. Lemon, 1975. An atypical tornado-producing cumulonimbus. Weather 31:337-347.

Donaldson, R. J. and W. E. Lamkin, 1963. Visual observations beneath a developing tornado. Mon. Weather Rev. 92:326-329.

Eskridge, R. E., and P. Das, 1976. Effect of a precipitation-driven downdraft on a rotating wind field: a possible trigger mechanism for tornadoes. J. Atmos. Sci. 33:70-84.

Gannon, R., 1973. Tornado! How science tracks down the dread twister. Pop. Sci. 203:64-66, 122-125.

Golden, J. H., 1974. The life cycle of Florida Keys' waterspouts. I. J. Appl. Meteorol. 13:676-692.

Golden, J. H., and B. J. Morgan, 1972. The NSSL/Notre Dame Tornado Intercept Program, spring 1972. Bull. Am. Meteorol. Soc. 53:1178-1179.

Knight, C. A., and N. C. Knight, 1974. Drop freezing in clouds. J. Atmos. Sci. 31:1174-1176.

Knight, C. A., and N. C. Knight, 1976. Hail embryo studies. Preprints, International Cloud Physics Conference, Boulder, Colorado. American Meteorological Society, Boston, Mass., 222-226.

Lemon, L. R., and C. A. Doswell, 1979. Severe thunderstorm evolution and mesocyclone structure as related to tornadogenesis. Mon. Weather Rev. 107:1184-1197.

Lilly, D. K., 1965. Experimental generation of convectively driven vortices. Geofis. Intl. 5:43-48.

Lilly, D. K., 1975. Severe storms and storm systems: scientific backgound, methods and critical questions. Pure Appl. Geophys. 113:713-734.

Moller, A. R., 1978. The improved NWS storm spotters' training program at Ft. Worth, Texas. Bull. Am. Meteorol. Soc. 59:1574-1582.

Moller, A., C. Doswell, J. McGinley, S. Tegtmeier, and R. Zipser, 1974. Field observations of the Union City tornado in Oklahoma. Weatherwise 27:68-77.

Morton, B. R., 1966. Geophysical vortices. In Progress in Aeronautical Sciences, Vol. 7, Pergamon Press, New York, 145-193.

NOAA (National Oceanic and Atmospheric Administration), 1977. Tornadoes: a spotter's guide. Movie available from Disaster Preparedness Office, National Weather Service, Silver Spring, Md.

NOAA (National Oceanic and Atmospheric Administration), 1980. Tornado: a spotters guide. Slide series supplement to movie available from Weather and Flood Warnings Coordination Program, National Weather Service, Silver Spring, Md.

Rossmann, F. O., 1960. On the physics of tornadoes. In Cumulus Dynamics, Pergamon Press, New York, 167-174.

Rossow, V. J., 1970. Observations of waterspouts and their parent clouds. Tech. Note D-5854, National Aeronautics and Space Administration, Washington, D.C., 63 pp.

Smith, M., 1974. Visual observations of a tornadic thunderstorm. Weatherwise 27:256-258.

Tegtmeier, S. A., 1974. The role of the surface, subsynoptic system in severe weather forecasting. Master's thesis, University of Oklahoma, Norman, 66 pp.

Vonnegut, B., 1960. Electrical theory of tornadoes. J. Geophys. Res. 65:203-212.

Ward, N. B., 1961. Radar and surface observations of tornadoes on May 4, 1961. Preprints, Ninth Weather Radar Conference, Kansas City, Missouri. American Meteorological Society, Boston, Mass., 175-180.

III. OBSERVATIONS FROM INSTRUMENTED AIRCRAFT

John McCarthy and Donald L. Veal

1. INTRODUCTION

In basic flight training, we are told in hundreds of ways, "Thunderstorms and airplanes do not mix!" Yet our knowledge of thunderstorms and of airplanes has grown in a nearly symbiotic relationship.

Although a history of the relationship between thunderstorms and aviation is given in Vol. 1, Ch. VI, a brief review is nevertheless useful. As the use of airplanes became well established for transportation in the 1930's and for weapon delivery systems during World War II, more close encounters with thunderstorms occurred. With good reason, pilots learned to fear them, avoiding them at almost any cost. As World War II came to a close, partly because of this fear little was known about thunderstorm interiors. Lightning and hail encounters were known from nearby passes alone.

As civil transportation and military needs expanded, aviators realized that complete avoidance of thunderstorms was impractical and thunderstorm research efforts were intensified. Analyses of data from the first comprehensive field program were reported in The Thunderstorm by Byers and Braham (1949). The exercise on which the study was based included the first research-oriented aircraft penetrations of thunderstorms. Results represented a substantial advance in understanding of thunderstorms; much of our knowledge concerning the cellular nature of thunderstorms came from the Thunderstorm Project and was a foundation of pilot training in aviation hazards.

As various aircraft types were developed and route coverage was increased, particularly in the 1950's and early 1960's, much practical experience was gained in unavoidable thunderstorms. The vast increase in flight numbers and range by piston engine aircraft such as the C-121 superconstellation, DC-6, and DC-7, and jet aircraft such as the Boeing 707, Convair 880, and DC-8, increased the emphasis on understanding thunderstorms and thunderstorm hazards. The use of radar to probe remote thunderstorms considerably increased our understanding of the structure of thunderstorms and made possible additional studies of thunderstorms using aircraft for direct probes.

In 1958, the U.S. Weather Bureau established the National Severe Storms Project in Kansas City, Mo. The operational arm of this project remained there as the National Severe Storms Forecast Center when the research arm moved to Norman, Okla., in 1964 to become the National Severe Storms Laboratory (NSSL). Since then, numerous thunderstorms have been penetrated by aircraft, usually of military type, bearing special instruments and operating in the NSSL program. Studies of the near-thunderstorm environment have also been conducted with instrumented aircraft not suitable for flight within thunderstorms.

Several major aircraft facilities have been developed and have devoted part of their effort toward understanding the thunderstorm. The Research Flight Facility (RFF) of NOAA was established in 1962, with initial and

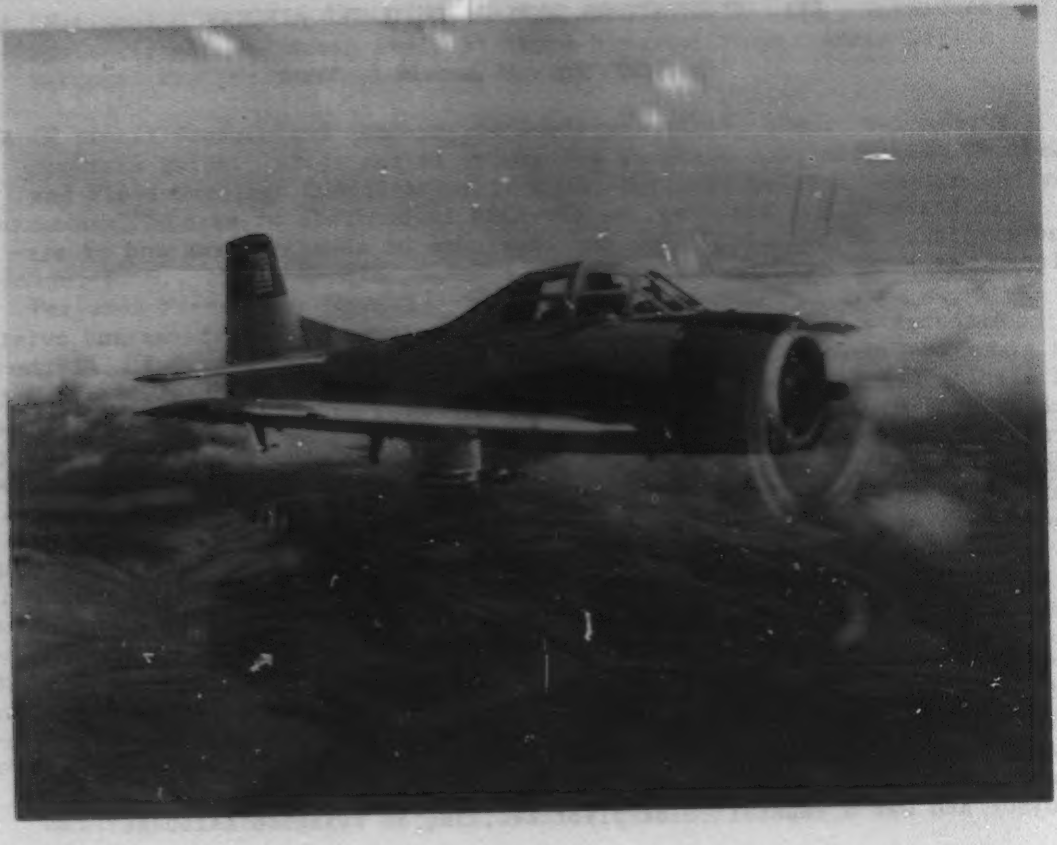

Figure 1.--T-28 armored hailstorm penetration airplane operated by the South Dakota School of Mines and Technology. Major focus of instrumentation system is microphysical measurements (photo by Brooks Martner and made available by Paul Smith, SDSMT).

primary emphasis on serving needs of hurricane operations and research. In 1964, the Research Aviation Facility (RAF) of the National Center for Atmospheric Research (NCAR) began flight operations in support of NCAR and university research. Important flight research programs have also been undertaken by the Illinois State Water Survey, Colorado State University, the Universities of Chicago, Nevada, Washington, and Wyoming, and the National Aeronautical Establishment of Canada, both alone and in collaboration with other groups such as NCAR and NSSL. Figures 1-3 show several research aircraft for storm penetrations and for flight in the near-thunderstorm environment. Table 1 lists parameters measured in recent thunderstorm research and the aircraft used as platforms for the measurements.

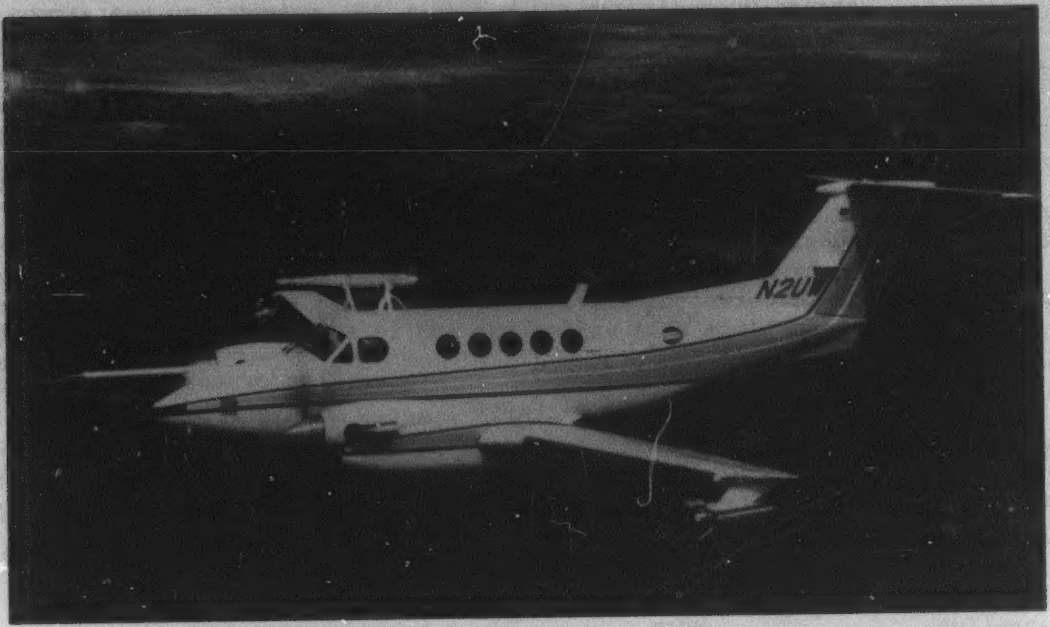

Figure 2.--Beech King Air cloud physics airplane developed by the University of Wyoming for the Bureau of Reclamation. This aircraft probably has the most sophisticated data recording and retrieval system of any meteorological aircraft.

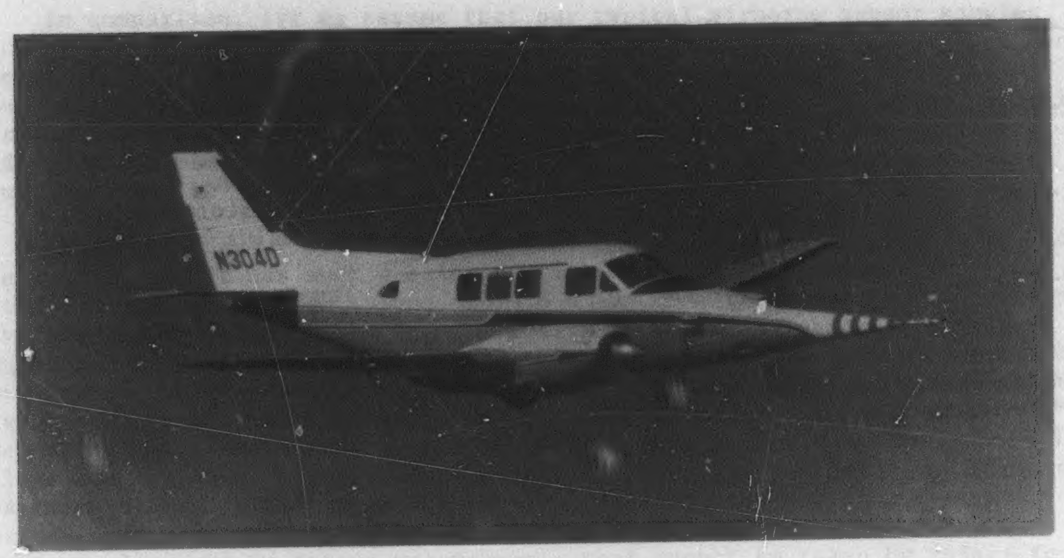

Figure 3.--Beech Queen Air, one of five instrumented aircraft operated by NCAR. The three-dimensional wind measuring system is one of the best in use (courtesy of Paul Spyers-Duran, NCAR).

Table 1.--Thunderstorm research platforms

Airplane	Facility	Profile
F4C Phantom	USAF	Thunderstorm penetration
F101 Voodoo	Colorado State University	Thunderstorm penetration
F101 Voodoo	NASA	Thunderstorm penetration
T-28*	South Dakota School of Mines	Thunderstorm penetration (cloud physics)
Beech King Air**	University of Wyoming	Thunderstorm environment (cumulus congestus)
Beech Queen Air	University of Wyoming	Thunderstorm environment (cumulus congestus)
Sabreliner	NCAR	Midlevel environment
Beech Queen Air†	NCAR	Cloudbase environment
Piper Navajo	Meteorology Research, Inc.	
Electra	NCAR	Subsynoptic environment
Lear Jet	University of Chicago	Thunderstorm top environment
Lear Jet	Colorado International Corp.	
C-130	NOAA	Thunderstorm-hurricane (cumulus congestus)
P-3 Orion	NOAA	Thunderstorm-hurricane (cumulus congestus)

* See Fig. 1.
** See Fig. 2.
† See Fig. 3.

2. COMPARISON OF AIRBORNE AND GROUND-BASED THUNDERSTORM PROBES

Why should aircraft be used in thunderstorm research? Would it not be more sensible to use a system for remote probing such as ground-based radar? Since radar is the most often used thunderstorm probe, a comparison of the two approaches is worthwhile.

An aircraft is used usually as a direct in situ probe; radar is indirect. (Airborne radar systems, of course, complicate our comparison.) The obvious advantage of ground-based radar is its relatively nonhazardous position compared with that of a penetrating aircraft. Furthermore, radar is able to sample a much larger volume of the atmosphere in a much shorter period of time.

Let us examine sample volume, sample time, and representativeness of sample. For simplicity, we treat a thunderstorm as a cubical volume, 10 km on a side. First consider the radar looking at our storm volume of 10^3 km^3 in approximately 1-min sample time. The radar samples an individual volume that is dependent on the illumination area A_i:

$$A_i = \frac{\pi R^2 \theta^2}{4} , \qquad (1)$$

where R is the range to the target and θ is the beamwidth in radians. The sample volume depends also on the pulse length h, typically 300 meters. The individual sample volume is $A_i(h/2)$; for a 1° beam and an average distance to the storm of 75 km, this is approximately 0.2 km^3. If our storm is sampled uniformly, in 1 minute we can obtain 5.0×10^3 total radar samples distributed throughout the storm.

In comparison, let us assume that our typical airborne sensor samples 1 cm^2 while flying through the storm at 150 m s^{-1} (a typical jet penetration speed); the horizontal penetration time would be 67 seconds. The total penetration sampling volume would be 10^6 cm^3 or 10^{-9} km^3. If the airplane instrumentation system were able to sense and record data at 8 Hz, then each individual sample would refer to 18.8×10^2 cm^3, and during the pass there would be 5.4×10^2 individual samples.

Clearly the radar sees a much larger volume than does the aircraft. However, the aircraft has much greater resolution along the flight path: the aircraft senses a minimum volume of 18.8×10^2 cm^3; the radar cannot resolve a volume smaller than 2×10^{14} cm^3. But is the aircraft observation representative of the storm? The ratio of the total aircraft sample volume to the total radar sample and storm volumes is 10^{-12}, but the airplane data have much higher resolution. As with most measurement systems, there are trade-offs: in the case of airborne instrumentation, we gain resolution at the expense of volume and representativeness of the sample. Also, ground-based and airborne instruments sense different weather parameters, and the airborne system serves relatively specialized needs. Nevertheless, the airborne in situ platform allows us to obtain measurements that cannot be taken by radar; for cloud microstructure, high-resolution velocity and turbulence, and atmospheric chemistry, there is no replacement for the airborne platform (Sec. 3a). Clearly, the proper use of an airborne system involves its combination with other measurement systems, such as conventional and Doppler radar, rawinsonde, and surface recording networks (see Sec. 5).

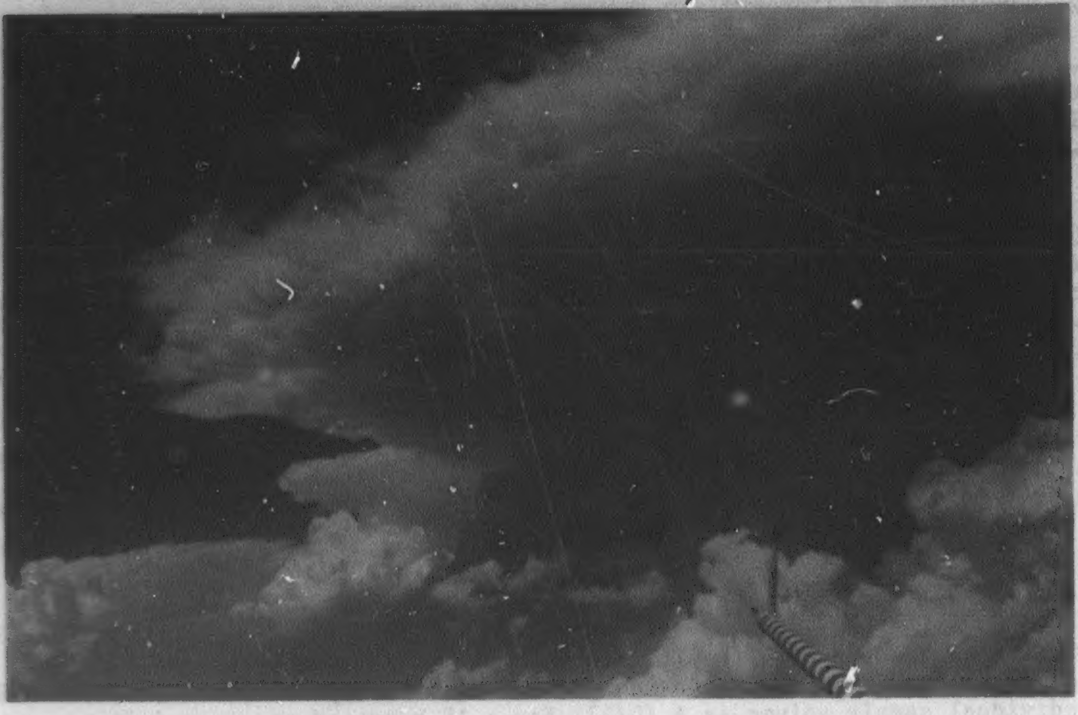

Figure 4.--Tornado-bearing thunderstorm as viewed from University of Wyoming Queen Air for a University of Oklahoma study of an Oklahoma dryline.

The unique visual perspective from aircraft is especially complementary to radar observations. The airborne observer is sometimes in a good position to direct the operation of data acquisition systems overall, and later to propose meaningful approaches to data synthesis. Also, a number of thunderstorm features (see, e.g., Fig. 4) are detected best by real-time visual observations; gust fronts, tornadoes, and tornado cyclones occurring in the subcloud region of the planetary boundary layer are easily seen from a low-flying airplane. Research mission objectives can be varied on the basis of these real-time visual observations.

3. MEASUREMENTS BY AIRBORNE SENSORS

a. State of the atmosphere

The synthesis of state-of-the-atmosphere parameters is basic to many important calculations in thunderstorm research. Thus measurements of these parameters are an essential part of the data obtained from the aircraft platform. Figure 5 shows a complement of state sensors mounted on an aircraft.

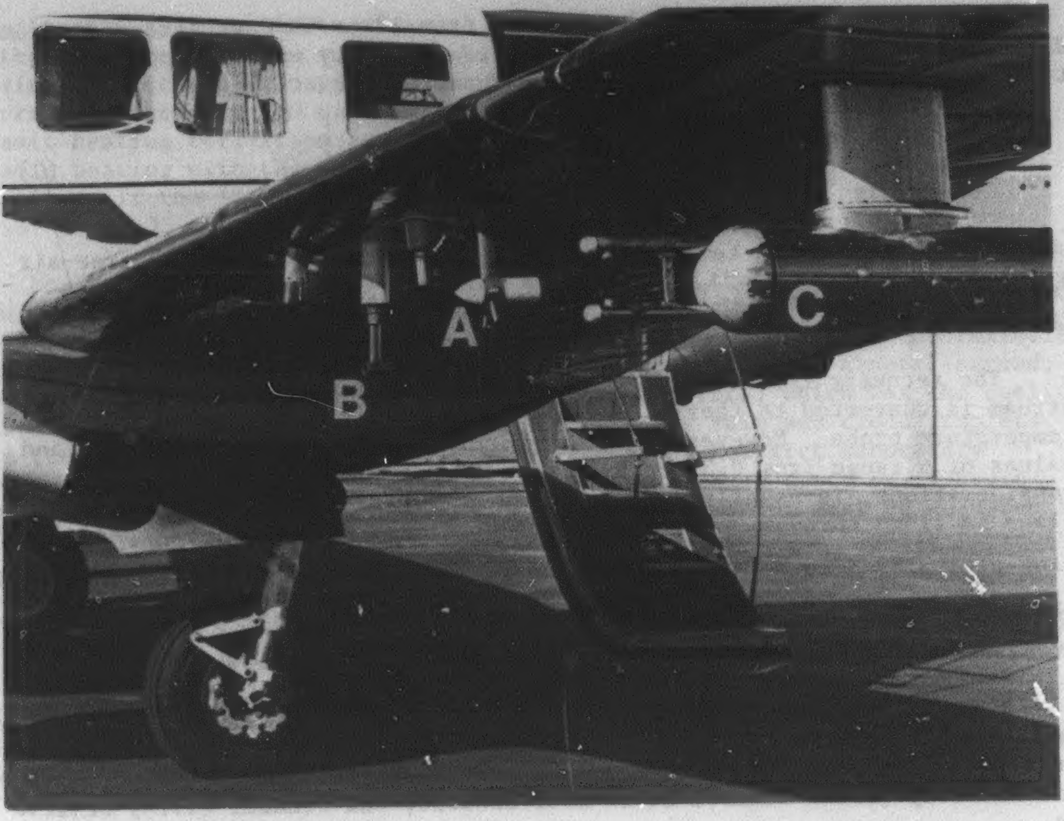

Figure 5.--Instruments mounted under the wing of NCAR Queen Air: (A) reverse flow probe for incloud temperature sensing; (B) Johnson-Williams Liquid Water Content Meter; and (C) PMS two-dimensional optical imaging probe (courtesy of NCAR).

(1) Temperature

The principal problem in measuring free-air temperature from an aircraft is placement of the measuring instrument on the airplane. The instrument is subject to dynamic heating, radiation, conduction and viscous effects, cloud and precipitation elements, and side effects of de-icing. A number of techniques have been attempted for observing free-air temperature, the most common involving a platinum resistance element mounted on an aircraft so as to be subjected to the airstream. This approach yields the total temperature, which is the actual temperature of the sensor and which yields the air temperature after corrections. These consider dynamic heating, or the rise in temperature in the airstream at the thermometer when it is brought momentarily to rest, and water or ice on the element. Effects of water and ice are particularly difficult to treat; hence the reverse flow probe of Rodi and Spyers-Duran (1972) has been devised, shown as A in Fig. 5. This probe shields the element from direct exposure to the airstream; the airflow is reversed with separation of the ice and water particles within the airstream, and the temperature-measuring element mounted in the probe is not wetted.

The dynamic heating factor can vary from 1° to 50°C at airspeeds from 85 kn to the speed of sound, so a correction clearly must be applied. A typical expression suitable for dynamic heating correction is

$$T_s = T_f + \alpha(1.3189 \times 10^{-4}\ \mathrm{TAS}^2)\ , \qquad (2)$$

where T_s is the sensor temperature in degrees Celsius, T_f is the free-air temperature in degrees Celsius, TAS is the true airspeed in knots, and α is the recovery factor.

The recovery factor reduces to 1.0 when all kinetic energy of the airstream is converted to thermal energy; the probe is then called a total-temperature probe. However, varying amounts of ventilation do occur, and values of α range from 0.5 to >0.9; α, presumably determinable by theoretical considerations, is usually determined by an empirical "speed run." The airplane is flown through potentially isothermal air at varying airspeeds, and a plot of $1.3189 \times 10^{-4}\ \mathrm{TAS}^2$ versus $T_s - T_f$ is made; α is the slope of the line of plotted points. Since TAS depends on T_f, an iterative procedure is actually required here, as indicated in the discussion following Eq. 6 below.

When a temperature sensor is flown through a cloud, the heating process cannot be assumed to remain free of wet-bulb effects. Whether this is a problem has been the subject of much discussion. Telford and Warner (1962) and McCarthy (1974) believe it is not; Lenschow and Pennell (1974) believe it is.

Finally, calibration of any temperature probe installed on an airplane involves not only the recovery factor, but also the baseline (DC) offset, if one exists in the data system. Flight past a tower at different temperatures and airspeed or immersion of the probe in an ice bath while on the ground establishes the appropriate offsets.

(2) Humidity

Humidity has been measured from aircraft in several ways: (1) use of wet- and dry-bulb thermometers; (2) direct measurement of dewpoint by deposition of dew or frost on a nonsorptive, inactive surface whose controlled temperature is the dewpoint when the dew or frost remains the same thickness; (3) measurement of the absorption cross section of water vapor in the Lyman-alpha spectral region with a spectral hydrometer; or (4) measurement of the microwave refractive index with a microwave resonance cavity.

Early airborne measurements of humidity used a pair of simple wet- and dry-bulb mercury thermometers mounted outside or through the skin of the aircraft. In the 1940's, mercury thermometers mounted in special housings were the standard humidity instruments for the United States. For slow aircraft, or when response time is not a problem, this type of instrumentation is moderately satisfactory. The wetted wick measurement must be used in the psychrometric equation, which relates various moisture parameters (List, 1958).

An alternate approach is to attach a wetted wick to platinum resistance wire or the thermocouples and expose it to the air either directly or mounted in a housing. For example, copper-constantan thermocouples were mounted in a reverse-flow housing and used to determine the wet-bulb depression, with a dynamic heating correction applied. This system must also be corrected for dynamic heating with the appropriate wick pressure used in the psychrometric equation. If the liquid water is not separated from the air before the sensor is read, the dry-bulb measurement has no significance.

Mullin and Wolber (1964) describe a hygrometer that measures directly by sensing dew or frost on a thermoelectrically cooled surface. The Cambridge Systems dewpoint hygrometer is now probably the most widely used and reliable instrument. The response time of this instrument is usually about 1 second; however, it may be much longer at low ambient dewpoints, which tax the cooling capacity of the instrument. An inlet that deflects rain and cloud droplets from the air sample has been developed by the Naval Research Laboratory (Ruskin and Scott, 1974). If the cooled surface becomes dirty or if hygroscopic material collects on the surface, the control point must be adjusted to yield the proper dewpoint. Periodic cleaning of the surface usually prevents this problem.

Ruskin (1967) and Buck (1973) describe the Lyman-alpha hygrometer, which responds in a few milliseconds to absolute humidity (g m^{-3}), which is convertible to other humidity units when pressure and temperature are known. This instrument has problems of drift of the source, detector performance, and window deterioration under moist conditions. These problems cause calibration instability, but if they can be overcome, the system should be ideal for airborne use.

With independent measures of pressure and temperature, humidity can be calculated also from the microwave refractive index. A microwave resonance cavity flushed with ambient air, which is separated from water drops, can be used to measure the microwave refractive index. The response time of this technique, several milliseconds, is a function of the flushing time and therefore is comparable with that of the Lyman-alpha instrument. An airborne refractometer has been operated by the Research Aviation Facility at NCAR.

(3) Pressure

In principle, pressure is the simplest atmospheric parameter to measure from an airborne platform. The most important problem is proper location of the static pressure source on the aircraft. Pitot-static probes have been designed in which the static ports are located symmetrically about the sideslip, or yaw axis. When a pitot-static probe is used, wind tunnel experiments can be conducted and empirical corrections established as a function of the angles of attack and sideslip. To minimize the reduction in static pressure resulting from increasing angles of attack and sideslip, the static-pressure source is often located on the empennage of the aircraft. However, for accurate measurements, the static-pressure defect or error must be experimentally evaluated; such evaluation can be accomplished by installing an accurate pressure device in the aircraft and flying at different airspeeds by a station (tower) at an altitude of known pressure. Depending on the aircraft and static-source location, corrections ranging from zero to 10 or more millibars may be necessary. Once the static-source errors are resolved, the determination of flight level pressure depends upon only the aircraft pressure sensor.

Pressure sensors are currently available that are stable over a wide range of environmental conditions, operate on various principles, and yield resolutions of fractions of millibars. A straightforward process converts the pressure values to pressure altitude using the ICAO (International Civil Aeronautical Organization, a UN affiliate) standard atmosphere or other pressure-height relationship.

b. State of the aircraft

(1) Indicated airspeed

Indicated airspeed (IAS) for an aircraft is determined from the difference between the pitot and static pressure at the aircraft flight level. Pitot pressure is not particularly difficult to observe, especially for small angles of attack and sideslip. For larger angles of attack, a pitot tube that aligns itself with the relative airflow can be used to minimize the errors. An additional source of error occurs in precipitation or in the presence of supercooled water. By heating the pitot probe, both effects can be minimized. The main error in IAS or pitot-static pressure difference is static-pressure defect or static-pressure error.

The conservation of energy in an airstream may be expressed as

$$C_p dT + d\left(\frac{V}{2}\right)^2 = 0 \ , \qquad (3)$$

where T is temperature, V true airspeed, and C_p heat capacity of air at constant pressure.

By using the Poisson relation between temperature and pressure for adiabatic processes, it can be shown that

$$V = \left\{2C_p T_f\left[\left(\frac{P + \Delta P}{P}\right)^{R/C_p} - 1\right]\right\}^{1/2} \ , \qquad (4)$$

where T_f is the free-air temperature, P the total pressure (static pressure), ΔP the differences between pitot pressure and static pressure, and R the gas constant of air,

Indicated airspeed may be defined as

$$IAS = \left\{2C_p T_a\left[\left(\frac{P_a + \Delta P}{P_a}\right)^{R/C_p} - 1\right]\right\}^{1/2} \ , \qquad (5)$$

where T_a and P_a are temperature and pressure of the ICAO standard atmosphere at sea level.

(2) True airspeed

For cases in which ΔP is much less than P, the indicated and true airspeed (TAS) are related by

$$TAS = IAS(\rho_o/\rho)^{1/2} \ , \qquad (6)$$

where ρ_o is the density of air at sea level of the standard atmosphere and ρ is the density of the air through which the aircraft is flying. Because evaluation of the density terms in Eq. 6 involves knowledge of the temperature, it is necessary to use an iterative procedure to solve Eqs. 4, 5, and 6 for T_f with desirable accuracy.

Examination of Eq. 5 indicates that errors in TAS are dependent on errors in static pressure, pitot-static difference, and free-air temperature. If accuracy in TAS is required, considerable care must be taken in selecting, locating, and calibrating the pressure and temperature sensors.

(3) Aircraft position

The simplest technique for position keeping involves continuous recording of two lines of position from two VOR* stations; this approach requires the aircraft always to be within radio reception range of both stations. It usually gives an aircraft track within 2 km of the true track, though accuracy is a function of range from the VOR station and calibration of the VOR receivers. Alternatively, one line of position (LOP) and the distance along the LOP can be continuously recorded from one VOR station. The VOR-DME† system locates the aircraft track with about the same accuracy as the dual VOR system. If two (preferably three) or more VOR stations are within radio range, multiple DME fixes can be obtained for better track accuracies (±0.5 km of true track). However, the need for reception of more than one VOR may be quite limiting since this enroute navigation system was laid out to provide navigation signals to a given area without much overlap, except in congested areas near metropolitan airports. Recent developments in very low frequency (VLF) navigation systems make aircraft position keeping reasonably inexpensive over a much wider range of altitudes and areas.

By integrating the groundspeed and drift angle defined by a Doppler navigation system, the position of the aircraft as a function of time can be estimated. Because of errors in groundspeed and drift angle during turns of the aircraft, and because these errors are cumulative, this technique is not suitable for long-term position keeping. It is, however, good for short-term dead reckoning, especially with frequent ground or other references.

An inertial navigation system (INS) comprises a gyro-stabilized platform and a computer. Accelerometers sense velocity changes along all three Cartesian axes, and hence define the quantities required to determine aircraft position at all times. The INS locates the aircraft during flight from a known position without reference to any signals from stations on the Earth's surface. Although the INS is the most accurate system for continuous tracking, position errors do occur and they accumulate with time. For greatest position accuracy, external position references (i.e., visual reference points) should be pro-

---

*Visual Omni Range is the national airspace principal navigation aid, which permits the determination of the aircraft's magnetic bearing to or from the ground VOR station. The system is line of sight.

†Distance Measuring Equipment allows the determination of the slant distance between the DME site on the ground and the aircraft in flight.

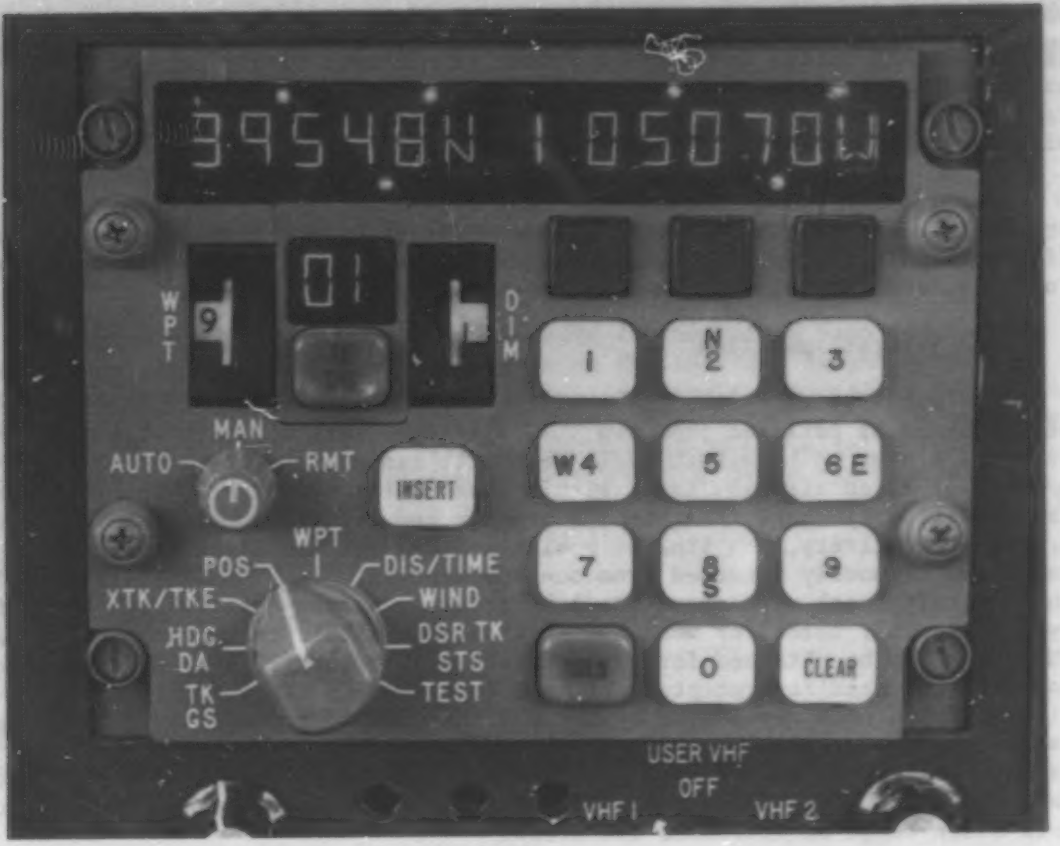
39548N 105070W
01
WPT 9
DIM
1
N 2
3
W4
5
6E
7
8 S
9
0
CLEAR
INSERT
MAN
AUTO
RMT
WPT 1
POS
DIS/TIME
XTK/TKE
WIND
HDG DA
DSR TK
STS
TK GS
TEST
USER VHF
OFF
VHF 1
VHF 2

Figure 6.--Display unit of the inertial navigation system (INS) on NCAR Queen Air. The device, a Litton LTN-51, is an important component in the wind-measuring system and in aircraft position determination (courtesy of NCAR).

vided at various points along the flight path. The "front-end" display of the NCAR inertial navigation system is shown in Fig. 6.

Real-time onboard display of the aircraft position can be accomplished by driving an x-y plotter or CRT display with any of the position-keeping techniques. An example of a reconstructed flight track using VOR-DME and airborne Doppler navigation radar is given in Fig. 7. Aircraft position information is particularly critical when an overall synthesis of data systems (i.e., aircraft and radar) is required. Too little emphasis has been placed on aircraft position in many research endeavors, and efforts should be made to upgrade this measurement.

c. Measurement of air velocities

Measurements of air motion are usually divided into three categories: (1) large-scale vertical motion, (2) large-scale horizontal motion, and (3) small-scale motion or turbulence. Large-scale vertical motion can be

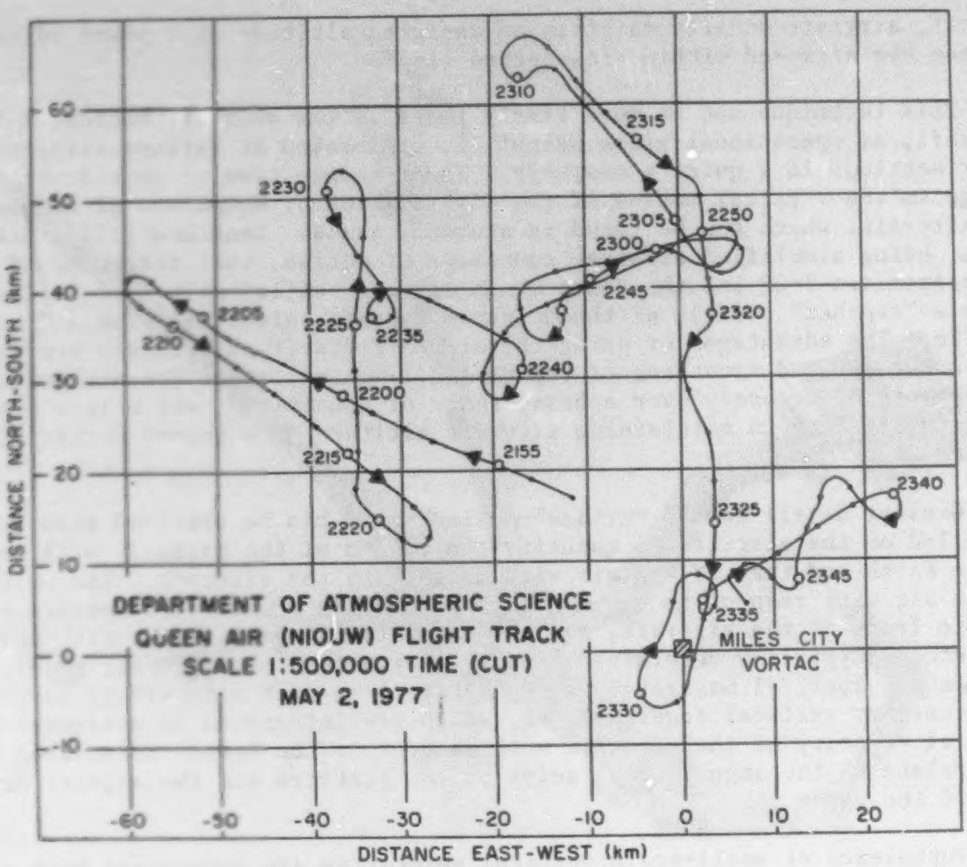
DEPARTMENT OF ATMOSPHERIC SCIENCE
QUEEN AIR (N10UW) FLIGHT TRACK
SCALE 1:500,000 TIME (CUT)
MAY 2, 1977
MILES CITY
VORTAC
2155
2200
2205
2210
2215
2220
2225
2230
2235
2240
2245
2250
2300
2305
2310
2315
2320
2325
2330
2335
2340
2345
DISTANCE NORTH-SOUTH (km)
60
50
40
30
20
10
0
-10
DISTANCE EAST-WEST (km)
-60
-50
-40
-30
-20
-10
0
10
20

Figure 7.--Flight track of Wyoming Queen Air, reconstructed using VOR-DME and airborne Doppler navigation radar. Aircraft position is with respect to Miles City, Mont., VORTAC navigation aid; the research supports the High Plains Experiment.

determined when the aircraft is in equilibrium with the vertical air motion: then either the aircraft itself can be used as a sensor, or various sensors that detect the motion of the aircraft with respect to the Earth as well as the relative motion of the air can be attached to the aircraft.

Horizontal air motion measurements require sensors such as an INS on the aircraft to measure the position or velocity of the aircraft with respect to the Earth with the INS capability coupled to airspeed and heading information. In general, if the measurements are made at the same point on the aircraft, the velocity of the air with respect to the ground is the sum of the velocity of the aircraft with respect to the Earth and the velocity of the air with respect to the aircraft.

The most elementary technique for observing large-scale vertical air motion uses the aircraft as the primary sensor and requires the pilot to maintain a constant airspeed and power setting, thus allowing the aircraft to move up and down with the vertical air motion field. This type of flying is

typical; aircraft usually maintain an assigned altitude with power adjustments to keep the airspeed within preselected limits.

This technique can be more finely tuned if the vertical motion of the aircraft, at operational gross weight, is calibrated at various airspeeds and power settings in a quiet atmosphere. The response time of an aircraft to a change in the vertical motion of the air is given by equations of motion of the aircraft, which can be found in standard texts. Lenschow (1976) has shown, using simplified airplane equations of motion, that responses of the North American T-28 and the Beech Queen Air are sufficiently fast to distinguish a "top-hat" profile of thunderstorm updraft velocities from a "smooth" profile. The advantages of using the aircraft itself as a sensor are simplicity, low cost, and smoothing of the vertical-motion data. The disadvantage is the lack of accuracy over a broad range of conditions, which is a result of the difficulty in maintaining aircraft altitude or airspeed within close tolerances.

Greater detail in the vertical-motion field can be obtained with sensors installed on the aircraft to quantify the motion of the aircraft with respect to the Earth and that of the air with respect to the aircraft. The velocity of the air with respect to the aircraft is usually measured by sensors on a boom in front of the aircraft, and the velocity of the aircraft with respect to Earth is typically determined from accelerometers or radar altimeter measurements. Inertial navigation systems have been used extensively to provide the necessary vertical accelerations, which are integrated to determine the vertical velocity of the aircraft with respect to the Earth. Associated problems relate to the angular accuracies of the platform and the angular drift rate of the gyros.

Turbulence or small-scale vertical velocities are determined with a gust probe, which consists of fast-response pitch and yaw vanes and a pitot tube. The vanes can be either rotating or constrained. The rotating vane turns freely in the wind gust, and the angular departure of the vane from level is related to accelerations. In the constrained vane, strain sensors are calibrated to accelerations. Gust probes sometimes use pressure sensors in place of vanes. The gust probe is always mounted on a forward boom to obtain measurements ahead of the flow affected by the aircraft. If the inertial platform is physically attached to a rigid boom, the velocity of the vanes with respect to the platform is found by a simple geometric calculation that takes rotation into account. If the inertial platform is well removed from the boom and/or the boom has oscillations independent of the platform, then the boom is referred to as a "floating" boom and must have vertical and lateral accelerometers attached to calculate the velocity of the vanes with respect to the platform. Figure 8 shows the NCAR gust probe mounted on a nose boom on the NCAR Electra.

Determination of horizontal air motion from an airborne platform requires knowledge of the track, heading, groundspeed, and true airspeed of the aircraft. Doppler navigation systems measure the groundspeed and drift angle (the angle between true course or ground track and true heading of the aircraft); when these are combined with the aircraft heading and true airspeed, horizontal wind can be determined. Without a yaw vane, the aircraft is the sensor that limits horizontal resolution of the wind field to the product of aircraft response time and horizontal speed. Since the Doppler system measures drift angle, errors in the compass heading affect determinations of wind direction rather than magnitude. If a yaw vane is used to account for rela-

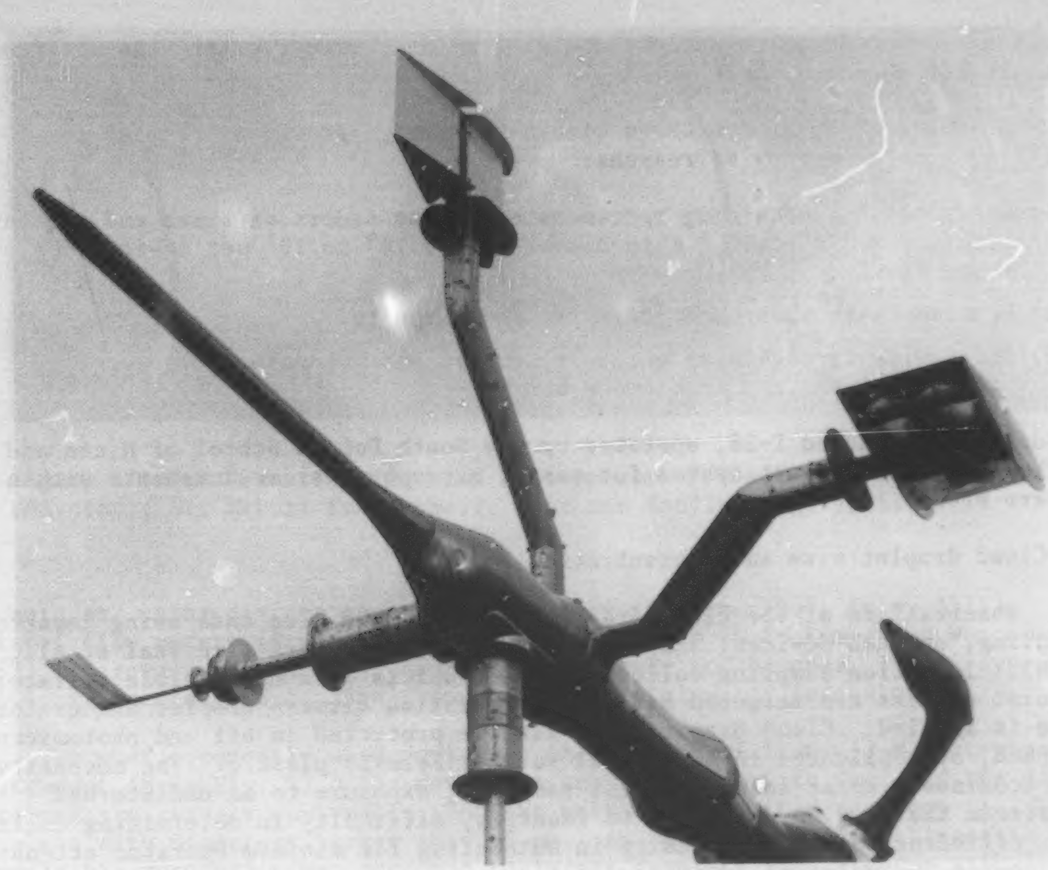

Figure 8.--Gust probe assembly of NCAR Electra aircraft, including fast-response pitot tube, fixed and rotating vanes for momentum sensing, and a fast-response temperature sensor (courtesy of NCAR).

tive air motion about the vertical axis of the sensor, resolution of the horizontal wind field is determined by the Doppler system response, which is a few hundred meters.

Several hybrid systems are now being tested. A hybrid system is one in which an independent measurement of the position of the aircraft is used to update the long-term drift inherent in state-of-the-art inertial navigation systems. Independent position measurements include pressure altitude, DME/VOR, multiple DME, VLF, and even multiple inertial navigation systems on the same aircraft.

4. MICROPHYSICAL MEASUREMENT TECHNIQUES

The basic microphysical parameters required for understanding of precipitation processes within severe storms are liquid water content and cloud droplet, raindrop, and ice particle size and concentration. Measurements of cloud condensation nuclei, ice nuclei, and electrical parameters are also desirable but are not addressed here.

Measurement of hydrometeors within the severe-storm environment is difficult for a variety of reasons:

(1) Difficulty in obtaining specimens over many orders of sizes and concentrations, 10^{-6} to 10^{-1} m in diameter, and 10^{9} to 10^{2} per cubic meter, respectively.

(2) Problems with instrument calibration stability.

(3) Difficulty in obtaining suitable sensors and aircraft sufficiently sturdy to withstand turbulence and hail.

To date, the armored T-28, operated by the South Dakota School of Mines and Technology, is the best system for making microphysical measurements within severe storms.

a. Cloud droplet size and concentration

Observations of the cloud droplet spectrum have been made using impactor sampling, optical devices, and electrostatic disdrometers (see Veal et al., 1978). Impaction sampling collects cloud droplets on a depressible surface; droplet craters are measured and a known relation between droplet and crater size is applied. Cloud droplets can also be protected in oil and photomicrographed, or replicated in a material such as Formvar plastic. The necessity for continuous or at least frequent sampling, exposure to an undisturbed airstream that may be difficult to identify, difficulty in determining collection efficiencies, and difficulty in automating for minimum operator attention all reduce the value of impaction devices.

At least three devices have been used for optical sensing of cloud droplet size and concentration: the Particle Measuring System spectrometer (Knollenberg, 1976), the Blau nephelometer (Blau et al., 1970), and the devices developed by Soviet scientists and described by Laktionov et al. (1972). These devices count individual cloud droplets by detection pulses of scattered light and determine their size by electronic analysis of pulse height.

The most important use of these devices is to observe droplet concentration and spectrum shape. The behavior of the tails of the spectrum (concentrations of larger droplets) is often of particular importance. Ease of data analysis and good spatial resolution of the spectrum are also highly desirable. The optical devices and the electrostatic disdrometer continually monitor the spectrum with about 2-mm size discrimination, and the main part of the spectrum is in readily analyzable form. Optical and disdrometer techniques are superior to any impaction technique with respect to sample continuity and ease of data analysis.

Figure 9 shows the Particle Measuring Systems, Inc., Forward Scattering Spectrometer Probe (FSSP), and Fig. 10 illustrates its optical system. FSSP incloud flight examples are given in Fig. 11.

b. Liquid water content

Liquid water content can be calculated by summation of drop size spectrum (observed by the previously discussed devices) or by direct bulk measurement

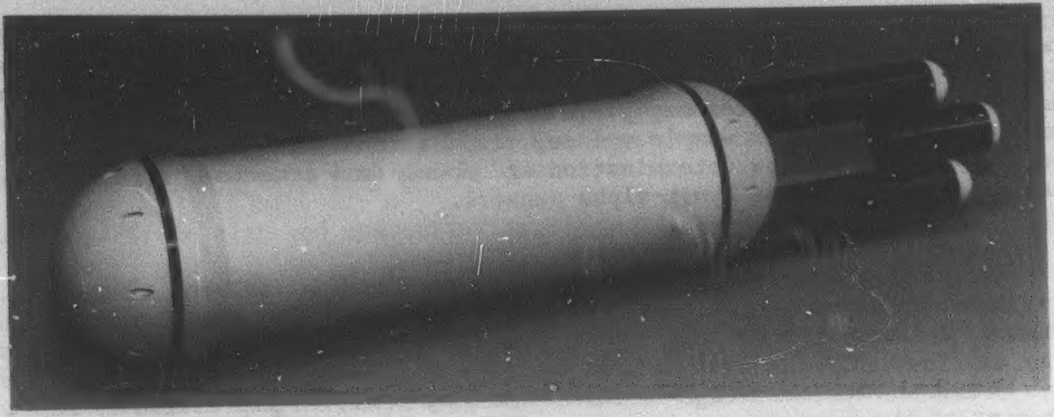

Figure 9.--PMS Forward Scattering Spectrometer Probe (FSSP) (courtesy of PMS, Inc., Dr. Robert Knollenberg; also see Knollenberg, 1976).

techniques, using devices such as evaporators (Ruskin, 1967; Kyle, 1975), optical flow meters (Brown, 1973), transmissometers (aufm Kampe and Weickmann, 1952), microwave radiometers, paper tapes (Warner and Newnham, 1952), synthetic filaments (Sasyo, 1968), and hot-wire total water indicators.

The most frequently used device is the Johnson-Williams (J-W) hot-wire instrument (B in Fig. 5). The device is very convenient to use, and the data obtained are readily analyzable, but the unit has a limited response to droplets with diameters larger than ~3 mm. An improved version alleged to have faster response time, response to larger droplets, and greater stability

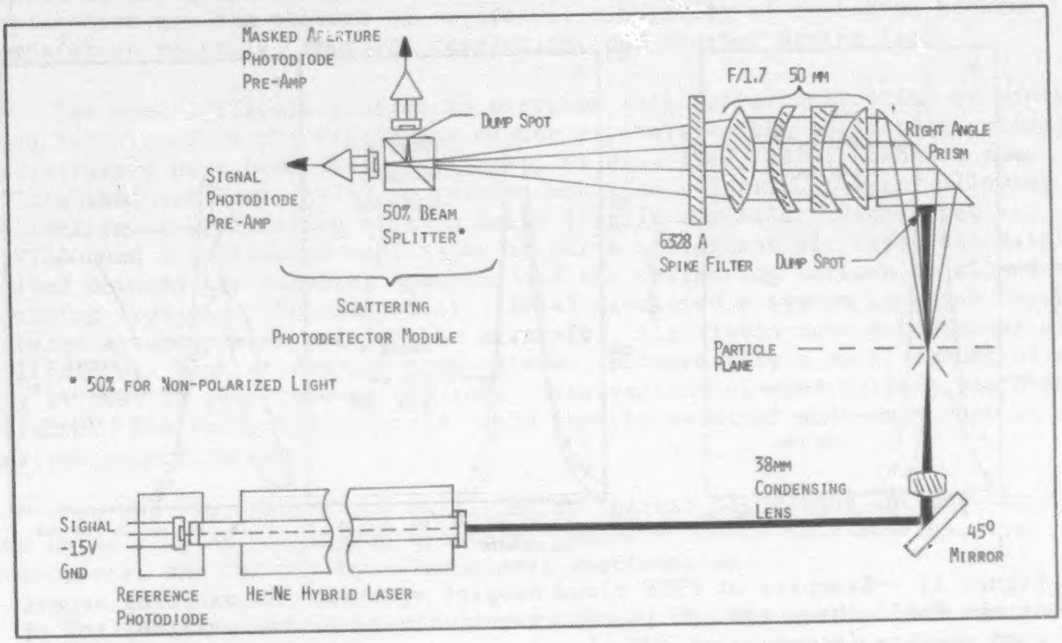
Masked Aperture
Photodiode
Pre-Amp
Dump Spot
F/1.7 50 mm
Right Angle
Prism
Signal
Photodiode
Pre-Amp
50% Beam
Splitter*
6328 A
Spike Filter
Dump Spot
Scattering
Photodetector Module
Particle
Plane
* 50% for Non-polarized Light
38mm
Condensing
Lens
Signal
-15V
Gnd
45°
Mirror
Reference
Photodiode
He-Ne Hybrid Laser

Figure 10.--Optics diagram for PMS FSSP probe (courtesy of PMS, Inc.).

has been developed by Merceret and Schricker (1975). The claimed characteristics, however, have not been well demonstrated. Because of poor response to larger droplets and because calibration and stability are difficult to maintain, the hot-wire devices may yield misleading information. Total water evaporators have better sample volume, response time, and sensitivity to all forms of water. Window determination and source and detector drift are potential problems with some Lyman-alpha sensors.

c. Raindrop size and concentration

Raindrop-sized hydrometeors can be measured by foil impaction, optical devices, and momentum sensing.

When hydrometeors hit lead foil backed by mesh, an impression is made. The size of the impression may be correlated with the size of the hydrometeor. The lower limit of detection is typically ~300 μm, and for 75 μm it is sometimes possible to distinguish water from ice on the basis of image shape (Knight et al., 1977). Impaction devices usually have adequate sample volume and can be either continuous or single shot. Reduction of the data is difficult to automate and is therefore time consuming.

Data from optical devices are available without extensive hand analysis. A device developed by Knollenberg (1970) uses a linear photodetector array onto which passing drops are imaged as shadows by a collimated light beam. The number of shadowed elements indicates the drop size, and the concentration is determined by counting the number of times one or more elements of the array are shadowed. A histogram of the drop spectrum can be viewed in real time, and the information can be recorded on magnetic tape for easy data analysis. The cloud droplet size distributions shown in Fig. 11 are similar to those obtained by the precipitation-sized drop sampler described here. One disadvantage of the Knollenberg instrument is that it does not discriminate between

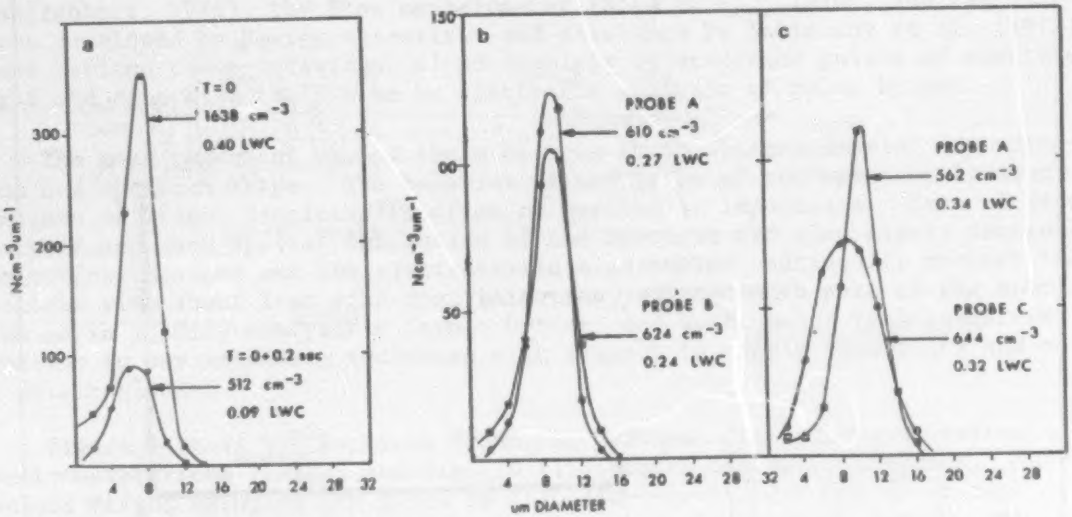

Figure 11.--Examples of FSSP cloud droplet spectra. An exciting aspect of the Knollenberg systems is the essentially real-time availability of such spectra (courtesy of PMS, Inc.).

liquid water and ice particles. In addition, when the image of a particle overlaps the end of the array, the event is disregarded. Because such events are thrown out, the sample volume is reduced by greater amounts for larger particles although we desire larger sample volumes for larger particles. An alternate approach is to employ two-dimensional optical imaging whereby the sample volume increases with particle size.

d. Ice particle size and concentration

Formvar replication was long the most frequently used technique for collecting ice crystals to measure their size and concentration. Ice crystals are captured in a solution of replicating material (Formvar), which hardens. The ice then sublimes, leaving a cast of the ice crystal. The replicas can be examined at room temperature using any desired magnification. Irregular drying of the Formvar solution and condensation of water on the evaporatively cooled formula sometimes cause artifacts, and insufficient contrast on small crystals sometimes makes interpretation of the replicas difficult. Sample volume for most Formvar systems is on the order of tens of liters per kilometer of flight path. This may not be adequate, especially when the ice crystal concentration is only a few per liter. Also, when continuous devices for sampling low concentrations of ice crystals are used, the particles are spread over considerable expanses of the film, making the analysis more difficult.

Weickmann (1947) practiced direct capture of ice crystals on oil-coated slides. This approach has also been used by scientists at the University of Wyoming for single-shot collections (Fig. 12). In this technique ice crystals are collected on a slide coated with mineral oil to ensure adherence, after which the slide is immersed in a silicone oil (Dow Corning 330 fluid) whose temperature is maintained below 0°C. Since mineral oil is insoluble in silicone oil, the crystals remain on the slide even under mechanical agitation; the silicone oil prevents evaporation. The original crystals can then be viewed at any desired magnification. The advantages of collection over replication are the absence of artifacts, simplicity of operation because of temperature controls, improved resolution, and shorter drying time.

The most difficult problem to overcome with either collection or replication techniques is the fracturing of ice crystals on the collection surface. Decelerators have been designed (Mossop et al., 1967, 1970; Hobbs et al., 1973; Davis and Veal, 1974) to reduce impaction velocity, thereby allowing collection or replication of even quite fragile crystals. Hanaway et al. (1972) used a continuous replicator in which a stagnant air layer was maintained between the sampling aperture and the collecting surface to slow down incoming crystals. Schreck et al. (1974) developed a system in which crystals entered a tube placed outside the aircraft. Air flowed into a container of silicone oil kept at dry-ice temperature. Because only a small amount of air was allowed to pass through the tube, deceleration of the crystals was accomplished. The collected crystals could then be examined in a cold room at any desired magnification.

Devices that detect ice particles by optical techniques include the MEE, the University of Washington counters, Cannon's camera (and others), the holocamera, and the PMS two-dimensional spectrometer.

The MEE (Sheets and Odencrantz, 1974) and the University of Washington (Turner and Radke, 1973) ice crystal counters use the property of an ice

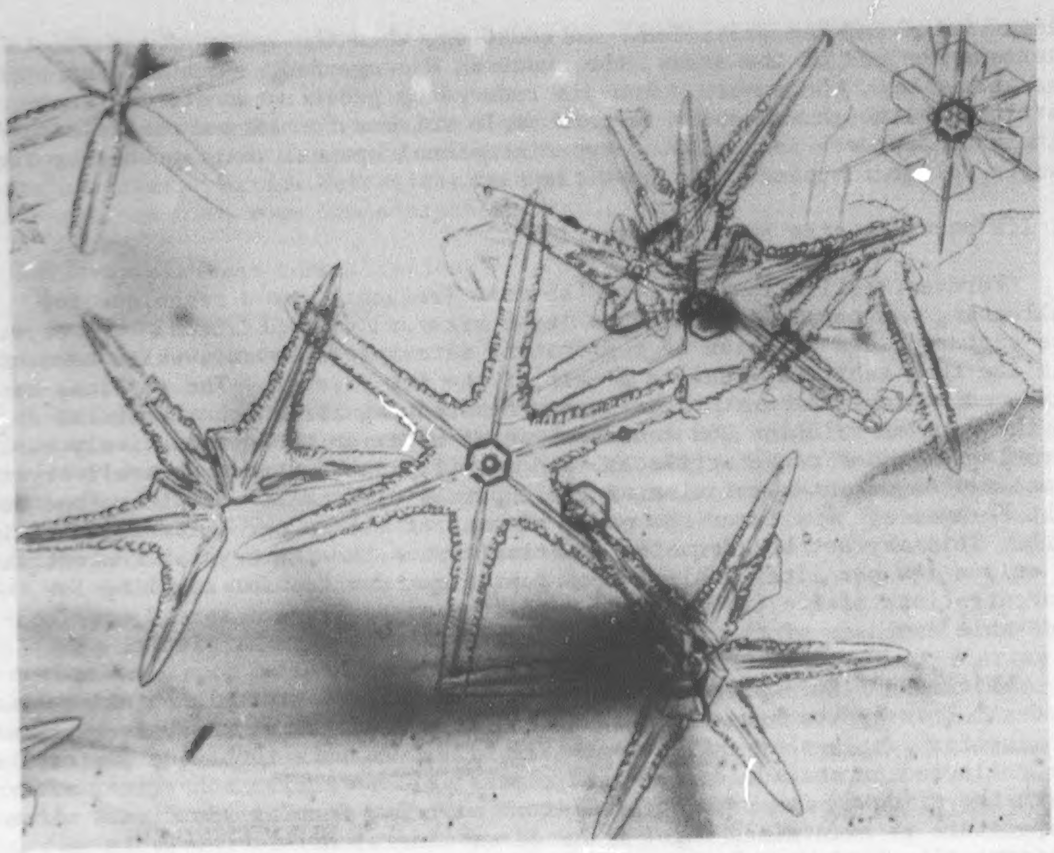

Figure 12.--Ice crystals captured by a single-shot oil-coated slide (courtesy of University of Wyoming).

crystal to rotate the plane of polarization of polarized light as the basis for their operation. Both devices make possible real-time display of ice crystal concentration and provide for rapid data reduction and analysis. Size information is not available from either instrument. Because of significant size-dependent efficiency corrections (Turner et al., 1975), which may also depend on crystal shape, independent shape and size information is desirable to obtain more reliable crystal concentrations.

The two-dimensional optical imaging probe developed by Particle Measuring Systems, Inc. (Knollenberg, 1976), is C in Figs. 5 and 13. This device incorporates an optical array similar to that in the liquid hydrometeor device described above. Particles shadow an array, and by frequently recording the status (shadowed or illuminated) of each element in the array as the particles pass, a two-dimensional picture can be reconstructed. The aircraft unit uses a 32-element array, with a typical resolution of about 25 mm per element. The maximum resolution per element is a function of aircraft velocity. Various configurations of the probes are available for detection of cloud sizes of precipitation size particles. Figure 14 is a block diagram of the optical system. The concentration of particles as well as the images can be displayed in real time in the aircraft. Examples of images obtained from rain and dendritic ice crystals are shown in Fig. 15.

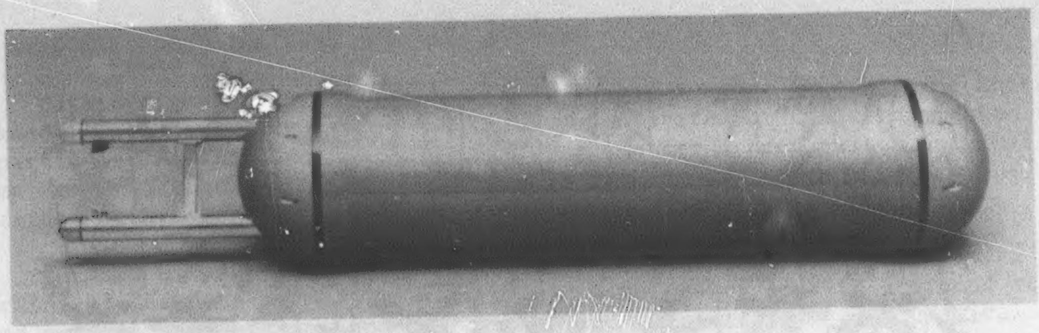

Figure 13.--Two-dimensional optical imaging probe on laboratory bench (mounted on the NCAR Queen Air in Fig. 5) (courtesy of PMS, Inc.).

The obvious advantages to obtaining direct photos of cloud elements are in situ sampling and more detailed information on the shape of the particles. The principal difficulties are achieving sufficient sample volumes with the required magnification and resolution and the necessity to "stop the motion" of the particles being photographed. Elliot (1974), McCullough and Perkins (1951), Lavoie et al. (1970), and Cannon (1974) describe various systems for photographing cloud elements. Analysis of the data collected using any of these systems is extremely demanding in time and manpower. It is possible, however, that with the aid of computerized analysis schemes the utility of direct photography of cloud elements could be considerably enhanced.

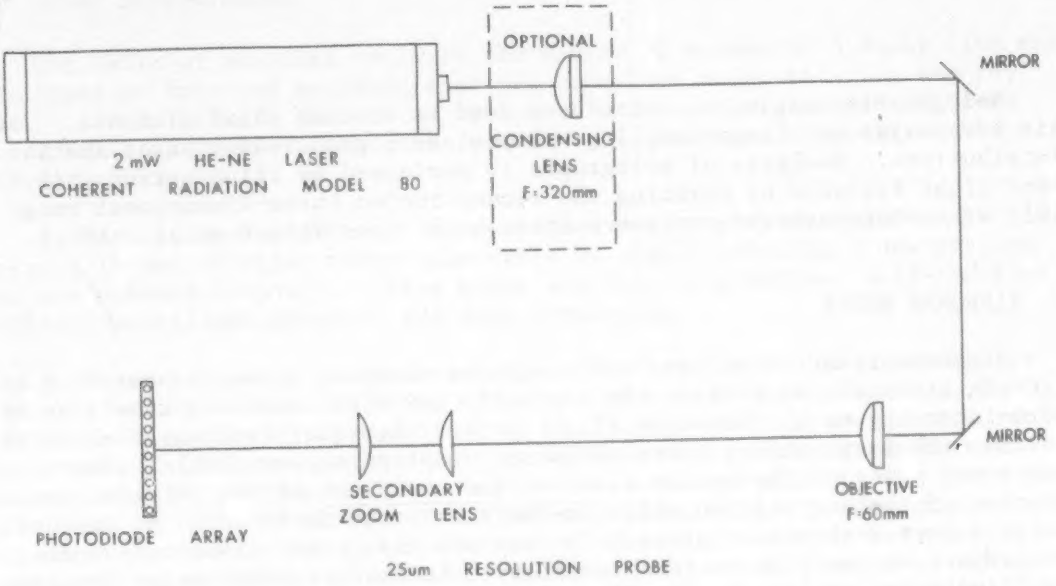
OPTIONAL
MIRROR
CONDENSING LENS F=320mm
2 mW HE-NE LASER
COHERENT RADIATION MODEL 80
MIRROR
SECONDARY ZOOM LENS
OBJECTIVE F=60mm
PHOTODIODE ARRAY
25um RESOLUTION PROBE

Figure 14.--Optics diagram for two-dimensional PMS probe (see Knollenberg [1976]) (courtesy of PMS, Inc.).

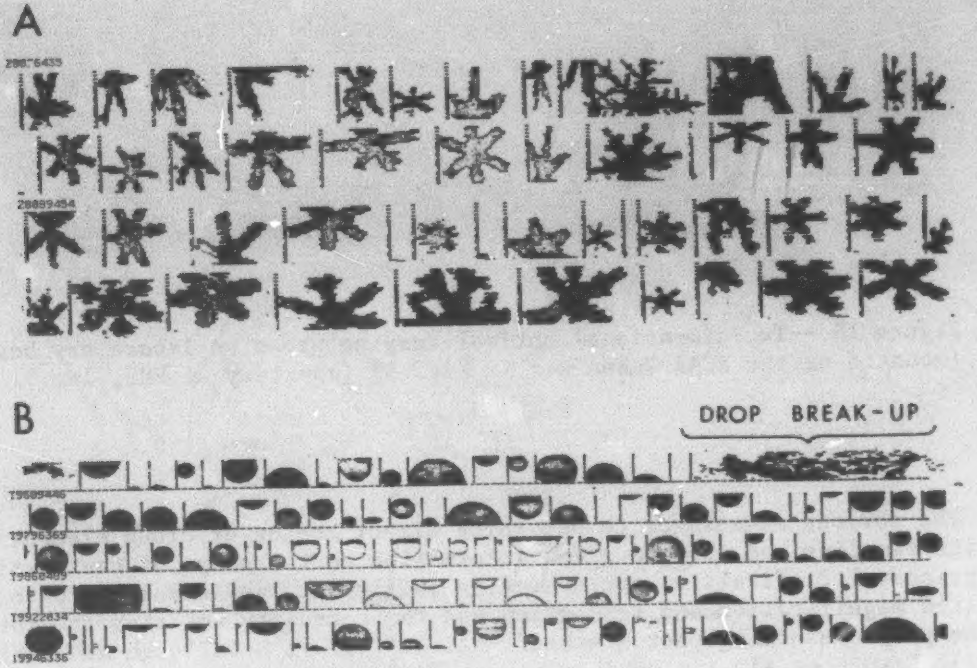

Figure 15.--Examples of PMS two-dimensional probe imaging: (A) snow sampling, such that ice crystal types can be identified and sized; (B) examples of rain sampling. Aircraft airspeed was 80 m s^{-1} (courtesy of University of Wyoming).

Holographic imaging has also been used to observe cloud elements. Its main advantages are large sampling volumes and a good rendition of spatial distributions. Analysis of holographs is performed by illumination with a laser light followed by scanning the reconstructed three-dimensional image field with a microscrope or camera arrangement (see Wilmot et al., 1974).

5. AIRBORNE RADAR

Airborne radar is an invaluable aid for studying severe storms with an aircraft since it can provide the aircraft crew with immediate knowledge of storm intensity on the intended flight path. High-quality commercial radar systems with many antenna sizes and scope displays are available. The frequency and power of the system selected are functions of the intended use and the size of the aircraft on which the unit is to be installed. An appropriate system allows weak-echo regions to be entered and allows close maneuvering near severe storms with reasonable safety. Several airborne radar displays are illustrated in Vol. 1, Ch. VI, and weather radar science and engineering are detailed in Vol. 3, Ch. VIII.

6. AIRBORNE COMMUNICATIONS AND DATA SYSTEMS

Data systems employed in atmospheric research range from keeping notes on a knee pad to sophisticated, computer-directed systems. Choice of system for a particular mission depends primarily upon whether a need exists for real-time decisions during the mission and upon the resolution required in the recorded data.

Because of weight or space limitations on research aircraft, onboard recording of the data may not be desirable. A telemetry link to a ground station can replace certain recording systems on the aircraft. The critical factor in a telemetry link is its range-altitude capability.

If the aircraft crew are to optimize observations of storms and interact with other personnel, descriptive parameters must be available in near real time. The best solution at present appears to be the use of a real-time system that provides for three important time scales, or learn-time cycles, of data use.

At the shortest time scale, the real-time cycle, the aircraft crew can use the measured parameters to aid the conduct of the research flight in real time and relay information to ground sites to aid in overall operation of the experiment. With the aid of a computer onboard the aircraft, the necessary conversions and corrections for the various parameters can be made and variables such as potential temperature, specific humidity, and wind can be determined and displayed.

The next scale in a research project is the single mission or one-day cycle. With a properly configured data system, hard copies of selected portions of the data can be had very soon after each flight, enabling the scientists to reconstruct and review mission highlights and compare their data with other observations.

The third or seasonal cycle is the review of accumulated daily data and many types of detailed analysis that may have been suggested from the real-time or single-mission learn-time cycles. In any case, the recorded data should be in the most fundamental form to facilitate new computations or analysis schemes.

Airborne computer-directed data systems are usually designed to be operated in one of three modes selectable by simply entering a new program into the onboard computer. These modes are data acquisition, self-check or preflight-postflight program, and data processing.

In the first mode, the sensor outputs are transferred to the computer through a multiplexer after being signal conditioned, then formatted and recorded. The computer also calculates various derived parameters for real-time display. Selected fault detection and identification during data collection can also be provided. Fault indications are desirable if the instantaneous values or rates of change of variables fall outside a predetermined range. The computer can also monitor the status of the tape recorder and perform a "read-after-write" check on the data recorder. If any malfunctions are detected, a signal or code that identifies the fault can be displayed in the aircraft.

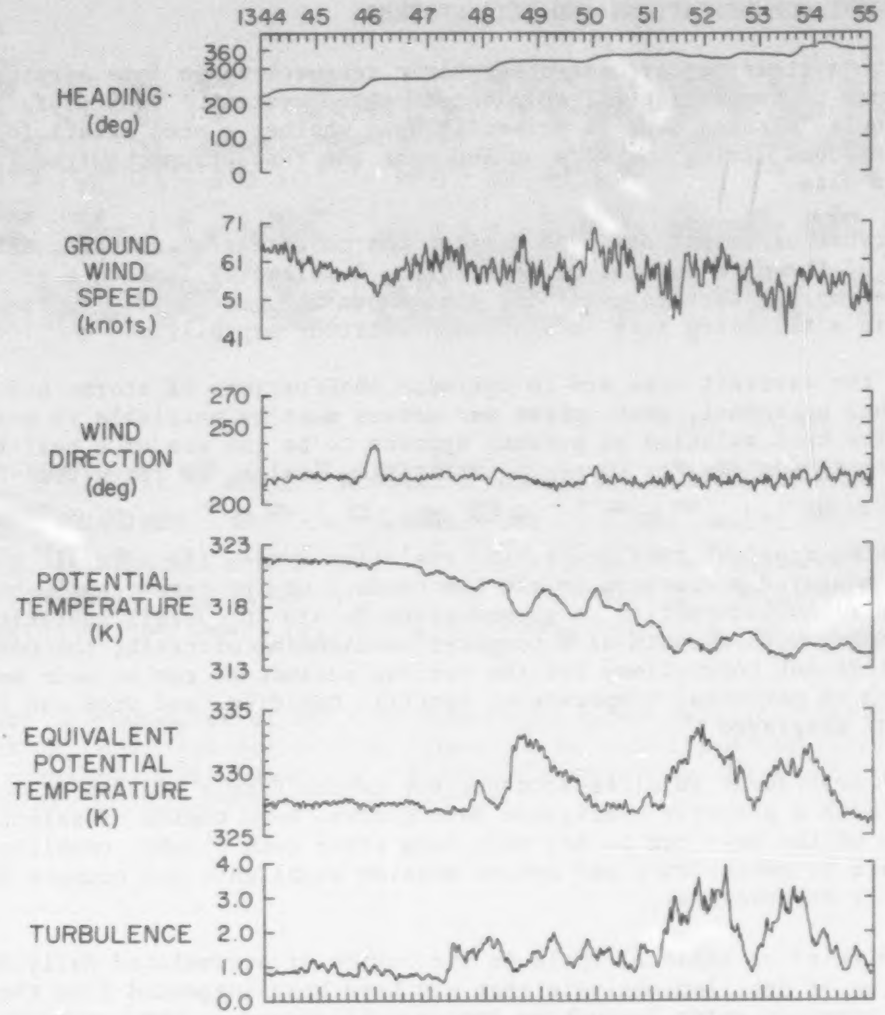

Figure 16.--Example of computer-processed meteorological variables as a function of time (Bensch and McCarthy, 1978).

The second mode of operation is very useful as a preflight-postflight or troubleshooting tool. The data system can be designed with sensor simulation circuitry that can be controlled by the computer to produce any desired output over the range of the sensor being simulated.

Operation in the third mode takes place on the ground after the mission. Line printers and teletypes are interfaced to the aircraft system, and processed data are obtained on hard copy. The ability to view data with only limited processing during field projects is often very useful. With computer-compatible formats, extensive processing of the data on other computer facilities is straightforward. Figure 16 is a typical example of the final derived parameter output from an airborne data system.

Internal and air-to-ground communications among the crew are usually a vital component of the data system and overall research mission, but are all too often neglected. Communications requirements for research often exceed the installed capacity in aircraft used principally for transportation. But for a flying laboratory to be effective, the scientific crewmembers and pilot must be able to communicate easily with each other. In addition, the system should allow each crewmember to isolate his conversation from others. This is required when the pilot communicates with FAA controllers while other crewmembers carry on other discussions.

Flying laboratories with computer-directed data systems and an array of modern sensors are especially valuable when versatile communications capabilites allow close coordination with other aircraft, ground mobile systems, ground radar systems, and FAA controllers.

7. SPECIAL USES OF AIRCRAFT IN THUNDERSTORM RESEARCH

a. Chaff as an air motion sensor

Since World War II, radar reflective chaff has been used to jam radar installations as an antiradar surveillance technique. It was soon discovered that chaff released from an airplane could be used as radar tracer elements to determine air motions. Jessup (1972) of NSSL made extensive use of point chaff packets to look at the thunderstorm environment wind flow. Marwitz (1973) of the University of Wyoming used chaff to trace vertical motions within the echo-free vaults of thunderstorms over the National Hail Research Experiment research area.

McCarthy et al. (1974) used chaff to fill a large volume of echo-free air in the near-thunderstorm environment. A unit of five chaff packets is dropped from an airplane; individual chaff packets are released every 500 meters during descent. The result is a column of chaff extending from near the airplane flight level to approximately 2,500 meters below flight level. By a series of releases, a large volume can be filled, and a Doppler radar system can measure the instantaneous winds in an otherwise nonreflective volume.

b. Lightning suppression experiments

Heinz Kasemir of NOAA has developed a technique of lightning suppression that uses chaff distributed from aircraft. The idea behind the technique is simple: the corona discharge property of a chaff fiber causes a silent conduction current and neutralizes separated charge centers. Results of several experiments have been promising, but not definitive, as noted in Vol. 2, Ch. XVI.

8. SYNTHESIS OF AIRBORNE DATA

Although we are not describing research achievements of thunderstorm flying in detail, we do offer several examples where instrumented aircraft data have been combined with other direct and remote sensors to yield valuable insight on thunderstorms. This combining of sensor data is an essential step in production of whole pictures.

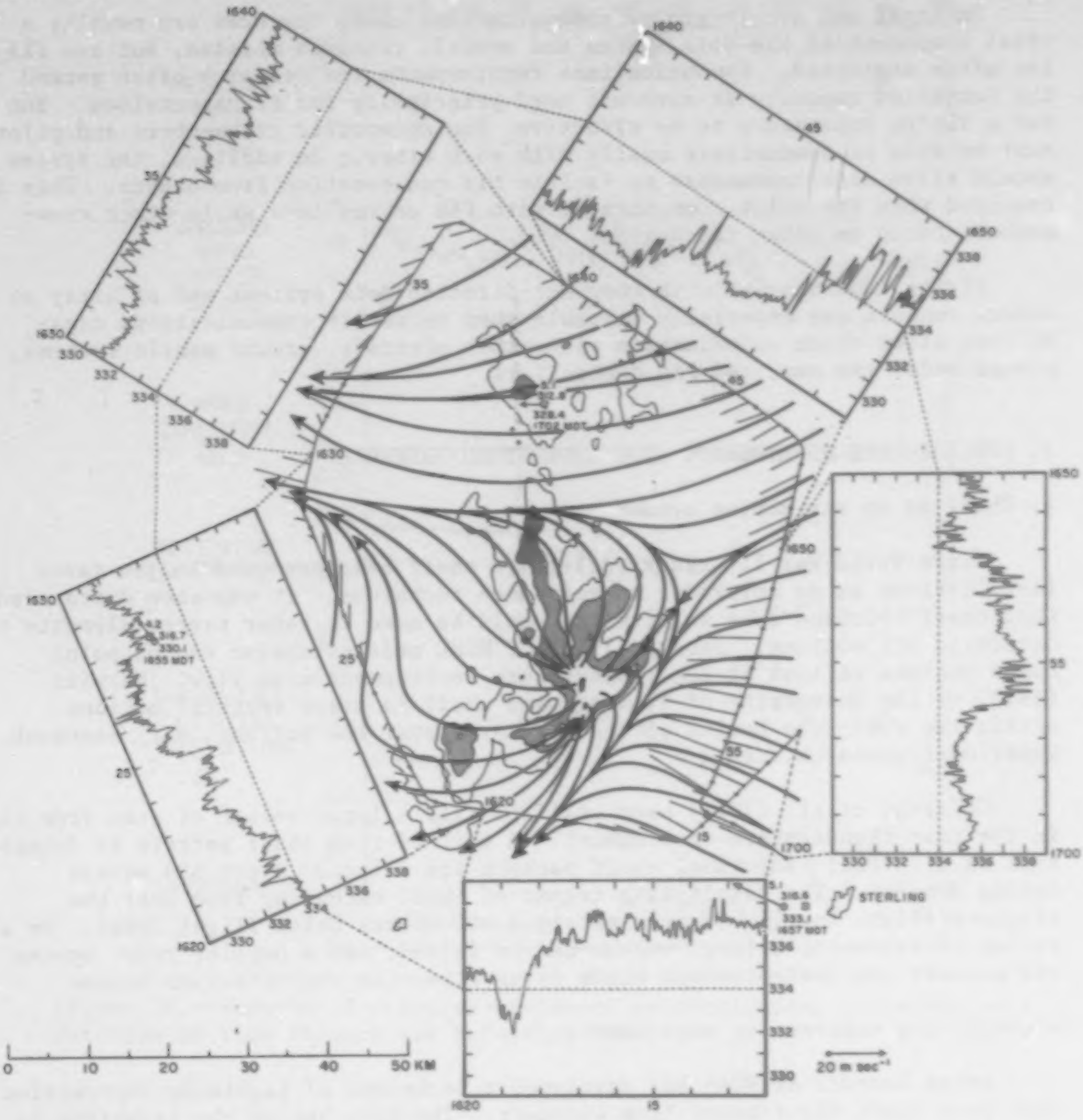

Figure 17.--NCAR de Havilland Buffalo aircraft data combined with other aircraft and radar data. Buffalo track is at 3.0 km, positioned relative to radar echo at 1655 LST. Wind vectors (scale at lower right) and streamline pattern represent flow relative to the storm. Equivalent potential temperatures based on variables measured along the track are distributed on surrounding panels as a function of time and space. Sharp gradients near 1618 and 1647 are interpreted as boundaries between inflowing and outflowing branches of circulation (Foote and Fankhauser,1973).

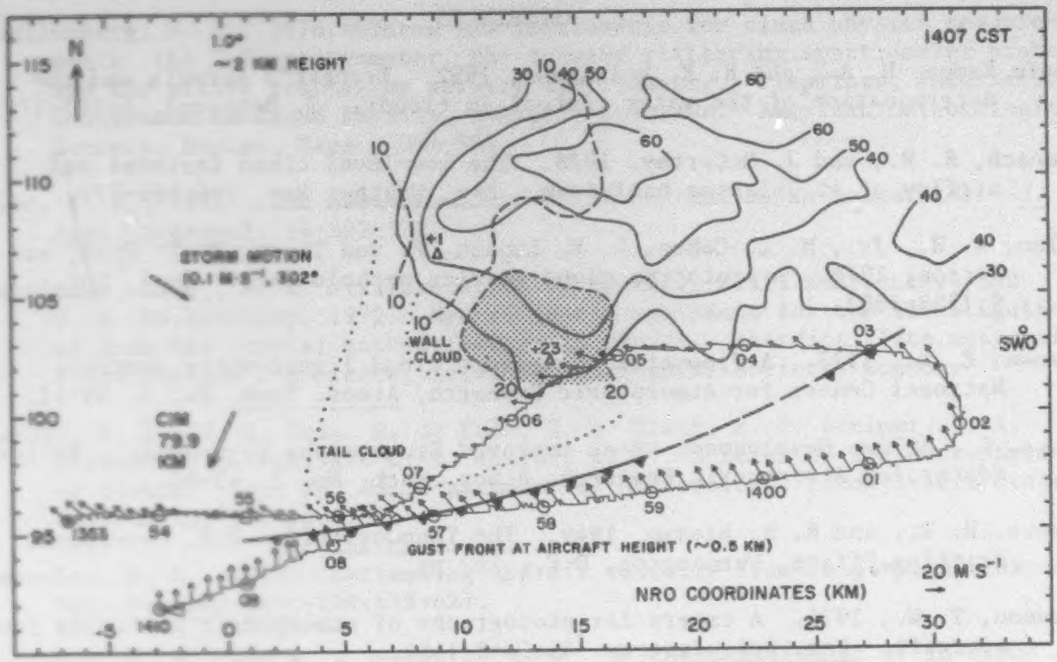

Figure 18.--Synthesis of NCAR Queen Air data and NSSL Doppler radar data: Cimarron Doppler radar 1.0-deg. elevation angle reflectivity (solid contours, dBZ) and radial velocities (corrected for storm motion) at 1407 CST. Maximum and minimum values of radial velocity are indicated by Δ symbols, and numerical values are shown. Area of radial velocities greater than 20 m s^{-1} is shaded. NCAR research aircraft storm relative track and wind vectors are shown for 1353-1410. The position of the inflow cloud was determined from aircraft photography. SWO indicates the location of the Stillwater Municipal Airport (Bensch and McCarthy, 1978).

The example in Fig. 17 is taken from research at NCAR, as part of the National Hail Research Experiment. A severe hailstorm was observed by surface-based radar, airborne instruments, and a variety of other surface sensors. NCAR de Havilland Buffalo aircraft data are superposed on other data. Radar intensities, airborne-measured equivalent potential temperature, and storm-relative airflow streamlines are shown. Such combined data present elements of storm structure at a level of detail that supports new inferences on the processes governing storm development.

Figure 18 is another example of synthesis, this time using NSSL Doppler radar data with the NCAR Queen Air aircraft. The position of the thunderstorm gust front has been deduced from aircraft-measured winds and superposed on NSSL Doppler wind and intensity measurements.

REFERENCES

aufm Kampe, H. A., and H. K. Weickmann, 1952. Trabert's formula and the determination of the water content in clouds. J. Meteorol. 9:167-171.

Bensch, R. R., and J. McCarthy, 1978. The low-level cloud features and airflow of an Oklahoma hailstorm. Mon. Weather Rev. 106:566-571.

Blau, H. H., Jr., M. L. Cohen, L. B. Lapson, P. von Thuna, R. T. Ryan, and D. Watson, 1970. A prototype cloud physics nephelometer. Appl. Opt. 9:1798-1803.

Brown, E. N., 1973. A flowmeter to measure cloud liquid water content. National Center for Atmospheric Research, Atmos. Tech. No. 1, 49-51.

Buck, L., 1973. Development of an improved Lyman-alpha hygrometer. National Center for Atmospheric Research, Atmos. Tech. No. 2, 43-46.

Byers, H. R., and R. R. Braham, 1949. The Thunderstorm. U.S. Government Printing Office, Washington, D.C., 287 pp.

Cannon, T. W., 1974. A camera for photography of atmospheric particles from aircraft. Rev. Sci. Instrum. 45:1448-1455.

Davis, C. I., and D. L. Veal, 1974. Decelerator design and testing. Inter. Prog. Rep. No. 9, Department of Atmospheric Resources, University of Wyoming, 10 pp.

Elliot, H. W., 1947. Cloud droplet camera. Rep. MI-701, Division of Mechanical Engineering, National Research Council of Canada, Ottowa.

Foote, G. B., and J. C. Fankhauser, 1973. Airflow and moisture budget beneath a northeast Colorado hailstorm. J. Appl. Meteorol. 12:1330-1353.

Hallett, J., R. W. Hanaway, and P. B. Wagner, 1972. Design and construction of a new cloud particle replicator for use on a pressurized aircraft. AFCRL-72-80410, Nevada University-Reno Laboratory of Atmospheric Physics.

Hobbs, P. V., R. J. Harper, and R. G. Joppa, 1973. Collection of ice particles from aircraft using decelerators. J. Appl. Meteorol. 12:522-528.

Jessup, E. A., 1972. Interpretations of chaff trajectories near a severe thunderstorm. Mon. Weather Rev. 100:653-661.

Knight, C. A., N. C. Knight, W. W. Grotewold, and T. W. Cannon, 1977. Interpretation of foil impactor impressions of water and ice particles. J. Appl. Meteorol. 16:997-1002.

Knollenberg, R. G., 1970. The optical array: an alternative to scattering or extinction for airborne particle size determination. J. Appl. Meteorol. 9:86-103.

Knollenberg, R. G., 1976. Three new instruments for cloud physics measurements: the 2-D spectrometer, the forward scattering spectrometer probe, and the active scattering aerosol spectrometer. Preprints, International Conference on Cloud Physics, Boulder, Colorado. American Meteorological Society, Boston, Mass., 554-561.

Kyle, T. G., 1975. The measurement of water content by an evaporator. *J. Appl. Meteorol.* 14:327-332.

Laktionov, A. G., N. K. Nikiforova, V. V. Smirnov, G. T. Schelchkov, and O. A. Volkovitsky, 1972. New automatic equipment for the investigation of drop and crystal microstructure in clouds. Abstract, International Cloud Physics Conference, Royal Meteorological Society, London.

Lavoie, R. L., J. A. Pena, R. de Pena, R. L. Riuth, R. P. Greiner, D. A. Corkum, J. L. Lee, and C. L. Hosler, 1970. Studies of the microphysics of clouds. Rep. No. 16, Department of Meteorology, Pennsylvania State University, 116 pp.

Lenschow, D. H., 1976. Estimating updraft velocity from an airplane response. *Mon. Weather Rev.* 104:618-627.

Lenschow, D. H., and W. T. Pennell, 1974. On the measurement of in-cloud and wet-bulb temperatures from an aircraft. *Mon. Weather Rev.* 102:447-454.

List, R. J., 1958. Smithsonian Meteorological Tables, Smithsonian Institution, Washington, D. C., 527 pp. (See, for example, pp. 365ff in the sixth revised edition.)

Marwitz, J. D., 1973. Trajectories within the weak echo regions of hailstorms. *J. Appl. Meteorol.* 1:1174-1182.

McCarthy, J., 1974. Field verification of the relationship between entrainment rate and cumulus cloud diameter. *J. Atmos. Sci.* 31:1028-1039.

McCarthy, J., G. H. Heymsfield, and S. P. Nelson, 1974. Experiment to deduce tornado cyclone inflow characteristics using chaff and NSSL dual Doppler radars. *Bull. Am. Meteorol. Soc.* 55:1130-1131.

McCullough, S., and P. J. Perkins, 1951. Flight camera for photographing cloud droplets in natural suspension in the atmosphere. (NACA RM E50K01a)

Meceret, F. J., and T. L. Schricker, 1975. A new hot-wire liquid cloud water meter. *J. Appl. Meteorol.* 14:319-326.

Mossop, S. C., and E. R. Wishart, 1970. Ice particles in maritime clouds near Tasmania. *Q. J. R. Meteorol. Soc.* 96:487-508.

Mossop, S. C., A. Ono, and K. J. Hefferman, 1967. Studies of ice crystals in natural clouds. *J. Rech. Atmos.* 3:45-64.

Mullin, R. A., and W. G. Wolber, 1964. A dewpoint hygrometer for micrometeorological range applications. Presented at the Fifth Conference on Applied Meteorology, March 2-6, 1964, Atlantic City, New Jersey. American Meteorological Society, Boston, Mass.

Rodi, A., and P. Spyers-Duran, 1972. Analysis of time response of airborne temperature sensors. J. Appl. Meteorol. 11:554-556.

Ruskin, R. E., 1967. Measurements of water-ice budget changes at -5°C in AgI seeded tropical cumulus. J. Appl. Meteorol. 6:72-81.

Ruskin, R. E., and W. D. Scott, 1974. Weather modification instruments and their use. In Weather and Climate Modification, W. N. Hess (ed.), John Wiley and Sons, New York, 842 pp.

Sasyo, Y., 1968. Studies and developments of meteorological instruments for cloud physics and micrometeorology (I). Pap. Meteorol. Geophys. (Japan) 19:587-598.

Schreck, R. I., V. Toutenhoofd, and C. A. Knight, 1974. A simple, airborne, ice particle collector. J. Appl. Meteorol. 13:949-950.

Sheets, R. C., and F. K. Odencrantz, 1974. Response characteristics of two automatic ice particle counters. J. Appl. Meteorol. 13:148-155.

Telford, J. W., and J. Warner, 1962. On the measurement from an aircraft of buoyancy and vertical air velocity in cloud. J. Atmos. Sci. 19:415-423.

Turner, F. M., and L. F. Radke, 1973. The design and evaluation of an airborne optical ice particle counter. J. Appl. Meteorol. 12:1309-1318.

Turner, F. M., L. F. Radke, and P. V. Hobbs, 1976. Optical techniques for counting ice particles in mixed-phase clouds. National Center for Atmospheric Research, Atmos. Tech. No. 8, 25-31.

Veal, D. L., W. A. Cooper, G. Vali, and J. D. Marwitz, 1978. Some aspects of aircraft instrumentation for storm research. In Hail: A Review of Hail Science and Hail Suppression, Meteorol. Monogr. 16, American Meteorological Society, Boston, Mass., 237-255.

Warner, J., and T. D. Newnham, 1952. A new method of measurement of cloud water content. Q. J. R. Meteorol. Soc. 78:46-52.

Weickmann, H. K., 1947 Die Eisphase in der Atmosphäre. Reps. Trans. No. 716, Ministry of Supply (A), Volkenrode, 244-247.

Wilmot, R. A., C. E. Cisneros, and F. L. Guiberson, 1974. High cloud measurements applicable to ballistic missile systems testing. Preprints, Sixth Conference on Aerospace and Aeronautical Meteorology, November 12-15, 1974, El Paso, Texas. American Meteorological Society, Boston, Mass., 194-199.

IV. PHOTOGRAMMETRY OF THUNDERSTORMS

Ronald L. Holle

1. INTRODUCTION

Clouds are visible tracers of atmospheric motion; for this reason, pictures of clouds are among the most revealing measures available to the meteorologist. When the pictures are combined with information from other sensors, the evolution of the condensation process can be followed, the influence of internal and external atmospheric motions on the cloud matter can be seen, and the ultimate disappearance of the cloud can be viewed. Film can capture the tracers of a wide variety of processes in an immediately comprehensible form. Although many atmospheric phenomena on larger and smaller scales are not directly visible, thunderstorm evolution is ideally suited to photographic description. The thunderstorm, in many cases, is small enough that the whole of one side is visible from one location.

A working definition is quoted here that appears in the American Society of Photogrammetry's monthly journal, Photogrammetric Engineering and Remote Sensing: "Photogrammetry is the art, science, and technology of obtaining reliable information about physical objects and the environment through processes of recording, measuring, and interpreting photographic images and patterns of electromagnetic radiant energy and other phenomena."

Analysis of photographs can proceed in as much detail as needed. Photogrammetry of every transient feature in thunderstorms is possible, but can be tedious. In many situations, qualitative information can be found easily from a photo without formal analysis. As in all scientific research, the motivation for study must be clearly in mind before analysis is begun. In most cases, the motivation is supplied by examination of the same clouds using meteorological data from other sources, and little is gained by detailed examination of aspects of a cloud not readily associated with other features of interest.

In view of the potential benefit from photographic analysis in conjunction with other data sources, every thunderstorm study should have a photography program. If the procedures of photographic analysis are known in advance, the photography program can be designed for the desired accuracy and the time available for analysis.

The use of photogrammetry for thunderstorm research has been widespread, but even wider use may have been prevented by problems and misunderstandings such as these:

(1) The impression that photo analysis is always very difficult.

(2) The inability to see inside large clouds or to photograph them at night or during days with poor visibility. (Radar is often a substantial aid, since it gives information on interior condensates. Other remote sensing techniques using various wavelengths can also be revealing, while photos show visible material on cloud exteriors.)

(3) The overabundance of data in photographs. Less detailed data sources provide general information about a cloud rather easily; pictures contain

so much data that photo analysis could be too time consuming if not carefully considered.

This survey of cloud photogrammetry covers pictures in the visible portion of the spectrum, as well as the use of various cameras and techniques.

2. BASIC EQUATIONS FOR PHOTOGRAMMETRIC ANALYSIS

The angular field of view of a camera as obtained from Wolf (1974, p. 63) is

$$\tan \frac{\alpha}{2} = \frac{d}{2f} , \qquad (1)$$

where α is the full horizontal or vertical angle of the lens, d is the horizontal or vertical dimension of the original film frame, and f is the focal length of the lens. Of course, the dimensions of d and f are in the same units, such as millimeters.

If the horizon is in the picture and the camera focal length is known, heights and widths of every cloud element can be calculated with appropriate equations dependent on camera tilt. For photos from an untilted camera, with the horizon in the center of the picture, McNeil (1954, Problem 43) gives

$$\tan \theta = \frac{x}{f} \qquad (2)$$

and

$$\tan \sigma = \frac{y \cos \theta}{f} , \qquad (3)$$

where θ is the horizontal angle to the right or left of the picture's center, σ is the vertical angle from cloud feature to horizon, and x and y, the coordinates of the measured cloud point, are the horizontal and vertical distances from vertical and horizontal lines that divide the picture into halves. In practical application, when the photograph is projected, x and y may be measured in millimeters, and f is multiplied by the amount of magnification M. The value of M is the ratio of the projected image size to the original film size.

When the picture is tilted, the equations are more complex. Then, to find angles to the cloud feature, one must find the camera tilt. First, find the exact center (the principal point P) of the entire photograph by locating the intersection of diagonals that connect the picture corners. Second, measure the perpendicular from point P to the horizon, at point A. Then, substitute into $\tan t = PA/f$ to find the camera tilt angle t above or below horizontal.

Exact equations for a cloud point on a picture tilted at angle t are

$$\tan \theta = \frac{x}{f \cos t - y \sin t} \qquad (4)$$

and

$$\tan \sigma = \frac{\cos \theta (y \cos t + f \sin t)}{f \cos t - y \sin t} \quad . \tag{5}$$

Tilt is 0° for a camera looking horizontally, 90° directly upward, etc. Note that when $t = 0°$, Eqs. 4 and 5 reduce to Eqs. 2 and 3. A derivation of a similar pair of equations is given by Wolf (1974, p. 366). McNeil (1954, Problem 43) gives almost the same equations for a different definition of t.

Heights of cloud features can be calculated, once the angles θ and σ are found from one of the two previous pairs of equations. To find the height, use

$$h = r \tan \sigma \quad , \tag{6}$$

where r is the range to the cloud feature. Methods of finding r are given in Secs. 3 and 4 below for several types of pictures. The importance of determining range as accurately as possible is seen clearly from Eq. 6. For example, for a change in r of 1 km, h changes by 360 meters when the cloudtop vertical angle is 20°. Effects of Earth curvature and atmospheric refraction should be included by using $C = 0.0676\ r^2$, where the correction C to the cloud height is in meters and range r is in kilometers. The value is always additive to the cloud height. C is substantial at large distances, but may be omitted for larger clouds at ranges less than 30 kilometers, where C is less than 60 meters.

The cloud width is found by determining the horizontal angle θ to the right and left sides of the cloud feature. Take the difference γ between these two angles, and use

$$w = r \tan \gamma \tag{7}$$

to find cloud width. Width is as sensitive as height to changes of range. No correction C is applied here because the atmospheric variations that cause refraction are systematic only in the vertical direction. The basic equations, Eqs. 1 through 7, are not difficult to use, although the preparation of an accurate diagram for measuring x and y can be time consuming. Considerably more complex expressions may be necessary for special applications or corrections to unique situations. Stereoscopic analysis, tornado photography, and downward-looking pictures usually use different mathematical expressions.

3. PHOTOGRAMMETRY OF GROUND-BASED PICTURES

In the following sections the broad categories of thunderstorm photography and analysis proceed from simplest to most difficult. The level of difficulty is defined by the time period, personnel, and equipment involved in data collection, and the expertise, equipment, and sophistication required for analysis. In any case, the product collected substantially determines the method to be followed in full use of a picture.

a. Handheld-camera pictures

The simplest photographic data collection involves still photography, as opposed to motion pictures.

Figure 1.--Handheld-camera picture taken from the surface at 1540 EDT on 18 June 1973 during the Florida Area Cumulus Experiment (FACE). At this time, an outdraft was moving across the mesonetwork at 15 m s^{-1} (photo from Michael Maier, Lightning Location and Protection, Inc., Tucson, Ariz.).

Field personnel can take pictures with very little time and expense, and the prospect for gathering a photo of the exact cloud of interest justifies the effort. A polarizing filter is often helpful for increased contrast between clouds and sky. The picture must be labeled with time and location, and the horizon must be visible. An example of a short-lived, rapidly moving cloud feature photographed during a field project is shown in Fig. 1.

Analysis of the picture may include qualitative documentation of cloud organization, orientation, timing, shear, and stage of life cycle. However, one may calculate the cloud's azimuth if the angle of view of the camera is known from Eq. 1 and angles to distant landmarks in the picture are measured. The analysis potential of handheld-camera photos is substantially improved if some supporting evidence gives distance to the cloud feature. For example, Holle and Maier (1980) took a series of pictures of a tornado. Its location was found by examining the patterns of rain gage reports and radar echoes in the vicinity and then combining this information with the photographs' views

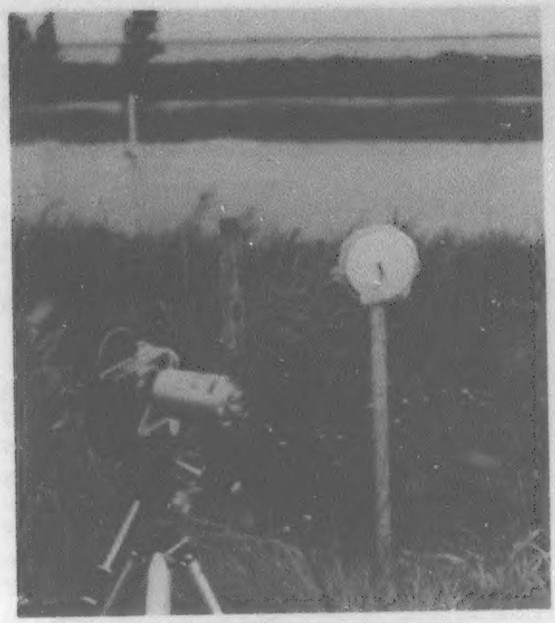

Figure 2.--Time-lapse 16-mm camera system operating at the University of Miami Doppler radar site at Pahokee, Fla., along the southeast shore of Lake Okeechobee. The camera is using color film. It is pointing toward an experimental seeding area and its related surface mesonetwork and tri-Doppler radar coverage region during FACE 1975.

of the relative positions of tornado and rainfall. The standard radar scan near 0.5° elevation angle is appropriate for determining r to lower levels in clouds. Vertically scanning radars, however, usually provide information on top locations, which may differ significantly from the lower level scan position of the cloud. Given range from these methods, or from pictures taken at another location, Eqs. 2 to 7 can be used to measure sizes of visible cloud features at picture time. Handheld-camera photographs from the ground have been taken and analyzed in virtually every thunderstorm study and can help in the selection of case study days on the basis of especially illustrative photographs such as Fig. 1.

b. Single time-lapse camera pictures

The time-lapse movie camera is the next simplest camera system to operate in the field. When an unattended camera is operated all day, it can be located next to a radar site or observation station. The camera should be pointed toward a mountain range that can be expected to produce afternoon thunderstorms, or along a lake shore or ocean beach, where large clouds may be produced by the lake or sea breeze convergence zone, or toward a target area for an experiment, as shown in Fig. 2. A frame from a time-lapse film of thunderstorms over mountains is shown in Fig. 3. The camera can be placed perpendicular to the wind, so that clouds move across the view, or toward an advancing cloud system. The least expensive system amenable to detailed analysis is the 16-mm camera (Fig. 2) with color film and a wide-angle lens, taking pictures at intervals ranging from one frame per second to one per minute, depending upon cloud motions. Automatic exposure controls can be used to cover different cloud lighting conditions. Such systems have been employed during many experiments over the last two decades.

An accurate record of the motion of condensed water vapor can be obtained by use of Eqs. 1 through 7 if several variables are known. The necessary

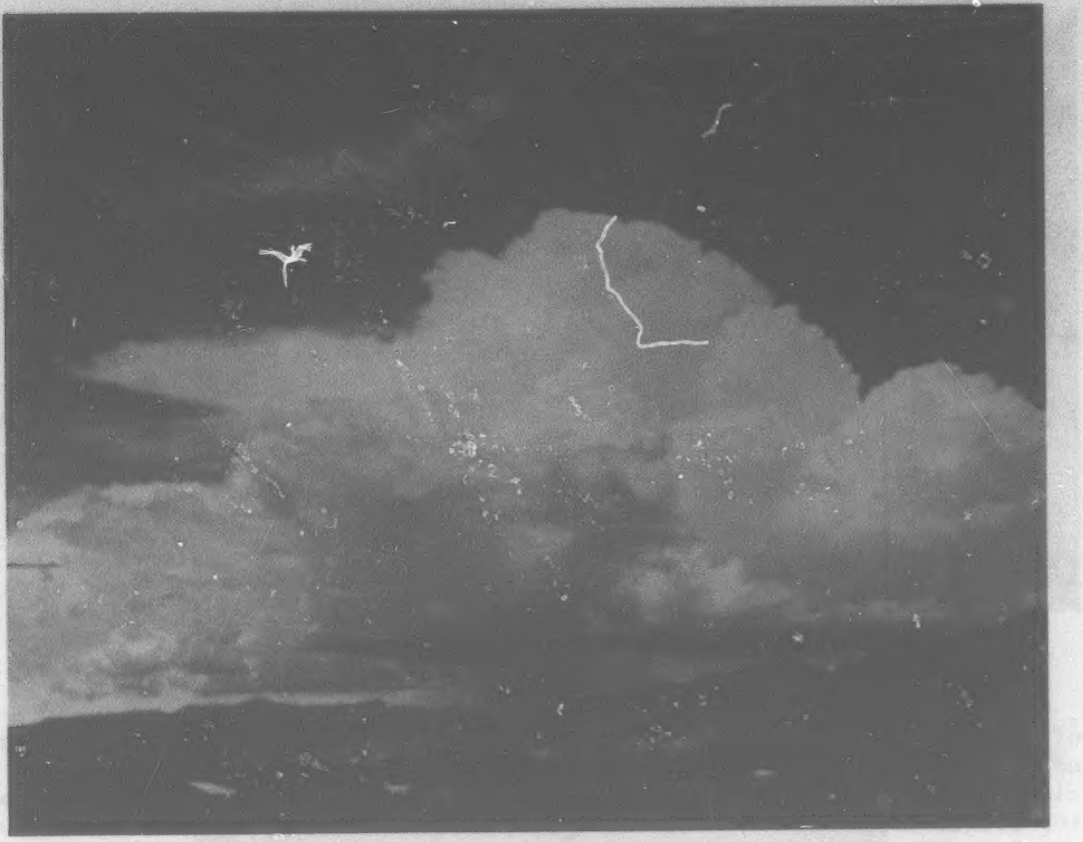

Figure 3.--Time-lapse picture, taken on 16 July 1975 from Socorro, N. Mex., with 16-mm color film. The thunderstorm was located over the Magdalena Mountains, where the Langmuir Laboratory is located (photo from Charles Moore, New Mexico Institute of Mining and Technology, Socorro).

information is similar to that needed for handheld cameras: the range to visible cloud features, angles to distant landmarks on the horizon (such as the trees in Fig. 2), lens focal length, and time recorded directly in the film to determine the exact frame rate. The stop-motion projector is the only special equipment needed to find precise heights and widths of clouds visible on a time-lapse film. A sequence of values can then be incremented to give horizontal and vertical growth rates of clouds. In addition, the following qualitative data can be estimated from time-lapse movies: differential cloud motion at various altitudes and locations, shear, organization, extent of glaciation, presence of rain, and the time history of each parameter. In one of many applications, Bhumralkar (1973) studied these qualitative factors from time-lapse film and related them to a model of flow over a heated island.

Readily available optics now permit attachment of all-sky lenses to movie cameras so that the entire sky from horizon to horizon can be seen in every direction. Cloud evolution, direction, speed, and cloud cover percentage can be documented quite easily from all-sky photos (Holle et al., 1979). However, the height and width of clouds near the horizon at a distance cannot be obtained, since such clouds cover a very small area of the picture, just as they cover a very small area of the actual sky. Horizontal-facing time-lapse cameras are needed to study clouds along the horizon.

The preceding data collection methods enable useful pictures to be obtained from the field on only a part-time basis. The following kinds of photographs require a nearly full-time photographer and/or increasingly sophisticated analysis equipment.

c. Panoramic photographs

Panoramic photographs of the sky at fixed intervals (e.g., hourly) provide benchmarks of cloud evolution in every direction from a single location. Ideally, a wide-angle camera with a large format and large vertical angle (such as the Hasselblad Super-wide) is used to take six to nine photographs with some overlap. A sunshade, polarizing filter, or other filter is usually desirable. Figure 4 shows a series of these panoramas taken on Grand Bahama Island during a field project. Thunderstorms grew over the center of the long E-W island and became well organized just north of the station. The three successive mosaics show clearly how clouds changed over the 3-h period, which was part of a day being studied for modeling the flow over a heated island. Directions are not in perfect alignment from one time to the next because individual pictures for the mosaics were cropped with respect to cloud entities and edges for good visibility of the whole system. Very accurate azimuths are available in the individual photos constituting the mosaics.

A photographer must be at the field site to take pictures at the appointed time; his time will be divided with other observing duties at a radar, upper-air, or communications site. Since the panoramic photos do not give fine time resolution, they are best used in combination with a time-lapse camera in a thunderstorm study. The time-lapse camera shows a narrower region of convection, and the panoramas document developments on the sides of the time-lapse camera's pictures that may be of great importance in understanding the narrower view.

As with photographic methods described previously, the analysis with Eqs. 1 to 7 requires only the usual parameters: horizon, lens focal length, and distance to cloud feature. Analysis is usually made on an enlarged print. Typically, some hundreds of panoramas are taken during an extensive field project so, for economy, they are taken in black and white. Contact prints are frequently examined by personnel from other subprograms of the field project; more often than not, it seems that interests in cloud parameters are not those anticipated in the original analysis program. Thousands of panoramas were taken in the Barbados area (Holle, 1968) for cloud population statistics, in FACE (Florida Area Cumulus Experiment), and in GATE, the GARP (Global Atmospheric Research Program) Atlantic Tropical Experiment.

d. Multiple time-lapse camera photographs

Multiple time-lapse camera photography of thunderstorms can be taken from either one or several locations with cameras usually operated unattended. If a specific cloud is to be kept in view, the cameras may need to be moved if the field of view (Eq. 1) is small. As additional cameras are set up, monitoring takes more time. If one photographer must oversee two or more sites

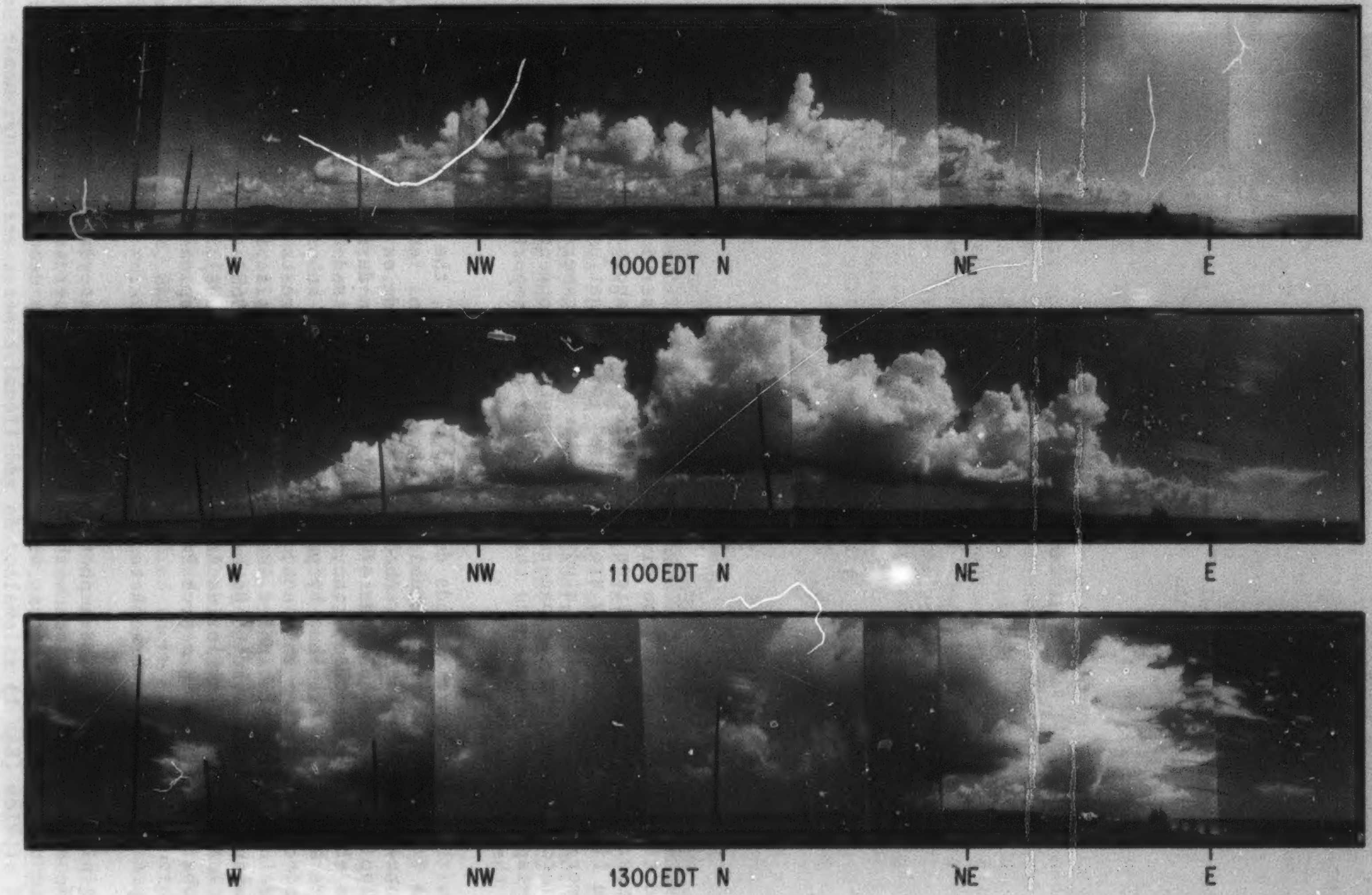
W
NW
1000EDT N
NE
E
W
NW
1100EDT N
NE
E
W
NW
1300EDT N
NE
E

Figure 4.--Mosaics of panoramic pictures of thunderstorms taken on the south coast of Grand Bahama Island on 20 August 1970 at 1000, 1100, and 1300 EDT. Mosaics from other days in this project are presented by Bhumralkar (1973).

best copy available

or three or more cameras, about half the day will be needed for setup, takedown, time checks, and other duties. Several time-lapse cameras looking in different directions from one site can provide nearly all the information that panoramic picture sets can give. However, one local storm or medium-sized shower may obscure the views of all cameras. If storms are isolated, but numerous, it may be better to place one camera in each of several locations. This situation prevails in the tropics and subtropics, especially in Florida, where during FACE 1975 there were as many as five time-lapse cameras at four locations (Staff, Cumulus Group, 1976), each positioned at a Doppler radar or operations center and all looking into a common region. It was rather unusual for all cameras to have their views blocked simultaneously by rain. In Socorro, N. Mex. (Fig. 3), where thunderstorms occur over the same mountain on most days, a network of three 16-mm cameras has been permanently installed, equally spaced, around the mountain (Aloway et al., 1970). In both Florida and New Mexico, additional cameras with larger film sizes have been established at some of the regular sites. Since 16-mm film provides relatively small negatives for enlargements, 35-mm cameras with timers and large magazines have been operated intermittently throughout the day when an especially good cloud view is apparent. The 16-mm time-lapse camera operates at one frame per 10 seconds all day, and the 35-mm time-lapse camera operates at one frame per minute for an hour.

e. Stereoscopic photographs

Stereoscopic photography has the advantage of producing its own distances to clouds and affords a qualitative view of relative distances without any analysis. There are proportional disadvantages in that more careful data collection and analysis are needed than for ordinary ground-based photography. For example, the lens focal lengths must be known very accurately and angles to distant landmarks must be measured precisely. Over a summer, the operation of a stereoscopic system during a field program requires a half-time photographer. In a typical field operation, an electronic signal fires two cameras simultaneously. A baseline of several kilometers is typically used to obtain useful parallax between pictures of the same thunderstorms located some tens of kilometers away. This baseline is a compromise between range resolution, needing a long baseline, and a view similar enough for common cloud elements to appear in both pictures, needing a short baseline. The optimum situation has the cloud subtending about 10° across the baseline. Closeness of two cameras increases the prospect that a local storm or cloud obscures the view of more distant clouds that must be visible on both cameras for a stereoscopic effect. This problem is considerably reduced in drier areas, since fewer cumuli block the view, and where storms grow over a fixed geographic location, such as a mountain range, where most stereoscopic systems have been placed. An example of a stereoscopic pair is shown in Fig. 5.

Different methods and equipment have been used for taking and analyzing stereoscopic pairs. For example, Shaw and Marshall (1972) employed two rotating-lens cameras with fields of view of 55° vertical by 140° horizontal. Warner et al. (1973) used two 16-mm time-lapse cameras and a specially designed analysis system for studying the Alberta clouds in Fig. 5. Such figures can be viewed either with an inexpensive pocket stereoscope or with the cross-eye method described by Fraser (1968). The latter technique requires no special equipment. Both viewing methods provide relative distance information, but do not measure any parameter directly.

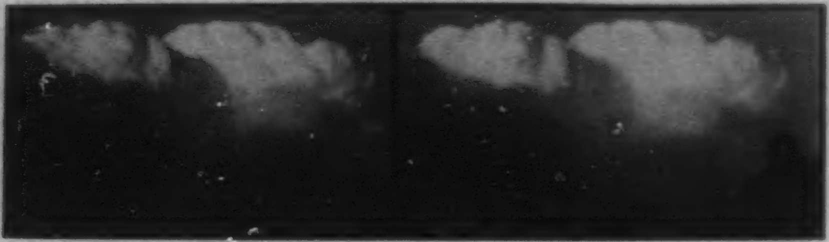

Figure 5.--Stereoscopic pair of pictures showing hailstorms over Stettler, Alberta, on 15 July 1968 at 1929 MST. This view looks east from two 16-mm color cameras located at Penhold, Alberta. The towers were growing explosively and produced hail of 1.5-cm diameter that fell briefly from the right tower and 1.0-cm hail from the left. The pair is properly oriented for viewing with a pocket stereoscope. (photos from Charles Warner, University of Virginia, Charlottesville; pictures were taken as part of the Alberta Hail Project).

Detailed measurements from stereoscopic pairs have been made with such a wide variety of devices and concepts that few generalizations can be made. One interesting approach is to use stereoscopic plotters commonly employed for mapping terrestrial features (roads, mountains, etc.) from stereoscopic aerial photography. These complex and costly machines normally measure phenomena that are stationary in time, as described by the American Society of Photogrammetry (1980). Adaptation of standard mapping procedures to stereoscopic cloud photos is not simple and varies from one plotter to another, but it holds promise for projects with large numbers of stereoscopic pairs to be analyzed.

f. Photos of tornadoes and severe weather

Movies and still photos from handheld cameras have given valuable information on tornadoes, waterspouts, hail, severe windstorms, and squall lines. Such pictures cannot be well planned in advance, so the analyst often encounters difficulties that result from incomplete data collection. A major problem in analyzing such pictures is introduced because the horizon and distance to storm are likely to be missing. In this situation, the sites of the photos and the tornado path must be marked and surveyed to determine the angles to power poles and other landmarks that are in the picture. In a research project, the pursuit of such pictures requires one or more dedicated photographers in an automobile, van, boat, or aircraft; contact may be maintained with other field personnel at, for example, a radar site. Such a tracking and photography project for gathering tornado pictures has been described by Golden and Morgan (1972). An example of an analyzed tornado photo is shown in Fig. 6. Photographs of tornadoes from the public have been analyzed by Fujita (1960, 1975; see also Vol. 1, Ch. III).

g. Summary

Considerable qualitative insight can be gained from still and time-lapse pictures with little more information than logs on time, location, and equipment. A good cloud observer can use photographs to prove a point of contention or to clearly disprove a possibility that other data had raised. The

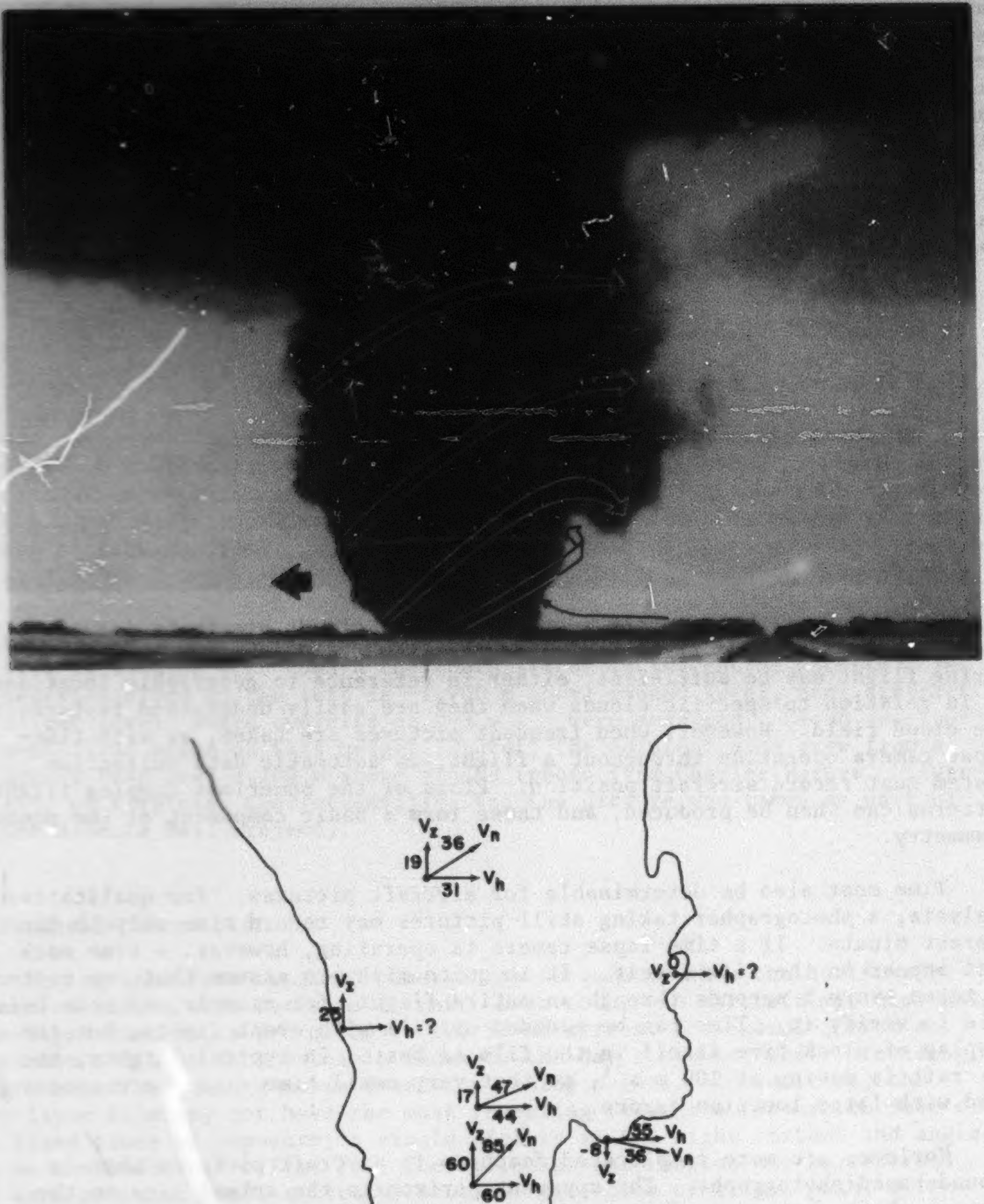
Vz
36
Vn
19
31
Vh
Vz
25
Vh=?
Vz
0
Vh=?
Vz
47
Vn
17
44
Vh
Vz
85
Vn
60
60
Vh
55
Vh
-8
36
Vn
Vz
500 m

Figure 6.--Great Bend, Kans., tornado of 30 August 1974. Above, the vortex from a 16-mm movie frame taken about 0005 GMT; debris trajectories are based on photogrammetry of the movie loops covering 0005 to 0010 GMT. Below, the most accurate vectors from a larger set of calculations, made during this period, which lead to trajectories above (Golden and Purcell, 1977).

latter is a frequent case in which pictures provide negative information--for example, the expected cloud configuration is clearly absent. It is sometimes very important to document absence of clouds. Limited quantitative information can be gained from one camera if the range is only roughly known; but if range is very accurate, single-picture analysis is easy and rather precise. Finally, sophisticated cameras and analytic procedures performed on stereoscopic pairs and handheld-camera pictures of rare targets of opportunity can provide highly detailed time histories. Ground photographs often provide the only way to see low-level thunderstorm features such as rainshafts, squalls, tornadoes, and cloudbases.

4. PHOTOGRAMMETRY OF AIRCRAFT-BASED PICTURES

a. Special considerations

Pictures from aircraft may show important aspects not visible from the ground. However, since an aircraft changes position continually and undergoes attitude changes such as roll while it is moving, analysis of airborne photography begins at a more difficult level than for ground photos. The additional parameters of aircraft altitude, location, time, and horizon must be considered.

The track of the aircraft must be known if clouds are to be located. Where only qualitative illustration of the cloud is needed, notes taken during flight may be sufficient, either in reference to geographic locations or in relation to specific clouds when they are easily understood features of the cloud field. However, when frequent pictures are taken, as with time-lapse camera operation throughout a flight, an automatic data collection system must record aircraft position. Plots of the sometimes complex flight patterns can then be produced, and these form a basic component of the photogrammetry.

Time must also be determinable for aircraft pictures. For qualitative analysis, a photographer taking still pictures may record time only to the nearest minute. If a time-lapse camera is operating, however, a time mark must appear on the film itself. It is quite risky to assume that one picture is taken every 5 seconds through an entire flight, for example, without being able to verify it. Time can be encoded on film with event lights, but the display of clock time itself in the film is best. In typical flights, the aircraft is moving at 100 m s^{-1}, so that very small time errors are associated with large location errors.

Horizons are more complicated features in aircraft pictures than in ground-based photographs. The apparent horizon is the actual line on the picture where sky and land meet, and the true horizon is at the intersection of the photo plane and the true horizontal plane containing the camera lens. From an aircraft, the observer's apparent horizon always dips below true horizontal in a manner dependent upon aircraft height. This difference, the dip angle, is more than 2° at 6-km altitude. The dip angle results mostly from Earth curvature, and there is also some contribution from atmospheric refraction. In addition, the apparent horizon is frequently not visible from an aircraft when there are thunderstorms, because of obscuring clouds. Consequently, calibration of the camera relative to the aircraft in flight is necessary during flight segments with clear views of the horizon.

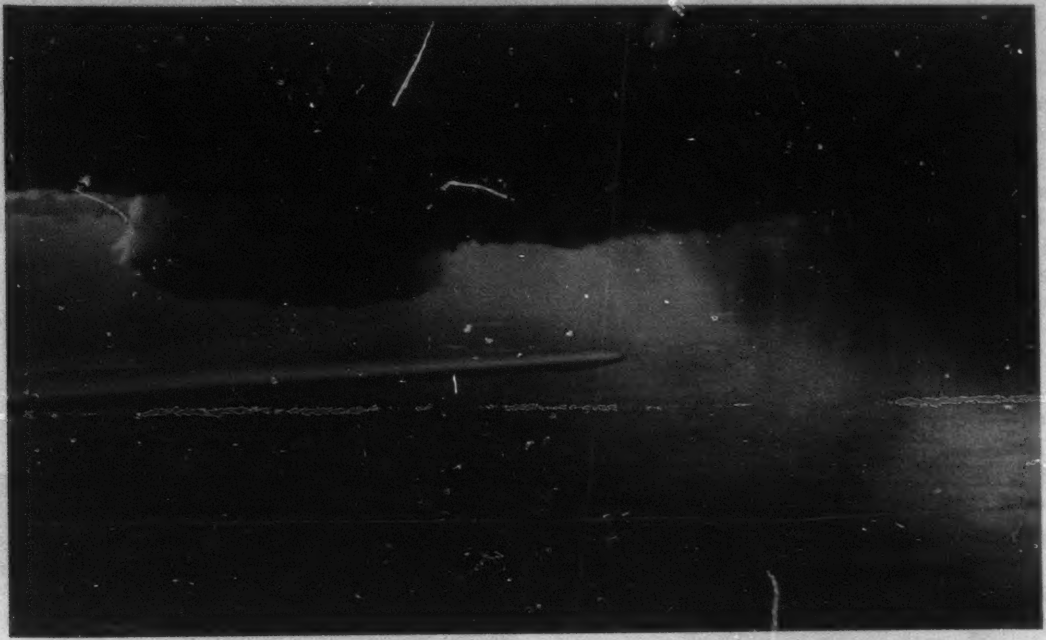

Figure 7.--Handheld-camera photo taken on 4 July 1976 at 1722 MDT. The view is looking west toward the foothills of south-central Alberta. The pedestal cloud on the left is ~1,700 m above ground level, near aircraft flight level, where updrafts of 2-3 m s^{-1} were measured. Cloud development first began at this height. Later, the adjacent area grew from a higher base near 2,700 m above ground (photo from Charles Warner, University of Virginia, Charlottesville, Va; the picture was taken as part of the Alberta Hail Project).

b. Handheld-camera pictures

Photographs from handheld cameras can frequently show the qualitative nature of clouds seen during a flight. Even though an aircraft may also have time-lapse cameras, a set of 50 to 100 35-mm slides, for example, from an afternoon's flight is a valuable index to the day's events, while providing larger negatives than a movie frame for making prints. In addition, the time-lapse film may not have the most revealing view of a feature because of its fixed times of exposure; a single picture at the right instant and angle can be invaluable (see Fig. 7). The following information may be recorded for each picture: time, aircraft location, direction of flight path, direction of camera, altitude, lens focal length, camera, photographer, film roll and picture numbers, and description of the meteorological condition that prompted the picture to be taken.

When the apparent horizon cannot be found, only the relative heights and dimensions of cloud portions can be determined, together with approximate location, organization, time history (from a series of photos), shear, and visible ice-water contrasts. In many situations these data are sufficient, or are all that can be recovered, as Warner (1977) reports for a qualitative study of Alberta thunderstorms. If the apparent horizon can be found, then the basic equations, Eqs. 1-7, are applicable to analysis.

c. Stereoscopic views

Stereoscopic pairs can be obtained in flight by a photographer looking from the side window. Proper stereoscopic parallax is gained in two steps. First, estimate the distance to the cloud of interest. Then, space the pictures along the flight path at an interval appropriate to the aircraft speed. An interval between 1 and 3 seconds will often be appropriate for pictures taken from a jet aircraft (Scorer, 1972). Fraser (1968) describes in more detail how to calculate the optimal time between pictures in a stereoscopic pair taken from aircraft. A useful equation for the time interval between pictures is

$$T = 300 \frac{D}{V} , \tag{8}$$

where T is the time in seconds, D is the distance to the closest cloud in miles, and V is the speed of the plane in miles per hour. Not every cloud in the view of a stereoscopic pair can be made to fuse in that pair alone. For closer or much more distant clouds, extra pictures may be needed.

Instruments for stereoscopic viewing include inexpensive pocket stereoscopes, sophisticated stereoscopes, or a small hand mirror; the cross-eye method can also be employed for stereoscopic viewing (Fraser, 1968). An example of the pocket stereoscope method is shown for ground-based pictures in Fig. 5. If a large number of stereoscopic pairs is required, it is preferable to operate an automatic time-lapse camera looking out the side of the aircraft. During analysis of side camera film, the distance to visible clouds will be roughly known. When depth perception is needed, an equation such as Eq. 8 can be used to choose the proper photos to print for stereoscopic viewing.

d. Time-lapse photographs

Airborne time-lapse cameras are the most sophisticated systems for taking thunderstorm pictures in the air. The cameras may look out the aircraft sides, front, or downward. A complete set of horizontal-facing pictures is shown in Fig. 8. The motion of the clouds across the screen, when the film is viewed at normal projection speeds, reduces the need for stereoscopic pairs in many, but not all, situations. Once the entire camera system is operational at the beginning of a flight, the cameras themselves may not need frequent checks in the air. But collection of coordinating data for complete analysis may require the attention of several personnel in flight. If only one time-lapse camera is available for an aircraft during a field project, the choice of direction depends upon the flight pattern. When flight tracks are complex, having, for instance, a turn every 5 minutes, the nose camera is the preferred single camera. It provides a superb visual record of clouds penetrated along the aircraft track, shows distant clouds ahead of the plane, and produces pictures that lend themselves to extensive analysis. The most common nose camera frame rate is one frame per 2 or 3 seconds, with slower rates at higher altitudes. This rate allows a sufficient number of frames to show an upcoming cloud in several frames, then indicate how many seconds the aircraft was in cloud during penetration; the rate is not unreasonably tedious on long, straight flights. Color 16-mm film has been almost universally used in nose cameras, although its quality is not as high as 35-mm, as Fig. 8 shows. Forward-looking cameras have one special complication: when

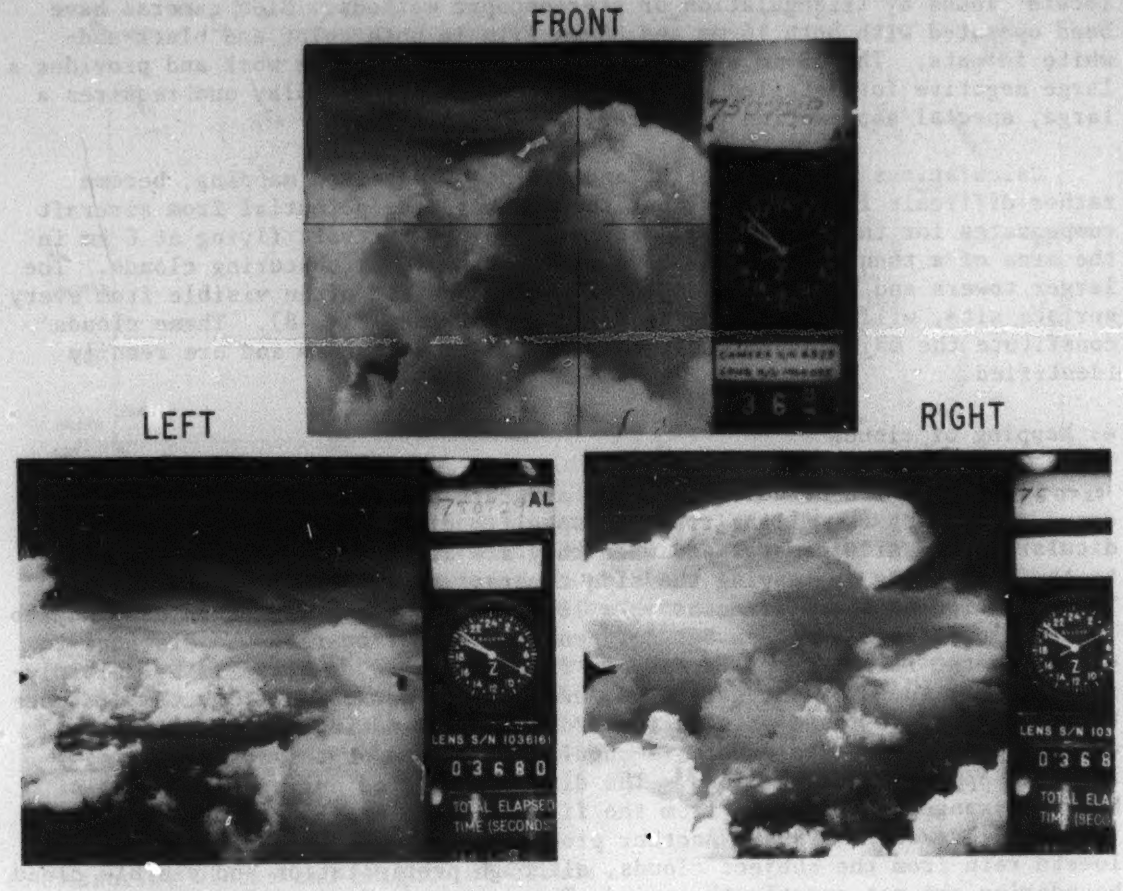

Figure 8.--Right, left, and nose camera views of Florida thunderstorms taken 29 July 1975 at 1951:20 GMT. The pictures were taken during FACE 1975 from the RFC DC-6 aircraft. Side camera photos were taken on 35-mm black-and-white film, and the nose camera used 16-mm color film; higher quality pictures come from the 35-mm film. Clock times are approximate, but the elapsed-time frame counters are exact. Lines in the front-facing photo are located in the image plane of the lens, but are not accurate; finding the picture center by crossed diagonals is the better method (see Eq. 3).

repeated penetrations are made of supercooled clouds, the window in front of the lens must be heated to remove the ice accumulation.

On long, straight flight legs, a complete record of clouds visible on one side of the aircraft track can be gained from a side camera looking exactly perpendicular to the aircraft track. Large areas are seen continuously, and detailed mapping can be accomplished similar to the Pacific cloud charts produced by Malkus and Riehl (1964). Side cameras are typically operated at a rate between one frame per 1 and 5 seconds. Although the side-looking wide-angle lens covers a large area, enough pictures must be taken to locate clouds by triangulation or stereoscopic methods. Side cameras have been operated with both 16-mm and 35-mm film in both color and black-and-white formats. The 35-mm system is excellent for precise work and provides a large negative for detailed prints (Fig. 8), but it is bulky and requires a large, special stop-motion projector for photo analysis.

Calculations of cloud height and width, or detailed mapping, become rather difficult from the air, but the greater data potential from aircraft compensates for the complexity. For example, an aircraft flying at 6 km in the area of a thunderstorm is above most of the lower obscuring clouds. The larger towers and the cloud complexes, which are not often visible from every surface site, will be penetrating flight level (see Fig. 8). These clouds constitute the major dynamic elements of the thunderstorm and are readily identified.

e. Mapping of clouds

Cloud maps can be developed from aircraft photos with the aid of lines drawn to connect the flight track to specific clouds when they are perpendicular to the side cameras and when they are at the azimuths corresponding to their entering or leaving the side cameras' view, as defined by Eq. 1. Triangulation of these azimuths on a large flight track map is an easy way to locate clouds that are seen but not penetrated. Of course, the distance to clouds on the flight track is easy to find from nose camera film by multiplying aircraft speed by the number of seconds to penetration. Or, the distance to a cloud may be found using a forward camera by noting the time interval needed for the cloud to double in angular dimension on the screen during aircraft approach to the cloud. The distance covered during this time is half the range to the cloud from the first view. These concepts are treated in detail by Ronne (1959). Another procedure is to use radar echoes to locate rain from the subject clouds, although precipitation and visible cloud boundaries are not exactly the same. The accuracy of aircraft navigation can be increased when geographical features are seen on radar. Warner (1978) described a method of mapping with nose camera film during straight and level flight.

Another tool for mapping unpenetrated clouds during level flight is the crossing-angle procedure developed by Ronne (1959) and expanded by Whitney and McClain (1967). This method uses side cameras to give range r to a cloud from

$$r = \frac{VFR}{2 \tan \frac{\alpha}{2}} , \qquad (9)$$

where V is the groundspeed of the aircraft along the portion of the track of importance, F is the number of frames that a cloud requires to cross the field of view of a side camera, R is the interval between frames in seconds, and α is the total horizontal angle of the lens from Eq. 1. Equation 9 can be the basis for some useful tables. The crossing-angle procedure and other mapping methods mentioned here have been used to produce the cloud maps in Fig. 9. It should be noted that some time-lapse projectors do not show the entire horizontal film frame.

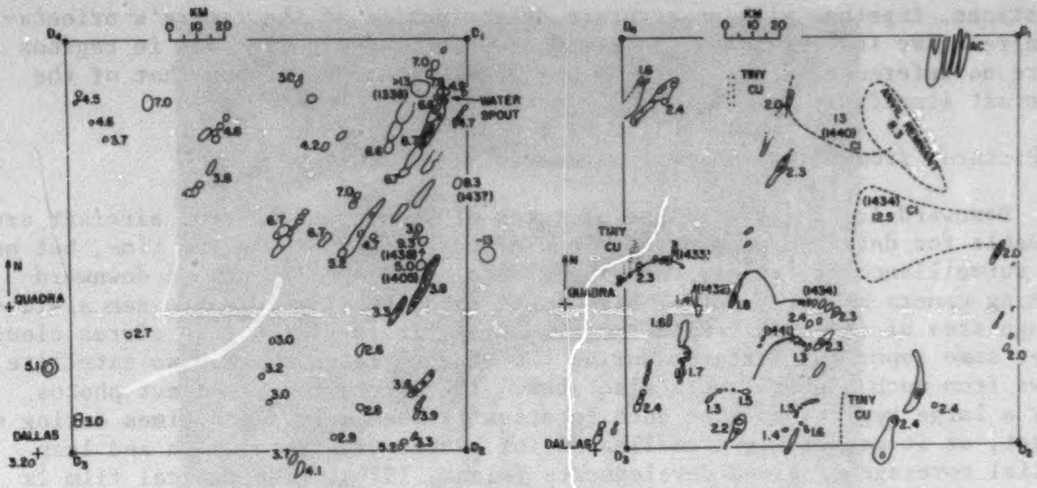

Figure 9.--Cloud maps made from aircraft time-lapse photographs during GATE on 18 September 1974 between 1300 and 1445 GMT. The pictures were taken using side and nose cameras aboard four of five aircraft flying the box circuit D_1 D_2 D_3 D_4, located between 8.6° and 9.9°N and 21.0° and 22.4°W. Left panel shows active cloudtops with heights from 2.5 to more than 13 km; right panel shows tops less than 2.5 km. Numbers are altitudes in kilometers and times of measurement. Thin solid lines represent arcs of clouds, and anvil shapes are dashed. GATE ships Quadra and Dallas are to the southwest (Warner et al., 1979).

f. Measuring widths and heights of clouds

Widths and relative heights are not difficult to measure from the air. One qualitative rule sometimes overlooked is that any cloud above the true horizon is above the aircraft flight level, and clouds below that level appear below the true horizon. However, the higher the aircraft, the greater the dip angle (see Sec. 4a), and this idea becomes less useful. Given distance to cloud from one of the techniques in the preceding paragraphs and the lens focal length, Eqs. 1-7 are appropriate. The only caveat is that tilt in Eqs. 4 and 5 must be known in order to use the equations exactly. Absolute heights and widths are calculable if the apparent horizon is visible, or if the camera has been calibrated to locate the true horizontal plane and aircraft roll was recorded. The Earth curvature and atmospheric refraction correction mentioned for Eq. 6 also must be applied for aircraft film. A graphical method, described by Cantilo and Woodley (1970), reduces the mathematics involved in the above procedures. It includes the use of grids, made for various aircraft rolls up to 24°. The method was used for the 35-mm side camera film shown in Fig. 8. A key step for photogrammetry is the calibration of the apparent horizon in clear-sky conditions at the desired altitude. This is an important consideration; once the horizon is located and cloud position is found from triangulation, measurements of absolute height may be made in cloudy areas where the apparent horizon is totally obscured. Then, absolute heights may be found rather quickly from the grids. However, the Cantilo-Woodley method is a solution for a specific problem. Other techniques have been devised (Fujita, 1974) that use basic photogrammetric equations, together with an accurate determination of the camera's orientation relative to horizontal, to allow cloud height measurements in regions where no reference is available to any absolute height except that of the aircraft itself.

g. Pictures from downward-looking cameras

Downward-looking time-lapse pictures of thunderstorms from aircraft are valuable for detailed mapping of cloud distributions at a given time, but not for surveillance of rapidly changing clouds. An aircraft with a downward-looking camera must fly rather high (more than 10 kilometers) to see a wide-enough area of interest. With thunderstorms, it is likely that cirrus clouds cover some important features during the storms' later stages, as satellite views from much higher levels also show. The aircraft may collect photos over a large region, so that each location is seen only a few times during a flight, or it may circle a small area for better time resolution and less spatial coverage of cloud developments (Plank, 1974). The typical film is black and white and rather large, ranging up to a 5" × 11" negative. Plank (1969) describes a project, with both vertical and oblique pictures, in which the vertical pictures provided cloud diameters and the heights of cloudbases from their shadows on the ground. Oblique pictures were taken with the horizon across the top of the photograph for finding cloud heights. Other downward-looking cameras have been used to take elongated pictures, sweeping from horizon to horizon, giving detail in a small area under the aircraft and less detail over larger areas toward the horizons (Fig. 10). Vertical or oblique photos can be difficult to analyze; use of special grids developed for specific cameras or larger stereoscopic plotting machines may prove economical only if there are many analyses.

5. CONCLUDING REMARKS

It is frequently anticipated that analysis of cloud pictures can be automated to eliminate time-consuming procedures. Although computers reduce the routine of long series of calculations, often only a few thunderstorm pictures taken with each type of camera from the same location are analyzed in the same way. Even more important, substantial automation is not feasible in many situations because of the nature of the clouds themselves. One must ask these questions: Where are the sides of a cloud? When have two elements become one? Can the same feature be seen from both ground and air? The meteorologist must be involved in the decision in light of experience, understanding of the storm from other data sources, and the level of detail that is required.

We have discussed photographic data collected in visible wavelengths from cameras situated near or below the tropopause. New methods of photography of terrestrial features from high-altitude aircraft and satellites are continually being developed. High-altitude balloons (near 30 km) have been used occasionally to gather downward-looking and oblique photos of thunderstorms with better time resolution than aircraft and better space resolution than satellites (Vonnegut, 1970). Although satellite views have somewhat supplanted high-altitude vertical photography for cloud mapping, this may be an appropriate time for new coordinated studies that match detailed vertical cloud views with high-resolution satellite pictures. Then, we may understand

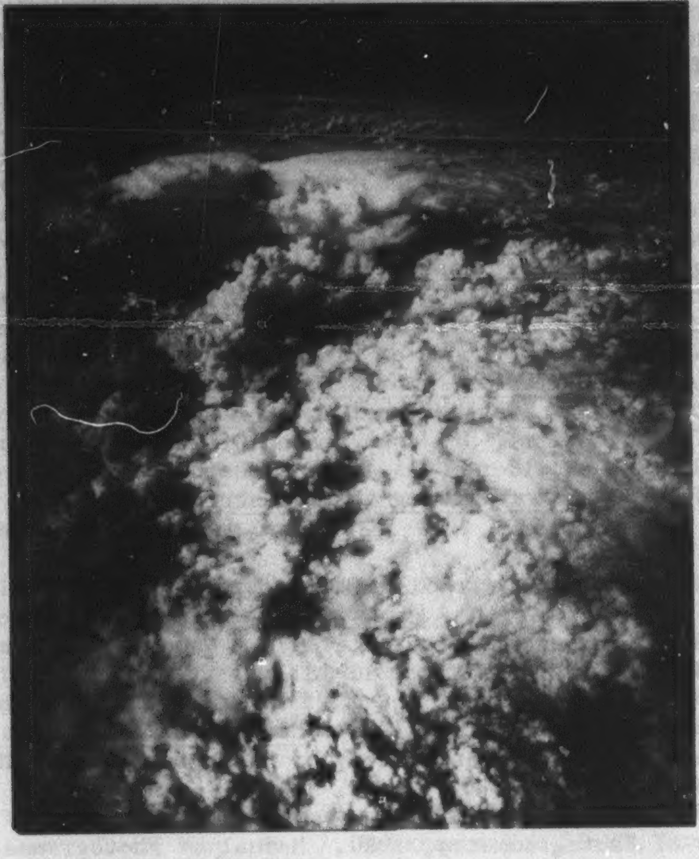

Figure 10.--View from downward-pointed camera aboard B57-F aircraft flying at 60,000 feet over western Oklahoma, 11 June 1967, 1445 CST. This is one-half of the full print and extends from the nadir (center of lower margin) to a horizon normal to the line of flight. Each full negative of the original film measures 5" × 11".

better the features of thunderstorm organization and structure shown by satellite imagery.

There is recent improvement in sensors for penetrating haze, poor visibility, and darkness with instrumentation outside the visible wavelength band. Such sensors and related techniques are given in the Manual of Remote Sensing from the American Society of Photogrammetry (1975). As new instrumentation and methods are developed, it is likely that renewed impetus will be provided to relate newly probed phenomena to more familiar visual records.

Conventional photo archives often represent some of the most interesting and cost-effective data in a thunderstorm study. Although newer cameras have replaced the Brownie in popularity, a comment of Ronne (1959) still holds true: "The lowliest box Brownie can measure off an angle or record a fact with an accuracy far greater than the eye or memory of the most skilled observer."

Acknowledgments

I am grateful to Dr. Joanne Simpson (NASA, Greenbelt, Md.), Dr. Michael Garstang (University of Virginia), and Dr. William Woodley (Office of Weather Research and Modification, NOAA/ERL, Boulder, Colo.) for providing the opportunity, encouragement, and time to become interested in and pursue photogrammetry of cumuli during the last decade. Great admiration and appreciation is extended to Claude Ronne, who for many years was associated with Woods Hole Oceanographic Institution and who has patiently described many of his ideas on cloud mapping from aircraft, as well as other basic concepts of photogrammetry. Dr. Charles Warner (University of Virginia) provided invaluable reviews of this manuscript based on his wide photogrammetric background. Dr. Charles Moore (New Mexico Institute of Mining and Technology) and Dr. Joseph Golden (NOAA/ERL, Boulder, Colo.) kindly provided illustrations of their photographic data. I also thank Michael Maier (Lightning Location and Protection, Inc., Tucson, Ariz.), Dr. John Brown (Office of Weather Research and Modification, NOAA/ERL, Boulder, Colo.) and Richard Decker (National Weather Service, Sterling, Va.) for reviewing the manuscript.

REFERENCES

Aloway, J., C. B. Moore, and B. Vonnegut, 1970. Cameras for time-lapse photography. Applied Optics 9:1811-1813.

American Society of Photogrammetry, 1975. Manual of Remote Sensing. R. G. Reeves (ed.), American Society of Photogrammetry, Falls Church, Va., 2144 pp.

American Society of Photogrammetry, 1980. Manual of Photogrammetry. 4th Ed., C. C. Slamo (ed.), American Society of Photogrammetry, Falls Church, Va., 1056 pp.

Bhumralkar, C. M., 1973. An observational and theoretical study of atmospheric flow over a heated island, Parts I and II. Mon. Weather Rev. 101:719, 731.

Cantilo, L. M. H., and W. L. Woodley, 1970. Cloud photogrammetry from airborne time-lapse photography. J. Soc. Motion Pict. Telev. Eng. 79:604-606.

Fraser, A. B., 1968. Stereoscopic cloud photography. Weather 23:505-514.

Fujita, T., 1960. A detailed analysis of the Fargo tornadoes of June 20, 1957. U.S. Weather Bureau Res. Paper No. 42, Washington, D.C., 67 pp.

Fujita, T., 1974. Overshooting thunderheads observed from ATS and Learjet. SMRP Res. Paper 117, University of Chicago, 29 pp.

Fujita, T., 1975. New evidence from April 3-4, 1974 tornadoes. Preprints, Ninth Conference on Severe Local Storms, Norman, Oklahoma. American Meteorological Society, Boston, Mass., 248-255.

Golden, J. H., and B. J. Morgan, 1972. The NSSL-Notre Dame Tornado Intercept Program, Spring 1972. Bull. Am. Meteorol. Soc. 53:1178-1180.

Golden, J. H., and D. Purcell, 1977. Photogrammetric velocities for the Great Bend, Kansas, tornado of 30 August 1974: accelerations and asymmetries. Mon. Weather Rev. 105:485-492.

Holle, R. L., 1968. Some aspects of tropical oceanic cloud populations. J. Appl. Meteorol. 7:173-183.

Holle, R. L., and M. W. Maier, 1980. Tornado formation from downdraft interaction in the FACE mesonetwork. Mon. Weather Rev. 108:1010-1028.

Holle, R. L., J. Simpson, and S. W. Leavitt, 1979. GATE B-scale cloudiness from whole-sky cameras on four U.S. ships. Mon. Weather Rev. 107:874-895.

Malkus, J. S., and H. Riehl, 1964. Cloud Structure and Distributions Over the Tropical Pacific Ocean. University of California Press, Berkeley and Los Angeles, 229 pp.

McNeil, G. T., 1954. Photographic Measurements: Problems and Solutions. Pitman Publishing Co., New York.

Plank, V. G., 1969. The size distribution of cumulus clouds in representative Florida populations. J. Appl. Meteorol. 8:46-67.

Plank, V. G., 1974. A photoreconnaissance technique for conducting time-lapse studies of the development and motions of cumulus cloud populations and systems. Air Force Cambridge Res. Lab. Rep. AFCRL-TR-74-0250, Bedford, Mass., 70 pp.

Ronne, C., 1959. On a method of cloud measurement from aircraft motion picture films. Tech. Rep. No. 7, Reference No. 59-29, Woods Hole Oceanographic Institute, Woods Hole, Mass., 23 pp.

Scorer, R. S., 1972. Clouds of the World. Stackpole Books, Harrisburg, Pa., 176 pp.

Shaw, R. W., and J. S. Marshall, 1972. Showers observed by stereo cameras and radar. Stormy Weather Group, Sci. Rep. MW-53, McGill University, Montreal, 21 pp.

Staff, Cumulus Group, 1976. 1975 Florida Area Cumulus Experiment (FACE): operational summary. Tech. Memo. ERL WMPO-28, NOAA Environmental Research Laboratories, Boulder, Colo., 186 pp.

Vonnegut, B., 1970. Time lapse photography of clouds from high altitude balloons. Appl. Optics 9:1814-1816.

Warner, C., 1977. Photos of seeded Alberta storms. Stormy Weather Group, Sci. Rep. MW-89, McGill University, Montreal, 27 pp.

Warner, C., 1978. Photogrammetry from aircraft nose camera movies. J. Appl. Meteorol. 17:1416-1420.

Warner, C., J. H. Renick, M. W. Balshaw, and R. H. Douglas, 1973. Stereo photogrammetry of cumulonimbus clouds. Q. J. R. Meteorol. Soc. 99: 105-115.

Warner, C., J. Simpson, D. W. Martin, D. Suchman, F. R. Mosher, and R. F. Reinking, 1979. Shallow convection on day 261 of GATE: mesoscale arcs. Mon. Weather Rev. 107:1617-1635.

Whitney, L. F., Jr., and E. P. McClain, 1967. Cloud measurements using aircraft time-lapse photography. ESSA Tech. Rep. NESC-40, Washington, D.C., 24 pp.

Wolf, P. R., 1974. Elements of Photogrammetry. McGraw-Hill Book Co., New York, 562 pp.

V. STORM ACOUSTICS

Roy T. Arnold

1. INTRODUCTION

Study of storm sounds is as old as science itself (Aristotle, 384-322 B.C.; Lucretius, 98-55 B.C.) and as new as the most recent technological advance. In modern probing of convective storms, this approach has been underexamined, and literature devoted to storm acoustics is relatively sparse. More atmospheric scientists should be aware of the merits and limitations of acoustical studies; this chapter is intended to serve as an introduction for those unfamiliar with the subject.

Storm acoustics research generally involves both active (e.g., acoustic sounding; Brown and Hall, 1978) and passive (e.g., study of thunder) techniques; this chapter is restricted to the passive methods. It is restricted also to audible frequencies, except for thunder studies, which include subaudible frequencies. Pressure waves at frequencies below the audible range (<20 Hz) are infrasounds. Infrasounds below 1 Hz from thunderstorms, discussed in Ch. VI, are ultralow-frequency waves that propagate with very little attenuation and probably have quite different origin than sounds and infrasounds described here.

Sounds most frequently associated with severe storms are generated primarily by lightning discharges (thunder) and by interactions of both precipitation and wind with terrain. There are undoubtedly other mechanisms that generate audible signals. For example, there have been reports of continuous rumbling (Arnold and Bass, 1977) apparently emanating from rather isolated storms and varied descriptions of unusual sounds from tornadoes and funnel clouds aloft (Flora, 1954). Verification and documentation of uncommon sounds is difficult, and records suitable for scientific analysis are practically nonexistent. Consequently this chapter is limited to descriptions of experimental and theoretical studies of thunder, analysis of sounds generated by severe tornadoes, and a brief comment on noise generated by wind.

2. PROPAGATION EFFECTS

Sound in the atmosphere is subject to the following alterations that affect the propagation direction and the amplitude of a pressure wave:

(1) Refraction caused by both temperature gradient and wind field.

(2) Spreading losses related to geometry of the sound source.

(3) Absorption in which sound energy is converted into random molecular motions.

(4) Reflections that occur at boundaries between air parcels having different physical characteristics, e.g., different density.

(5) Reflection and absorption at the Earth's surface.

Many important physical characteristics of the atmosphere near a severe convective storm are unknown, and it is difficult to treat propagation effects quantitatively. Some insight can be gained into just how important the effects are by using mean values of temperature, pressure, humidity, and wind field velocities in propagation analyses. It is also useful to consider some propagation effects applied to a sound source (such as a lightning channel segment) located a few kilometers above the ground: initially sound is radiated outward from the source in directions determined by the shape of the source; e.g., spherical and point sources radiate energy equally in all directions. As waves travel from source to recording station, refraction occurs because the velocity of sound is temperature dependent and because sound direction is altered by winds. Sound refracted upward in the mean vertical-temperature field accounts for some observed effects, e.g., the lack of sound from a nearby cloud-to-ground lightning flash. Variations in the wind field and turbulence produced by wind changes might account for other observations, e.g., seeing a cloud-to-ground lightning flash in one direction and hearing the thunder from another.

Sound velocity in a gas can be expressed as

$$c = \sqrt{\gamma r T} \, , \qquad (1)$$

where c is the speed of sound, γ is the ratio of the specific heat of the gas at constant pressure to that at constant volume, r is a constant whose value depends on the particular gas involved, and T is the absolute temperature in kelvins (Kinsler and Frey, 1962). In most instances of importance in storm acoustics, changes in sound velocity in the atmosphere are much more strongly influenced by variations in temperature than by variations in composition and pressure. For air at 1,013-mb pressure we may write

$$c = c_o \sqrt{T/273} \, , \qquad (2)$$

where c_o, the speed of sound in air at 0°C, is 331.6 m s^{-1}. Equation 2 may be applied to any region of the troposphere with good accuracy.

The importance of temperature-related refraction can be easily illustrated. We rewrite Eq. 2 as

$$c = c_o \left(\frac{T_s - ay}{273} \right)^{\frac{1}{2}} \, , \qquad (3)$$

where T_s is surface temperature, a is lapse rate, and y is altitude above the surface. Binomial expansion of the radical in Eq. 3 shows that the speed of sound is approximately a linear function of temperature over the vertical extent of the troposphere, if one assumes a constant lapse rate no greater than 6.5 K km^{-1}. Consequently, the vertical velocity gradient, g_T, is approximately constant and is given by

$$g_T = \frac{dc}{dy} = \frac{-ac_o}{2} (273 \, T_s)^{-\frac{1}{2}} \, . \qquad (4)$$

It is clear from Eq. 4 that in this model of the troposphere sound velocity decreases with altitude and rays will refract upward. To demonstrate the effect's importance, we consider an initially horizontal ray at ground level radiated from a cloud-to-ground lightning flash. Near the ground a ray will follow (approximately) a circular arc of radius R ($R = c_0/gt$) if the velocity gradient is constant. For a ray at ground level that has propagated horizontally 1 kilometer, the ray path will be approximately 6 meters above the ground with a direction of travel about 0.65° above the horizontal.

To illustrate refraction by wind velocity gradients, we select a plane boundary of given thickness between two layers of air moving in opposite directions with identical speeds. The wind velocity gradient in a direction perpendicular to the boundary is assumed constant. A sound ray incident normally on the boundary will follow a curvilinear path until it reaches the second boundary, then continue straight-line propagation with a sound velocity component in the prevailing wind direction. A 100-m layer between two airmasses moving at speeds of ± 15 m s^{-1} would produce an angular deflection of approximately 7.5° for a normally incident ray. Therefore, one can see that wind effects are often quite pronounced, but because of lack of knowledge of wind fields they are difficult to evaluate. Relative importance of temperature and wind field refraction effects in a storm environment has not been determined.

Reflection and scattering of sound by the Earth's surface is an important modifier of sound signals received near the surface. Sound arriving at a receiver is composed of a direct wave from the sound source and a reflected wave from the surface. Interference between direct and reflected waves is frequency dependent because phase shift upon reflection is frequency dependent. The phase shift upon reflection, the magnitude of which is a function of both the angle of incidence and the surface acoustic impedance, is π at very low frequencies and falls off slightly with frequency increase. A phase change of approximately π occurs at nearly all frequencies for grazing incidence ($\lesssim 5°$), in which case almost complete cancellation occurs. Consequently, at distances beyond 10 km on a relatively flat terrain, almost no direct sound can be heard from the visible portion of a cloud-to-ground lightning flash. Similarly, tornado noises that emanate from very near the ground will be greatly diminished by interference only a few kilometers away. A detailed review of sound propagation near the Earth's surface is presented by Piercy et al. (1977).

Sound waves are attenuated with distance because sound energy is lost to molecular motions in the atmosphere. Absorption of higher acoustic-wave frequencies is most rapid and is determined by temperature, pressure, and molecular composition of the atmosphere. Reliable calculations of the absorption coefficient for sounds propagating in the atmosphere can be incorporated into storm acoustics (Bass and Losey, 1975; Arnold et al., 1976). Total absorption of sound in air as a function of frequency and relative humidity is presented in Fig. 1; note the magnitude of attenuation.

Sound traveling outward from a source is also subject to spreading losses; i.e., the intensity of sound emanating from either a point or spherical source diminishes proportional to the inverse square of the propagation distance.

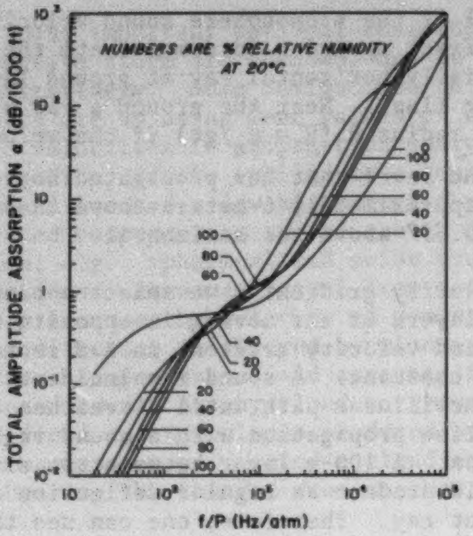

Figure 1.--Total absorption of sound in air as a function of frequency (after Evans et al., 1972).

Some other propagation effects also modify sound waves in the atmosphere. Reflection of sound at boundaries between airmasses with different temperature and/or wind fields undoubtedly contributes to echoes and variations in sound amplitude such as rumbles of thunder. Large-amplitude effects such as wave steepening and increased absorption are important when the wave overpressure is large (>1 mb). In addition, ducting of sound in a layered atmosphere, diffraction, and interference from multiple sources are often effects to be considered in some problems.

3. THUNDER

Thunder is a mechanical disturbance generated by great overpressure within the segments of a lightning channel. There is first a shock wave propagating outward somewhat faster than the speed of sound (Zel'dovich and Raizer, 1967). With both absorption and spreading losses, the mechanical wave passes from a strong-shock into a weak-shock regime and finally evolves into a finite-amplitude acoustic wave from which thunder follows. Other mechanical disturbances can be generated by a lightning discharge. For example, neutralization of charge droplets in a large volume can produce an observable pressure pulse as the region undergoes partial collapse (Wilson, 1920).

Thunder and infrasonic pressure variations associated with lightning have been studied by numerous investigators. Uman (1969) surveyed the thunder literature. Few (1969; 1970; 1974b), Holmes et al. (1971), Bohannon et al. (1977), and Dessler (1973) list pertinent research papers.

a. Sounds of thunder

(1) Audible thunder

Claps and rumbles are the characteristic thunder sounds. Thunderclaps are abrupt changes in loud sounds that occur when the observer is located where sound from major channels and branches is at a maximum. Occasionally, when one is very near a vertical channel, absorption of high-frequency components of sound is diminished and a loud crack is heard. Rumbles occur because of arrival of many erratic sound signals from the entire extent of channels and branches. Major channel elements are approximately 50 or more meters long, and the minor segments are a few meters or less in length (Hill, 1968). Channel segments represent individual cylindrical sound sources that radiate energy perpendicular to the channel axis, and the sound one hears originates in thousands of sources along the lightning channel; thus thunder following a lightning flash is perceived as a superposition of sounds from many segments of a very tortuous lightning channel (Few, 1974b). Consequently, pressure variations produced by lightning are very complex, and careful recording and data reduction techniques are required before analytical benefits can be derived. More complete qualitative descriptions of what we hear as thunder can be found in Few (1974b; 1975) and Uman (1969).

Loudness, a qualitative aspect of audible thunder, merits a brief description. Excluding propagation effects, what we perceive as loudness is not only a function of sound wave intensity but also a function of frequency content of the wave, sound duration, and spectral response of the ear. Consequently, comparison of thunder with other noises common in our experience is of little value unless we consider each variable.

Frequency content of typical thunder sounds is shown in Fig. 2a. Note that the spectrum peaks at about 100 Hz, and most of the acoustic energy is within a frequency band approximately 200 Hz wide. If we correct the power spectrum in Fig. 2a for the frequency variations of the ear's response, the peak maximum is shifted to 250 Hz and the frequency interval of significant power contributions is 300 Hz. The corrected total acoustic intensity is 2.7 ergs cm^{-2} s^{-1}, which corresponds to a loudness of 94 dBA.* In overpressure, this acoustic intensity is 1.3×10^{-6} atm. It is not uncommon to have overpressures of 10^{-3} to 10^{-4} atm for nearby lightning (Uman, 1969). This means that the peak loudness might be as high as 123 dBA (3 dB above the threshold of pain), but more commonly one might expect values between 90 dBA (corresponding roughly to the sound of an elevated train) and 110 dBA.

Until the duration of sound exceeds a few oscillation periods of the wave, sounds are perceived as clicks. If duration is longer than about 0.5 second, loudness is independent of duration except for a slight diminution of loudness if the sound persists for several seconds. For duration shorter than 0.5 second, the time required to reach maximum loudness is frequency dependent, higher frequencies reaching maxima first. For typical thunder (as presented in Fig. 2), the duration of the peak intensity is 0.5-1 second; it has little or no effect on loudness. However, very near the lightning channel the duration can be substantially less than 0.5 second. There are two effects: what we hear is shifted to higher frequencies, and the perceived loudness is diminished. To calculate a value of loudness would require an exact knowledge of the sound wave form. For further considerations of sound perception and loudness, see Kinsler and Frey (1962).

---

*To provide measurements of noise as perceived by the ear, a weighted, relative, logarithmic sound pressure scale is used that corrects direct noise levels in dB for the acoustic response of the human ear. This corrected scale is called dBA (Kinsler and Frey, 1962).

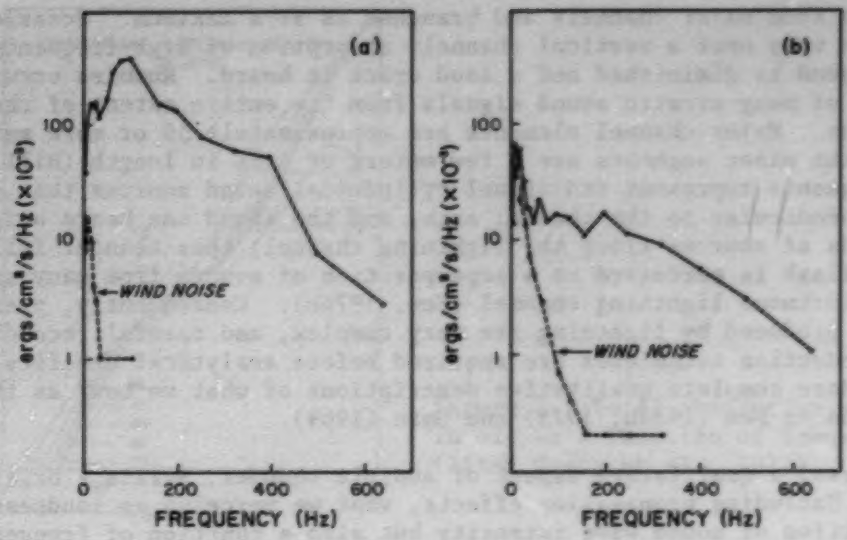

Figure 2.--(a) A typical analog thunder spectrum with a peak frequency of 100 and a wind-noise spectrum. (b) A thunder spectrum with a low-frequency peak due to wind noise. The wind-noise analysis is based on the pressure data just preceding the thunder (after Holmes et al., 1971).

(2) Infrasonic thunder

Pressure waves at both audible and subaudible frequencies are associated with lightning. No reports of significant energy content in thunder at frequencies above ~600 Hz have been published as of this writing, but several workers (e.g., Uman, 1969) have reported pressure variations at frequencies well below the lower limit of the audible range (<20 Hz), and other interest in infrasonic thunder has blossomed (Bohannon et al., 1977; Dessler, 1973; Holmes et al., 1971; Colgate and McKee, 1969). Although our perception of thunder is based mainly on audible pressure changes, we often do sense that significant infrasonic energy is present even when audible frequencies are dominant. We literally "feel" thunder even when audible sound is not excessive. Most subaudible sounds associated with a lightning flash are greater than 0.1 Hz and less intense than the much lower frequency sounds produced by the convective storm as a whole (see Ch. VI). Evidence suggests that at least a part of the infrasonic wave observed after a lightning flash does not originate in the rapidly expanding shock wave but is generated prior to the flash itself (Bohannon et al., 1977).

b. Measurements and theory

Description of experimental and theoretical work is divided here on the basis of measurement techniques required to obtain useful data.

(1) Thunder power spectra

One might think that recording thunder is an almost trivial undertaking, but in any measurement of thunder, a very difficult experimental problem is posed by noise from mechanical interaction between wind and microphone and from pressure fluctuations (turbulence) in the wind itself. One would appropriately use a microphone and recorder, having uniform frequency response between 0.1 and 600 Hz. Enclosure resonances and interference between direct and reflected waves can be minimized if the microphone is placed on the ground far from other major reflecting surfaces such as buildings. Rain damage to the microphone's sensitive element is easily eliminated by use of a rainshield, but both microphone and rainshield are directly exposed to surface winds, and interaction between them and the wind produces significant background noise. Most commonly, noises associated with the terrain (e.g., grass and bushes) do not pose problems as serious as wind-microphone interactions unless windspeeds are quite high (>20 knots) or there is unusually thick vegetation.

To minimize interaction between wind and microphone, two techniques are commonly used. A windscreen similar to those used on voice mikes provides an 8- to 15-dB noise reduction in the frequency interval of concern. A second technique is to mount the microphone as near as possible to the ground, where wind is at a minimum. A microphone mounted on a flat, hard surface is almost ideal for a single-microphone recording station. Thunder is most easily heard in a storm's cool outflow, but in this region the surface winds are often strong. Good data can often be gathered in the region of surface inflow, where winds are milder, except in some severe storms.

Turbulence advected by the wind field generates the dominant wind noise once the wind-microphone interaction has been dealt with satisfactorily. For low-to-moderate windspeeds the noise is principally below 3 Hz and cannot be removed by electronic filtering techniques without losing the low-frequency thunder data. One possible way to reduce this noise is to add signals from an array of microphones and employ spatial averaging. If the wind noise is random at each point in the array, then the wind noise will tend to cancel and the thunder signal will add constructively; i.e., there will be an increase in the signal-to-noise ratio. Whether or not this is the approach taken, wind noise is a problem that must be solved if very-low-frequency data are to be obtained.

Figure 2 shows power spectra of two separate thunder events recorded for a convective storm; it is evident that wind-associated noises can be appreciable.

Experimental recordings of the thunder power spectrum are described by Holmes et al. (1971), Uman (1969), Few (1968), and Few et al. (1967). Typically a four-channel FM magnetic tape recorder is used: a voice channel for supplementary data, a channel for time code, a channel for electric field change and a channel for the sound. Putting thunderstorm data in digital form facilitates theoretical study. This can be done in different ways, but one particularly useful scheme is to present the analog data to a real-time spectrum analyzer, which digitizes the thunder power spectrum directly.

The starting point for theoretical calculation of the power spectrum for thunder is the sound source, i.e., the lightning channel. Many have attempted to approximate the evolution of the shock wave into a sound wave by treating the lightning channel as a cylindrical acoustic wave source (Bass, 1980; Few et al., 1970; Troutman, 1969; Remillard, 1969; Colgate and McKee, 1969; Bhartendu, 1968, 1969; Jones, 1968; Jones et al., 1968). Because the lightning channel is so tortuous (i.e., the channel is broken up into many short, straight segments; see Hill [1968]), the cylindrical calculation is invalid for sound recorded farther than a few segment lengths from the channel. Few (1969) considered the effect of channel tortuosity on the evolution of thunder and concluded that the channel is more properly considered a series of short cylindrical segments that at distances greater than a segment length appear more like a string of spherical wave sources (string-of-pearls model) than a cylinder. Later Few et al. (1970) illustrated the effect of lightning channel tortuosity photographically. The string-of-pearls model accounts for the varying sounds of thunder, i.e., claps and rumbles.

Few (1969) calculated the acoustic power spectrum for a short line source of sound, choosing the total mechanical energy available per unit length to be 10^6 J m^{-1}. Qualitative arguments infer the actual thunder power spectrum, and thunder data are in general agreement with qualitative predictions of the string-of-pearls model. However, a detailed comparison of individual thunder spectra with calculated spectra is needed if the model is to be analyzed critically. Calculations based on the model reveal that the peak frequency in the acoustic-power spectrum varies inversely as the square root of the energy per unit length along the channel. That is, the frequency of the power spectrum maximum is given by

$$f_m = (0.63)c(P_o/E_1) \ , \qquad (5)$$

where c is the local speed of sound, P_o is the atmospheric pressure, and E_1 is the energy per unit length of the channel available to thunder. Holmes et al. (1971) observed low-frequency peaks (5 Hz and lower) apparently inconsistent with the mean energy input into the lightning channel as measured independently by electrical means. A conclusion is that in some instances thunder energy is contributed by a process other than channel expansion, a matter not easily resolved on the basis of power spectra alone.

Theoretical calculations of the thunder power spectrum are far from complete. Evolution of high overpressure in a lightning channel into a shock wave is not understood. In any theoretical treatment of the evolution of a shock wave into an acoustic wave, one must first choose a suitable initial pressure profile for the wave, which is a formidable task in itself. Calculation of the pressure as the wave evolves in time is then involved but straightforward, although propagation effects for a real atmosphere are difficult to include quantitatively (Few, 1969; Bass and Losey, 1975; Bass, 1980). Fourier analysis of the waveform (Fig. 3b) provides an acoustic-power spectrum of the pressure wave (Fig. 3a). But how to choose an initial pressure pulse will be subject to question for some time. The waveform in Fig. 3b is comparable with the general wave shape observed for laboratory sparks (Klinkowstein, 1974; Uman et al., 1970; Dawson et al., 1968; Wright and Mendendorp, 1967), but laboratory sparks are different in many ways from a lightning discharge. Extreme overpressure present in a lightning discharge might generate a pressure profile that is independent of the detailed structure of the lightning channel. In this case, thunder power spectra would contribute little detail about the actual electrical discharge process; i.e.,

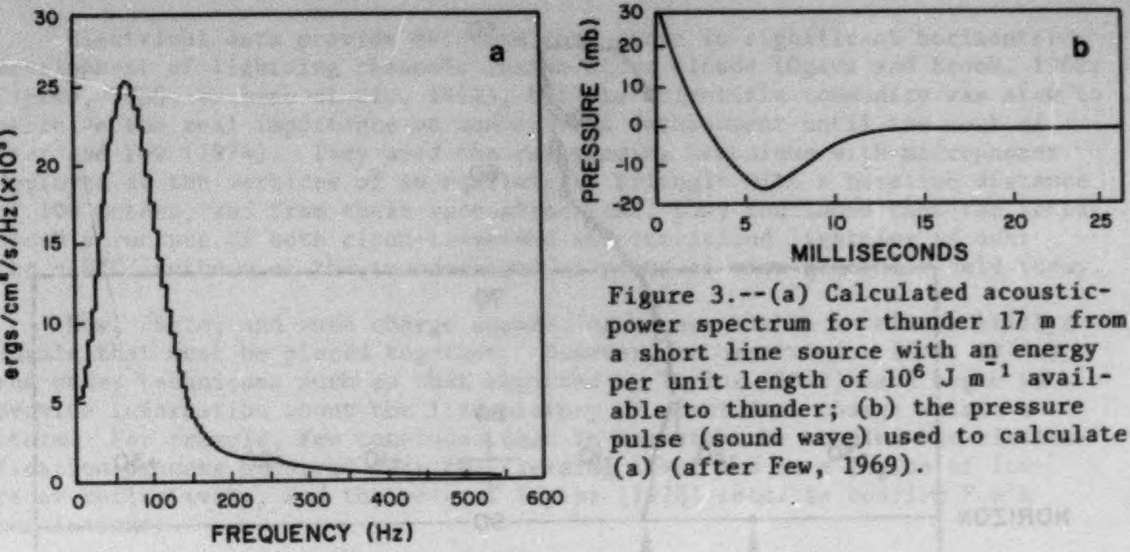

Figure 3.--(a) Calculated acoustic-power spectrum for thunder 17 m from a short line source with an energy per unit length of 10^6 J m^{-1} available to thunder; (b) the pressure pulse (sound wave) used to calculate (a) (after Few, 1969).

the evolution of a high channel overpressure into audible sounds would be more strongly influenced by propagation effects than by the detailed atomic and molecular processes of the lightning channel.

(2) Lightning channel reconstruction

The output of an array of microphones can be used to reconstruct the geometry of lightning channels (Few, 1970), and studies have been conducted on channel reconstruction for both audible and infrasonic thunder (Bohannon et al., 1977; Few and Teer, 1974; Few, 1974b; Teer and Few, 1974; Nakano, 1973; Teer, 1973). Further investigation is in progress, but Few and Teer (1974) have concluded that the shape of a lightning channel can be determined accurately, especially if one properly includes the effects of wind and temperature. An example of channel reconstruction results compared with a lightning channel photograph is shown in Fig. 4 (Few and Teer, 1974). The reconstruction technique proves to be an important tool in studying spatial and temporal evolution of lightning, which adds to our knowledge of how electrical charge changes in space and time in convective storms.

In one reconstruction technique an array of microphones used in a ray-tracing technique may include three microphones deployed at the vertices of an equilateral triangle 100 meters on a side (Teer, 1973). Sound waves generated as shock waves propagate outward from a lightning channel and pass over the microphone array. The waves can be treated as plane waves if the source is distant compared with the microphone spacing. A quantitative measure of similarity between two different signals shifted in time relative to one another is provided by cross correlation. The peak cross correlation of thunder signals defines relative time of arrival of wavefronts at each microphone, and if the speed of sound is known, then the wave vector for an incident wave can be determined. The time lapse between the lightning flash and the sounds of thunder can be used to calculate the range of the source from the array, thus locating the wave source. Space between microphones is no more than about 100 meters since wave fronts become incoherent if spaces are greater. Maximum spacing is also limited by atmospheric turbulence and by the lengths of discrete sources in major lightning channels (Few, 1974a).

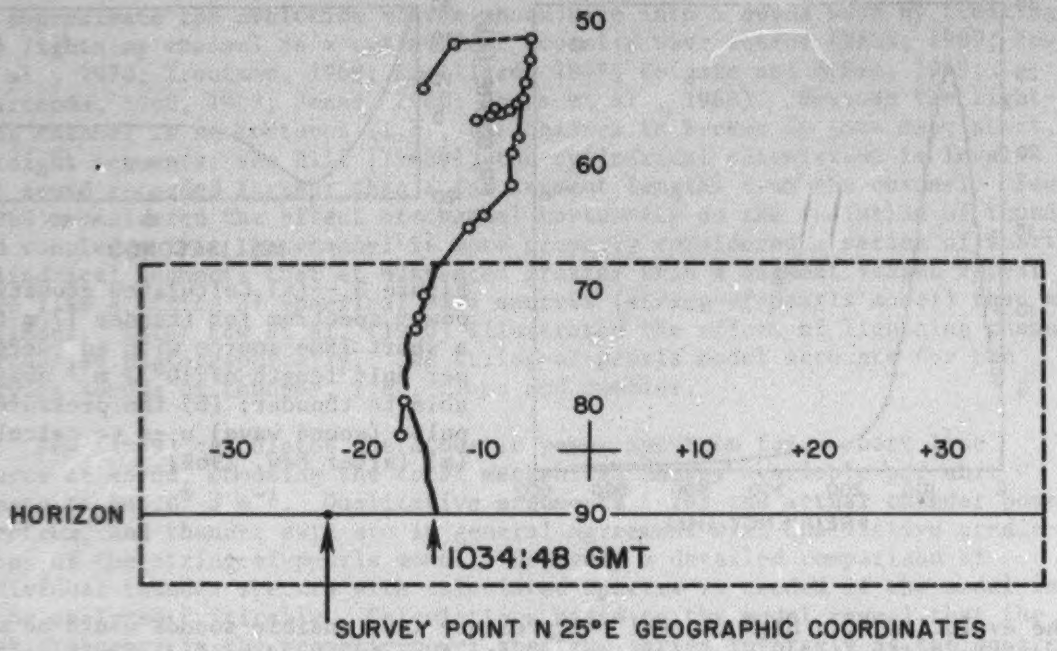

Figure 4.--Overlay of an acoustically reconstructed lightning channel on the photographed channel. The field of view of the camera system is indicated by the dashed-line rectangle, the look direction of the camera is given by cross hairs in the center, and angles of azimuth from the look direction and from the zenith are indicated in degrees. The open circles are the reconstructed source points for the thunder; to produce this reconstruction, a model atmosphere based upon rawinsonde measurements was used (after Few and Teer, 1974).

A second reconstruction technique employed by Few (1974a) has been aptly termed thunder ranging. Microphones are placed at the corners of a right triangle with sides of approximately 1-2 kilometers. Time of arrival of a thunderclap at each detector is measured by comparing the time of the thunder record with the time of origin as recorded in terms of electric field change. Range from the lightning channel segment is computed from

$$R_i = ct_i , \qquad (6)$$

where R_i is the distance of the i^{th} detector from the source, t_i is the time for the sound of thunder to travel from the source to the i^{th} detector, and c is the mean speed of sound between the source and detector. Separation of the microphones can be increased since coherence of the acoustic waves is not important, and as a consequence, accuracy in locating the sound source is greatly improved. Source location is at the intersection of arcs with radii R_i around each microphone. Accuracy of the calculated source position is a function of the relative positions of source and detectors; the technique is an exciting addition to thunder measurements.

Electrical data provide evidence that there is significant horizontal development of lightning channels inside storm clouds (Ogawa and Brook, 1969; Pierce, 1955; Workman et al., 1942), but the scientific community was slow to perceive the real importance of nonvertical development until the work of Teer and Few (1974). They used the ray-tracing technique with microphones deployed at the vertices of an equilateral triangle with a baseline distance of 100 meters, and from their reconstructions, they concluded that the intracloud structure of both cloud-to-ground and intracloud lightning is near the -10°C isotherm of the thundercloud, a point of view generally held today.

How, where, and when charge separation occurs within a cell is still a puzzle that must be pieced together. However, reconstruction (Few, 1974a) and other techniques such as that reported by Taylor (1978) have begun to provide information about the life history of electrical charge within a storm. For example, Few concluded that in one storm he studied the electrification process occurred near the freezing level and in a region of low radar reflectivity, and the work of Taylor (1978) seems to confirm Few's conclusions.

(3) Infrasonic thunder

Dessler (1973) has considered the possibility of infrasonic thunder that may arise from a mechanism quite different from rapid expansion of a lightning channel. Before the discharge by lightning, equilibrium between electrostatic forces and fluid dynamic forces defines the charged volume. Following charge neutralization by the discharge, a new equilibrium is reached only by a fluid adjustment (in this case a collapse) in response to the reduction of electrostatic force, and a low-frequency acoustic pulse is generated. Wilson (1920) first considered this process, and others (Colgate and McKee, 1969; Holmes et al., 1971; Colgate, 1967) have discussed it as a possible explanation of infrasonic signals sometimes observed in thunder. Bohannon et al. (1977) used ray-tracing techniques on a storm on 12 August 1975 near Socorro, N. Mex., and observed that infrasonic emissions are indeed associated with the lightning process. On the basis of the absence of infrasonic signals from the vertical portion of cloud-to-ground flashes, they concluded that the waves do not arise from channel heating and subsequent expansion.

4. TORNADO ACOUSTICS

In contrast to thunder, tornado acoustics, a relatively new subject of study, has received very little analytical attention. Experimental (Arnold et al., 1976) and theoretical (Abdullah, 1966) treatments of acoustic emissions from tornadoes indicate a lack of data. For the most part, eyewitness descriptions cite loud-noise sources of the times (e.g., a freight train or a jet plane; see Abdullah, 1966; Flora, 1954), although tornadoes are often seen and not heard. Qualitative descriptions of tornadic sounds have provided little insight into the nature of the sound source.

a. Tornadic sounds

Major interruptions in fluid flow by ground obstacles as the base of a funnel moves along the Earth's surface are most likely what produce the principal audible tornado sounds. Eddying of the flow generates sound, and acoustic power output is determined by the flow velocity (Powell, 1964;

Lighthill, 1952, 1954). Other sounds might arise from resonant behavior of the vortex itself (Abdullah, 1966; Sozou, 1968). Abdullah made a serious attempt to predict fundamental frequencies of tornado sounds, but there has been no quantitative calculation of acoustic-power emissions. Interest in genesis of tornadic sounds has not been high because of complexity and paucity of experimental data; whether activity increases in the future will be influenced by the supply of sound recordings to the scientific community.

Existing data for tornadic sounds are derived from recordings made by the public.* Each recording has utility limited primarily by poor frequency response of the recording microphone (Arnold et al., 1976), and information below 100 Hz is nonexistent. Figure 5 presents the estimated relative acoustic-power spectrum for a very damaging nocturnal tornado that went through Guin, Ala., on 3 April 1974; in spite of large errors reported, it is evident that virtually all of the energy was below 500 Hz. Abdullah's (1966) hypothesis that the airmass involved in the tornado circulation executes free vibrations provides a simple formula for the fundamental frequency in the special case of radially symmetric vibrations:

$$v_{max} = \frac{207}{a} , \qquad (7)$$

where a is the vortex radius expressed in meters. For the Guin tornado, whose damage path was about 200 meters wide, the maximum frequency of a free oscillation would be near 1 Hz. Analysis of the power spectrum shown in Fig. 5 offers little insight into the accuracy of Abdullah's prediction because of the low fidelity of the recording.

Instrumentation required for making a high-fidelity tornado sound recording is basically the same as that for recording thunder, but it is good to employ a microphone with a broad frequency response since the nature of tornadic sounds is unknown. Arnold and Bass (1977), working in conjunction with the National Severe Storms Laboratory, used storm-tracking techniques similar to those reported by Golden and Morgan (1972) (see Ch. II). A sound-recording package with a uniform frequency response between 10 Hz and 10 KHz is used. Since the recording system might be damaged or lost, microphone fidelity has been sacrificed for economy. The nearest the sound package has been placed to a tornado track is about 2 kilometers, and background wind noise on that occasion masked any audible tornado sounds that might have been detected otherwise. As more tornado-producing storms are encountered, a high-quality recording will eventually be obtained, and the value of recorded tornadic sounds as a data base from which we study the tornado can be assessed.

Propagation effects are also important for interpretation of acoustic emissions from tornadoes. What is observed at a recording station not only will be a function of the intervening atmosphere but also will depend on the

---

*Sound tracks have been made by various persons for the following tornadoes: Carrol County, Ind., 20 March 1976; Omaha, Nebr., 6 May 1975; Tulsa, Okla., 8 June 1974; Xenia, Ohio, 3 April 1974; Guin, Ala., 3 April 1974; Clay Center, Kan., 25 September 1973; Alto, Ind., 11 April 1965; and Winfield, Kan., 1964. Copies of these recordings are with the author.

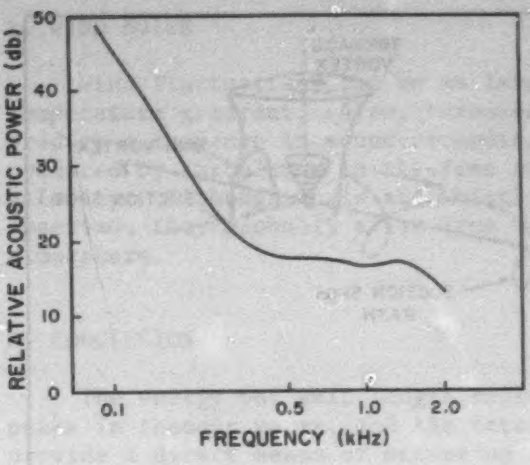

Figure 5.--Tornado relative power spectrum for the Guin, Ala., tornado. Corrections have been made for microphone response (after Arnold et al., 1976).

terrain, since sound originates very near the ground. Further, refraction of sound by the tornado core might well influence the direction of sound travel (Georges, 1971).

b. Temporal evolution of tornadic sounds

At present the most promising analysis of available tornado sound tapes is the study of how the sounds evolve in time (Arnold et al., 1976). As a tornado moves relative to a recording station, both frequency content and sound intensity change, because distance changes when the tornado describes a complex path and because the vortex evolves. The most important sources of sound to be found on a tornado recording are these: (1) wind-surface noises, (2) noises from within the tornado vortex, and (3) noises associated with the parent storm. Arnold et al. (1976) consider only the first of these sound sources in the analysis of evolution of tornadic sounds. Figure 6 shows the geometry assumed for the track of the Guin tornado, and Figure 7 shows the measured temporal variation in the relative acoustic power at 350 Hz. In the rather speculative model, sounds are assumed to be generated both by a small vortex moving about a larger vortex and by the larger vortex itself. It is also assumed that the source of noise is the interaction of the vortices with terrain. In calculating the relative power received, absorption by terrain and atmosphere was an important correction. Figure 8 shows a comparison of observations and calculations. Agreement is far from perfect, and the regular variations are suspect because they are twice the observational interval; i.e., they may represent analysis error rather than a true physical phenomenon. However, if the loudest sounds were assumed to coincide with the point of nearest approach by the main vortex, then the shift in phase of the regularly spaced intensity peaks coincident with the tornado's passage supports the contention that the variations are real. Consequently, it is reasonable from sound study alone to postulate that there was multiple vortex structure. A more complete analysis can be made when the assumed vortex tracks can be compared with the actual tornado damage survey.

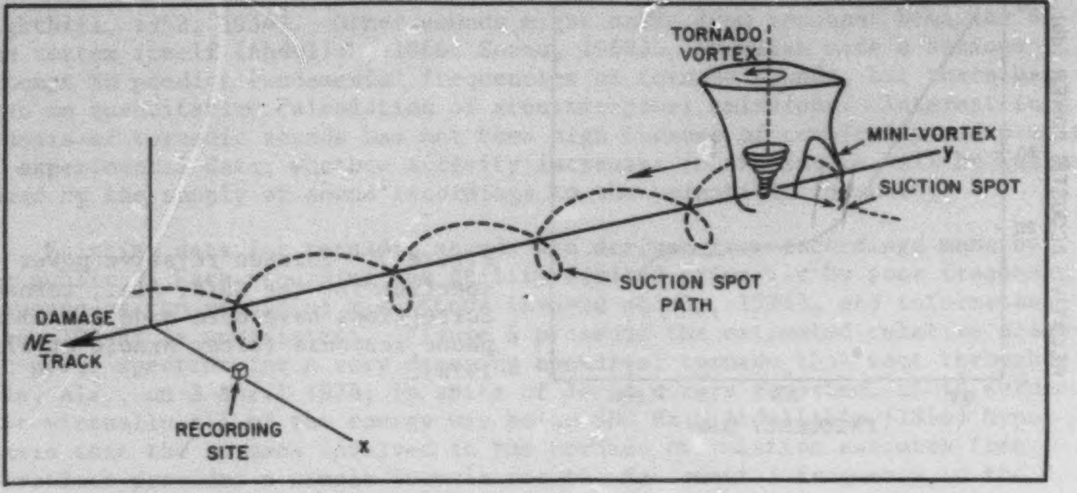
TORNADO VORTEX
MINI-VORTEX
y
SUCTION SPOT
SUCTION SPOT PATH
DAMAGE
NE
TRACK
RECORDING SITE
x

Figure 6.--Geometry assumed for the track of the Guin, Ala., tornado (3 April 1974) and a possible minivortex. Variations in elevation (-10 to +7 meters) were neglected (after Arnold et al., 1976).

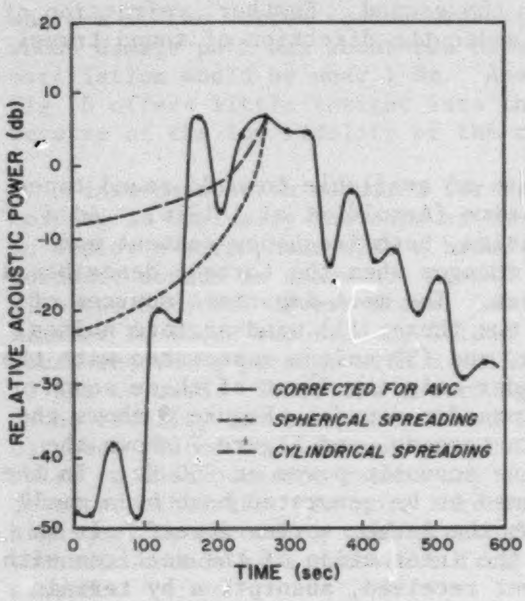

Figure 7.--Temporal variations in the relative acoustic power at 350 Hz for the Guin tornado compared with power variations expected for spherical and cylindrical spreading. The tornado vortex was assumed to track at a constant speed of 96 km h^{-1} in computing spreading losses. The relative power for the tornado has been corrected for atmospheric absorption, assuming 90% humidity at 20°C (after Arnold et al., 1976).

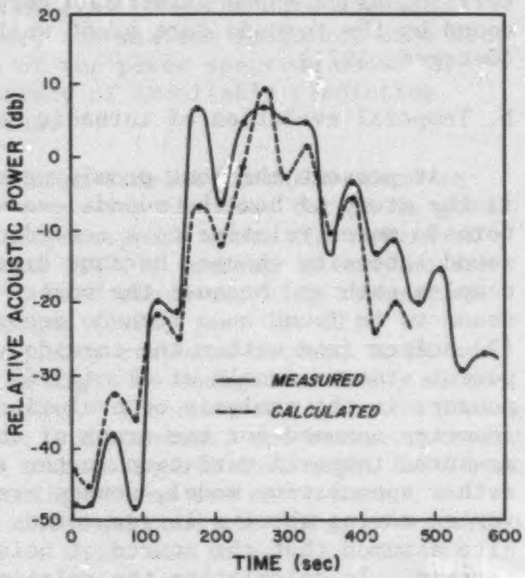

Figure 8.--Temporal variations in the relative acoustic power at 350 Hz for the Guin tornado compared with the variation expected from two point ground sources, i.e., from the large and small vortices (after Arnold et al., 1976).

5. WIND NOISE

Wind fluctuations can be as large an influence in sound refraction as a temperature gradient. Also, turbulence itself generates pressure waves, which produce a response in sound-recording equipment. The intensity of sound produced by turbulence in the free atmosphere depends strongly on the wind velocity. Although howls and whistles associated with high winds are commonly observed, they probably arise from surface features and not in the free atmosphere.

6. CONCLUSION

The energy per unit length released in a lightning flash, determined from peaks in thunder power, and the total channel length from reconstruction provide a direct means of measuring the mechanical energy produced by a lightning discharge. Observations of power peaks at infrasonic frequencies have led to an explanation of low-frequency thunder based on electrostatic collapse of a charged volume rather than on channel expansion. Reconstruction analysis of lightning channels from thunder data shows great promise in studies of space-time evolution of lightning in convective storms.

Thunder studies, however, cannot alone provide a complete picture of what are inherently electrical processes within storms. It is important that both active and passive electromagnetic mapping techniques be studied simultaneously with sound measurements. Future experiments might use the lightning flash as source of intense sound with which to probe the atmosphere in and near a severe storm.

Recorded sounds from a tornado are in short supply, but there is encouraging evidence from the one sound analysis reported in the literature that useful information on the tornado itself can be derived from detailed sound study.

Acknowledgments

Active storm research at the University of Mississippi would not be possible without support from the Office of Naval Research, National Science Foundation, Nuclear Regulatory Commission, and National Severe Storms Laboratory. To each I express a sincere thank you. A special note of thanks to my colleague Henry Bass for his constructive critique.

REFERENCES

Abdullah, A. J., 1966. The "musical" sound emitted by a tornado. Mon. Weather Rev. 94:213-220.

Aristotle, 384-322 B.C. Meteorologica. Translated by H.P.D. Lee, Loeb Classical Library, Harvard University Press, Cambridge, Mass., 1951.

Arnold, R. T., and H. E. Bass, 1977. Unusual storm acoustics. Res. Rep. 77-1, Department of Physics, Univ. of Mississippi, University.

Arnold, R. T., H. E. Bass, and L. N. Bolen, 1976. Acoustic spectral analysis of three tornadoes. J. Acoust. Soc. Am. 60:584-593.

Bass, H. E., 1980. The propagation of thunder through the atmosphere. J. Acoust. Soc. Am. 67:1959-1966.

Bass, H. E., and R. E. Losey, 1975. Effect of atmospheric absorption on the acoustic power spectrum of thunder. J. Acoust. Soc. Am. 57:822-823.

Bhartendu, 1968. A study of atmospheric pressure variations from lightning discharges. Can. J. Phys. 46:269-281.

Bhartendu, 1969. Audio frequency pressure variations from lightning discharges. J. Atmos. Terr. Phys. 31:743-747.

Bohannon, J. L., A. A. Few, and A. J. Dessler, 1977. Detection of infrasonic pulses from thunderclouds. Geophys. Res. Lett. 4:49-52.

Brown, E. H., and F. F. Hall, Jr., 1978. Advances in atmospheric acoustics. Rev. Geophys. Space Phys. 16:47-110.

Colgate, S. A., 1967. Enhanced drop coalescence by electric fields in equilibrium with turbulence. J. Geophys. Res. 72:479-487.

Colgate, S. A., and C. McKee, 1969. Electrostatic sounds in clouds and lightning. J. Geophys. Res. 74:5379-5389.

Dawson, G. A., C. H. Richards, and E. P. Knider, 1968. Acoustic output of a long spark. J. Geophys. Res. 73:815.

Dessler, A. J., 1973. Infrasonic thunder. J. Geophys. Res. 78:1889-1896.

Evans, L. B., H. E. Bass, and L. C. Sutherland, 1972. Atmospheric absorption of sound: theoretical predictions. J. Acoust. Soc. Am. 51:1565-1575.

Few, A. A., 1968. Thunder. Ph.D. thesis, Rice University, Houston, Tex.

Few, A. A., 1969. Power spectrum of thunder. J. Geophys. Res. 74:6926-6934.

Few, A. A., 1970. Lightning channel reconstruction from thunder measurements. J. Geophys. Res. 75:7517-7523.

Few, A. A., 1974a. Lightning sources in severe thunderstorms. Preprints, Conference on Cloud Physics, Tucson, Arizona, 21-24 October. American Meteorological Society, Boston, Mass., 387-390.

Few, A. A., 1974b. Thunder signatures. EOS 55:508-514.

Few, A. A., 1975. Thunder. Sci. Am. 233:80-90.

Few, A. A., and T. L. Teer, 1974. The accuracy of acoustic reconstructions of lightning channels. J. Geophys. Res. 79:5007-5011.

Few, A. A., A. J. Dessler, D. J. Latham, and M. Brook, 1967. A dominant 200-hertz peak in the acoustic spectrum of thunder. J. Geophys. Res. 72:6149-6154.

Few, A. A., H. B. Garrett, M. A. Uman, and L. E. Salanave, 1970. Comments on letter by W. W. Troutman. *J. Geophys. Res.* 75:4192-4195.

Flora, S. D., 1954. *Tornadoes of the United States*. University of Oklahoma Press, Norman.

Georges, T. M., 1971. Acoustic ray paths through a model vortex with a viscous core. *J. Acoust. Soc. Am.* 51:206-209.

Golden, J. H., and B. J. Morgan, 1972. The NSSL/Notre Dame Tornado Intercept Project, spring 1972. *Bull. Am. Meteorol. Soc.* 53:1178-1180.

Hill, R. D., 1968. Analysis of irregular paths of lightning channels. *J. Geophys. Res.* 73:1897-1906.

Holmes, C. R., M. Brook, P. Krehbiel, and R. McCroy, 1971. On the power spectrum and mechanism of thunder. *J. Geophys. Res.* 76:2106-2115.

Jones, D. L., 1968. Comments on paper by A. A. Few, A. J. Dessler, D. J. Latham, and M. Brook, "A dominant 200-hertz peak in the acoustic spectrum of thunder." *J. Geophys. Res.* 74:5555.

Jones, D. L., G. G. Goyer, and M. N. Plooster, 1968. Shock wave from a lightning discharge. *J. Geophys. Res.* 73:3121-3127.

Kinsler, L. E., and A. R. Frey, 1962. *Fundamentals of Acoustics*. John Wiley & Sons, Inc., New York, 464 pp.

Klinkowstein, R. E., 1974. A study of acoustic radiation from an electrical spark discharge in air. Master's thesis, Massachusetts Institute of Technology, 75 pp.

Lighthill, M. J., 1952. On sound generated aerodynamically, I. *Proc. R. Soc. A.* 211:564-587.

Lighthill, M. J., 1954. On sound generated aerodynamically, II. *Proc. R. Soc. A.* 222:1-32.

Lucretius, T., 98-55 B.C. *On the Nature of Things*. Translated by H. A. J. Munro, Book VI, Great Books of the Western World, William Benton (ed.), Chicago, 1952.

Nakano, M., 1973. Lightning channel determined by thunder. *Proc. Res. Inst. Atmos. Nagoya Univ.* 20:1-7.

Ogawa, T., and M. Brook, 1969. Charge distribution in thunderstorm clouds. *Q. J. R. Meteorol. Soc.* 95:513-525.

Pierce, E. T., 1955. The development of lightning discharges. *Q. J. R. Meteorol. Soc.* 81:229-240.

Piercy, J. E., T. F. W. Embleton, and L. C. Sutherland, 1977. Review of noise propagation in the atmosphere. *J. Acoust. Soc. Am.* 61:1403-1418.

Powell, A., 1964. Theory of vortex sound. *J. Acoust. Soc. Am.* 36:177-195.

Remillard, W. J., 1969. Comments on paper by A. A. Few, A. J. Dessler, D. J. Latham, and M. Brook, "A dominant 200-hertz peak in the acoustic spectrum of thunder." J. Geophys. Res. 74:5555.

Sozou, C., 1968. Symmetrical normal modes in a Rankine vortex. J. Acoust. Soc. Am. 46:814-818.

Taylor, W. L., 1978. A VHF technique for space-time mapping of lightning discharge processes. J. Geophys. Res. 83:3575-3583.

Teer, T. L., 1973. Lightning channel structure inside an Arizona thunderstorm. Ph.D. thesis, Rice University, Houston, Tex.

Teer, T. L., and A. A. Few, 1974. Horizontal lightning. J. Geophys. Res. 79:3436-3441.

Troutman, W. W., 1969. Numerical calculation of the pressure pulse from a lightning stroke. J. Geophys. Res. 74:4595-4596.

Uman, M. A., 1969. Lightning. McGraw-Hill, New York, 264 pp.

Uman, M. A., A. H. Cookson, and J. B. Moreland, 1970. Shock wave from a 4-meter spark. J. Appl. Phys. 41:3148-3155.

Wilson, C. T. R., 1920. Investigations on lightning discharges and on the electric field of thunderstorms. Phil. Trans. R. Soc. London, Ser. A. 221:73-115.

Workman, E. J., R. E. Holzer, and C. T. Pelson, 1942. The electric structure of thunderstorms. National Advisory Committee for Aeronautics, Tech. Note 864 (available from National Technical Information Service, Springfield, Va.), 47 pp.

Wright, W. M., and N. W. Mendendorp, 1967. Acoustic radiation from a finite line source with N-wave excitation. J. Acoust. Soc. Am. 43:966-971.

Zel'dovich, Y. B., and Y. P. Raizer, 1967. Physics of Shock Waves and High-Temperature Hydrodynamic Phenomena. Academic Press, New York, 636 pp.

VI. INFRASOUND FROM THUNDERSTORMS

T. M. Georges

1. INTRODUCTION

Everyone is familiar with the sounds for which thunderstorms are named; thunder is probably the loudest natural sound we are regularly exposed to. Chapter V reviews some of the physics of thunder and other acoustic emissions from storms, but the attention of that chapter is confined mainly to audible storm sounds and entirely to waves whose frequencies exceed about 1 Hz. This chapter is concerned with storms that emit acoustic waves at infrasonic frequencies, specifically at frequencies less than 1 Hz.

If we "listen" to these ultralow frequencies with suitable instruments, we find acoustic waves whose intensities are comparable with those of natural audible sounds. But we also find an interesting property not shared with the audible spectrum. Sounds like thunder are detectable no more than a few tens of kilometers from their sources, because of strong atmospheric attenuation; infrasound below about 1 Hz can travel hundreds or thousands of kilometers relatively unattenuated. The difference occurs because the classic coefficient of acoustic absorption is proportional to the square of the wave frequency (Reed, 1972; Procunier and Sharp, 1971). Thus, infrasound sensors can monitor events not just on a local scale, but on a global scale. This chapter explores the remote-sensing potential of such a capability, with particular application to severe storms.

2. HISTORICAL PERSPECTIVE

As is often the case in scientific discoveries, natural infrasound was initially regarded as interference on instruments designed to observe something else--in this case acoustic-gravity waves from distant nuclear explosions. But as better ways to monitor nuclear tests evolved, attention turned to the sources of the natural background "noise." Empirical associations with various known geophysical events soon uncovered a whole "zoo" of infrasonic wave types. Attempts to classify the different species have been published by Cook and Young (1962) and by Georges and Young (1972). For a bibliography on natural and manmade infrasound and related subjects, see Thomas et al. (1971).

One source turned out to be severe thunderstorms, some over 1,000 kilometers from the sensors (Chrzanowski et al., 1960; Goerke and Woodward, 1966; Bowman and Bedard, 1971; McDonald, 1974). The waves often had pressure amplitudes of a few microbars and periods of tens of seconds, and often lasted for hours. They were distinguished from local pressure fluctuations because they traveled at essentially the speed of sound. The association with storms was established by comparing the times and directions of arrival of a certain kind of infrasound event with severe-storm reports and with national weather radar charts.

Another quite different manifestation of severe-storm infrasound was independently discovered in 1967. During a survey of wavelike ionospheric motions revealed by HF-CW (high-frequency, continuous-wave) Doppler soundings at Boulder, Colo., certain nearly monochromatic oscillations of approximately 3-min period and durations of several hours emerged as a distinct type of event. Georges (1968a, 1968b) correlated observations of these ionospheric waves with the occurrence of severe thunderstorms below the ionospheric observation point. He also explained the waves' frequency content in terms of a narrow-band "window" for acoustic waves reaching the ionosphere from the troposphere. These observations have been since confirmed by Detert (1969), Baker and Davies (1969), Davies and Jones (1971, 1972a, 1972b), Prasad et al. (1975), Smith and Hung (1975), and Hung et al. (1975).

Davies and Jones (1972a) observed that frequency spectra of the ionospheric waves consistently reveal a "fine structure" with distinct peaks near 3.5- and 4.5-min periods. Chimonas and Peltier (1974) recognized that these peaks occur at the frequencies of modal resonances revealed by theoretical analyses of acoustic waveguide propagation in the atmosphere's temperature structure (e.g., Francis, 1973). Jones and Georges (1976) constructed a mathematical model of an acoustic window to the ionosphere that explains the major features of the observed spectra. Moo and Pierce (1972) have proposed a competing source mechanism that does not invoke atmospheric filtering but is based on buoyancy oscillations and nonlinear frequency doubling inside storms.

Georges (1973) cataloged the phenomenologies of these two kinds of severe-storm waves, i.e., the waves in air pressure at the surface and wave-like ionospheric motions, and found that they share many features, leading him to suggest that they may be just two different manifestations of the same emission process. He also reported some examples of simultaneous observations of the two different kinds of waves from the same storm system. Possible use of the emissions for storm warning has been examined by Georges and Greene (1975), and Georges (1976) has critically examined several proposed emission mechanisms.

3. INSTRUMENTATION AND SOME REPRESENTATIVE OBSERVATIONS

a. Surface pressure

Modern microbarographs can record pressure changes of less than 10^{-8} atmospheres (Matheson, 1964; Cook and Bedard, 1971; Hubbard and Bedard, 1969; Bedard, 1971). For comparison, the threshold of hearing, 0 dB, is 2.2×10^{-10} atm. The infrasound from severe storms has pressure amplitudes that are very small in meteorological terms, but are comparable with those of ordinary speech (about 60 dB or 0.22 μb). But because its frequency is much lower (0.1 to 0.004 Hz, or 10- to 250-s wave period), it must compete with much higher levels of nonacoustic atmospheric pressure fluctuations, or "noise."

Because the power spectrum of atmospheric pressure fluctuations exhibits something like an inverse-square frequency dependence (Kimball and Lemon, 1970; Meecham, 1971), bandpass filtering is normally used to focus on the particular decade or so of interest; otherwise long-period pressure fluctuations tend to dominate. Signal-to-noise ratios are usually less than unity, so that cross correlation of pressure fluctuations obtained at spatially separated microbarographs is required to separate acoustic waves from the noise produced at the sensors by wind-advected turbulence. Optimum separation is determined by the spatial coherence of the acoustic waves; for severe-storm infrasound, a sensor spacing of about 10 kilometers has been found to be the best compromise between angular resolution and spatial decorrelation.

Sampling the atmosphere through long pipes (300 meters or more) with resistive ports spaced approximately every meter provides additional spatial filtering to smooth out small-scale pressure fluctuations (Daniels, 1959; Priestley, 1966; Burridge, 1971; Grover, 1971; McDonald et al., 1971). This technique reduces the effects of pressure fluctuations whose temporal scales fall in the frequency band of interest but whose spatial scales are much smaller than the wavelengths of acoustic waves of the same frequency. (At 0.1 Hz, the acoustic wavelength is more than 3 km.)

Arrays of microbarographs lend themselves to analog and digital array-processing techniques, which transform an array of pressure-time data into spatial and temporal spectra (Brown, 1963; Young and Hoyle, 1975; Smart and Flinn, 1971). This permits automatic searching and filtering in frequency-wavenumber space and greatly simplifies the task of identifying particular kinds of waves from particular directions.

One way to display infrasonic waves from severe storms is shown in Fig. 1, which is the superposition of four analog recordings of pressure vs. time made at Boulder, Colo., with a quadrilateral array of microbarographs whose average spacing is about 8 kilometers. The four pressure traces have been shifted a few seconds in time with respect to each other; the shifts correspond to the acoustic delay across the sensor array for a wave arriving from an azimuth of 128° at a speed of 340 m s^{-1}. The frequency passband used to make this record has 20-dB response points at wave periods of about 2 and 100 seconds. These particular fluctuations were associated with a severe-storm system about 800 kilometers away near Oklahoma City. Emissions from this storm were recorded at seven different observatories, the most distant at College, Alaska. The Boulder observatory recorded the emissions for more than 5 hours. This was an exceptionally strong and long-lived event; the estimated maximum acoustic power radiated by this storm was 5×10^7 W (watts). However, a typical severe storm cell might release latent heat at an average rate of about 10^{13} W (Georges, 1976), nearly a million times the observed acoustic power.

Wind noise now imposes the most severe limitation on the sensitivity of microbarographs at infrasonic frequencies. A statistical study of the sensitivity of the NOAA microbarograph array near Boulder, Colo., showed that the wind-noise level exceeded 0.5 μb (about the average level of severe-storm waves) about 50% of the time. (The sensors themselves can detect 0.01 μb.) Boulder is a very "quiet" location, and the array is equipped with 300-m noise suppression pipes. Average wind-noise levels at two other locations were two to three times as great (Georges and Greene, 1975).

Because the average sensitivity of such arrays is wind-noise limited, advances in infrasound measurement technology should focus on the development of noise-reducing probes (Smith and Bauer, 1970; Elliott, 1972) and on assessing the effects of meteorology, terrain, and vegetation on the noise level at a given location.

b. Ionospheric waves

The ionospheric effects of severe-storm infrasound were discovered on records of HF-CW Doppler sounders, a technique invented by Watts and Davies

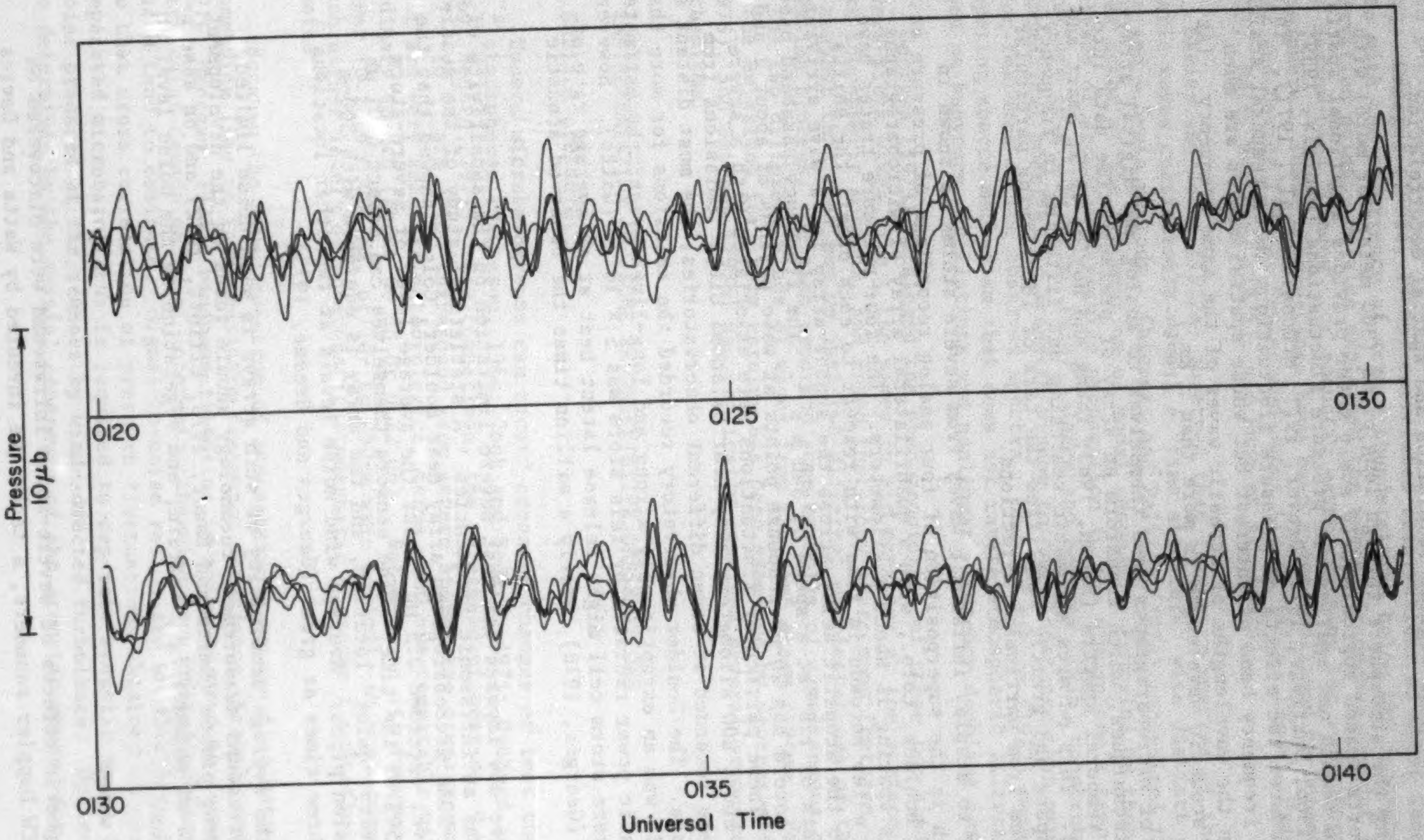

Figure 1.--Four superimposed microbarograph traces recorded at Boulder, Colo., during a severe-weather outbreak (including tornadoes) in Oklahoma on 5 June 1973. The four traces have been shifted in time for a maximum cross correlation; the shifts correspond to delays appropriate to a plane acoustic wave passing over the sensor array at 340 m s^{-1} from 128° azimuth.

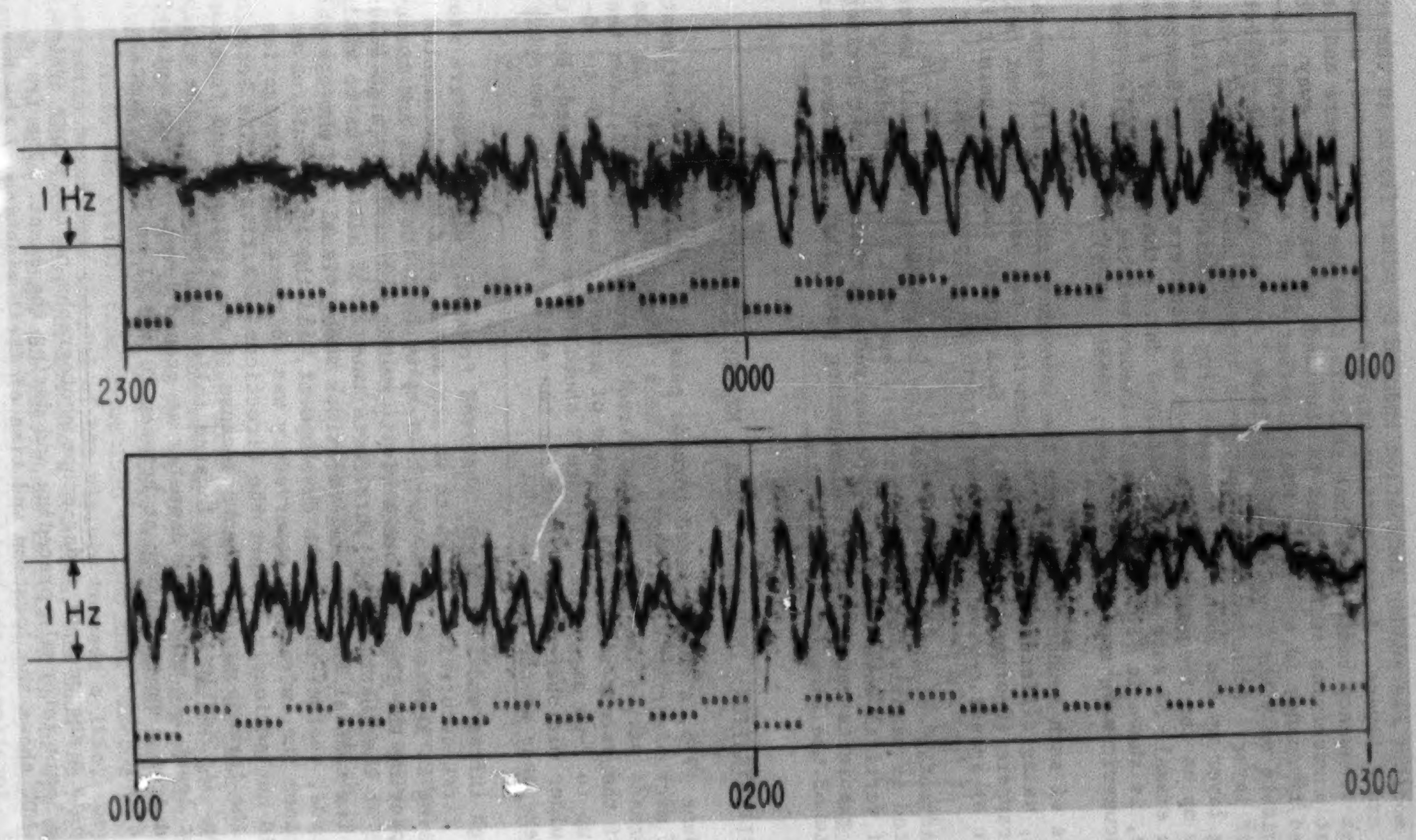

Figure 2.--Frequency fluctuations of a 3.3-MHz radio wave reflected from the ionosphere during a 4-h period on 27-28 June 1969. The undulations whose period is about 4 minutes (2300 UT to 0300 UT) are unusually periodic and are attributed to the upward passage of severe-storm acoustic waves through the reflecting ionospheric layer (after Davies and Jones, 1972a).

(1959) to monitor the sudden ionization induced by solar flares in the ionospheric E and F layers. A transmitting station emits a continuous, unmodulated, high-frequency radio wave that reflects from the ionosphere and is detected at a receiving station tens to thousands of kilometers away. The transmitted frequency is so stable that fluctuations of the received frequency indicate only the Doppler shifts imposed by motions of the reflecting ionospheric layer. Acoustic waves that pass through the ionosphere move the reflecting layer up and down, and the resulting periodic frequency fluctuations show up on the frequency-time records the sounders produce (Georges, 1973). An example of such a record, obtained during the passage of a severe-storm wave, is shown in Fig. 2. A simple theory relates the Doppler fluctuations to acoustic-wave amplitude (Georges, 1968b, 1973).

Arrays of such sounders can probe the ionosphere at spatially separated points and, using different sounding frequencies, can probe different heights in the ionosphere (Georges, 1967, 1968a). Such spaced soundings permit the measurement of acoustic-wave speeds and directions of propagation.

A disadvantage of the method is that the height where the radio waves are reflected is usually not known accurately and must be independently measured if vertical wave velocities are desired. Another is that horizontal ionization gradients cause nonvertical sounding paths that introduce error in the estimate of the location being probed.

4. A CASE ILLUSTRATION: INFRASOUND FROM A NEARBY TORNADIC STORM

On 4 June 1976, a medium-sized tornado passed 27 kilometers northeast of an array of microbarographs near Boulder, Colo. Immediately following the time the tornado was on the ground, the microbarographs recorded, from the direction of the parent storm, the passage of acoustic waves of 20- to 30-s period and up to 7-μb amplitude. Figure 3 shows three superimposed, but time-shifted, Boulder microbarograph traces for the entire event. No ionospheric soundings were made at the time.

Although infrasound is commonly observed from more distant severe storms, this is the first occurrence, of which we are aware, of a well-documented tornado passing so near a microbarograph array without the winds and turbulence accompanying the thunderstorm activity causing excessively high acoustic noise levels at the instruments. This fortuitous event allowed us to study in more detail the spatial and temporal relations among visual and photographic tornado records, weather-radar echo development, and the infrasonic waves, especially since the infrasound observatory was so close that propagation effects could not seriously distort the directions of arrival. The location and size of the tornado are well known because it was photographed from two locations, and its damage track was located following the storm. The visible funnel was at least 375 meters in diameter at ground level, and its intensity was estimated from a damage survey at between F0 and F1 on Fujita's scale (see Vol. 1, pp. 47-48).

Figure 4 is a sequence of radar-scope photographs of the storm system at approximately 5-min intervals preceding and during the event. The frame labeled 1530 MDT shows the location and time of first sighting of the tornado (T) and the location of the Boulder microbarograph array (B). The precipitation cell associated with the tornado shows an extraordinary growth rate compared with any other storm echoes in the sequence.

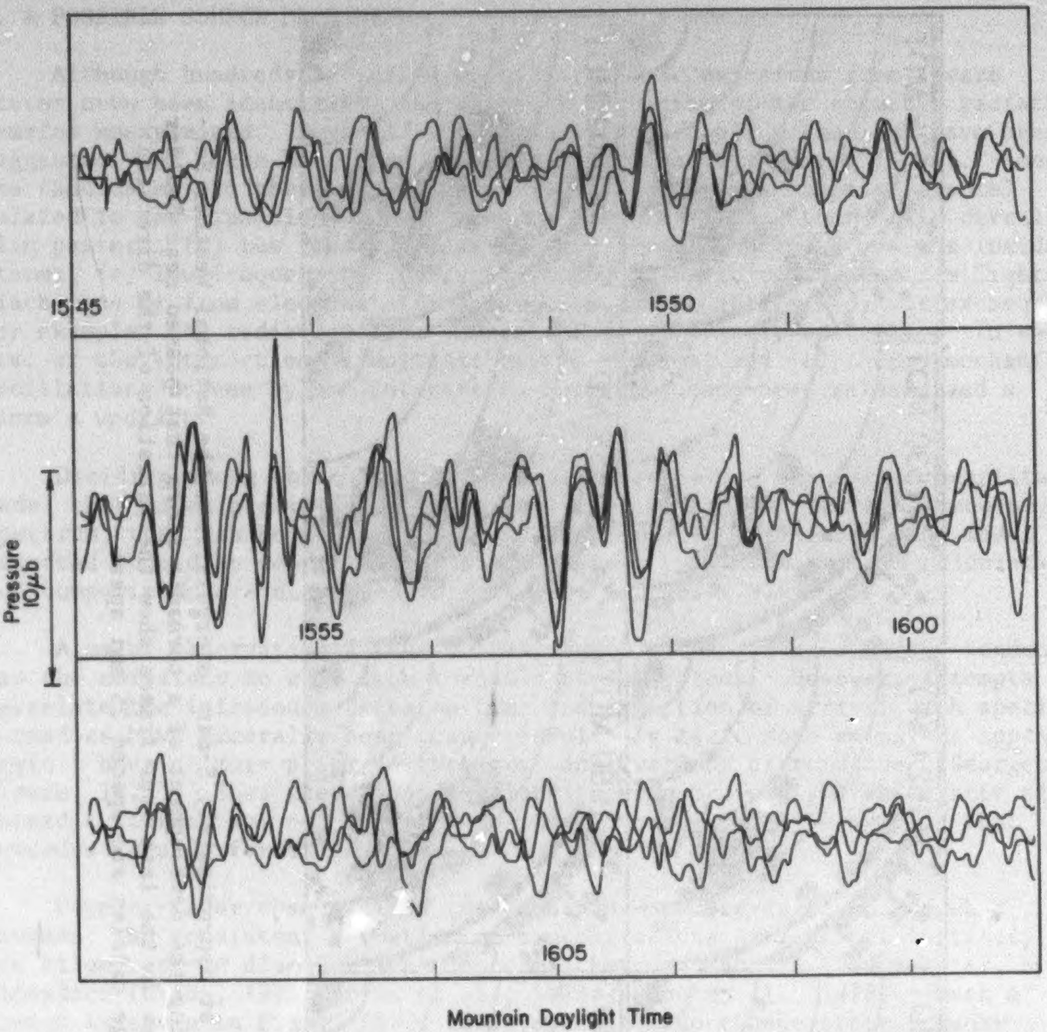

Figure 3.--Three superimposed microbarograph traces recorded at Boulder, Colo., on 4 June 1976 during the passage of a tornado about 27 km NE of the observatory. The traces have been shifted in time to correspond to a plane acoustic wave from 71° azimuth at 360 $m\ s^{-1}$, which coincides with the direction of the tornadic storm.

The direction of infrasound arrival was measured at about 5-min intervals between 1545 and 1605 MDT. The wave arrival direction changed smoothly from about 60° at 1545 MDT to about 95° at 1605. The bearing of the tornado's ground damage track from the observatory was between 60° and 65° azimuth, and the tornado was visible from about 1530 to 1540 MDT. Therefore, the emissions apparently began near the end of the visible tornado's life; they appeared at first to come from near the tornado's location, but then the apparent source moved clockwise. Perhaps the infrasound is related to the appearance of the appendage to the tornadic cell that appeared on radar at about 1540 MDT and then grew to join the larger cells to the southwest. This feature of the emissions is common: they are apparently connected with the tornadic storm, but not with the location and time of the tornado itself.

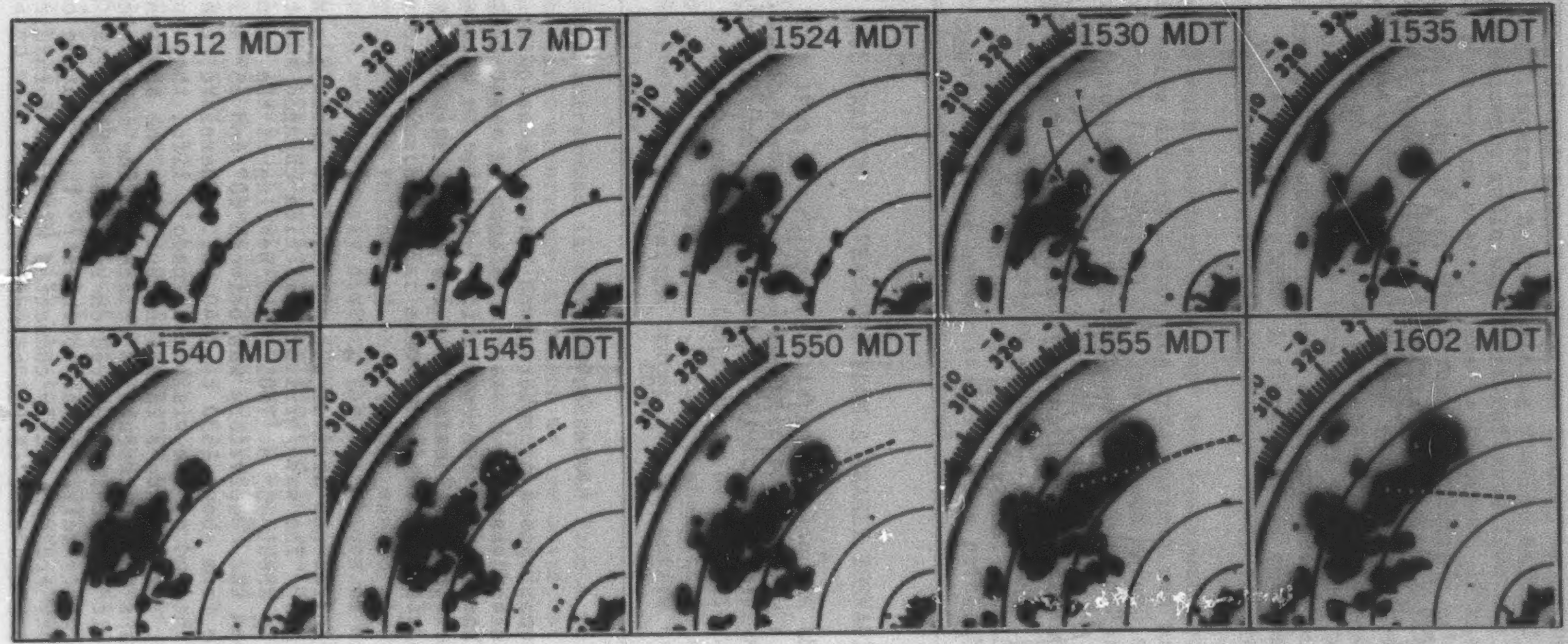

Figure 4.--Weather radar echoes at approximately 5-min intervals from the National Weather Service radar at Limon, Colo., during the development of a tornadic storm that passed near Boulder on 4 June 1976. The dashed lines in the last four frames show the variation of the direction of infrasound arrival. The range circles are spaced 25 nmi apart.

5. A POSSIBLE SOURCE MECHANISM

Although hundreds of instances of infrasonic emissions from severe storms have been identified, the physical mechanism of the acoustic radiation remains unexplained. Several superficially reasonable mechanisms have been suggested, and these have been critically examined by Georges (1976). Among the candidates are these: (a) simple acoustic sources (monopole, dipole) related to the expansion of heated storm air and to the storm-scale circulation pattern; (b) the random acoustic noise from "turbulent" motions inside storms; (c) low-frequency thunder, i.e., the acoustic radiation from lightning discharges or from electrostatic relaxation inside storms; (d) vortex sound, for example, the radiation from several kinds of dynamic instability in vortices, or the interaction of multiple-vortex systems; and (e) thermo-mechanical oscillations driven by the interaction between latent-heat release and a storm's updraft.

Deciding among these candidates means formulating for each a quantitative model that makes predictions, for example, of radiated power and frequency spectrum, that can be compared with observations. Furthermore, the model selected should be compatible with known storm processes. These calculations and comparisons are discussed in detail by Georges (1976).

A major observational clue to the source mechanism is a marked tendency for the emissions to come from tornadic storm systems. However, attempts to correlate the infrasound emission time and direction of arrival with specific tornadoes have generally been unsuccessful. In fact, some emissions appear to begin 1 hour or more prior to the first observations of tornadoes (Georges and Greene, 1975). Thus the evidence points to some process characteristic of tornadic storms, but not the tornado itself, and possibly a process that precedes tornado formation.

Doppler-radar observations inside storms have revealed just such a process: the consistent formation of concentrations of vertical vorticity a few kilometers in diameter inside storms that, as much as 1 hour later, spawn tornadoes (Kraus, 1973; Brown et al., 1973; Lemon et al., 1978). Such a vortex is shown in Fig. 5 for a nonsevere Colorado thunderstorm. Radar resolution is insufficient to reveal any subvortex structure. Agee et al. (1976) have suggested that such mesoscale vortices are members of a hierarchy of vortices of decreasing diameter that characterize some tornadic storms. The hierarchy extends through (a) the mesoscale tornado cyclone just mentioned, which probably coincides with radar hook echoes and may be exhibited visually in the wall or pedestal clouds that often accompany tornadoes; (b) a minitornado cyclone, perhaps several hundred meters in diameter, corresponding to the parent of multiple tornadoes; (c) tornadoes themselves, up to a few tens of meters in diameter; and (d) the subtornado-scale suction vortices, up to a few meters in diameter, proposed by Fujita (1970, 1971) and Agee et al. (1975). The members of this hierarchy could be linked by a dynamic instability that causes large vortices to decompose into a few satellite vortices instead of being dissipated by turbulence. Many such instabilities are known in the theory of rotating flows (Lord Kelvin, 1910; Davy et al., 1968).

Ward (1972) has investigated the conditions under which multiple vortices form from larger ones in a laboratory model simulating tornado flow. He found that certain relations between the inflow angle and the updraft speed in his apparatus favored the formation of multivortex flows, in which several vor-

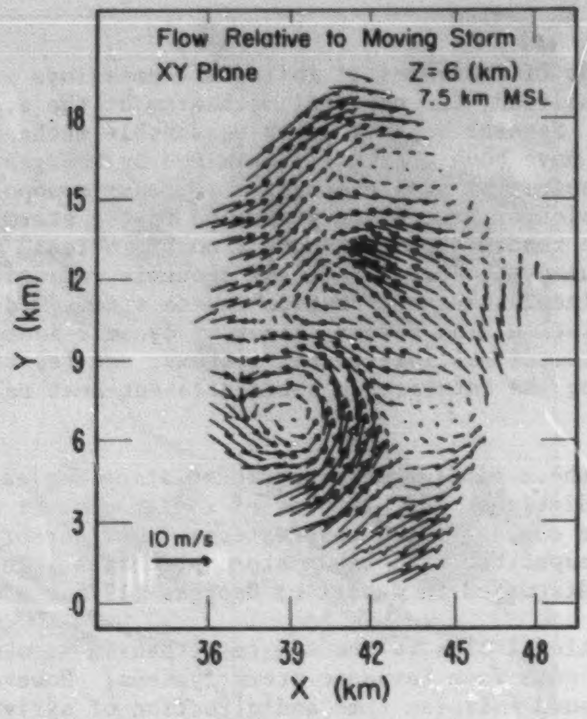

Figure 5.--A map of horizontal air velocity vectors 6 km above ground inside a Colorado thunderstorm. The velocity field was mapped with the WPL dual Doppler radar (Kropfli and Miller, 1976). The size of each vector is proportional to airspeed, with mean removed, at that location, with the highest speeds reaching 10 m s^{-1}. A strong vortex is visible at the lower left, and two weaker ones at the top and at the lower right can also be seen. The radar resolution does not allow the subvortex structure to be seen with any detail.

tices rotate about a common center. Furthermore, changing a parameter such as the inflow angle could cause single vortices to decay into multivortex systems. These simulations suggest that, under the conditions that exist in the vicinity of some severe thunderstorms, transitions through successive stages of the vortex hierarchy described by Agee et al. (1976) may be common.

Multivortex systems suggest a simple model from which the acoustic radiation is readily calculated. Consider, for example, the radiation from a corotating vortex pair, as calculated by Powell (1964). The radiated acoustic power is

$$\Pi = \frac{16}{15\pi} \frac{\rho}{c^5} \left(\frac{\Gamma}{4\pi r}\right)^8 \ell^2 \quad ,$$

where Γ is the vortex strength (circulation), $2r$ is the distance separating the pair, ℓ is their axial length, and ρ and c are the atmospheric density and sound speed. The quantity $\Gamma/4\pi r$ is the tangential speed u at which the vortices spin about their common axis, so that the rotation frequency is $u/2\pi r$. Powell shows that the pair radiate acoustically like a rotating acoustic quadrupole*. The radiated frequency is thus twice the rotation frequency or $u/\pi r$. For example, if $u = 43 \text{ m s}^{-1}$ and $\ell = 3$ km, then $\Pi = 10^7$, and the vortex separation required for radiation at a 30-s wave period is about 820 meters. The required source power estimated by Georges (1973) for infrasonic waves of about 0.6-μb amplitude observed at a distance of 500 km is approximately 2.3×10^7 W. More realistic models could be constructed, but not without guidance that can be supplied only by more detailed measurements of storm vortex structure and breakdown dynamics.

6. IS IT USEFUL FOR STORM WARNING?

Georges and Greene (1975) examined the storm warning potential of the infrasound observed at ground level by comparing the observability of the waves at three observatories (spaced about 550 km apart) with weather-radar data and severe-storm reports. They evaluated their results on the basis of four "indices of usefulness":

(1) False-alarm rate, which tells how often infrasound from other sources is mistaken for that from storms. They devised a sorting procedure that reduces the false-alarm rate to 15%-20%, and even lower rates seem achievable.

(2) Detection rate, which tells what fraction of all severe storms in a specified region is detected. Here the major problems are defining severe storms objectively and verifying their occurrence. They estimated a 65% detection rate for tornadic storms, a 31% detection rate for tornadoes themselves, and a 33% detection rate for storms with radar tops above 50,000 ft.

(3) Timeliness, which tells how much advance warning the emissions might give of dangerous storm effects. Only tornadoes were considered from this viewpoint, because of the difficulties of specifying onset time for other storm features. It was discovered that many infrasound emissions begin 1 hour or more prior to tornado sightings, with some emissions preceding tornado onset by many hours (Fig. 6). However, the relatively slow speed of acoustic waves (about 1,000 km per hour) imposes a fundamental limitation on the density of a practical observing network. Furthermore, some emissions apparently come after tornado formation.

(4) Location accuracy, which tells how well the emissions could be used to locate and track storms. Of 177 events that were classed as storm emissions during 1 season, fewer than expected (about 18%) were recorded at more than 1 observatory, and fewer than 3% were recorded at all 3

---

*A monopole would represent local fluctuations of mass or energy; a dipole would represent a local flux of mass or energy, for example, an oscillating fluid parcel; a quadrupole would represent a cloverleaf-shaped distribution of fluid density, for example, with alternating positive and negative lobes.

stations. Therefore, source location by triangulation was not usually possible. Source identification was usually made by comparing the apparent source direction measured at one observatory with national weather radar charts. When triangulation was possible, the indicated intersections usually fell close to radar-indicated severe-storm system but positive identification and tracking of a particular storm was seldom possible. Atmospheric refraction of the acoustic waves in azimu apparently permits no better than about 100-km accuracy in source location at a nominal range of 700 km.

If ways to reduce background noise can be found, severe-storm detection rates should improve, and it may be practical to consider deploying a prototype network of microbarograph observatories in something like a 1,000-km grid to supplement the present storm warning system. Compared, for example, with a radar station, the costs and complexity of a microbarograph observator are modest indeed, and the automation of all its signal-processing tasks seem straightforward. Integration of such a capability into the existing storm sensing and warning system may be a cost-effective way to improve the reliability and timeliness of tornado warnings.

The warning potential of the ionospheric waves seems more remote than that of the ground level waves, mainly because the ionospheric effects appear to be more localized (generally within a few hundred kilometers of the source

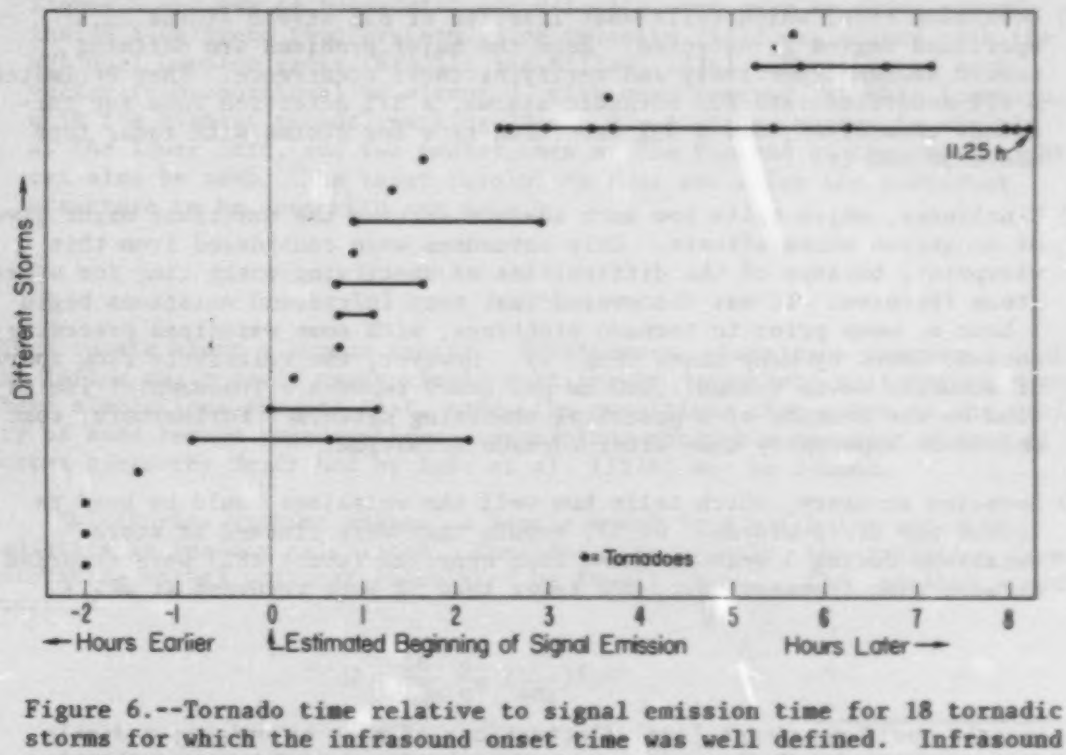

Figure 6.--Tornado time relative to signal emission time for 18 tornadic storms for which the infrasound onset time was well defined. Infrasound travel time has been removed from these estimates. The horizontal lines connect different tornadoes (dots) occurring within the same storm system.

storm), and because directional information is more difficult to extract (Davies and Jones, 1972a).

7. CONCLUSION

Although the acoustic energy that a storm radiates represents only a minuscule part of a storm's energy budget, the emissions are interesting and possibly useful from several viewpoints:

(1) They may be a usable precursor of tornadoes.

(2) As a remote indicator of vorticity concentration inside storms, they may supplement meteorologists' array of storm research sensors.

(3) They have helped us formulate a model of acoustic propagation into the upper atmosphere.

(4) And finally, they have provided a recurring example of the natural aerodynamic generation of strong infrasound. A complete explanation of the storm emission process may also help explain other natural infrasound, such as the emissions traced to several windy, mountainous regions of the Earth (Larson et al., 1971).

Acknowledgments

I thank Gary Greene for processing the infrasound records of the case illustrations and Joe Golden for providing the tornado observations he collected.

REFERENCES

Agee, E., C. Church, C. Morris, and J. Snow, 1975. Some synoptic aspects and dynamic features of vortices associated with the tornado outbreak of 3 April 1974. Mon. Weather Rev. 103:318-333.

Agee, E. M., J. T. Snow, and P. R. Clarke, 1976. Multiple vortex features in the tornado cyclone and the occurrence of tornado families. Mon. Weather Rev. 104:552-563.

Baker, D. M., and K. Davies, 1969. F2-region acoustic waves from severe weather. J. Atmos. Terr. Phys. 31:1345-1352.

Bedard, A. J., 1971. Seismic response of infrasonic microphones. J. Res. NBS 75C:41-45.

Bowman, H. S., and A. J. Bedard, 1971. Observations of infrasound and subsonic pressure disturbances related to severe weather. Geophys. J. R. Astron. Soc. 26:215-242.

Brown, R. A., D. W. Burgess, and K. C. Crawford, 1973. Twin tornado cyclones within a severe thunderstorm: single Doppler radar observations. Weatherwise 26:63-69.

Brown, R. F., Jr., 1963. An automatic multichannel correlator. J. Res. NBS 67C:33-38.

Burridge, R., 1971. The acoustics of pipe arrays. Geophys. J. R. Astron. Soc. 26:53-69.

Chimonas, G., and W. R. Peltier, 1974. On severe storm acoustic signals observed at ionospheric heights. J. Atmos. Terr. Phys. 36:821-828.

Chrzanowski, P., J. M. Young, and H. L. Marrett, 1960. Infrasonic pressure waves from tornadic storms. NBS Rep. 7035, National Bureau of Standards, Washington, D.C. (Unpublished.)

Cook, R. K., and A. J. Bedard, 1971. On the measurement of infrasound. Geophys. J. R. Astron. Soc. 26:5-11.

Cook, R. K., and J. M. Young, 1962. Strange sounds in the atmosphere, part 2. Sound 1:25-33.

Daniels, F. B., 1959. Noise-reducing line microphone for frequencies below 1 cps. J. Acoust. Soc. Am. 31:529-531.

Davies, K., and J. E. Jones, 1971. Ionospheric disturbances in the F2 region associated with severe thunderstorms. J. Atmos. Sci. 28:254-262.

Davies, K., and J. E. Jones, 1972a. Ionospheric disturbances produced by severe thunderstorms. Prof. Paper No. 6, NOAA Environmental Research Laboratories, Boulder, Colo., 47 pp.

Davies, K., and J. E. Jones, 1972b. Infrasound in the ionosphere generated by severe thunderstorms. J. Acoust. Soc. Am. 52:1087-1090.

Davy, A., R. C. DiPrima, and J. T. Stuart, 1968. On the instability of Taylor vortices. J. Fluid Mech. 31:17-52.

Detert, D. G., 1969. A study of the coupling of acoustic energy from the troposphere to the ionosphere. AVCO Corp. Final Rep. to Marshall Space Flight Center, Huntsville, Ala., 15 February 1969.

Elliott, J. A., 1972. Microscale pressure fluctuations measured within the lower atmospheric boundary layer. J. Fluid Mech. 53:351-383.

Francis, S. H., 1973. Acoustic-gravity modes and large-scale traveling ionospheric disturbances of a realistic, dissipative atmosphere. J. Geophys. Res. 78:2278-2301.

Fujita, T., 1970. The Lubbock tornadoes: a study of suction spots. Weatherwise 23:160-173.

Fujita, T. T., 1971. Proposed mechanism of suction spots accompanied by tornadoes. Preprints, Seventh Conference on Severe Local Storms. American Meteorological Society, Boston, Mass., 208-213.

Georges, T. M., 1967. Ionospheric effects of atmospheric waves. ESSA Tech. Rep. IER 57-ITSA 54, U.S. Government Printing Office, Washington, D.C.

Georges, T. M., 1968a. HF Doppler studies of traveling ionospheric irregularities. *J. Atmos. Terr. Phys.* 30:735-746.

Georges, T. M., 1968b. Short-period ionospheric oscillations associated with severe weather. Proceedings, Symposium on Acoustic-Gravity Waves in the Atmosphere. U.S. Government Printing Office, 171-178.

Georges, T. M., 1973. Infrasound from convective storms: examining the evidence. *Rev. Geophys. Space Phys.* 11:571-594.

Georges, T. M., 1976. Infrasound from convective storms, part 2: a critique of source candidates. Tech. Rep. ERL 380-WPL 49, NOAA Environmental Research Laboratories, Boulder, Colo.

Georges, T. M., and G. E. Greene, 1975. Infrasound from convective storms, part IV: is it useful for storm warning? *J. Appl. Meteorol.* 25:1303-1316.

Georges, T. M., and J. M. Young, 1972. Passive sensing of natural acoustic-gravity waves at the earth's surface. In *Remote Sensing of the Troposphere*, V. E. Derr (ed.), U.S. Government Printing Office, Washington, D.C., 21-1 to 21-20.

Goerke, V. H., and M. W. Woodward, 1966. Infrasonic observations of a severe weather system. *Mon. Weather Rev.* 94:395.

Grover, F. H., 1971. Experimental noise reducers for an active microbarograph array. *Geophys. J. R. Astron. Soc.* 26:41-52.

Hubbard, E. K., and A. J. Bedard, 1969. A pressure transducer for use as a component of an infrasonic microphone. ESSA Tech. Memo. ERLTM-WPL 4, NOAA Environmental Laboratories, Boulder, Colo.

Hung, R. J., R. E. Smith, G. S. West, and B. B. Henson, 1975. Detection of upper atmospheric disturbances in northern Alabama during extreme tornado outbreak of April 3, 1974. Preprints, Ninth Conference on Severe Local Storms, American Meteorological Society, Boston, Mass., 294-300.

Jones, R. M., and T. M. Georges, 1976. Infrasound from convective storms, part III: propagation to the ionosphere. *J. Acoust. Soc. Am.* 59:765-779.

Kelvin, Lord, 1910. Vibrations of a columnar vortex. In *Mathematical and Physical Papers*, Cambridge University Press, 152-165 (also in *Phil. Mag. [1880]* 5:155-168).

Kimball, B. A., and E. R. Lemon, 1970. Spectra of air pressure fluctuations at the soil surface. *J. Geophys. Res.* 75:6771-6777.

Kraus, M. J., 1973. Doppler radar observations of the Brookline, Massachusetts tornado of 9 August 1972. Bull. Am. Meteorol. Soc. 54:519-524.

Kropfli, R. A., and L. J. Miller, 1976. Kinematic structure and flux quantities in a convective storm from dual-Doppler radar observations. J. Atmos. Sci. 33:520-529.

Larsen, R. J., L. B. Craine, J. E. Thomas, and C. R. Wilson, 1971. Correlation of winds and geographic features with the production of certain infrasonic signals in the atmosphere. Geophys. J. R. Astron. Soc. 26:201-214.

Lemon, L. R., D. W. Burgess, and R. A. Brown, 1978. Tornadic storm airflow and morphology derived from single-Doppler radar measurements. Mon. Weather Rev. 106:48-61.

Matheson, H., 1964. Instructions for the operation of NBS infrasonic equipment. NBS Rep. 8519, National Bureau of Standards, Washington, D.C. (Unpublished.)

McDonald, J. A., 1974. Naturally occurring atmospheric acoustical signals. J. Acoust. Soc. Am. 56:338-351.

McDonald, J. A., E. J. Douze, and E. Herrin, 1971. The structure of atmospheric turbulence and its application to the design of pipe arrays. Geophys. J. R. Astron. Soc. 26:99-109.

Meecham, W. C., 1971. On aerodynamic infrasound. J. Atmos. Terr. Phys. 33:149-155.

Moo, C. A., and A. D. Pierce, 1972. Generation of anomalous ionospheric oscillation by thunderstorms. Effects of atmospheric acoustic-gravity waves on electromagnetic wave propagation, Advisory Group for Aerospace Research and Development, Conference Proceedings No. 115, North Atlantic Treaty Organization, Geneva, Switzerland.

Powell, A., 1964. Theory of vortex sound. J. Acoust. Soc. Am. 36:177-195.

Prasad, S. S., L. J. Schneck, and K. Davies, 1975. Ionospheric disturbances by severe tropospheric weather storms. J. Atmos. Terr. Phys. 37:1357-1363.

Priestley, J. T., 1966. Calculation of the effectiveness of infrasonic line microphones for reducing wind noise. NBS Rep. 9380, National Bureau of Standards, Washington, D. C. (Unpublished.)

Procunier, R. W., and G. W. Sharp, 1971. Optimum frequency for detection of acoustic sources in the upper atmosphere. J. Acoust. Soc. Am. 49:622-626.

Reed, J. W., 1972. Attenuation of blast waves by the atmosphere. J. Geophys. Res. 77:1616-1622.

Smart, E., and E. A. Flinn, 1971. Fast frequency-wavenumber analysis and Fisher signal detection in real-time infrasonic array data processing. Geophys. J. R. Astron. Soc. 26:279-284.

Smith, A. M. O., and A. B. Bauer, 1970. Static-pressure probes that are theoretically insensitive to pitch, yaw and Mach number. J. Fluid Mech. 44:513-528.

Smith, R. E., and R. J. Hung, 1975. Observation of severe-weather activities by Doppler-sounder array. J. Appl. Meteorol. 14:1611-1615.

Thomas, J. E., A. D. Pierce, E. A. Flinn, and L. B. Craine, 1971. Bibliography on infrasonic waves. Geophys. J. R. Astron. Soc. 26:399-426.

Ward, N. B., 1972. The exploration of certain features of tornado dynamics using a laboratory model. J. Atmos. Sci. 29:1194-1204.

Watts, J. M., and K. Davies, 1959. Rapid frequency analysis of fading radio signals. J. Geophys. Res. 65:2295-2301.

Young, J. M., and W. A. Hoyle, 1975. Computer programs for multidimensional spectra array processing. Tech. Rep. ERL 345-WPL 43, NOAA Environmental Research Laboratories, Boulder, Colo.

blank page

VII. SFERICS AND OTHER ELECTRICAL TECHNIQUES FOR STORM INVESTIGATIONS

E. T. Pierce

1. INTRODUCTION

An atmospheric is the electromagnetic signal radiated by a complete lightning discharge or by any subsidiary phase of the flash. The abbreviated form "sferic" is often used. The plural "sferics," however, has a different and more specialized meaning, and it is this meaning that is the main subject of this chapter. We define sferics as referring to techniques using atmospherics for the detection of lightning occurrence and--in more sophisticated applications--for the location of the flash position.

The use of sferics methods ranges from use within largely social contexts through more technical applications to basic research. An example of the social use of sferics techniques is their potential utility in warning populated areas of the approach of severe storms. A typical technical application is the identification in forestry of areas of potential lighting-caused fires. Many sferics studies of storms less than 200 km away in particular have the research objective of better defining the electrical characteristics of the storm; an example is the mapping of the lightning channels within a thundercloud.

Sferics techniques can be conveniently distinguished in three categories according to distance: long distance (>1,000 km), intermediate (200-1,000 km), and close (<200 km).

2. LONG-DISTANCE TECHNIQUES

a. Introduction

Sferics methods have been used to locate storm centers at great distances (>1,000 km) for two main reasons. First, they are adjunct input to meteorological forecasting, supplying immediate data for regions where surface observations are not readily available. Coverage by satellite meteorology has greatly diminished the need for such sferics information in routine forecasting. Nevertheless some past successes have been substantial, notably the hourly location for many years of any eastward-moving active frontal system in the North Atlantic by the British sferics network. The second motivation for long-distance sferic studies, less immediate and in some respects more basic, is to establish the climatology of thunderstorm occurrence ideally on a worldwide basis. Such information can be applied to fundamental studies of the global circuit in atmospheric electricity (Vol. 2, Ch. XIII).

There are possibilities for the global monitoring of thunderstorms by sferics systems carried in satellites. These systems would operate at frequencies in the VHF (30-300 MHz) band or higher so that the source signals would pass through the ionosphere. However, for various reasons the resolution that can be achieved from a satellite is limited, and for the accurate sferics location of distant lightning, ground-based observations are now preferred. This implies reliance on lightning signals in the LF (300-30 kHz), VLF (30-3 kHz), and ELF (<3kHz) bands, and consequent restriction of sferics location to that obtained from the lightning return stroke. It is only at frequencies below 300 kHz that propagation is relatively stable and well understood and propagation losses are sufficiently low for the source properties to be recognizable and detectable at great distances, and to be therefore useful in sferics studies.

Propagation below 300 kHz is channeled in the waveguide formed by the Earth and the lower ionospheric D region (Wait, 1970). A general description of the propagation has already been given (Vol. 2, Ch. XIII); some further details of particular significance in sferics methods are added here.

Waveguide propagation is frequency-selective in its attenuation properties. There are two windows of minimum attenuation: below 300 Hz and between about 10 and 30 kHz. Figure 1 illustrates the influence of these windows on the received-sferic spectrum. The source spectrum at d = 100 km is typical of a return stroke in which the initial violent current surge is succeeded by an intermediate current. The maximum amplitude is at 5 kHz. After propagation, the spectrum at 3,000 km has split into two components corresponding to the two windows of minimum attenuation at ELF and VLF. Note the shift in the maximum amplitude from 5 kHz to 10 kHz with propagation.

The behavior shown in Fig. 1 results from attenuation in two dominant waveguide modes in which the magnetic field is transverse to the direction of propagation (TM modes). Other modes have only subsidiary effects. Each mode, besides having its own frequency-selective attenuation characteristic, is also dispersive; i.e., propagation speed varies with frequency. This variation is complicated, but the ELF component lags increasingly behind the VLF signal as the propagation distance increases.

b. Single-station methods

A common approach to all single-station techniques for locating a lightning source is to establish separately the azimuth of the incoming sferic and the distance, d, of the discharge. The range is deduced from some property of the incoming sferic that is distance-dependent.

(1) Crossed loops

All long-distance, single-station sferics techniques rely on a crossed-loop antenna system to yield the azimuth information. In such a system, two identical vertical loop antennas are oriented N-S and E-W. Consider an incoming atmospheric with its electrical field in the plane of propagation and the magnetic field transverse to this plane. Such a vertically polarized atmospheric incident at an azimuth angle Φ with respect to north will induce signals in the loops proportional respectively to $\cos \Phi$ and $\sin \Phi$. This information can be displayed as an azimuth on a cathode ray tube by applying the loop outputs after suitable amplification to the respective plates of the tube. The information can also be digitized and the value of Φ indicated accordingly. In its simplest form, the loop antenna system includes an ambiguity of 180° in direction of arrival, which can be removed by adding an auxiliary vertical whip antenna and using the output suitably phased to eliminate the appropriate diametrical half.

Polarization, the orientation of the vibration vector of the electric field, can introduce errors in the operation of a crossed-loop system. An

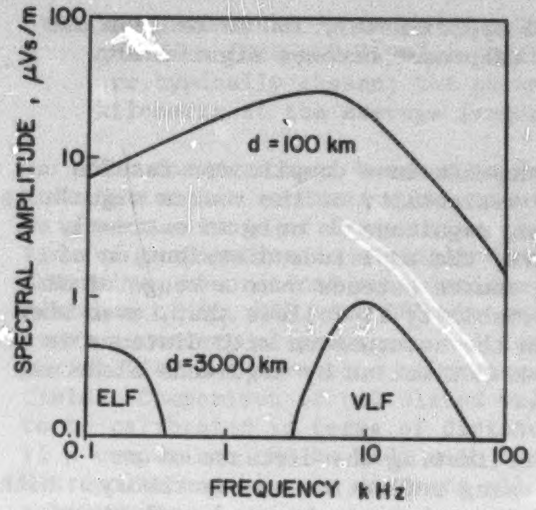

Figure 1.--Return stroke sferic spectra at two distances.

incoming atmospheric will produce a clear-cut response in the system only if the signal does not include horizontally polarized components; when such components are present, the response on a cathode ray tube display, for example, is elliptical and not linear. Horizontal polarization results from lightning channel orientation and propagation effects. During propagation there is a conversion of polarization state by ionospheric reflections so that even an initially vertically polarized signal will develop horizontally polarized components. Because of the propagation the later stages of an atmospheric of distant origin are particularly liable to include abnormally polarized components. For this reason, gating techniques in which the azimuth is effectively determined from the earlier parts of the waveform are of some use. However, with an optimum choice of frequency of operation, the errors due to polarization and channel orientation are rarely serious. Both experience and theory indicate that, within the VLF band, operation at or near a frequency of 10 kHz is a satisfactory choice for minimizing errors in direction finding on distant atmospherics, if the bandwidth is relatively wide.

Errors in crossed-loop work are also introduced at the site (Horner, 1964). Even topographical irregularities that are small compared with the wavelengths involved introduce distortion of the wavefront and consequent abnormal signals into the loop system. The site should be not only level but also as electrically homogeneous as possible. Long lengths of cable, buried or exposed, are very likely to produce errors, because the cables represent preferred paths for the currents induced by the impressed sferic, and the resultant reradiation is a source of unwanted abnormal signals in the loop system. As a final source of errors with a crossed-loop system, there is the possibility, with tuned loop receivers, of the disturbance or ringing response produced by an incoming sferic not having decayed completely before another sferic arrives. The duration of the disturbance is inversely proportional to the bandwidth, so that with a typical system of 1 or 2 kHz bandwidth the ringing is on the order of 1 millisecond. This time is not usually sufficiently long for interference between successive bearings to be a problem. Even if signals were accepted from all the global lightning activity (100 flashes per second) the average interval between return stroke pulses is still several milliseconds. However, if narrow bandwidths of approximately 100 Hz or less are employed, interference between successive responses becomes significant.

(2) Distance-dependent parameters

The magnitude of an incoming sferic depends in a complicated fashion on the distance of its origin. However, the variability of the source signals is such that, even when the distance is known, magnitude is only an extremely crude indication of distance. For instance, the amplitude distribution of broadband VLF return stroke pulses at the source extends over a range of at least 20 to 1. With this great source variability it follows that, even when a specific frequency is selected for which the attenuation with distance is considerable, the uncertainties in distance estimation by magnitude alone are immense.

A historically well-tried method of estimating the distance of an atmospheric is to interpret the waveform using reflection or ray theory. With this approach, and assuming the Earth and ionosphere to be good reflectors, the waveform will consist of a series of pulses whose sequence of temporal arrival is uniquely defined by the height of the ionospheric layer and the great circle distance. Unfortunately, the few waveforms suitable for analysis by the reflection mechanism are usually restricted to short ranges and/or a night environment (Kinzer, 1974). Under other conditions the pulses are severely modified by the ionospheric reflection. The ionosphere cannot ever be regarded as a surface of constant height since there are changes with pulse order and obliquity of incidence, and there is much superposition of pulses. The waveform analysis method, although of historical interest, cannot now be regarded as of practical importance.

Examination of the spectral content and dispersion of an atmospheric provides significant ways of estimating distance. As indicated in Fig. 1, the attenuation with distance is a function of frequency. Thus if the source spectral distribution--not its magnitude--is constant and established and the attenuation as a function of frequency and distance is known for the specific propagation conditions, then the ratio of received amplitudes at two frequencies, for example, is potentially a sensitive indicator of distance. Potentially is a key word because of the assumed constraints of source spectral shape constancy and knowledge of the propagation factors. Dispersion in an atmospheric depends on distance, but the method can be accurately applied only if the dispersion at the source is constant and the propagational dependence of the dispersion is known.

(3) The atmospherics analyzer

The equipment to analyze atmospherics is the most elaborate yet devised for single-station sferics work. It has been extensively developed (see, for example, Harth [1972]) since the original concept by Heydt and Volland (1964). The equipment combines separate measurements of three distance-dependent parameters as a function of azimuth for all incident atmospherics exceeding a certain threshold level. The chosen parameters are these:

(1) The amplitude at a specific frequency (Spectral Amplitude--SA). A typical choice would be 9 kHz.

(2) The ratio of the amplitudes at selected frequency pairs (Spectral Amplitude Ratio--SAR). The selection might be 5 and 9 kHz.

(3) The difference in times of arrival of the signals on two adjacent frequencies (Group Delay Time Difference--GDD). Frequencies of 6 and 8 kHz are typically chosen; the parameter is expressed in milliseconds per kilohertz at the average frequency of the selected pair.

The conversion of basic data from the atmospherics analyzer into distance information has received much attention. Since the measurements are confined to a narrow range of frequencies in the lower part of the VLF band, the assumption of propagation in a single dominant waveguide mode is not reasonable. Extensive, theoretical calculations for this mode yielding the variation with distance of SA, SAR, and GDD are available (Wait, 1970). These calculations cover a variety of propagational conditions including ionospheric temporal variability and direction of propagation with respect to the geomagnetic field. Comparison of calculated values with actual data enables the analyzer to be calibrated in terms of distance. The calibration is particularly sound if a comparison can be made with independent estimates of storm location. Extrapolations at zero distance allow estimations of the average source characteristics.

The information from the atmospherics analyzer is usually presented on an oscilloscope. One deflection represents azimuth and the other the specific distance parameter being studied. Each incoming atmospheric brightens the tube so that a photographic record of the screen, taken over a few minutes, reveals clusters of dots corresponding to the respective storm centers. These clusters are usually much more elongated in the distance direction than in the azimuthal coordinate. Undoubtedly much of this elongation is due to source variability between individual atmospherics in SA, SAR, and GDD. The extent of this source variability is far less well understood than are the propagational factors. Further improvements in the precision with which the atmospherics analyzer can identify storm centers are likely once the extent of the source variability in the different parameters is established. However, the very existence of the source variability means that the analyzer can never locate an individual atmospheric with accuracy, but can only fix the position, on a statistical basis, of an aggregate of atmospherics that is a storm center.

c. Multistation techniques

The standard method of fixing the position of an atmospheric is to use crossed-loop systems at two or more stations. Intersection of the respective bearings then yields the location. All the errors already discussed in relation to a single crossed-loop installation apply; for this reason, the redundancy furnished by more than two stations is very desirable. Typically, stations are separated by 500 km or more to obtain good fixes at distances beyond 1,000 km. The accuracies are approximately 10%. Some form of interstation timing is necessary to ensure that bearings are taken on the same atmospheric at the different stations. However, this requirement is not severe; a timing accuracy of 10 ms is usually quite adequate. Indeed, if the location information is not quickly required, the patterns of pulse reception at the different stations can often be matched, particularly when there is no local activity. In these circumstances the need for interstation timing is eliminated.

A time-of-arrival (TOA) method is by far the most accurate way of fixing the source of an individual sferic. It is also, understandably, the most elaborate and expensive. Suppose we have two stations and measure the difference in the times of arrival of the same feature--preferably the start--of an atmospheric waveform. Then a given time difference implies that the source lies on a certain hyperbola, with the stations as foci (Hughes and Gallenberger, 1974). Two time differences can be achieved with three stations arranged in two pairs, thus providing two hyperbolas, but four stations (three hyperbolas) are necessary if all ambiguity is to be avoided. TOA systems are much less subject to errors than are crossed-loop techniques. Polarization errors are effectively nonexistent; site errors are very small. However, if the potential accuracy of a TOA system is to be realized and confusion between separate atmospherics is to be avoided, interstation timing of approximately 10 μs is required. This implies the installation of accurate time standards at each station. Futhermore, the hyperbolic geometry involved makes plotting and fixing more difficult than with the straightforward directions yielded by crossed loops. Also, the TOA approach requires more stations than does a crossed-loop system. All these considerations suggest that, unless exceptional accuracy is required for special reasons, a crossed-loop multistation system is economically preferable to the TOA approach.

3. INTERMEDIATE DISTANCES

Many of the long-distance techniques discussed operate equally well or even better at shorter distances. This is so for multistation time-of-arrival systems, as well as for some of the methods of estimating distance from a single station. Among these, the successive reflection technique is more powerful at intermediate distances (200-1,000 km). The spectral-amplitude-ratio method can also be effectively used, although the pair of frequencies must be chosen with care. A compromise is necessary between pairs of frequencies that are insufficiently sensitive to distance changes and pairs that are overattenuated.

Conventional crossed-loop techniques tuned to 10 kHz give serious polarization errors at shorter distance for two main reasons. The loop antennas sense the abnormal fields due to long horizontal sections of channel before these have been attenuated by propagation. Also, the ground and ionospherically reflected waves containing horizontally polarized components are of comparable amplitude and arrive almost in superposition. Consequently, polarization errors of many degrees are common at close distances.

Gating techniques in which only the first part of the lightning signal is sampled are relatively ineffective at VLF, since most of the VLF signal originates at a later stage of the return stroke. However, a crossed-loop system has been perfected by Krider et al. (1976) in which a gating method is used at broadband. This system represents a very sophisticated development that is being extensively applied in forestry for locating potential lightning-caused fires.

The principle of the gating method devised by Krider et al. (1976) is easily understood. Records of the magnetic field due to the return stroke of a close flash to the ground show that the peak value is attained within 1 to 5 μs of the start of the return stroke. Suppose we assume a zero-to-peak time of 3 μs. Then since a typical return stroke upward velocity is 5×10^7 m s^{-1}, it follows that the initial peak fields must originate in channel length of only 150 meters above ground level. This channel length close to ground will almost always be approximately vertical, so that the complications of horizontal polarization are avoided if the azimuth information from the loop antennas is obtained by sampling close to the initial radiation field peak.

Broadband antenna systems are essential, and the loop antennas involved cover a frequency range of approximately 1 kHz to 10 MHz. The combined signals from the antennas trigger a sample gate whenever they exceed a certain threshold value. At the same time the azimuthal information from the loops is tracked pending the initiation of a display gate. In the preferred mode of operation, the display is initiated by a coincidence of the sample gate and the first zero crossing of the differentiated signal, i.e., at the peak output. Display initiation holds the azimuth information at the instant of initiation; this information is then presented as a bearing with a decay constant of 1 ms on an oscilloscope.

In the application to forestry the interest is in cloud-to-ground lightning alone and therefore in return strokes. For this reason various discriminants against background noise and intracloud lightning are incorporated into the direction finder. A return stroke pulse from the first stroke of a flash rises abruptly to a peak and then decays through a series of subsidiary peaks. The discriminants are such that only pulses characteristic of this temporal and peak sequence behavior are accepted.

There have been extensive tests of the broadband direction finder, involving comparisons with visual observations and television scanners and also, from greater distances, with storm locations revealed by weather radar. Generally the results have been excellent. Bearing errors of 1° or less are usual for ranges from 10 to 600 km. The principal exception is for discharges in mountainous terrain when errors of a few degrees are possible.

4. CLOSE DISTANCES

a. Lightning mapping

Quite recently some very interesting applications of sferics techniques at VHF have been made, making it possible, for the first time, to map the VHF sources within a cloud. The principle of the method--a time-of-arrival technique--was first formulated by Oetzel and Pierce (1969). It is illustrated in Fig. 2 for a baseline very short compared with the distance to the flash. Under these circumstances the hyperbolas of a conventional time-of-arrival system degenerate into asymptotic straight lines. With the illustrated three-antenna system, the difference in times of arrival of the same impulse at antennas S_1S_2 and S_2S_3, respectively, are given by

$$\Delta t_1 = (2\ell/c) \cos\theta$$

and (1)

$$\Delta t_2 = (2\ell/c) \sin\theta ,$$

where 2ℓ is the baseline and c the velocity of light. Short baselines (<100 meters) are desirable in order to avoid ambiguities, to ensure similarity

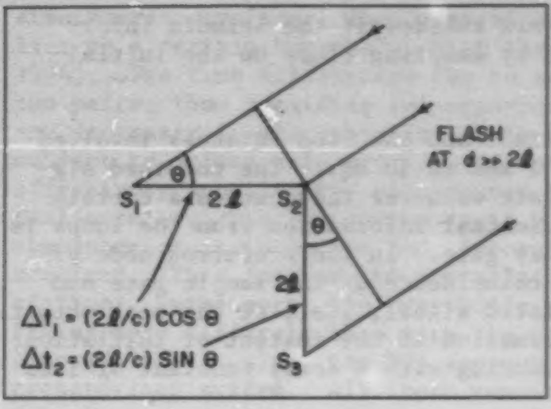
FLASH
AT d ≫ 2ℓ
θ
S_1
2ℓ
S_2
θ
2ℓ
$\Delta t_1 = (2\ell/c)\cos\theta$
$\Delta t_2 = (2\ell/c)\sin\theta$
S_3

Figure 2.--Illustrating principle of time-of-arrival VHF azimuth indicator.

of pulses at each end of the baseline, to preserve the approximate geometry, to achieve compactness, and so on. However, the shorter the baseline the less the accuracy. Fortunately, fast logic circuitry components now available can measure times of arrival to 1 ns. It follows that even with antennas separated by only 15 meters, cos θ or sin θ is measured to 0.02 and the bearing accuracy is therefore approximately 1 degree.

Taylor (1978) has extended the short-baseline arrangement to measure azimuth and elevation for incoming VHF pulses. His equipment covers a bandwidth of 20 to 80 MHz and uses baselines of only 13.74 meters for both the vertically separated (elevation) and horizontally spaced (azimuth) antennas (Fig. 3). The angle of elevation ϕ is obtained from

$$\phi = \text{arc sin } \left(\frac{c}{L_1} T_{el.}\right) , \qquad (2)$$

where c is the velocity of light, and

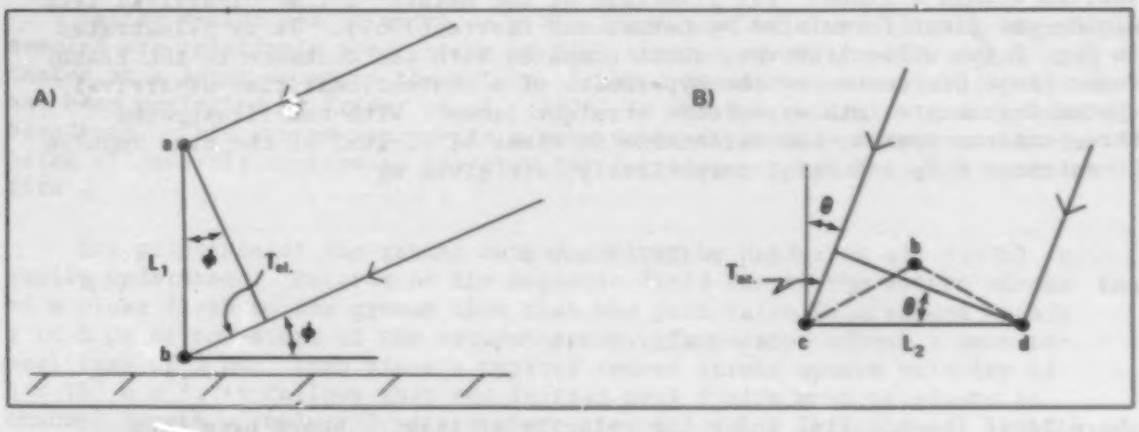

Figure 3.--Antenna arrangements showing how the (A) elevation and (B) azimuth angles are related to the time-of-arrival differences.

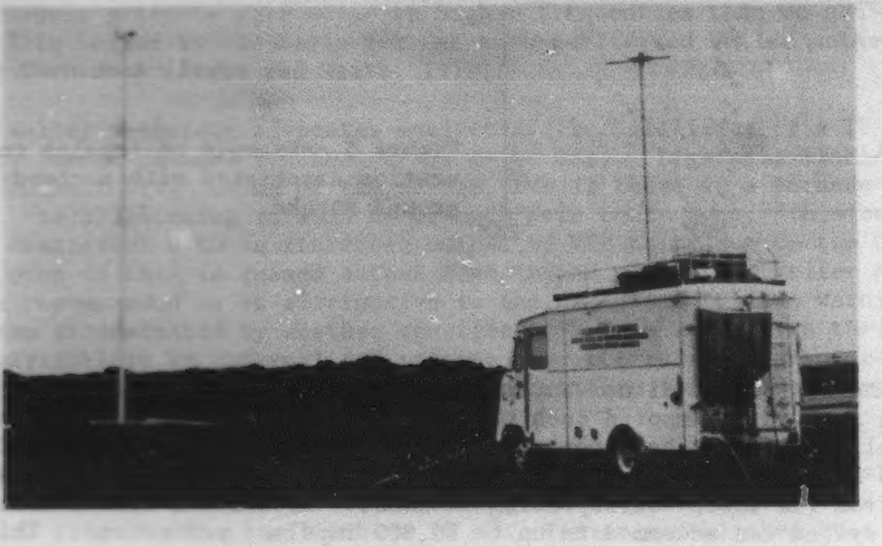

Figure 4.--Mapping site antenna mast and equipment van.

$$T_{el.} = t_b - t_a \,, \qquad (3)$$

where t_a and t_b are the times of arrival of an impulse at antennas a and b. The azimuthal angle of arrival is obtained by

$$\theta = \text{arc sin} \left(\frac{c}{L_2} \frac{T_{az}}{\cos\phi}\right) , \qquad (4)$$

where

$$T_{az} = t_c - t_d \,, \qquad (5)$$

and where t_c and t_d are the times of arrival of an impulse at antennas c and d. L_1 and L_2 are the separations between corresponding antenna pairs used in obtaining the elevation and azimuth angle.

Figure 4 is a picture of one observing site at the Kennedy Space Center in 1976. The mast at the left supports antenna a at the top, with antenna b situated at the base. Twelve other antennas surround the mast and are electrically selected corresponding to antennas c and d to restrict impulse acceptance to a 60° azimuthal sector that can be shifted in 30° increments. The antenna on top of the van is for communications.

Although there is no problem with ambiguity in determining elevation angles using only two antennas, a third antenna must be used to eliminate ambiguity in measuring azimuth. A simple solution is to use antenna b, as shown in Fig. 3. By requiring that the received impulses arrive at antenna

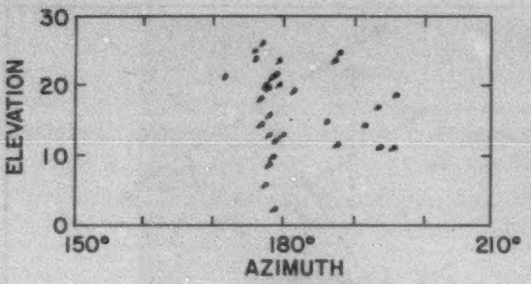

Figure 5.--Example of impulse configuration associated with a cloud-to-ground stroke.

b prior to arrival at either antenna c or d, ambiguity is eliminated and a limit in azimuth is imposed such that only impulses from within a preferred azimuthal sector will be accepted. This sector width is 180° minus the angle c-b-d in Fig. 3B, unless relative time delays are imposed in the signals received from the three corresponding antennas. Accuracies of 0.5° are obtained, and the system can accommodate up to 25,000 impulses per second. This corresponds to times somewhat shorter than the usual VHF pulse separation of 50 to 100 μs within a flash.

An example of a cloud-to-ground stroke with associated intracloud processes is shown in Fig. 5, a pictorial view in elevation and azimuth obtained at a range of about 14 km. The highest dot represents the source of an impulse located at a height of 7.1 km. There appear to be three branches to the right of the main vertical configuration of dots. The lowest branch, containing three dots, is at 2.7 km. Below this height there are four dots representing the main return stroke channel.

At times pulses can occur as short as 10 μs apart. This means that with baselines exceeding 3 km the possibility of confusion arises. However, this will not always be the case, and an elaborate VHF locating system known as LDAR (Lightning Detection and Ranging System) that uses baselines of approximately 10 km has been constructed and successfully operated at Kennedy Space Center. Five stations are employed, one central and four peripheral. The information from any four of the stations yields the location of the VHF signal using true three-dimensional hyperbolic geometry; the asymptotic approximations are not applicable since the baselines are now not short compared with the distance to the flash. Various discriminants are incorporated in the LDAR system to ensure that the measured times employed in computing a location are physically realistic and that confusion between unrelated pulses is avoided. Time differences are measured to within 50 ns. The accuracy of the system varies with the configuration of the selected stations and with the range and altitude of the source. Typically, for a range of 32 km and an altitude of 10 km, errors of 2% are obtained in each parameter. However, the errors in altitude estimation are much greater for low sources.

b. Warning techniques

Perhaps of most public interest is the use of sferics in monitoring the approach of severe weather. Thunderstorms emit radio signals over almost the entire radio frequency spectrum, but there are strong indications that the spectral distribution of the emitted noise varies with the severity of the storm. In particular there is now some belief that severe storms that may spawn tornadoes generate more noise at higher frequencies than do non-tornadic storms. This belief is the basis for the much-publicized Weller method of detecting tornadoes (Biggs and Waite, 1970).

The Weller technique advocates monitoring the brilliancy of a TV receiver set at its lowest channel (channel 2--54 to 60 MHz). Lightning flashes produce a transient brightening of the screen, but if there is a tornado in the vicinity, the brightening is said to be much more continuous. This behavior would be consistent with an increased output of VHF noise due to the tornado. However, even if this increased output does indeed occur, the Weller method cannot be recommended as an alternative to the organized tornado warning information disseminated by weather agencies. TV receivers, with their intrinsic variability in internal and antenna characteristics, cannot really be used as precision indicators. They are no substitute for equipment specifically designed for warning purposes.

Taylor (1973) has made some thorough studies of the utility of sferics as detectors of severe storms. After examining the outputs of receivers at frequencies from 10 kHz to well above 10 MHz, Taylor established that the channels at frequencies exceeding 1 MHz were uniformly more responsive to severe storms. In particular, the burst rate at 3 MHz was a sensitive indicator of the severity of a storm. With a given threshold level, corresponding typically to a storm at 70 km, a burst occurs when the received signals exceed the threshold level at a rate greater than 500 per second over a time of more than 0.1 second. Burst rates exceeding 20 per minute were present in 82% of tornadic storms, in about 22% of other severe storms (funnel clouds, hail, and/or strong winds), and in only 1.4% of nonsevere thunderstorms. This apparently favorable result is, however, tempered by the fact that the vast majority of storms are nonsevere. In fact, if the 20-per-minute burst rate were used as an indicator of tornadoes, the false-alarm rate would be about 70%. This result is, however, for an omnidirectional arrangement. The addition of a directional capability reduces the false-alarm rate since much of this is due to the aggregation of several nonsevere storms simultaneously active at similar ranges.

Sometimes the severity of the storm is not a prime consideration in warning techniques, for example, for operations in which lightning is a hazard, and for which, in consequence, all thunderstorms are dangerous. Typical of such operations would be a protracted loading or unloading of explosives. Under such circumstances a simple omnidirectional threshold sferics warning device can be useful. It is best for the device to function in the "near-field" regime within its operating range. This enables the range to be better defined; the operation thus depends inversely on the cube of distance on the near-field electrostatic component, rather than inversely with distance as with the far-field radiation component. Choice of the electrostatic field regime implies selection of an extremely low frequency for the warning device. This is dictated by the near-field requirement $f < (c/2\pi R)$, where f is the frequency, R the range, and c the velocity of light. Thus a nominal range of 50 km would entail a device functioning at frequencies of less than 1 kHz.

c. Studies of electric fields and field changes

The preferred methods for research studies of the electrical effects of close thunderstorms do not fall under what is conventionally referred to as sferics. However, no account of experimental studies would be complete without some discussion of methods of the measurement of the electric fields associated with storms and of the field changes caused by lightning.

The standard instrument for measuring electrical field is the field mill. Many designs of field mills exist, but all operate on similar principles (Chalmers, 1967). Consider a conducting plate of area A exposed to the Earth's field E. Under the influence of the field a surface charge of $\varepsilon_o EA$ will reside on the plate, where ε_o is permittivity of free space. If the plate is alternately exposed to and shielded from the field, the bound surface charge will vary alternately with an amplitude that is proportional to E. The alternating charge is conveniently amplified and then demodulated to produce an output signal dependent on E.

A typical field mill consists of a set of insulated plates alternately shielded from and exposed to the ambient field by a sectored rotor. The rotor is often driven at a speed of some 2,000 rpm, and in the usual arrangement, the exposed area A(t) of the plates varies as a triangular function of time. A synchronous signal derived from the rotor is used for demodulation after the ouput from the sensing plates has passed through a charge amplifier.

The modulating frequency of a field mill depends on the number of sectors in the rotor and rotor speed and is typically about 100 Hz. However, the output of the mill is usually integrated over several modulation cycles to give a time constant exceeding 0.1 second. This integration, and the basic limitation that the exposed plate area does not remain constant but varies with time, renders the field mill unsuitable for studying the rapid field changes due to lightning. These must be investigated with some kind of fixed antenna system.

Many antenna arrangements are possible, including vertical whips, ball antennas, and plates. With some of these arrangements calibration in terms of the ambient field is very straightforward, notably so for the case of a plate antenna of area A mounted flush with the Earth's surface. As in the case of a field mill sensor, there is a bound charge $\varepsilon_o E(t)A$ on the antenna and the output voltage of a charge amplifier will be proportional to $\varepsilon_o E(t)A/C$, where C is the capacitance of the antenna system. The capacitance will be shunted by a resistor R to produce a time constant RC. Choice of a time constant appropriate to the lightning phenomenon being studied is a fundamental requisite; the time constant should be at least 10 times the duration of the event being investigated. Thus if the field variation over the entire discharge (duration ~1 second) is being examined, a 10-s time constant is reasonable. An antenna with this value is termed a slow antenna. At the other extreme a fast antenna with a time constant of about 100 μs is appropriate for studying the rapid (<10 μs) changes accompanying return strokes.

Whatever the type of antenna or field mill being used, the choice of a site is of prime importance. The area should be flat, and there should be no shielding of the antenna or mill by adjacent objects. An artificial ground plane surrounding the antenna helps to ensure correct operation and to simplify calibration. For a plate antenna, mounted flush with the Earth and surrounded by a ground plane, calibration is simply effected by using an insulated screen above the antenna. Calibrating voltages, preferably in the form of square waves, are applied to the screen. The dimensions of the screen should be appreciably larger than the size of the antenna to avoid fringing effects.

REFERENCES

Biggs, W. G., and P. J. Waite, 1970. Can TV really detect tornadoes? Weatherwise 23:120-124.

Chalmers, J. A., 1967. Atmospheric Electricity. Pergamon Press, New York, 515 pp.

Harth, W., 1972. VLF-atmospherics: their measurement and interpretation. Z. Geophys. 38:815-849.

Heydt G., and H. Volland, 1964. A new method for locating thunderstorms and counting their lightning discharges from a single observing station. J. Atmos. Terr. Phys. 32:609-621.

Horner, F., 1964. Radio noise from thunderstorms. In Advances in Radio Research, Vol. 2, J. A. Saxton (ed.), Academic Press, New York, 121-204.

Hughes, H. G., and R. J. Gallenberger, 1974. Propagation of extremely low-frequency (ELF) atmospherics over a mixed day-night path. J. Atmos. Terr. Phys. 36:1643-1661.

Kinzer, G. D., 1974. Cloud-to-ground lightning versus radar reflectivity in Oklahoma thunderstorms. J. Atmos. Sci. 31:787-799.

Krider, E. P., R. C. Noggle, and M. A. Uman, 1976. A gated wideband magnetic direction finder for lightning return strokes. J. Appl. Meteorol. 15:301-306.

Oetzel, G. N., and E. T. Pierce, 1969. VHF technique for locating lightning. Radio Science 4:199-201.

Taylor, W. L., 1973. Electromagnetic radiation from severe storms in Oklahoma during April 29-30, 1970. J. Geophys. Res. 78:8761-8777.

Taylor, W. L., 1978. A VHF technique for space-time mapping of lightning discharge processes. J. Geophys. Res. 83:3575-3583.

Wait, J. R., 1970. Electromagnetic Waves in Stratified Media. Pergamon Press, New York.

blank page

VIII. OBSERVATION AND MEASUREMENT OF HAILFALL

Griffith M. Morgan, Jr.

1. INTRODUCTION

The development of adequate measurement techniques is an important early milestone in any scientific endeavor. Prior to this stage a science consists of little more than a collection of stories and impressions. The study of hailfall sits, at the moment, astride the measurement milestone. It is only since the last part of the preceding century that networks of specifically instructed observers have attempted organized observations of hailstorms in Europe, and less than 25 years since the first networks of hail-observing instruments were brought into use in North America.

Most modern data on hailfall have come from the few research groups that have established the necessary extensive field observing networks. These groups are in Alberta, Canada; Pretoria, South Africa; Illinois; and Colorado. New large-scale efforts under way in Switzerland, France, Italy, Hungary, and Yugoslavia should offer interesting results in the next few years. Interest in hailfall measurement is spreading as more countries become concerned about hail suppression testing, as indicated by the holding of the First International Workshop on Hailfall Measurement at Banff, Alberta, in October 1977 (Goyer, 1978).

Complete description of a hailfall would include the parameters for each stone falling on a representative area: time and place of arrival, size, shape, ice and liquid water content, content and distribution of air bubbles and foreign substances, hardness, crystal structure, velocity, rotation, and perhaps more. In most hail research, much less complete information is required, and only a few parameters suffice to describe an entire hailfall at a point. For example, the total kinetic energy of the hail integrated during a hailfall event has been used as the primary measure for hail prevention experimentation (Schleusener and Jennings, 1960) because of a presumed relationship between kinetic energy and crop damage. The National Hail Research Experiment (NHRE) based its hailfall documentation on measurements of the time-integrated volume (or mass) of hail owing to theoretical arguments about the effect of cloud seeding on that parameter.

2. HAIL OBSERVATION BY CONVENTIONAL WEATHER STATION NETWORKS

Hail is observed and reported by the weather-observing networks that furnish information on which the familiar weather forecasts are largely based, and much of the readily available climatology of hail is based on these observations (Stout and Changnon, 1968). Although the stations are approximately 25 to 100 miles apart, depending on the region, so many hailstorms occur each year that some of them are observed at each station. The value of the stations' hail reports lies primarily in the length of the observations (50 to 80 years at some stations). To show their importance it is necessary to explain the relationship between point hail frequency and areal hail frequency.

The average number of times hail occurs at a given weather station is the point hail frequency. Though it does not directly define the number of hail-

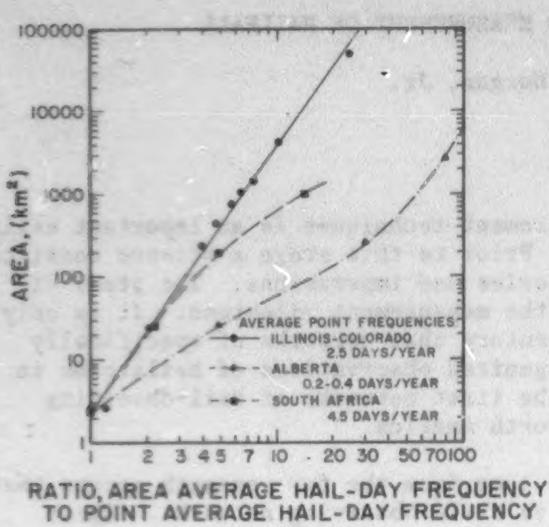

Figure 1.--Relationship between areal hailfall frequency and point frequency for Illinois-Colorado (Changnon, 1971b), South Africa (Douglas, in Hitschfeld, 1971), and Alberta (Carte and Held, 1978).

storms taking place in the vicinity of the station, it is an indicator of generalized hailstorm frequency. By comparing point frequencies with hail data from other sources, such as hail insurance reports and observer networks, it is possible to determine the average relationship between the local point frequencies and the frequency of hail in areas of specified sizes. Figure 1 shows the point-area relationship based on data from Illinois and one point in Colorado, and similar relations derived from data for South Africa and Alberta. The curve for Illinois and Colorado approximates a straight line; South Africa and Alberta show higher area-point ratios for equal areas. The differences between these curves should be due to differences in the characteristic sizes of hail areas (and their variations) from place to place, but probably reflect effects due to nonuniformities of the point hail frequency within the areas studied and ordinary sampling problems. The large-scale point frequency distribution in Illinois is rather uniform, with point values generally between 2 and 3 days per year. Both the Alberta and South Africa areas contain both high and low average frequencies within the areas of study. Maps of point frequency of hailfall such as those found in Stout and Changnon (1968) are valid and useful for comparing one area with another. Point frequencies reliably indicate regions of high or low hail incidence.

3. HAILFALL AND CROP DAMAGE

Crop damage is the most important economic impact of hailfall. Much has been learned about hailstorms by studying damage to crops, but there are some important complications to be understood in order to interpret such information.

Hail damages crops because hailstones are fast-moving missiles. Each stone has some degree of potential for puncturing or removing leaves, breaking stems and branches, crushing stalk fibers, and smashing fruit. This damage potential depends on the hailstone itself (mass, shape, hardness, speed), the plant that is exposed to it (type of plant, stage of growth, mode of planting, and condition), and other factors such as wetting by previous or concurrent rain. The wind that accompanies hail also has a strong influence on damage primarily because it can impart a velocity component to the hailstones several times that acquired through free fall alone. Added horizontal velocity increases the path length of the stone through the crop and, hence, the probability of its striking a plant, and increases the number of stones that have enough energy to do damage. The wind can also cause the plant to present a different cross section to the hail than it would in the absence of wind. A very impressive fall of hail might do little or no damage to a crop if the wind is very light; a lesser fall of hail might completely destroy it if accompanied by a strong enough wind. An observed increase in crop damage from one side of a field to another could be due to an increase in the same sense of either hail or wind.

Lack of wind information has hindered efforts to determine relationships between crop damage and hailfall characteristics such as stone sizes and energies (Changnon, 1971a; Garcia et al., 1976; Morgan and Towery, 1976a).

a. Hailfall inferred from kinetic energy

Most attempts to express hailfall parameters in terms of equivalent crop loss have been based on the assumption that damage is a simple function of the sum of the kinetic energy of the hailstones falling on a unit area. That energy, for an arbitrary hailfall in the absence of wind, is

$$KE = 1/2 \Sigma m_i v_i^2 ,$$

where m_i and v_i are the masses and fallspeeds of individual stones striking a unit horizontal area. Since stones are assumed to fall at their terminal fallspeeds, given by $v_i = k\, d_i^{\frac{1}{2}}$, where k is a constant and d_i is the diameter of the i^{th} stone,

$$KE = \frac{\pi}{12} k^2 \ \rho_i \ \Sigma d_i^4 .$$

This analytical approach to hail damage has been further developed by Morgan and Towery (1976b), who have shown how a windblown hailfall can be divided into its component fluxes of kinetic energy for analysis. With no wind, there is only a vertical flux of vertically directed kinetic energy. When wind blows with hail, five new flux components can be defined, each of which can be greater than the no-wind energy flux.

Even if we neglect the complications due to wind, the damage is actually a function of more than the kinetic energy. First, the geometry of the plant is not taken into account. Second, although the largest stones carry the most energy, they are few in number (and for that reason alone may not play a strong role in crop damage) and their numbers are not well estimated. The damage will be more dependent on some intermediate-sized stones that are both great in number and large enough to do damage (Morgan and Towery, 1976a).

An example of an attempt to relate hail kinetic energy to crop damage is seen in Fig. 2. This shows that there is a threshold of about 50 J (joule) m^{-2} below which little or no damage is done to crops and that above about 450 J m^{-2} the crops are totally destroyed. Between these limits, however, the actual data show no regular relationship between hail kinetic energy and crop damage.

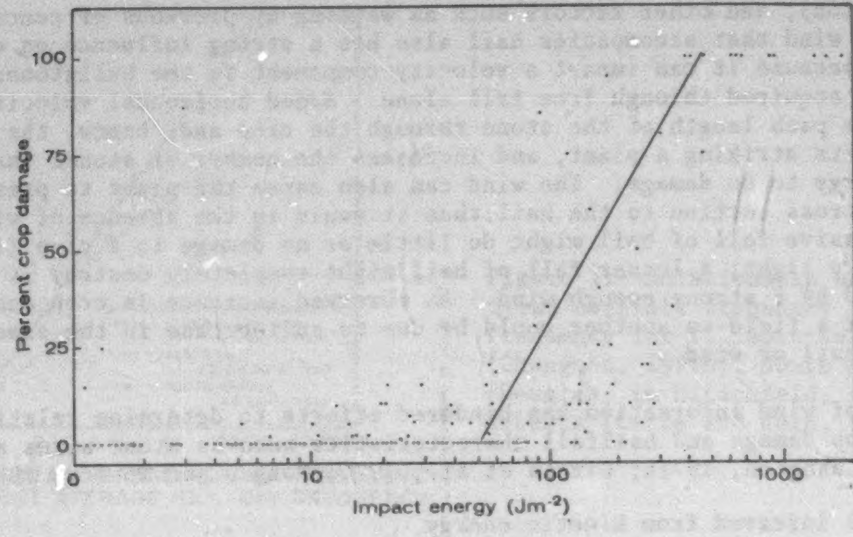

Figure 2.--Crop damage in Alberta as a function of hailfall kinetic energy (Strong and Lozowski, 1977).

Vento and Morgan (1976) used hailcube (see Sec. 5) measurements to estimate the enhancement of hailfall kinetic energy by wind. The kinetic energy contributed by wind exceeded that due to fallspeeds alone in 33% of 524 observations made in the Po Valley of Italy and in almost all 88 measurements made in hailstorms in Nebraska.

Wojtiw and Renick (1973) used both hail and wind observations to determine the probability of damage. From the reports of wind (strong, moderate, etc.), hailstone size, ground coverage, and crop damage, they estimated the total (fallspeed plus wind) impact energy (KE) received by a unit horizontal surface. Table 1 shows their results for the probability of damage of four classes of intensity as a function of the total impact energy.

b. Hailfall inferred from insurance records

Insurance records of crop loss are an invaluable source of hailfall information. CHIAA (1978) gives a detailed account of the terminology and technical characteristics of crop hail reports. Without a full understanding of these one could acquire some very misleading ideas about hailfall from using insurance information. Not all hail produces damage, so that the hail area shown by insurance data will be smaller (at times considerably) than the area over which hail actually fell. Insurance against hail normally includes a deductible clause whereby no payment is made for damage less than a certain percent, and this can further reduce the inferred hail area.

Crop hail insurance reports represent an almost continuous distribution of observers at times when all farms have hail-sensitive crops, but there must be crops to experience damage for insurance claims to reveal the occurrence of a hailfall.

Table 1.--Relationship between total impact energy and hail damage in Alberta

Total impact energy ($J\ m^{-2}$)	Probability (%) of damage category occurring			
	Nil	Slight	Moderate	Heavy-severe
$<10^{-2}$	98.8	0.3	0.0	1.2
10^{-2} - $<10^{-1}$	94.2	4.3	1.4	0.0
10^{-1} - $<10^{0}$	81.2	16.1	1.1	1.7
10^{0} - $<10^{1}$	67.8	19.1	10.1	3.0
10^{1} - $<10^{2}$	46.2	29.6	14.8	9.4
10^{2} - $<10^{3}$	23.0	23.3	27.8	25.9
10^{3} - $<10^{4}$	12.7	13.0	23.9	50.4
10^{4} - $<10^{5}$	10.6	6.4	6.4	76.6

Figure 3 shows the average number of hail days per month in a 26,500-mi^2 (67,800-km^2) area of central Illinois from 1967 to 1973 both with and without the incorporation of hail insurance data. In March, when no crops are exposed and susceptible, the insurance data add nothing, but in June, when crops are susceptible, they double the number. This illustrates simultaneously the effect of high observation density on the number of observed hail days and a shortcoming of insurance data as a source of information for the researcher. When insurance data is most effective, it seems (in the example of Fig. 3) that the monthly number of hail days is doubled. On this basis, one may deduce true peaks of about 15 hail days per month in April and May.

An insurance adjuster generally makes estimates of one or two types of physical damage to the crop, such as percentage of leaf loss and percentage of

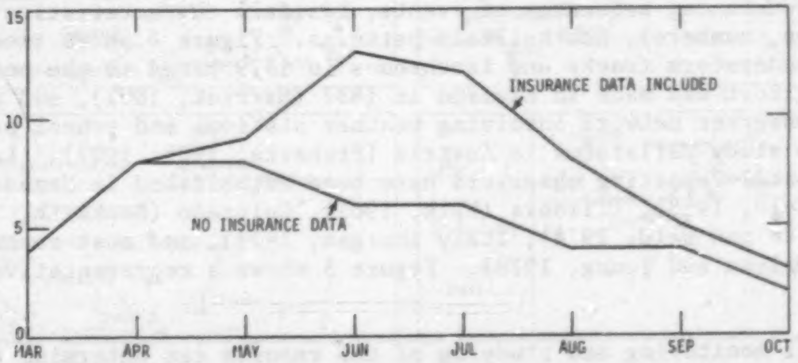

Figure 3.--The average number of hail days per month in a 26,500-mi^2 (67,800-km^2) area of central Illinois, 1967-73, with and without reports of insurance losses (Changnon and Morgan, 1976).

plants completely destroyed and then, with the aid of empirically derived tables and graphs, estimates the percent loss of crop yield. These forecast losses are, at times, seriously in error. The relationship between these forecast values and the actual physical damage depends on factors (potential for plant recovery, for example) not related solely to the physical damage. Plants go through stages in their development during which they are sensitive in varying degrees to damage by hail. For instance, large leaf loss to corn may have a strong influence on net yield at one stage of its life and none at all at a later stage.

c. Hailfall inferred from aerial photography of crop damage

An interesting observation technique, which within very few trials led to some surprising new insights about hail patterns, is aerial photography of damaged crops. Changnon and Barron (1971) employed aerial photography with both infrared and conventional color film in an exploratory study and found that with careful interpretation damage areas could be well delineated. A study by Towery et al. (1976) examined the utility of aerial photography using false-color infrared film as an aid to hail insurance companies in storm assessments. The results were encouraging enough that the sponsoring group uses the technique on a quasi-routine, trial basis. Some of the insights about surface hailfall that have come from studies of aerial photographs are described in Vol. 2, Ch. XI.

4. HAIL DATA FROM OBSERVERS' REPORTS

Collation of witnesses' accounts probably gave the first indications of the strange and variable patterns of hailfall. Studying such accounts is still an exciting and valuable way to learn about hailfall patterns, as well as people's attitudes and perceptions of hailstorms. The use of large networks of trained observers, however, has produced greater scientific knowledge of hailfall.

Networks of observers have been organized over large areas since late in the last century. In 1874 a network of postal-reporting observers, augmented by hail insurance adjusters, military volunteers, and railroad employees, was established to cover northern Italy (Pini, 1885). Until World War I, it furnished valuable documentation of thunderstorm motions (speeds and directions), times of occurrence, sequences of events, hailfall characteristics (stone sizes, types, numbers), and hailfall patterns. Figure 4 shows reconstructions of some thunderstorm tracks and isochrones in 1879 based on the postal reports. A similar effort was made in England in 1887 (Marriot, 1892), and still later a notable observer network involving weather stations and school principals was used to study hailstorms in Austria (Prohaska, 1905; 1907). Large networks of postal-reporting observers have been established in Canada (Douglas and Hitschfeld, 1958), Illinois (Wilk, 1961), Colorado (Beckwith, 1960), South Africa (Carte and Held, 1978), Italy (Morgan, 1973), and most recently, Oklahoma (Nelson and Young, 1978). Figure 5 shows a representative reporting card.

Careful monitoring and studying of the reports can determine the reliability of each observer (see Carte et al. [1963]). The observer reports of hailfalls are subjective, and certain average biases must be considered for them to be useful. Douglas (Carte et al., 1961) noted that observers tend to round off times to the nearest 5 minutes. Changnon (1971a) also showed that

TAV. IV

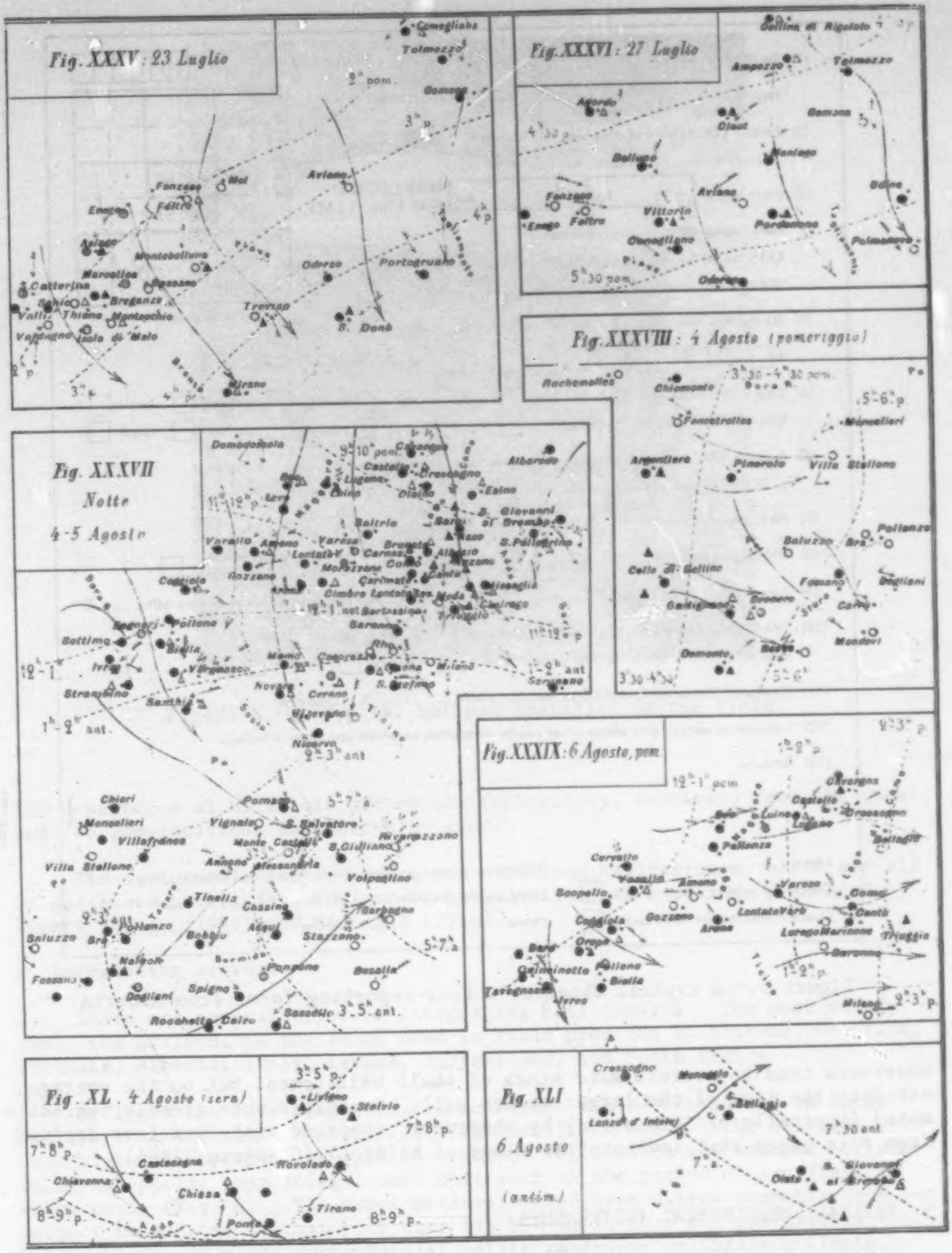
Fig. XXXV : 23 Luglio
Comeglians
Tolmezzo
Gemona
2h pom.
3h p.
4h p.
Aviano
Fonzaso
Mel
Enego
Feltre
Asiago
Montebelluna
Marostica
Bassano
S. Catterina
Schio
Breganze
Valli
Thiene
Montecchio
Valdagno
Isola di Malo
Oderzo
Portogruaro
Treviso
S. Donà
Piave
Tagliamento
Brenta
Mirano
Fig. XXXVI : 27 Luglio
Collina di Rigolato
Ampezzo
Tolmezzo
Agordo
Cleut
Gemona
4h 30 p.
Belluno
Maniago
Udine
Fonzaso
Feltre
Enego
Aviano
Vittorio
Pordenone
Conegliano
Palmanova
Piave
Oderzo
5h 30 pom.
Fig. XXXVIII : 4 Agosto (pomeriggio)
Rochemolles
Chiomonte
3h 30 - 4h 30 pom.
5h-6h p.
Fenestrelles
Moncalieri
Argentiera
Pinerolo
Villa Stellone
Saluzzo
Bra
Pollenzo
Colle di Sollino
Fossano
Dogliani
Castiglione
Busca
Cuneo
Carrù
Mondovì
Demonte
3h 30-4h 30
5h-6h
Fig. XXXVII Notte 4-5 Agosto
Domodossola
9h-10h pom.
Cavergno
Castello
Lugano
Crescagno
Albarado
Olsio
Esino
Beltrio
S. Giovanni al Brembo
Varallo
Arona
Varese
Brunate
Lentate
Como
S. Pellegrino
Gozzano
Morazzone
Cantù
Carimate
Cimbro
Lentate
Seveso
Trezzo
Cossato
Biella
Pollone
Settimo
Ivrea
Strambino
Sambia
Vergnasco
Novara
Cerano
Saronno
Rho
Milano
S. Stefano
Seregno
Vigevano
Nicorvo
12h-1h
1h-2h ant.
2h-3h ant
11h-12h p.
1h-2h ant
Po
Chieri
Moncalieri
Villafranca
Villa Stellone
Pomaro
Vignale
S. Salvatore
Monte Castello
S. Giuliano
Rivarazzano
Annone
Alessandria
Volpedino
Tinella
Cassine
Garbagna
Saluzzo
Bra
Pollenzo
Bobbio
Acqui
Stazzano
Bormida
Narzole
Ponzone
Busalla
Fossano
Dogliani
Spigno
Rocchetta
Cairo
Sassello
2h-3h ant
5h-7h a.
3h-5h ant.
Fig. XXXIX : 6 Agosto, pom
12h-1h pom
1h-2h p.
2h-3h p.
Cavergno
Castello
Lugano
Luino
Crescagno
Bellagio
Pallanza
Cervatto
Varallo
Arona
Varese
Como
Scopello
Gozzano
Lentate
Cantù
Coggiola
Arona
Lurago Marinone
Triuggio
Saronno
Oropa
Pollone
Biella
Ivrea
Bard
Quincinetto
Tavagnasco
Milano
Ticino
1h-2h p.
Fig. XL . 4 Agosto (sera)
3h-5h p.
Livigno
Stelvio
7h-8h p.
Castasegna
Chiavenna
Roveleto
Chiesa
Tirano
Ponte
8h-9h p.
Fig XLI 6 Agosto (antim.)
Crescagno
Menaggio
Bellagio
Lanzo d'Intelvi
7h 30 ant
7h a.
S. Giovanni al Brembo
Olsio
Lario

Figure 4.--Analyses of postal observers' reports of thunderstorms and hail in northern Italy in 1879. Dashed lines are isochrones; arrows indicate direction of propagation; lightning, rain, and hail symbols are like those in current usage. Barbed arrows indicate winds with storms.

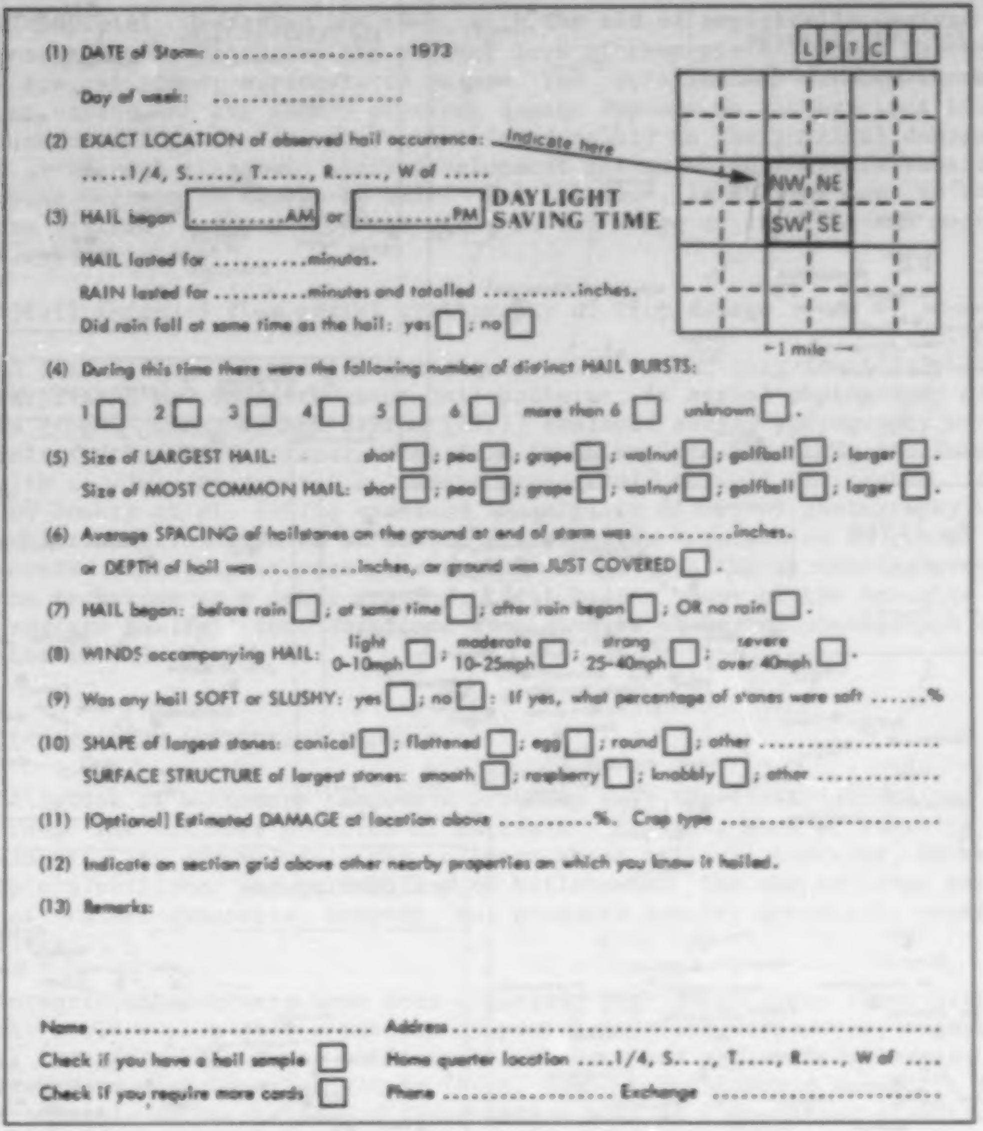
L
P
T
C
Indicate here
NW
NE
SW
SE
←1 mile →

(1) DATE of Storm: 1973

Day of week: ....

(2) EXACT LOCATION of observed hail occurrence:

.....1/4, S......, T......, R......, W of .....

(3) HAIL began ☐ ....AM or ☐ ....PM DAYLIGHT SAVING TIME

HAIL lasted for ....minutes.

RAIN lasted for ....minutes and totalled ....inches.

Did rain fall at same time as the hail: yes ☐; no ☐

(4) During this time there were the following number of distinct HAIL BURSTS:

1 ☐ 2 ☐ 3 ☐ 4 ☐ 5 ☐ 6 ☐ more than 6 ☐ unknown ☐.

(5) Size of LARGEST HAIL: shot ☐; pea ☐; grape ☐; walnut ☐; golfball ☐; larger ☐.

Size of MOST COMMON HAIL: shot ☐; pea ☐; grape ☐; walnut ☐; golfball ☐; larger ☐.

(6) Average SPACING of hailstones on the ground at end of storm was ....inches.

or DEPTH of hail was ....inches, or ground was JUST COVERED ☐.

(7) HAIL began: before rain ☐; at same time ☐; after rain began ☐; OR no rain ☐.

(8) WINDS accompanying HAIL: light 0-10mph ☐; moderate 10-25mph ☐; strong 25-40mph ☐; severe over 40mph ☐.

(9) Was any hail SOFT or SLUSHY: yes ☐; no ☐: If yes, what percentage of stones were soft ......%

(10) SHAPE of largest stones: conical ☐; flattened ☐; egg ☐; round ☐; other ....

SURFACE STRUCTURE of largest stones: smooth ☐; raspberry ☐; knobbly ☐; other ....

(11) [Optional] Estimated DAMAGE at location above ....%. Crop type ....

(12) Indicate on section grid above other nearby properties on which you know it hailed.

(13) Remarks:

Name .... Address ....

Check if you have a hail sample ☐ Home quarter location ....1/4, S...., T...., R...., W of ....

Check if you require more cards ☐ Phone .... Exchange ....

Figure 5.--A typical observer's hail-reporting form, from Alberta.

observers tend to overestimate sizes of small hailstones, but on the average, estimate the size of the larger stones well. Durations were greatly overestimated (typically by 10 minutes) by observers, compared with durations derived from rain gages that indicate the times of hailfall (Changnon, 1966).

5. HAILFALL MEASUREMENT INSTRUMENTS

Difficulties encountered in surface hail measurements derive from these: (1) rarity of hail occurrence, so that highly dependable instruments and large study areas are required; (2) great horizontal variability of hailfall parameters, which places demands on the sensing areas and numbers of instruments;

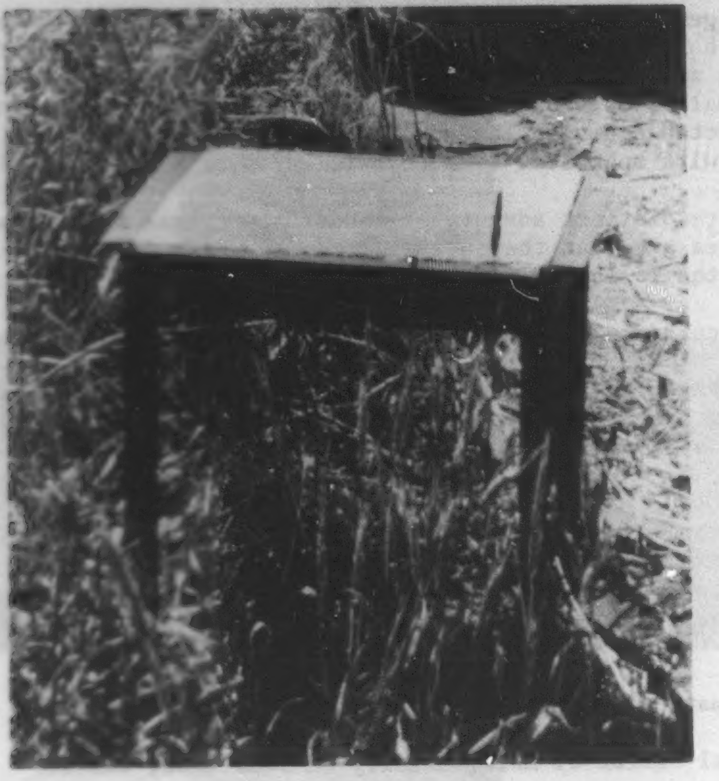

Figure 6.--A typical hailpad installed in the field.

(3) departures of hailstone properties (sphericity, hardness) from the ideal; and (4) complications introduced by wind.

The instruments for recording and measuring hailfall now in use are all of quite recent origin. Reviews of hail instruments have been presented by Towery et al. (1976) and Nicholas (1978).

a. Integrating sensors

There are several types of integrating hail sensors. The most widely used, the hailpad, is now being used in field programs in Montana, Colorado, Illinois, Alberta, Italy, France, Switzerland, and South Africa.

Hailpads are very simple instruments that can be fabricated in large numbers from inexpensive materials. In most field studies the hailpads have been slabs of Styrofoam wrapped in aluminum foil, which are mounted horizontally on special supporting frames that rest on the ground or are fixed to fence posts (Fig. 6). The exact materials used have varied somewhat from one project to another so that each user has had to perform his own calibration. The problems and minor controversial points regarding calibration (Vento, 1976; Lozowski and Strong, 1978) are not essential to this discussion. Descriptions of various combinations of materials used in hailpads can be found in Schleusener and Jennings (1960), Towery et al. (1976), Roos (1978), and Lozowski et al. (1978).

Goyer (personal communication) experimented with pressure-sensitive paper backed by a hard Masonite surface as a potential replacement for the hailpad. This sensing surface worked well for hard, plastic spheres, but is useless for recording real hailstones, because of their variable shapes and hardness. He also constructed a device intended to sort hailstones by size, which functioned well with spherical test objects but poorly with actual hailstones.

There are distinct advantages and disadvantages to the use of hailpads. The advantages are that they are inexpensive, easy to service and work with, and provide the following information:

(1) Hail occurrence (yes-no).

(2) The number of hailstones ($\geq$0.1-cm diameter) per unit area, determined by counting dents. The upper limit on number is about 10^4 stones per square meter; beyond this number it becomes difficult to distinguish individual stones.

(3) An estimate of stone size, made by measuring dent size.

(4) An estimate of the vertical kinetic energy and momentum imparted by hailstones (based on observed dent size and theoretical values of fall-speed).

(5) An estimate of the accumulated mass of hail.

(6) The areal extent of hail, usually on a hail day basis.

If data are collected over a period of years, the above information can provide valuable climatological information about hail occurrences, which is important in evaluating hail suppression projects.

Disadvantages of hailpads include the following:

(1) All hail falling between pad changes will be recorded. Should more than one hailfall occur, one cannot separate the hail events.

(2) Stone frequency errors occur if stones cause overlapping dents, a major problem with very large numbers of stones.

(3) No information is obtained about windblown stones.

(4) No information is obtained on the time of hail, a distinct problem in the study of individual storms. An attempt has been made to overcome this problem by installing hailpads near weighing-bucket recording rain gages that have been altered (evaporation funnel removed) so that hailstones hit into the bucket, deflect the pen arm, and leave a spike on the rainfall trace. This spike can give a reasonably accurate estimate of time and duration of hail (Chagnon, 1966), but some judgment is required to identify spurious signatures that occasionally occur because of strong, gusty winds.

Another variation of the hailpad has been adapted for quantitative analysis of windblown hail. Figure 7 shows a hailcube, a five-sided hail sensor, which has been distorted for ease of viewing. It is an adaptation of a device

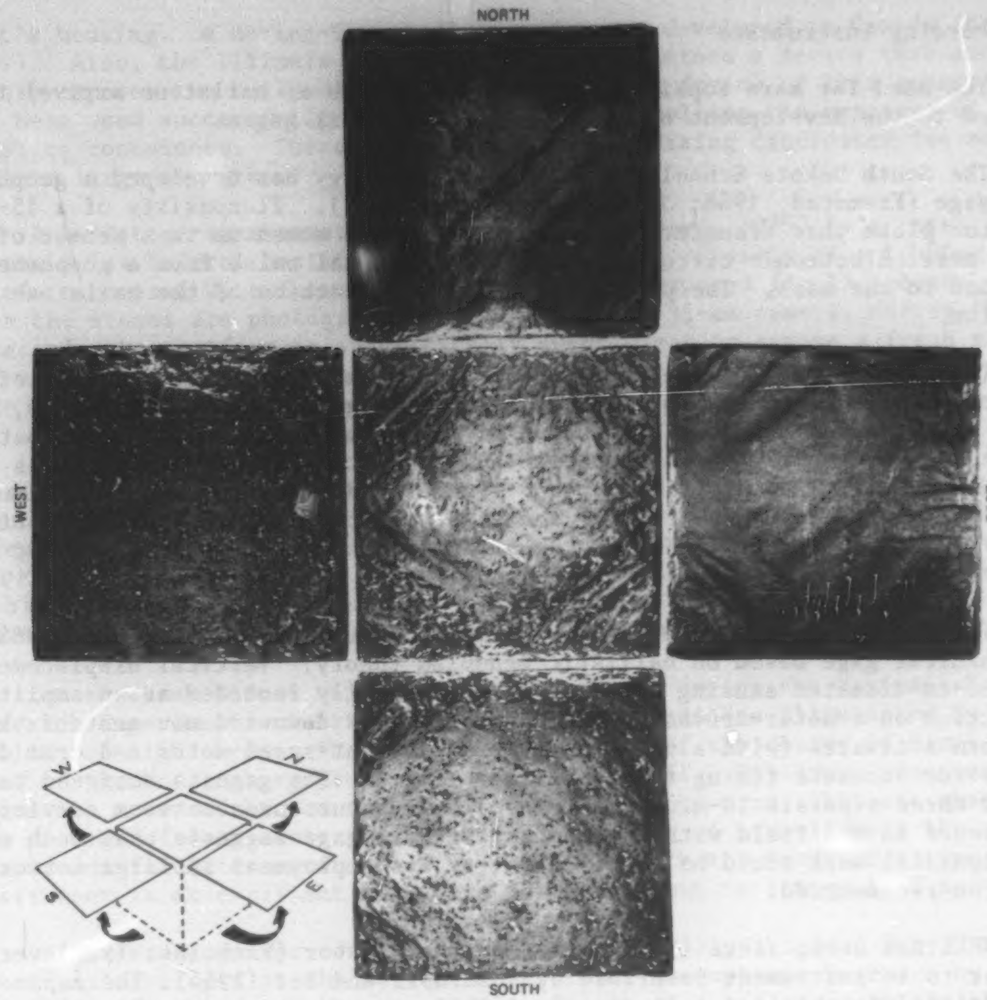

Figure 7.--The five-sided hailcube. Example from a hailstorm in southwestern Nebraska on 22 July 1973.

extensively employed in Italy. Vertical and azimuthal angles of hailfalls are obtained by means of a relationship between the number of stones that occur on the vertical and horizontal sensing surfaces (Morgan and Towery, 1976b; Vento, 1972). The horizontal components of hailstone velocity, momentum, and kinetic energy can also be calculated. A minor disadvantage is transporting five times as many hailpads as required by the single hailpad technique. Hailcube analysis, described in detail by Morgan and Towery (1976b), typically requires about 20% more time than that required to analyze single horizontal hailpads. Hailcubes have been employed in field projects in the United States, Canada, and Western Europe; in the late 1970s a network of 300 hailcubes was installed in support of a hail prevention project near Pecs, in southern Hungary.*

---

*Personal communication from Dr. Endre Wirth, Director of the Hungarian Hail Prevention Project, Pecs, Hungary.

b. Recording instruments

The need for more sophisticated hail data such as hailstone arrival times has led to the development of several recording hail gages.

The South Dakota School of Mines and Technology has developed a geophone hail gage (Fremstad, 1968; Johnson and Smith, 1978). It consists of a 15-cm-diameter plate that transfers the hailstone impact momentum to a sensor of large mass. Electronic circuits derive an electrical pulse from a geophone attached to the mass. The pulse amplitude is a function of the hailstone momentum.

The geophone hail gage gives information on size, number, and time of occurrence of hailstones, covers a reasonable range of vertical momentum, gives a unique and reproducible output of momentum values, operates on batteries, and records the data on magnetic tape (resulting in reduced analysis time and cost). Time distribution and size provide information useful in assessing hail suppression efforts and hailstorm characteristics. The primary disadvantage to this hail gage is the small sensing area, which may yield a somewhat unrepresentative stone size distribution (Changnon and Staggs, 1969).

The Illinois State Water Survey hail gage (Mueller and Changnon, 1968) is a mechanical gage based on ballistic pendulum theory. Vertical displacement of a 36-cm-diameter sensing platform is mechanically recorded as an amplitude deflection on a motor-driven recording chart. The downward movement of the platform activates (with a start magnet) a constant-speed motor and drum drive to provide accurate timing for a hailfall record. The gage is designed to record three separate 10-min (or shorter) hail occurrences between servicings. Experience in the field with the mechanical hail gage suggests that much more developmental work would be required before its employment in large networks could be recommended.

NHRE has used, since 1972, a hail-rain separator (Nicholas, 1978) very similar to an instrument described by Kozminski and Bac (1964). The separator was designed to obtain a measurement of the mass of rain and hail. Recording and nonrecording types have been designed, with a 36-cm^2 opening that receives the rain and hail. The rain passes through a screen into a container, and the hailstones roll or slide down the screen into a second container. The nonrecording hail separators can be automatically closed at a specified time by a spring-loaded lid. The precipitation from the rain and the hail containers is measured daily. In the recording hail separator, the hailstones fall into a water-filled container, and the amount of water displaced is equal to the mass of hail. The displaced water flows into a calibrated, automatic siphon device; the amount is recorded digitally on 35-mm film, allowing estimation of the hail rate and duration. The rain-receiving portion of the separator allows similar recording of rainfall.

Admirat* (personal communication) has developed a time-resolving hail recorder. The instrument consists of several conventional hailpads mounted on a drum that rotates in steps on command from a timing device. One hailpad at a time is exposed to the hail through an opening in the top of the instrument's housing. A moving-foil hail recorder was developed in Canada (Koren, 1969). Also, the Illinois State Water Survey examined a device that successively exposes two hailpads for 24 hours each. A device of this general type has been used successfully in the field for controlling the exposure of rain-sampling containers. These devices are very promising candidates for employment in large networks.

---

*Personal communication from Dr. Pierre Admirat, Institute of Glaciology, University of Grenoble, France.

A hailstone spectrometer (Federer and Waldvogel, 1975) is a research tool at the Swiss Federal Institute of Technology. It consists of a 1,650-cm^2 platform covered with foam rubber. The area is exposed for 27 seconds, and then the stones are photographed by an automatic 35-mm camera; during the next 3 seconds the platform is automatically swept clean to expose a fresh surface for another 27 seconds. The spectrometers are portable and require the presence of an operator during observations.

Rosini (personal communication) constructed and tested in Italy a device consisting of a collecting funnel and a clock-driven (stepwise) rotating elbow spout that would deliver all hailstones falling in fixed time periods to receptacles filled with chilled kerosene; this procedure would thus preserve all stones entering the collector in each period. This device suffered from problems with the collection funnel such as bouncing of stones, but otherwise functioned well and might serve well in limited scientific applications.

An electro-optical hail recorder considered during the National Hail Research Experiment consists of an array of photodiodes illuminated by a collimated light beam. The operating principle of the device is similar to that of the Knollenberg probe discussed in Ch. III. Hailstone size and fall-speed are measured by the number of elements of the array that are shaded by the passage of each stone and by the stone's time of transit past the array. Despite difficulties encountered in the field with the first prototypes, this instrument is an excellent candidate for deployment in future hail networks.

A hailstone sensor consisting of an electrically shielded Butyl rubber sheet was developed at the National Center for Atmospheric Research by Buck and Goyer (Changnon and Staggs, 1969). Impact of a hailstone on the sheet produces a pulse whose amplitude is a function of the size of the hailstone. Though the sensor had many desirable properties such as ruggedness, it was insensitive to stones less than 0.5 in (1.25 cm) in diameter and the output response to impact was not uniquely related to input.

The Illinois State Water Survey is conducting tests on two devices that record the time and duration of hailfall, using a piezoelectric sensing element attached to a 30-by-30-cm Plexiglas impaction surface horizontally supported above the ground. Proper thresholding of the output of this sensor permits a very reliable distinction between hail and rain. In one of the devices, a standard weighing-bucket recording rain gage with an additional pen arm is used for recording the hail occurrence times. This device has been successfully tested in Illinois and Colorado. For hail timers at locales without rain gages, a second version has an inexpensive digital memory for the recording medium. Both devices can be used with a standard hailpad to obtain hailstone frequency and size estimates.

c. Remote-sensing techniques

McNeil and Houston (1966) discussed their preliminary investigation of interesting ideas for remotely sensing hail. They reported that exploratory studies of seismic and acoustic techniques indicated that, though sound in concept, they would be usable only to ranges of about 0.25 miles (0.4 km) and therefore were not worth pursuing. They also discussed and rejected techniques based on radar sensing of the changes in reflectivity of a passive target due to hail impacts. Another technique considered was allowing the impact of hail to switch on an inexpensive VHF transmitter whose output could be sensed by a remote receiver. They believed the main problem with such an approach would be that of frequency multiplexing an array of several hundred such sensors to know which of them was transmitting at a given time.

An interesting remote sensing approach to hail detection and measurement pursued by Weickmann (1969), Goyer (1970; 1971), and Roads (1973) is the mapping of melting hail on the ground by airborne infrared radiometric devices. Under ideal circumstances this technique can produce a good estimate of the extent of hail on the ground; in general, however, it is of limited applicability.

Weather radar has been an indispensable remote-sensing tool in the study of hailstorms and other forms of severe weather. Radar allows rather approximate localization of hail areas; Fig. 8 shows radar echo tracings of a large and severe hailstorm that took place on the high plains of Colorado and Kansas on 21 June 1972. Weather radar research has included developing methods of measuring both rainfall and hailfall at the ground (in terms of rainfall rate, rate of hailfall mass deposition, or measures of hailfall damage potential such as kinetic energy flux). The detection and measurement of hail by radar is fraught with complications, and radar cannot yet be recommended for routine monitoring and measurement of hailfall.

The correspondence between location of hail at the ground and low-angle radar echo has been investigated by many, and no clear picture has emerged. Waldvogel et al. (1978) have reported some success at estimating hail kinetic energy with radar, the basic assumption being that hail, when it occurs, is associated with the strongest radar echo at the lowest angle of scan.

In Illinois (Changnon and Morgan, 1976) strong hailfall at the ground was associated with strong low-altitude gradients of 3-cm wavelength reflectivity. Carte and Held (1978) reported 86% of surface hail occurrences were in the strong gradient (10-cm wavelength) regions; 38% occurred on the storm's left flank (N.B., these are Southern Hemisphere observations); and 39% on the leading edge, with hail occasionally occurring at the rear.

The tendency of hail to appear in the strong gradient portions of the echoes might be explained by wind displacement below the radar beam; it has been shown in Vol. 2, Ch. XI, that hail tends to be blown to the right (in Illinois, Northern Hemisphere) of the direction of hailshaft motion. However, aircraft penetrating hailstorms (Musil et al., 1976) have found hail aloft on the edges of updrafts in regions of strong gradient of radar reflectivity.

A major effort in remote hail detection has been the dual-wavelength radar hail detection technique proposed by Eccles and Atlas (1969). This elegantly simple approach to hail detection based on the different scattering properties of hail at different radar wavelengths (Atlas and Ludlam, 1961) has had some limited success but also some practical difficulties. Another radar hail detection technique is based on the depolarization of microwave radiation by nonspherical hailstones (Atlas et al., 1953). Tests of this approach in

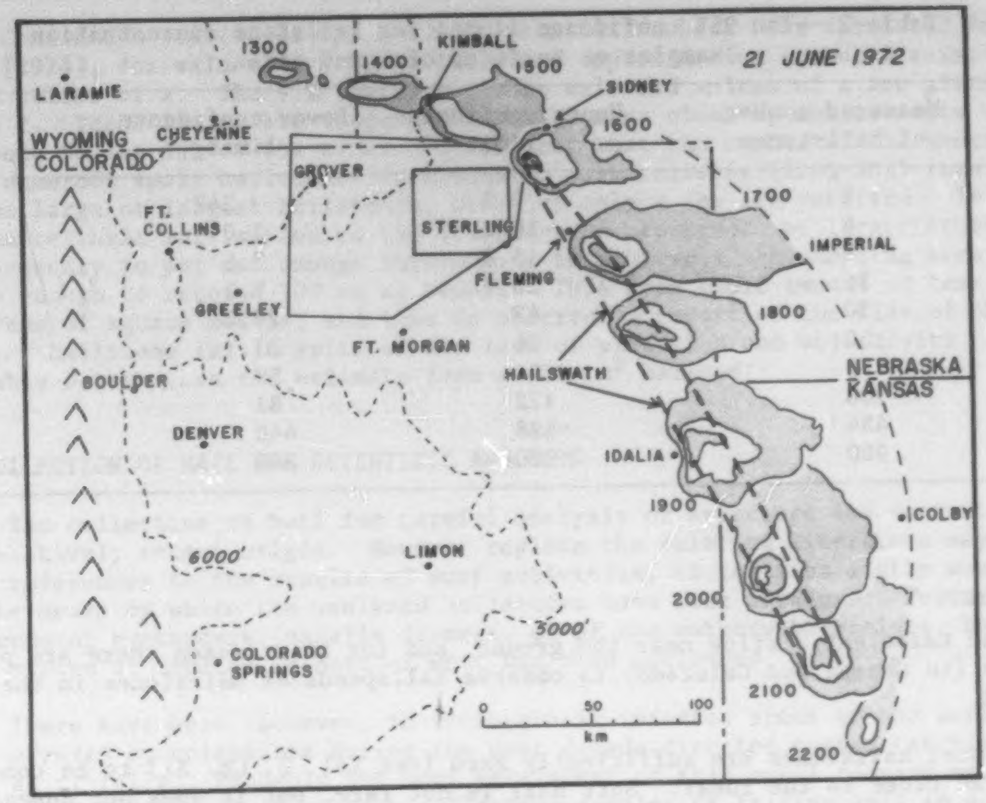
1300
1400
KIMBALL
1500
21 JUNE 1972
LARAMIE
SIDNEY
WYOMING
COLORADO
CHEYENNE
1600
GROVER
FT. COLLINS
STERLING
1700
IMPERIAL
FLEMING
GREELEY
1800
FT. MORGAN
HAILSWATH
NEBRASKA
KANSAS
BOULDER
DENVER
IDALIA
1900
COLBY
LIMON
6000'
2000
3000'
COLORADO SPRINGS
2100
0
50
100
km
2200

Figure 8.--Hourly positions of a large hailstorm as determined by radar. The approximate limits of the hailswath are indicated by the bold dashed line. Outer contours are 20 dBZ. Successive contours are at intervals of 12 dB (i.e., 32, 44, etc.) (Browning and Foote, 1975).

Alberta (Barge, 1970) have lent support to its validity, but evaluation is still under way.

A review of radar sensing of hailfalls and hail areas is provided by Changnon (1972) and Srivastava and Jamieson (1977).

d. Limits to accuracy of point hailfall measurements with instruments

Instruments such as hailpads are calibrated under controlled laboratory conditions, where uncertainties of measurement can be evaluated and are usually quite small (about 10%; Lozowski et al., 1978). Other errors or sources of uncertainty, which occur in real field conditions, probably dwarf the basic measurement errors.

Since ideal properties of hailstones are assumed in calibrating instruments, departures from ideal result in errors. Large departures from sphericity (see Vol. 2, Ch. XI) are infrequent, and the normal range of shapes does not suggest that this is a large source of error. Deviations of fallspeeds at impact from the theoretical terminal fallspeeds, however, seem likely to occur

Table 2.--The 95% confidence limits for hailstone concentration samples on surfaces of fixed size

Measured number of hailstones	Upper confidence limit	Lower confidence limit
2	7.2	.242
4	10.2	1.09
8	15.8	3.5
16	26.0	9.1
30	43	20.2
50	66	37.1
75	94	59
100	122	81
484	~528	440
900	~960	840

in the turbulent airflow near the ground, and for this reason there are programs (in Canada and Colorado) to observe fallspeeds of hailstones in the field.

Most hailstones are sufficiently hard (see Vol. 2, Ch. XI) to be considered close to the ideal. Soft hail is not rare, but it does not appear to be a frequent source of measurement uncertainty.

These problems and any others unforeseen will produce a net uncertainty (or instrumental error variance) in the measurements. Attempts are under way in Europe and the United States to evaluate this uncertainty (for hailpads) by performing calibrations in the field. These consist of catching or photographing all the stones that strike a hailpad and comparing their dimensions with the dents on the pads.

Another source of error, characteristic of any instrument of small surface area, is purely statistical. It is reasonable to expect the statistics of hailstone concentration in the air (per cubic meter) at any instant to vary from one small volume to another in a random fashion that can be described by the Poisson probability distribution, which has found validity in problems similar to hailfall, such as sedimentation of particles, fluctuations in the concentration of molecules of a gas, and, more closely, fluctuations in raindrop concentrations (Joss and Waldvogel, 1969). The distribution law is given by

$$p(x) = \frac{m^x e^{-m}}{x!} ,$$

where p(x) is the probability of finding x hailstones in any of many equal volumes, and m is the mean of x over many volumes. The same distribution should be equally valid for the total number of hailstones per unit area on the ground, or for that matter, for the number of hailstones in any selected size interval.

Confidence limits for the Poisson distribution have been tabulated (e.g., Crow [1974], for values of x up to 100), and approximation formulas exist for large values of x. The 95% limits for some selected values of x are given in Table 2. These limits are those within which many close-by measurements would be found to lie 95% of the time. It is clear that the number of the generally more numerous small hailstones is estimated more reliably (±10%-20%) than that of the large or largest hailstones, of which only a few are detected. To obtain reliable information on the frequency of occurrence of larger stones it is necessary to put out enough instruments to achieve a net sampling area large enough to receive 100 or so stones. This area could amount to tens or hundreds of square meters, and thus an observer's report of the size of the largest hailstone is, in spite of its lack of precision and objectivity, probably better than the estimate from a 900-cm^2 hailpad.

6. COLLECTION OF HAIL FOR SCIENTIFIC ANALYSIS

The collection of hail for careful analysis of structure and content is of relatively recent origin. However replete the relevant literature may be with references to the results of such activities, it contains little mention of the means by which the analyzed hailstones have been obtained. Fortuitous presence of bystanders, usually farmers, or of the authors themselves, has been stated or implied in most of what has been published.

There have been, however, in various hail-infested areas of the world, some efforts by scientists during the past decade directed toward catching hail as it falls. Probably the most persistent of this small company must be Knight and Knight, who have been collecting samples of falling hail in northern Colorado, Oklahoma, and the lowveld of South Africa for more than 10 years. One of the reasons for the Knights' work has been to remove that element of fortuity from studies of hailstone structures. Bystanders tend always to collect the largest stones in any given samples. More important than this size bias, however, is the lack of other information to which the results of the analyses may be related. All attempts to collect hail on any organized basis, therefore, have been connected with projects in severe-storm research in which data from radar, aircraft, and ground networks are also available.

One of the few published reports of hail chasing is given by Browning et al. (1968), who describe problems associated with interception of hailstorms in the vicinity of, and in cooperation with, the National Severe Storms Laboratory in Norman, Okla.

Browning and his colleagues examined hailstones in the field but, in most cases, the stones were just collected, stored, and later examined in the laboratory. Because the crystal structure of a hailstone changes rapidly at temperatures close to 0°C in a process known as recrystallization, the stones must be collected in a manner that will preserve their original structure (Knight and Knight, 1968). This is usually done by letting the stones fall into liquid hexane at dry-ice temperature (-78°C), which freezes, immediately and in situ, any liquid water contained in the hailstone.

A number of vehicles have been designed to intercept severe storms and to sample various types of precipitation. The more elaborate of these have also contained instruments to measure and record the standard meteorological parameters such as temperature, pressure, windspeed and direction, humidity, and rainfall rate. Ambient air filter samplers, rain drop disdrometers, hail cameras, and even pibals are also sometimes carried on the vehicles.

When they first began chasing hailstorms in northeastern Colorado, Knight and Knight used an ordinary delivery van and set out catchers on the ground. In time, radios were added to permit communication with a radar center at Grover, Colo., and project aircraft. A simple device was later mounted on top of the van to funnel the hailstones inside, at once allowing them to observe the storm from inside the vehicle and providing time-resolved samples.

The complexity of the instrumentation contained in any one vehicle depends primarily upon its mission. One of the first vehicles designed to sample both rain and hail was used in the Alberta Hail Studies Program for several years (Summers, 1968). In 1969, Morgan designed a similar but more complicated vehicle for a research program conducted in Verona, Italy. A still more elaborate vehicle was designed by the University of Wyoming (Veal, 1970) and used in cooperation with the National Hail Research Experiment (NHRE) in northeastern Colorado from 1971 to 1976, as were a number of more spartanly equipped vehicles designed by the Desert Research Institute to collect rain and hail samples for silver analysis in connection with weather modification projects. A more recent addition to the vehicle fleet has been built by Federer and Waldvogel for use in Grossversuch IV, a hail research program conducted in Switzerland (Federer and Waldvogel, 1975).

Successful interception of a severe storm requires a great deal of cooperation and communication between the mobile units and those who are monitoring the progress of the storm by radar or aircraft. In an ideal situation, storm occurrence and motion must be forecast in sufficient time to allow mobiles to be deployed into the area where the storm is expected to occur. As the storm materializes and grows, its development is relayed to the mobile units, which maneuver into a position in front of the storm, where the core of highest radar reflectivity may be expected to pass overhead.

In reality, nature rarely cooperates in such a straightforward way, and hail chasing is often a game of "catch-up." There are hazards involved in chasing hail, not the least of which is the necessity of driving over miles of wet, unpaved farm roads that, during storms, turn into rivers of slithery gumbo. There are meteorological hazards as well: gust fronts, blowing dust, and lightning. In areas such as Oklahoma, where hail is often associated with tornadoes, one must always be especially aware of the vehicle's position with respect to the storm. Large hail often falls just to the north of a tornado. In such circumstances, it is obvious that the technique employed for catching hail differs somewhat from that employed in less violent storms. One approaches from the north, drives into the precipitation shaft but never through it, collects hail, and returns to the north again, turning away from the storm. Clear escape routes, preferably in more than one direction, are extremely important.

7. DESIGN OF NETWORKS FOR HAILFALL OBSERVATION

The principal characteristic of a network is its station density, or the number of stations per unit area (sometimes expressed as its inverse, the area represented by each station, or as the mean separation between stations). This must be great enough that a number (to be specified) of observation points will fall within any significant hail entity (e.g., a hailstreak) that occurs within the network. Figure 9 shows networks of three different station densities operated by the Illinois State Water Survey in 1974.

Clearly, the perfect network would be dense enough to allow a description of every hailfall event to any desired degree of detail. The network density actually required to achieve an acceptable network sampling variance depends on these: a) the statistical characteristics of the hailfall in the network area, described by the distribution of sizes (lengths, widths, areas) of hailfall entities and the typical scales of variability within entities of the desired measures of hailfall; and b) the purpose the measurements must serve. For example, a network intended to estimate the total mass of hail falling from an ensemble of 50 hailstorm days need not be as dense as one intended to describe in detail a single hailfall.

a. An example of the effect of sampling density on estimates of areal extent of damaging hail

Two areas in central Illinois, one comprising 4,000 square miles and the other 1,000 square miles, located inside the larger area, were chosen for study by Changnon (1968). More than 85% of the total area was covered by insurance over an 11-yr period. Maps for each storm day were prepared, showing the actual areas of paid losses using all the available insurance data that represented a sampling density of four observation points per square mile. Transparent overlays at the same map scale with evenly distributed points representing observation sites with densities of 0.5, 1.0, 3.0, and 9.0 square miles per point were placed on each damage map to determine the area of damage per storm day for each density.

The average values for the areal extent of damaging hail on storm days showed a considerable variation with sampling density. In the 4,000-mi^2 area, 16,000 sampling points (36 points per 9 square miles) indicated that the average daily areal extent of damaging hail was 36.1 square miles, whereas 445 points (1 point per 9 square miles) measured only 6.3 square miles of damaging hail. This is because of the tendency for hail to fall in isolated scattered patches. At low station density many of the patches escape detection by the network.

The seasonal average areal extents of damaging hail defined by different densities were expressed as percentages of the total damaged hail area, as defined by four points per mile (see Table 3). On the average, a hail network with a density of one point per 9 square miles in a 1,000-mi^2 area measures 11% of the actual area of damaging hail in a season. A network with this density measured a 1-yr high of 13% and a 1-yr low of 8%. These results indicate that a network comprising one or two observation sites per square mile is necessary to measure adequately the areal extent of damaging hail.

b. An example of degradation of hailfall pattern with decreasing network density

Long (1978) studied the variation of estimates of total hailfall mass for a storm that occurred on 22 June 1976 over the NHRE hail network in northeastern Colorado. On that day 551 hailpads registered hail, and the topography of mass of hail (in millimeters of rainfall equivalent) based on all of them is shown in Fig. 10. The dots represent the hailpad locations. Figure

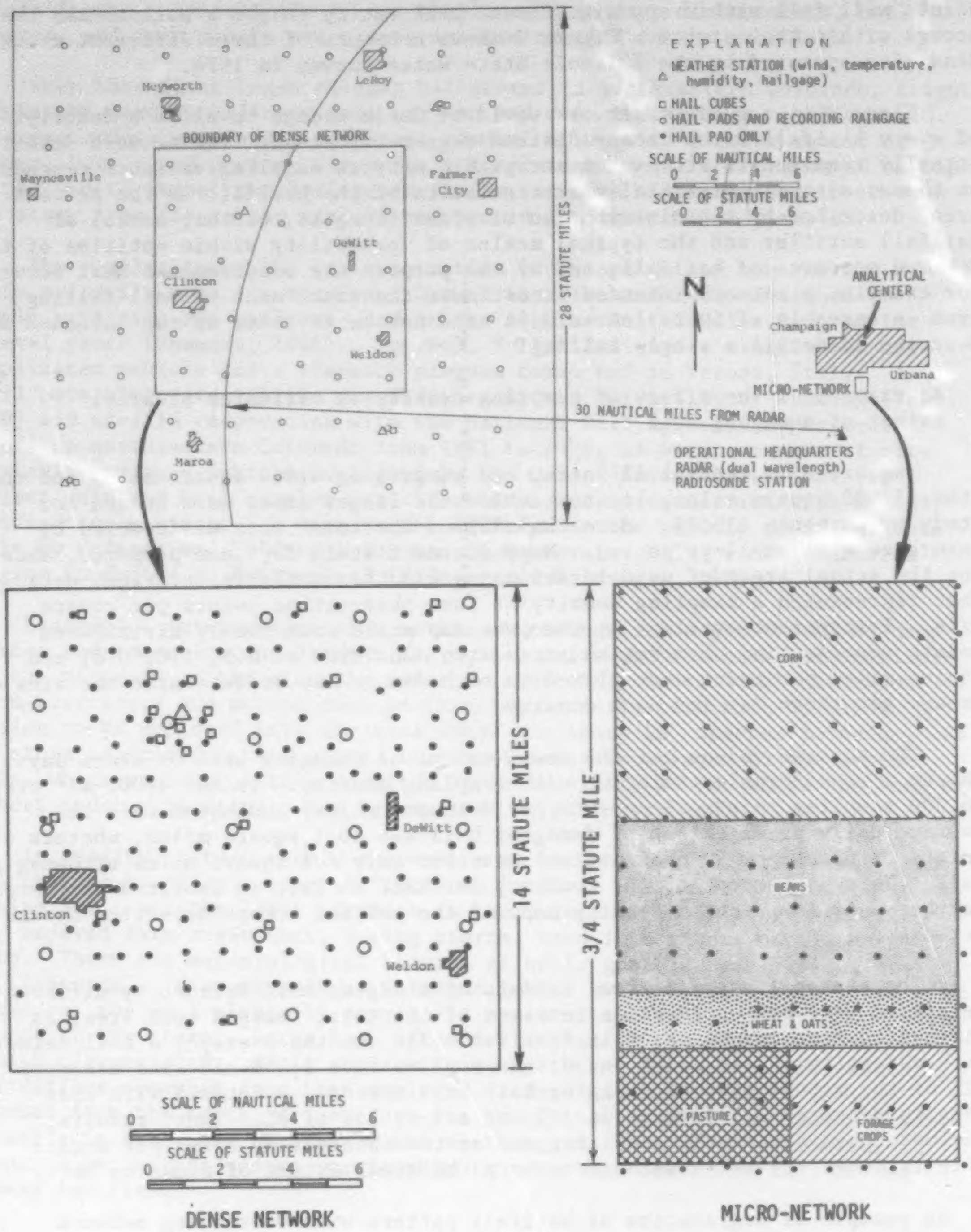
Heyworth
LeRoy
BOUNDARY OF DENSE NETWORK
Waynesville
Farmer City
DeWitt
Clinton
Weldon
Maroa
28 STATUTE MILES
EXPLANATION
△ WEATHER STATION (wind, temperature, humidity, hailgage)
□ HAIL CUBES
○ HAIL PADS AND RECORDING RAINGAGE
• HAIL PAD ONLY
SCALE OF NAUTICAL MILES
0 2 4 6
SCALE OF STATUTE MILES
0 2 4 6
N
ANALYTICAL CENTER
Champaign
Urbana
MICRO-NETWORK
30 NAUTICAL MILES FROM RADAR
OPERATIONAL HEADQUARTERS
RADAR (dual wavelength)
RADIOSONDE STATION
14 STATUTE MILES
Clinton
DeWitt
Weldon
SCALE OF NAUTICAL MILES
0 2 4 6
SCALE OF STATUTE MILES
0 2 4 6
DENSE NETWORK
3/4 STATUTE MILE
CORN
BEANS
WHEAT & OATS
PASTURE
FORAGE CROPS
MICRO-NETWORK

Figure 9.--Networks of three different sizes and densities operated by the Illinois State Water Survey in 1974 (Changnon and Morgan, 1976).

Table 3.--Percent of total area of damaging hail in 1000-m^2 (2560-km^2) area, measured by different densities of observation points during a crop season

	Density (mi^2 /sampling point)			
	9	3	1	0.5
Average	11	25	67	85
Highest	13	30	76	91
Lowest	8	20	62	80

10 is an example of the realistic compromises that must be made between the ideal network configuration and the road system that is available. In this case, the roads are very widely separated. An attempt has been made to offset this by spacing the stations very closely, as close as 400 meters, along the roads. The mean spacing turns out to be 1.0 km.

In Figs. 11 and 12, stations are removed from the map and new analyses performed. Figures 10, 11, and 12 show how the pattern of hailmass becomes more and more degraded as the number of stations (N) decreases.

c. An illustration of the evaluation of network sampling performance

Area and pattern are only two aspects of hailfall. For example, predicting the results of trials of hail suppression techniques requires quantitative estimates of hailfall intensity and amount.

Changnon and Barron (1971) studied the patterns of crop damage within single hailstreaks, making as many as 45 point estimates in a single 20-acre field and in one case 198 estimates in a 5.4-mi^2 streak (Fig. 13). These measurements show a damage pattern with large variations over small distances. Morgan and Towery (1975) determined the distribution of these loss estimates and the average gradients of loss over this streak. There was a large number of points (Fig. 14) with small loss and a broad peak, representing a fraction of all the points, with values between 40% and 90%. The average N-S loss gradient of damage was 6.5% per 150 meters. A Monte Carlo simulation was performed in which the pattern was sampled 100 different times by a 1-mi-grid network and also by 0.5- and 2.0-mi-grid networks. The process can be visualized by imagining the grid formed by the intersections of the 4 straight lines in Fig. 13 to be moved around on the damage pattern to 100 different positions. The variance of the areal estimates in this kind of simulation is called network sampling variance. This simulation showed (Fig. 15) that the total damage (the integral over area of the percentage loss) would be estimated to within 20% of the true value 80% of the time by a 1-mi-grid network. This is the only available evaluation of the performance of a given network in estimating the areal total damage from a single hailstreak. The result is highly specific to the damage distribution that was used and is not necessarily representative.

An important parameter in determining the network performance is undoubtedly the ratio between the area of the hailstreak and the area represented by

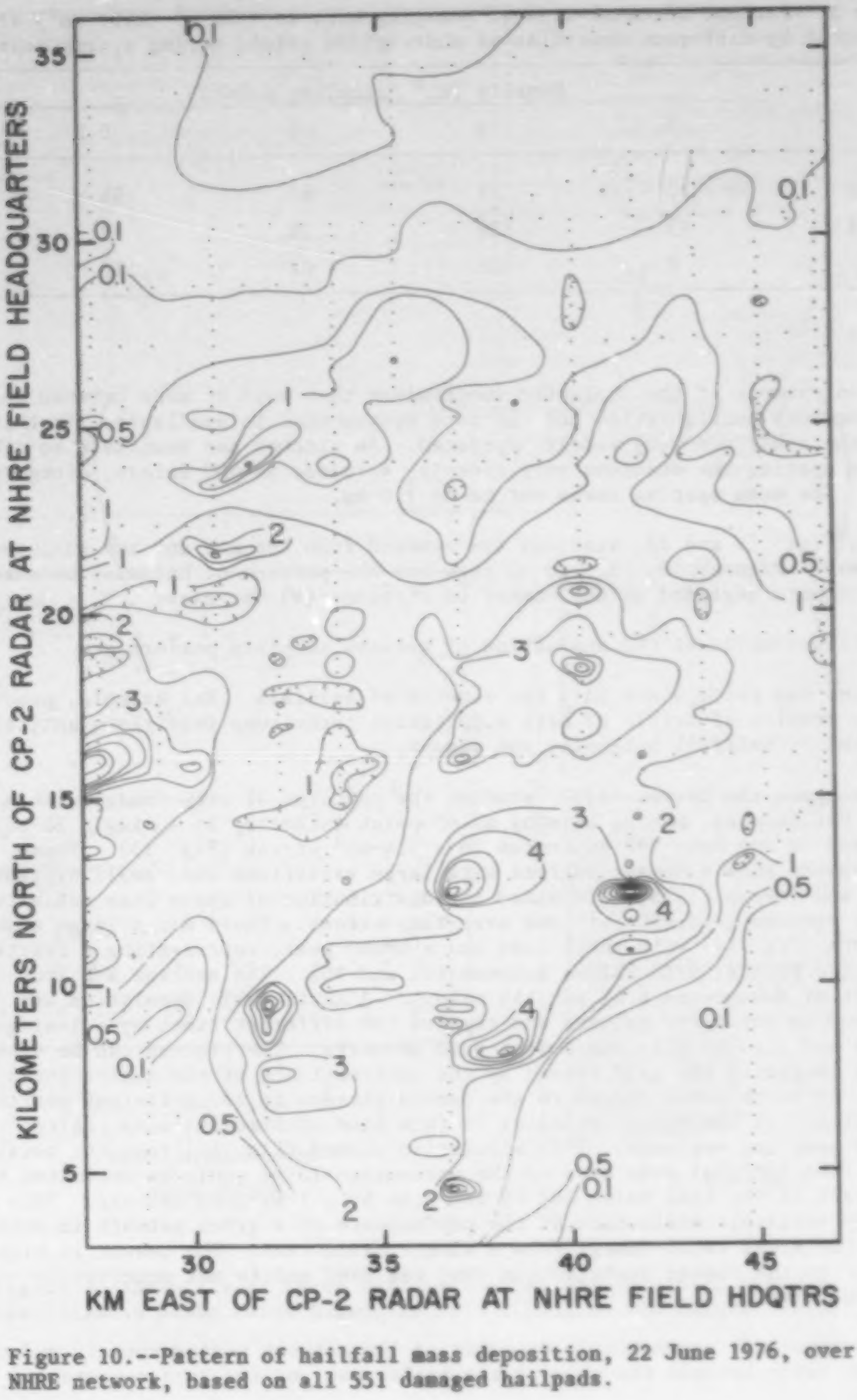
KILOMETERS NORTH OF CP-2 RADAR AT NHRE FIELD HEADQUARTERS
KM EAST OF CP-2 RADAR AT NHRE FIELD HDQTRS
35
30
25
20
15
10
5
30
35
40
45
0.1
0.5
1
2
3
4

Figure 10.--Pattern of hailfall mass deposition, 22 June 1976, over the NHRE network, based on all 551 damaged hailpads.

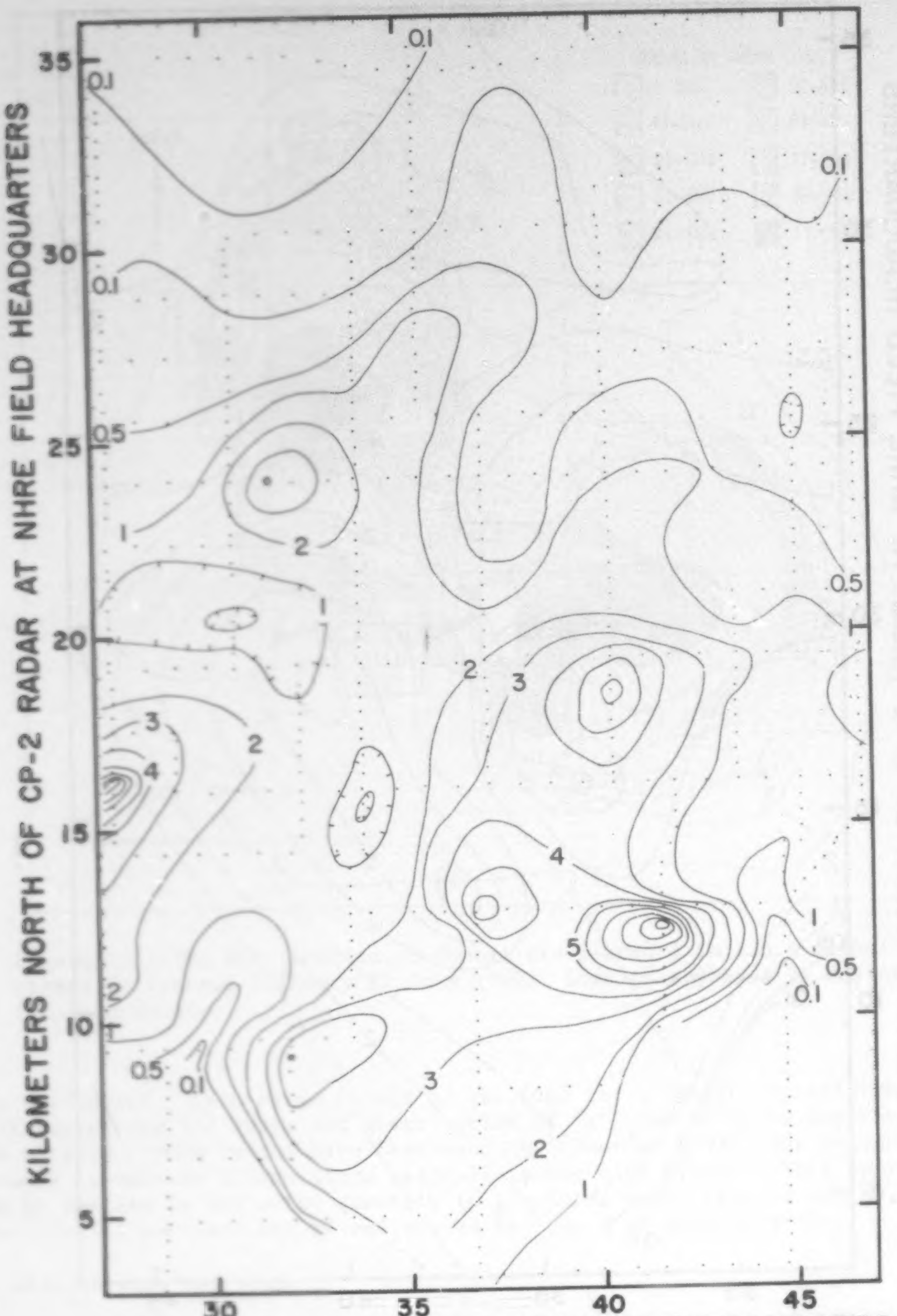

KILOMETERS NORTH OF CP-2 RADAR AT NHRE FIELD HEADQUARTERS
KM EAST OF CP-2 RADAR AT NHRE FIELD HDQTRS
35
30
25
20
15
10
5
30
35
40
45
0.1
0.5
1
2
3
4
5

Figure 11.--Pattern of hailfall mass deposition based on one-quarter of the observations in Fig. 10.

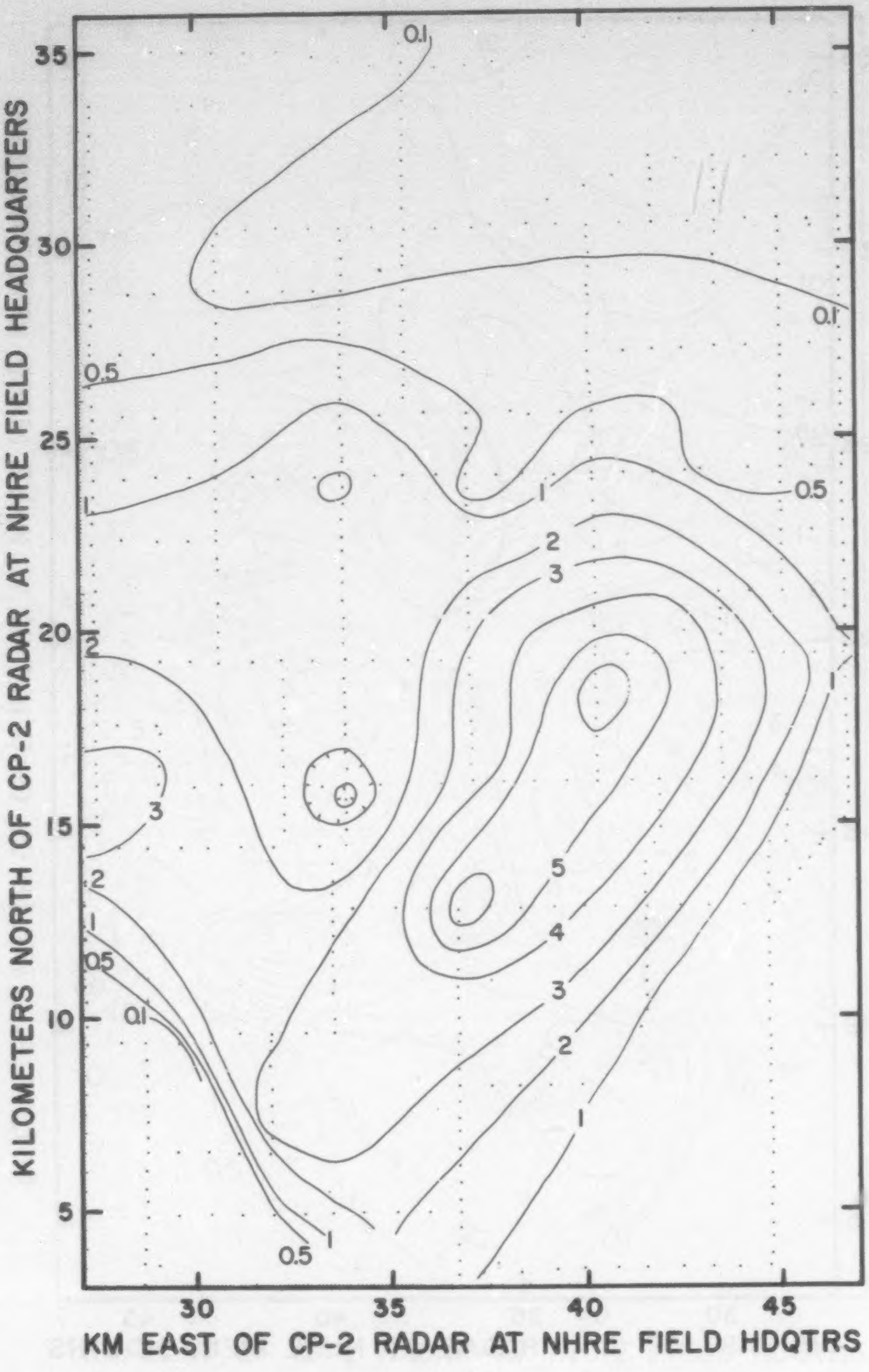

Figure 12.--Pattern of hailfall mass deposition based on one-sixteenth of the observations in Fig. 10.

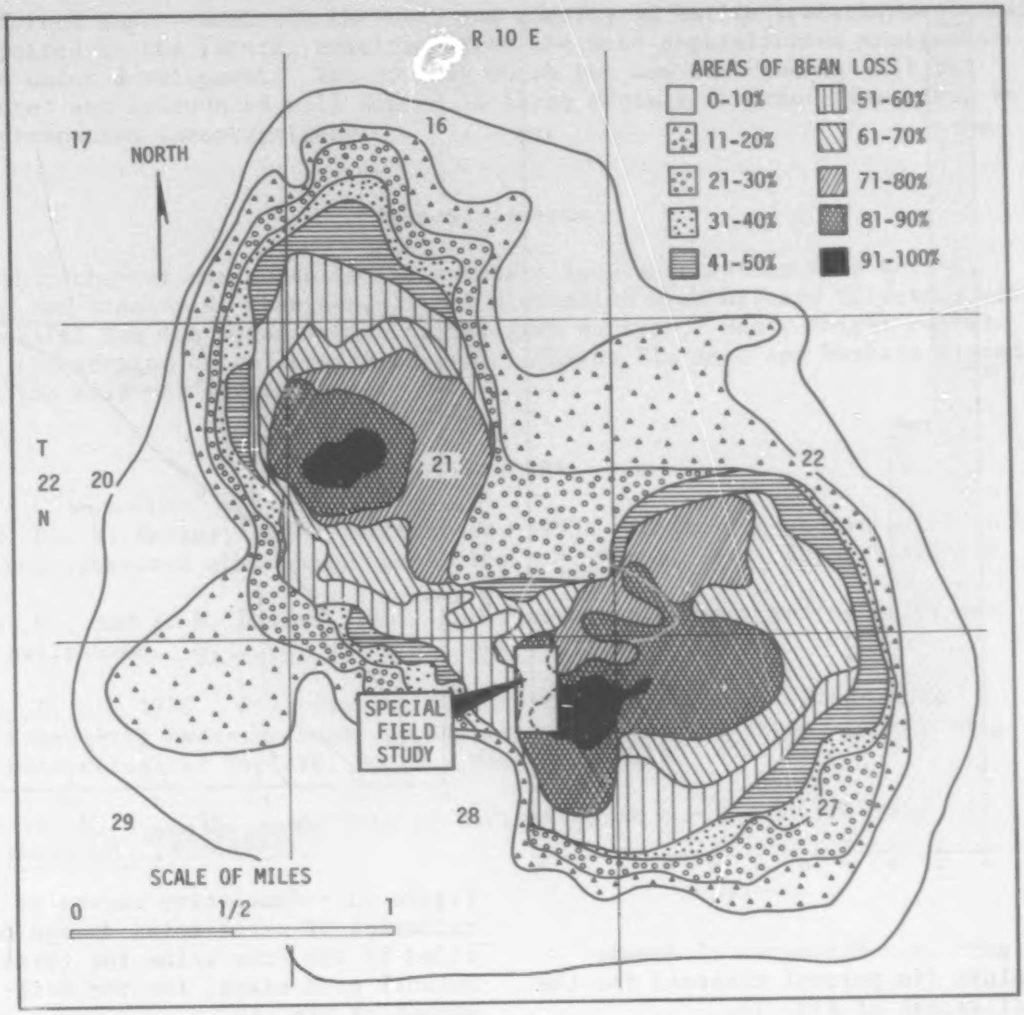
R 10 E
AREAS OF BEAN LOSS
0-10%
11-20%
21-30%
31-40%
41-50%
51-60%
61-70%
71-80%
81-90%
91-100%
17
16
NORTH
T
22
N
20
21
22
SPECIAL FIELD STUDY
29
28
27
SCALE OF MILES
0
1/2
1

Figure 13.--The distribution of damage (in percent) in a 5.4-mi hailstreak in Central Illinois 11 July 1969. Loss to soybeans is defined by 198 assessments.

one grid point. This ratio should be obtained for a sample of hailstreaks that represents the range and distribution of hailstreaks to be expected in the network. Such ratios have been used by Silverman (1981) for designing a network to measure thunderstorm rainfall in the high plains. This approach can be applied to any areal quantity (e.g., total mass, kinetic energy, or the area itself) and need not be restricted to square or uniform grids.

d. Network size and shape

The size of network required for a given purpose rests on information derived from Fig. 1, which shows the number of hail days per year as a function of area. The main importance of area size is in determining the number of study events available each year and the number of instruments required to monitor them. These have obvious effects on the cost of the experiment.

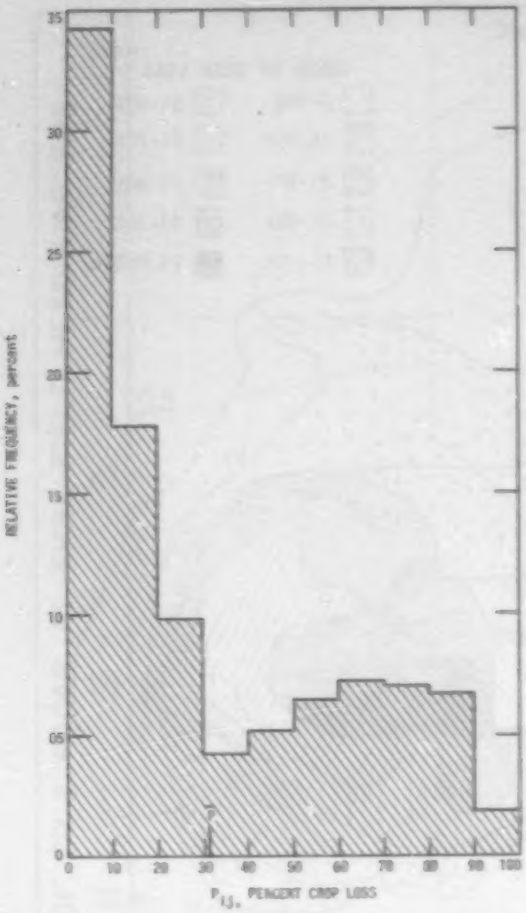

Figure 14.--Histogram of damage values (in percent classes) for the hailstreak of Fig. 13.

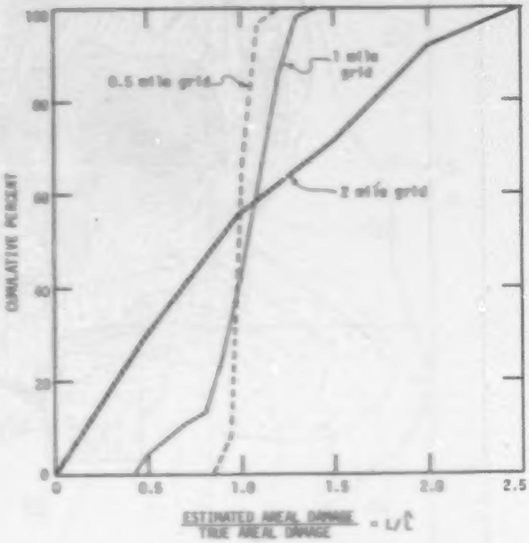

Figure 15.--Cumulative curves of the estimates of areal total damage divided by the true value for three network grid sizes, for the hailstreak of Fig. 13.

Schickedanz and Changnon (1971) arrived at 700 square miles (1972 square kilometers) as the optimum network size for a randomized hail prevention experiment in Colorado. This assures a good probability of enough seeded and unseeded storm days to achieve a statistically significant result in a 5-yr experiment. The shape and orientation of a hail network are influenced by the typical directions of storm propagation and local inhomogeneities in storm distribution.

8. CONCLUSION

Techniques for measuring hailfall have undergone rapid improvements in the last 25 or 30 years through the introduction of simple but effective instruments in well-designed networks. The improvements have come about to meet the needs of weather modification research. For some purposes volunteer observer networks of the type introduced 100 years ago are still useful.

Marked improvements in the type and quality of hailfall measurements can be expected in the future, resulting from the more sophisticated instrumentation under development. The rate at which the new instruments will be perfected and introduced will depend in large measure on priorities given to hail prevention investigations.

Acknowledgments

This chapter owes much to the author's long association with Neil G. Towery and Stanley A. Changnon, Jr. A discussion with Bernard Silverman was very useful for the organization of the last section. Nancy Knight contributed the section on collection of hail. Sharon Blackmon and Barbara Strand typed the original manuscript.

REFERENCES*

Atlas, D., M. Kerker, and W. Hitschfeld, 1953. Scattering and attenuation by non-spherical atmospheric particles. J. Atmos. Terr. Phys. 3:108-119.

Atlas, D., and F. H. Ludlam, 1961. Multiwavelength radar reflectivity of hailstorms. Q. J. R. Meteorol. Soc. 87:523-534.

Barge, B. L., 1970. Polarization observations in Alberta. Preprints, Fourteenth Radar Meteorology Conference, Tucson, Arizona. American Meteorological Society, Boston, Mass., 221-224.

Beckwith, W. B., 1960. Analysis of hailstorms in the Denver network. J. Meteorol. 23:348-353.

---

*The Illinois State Water Survey bibliography on hail and hail prevention is available to bona fide researchers at a small cost. For information contact

Professor Stanley A. Changnon, Jr.
Head, Atmospheric Science Section
Illinois State Water Survey
P.O. Box 203
Urbana, Illinois 61801.

The March 1978 issue of Atmosphere-Ocean, the largest single-volume collection of papers on hailfall measurement, can be obtained from

The University of Toronto Press
Journals Department
5201 Dufferin Street
Toronto, Canada M3H 5T8.

Browning, K. A., and G. B. Foote, 1975. Airflow and hailgrowth in supercell storms and some implications for hail suppression. Tech. Rep. 75/1, National Center for Atmospheric Research, Boulder, Colo., 75 pp.

Browning, K. A., J. Hallett, T. W. Harrold, and D. Johnson, 1968. The collection and analysis of freshly fallen hailstones. *J. Appl. Meteorol.* 7:603-612.

Carte, A. E., and G. Held, 1978. Variability of hailstorms on the South African plateau. *J. Appl. Meteorol.* 17:365-373.

Carte, A. E., R. H. Douglas, R. C. Srivastava, and G. N. Williams, 1963. Alberta hail studies, 1962/63. Sci. Rep. MW-36, McGill University, Montreal, 98 pp.

Carte, A. E., R. H. Douglas, C. East, K. L. S. Gunn, W. Hitschfeld, J. S. Marshall, E. J. Stansbury, 1961. Alberta hail studies, 1961. Sci. Rep. MW-35, McGill University, Montreal.

Changnon, S. A., Jr., 1966. Note on recording hail occurrences. *J. Appl. Meteorol.* 5:899-901.

Changnon, S. A., Jr., 1968. Effect of sampling density on areal extent of damaging hail. *J. Appl. Meteorol.* 7:518-521.

Changnon, S. A., Jr., 1971a. Note on hailstone size distributions. *J. Appl. Meteorol.* 10:168-170.

Changnon, S. A., Jr., 1971b. Means for estimating areal hail-day frequencies. *J. Weather Modif.* 3:154-159.

Changnon, S. A., Jr., 1971c. Hailfall characteristics related to crop damage. *J. Appl. Meteorol.* 10:270-274.

Changnon, S. A., Jr., 1972. Illinois radar research for hail suppression applications, 1967-1969. Invest. Rep. 71, Illinois State Water Survey, Urbana, 23 pp.

Changnon, S. A., Jr., and N. A. Barron, 1971. Quantification of crop-hail losses by aerial photography. *J. Appl. Meteorol.* 10:86-96.

Changnon, S. A., Jr., and G. M. Morgan, Jr., 1976. Design of an experiment to suppress hail in Illinois. Bull. 61, Illinois State Water Survey, Urbana, 194 pp.

Changnon, S. A., Jr., and D. W. Staggs, 1969. Recording hailgage evaluation. Final Rep. NSF-GA-1520, Illinois State Water Survey, Urbana, 47 pp.

CHIAA, 1978. *Crop-Hail Insurance Statistics*. Crop Hail Insurance Actuarial Association, Chicago, Ill., 75 pp.

Crow, E. L., 1974. Confidence limits for digital error rates. OT Rep. 74-51, Department of Commerce, U.S. Government Printing Office, Washington, D.C., 67 pp.

Douglas, R. H., and W. Hitschfeld, 1958. Studies of Alberta hailstorms. Sci. Rep. MW-27, McGill University, Montreal, 79 pp.

Eccles, P. J., and D. Atlas, 1969. A dual wavelength radar hail detector. Tech. Rep. 14, Lab. for Atmos. Probing, University of Chicago, Chicago, Ill., 66 pp.

Federer, B., and A. Waldvogel, 1975. Hail and raindrop size distributions from a Swiss multicell storm. J. Appl. Meteorol. 14:91-97.

Fremstad, P. G., 1968. Transducer for measuring hailstone momentum. Rep. 68-4, Institute for Atmospheric Sciences, South Dakota School of Mines and Technology, Rapid City, 47 pp.

Garcia, R. R., B. E. Weiss, and A. H. Murphy, 1976. Relationships between crop damage and hailfall parameters on the high plains. NHRE Tech. Rep. NCAR-7100-76/4. National Center for Atmospheric Research, Boulder, Colo., 28 pp.

Goyer, G. G., 1970. The testing of airborne infrared detection systems for mapping hailswaths and measuring hailfall coverage at the ground. The Joint Hail Research Project-Summer 1969-Summary Report. NCAR Internal Rep., February 1970, 24-29.

Goyer, G. G., 1971. The Joint Hail Research Project-Summer, 1970. NCAR Internal Rep., March 1971, 44-53.

Goyer, G. G., 1978. Meeting review: The First International Workshop on Hailfall Measurement, Banff, Alberta, Canada, 22-26 October 1979. Bull. Am. Meteorol. Soc. 59:297-298.

Hitschfeld, W. F., 1971. Hail research at McGill, 1956-1971. Sci. Rep. MW-68, Stormy Weather Group, McGill University, Montreal, 67 pp.

Johnson, G. N., and P. L. Smith, Jr., 1978. Measurement of hailfall intensity with a self-contained hailstone momentum sensor. Atmosphere-Ocean 16:86-93.

Joss, J., and A. Waldvogel, 1969. Raindrop size distribution and sampling size errors. J. Atmos. Sci. 26:566-569.

Knight, C. A., and N. C. Knight, 1968. The final freezing of spongy ice: hailstone collection techniques and interpretations of structures. J. Appl. Meteorol. 7:875-881.

Koren, D., 1969. Development of a moving aluminum foil hail recorder. TEC 711, Meteorological Branch Downsview, Toronto, Ontario, 7 pp.

Kozminski, C., and S. Bac, 1964. Prototype de grêlimètre enregistreur. J. Rech. Atmos. 1:55-56.

Long, A. B., 1978. Design of hail measurement networks. Atmosphere-Ocean 16:35-48.

Lozowski, E. P., and G. S. Strong, 1978. On the calibration of hailpads. J. Appl. Meteorol. 17:521-528.

Lozowski, E. P., R. Erb, L. Wojtiw, M. Wong, G. S. Strong, R. Matson, A. ong, D. Vento, and P. Admirat, 1978. The hail sensor intercomparison experiment. *Atmosphere-Ocean* 16:94-106.

Marriott, W., 1892. Report on the thunderstorms of 1888 and 1889. *Q. J. R. Meteorol. Soc.* 18:23-29.

McNeil, R. D., and J. E. Houston, 1966. A survey of methods of remote detection of hail. Project Hailswaths, Final Rep. 66-9, Institute for Atmospheric Sciences, South Dakota School of Mines and Technology, Rapid City.

Morgan, G. M., Jr., 1969. Thunderstorm studies at Verona, Italy. Preprints, Sixth Conference on Severe Local Storms, Chicago, Illinois. American Meteorological Society, Boston, Mass., 332-337.

Morgan, G. M., Jr., 1973. A general description of the hail problem in the Po Valley of northern Italy. *J. Appl. Meteorol.* 12:338-353.

Morgan, G. M., Jr., and N. G. Towery, 1975. Small scale variability of hail and its significance for hail prevention experiments. *J. Appl. Meteorol.* 14:763-770.

Morgan, G. M., Jr., and N. G. Towery, 1976a. Crop damage-hailpad parameter study in Illinois. Final Rep. NSF S-5015, Urbana, 56 pp.

Morgan, G. M., Jr., and N. G. Towery, 1976b. On the role of strong winds in damage to crops and its estimation with a simple instrument. *J. Appl. Meteorol.* 8:891-898.

Mueller, E. A., and S. A. Changnon, Jr., 1968. A recording hailgage for use in hail modification projects. Preprints, First National Conference on Weather Modification. American Meteorological Society, Boston, Mass., 494-502.

Musil, D. J., E. L. May, P. L. Smith, Jr., and W. R. Sand, 1976. Structure of an evolving hailstorm; part IV: internal structure from penetrating aircraft. *Mon. Weather Rev.* 104(5):596-602.

Nelson, S. P., and S. K. Young, 1979. Characteristics of Oklahoma hailfalls and hailstorms. *J. Appl. Meteorol.* 18:339-347.

Nicholas, T. R., 1978. A review of surface hail measurement. In *Hail: A Review of Hail Science and Hail Suppression*, Meteorol. Monogr. 16, American Meteorological Society, Boston, Mass., 257-267.

Pini, E., 1885. Sui temporali osservati nell' Italia superiore durante l'anno 1879. Publ. Reale Osserv. Brera di Milano, No. 18, Hoepli, Milano, 150 pp.

Prohaska, K., 1905. Prohaska uber Zugrichtung, Starke und Geschwindigkeit der Hagelwetter, Dauer des Hagelfalles 1902 und im Mittle. *Met. Zeit.* 22:519-523.

Prohaska, K., 1907. Die hagelfalle des 6 Juli 1905 in den Ostalpen. *Met. Zeit.* 24:13-201.

Roads, J. O. 1973. A study of hailswaths by means of airborne infrared radiometry. J. Appl. Meteorol. 12:855-862.

Roos, D.v.d.S. 1978. Hailstone sizes inferred from dents in cold-rolled aluminum sheets. J. Appl. Meteorol. 17:1234-1239.

Schickedanz, P. T., and S. A. Changnon, Jr., 1971. The design and evaluation of the NHRE, in northeast Colorado. J. Weather Modif. 3:160-176.

Schleusener, R. A., and P. C. Jennings, 1960. An energy method for relative estimates of hail intensity. Bull. Am. Meteorol. Soc. 41:372-376.

Silverman, B., 1981. On the sampling variance of precipitation gage networks. J. Appl. Meteorol. 20(12).

Srivastava, R. C., and A. R. Jameson, 1977. Radar detection of hail. In Hail: A Review of Hail Science and Hail Suppression, Meteorol. Monogr. 16, American Meteorological Society, Boston, Mass. 269-277.

Stout, G. E., and S. A. Changnon, Jr., 1968. Climatology of hail in the central United States. CHIAA Res. Rep. No. 38, Crop Hail Insurance Actuarial Association, Chicago, Ill. 49 pp.

Strong, S., and E. P. Lozowski, 1977. An Alberta study to objectively measure hailfall intensity. Atmosphere 15:34-53.

Summers, P. W. (ed.), 1968. Alberta hail studies 1967 field program. Unpublished report, Research Council of Alberta, Edmonton.

Towery, N. G., S. A. Changnon, Jr., and G. M. Morgan, Jr., 1976. A review of hail measuring instruments. Bull. Am. Meteorol. Soc. 57: 1132-1140.

Towery, N. G., R. E. Eyton, C. L. Dailey, and D. E. Luman, 1976. Annual report of remote sensing of crop-hail damage. Report of Research for the Country Companies. Urbana, Ill., 68 pp.

Veal, D. L., 1970. Proposed programs of hailstorm research in association with the NHRE. A proposal by Natural Resources Research Institute, College of Engineering, University of Wyoming, Laramie, 39 pp.

Vento, D., 1972. La determinazione della energia di impatto della grandine. Rev. Ital. Geofis. 21:73-77.

Vento, D., 1976. The hailpad calibration for Italian hail damage documentation. J. Appl. Meteorol. 15:1018-1022.

Vento, D., and G. M. Morgan, Jr., 1976. Statistical evaluation of energy imparted to hail by wind in Europe and United States. Second WMO Scientific Conference on Weather Modification, WMO-No. 443, World Meteorological Organization, Geneva, 281-285.

Waldvogel, A., B. Federer, W. Schmid, and J. F. Mezeix, 1978. The kinetic energy of hailfalls, part II: radar and hailpads. J. Appl. Meteorol. 17:1680-1693.

Weickmann, H. K., 1969. ESSA-1968-Colorado hail research. Preprints, Sixth Conference on Severe Local Storms, Chicago, Illinois. American Meteorological Society, Boston, Mass., 314-319.

Wilk, K. E., 1961. Radar investigation of Illinois hailstorms. Sci. Rep. 1, USAF 19(604)-4940, Illinois State Water Survey, Urbana, 42 pp.

Wojtiw, L., and J. H. Renick, 1973. Hailfall and crop damage in Alberta. Preprints, Eighth Conference on Severe Local Storms, Denver, Colorado. American Meteorological Society, Boston, Mass., 138-141.

IX. WEATHER RADAR

Richard J. Doviak, Dale Sirmans, and Dusan Zrnic'

1. INTRODUCTION

Radars were originally developed to detect and determine range of aircraft by radio techniques (Radio Detection And Ranging). As they became more powerful, their beams more directive, receivers more sensitive, and transmitters more coherent, radars were successfully applied in mapping the Earth's surface and weather; their signals have even reached out into space to explore surface features of our planetary neighbors. The radar beam penetrates thunderstorms and clouds to reveal, like an X-ray photograph, their inside structure. Pulsed Doppler radar techniques have been applied to map severe-storm structures with some astounding success, particularly in showing, in real time, the development of incipient tornado cyclones (Donaldson, 1970; Doviak et al., 1974; Burgess, 1976). Such observations should enable weathermen to provide better forecasts and warnings, and researchers to understand the life cycle and dynamics of storms.

The most comprehensive treatment of radar techniques is found in the collected works compiled by Skolnik in his Radar Handbook (1970). Battan's text (1973) on weather radar applications is probably the most widely used by meteorologists, and Atlas (1964) also gives a concise and informative review of many weather radar topics. Both emphasize electromagnetic scatter and absorption by hydrometeors. Nathanson (1969) emphasizes the total radar environment as well as radar design principles. The radar environment causes unwanted reflection (clutter) from sea and land areas (precipitation produces clutter when aircraft are the targets of interest); Nathanson treats precipitation echoes comprehensively. Anomalous propagation of radar signals enhances ground clutter. A good general reference on propagation of electromagnetic waves through the stratified atmosphere is Bean and Dutton (1966).

We provide here a foundation of weather radar principles and relate the radar parameters and signal characteristics to the target's meteorological properties. We lightly touch upon subjects comprehensively treated elsewhere (e.g., scattering properties of hydrometeors), present techniques used in extracting a target's properties from its echoes, and relate radar parameters and echo power to the weights given to a hydrometeoric target's backscatter cross section. To accomplish this we tour the radar signal path starting from the transmitter, through the antenna, along the beam to the target, and return to the receiver, highlighting along the way the important signal properties.

We discuss the pulsed Doppler radar and consider a discrete target to develop radar principles and the radar equation. The theory for conventional non-Doppler radar is also included. These principles are then extended to the more complex weather target, which is a conglomerate of discrete targets producing a continuous stream of echoes with rapidly fluctuating amplitude and phase. The origin of these fluctuations is shown, and the weather radar equation is developed.

We relate the weather Doppler spectrum and its principal moments to the spatial distribution of target reflectivity and its velocity. Finally, we show example analyses of radar data from severe storms.

2. PRINCIPLES OF RADAR

Weather radar illuminates the atmosphere around it with a series of pulses of focused electromagnetic radiation, directed with an antenna mechanically rotated in azimuth and elevation. Alternately transmitting and receiving, a radar is equipped to display echoes from precipitation particles and other targets in relation to the time delay between pulse transmission and echo arrival, hence indicating range. Echo amplitude is a measure of precipitation intensity or, in the case of a discrete target, its size. Coherent radars can go one important step further: they gage the phase of successive echo signals to determine the Doppler shift and hence radial velocity of the hydrometeors. Pulsed Doppler radars with advanced signal-processing equipment using solid-state digital hardware can estimate precipitation intensity, radial velocity, and atmospheric turbulence at about 1,000 contiguous but independent locations every second. Although massive amounts of data are gathered and need to be processed in relatively short periods of time, much of the data is redundant and contains few bits of meteorologically significant information. Therefore these large data fields are easily assimilated by the human to interpret data patterns and relate these to meteorological phenomena.

a. Electromagnetic waves

Electromagnetic or radio waves from radar are electric, E, and magnetic, H, force fields that propagate through space at the speed of light and interact with matter along its path. These interactions cause the scattering, diffraction, and refraction also common to visible electromagnetic radiation (light). The waves, focused into beams by the antenna system, have sinusoidal spatial and temporal variations--the distance and time between successive wave peaks of electric (magnetic) force defines the wavelength, λ, and wave period (i.e., the reciprocal of frequency, f, in hertz). These two important electromagnetic field parameters are related to propagation speed:

$$c = \lambda f = 3 \times 10^{8} \text{ m s}^{-1} \, . \qquad (2.1)$$

Microwaves are electromagnetic forces having wavelengths between 10^{-3} and 10^{-1} m--visible radiation has a wavelength of about 6×10^{-7} m. The upper end (0.01 to 0.1 m) of the microwave band is used in weather and aircraft surveillance radars (Fig. 2.1).

The electric field wave far from the transmitting antenna has a time t and range r dependence, generally given by

$$E(r,\theta,\phi,t) = \frac{A\,(\theta,\phi)}{r} \cos \{2\pi f[t - r/c] + \psi\} \ (\text{V m}^{-1}) \, , \qquad (2.2\text{a})$$

where A depends upon θ,φ, the direction of r from the radiation source, and ψ is usually an unknown but constant phase. The dependence of E on r, t, and θ,φ is characteristic of all electromagnetic waves propagating in space devoid of matter, be it radio or light waves (Jordan, 1950, p. 559). For waves propagating through our atmosphere, Eq. 2.2a approximates well the wave properties at weather radar frequencies. Since force has a direction, E is a

best copy available

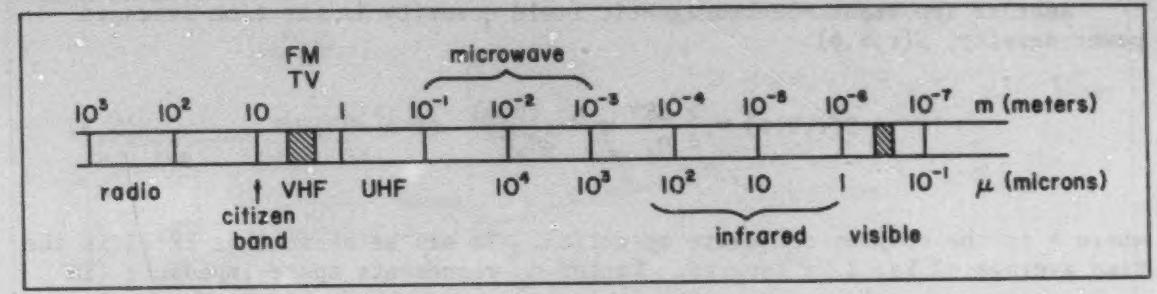
FM
TV
microwave
10^3
10^2
10
1
10^{-1}
10^{-2}
10^{-3}
10^{-4}
10^{-5}
10^{-6}
10^{-7}
m (meters)
radio
citizen band
VHF
UHF
10^4
10^3
10^2
10
1
10^{-1}
μ (microns)
infrared
visible

Figure 2.1.--Electromagnetic spectrum showing location of microwave band of radar wavelengths relative to radio frequency and optical bands.

vector quantity, and Eq. 2.2a represents one component of this force. The waves propagate in the direction of r--that is, an observer's range r must increase at rate c in order to stay on a wave crest (t - r/c = const.) The E and H vectors are always perpendicular to r and to each other when r is large compared with the antenna dimensions.

Because the principal factors characterizing periodic electric fields are amplitude, $A(\theta,\phi)/r$, and phase, $2\pi f(t - r/c) + \psi$, it is convenient to use complex number or phasor notation to describe these parameters (Jordan, 1950, p. 116). The electric field (Eq. 2.2a) is then expressed as

$$E = \frac{A\ (\theta,\phi)}{r}\ e^{\,j2\pi f(t - r/c) + j\psi}\ , \qquad (2.2b)$$

which, by Euler's formula, can be represented in a two-dimensional phasor diagram (Fig. 2.2). This diagram clearly presents the time and space dependence of amplitude and phase to within an integral multiple of 2π. E and H are real, measurable quantities, and it is understood that we need to take the real part of Eq. 2.2b, or of any other phasor we may introduce, in order to have the real time and space dependence. The time dependence of phase is of paramount importance in understanding the principles of Doppler radar.

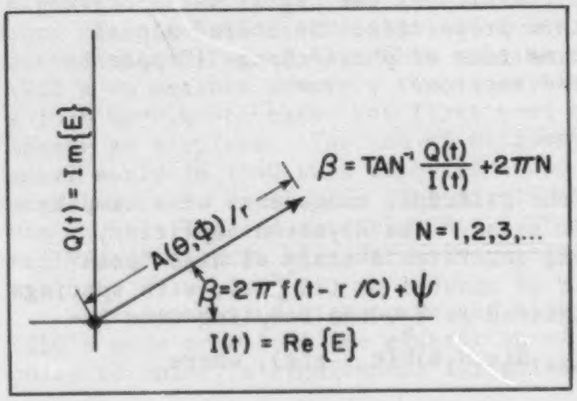
$Q(t) = \mathrm{Im}\{E\}$
$\beta = \mathrm{TAN}^{-1}\frac{Q(t)}{I(t)} + 2\pi N$
$A(\theta,\Phi)/r$
$N = 1,2,3,\ldots$
$\beta = 2\pi f(t - r/C) + \psi$
$I(t) = \mathrm{Re}\{E\}$

Figure 2.2.--The phasor diagram. Re {E} is the real part of the complex electric field E and Im {E} the imaginary part.

Another important electromagnetic field quantity is the time-averaged power density, $S(r,\theta,\phi)$:

$$S(r,\theta,\phi) = \frac{1}{2}\frac{EE^*}{\eta_o} = \frac{A^2(\theta,\phi)}{2\eta_o r^2} \quad (\mathrm{W\ m^{-2}}) \ , \qquad (2.3)$$

where * is the complex conjugate operation. It can be shown that $EE^*/2$ is the time average of Eq. 2.2a squared. Factor η_o represents space impedance (in space or Earth's atmosphere at radar wavelengths, η_o is a constant equal to 377 ohms), and simply relates the electric field intensity required to advance the power density S. Time averages represented by Eq. 2.3 are averages of power over a cycle or period f^{-1} of the wave, and Eq. 2.3 is usually called peak power density of an electromagnetic packet of waves if power is pulsed (i.e., transmitted in a burst of energy). The significance of $S(r,\theta,\phi)$ is that it represents the power density flowing outward from a source, either continuously or in bursts, and products of S with areas, later to be specified, represent power that is received, absorbed, scattered, etc.

Spatial resolution of observations, i.e., discrimination between two adjacent similar objects, is dependent on wavelength and antenna size. The angular resolution or diameter of the first null in a circular diffraction pattern is well approximated by

$$\Delta\theta \sim \frac{140\lambda}{D} \ (\text{degrees}) \ , \qquad (2.4)$$

where D is the diameter of the antenna system (Born and Wolf, 1964, p. 415). Thus radio waves (i.e., $\lambda = 10^2$-10^3 m) require huge antenna installations to achieve an angular resolution of a few degrees--rather poor for optical antenna systems. For example, the human eye has an angular resolution of about 0.02°.

The essential distinguishing feature favoring microwaves for weather radars is their ability to penetrate rain and cloud, and thus provide a view inside showers and thunderstorms, day or night. Rain and cloud do attenuate microwave signals, but only slightly (for $\lambda \geq 0.05$ m) compared with the almost complete extinction of optical signals. Raindrops scatter electromagnetic energy, and the portion scattered constitutes the signal whose characteristics are diagnosed to determine storm properties. Scattered signal strength measures rain intensity, and time rate of phase change (Doppler shift) measures raindrop speed in the r direction.

b. Doppler radar transmitting aspects

Figure 2.3 shows in block diagram the principal components of a simplified, but representative, pulsed Doppler radar. The Klystron amplifier, turned on and off by the pulse modulator, generates a train of high "peak" power microwave pulses having duration τ of about 1 μs (10^{-6} s), with spacings at the pulse repetition time (PRT) designated as T_s, the sampling time interval. The pulse of peak power density, $S(r,\theta,\phi)U(t - r/c)$, where

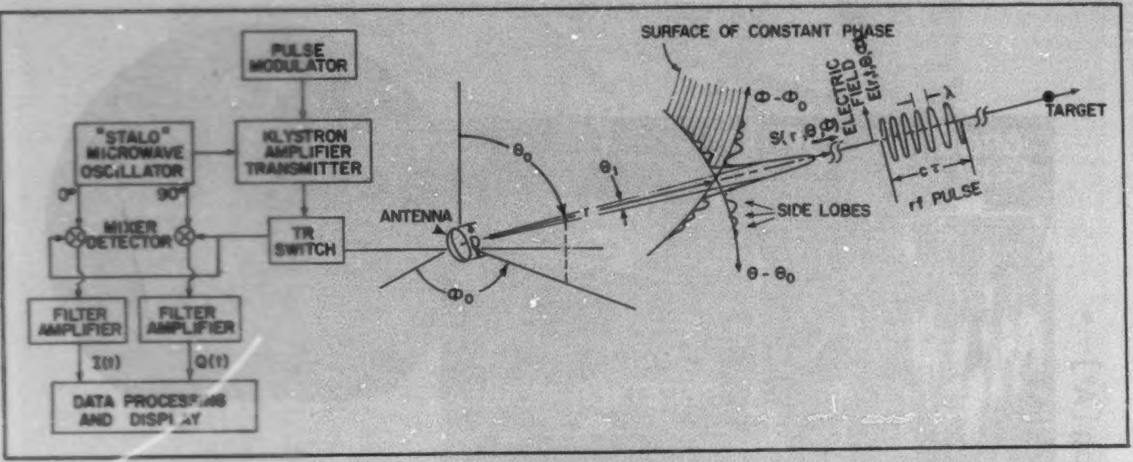
PULSE MODULATOR
"STALO" MICROWAVE OSCILLATOR
KLYSTRON AMPLIFIER TRANSMITTER
0°
90°
MIXER DETECTOR
TR SWITCH
FILTER AMPLIFIER
FILTER AMPLIFIER
I(t)
Q(t)
DATA PROCESSING AND DISPLAY
ANTENNA
θ₀
θ₁
r
Φ₀
SURFACE OF CONSTANT PHASE
Φ - Φ₀
θ - θ₀
S(r, θ, Φ)
ELECTRIC FIELD E(r,θ,Φ)
SIDE LOBES
λ
cτ
rf PULSE
TARGET

Figure 2.3.--Simplified Doppler radar block diagram.

$$U(t - r/c) = \begin{cases} 1, & r/c \leq t \leq r/c + \tau \\ 0 & \text{otherwise,} \end{cases} \qquad (2.5)$$

illuminates objects (targets) as it propagates within a narrow beam, and a tiny fraction of this radiation is scattered by targets toward a receiver that, in most instances, is located at the transmitter site. Furthermore, for economic reasons, the same antenna is shared by the transmitter and receiver.

The transmit-receive (TR) switch connects the transmitter to the antenna during the period τ, whereas the receiver (i.e., mixer-detector plus amplifiers) is connected during the time interval $T_s - \tau$, the listening period. The TR switching is not performed instantaneously, and there is a period of time (usually a few tens of microseconds) when the receiver does not have full sensitivity for detection.

When targets are small (compared with $c\tau$), few, and well separated (no two targets within $r \pm c\ \tau\sqrt{2}$), the scattered energy or echoes are replicas of the transmitted pulse. These echoes, modified by the receiver to enhance signal-to-noise ratio (see Sec. 2f[1]), are displayed on video equipment to show their relative strengths and delay referenced to the time of the transmitted pulse (Fig. 2.4). This echoing principle was first applied in the late 1920's to measure remotely the properties of the ionosphere, and in late 1934 a 10-m wavelength radar was first used by the Naval Research Laboratory to locate an airplane. The use of microwaves in radars did not become practical until early in 1940 when a powerful and efficient transmitting tube, the magnetron, was developed. The first detection of storms by microwave radar was made in England in early 1941. There is an excellent historical review of early developments in radar meteorology in Atlas (1964).

Development of high-power and high-gain Klystron amplifiers in the 1950's made practical the generation of microwaves that are phase coherent pulse to pulse, a requirement for pulsed Doppler radars if velocity of targets

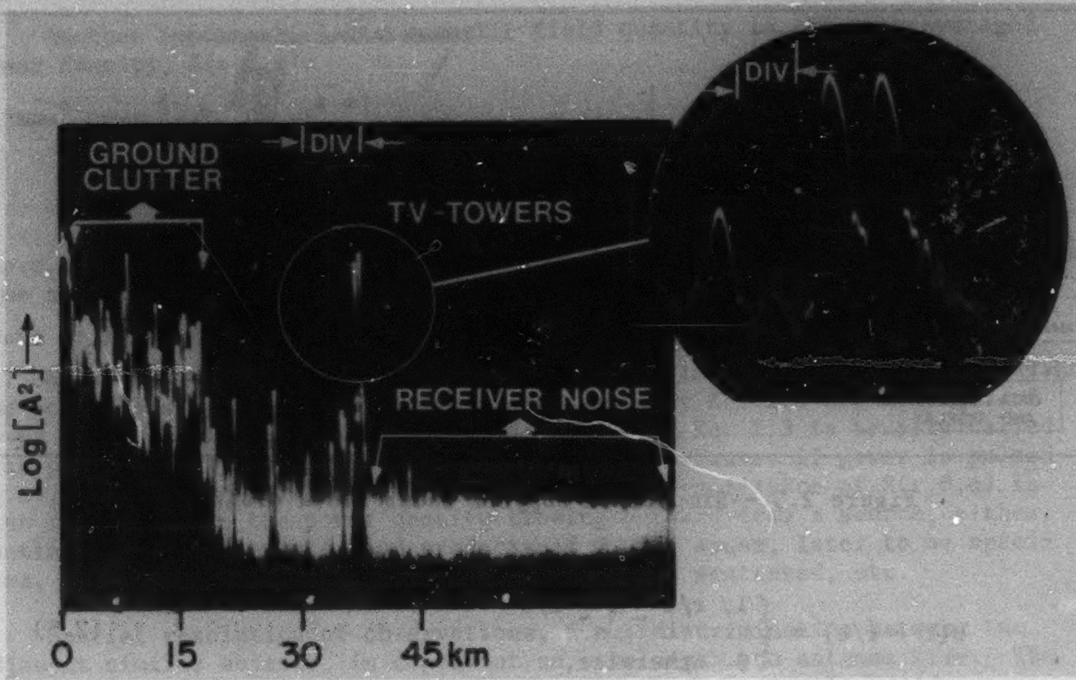

Figure 2.4.--Time delay and strengths of echoes from discrete targets (e.g., TV towers at about 40 km) from the radar site. Ground clutter is a conglomerate of usually indistinguishable echoes from targets on the ground. Vertical scale is proportional to the logarithm of echo power; time scale is 50 μs/DIV. Transmitter pulse width τ is 1.2 μs. In expanded (in range) view of tower echoes, scale is 5 μs/DIV.

beyond the first trip (i.e., $r \geq cT_s/2$) is to be measured as well as velocity of first-trip targets. Radar signals are phase coherent from pulse to pulse if the distance (or time) between wave crests of successive transmitted pulses is fixed. Magnetrons are not phase coherent from pulse to pulse, but if the phase of each transmitted pulse is measured and stored, these inherently incoherent oscillators can be used in radars to measure velocity of targets at all ranges.

(1) The electromagnetic beam

The microwave pulse leaves the antenna in an essentially collimated beam of diameter D equal to that of the antenna-reflector (Fig. 2.5). However, because of diffraction, the electromagnetic beam begins to spread at a range $r = D^2/\lambda$ into a conical one having an angular spread or beamwidth, θ_1, given approximately by Eq. 2.4. The beamwidth θ_1 is commonly specified as the angle within which the microwave radiation is at least one-half its peak intensity (3-dB width).

The radiation pattern $S(\theta,\phi)$ specifies the angular distribution of power density (W m^{-2}) that emanates from the antenna. It is impossible to confine

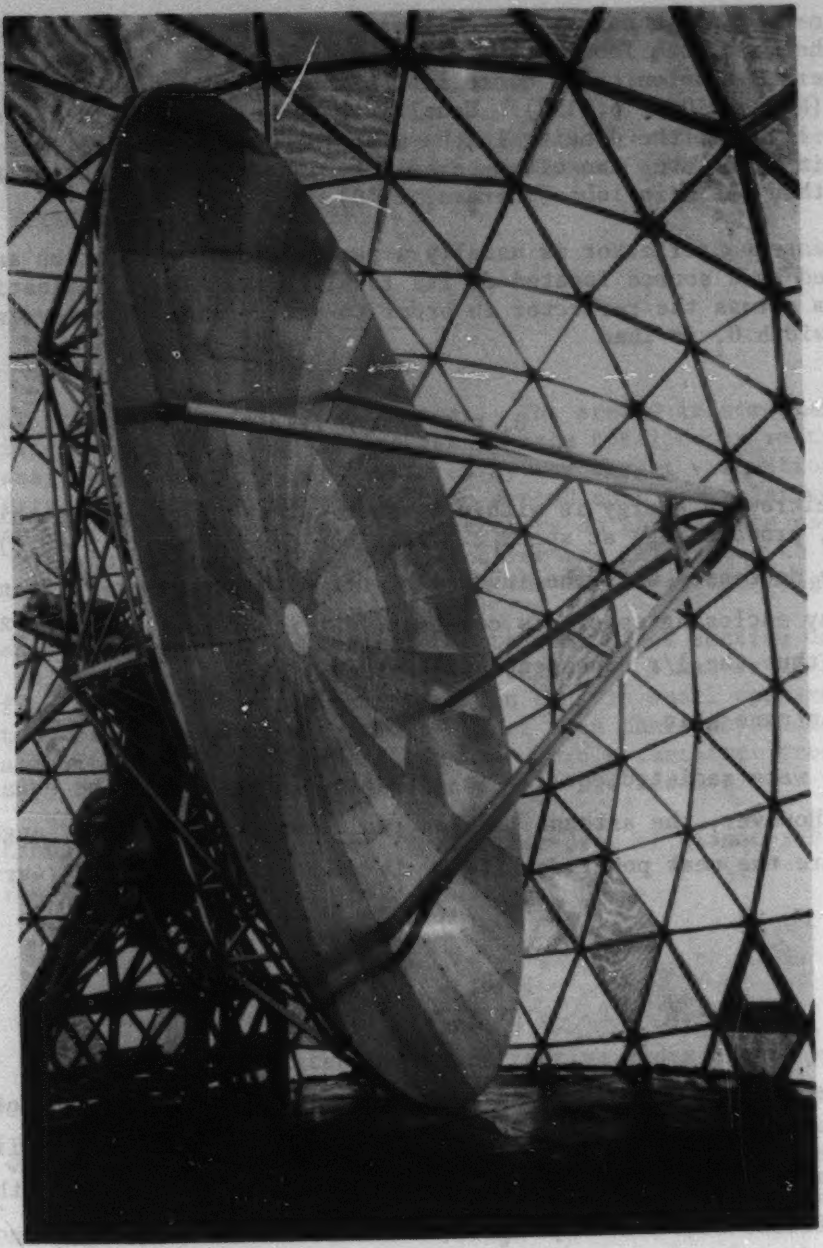

Figure 2.5.--The National Severe Storms Laboratory's weather radar antenna-reflector inside its protective radome. The reflector, a paraboloid of revolution, has a 9.14-m diameter. The radiation source is the "horn" at the end of the curved (black) waveguide. The tubes extending to the right support the source and waveguide.

all the energy into a narrow conical beam, and some of it inevitably falls outside the main beam lobe into side lobes (Fig. 2.3). The main lobe is that region where S monotonically decreases, although other definitions have been proposed (Kraus, 1966, p. 154). Usually the power density in any side lobe is less than 1/100 of the density in the main lobe. Furthermore, the sum total of power in side lobes can often be held to just a few percent of that transmitted within the main lobe (Sherman, 1970).

The antenna reflector is usually a paraboloid of revolution and is illuminated by a source located at its focal point. The illumination is made nonuniform across the reflector in order to reduce side-lobe levels, and the 3-dB beamwidth θ_1 is then

$$\theta_1 = 1.27\ \lambda/D\ (\mathrm{rad})\ . \tag{2.6}$$

The microwave energy is within a spherical shell $c\tau$ meters thick expanding (i.e., propagating) at speed c. Thus the power density $S_i(\theta,\phi)$ incident on targets decreases with the inverse of r^2, although power P_t' transmitted through any enclosing sphere is constant. S_i is proportional to E^2 (see Eq. 2.3), thus the 1/r dependence of E in Eq. 2.2.

(2) Antenna gain

If P_t' were radiated equally in all directions, S would be equal to $P_t'/4\pi r^2$. However, the antenna focuses radiation into a narrow, angular region where the peak power density S_p is much stronger than $P_t'/4\pi r^2$. The ratio

$$\frac{S_p}{P_t'/4\pi r^2} = g_t' \tag{2.7}$$

defines the maximum directional gain of the antenna. Measurement of P_t' is difficult, and the antenna engineer therefore measures power P_t delivered to the antenna system and S_p at distances far (i.e., $r \geq 2D^2/\lambda$) from the antenna. In this case the computed gain g_t accounts for losses of energy associated with the antenna system (e.g., radome, waveguide). Then the incident radiation power density at range r is given by

$$S_i(\theta,\phi) = \frac{P_t\ g_t\ f^2(\theta,\phi)}{4\pi r^2}\ , \tag{2.8}$$

where $f^2(\theta,\phi)$ is the normalized power gain function (i.e., $f(\theta,\phi) = 1$ at θ_o,ϕ_o; Fig. 2.3), and g_t is simply the antenna gain along the beam axis.

c. The target

(1) Scattering cross section

The cross section σ of a target is a fictitious area that intercepts a power σS_i, which is assumed to radiate isotropically to produce in the direction of the receiver a power density,

$$S_e = \frac{S_i \sigma(\theta',\phi')}{4\pi r^2} , \qquad (2.9)$$

equal to that scattered by the actual target. The area σ is sometimes called a differential cross section to distinguish it from total cross section, which is proportional to the total power scattered by the target. Equation 2.9 shows that target cross section $\sigma(\theta',\phi')$ can depend upon the relative location of the transmitter and receiver because scatterers do not radiate power isotropically. The polar angles θ',ϕ' to a receiver are referenced to an axis drawn from the transmitter to the target with the target at the origin.

It is easy to deduce that a target's scattering cross section may have no resemblance to the target's physical cross section. As a matter of fact, thin metallized fibers (chaff) of real cross section that is small compared with λ^2 have scatter cross sections many times larger than their physical area. On the other hand, a large metallic sheet can have zero backscatter cross section when it is oriented so as not to scatter energy to the receiver.

The backscatter cross section σ_b for a water drop of diameter D_i that is small compared with λ (i.e., $D_i \lesssim \lambda/16$) is

$$\sigma_b = \frac{\pi^5}{\lambda^4} \left| K_w \right|^2 D_i^{\,6} , \qquad (2.10)$$

where $\left|K_w\right|^2$ is a parameter, related to the refractive index of the water, that varies between 0.91 and 0.93 for wavelengths between 0.01 and 0.10 m and is practically independent of temperature (Battan, 1973, p. 39). Ice spheres have $\left|K_w\right|^2$ values of about 0.18 (for density 0.917 g cm^{-3}) independent of temperature as well as wavelength in the microwave region. The backscattering cross section (Eq. 2.10) is called the Rayleigh approximation because it is similar to the scattering cross section of atmospheric molecules whose diameters are small compared with the optical wavelengths. Equation 2.10 shows that waves at shorter λ are more strongly scattered--a fact that Rayleigh used to explain why the sky is blue.

If the target is small compared with wavelength, the scatter energy is radiated nearly isotropically. Large targets have a much more directive scatter radiation pattern, and often more radiation flows in directions other than back to the transmitter. For example, scattered power density in the direction of r (forward scatter) can be 100 to 1,000 times larger than that returned in the direction of the source and is known as the Mie effect (Born and Wolf, 1964).

Battan (1973) and Atlas (1964) have reviewed the abundance of experimental and theoretical work that relates a particle's scattering cross section to its shape, size relative to wavelength when $D_i \geq \lambda/16$, temperature, and mixture of phases (e.g., water-coated ice spheres).

(2) Doppler shift

When the pulse of radiation impinges upon a target (e.g., a raindrop), it forces molecular vibrations in synchronism with the electric and magnetic fields. If the drop is stationary or moving along a surface of constant phase (i.e., r is fixed; see Fig. 2.3), its molecules vibrate at the frequency of the radiation field; if it is moving toward the transmitter at velocity v_r, its vibrational frequency is higher by v_r/λ Hz because the target molecules experience more rapid fluctuations of electric and magnetic force. The vibrating molecules themselves generate electromagnetic fields that in turn radiate outward from the target.

For monostatic radar, the usual case with transmitter and receiver colocated, the frequency of scattered radiation is Doppler shifted by an amount

$$f_d = -2v_r/\lambda \quad (\text{Hz}) , \tag{2.11}$$

where v_r is the radial component of velocity--positive being away from the radar. The factor 2 in Eq. 2.11 is a result of two-step increase (for targets moving toward the radar) in frequency; first, the target's electric vibrational frequency is increased by v_r/λ, and second, the frequency of its radiation field in the direction of the radar is increased by v_r/λ, because target motion decreases the distance between radiated electric field crests along this direction. Similar reasoning shows that there is no Doppler shift in the scattered electromagnetic field along a straight line between the transmitter and target at points beyond the target (i.e., the forward scatter path) even though the target's vibrational frequency is different from the transmitter's frequency.

d. Attenuation

Were it not for electromagnetic energy absorption by water or ice drops, radars with shorter wavelength radiation would be much more in use because of their superior spatial resolution (Eq. 2.6). Short-wavelength (e.g., $\lambda = 3$ cm) radars suffer echo power loss that can be 100 times larger than radars operated with $\lambda \geq 10$ cm.

Each drop absorbs an amount of power that can be expressed as

$$P_L = \sigma_a S_i , \tag{2.12}$$

where σ_a is the absorption cross section that intercepts a power equal to the power dissipated as heat in the drop. But the incident wave suffers power loss from both energy absorption and scatter. Analogous to the backscatter cross section is a total scatter cross section σ_t that accounts for the total power scattered by a drop. σ_t is proportional to the integral, over a sphere enclosing the target, of the scattered power density $S_e(\theta',\phi')$; for small spherical drops, $\sigma_t = 2\sigma_b/3$. Thus the total power extracted from a wave is proportional to $\sigma_a + \sigma_t$. In contrast with Eq. 2.10, there is no simple formula for σ_a that can be used for different wavelength radars and for different drop temperatures; we must resort to tabulations (Herman et al., 1961) or measurements.

If we assume that the presence of drops within an elemental volume $\Delta V(r)$ does not significantly alter the incident power density S_i within this volume (i.e., we can neglect scattering of the scattered field--the Born approximation), then the power density change in a wave propagating a short distance Δr through the volume is

$$\Delta S_i = -\frac{\Delta r}{\Delta V} \sum_{n=1}^{N} (\sigma_{an} + \sigma_{tn}) S_i \, , \tag{2.13a}$$

where the summation extends over all N drops within ΔV, and σ_{an} and σ_{tn} are the absorption and scatter cross sections of the n^{th} particle. The rate of power density loss is then

$$\lim_{\Delta r \to 0} \left(\frac{\Delta S_i}{\Delta r} \right) = \frac{-1}{\Delta V} \sum_{n=1}^{N} (\sigma_{an} + \sigma_{tn}) S_i \, . \tag{2.13b}$$

In the limit $\Delta r \to 0$, S_i can be considered a constant within ΔV and thus can be placed outside the summation. Then the power density at any range r is the integral solution of Eq. 2.13b:

$$S_i(r_2) = S_i(r_1) \exp \left(- \int_{r_1}^{r_2} k \, dr \right) , \tag{2.14}$$

where $k \equiv (\Delta V)^{-1} \Sigma (\sigma_{an} + \sigma_{tn}) (m^{-1})$ is the attenuation rate. This rate expressed in decibels per kilometer is

$$K \equiv \frac{d}{dr_2}\left[10 \log \frac{S(r_1)}{S(r_2)}\right] = 4.34 \times 10^3 k \ . \qquad (2.15)$$

Values of K have been tabulated by Bean and Dutton (1966, pp. 292-296) for various rainfall rates and radar wavelengths.

Data on cloud attenuation rate versus wavelength and temperature are given by Gunn and East (1954). Although attenuation through ice clouds is usually negligibly small, it should not be ignored for water clouds, where the attenuation rate is generally an order of magnitude larger.

When drop diameters are small compared with wavelength, attenuation becomes independent of drop size distribution and depends only on cloud liquid mass density. Clouds between the radar and a distant storm can produce measurable attenuation even at $\lambda = 10$ cm (e.g., 1.8 dB for two-way propagation through 100 km of 1.0 g m^{-3} liquid water) and thus could cause underestimates of rain in the distant storm.

Besides attenuation due to rain and/or cloud droplets, there is attenuation due to energy absorbed by the atmosphere's molecular constituents, mainly water vapor and oxygen. This gaseous attenuation rate k_g is not negligible when storms are far away ($r \geq 60$ km) and beam elevation is low, even at $\lambda = 10$ cm if accurate cross-section measurements are required. In such a case a correction of 1-2 dB is typically required.

Combining Eqs. 2.8, 2.9, and 2.14, we deduce that the echo power density at the radar antenna is

$$S_e(r,\theta,\phi) = \frac{P_t \, g_t \, f^2 \, (\theta,\phi)\ell^2\sigma_b}{(4\pi r^2)^2} \quad (\mathrm{W\ m^{-2}}) \ , \qquad (2.16)$$

where $\ell = \exp - \int (k_g + k)dr$ is the one-way loss factor due to gaseous and droplet (both cloud and precipitation) attenuation. Brandes and Wilson (Ch. X) give expressions for attenuation due to water and gas.

e. Doppler radar receiving aspects

The echo power P_r collected by the antenna system from a wave scattered by a target at r,θ,ϕ, is

$$P_r = S_e(r,\theta,\phi)\ A_e(\theta,\phi) \ , \qquad (2.17)$$

where A_e is the effective aperture area of the antenna for radiation from direction θ,ϕ. Theoretically (Silver, 1949; Sherman, 1970, p. 9-12),

$$A_e = \frac{g_r \lambda^2}{4\pi} \; f^2(\theta,\phi) \; , \qquad (2.18)$$

where g_r, the gain of the receiving antenna, is equal to g_t if the transmitting antenna is used for echo reception and P_r is measured at the same location as P_t. For large-aperture antennas and targets along the beam, A_e is roughly the physical area of the antenna reflector. For example, the National Severe Storm Laboratory's (NSSL) Doppler radar antenna (Fig. 2.5) has an $A_e = 42$ m^2, but its physical area is 65.7 m^2. The significantly smaller A_e is caused principally by tapering the illumination of the reflector, which is equivalent to weighting the power density reflected from the parabolic surface. Furthermore, radome and waveguide losses cause A_e to be smaller than the physical area (omitted in our example).

(1) The radar equation

Combining Eqs. 2.16-2.18 gives the radar equation for a discrete target having backscatter cross section σ_b:

$$P_r = \frac{P_t \, g^2 \, \lambda^2 \, \ell^2 \, \sigma_b \, f^4(\theta,\phi)}{(4\pi)^3 r^4} \quad (\mathrm{W}) \; , \qquad (2.19)$$

where we have substituted $g_t = g_r = g$. This equation relates echo power P_r to the radar parameters and target location.

Here is an example of the tremendous sensitivity that radar has for detection of some extremely small targets. NSSL's 10-cm ($\lambda = 0.1$ m) radar receivers can detect echo power as weak as 10^{-14} W; the transmitted peak power is 10^6 W and antenna gain is 4×10^4. Thus, using Eq. 2.19, the minimum detectable cross section at a range of 20 km is

$$\sigma_b(\min) = 2 \times 10^{-7} \text{ m}^2 \; .$$

That is, a single water drop with diameter 6.3 mm could be detected at 20 km. Thus it would not take a very large number of drops to provide a detectable signal at larger range (e.g., 200 km)--and, at that, the transmitted power and receiver performance of the NSSL radars are only moderate in relation to advanced systems in use today (as deep-space probes, for example).

(2) The received waveform (inphase and quadrature components)

Consider a single target. If receiver bandwidth is sufficiently large (see Sec. 2f[1]), the echo signal voltage V(t) replicates the transmitted electric field waveform E and is proportional to it:

$$V(t,r) = A \, \{\exp[j2\pi f(t - 2r/c) + j\psi]\} \; U(t - 2r/c) \; , \qquad (2.20)$$

where 2r is the total path traversed by the incident and scattered waves, A is the prefilter (Fig. 2.3) echo amplitude, and, as before, U = 1 when its argument is between 0 and τ, otherwise it is zero. Range-time $\tau_s \equiv 2r/c$ specifies in units of time, the target location. The total phase of the echo,

$$\beta = 2\pi f(t - 2r/c) + \psi \, , \tag{2.21}$$

is dependent upon t as well as r.

An important radar component is the STALO (stabilized local oscillator), which oscillates at the transmitted frequency f plus (or minus) a small but fixed offset frequency f_Δ. (For simplicity Fig. 2.3 shows homodyning wherein STALO frequency is the same as the transmitted frequency; i.e., $f_\Delta = 0$.) A portion of its signal is mixed (heterodyned) with the echo signal, whose strength is weak relative to the STALO's. (Heterodyne receivers have better sensitivity than homodynes.) As a result of mixing (an additive process), detection (a nonlinear process), and filtering, a signal is generated that replicates in both phase and amplitude the received echo signal (which has carrier frequency f), but it has a new carrier frequency f_Δ (Rideout, 1954, p. 311). Detection and filtering are necessary to retrieve this signal and to remove the carrier frequency f (plus harmonics generated in the detection process). Thus at the filter output (Fig 2.3) we obtain a signal

$$V_o(t) = Ae^{-j(4\pi r/\lambda - \psi)}U(t - 2r/c)e^{j2\pi f_\Delta t} \, . \tag{2.22}$$

We assume for now that the filter rejects all harmonics of f, $f + f_\Delta$, as well as the harmonics of the sum and difference frequencies, but has sufficient bandwidth so that we can ignore loss of frequencies that constitute Eq. 2.22 (see Taylor and Mattern, 1970). Thus heterodyning and detection serve only to shift the carrier frequency (f to f_Δ) without affecting the modulation envelope AU(t). The STALO signal is cw (continuous wave) so that whenever an echo arrives, a STALO signal is mixed with it. A Doppler radar usually has two channels (without which direction of the target toward or away cannot be determined); in one the STALO signal is phase shifted by 90° before mixing so that its detected and filtered output is (assuming $f_\Delta \equiv 0$; Fig. 2.3)

$$V_o(t) = A\, e^{-j\left(\frac{4\pi r}{\lambda} - \psi + \frac{\pi}{2}\right)}\, U(t - 2r/c) \, . \tag{2.23}$$

Now the actual signals from each mixer are the real parts of Eqs. 2.22 and 2.23, which are designated

$$I(t) = \frac{A}{\sqrt{2}}\, U(t - 2r/c) \cos\left(\frac{4\pi r}{\lambda} - \psi\right) \tag{2.24a}$$

and

$$Q(t) = \frac{-A}{\sqrt{2}} U(t - 2r/c) \sin\left(\frac{4\pi r}{\lambda} - \psi\right), \qquad (2.24b)$$

the inphase I(t) and quadrature Q(t) components (see Fig. 2.2) of the complex signal V(t). Echoes from stationary targets have complex signals in which phase, $\gamma = -(4\pi r/\lambda) + \psi$, is time independent. If r increases with time, the phase decreases and the time rate of phase change,

$$\frac{d\gamma}{dt} = -\frac{4\pi}{\lambda}\frac{dr}{dt} = -\frac{4\pi v_r}{\lambda} = \omega_d , \qquad (2.25)$$

is the Doppler shift (in radians per second), a result we deduced in Eq. 2.11.

It is relatively easy to see from Eq. 2.24 that, for usual radar conditions (i.e., $\tau \sim 10^{-6}$ s) and meteorological target velocities on the order of tens of meters per second, the change in the trigonometric functions is extremely small during the time τ when U(t - 2r/c) is nonzero. Thus we measure target phase change during the longer time, $T_s \sim 10^{-3}$ s, from echo pulse to echo pulse rather than during a pulse period. Thus the pulsed Doppler radar becomes a phase- as well as an amplitude-sampling device; samples are at $t = \tau_s + (n - 1) T_s$, where τ_s is the time delay between the n^{th} transmitted pulse and its echo. τ_s is called "range time" because it is proportional to range (i.e., $\tau_s = 2r/c$). It is convenient to introduce another time scale, "sample time," wherein time is incremented in discrete T_s steps after $t = \tau_s$. It is important to realize that echo phase and amplitude changes are examined in sample time space at the discrete instants $(n - 1)T_s$ for a target echo at range time τ_s. Figure 2.6 shows a sample of I(t) and Q(t) changes for stationary and moving targets. It is quite evident that if Q(t) were negative and increasing in a positive direction while I(t) was positive, the Doppler shift would be positive (i.e., angle γ increasing in a counterclockwise direction) and the target would be moving toward the radar.

f. Radar measurement limitations

The discussion above treats an ideal radar to facilitate understanding of radar principles, but it omits some important limitations in radar measurements.

(1) Receiver noise, bandwidth, and signal-to-noise ratio

In an ideal noiseless radar receiver, there is no lower limit in detecting the weakest echo signals. However, all receivers have a power detection limitation usually imposed by the random electrical signals associated with thermal agitation of electron motion in each receiver's front end (in Fig. 2.3 it is the mixer-detector). Some high-performance receivers with parametric amplifiers or other low-noise amplifiers before the mixer-detector have so small a thermal noise that microwave emission from the Earth's surface and

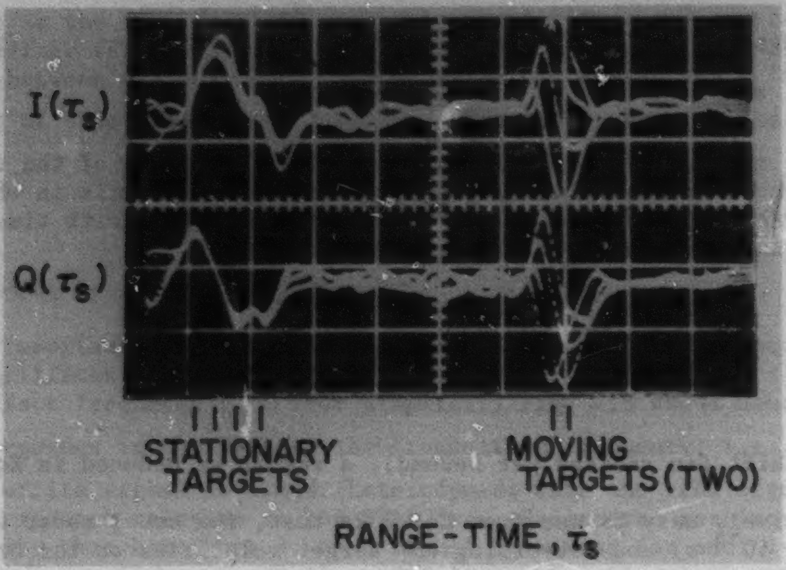

Figure 2.6.--Samples of inphase $I(\tau_s)$ and quadrature phase $Q(\tau_s)$ components of the echo signal for moving and stationary targets. Four successive sampling intervals T_s have been superimposed to show the relative change of amplitude from echo sample to echo sample of targets at range-time τ_s. Vertical scale is linear in voltage, and range-time scale, τ_s, is 2 μs/DIV.

outer space can be the more significant contributor to the overall noise power referred to each receiver's input. Furthermore, emission from lightning and signals from other extraneous sources are noise to the radar. However, in most weather radar systems thermal noise power N limits receiver performance, and its value,

$$N = kT_eB_n\ , \tag{2.26}$$

is a characteristic constant of the radar, where k is Boltzmann's constant, (1.38×10^{-23} W s K^{-1}), B_n is the receiver's noise bandwidth, and T_e is the effective system temperature at the receiver's front end. The system temperature includes thermal-power contributions from environmental noise received by the antenna, thermal radiation due to losses in the antenna's transmission line and protective radome, as well as thermal noise within the receiver itself (Blake, 1970, p. 2-29).

The echo pulse, as well as any signal, can be synthesized in terms of its Fourier spectral coefficients. The receiver amplifies only a band of these spectral or frequency components; i.e., the receiver has a finite bandwidth. The receiver's filter (Fig. 2.3) response G(f) is usually a monotonically decreasing function of frequency, and its width, B_6, is best specified as the frequencies within which G(f) is larger than one-fourth of its highest level--its 6-dB width (Taylor and Mattern, 1970). Noise bandwidth B_n is not so simply specified because it depends upon G(f) as well as noise power spectrum, but in practice it is nearly equivalent to the 3-dB width if noise power is white, i.e., independent of frequency (Kraus, 1966, p. 265).

The larger the B_6, the better the fidelity of the echo pulse shape, but noise power increases in proportion to B_n. We also run the risk of accepting unwanted products of the mixer output. Usually it is not important to detect the return echo with nearly perfect fidelity, nor is it advisable to reduce noise excessively by decreasing B_6 because, as we show below, smaller filter bandwidth coarsens resolution.

An important measurement made with radar is range to the target. The radar often needs to resolve targets that are closely spaced and have largely different backscatter cross sections. For a noiseless receiver of infinite bandwidth, targets are resolved if their spacing is wider than one-half the spatial pulse width (i.e., $c\tau/2$), and targets so spaced return echoes that arrive at separate and distinct time intervals. Finite bandwidth receivers distort the echo pulse by reverberating echo power within the receiver in amounts decreasing with time after the peak echo signal (for example, Fig. 2.4). This causes the receiver output signal to have widths larger than τ, and weak echoes could then be masked by strong ones.

An important echo parameter is the ratio of peak signal power to noise power, which can be shown to be (Doviak and Zrnic', 1979)

$$\mathrm{SNR} = \frac{(I_o^2 + Q_o^2)\,\mathrm{erf}^2\,(aB_6\tau/2)}{kT_eB_n}, \qquad (2.27)$$

where I_o and Q_o are the prefilter echo amplitudes $A/\sqrt{2}$ (Eq. 2.24), τ is the pulse width, $a=\pi/2\sqrt{\ell n2}$, and erf ( ) is the error function (Abramowitz and Stegun, 1964).

(2) Ambiguities

Two kinds of ambiguity are in Doppler radars: range and velocity. Often Doppler radars are operated with uniform PRT (i.e., T_s). Under these conditions, when targets have range r larger than $cT_s/2$, their echoes for the n^{th} transmitted pulse are received after the $(n + 1)^{th}$ pulse is transmitted. Therefore, these echoes are received during the same time interval that targets at $r < cT_s/2$ return echoes from the $(n + 1)^{th}$ pulse Thus range r to the distant target has an apparent value $r' = r - (N_t - 1)r_a$ and is ambiguous with targets at $r = r'$. (N_t is the trip number and $N_t - 1$ designates the whole number of $cT_s/2$ intervals between the target and receiver; $r_a = cT_s/2$ is that range within which all targets must lie to have their ranges unambiguously measured.) Targets for which $N_t = 2$ produce what are called "second-trip"

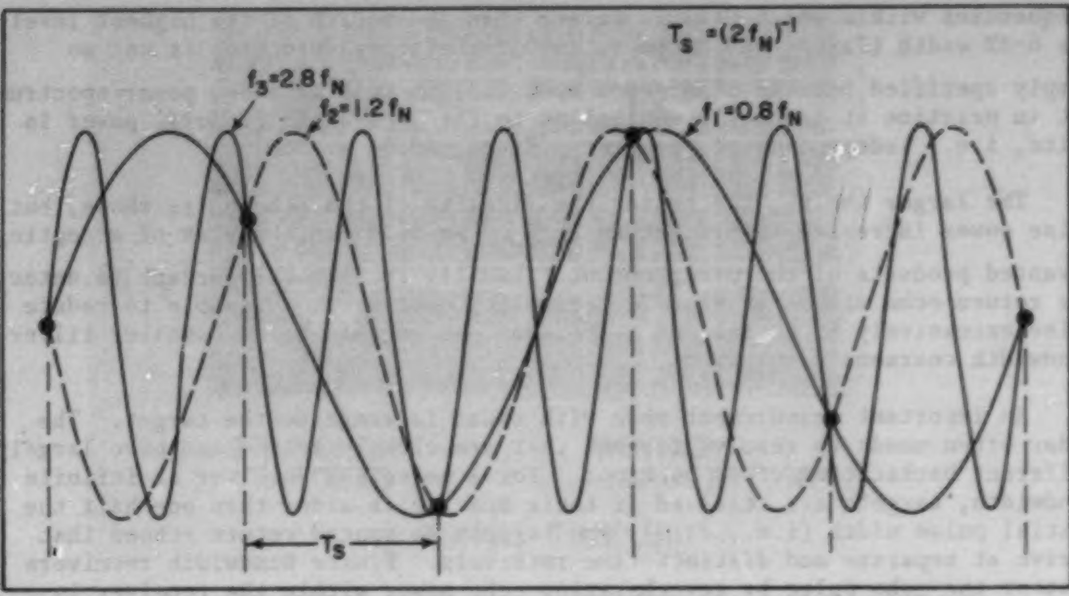

Figure 2.7.--Signals at three different Doppler frequencies that yield, when sampled, the same set of data. These Doppler frequencies are aliases of each other. If both I and Q signals were sampled it can be shown that the signal with f_2 would be an alias not of the one with f_1 but of the one having a frequency $-2f_N + f_1$. $T_s = (2f_N)^{-1}$.

echoes. We emphasize that r_a does not necessarily limit the range to which the pulsed Doppler radar can achieve useful measurement. If its STALO (Fig. 2.3) is phase coherent over many T_s intervals, the radar can accurately measure velocities of targets far beyond r_a, but interference occurs when echoes from targets in different trips are received simultaneously.

The second ambiguity relates to measurement of target velocity. As discussed in Sec. 2e(2), the target's phase γ is sampled at intervals T_s and its change $\Delta\gamma$ over the interval T_s is a measure of the Doppler frequency $f_d = \omega_d/2\pi$. Unfortunately, given a set of sampled phases (computed from I, Q samples), we cannot relate them to a unique Doppler frequency. As Fig. 2.7 shows, the same set of samples could have resulted from any one of the signals having three different Doppler frequencies. Signals that fit the sample data set are called aliases, and $f_N = (2\ T_s)^{-1}$ is the Nyquist (or aliasing) frequency. Doppler frequencies between $\pm f_N$ are the principal aliases, and any frequency higher than f_N is ambiguous with one between $\pm f_N$. Thus target velocities must lie within $v_a = \lambda/4T_s$ to avoid velocity ambiguity. However, transmission of pulses at two interlaced PRF's and signal processing can extend the maximum velocity unambiguously measured (Doviak et al., 1978).

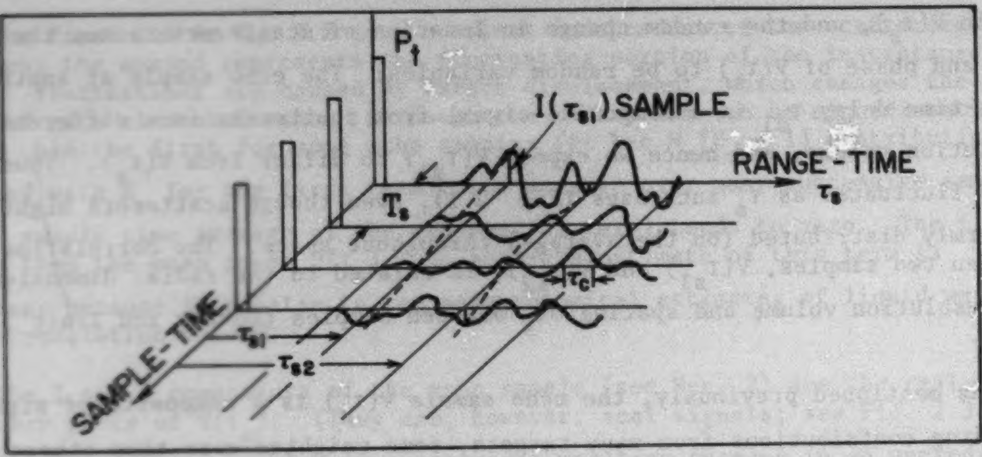

Figure 3.1.--Idealized traces for the inphase component, $I(\tau_s)$, echoes from distributed targets. Each trace represents echoes from a single transmitted pulse P_t. Instantaneous samples are taken at τ_{s1}, τ_{s2}, etc. Dashed line indicates probable time dependence of sample at τ_s if sampling rate T_s^{-1} were increased and ambiguities resolved. τ_c depicts signal correlation time along τ and is related to $B_6\tau$. Samples at fixed τ_s taken at T_s intervals are used to construct Doppler spectra for scatterers located about the range $c\tau_s/2$.

3. WEATHER ECHO SIGNALS

Section 2 delineated the radar signal properties of waves scattered from discrete targets whose dimensions are considerably smaller than the wavelength and whose spacing is more than one-half the spatial pulse width $c\tau/2$. Targets satisfying these conditions are called point targets. Rain, snow, hail, etc., produce a return signal that is a composite of echos from many closely spaced hydrometeors, each of which can be considered a point target. Collectively they are distributed targets or clutter. Echos are received continuously during twice the time required for the microwave pulse to propagate across the volume containing scatterers. We cannot resolve the individual hydrometeors, but we can sample the composite echo at selected range-time delays τ_s (usually spaced τ apart) after the transmitted pulse (Fig. 3.1).

a. The echo sample

Each sample at τ_s represents a composite of discrete echoes from all the scatterers inside the range $c\tau_s/2$; each echo has a weight determined by the radiation pattern $f^4(\theta,\phi)$ and receiver bandwidth-transmitted pulse width product $B_6\tau$. These weighting functions determine a resolution volume in space, where targets significantly contribute to the echo sample at τ_s.

Echo signals from each particle in the resolution volume constructively and/or destructively interfere with each other to produce a composite echo sample $V(\tau_s)$, and the random change in location of scatterers causes the amplitude and phase of $V(\tau_s)$ to be random variables. The echo sample at another range-time delay τ_{s1} is a composite signal from scatterers in a different resolution volume, and hence we expect $V(\tau_{s1})$ to differ from $V(\tau_s)$. Thus $V(\tau_s)$ fluctuates as τ_s increases (Fig. 3.1), even though scatterers might be uniformly distributed (on the average) throughout space. The correlation between two samples, $V(\tau_{s1})$ and $V(\tau_{s2})$, is related to the radial dimensions of the resolution volume and spacing $\delta\tau_s$ between samples (Doviak and Zrnic', 1979).

As mentioned previously, the echo sample $V(\tau_s)$ is a composite of signals including contributions from many targets, some weighted more than others:

$$V(\tau_s) = \sum_i A_i W_i e^{j4\pi r_i/\lambda} \; . \qquad (3.1)$$

In this and following equations we assume that the antenna's gain-weighting function $f^2(\theta,\phi)$ is part of A_i and that W_i is strictly a range-dependent weight determined by the transmitted pulse shape and receiver bandwidth. The echo sample power averaged over an r-f cycle is proportional to (see Eq. 2.3)

$$P(\tau_s) \propto \frac{1}{2}\,[VV^*] = \frac{1}{2} \sum_{i,k}^{N_s} A_i A_k^* W_i W_k^* e^{j4\pi(r_i - r_k)/\lambda}$$

$$= \frac{1}{2} \sum_i^{N} |A_i|^2 \, |W_i|^2 + \frac{1}{2} \sum_{i \neq k} A_i A_k^* W_i W_k^* \, e^{j4\pi(r_i - r_k)/\lambda} \; , \qquad (3.2)$$

the instantaneous echo power at range-time delay τ_s for one transmitted pulse, where N_s is the number of scatterers and $|A_i|^2$ is the magnitude squared of A_i. When scatterers move relative to one another, the echo sample at range time τ_s will differ for each transmitted pulse, and the amount of change depends upon the sampling time interval T_s (the interval between transmitted pulses) and the relative velocity of the scatterers. The equation defining $P(\tau_s)$ for successive transmissions will have the same form, but r_i's and r_k's will have changed because of scatterer motion. If scatterers within a resolution volume are randomly displaced a significant fraction of a wavelength (e.g., $\lambda/4$) between successive transmissions, each successive echo sample $V(\tau_s)$ (spaced T_s) will be essentially uncorrelated and the target volume is said to scatter incoherently. In order to make coherent Doppler measurements of the scatterers' mean radial speed, T_s between successive samples must be small so that successive echoes, at fixed delay τ_s, are correlated.

The first sum in Eq. 3.2 is a constant independent of the scatterers' position; the second represents the fluctuating portion of the instantaneous power. Fluctuations are caused by target displacement, which changes the phase of each elemental echo. Although the second sum can be significantly larger than the first for some echo samples (it has $N_s[N_s - 1]$ contributions compared with N_s for the first term), its average over many successive samples (i.e., sample time average of the exponential term) tends to zero. The first sum is then the mean power $\bar{P}(\tau_s)$. An accurate estimate of this term is important because it relates to the meteorological estimates of liquid water in the resolution volume.

The I and Q components of the echo sample (see Sec. 2) are the real and imaginary parts of $V(\tau_s)$. (They are, however, real signals; see Fig. 2.3.) I and Q are random variables if scatterers' position changes in an unpredictable way. Because I and Q are made up of many contributions, each of which is not a significant portion of the whole, we can invoke the central limit theorem (Papoulis, 1965, p. 266) to deduce that I and Q amplitudes have a Gaussian probability distribution with zero mean. Thus I and Q are jointly normal (Papoulis, 1965, p. 182) random variables, and their correlation is not easily deduced. But it can be shown that when scatterers' position and cross section are independent random variables and target positions produce a uniform distribution of phases across 2π, the correlation of I and Q is zero. Therefore the joint probability distribution of I and Q is the product of individual probabilities:

$$\mathrm{Prob}(I,Q) = \frac{1}{2\pi\sigma^2} e^{-(I^2/2\sigma^2) - (Q^2/2\sigma^2)} , \qquad (3.3)$$

where σ^2 is the mean square value of I (equal for Q). Because $P(\tau_s) = (I^2 + Q^2)$, it follows from Eq. 3.3 that instantaneous power is exponentially distributed and its mean value is $\bar{P} = 2\sigma^2$, where $\bar{P}$ is given by the first term of Eq. 3.2.

b. The weather radar equation

We are now in a position to relate the sample time average of echo power $\bar{P}(\tau_s)$ to the radar parameters and target cross section. The contribution to average echo power from each scatterer is

$$P_i = \frac{1}{2} |A_i|^2 \, |W_i|^2 , \qquad (3.4)$$

where $|A_i|^2/2$ is the prefilter echo power and hence can be expressed directly in terms of radar parameters and target cross section through use of Eq. 2.19. Thus the sample time average power at delay τ_{s1} is

$$\bar{P}(\tau_{s1}) = \frac{P_t g^2 \lambda^2}{(4\pi)^3} \sum_i \frac{\ell_i^2 \sigma_{bi} f^4(\theta_i,\phi_i) \, |W(r_i)|^2}{r_i^4} , \qquad (3.5)$$

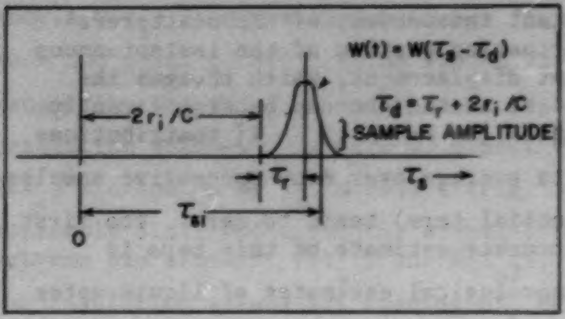

Figure 3.2.--Realistic receiver response to point target echo of a rectangular transmitter pulse. Time delays relate to target range r_i, receiver response delay τ_r, and the sample range-time delay τ_{sl}. τ_s=0 is the time at which the transmitter signal is emitted from the antenna.

where r_i is the i^th^ scatterer's range and θ_i,ϕ_i are its angular displacements from the beam axis at θ_o,ϕ_o. When scatterers are nearly identical, the ones that contribute most to $\bar{P}(\tau_{sl})$ have range $r_i = r_o$ and

$$r_o = c(\tau_{sl} - \tau_r)/2 \ , \tag{3.6}$$

where τ_r is the delay a point target echo experiences passing through the radar's transmission lines and receiver (i.e., the time to obtain peak signal after the echo pulse reaches the antenna; see Fig. 3.2).

We now consider an elemental volume ΔV containing many drops. The summation of σ_{bi} over this volume normalized to ΔV defines target reflectivity:

$$\eta = (\Delta V)^{-1} \sum_{\Delta V} \sigma_{bi} \quad m^{-1} \ . \tag{3.7}$$

Replacing the sum by an integration because particles are usually closely spaced compared with the scale of the weighting function, the weather radar equation is

$$\bar{P}(\vec{r}_o) = \frac{P_t g^2 \lambda^2}{(4\pi)^3} \int_0^{\infty} \int_0^{\pi} \int_0^{2\pi} \frac{\eta(\theta,\phi,r)\ell^2}{r^4} f^4(\theta,\phi) \left| W(r_o - r) \right|^2 dV \ , \tag{3.8a}$$

where $dV = r^2 dr \sin\theta \, d\phi d\theta$ and $\vec{r}_o$ is the vector range to the center of the resolution volume. Targets at range $r_i \geq c\tau_{sl}/2$ do not contribute to the echo sampled at τ_{sl} (see Fig. 3.2). Even though we made the upper limit on the r integral infinite, $W(r_o - r)$ gives zero weight to targets at ranges $r_i \geq c\tau_{sl}/2$, although all targets at closer ranges contribute to $\bar{P}(r_o)$. In general n and ℓ are functions of r, θ, and ϕ, but we assume that $f^4(\theta,\phi)$ $|W(r)|^2$ has a scale (resolution volume dimensions) such that the reflectivity and attenuation can be considered constant over the region that contributes most to $\bar{P}(r_o)$. Furthermore, we assume range-to-resolution volume large compared with its range extent. Thus we can approximate Eq. 3.8a by

$$\bar{P}(r_o,\theta_o,\phi_o) \simeq \frac{P_t g^2 \lambda^2 \ell^2 \eta}{(4\pi)^3 r_o^2} \int_0^\infty |W(r_o - r)|^2 dr \int_0^{2\pi} \int_0^{\pi} f^4(\theta,\phi) \sin\theta \, d\theta d\phi \ , \qquad (3.8b)$$

where ℓ and η smoothly depend upon the coordinates θ_o, ϕ_o, and r_o, the center of the resolution volume. When antenna patterns are circularly symmetric and have a Gaussian shape, it can be shown (Probert-Jones, 1962) that

$$\int_0^{\pi} \int_0^{2\pi} f^4(\theta,\phi) \sin\theta \, d\theta d\phi = \frac{\pi\theta_1^2}{8\ell n 2} \ , \qquad (3.9)$$

where θ_1 is the 3-dB width (in radians) of the one-way pattern.

The range-weighting integral in Eq. 3.8b causes a loss in weather echo strength. This loss, due to finite receiver bandwidth, was first enunciated by Nathanson and Smith (1972) to explain residual discrepancies between measurements and theory. Probert-Jones' solution accounted for most of the discrepancy and, in the case $B_6 >> \tau^{-1}$ often used in conventional non-Doppler radar systems, for practically all differences. If the filter has Gaussian frequency response, it can be shown (Doviak and Zrnic', 1979) that a form of the weather radar equation is

$$\bar{P}(r_o,\theta_o,\phi_o) = \frac{P_t g^2 \lambda^2 \ell^2 \eta}{(4\pi)^3 r_o{}^2} \left[\coth(2b) - \frac{1}{2b}\right] \frac{\pi\theta_1^2}{8\ell n 2} \ \frac{c\tau}{2} \ , \qquad (3.10)$$

where $2b = \pi B_6 \tau / 2\sqrt{\ell n 2}$. Equation 3.10 shows the dependency of averaged echo power $\bar{P}$ upon measurable quantities for the radar. The term in the brackets is the receiver loss, $L_r = -10 \log \ell_r$, due to finite receiver bandwidth (plotted in Fig. 3.3). This loss is a function of both transmitted pulse width τ and receiver bandwidth B_6 analogous to the two measurable parameters, g and θ_1, of the antenna. For radar receivers having B_6 nearly equal to τ^{-1} or less, ℓ_r is significant and needs to be accounted for in the weather radar equation.

(1) Resolution volume

It is useful to define a resolution volume V_6 as that circumscribed by the 6-dB contour. Thus the resolution volume is a cylinder having a 6-dB diameter $r\theta_1$ and a range extent of

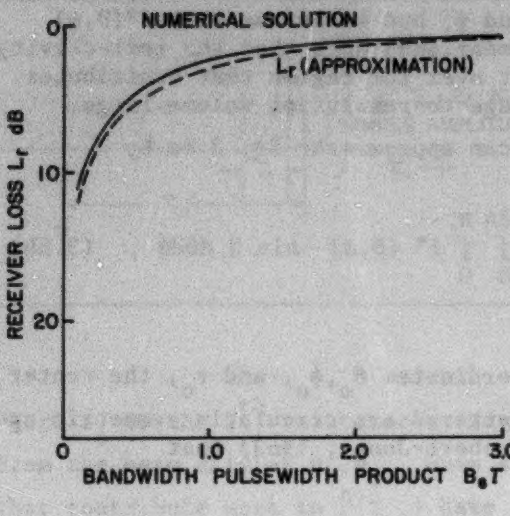

Figure 3.3.--Receiver signal power loss L_r (dB) because of finite bandwidth. Receiver frequency transfer is Gaussian and echo pulse rectangular. The solid curve is a numerical solution of the exact response function, and the dashed curve is obtained from an analytical approximation (see Eq. 3.10).

$$r_6 = \frac{c\tau/2}{aB_6\tau} \cosh^{-1} (2 + \cosh aB_6\tau) \ . \tag{3.11}$$

When the receiver's bandwidth B_6 is matched to the transmitted pulse width τ (i.e., $B_6\tau = 1$), r_6 is about 20% larger than $c\tau/2$, the resolution for $B_6 \to \infty$. From Eq. 3.11 we note that both B_6 and τ determine the range distribution of weights, as g and θ_1 determine the angular distribution. The resolution volume is 0.1 km^3 for $\theta_1 = 1°$, $r = 50$ km, $B_6 = 1$ MHz, and $\tau = 1$ μs. Outside this volume, reflectivity is weighted by factors less than one-fourth, because of antenna pattern and receiver response.

(2) Reflectivity factors

Radar meteorologists need to relate reflectivity (η) to factors that have meteorological significance. If scattering particles are known to be spherical and have diameters small compared with wavelength (i.e., the Rayleigh approximation), then we can substitute Eq. 2.10 into Eq. 3.7 to obtain

$$\eta = \frac{\pi^5}{\lambda^4} \left|K_w\right|^2 Z \ , \tag{3.12a}$$

where

$$Z \equiv \frac{1}{\Delta V} \sum_i D_i^{\,6} \ , \tag{3.12b}$$

the reflectivity factor. Whenever the Rayleigh approximation does not apply, and this is usual for short-wavelength (λ < 10 cm) radars measuring thunderstorm precipitation,

$$Z_e \equiv \frac{\lambda^4}{\pi^5} \left| K_w \right|^{-2} \eta \tag{3.12c}$$

where Z_e is the effective reflectivity factor.

Reflectivity factors do not relate radar echo power to meteorologically significant factors such as rainfall rate or liquid water content because one more essential parameter needs to be known in addition to substance phase (i.e., $\left| K_w \right|^2$): the drop size distribution (see Ch. X). Although η or Z_e could be used in the radar equation, radar meteorologists have chosen Z_e. Z should not be used in the radar equation unless one is sure that all hydrometeors contributing to the echo sample have a diameter small compared with wavelength (i.e., $D < \lambda/16$).

(3) A useful form of the weather radar equation

Incorporating Eq. 3.12c into Eq. 3.10, we have the modified weather radar equation that gives average echo power in terms of Z_e (m^3):

$$\bar{P}(\vec{r}_o) = \frac{\pi^3 P_t g^2 \ell^2 \ell_r \theta_1^2 c\tau \left| K_w \right|^2 Z_e}{2^{10}(\ell n 2)\lambda^2 r_o^{\,2}} , \tag{3.13a}$$

where all units are in the MKS system (i.e., meters, seconds, and watts). θ_1 is in radians, g is dimensionless, and r_o is taken to be the center of the radiation volume.

However, it is common to express Z_e in $mm^6\ m^{-3}$, θ_1 in degrees, r in kilometers, λ in centimeters, τ in microseconds, P_t in watts, and $\bar{P}$ in milliwatts. Thus, using units conventional to the radar meteorologist, the mean weather echo power for resolution volume at r_o, θ_o, ϕ_o is

$$\bar{P} = \frac{\pi^5 10^{-17} P_t g^2 \ell^2 \ell_r \tau \theta_1^2 \left| K_w \right|^2 Z_e}{6.75 \times 2^{14}(\ell n 2) r_o^{\,2} \lambda^2} . \tag{3.13b}$$

c. Signal-to-noise ratio for weather targets

The signal-to-noise ratio (SNR) for weather echoes is Eq. 3.10 divided by kTB_n. Again consistent with the above approximations, we find that SNR depends upon B_6 as

$$\mathrm{SNR} = \frac{C_o}{r^2} \left[\coth(2b) - \frac{1}{2b}\right] \frac{\tau^2}{B_6 \tau} , \tag{3.14}$$

where C_o contains constants pertaining to the radar. If $B_6\tau$ is a constant of 1 (a reasonable selection because this "matches" the receiver bandwidth to the transmitted pulse width producing a maximum SNR for point targets), SNR is proportional to the square of the transmitted pulse width. But it can be shown that maximum SNR is obtained as $B_6 \rightarrow 0$, in contrast to point target measurements where we obtain a maximum SNR at $B_6\tau = 1$ (see Eq. 2.27). Even though SNR increases monotonically as B_6 decreases, resolution r_6^{-1} worsens. Zrnic' and Doviak (1978) define an optimum B_6 as the value that maximizes SNR for a given resolution.

4. DOPPLER SPECTRA OF WEATHER ECHOES

The Doppler spectrum is a reflectivity-weighted distribution of the radial velocities of the scatterers that lie mostly within the resolution volume. The reflectivity weight depends not only on the cross section of each scatterer, but also on the weighting given to scatterers by the antenna pattern, the transmitted pulse width, and the receiver bandwidth. A derivation leading to a relationship among the velocity and reflectivity fields, the resolution volume weighting functions, and the Doppler spectrum was first put forward by Sychra (1972). Doviak et al. (1979) derive identical results using a different approach. They show that the power spectrum density $\bar{S}(v)$ of the Doppler velocities is

$$S\,(\vec{r},v) = \iint_A \eta(\vec{r}_1) I(\vec{r},\, \vec{r}_1)\ \left|\text{grad } v(\vec{r}_1)\right|^{-1} dA \quad , \tag{4.1a}$$

where $\vec{r}$ and $\vec{r}_1$ are the radius vectors to the resolution volume center and the elemental scattering volume. A is an area on a surface of constant Doppler velocity $v(\vec{r}_1)$, and $I(\vec{r},\vec{r}_1)$ is the illumination function,

$$I(\vec{r},\vec{r}_1) = C_1\, f^4(\theta,\phi)\, W^2(r - r_1)/r_1^4 \ , \tag{4.1b}$$

where C_1 is a constant.

Equation 4.1 is fundamental and worthy of more discussion. The area A consists of all isodop surfaces (surfaces of constant Doppler velocity); i.e., it is a union of such surfaces. At each point $\vec{r}_1$ on the surface, the reflectivity is multiplied with the corresponding weighting function. The gradient term adjusts the isodops' contribution according to their density; i.e., the closer the isodop surfaces the smaller the weight applied to the spectral components in the velocity interval between two isodops.

For calculation of the mean velocity and the spectrum width, the normalized $\bar{S}_n(\vec{r},v)$ version of Eq. 4.1 is used:

$$\bar{S}_n(\vec{r}, v) = \frac{\bar{S}(\vec{r},v)}{\int_{-\infty}^{\infty} \bar{S}(\vec{r},v)\,dv} . \tag{4.2}$$

Note that the integral in the denominator is the total power and equals the volume integral, Eq. 3.8. Even though we have indicated infinite limits, all power is contained within the Nyquist interval $\pm\lambda/4T_s$. The weighted average reflectivity $\bar{\eta}(\vec{r})$ is

$$\bar{\eta}(\vec{r}) \equiv \frac{\iiint \eta(\vec{r}_1) I(\vec{r},\vec{r}_1)\,dV}{\iiint I(\vec{r},\vec{r}_1)\,dV} . \tag{4.3}$$

The integral value in the denominator of Eq. 4.3 can be obtained from Eq. 3.10 for weather radar parameters usually met in practice. Now the mean Doppler velocity is defined as

$$\bar{v}(\vec{r}) \equiv \int_{-\infty}^{\infty} v\,\bar{S}_n(\vec{r},v)\,dv , \tag{4.4}$$

a combination of reflectivity (power) and illumination function weighted velocity that could be quite different from the $I(\vec{r}, \vec{r}_1)$ weighted velocity. The velocity spectrum width $\sigma_v(\vec{r})$ is obtained from

$$\sigma_v^2(\vec{r}) = \int_{-\infty}^{\infty} [v - \bar{v}(\vec{r})]^2\,\bar{S}_n(\vec{r},v)\,dv . \tag{4.5}$$

The relationship between the point velocities $v(\vec{r}_1)$ and the power-weighted moment $\bar{v}(\vec{r})$ is obtained by substituting Eq. 4.2 into Eq. 4.4:

$$\bar{v}(\vec{r}) = \frac{\iiint v(\vec{r}_1)\,\eta(\vec{r}_1)\,I(\vec{r},\vec{r}_1)\,dV}{\iiint \eta(\vec{r}_1)\,I(\vec{r},\vec{r}_1)\,dV} . \tag{4.6}$$

Unlike the pulse volume-averaged reflectivity, this is the average of point velocities weighted by both reflectivity and the illumination function. Similarly the width (Eq. 4.5) reduces to

$$\sigma_v^2(\vec{r}) = \frac{\iiint v^2(\vec{r}_1)\,\eta(\vec{r}_1)\,I(\vec{r},\vec{r}_1)\,dV}{\iiint \eta(\vec{r}_1)\,I(\vec{r},\vec{r}_1)\,dV} - \bar{v}^{\,2}(\vec{r}) \tag{4.7}$$

and corresponds to a weighted deviation of velocities from the averaged velocity.

The mean Doppler velocity (Eq. 4.4) depends on the distribution of scatterers' cross section within the resolution volume and its weighting functions. Thus $\bar{v}(\vec{r})$ cannot in general be equated to a spatial mean velocity. However, if wind distribution is symmetrical about the resolution volume center and reflectivity is uniform, then $\bar{v}(\vec{r})$ can be considered a very good approximation of the true radial component of wind at the volume center. But hydrometeor fall velocity must be either insignificant or known (see Sec. 5a[1]).

a. Estimating Doppler power spectra

In order to measure the power-weighted distribution of velocities, frequency analysis of $V(\tau_s)$ is needed and can be accomplished by estimating its power spectrum. Bear in mind that the frequency analysis is performed along the sample time axis for samples $V(\tau_s)$, at fixed τ_s. Thus we have discrete samples $V(\tau_s, mT_s)$, spaced T_s apart, of a continuous random process. Next we shall make some general statements concerning spectral analysis of continuous random signals.

The power spectrum density is the Fourier transform of the signal's autocovariance function $R(T_\ell)$:

$$\bar{S}(f) = \int_{-\infty}^{\infty} R(T_\ell) e^{-j2\pi f T_\ell} \, dT_\ell \, , \tag{4.8}$$

where T_ℓ is a time lag.

The autocovariance function of a stationary signal (statistics do not change during the time of observation) is found from the time average:

$$R(T_\ell) = \lim_{T\to\infty} \frac{1}{T} \int_{T/2}^{T/2} V^*(t) V\,(t + T_\ell) dt \, . \tag{4.9}$$

Because V(t) has zero mean, autocorrelation and autocovariance are identical. Note that conservation of power relates the Doppler spectrum $\bar{S}(v)$ to the power spectrum $\bar{S}(f)$ through

$$\bar{S}(v) = \frac{2}{\lambda} \, \bar{S}(f) \, . \tag{4.10}$$

When the spectrum or the autocovariances are known, all pertinent information (e.g., mean Doppler velocity) can be readily obtained. Neither $\bar{S}(v)$ nor $R(T_\ell)$ is available; they must be estimated from the ensemble of samples

$V(\tau_s, mT_s)$ spaced T_s apart. Because radars observe any resolution volume for a finite time, one is faced with estimating at a given range, $c\tau_s/2$, the spectrum and its parameters from a finite number M of time samples $V(mT_s)$. We delete the range time argument τ_s, and $V(mT_s)$ designates an ensemble sample at the implicit delay τ_s and T_ℓ increments in steps of T_s.

Samples $V(mT_s)$, often multiplied by a weighting factor $W(mT_s)$, are Fourier transformed, and the magnitude squared of this transformation is a power spectrum estimate $\hat{S}(k)$ commonly known as the periodogram:

$$\hat{S}(k) = \frac{1}{M} \left| \sum_{m=0}^{M-1} W(mT_s)V(mT_s)e^{-j2\pi km/M} \right|^2 , \qquad (4.11)$$

where k and m are integers.

The finite number of time samples from which the periodogram is computed limits velocity resolution and creates an undesirable "window effect"; i.e., one may imagine that the time series extends to infinity but is observed through a finite length window. The magnitude squared of the data window transform is referred to as the spectral window and is significant because its convolution with the true spectrum equals the measured spectrum.

Figure 4.1 illustrates a weather signal weighted with a uniform window and one with a von Hann (raised cosine) window, showing considerable difference in the spectral domain, especially in spectral skirts. Since the von Hann window has a gradual transition between no data and data points, its spectral window has a less concentrated main lobe and significantly lower side lobes. The resulting spectrum retains these properties and enables us to observe weak signals to more than 40 dB below the main peak. This is very significant when one is trying to estimate the peak winds of tornadoes or other severe weather (Zrnic', 1975a) within the resolution volume; power in spectral skirts due to high velocities is rather weak and would be masked by the strong spectral peaks seen through the window side lobes unless a suitable window were applied. The apparent lack of randomness of coefficients in the spectral skirts for the rectangularly weighted data is due to the larger correlation between coefficients. This correlation is attributed to the strong spectral powers seen through the nearly constant level window side lobes (Zrnic', 1975a).

The example in Fig. 4.1 is from a tornadic circulation with translation; the broad spectrum results from high-speed circulatory motion within the resolution volume. The envelope shape $|\sin x/x|^2$ is readily apparent for the rectangular window (at negative velocities), and the dynamic range for spectrum coefficients is about 30 dB. This is in contrast to more than 45 dB of dynamic range with the von Hann window, which also defines better the true spectrum and the maximum velocity (60 m s^{-1}).

Besides the window effect, which is intimately tied to signal processing, there are several spectral artifacts due to the radar hardware, which are discussed in Zeoli (1971), Zrnic' (1975b), and Zrnic' and Bumgarner (1975).

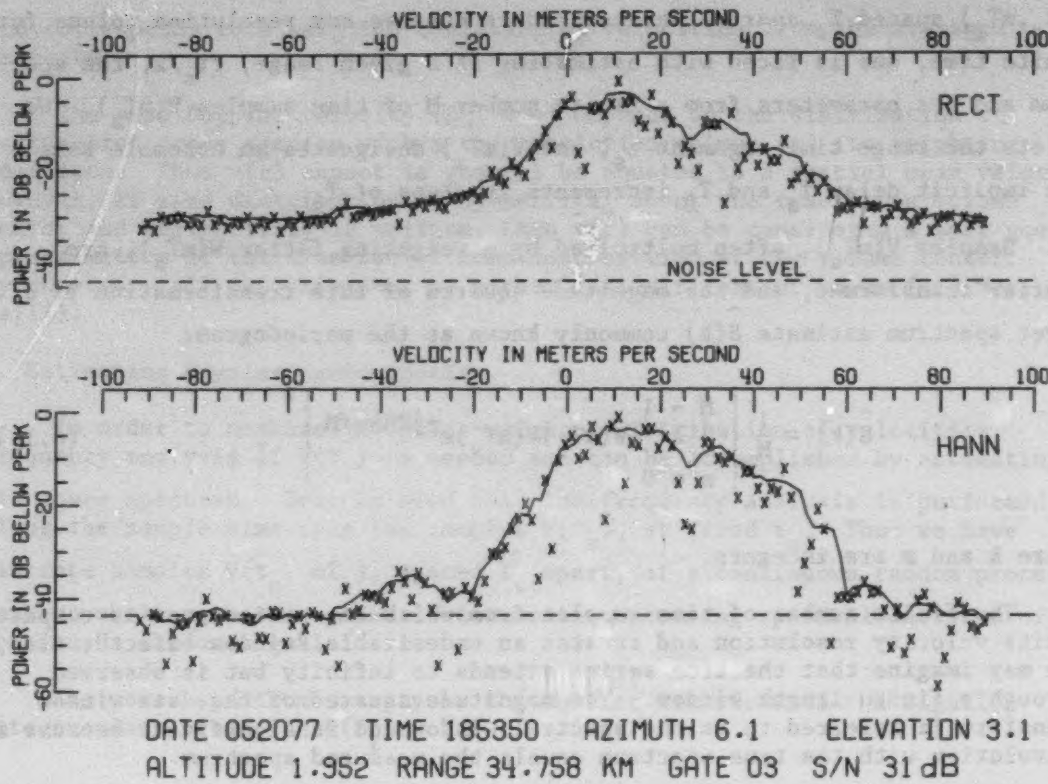

Figure 4.1.--Power spectra of weather echoes showing statistical fluctuations in spectral estimates (x). RECT (above) signifies spectra of echo samples unweighted, whereas HANN (below) signifies samples weighted by a von Hann window. Solid curves are five-point running averages of spectral powers.

b. Velocity spectrum width, shear, and turbulence

The velocity spectrum width (i.e., the square root of the second spectral moment about the mean velocity) is a function of radar system parameters such as beamwidth, bandwidth, and pulse width, and meteorological parameters that describe the distribution of hydrometeor density and velocity within the resolution volume (Atlas, 1964). An excellent explanation and assessment of each can be found in Waldteufel (1976).

Relative radial motion of targets broadens the spectrum. For example, turbulence produces random relative radial motion of drops. Wind shear can cause relative radial target motions as can differences in fallspeeds of various size drops. The beam sweeping through space also contributes to spectrum width (i.e., the radar does not receive echoes from identically weighted targets on successive samples). This change in resolution volume V_6 location from pulse to pulse results in a decorrelation of echo samples and consequent increase in spectrum width σ_v. The echo samples are uncorrelated more quickly (independent of particle motion inside V_6) the faster the antenna

is rotated. Thus spectrum width increases in proportion to the antenna angular velocity.

If all the above spectral-broadening mechanisms are independent of one another, the square of the velocity spectrum width σ_v can be considered the sum of all (Hitschfeld and Dennis, 1956):

$$\sigma_v^2 = \sigma_s^2 + \sigma_r^2 + \sigma_d^2 + \sigma_t^2 \quad , \tag{4.12}$$

where σ_s^2 is due to shear, σ_r^2 to antenna rotation, σ_d^2 to different drop size fallspeeds, and σ_t^2 to turbulence. The relation of the above terms to the meteorological and radar parameters is derived and discussed in Nathanson (1969) and Doviak et al. (1979).

Doviak et al. (1978) measured velocity spectrum widths σ_v in severe tornadic storms. Their data (Fig. 4.2) show a median width value of about 4 m s^{-1} and about 20% of widths larger than 6 m s^{-1}. They deduced that these large widths are most likely caused by turbulence that is not homogeneous and isotropic, thereby suggesting the presence of energetic eddies of scale size small compared with radar resolution volume. For these experiments, $\theta_1 = 0.8°$ and $\tau = 1$ μs, so weather radars not having better resolution should obtain similar width distributions in severe storms.

Frisch and Strauch (1976) measured widths up to 5 m s^{-1} in a convective storm (3-cm wavelength radar, beamwidth 0.9°, range up to 55 km). It is significant that those maxima were in the transition region between updrafts and downdrafts and close to the reflectivity core.

It is extremely important to relate widths to severe turbulence so that radars can give reliable measure of turbulence hazardous to aircraft. Analysis by J. T. Lee at the National Severe Storms Laboratory (NSSL) (Lee, 1977) suggests a strong connection between spectral width and aircraft penetration measurements of turbulence. When aircraft-derived gust velocities exceeded 6 m s^{-1}, corresponding to moderate or severe turbulence, the spectral width exceeded 5 m s^{-1} in every case for aircraft within 1 km of the radar resolution volume. Not all storm regions of large spectral width produce aircraft turbulence, however. When σ_v was less than 4 m s^{-1}, the aircraft experienced only light turbulence in more than 50 thunderstorm penetration flights. Accurate estimates of turbulence and shear, as well as of rain and hail hazards, should allow safer flights through showers produced by thunderstorms.

For most situations, the combination of radar characteristics and meteorological parameters results in negligible contribution from all mechanisms in Eq. 4.12 except radial velocity shear and turbulence (Sirmans and Doviak, 1973). Because shear can be determined directly from the angular dependence of the mean radial velocity, the component due to turbulence can be extracted from spectral width. NSSL's Doppler velocity fields show that shears of about 1 to 2 × 10^{-2} s^{-1} typify mesocyclone regions of tornadic storms.

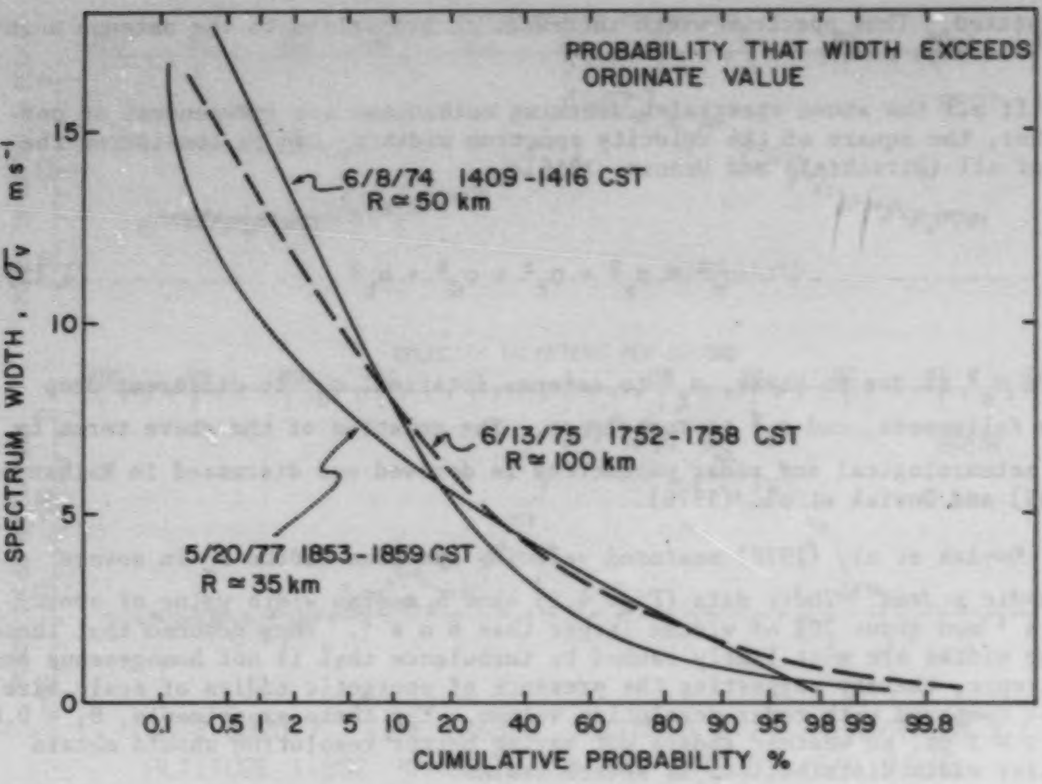

Figure 4.2.--Cumulative probability of unbiased spectrum widths for echoes from three tornadic storms. Spectrum widths are derived from spectra computed using discrete Fourier transforms of echo samples having S/N $\geq$ 15 dB. Antenna beamwidth $\theta_1 = 0.8°$.

5. OBSERVATION OF WEATHER

The great utility of storm observation with centimeter wavelength pulsed Doppler radar derives from its capacity to map reflectivity η and mean radial velocity $\bar{v}$ inside the storm's shield of clouds. A three-dimensional picture of a single storm takes about 2 to 5 minutes of data collection time not only because of antenna rotation limitations, but also because many echoes from each resolution volume must be processed to reduce the statistical uncertainty in the η and $\bar{v}$ estimates. Although storm structure can change significantly during this period with distortion in the radar's image of the true reflectivity and velocity fields, highly significant achievements have been made in depicting the structure and evolution of the thunderstorm.

But the meteorologically interesting variables are not η or $\bar{v}$ but parameters such as rainfall rate (on the ground) and wind. Pulsed Doppler radar measures the radial speed of hydrometeors, not air, and in certain situations (e.g., with vertically directed beams) these speeds can differ significantly from the radial component of wind. Surface rainfall rate estimates are also

not easily related to η, and often radar reflectivity measurements are supplemented by surface rain gages (Brandes, 1975; Crawford, 1977).

Incoherent radars map η and, if their resolution volume is sufficiently small and reflectivity estimates are accurate, can track prominent reflectivity structures to map winds that steer cells (Crane, 1979). However, Doppler radar measures, practically instantaneously, velocities in each resolution volume and hence can provide far better resolution of the velocity field.

a. Dual Doppler radar

A single Doppler radar maps a field of a velocity component directed toward (or away from) the radar. A second Doppler radar, spaced far from the first, provides a field of different radial velocities, because the wind vector is projected on different radials. The two radial-velocity fields can be vectorially synthesized to retrieve the two-dimensional velocities in the plane containing the radials (Armijo, 1969). The synthesis is usually accomplished on common grid points to which radar data are interpolated. Radial velocities in each of the radar's resolution volumes surrounding a grid point are not measured simultaneously but are separated up to the few minutes required for each radar to scan the common volume. The respective resolution volumes are also usually quite different in size and orientation.

Nevertheless, useful estimates of wind can be made on scales of air motion large compared with the biggest resolution volume dimensions, if the velocity field is preserved during the period required for data collection. Targets such as water drops having small mass quickly respond to horizontal wind forces and faithfully trace the wind. Stackpole (1961) has shown that for energy spectrum of wind scales following a -5/3 law to at least 500 meters, more than 90% of the rms wind fluctuations are acquired by the drops if their diameters are less than 3 mm. When radar beams are at low elevation angles, target terminal velocity (i.e., the steady-state vertical velocity of the target relative to the air) gives negligible error in the radial wind component. At high elevation angles, terminal velocity must be considered.

(1) Reconstruction of wind fields

The dual Doppler radar technique to derive quasi-horizontal winds was first illustrated by Lhermitte (1970) and later extended by Frisch et al. (1974) to display all three Cartesian wind components. Wind field determination is greatly simplified if the synthesis is performed in cylindrical coordinates with an axis being the line connecting the two radars. That is, radial velocities at data points (centers of resolution volumes) are interpolated to nearby grid points on planes having a common axis (the COPLAN technique) (Lhermitte, 1970). Cartesian wind components can be derived from these synthesized cylindrical components. Solving directly for Cartesian wind components necessitates a solution of an inhomogeneous, hyperbolic partial differential equation to derive vertical wind (Armijo, 1969).

The cylindrical coordinate system is illustrated in Fig. 5.1. The mean Doppler velocity must be corrected for the scatterers' terminal velocity v_t relative to the air in which they are located. The corrected radial velocity estimate is

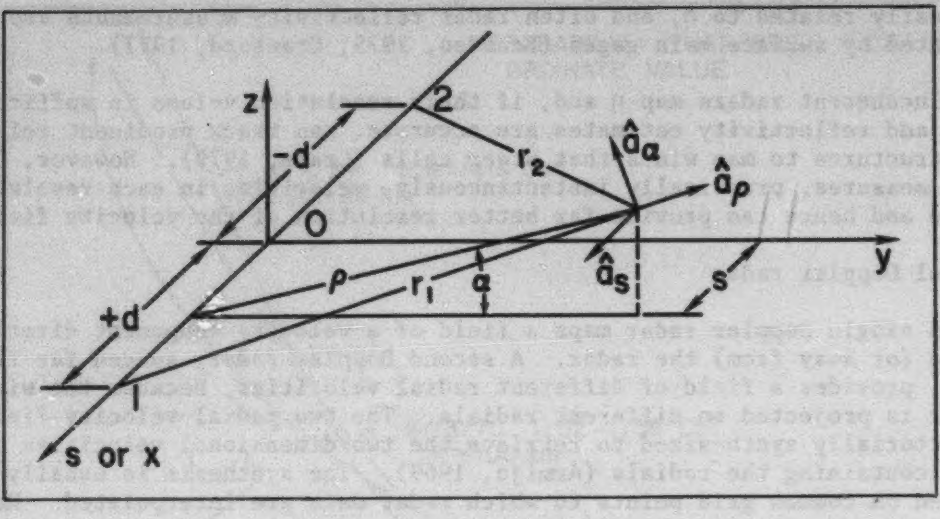

Figure 5.1.--Cylindrical coordinate system used for dual radar data analysis. The radars are located at the points 1 and 2; $\hat{a}_\rho$, $\hat{a}_s$, and $\hat{a}_\alpha$ are the unit normals defining directions of the three orthogonal velocity components.

$$v_{1,2} = v'_{1,2} + v_t \sin\theta \ , \qquad (5.1)$$

where $v'_{1,2}$ are the mean Doppler target velocities measured by radars 1,2 at data points and θ_e is the elevation angle. To estimate v_t for each resolution volume, one could use the empirical expression (Atlas et al., 1973)

$$v_t = 2.65 \ Z^{0.114} \left[\frac{\gamma_o}{\gamma} \right]^{0.4} \quad (\mathrm{m\ s^{-1}}) \ , \qquad (5.2)$$

where the parenthetical term is that suggested by Foote and duToit (1969) to account for height-dependent air density γ and Z is the reflectivity factor. This relation well represents experimental data over a large range of Z (i.e., $1 \le Z \le 10^5$ $\mathrm{mm^6\ m^{-3}}$) for regions of liquid water, but large errors up to several meters per second in v_t estimates can be caused by erroneously relating regions of hail with a v_t,Z relation appropriate for liquid water. Usually there is little or no information to identify these regions uniquely, and errors in vertical wind w_z can result. However, it has been shown for typical arrangements of storms relative to the two-radar placement that the error in w_z is significantly smaller than errors in v_t (Doviak et al. 1976).

The estimated radial velocities $v_{1,2}$ of the air can be interpolated to uniformly spaced grid points in planes at angle α to the horizontal surface

containing the baseline. Interpolation filters the data and reduces variance. The cylindrical wind components in the ρ,s plane are related to $\bar{v}_1, \bar{v}_2$ as

$$w_\rho = \frac{(s + d)r_1\bar{v}_1 + (s - d)r_2\bar{v}_2}{2d\rho} \tag{5.3}$$

and

$$w_s = \frac{r_2\bar{v}_2 - r_1\bar{v}_1}{2d} \ , \tag{5.4}$$

where $\bar{v}_{1,2}$ are the interpolated Doppler velocities of air.

The wind component, w_α, normal to the plane, is obtained by solving the continuity equation in cylindrical coordinates,

$$\frac{1}{\rho}\frac{\partial}{\partial\rho}(\rho\gamma w_\rho) + \frac{1}{\rho}\frac{\partial}{\partial\alpha}(\gamma w_\alpha) + \frac{\partial}{\partial s}(\gamma w_s) = 0 \ , \tag{5.5}$$

with an appropriate boundary condition (Ray et al., 1975). The mass density γ is given by

$$\gamma = \gamma_o \exp\left[-g_o M\rho \sin\alpha/(R^*T)\right] \ , \tag{5.6}$$

where g_o is the gravitational constant (9.8 m s^{-2}), M the mean molecular weight of air (29 g mol^{-1}), T the absolute temperature (K), and R* the universal gas constant (8.314 J mol^{-1} K^{-1}). Appropriate values of γ_o and T can be obtained from surface site and upper-air soundings. The Cartesian components of wind can then easily be obtained from w_ρ, w_s, and w_α.

(2) Observation of a tornadic storm

The first dual Doppler radar observations of a tornadic storm were made on 20 April 1974 with NSSL's 10-cm radars. These radars provide a large unambiguous range and velocity capability well suited for observation of the large and severe thunderstorms that frequent the high plains of the United States.

Figure 5.2 locates the two radars, one at Cimarron airfield in Oklahoma City and the second at NSSL's headquarters in Norman, Okla. It also shows reflectivity contours and the horizontal wind field synthesized using a slight modification of the above outlined scheme (Ray et al., 1975). (Terminal velocity corrections were obtained from interpolated reflectivity factor values, and a slightly different v_t,Z relationship was used.) Streamlines have been drawn in addition to velocity vectors, whose lengths are proportional to windspeed. The curvature in the streamlines shows appreciable local vorticity in the region near the grid point (30.0, 24.0).

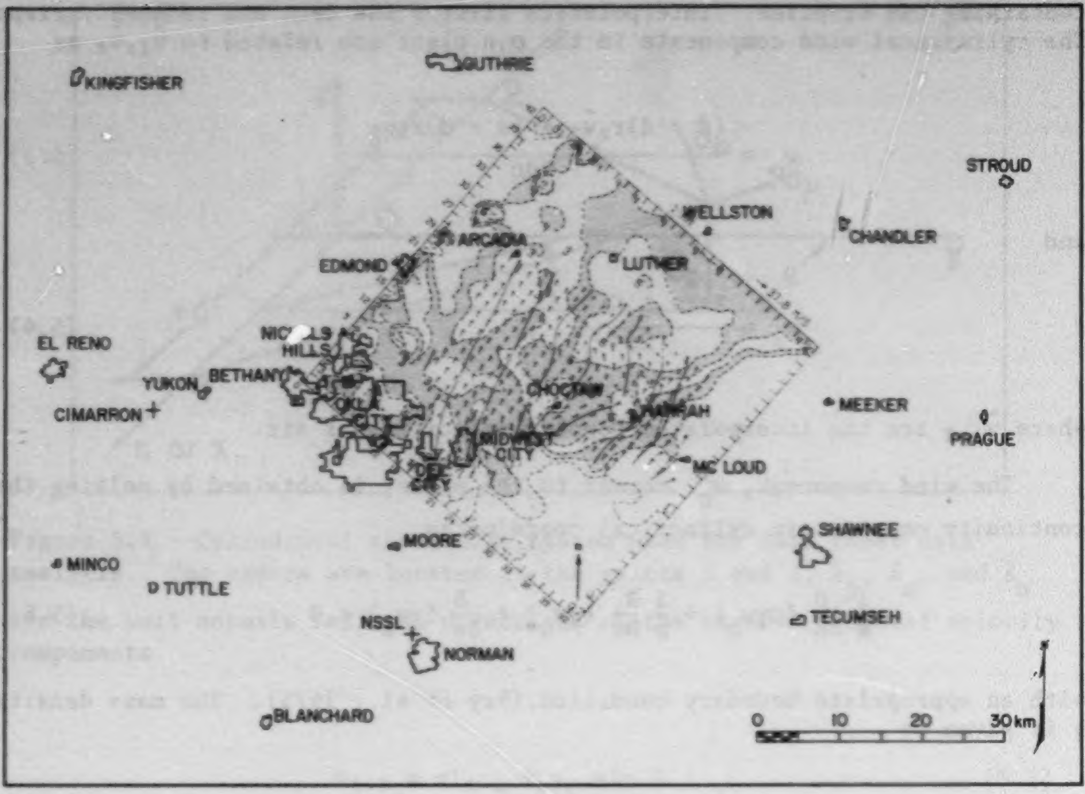
KINGFISHER
GUTHRIE
STROUD
WELLSTON
CHANDLER
ARCADIA
EDMOND
LUTHER
EL RENO
NICHOLS HILLS
YUKON
BETHANY
CIMARRON
OKLA CITY
CHOCTAW
HARRAH
MEEKER
PRAGUE
MIDWEST CITY
DEL CITY
MC LOUD
MOORE
SHAWNEE
MINCO
TUTTLE
NSSL
TECUMSEH
NORMAN
BLANCHARD
0 10 20 30 km

Figure 5.2.--Map of central Oklahoma with reflectivity field (shaded areas) and winds relative to the ground at a height of 1 km. Radar locations are marked with +. At this height maximum velocity was 37.8 m s^{-1}. Reflectivity contours (dashed lines) are labeled log Z (Ray et al., 1975).

To discern the storm's kinematic structure at several altitudes, the mean wind at each height is subtracted from the wind vector at each grid point. This perturbation velocity field is displayed at two heights in Fig. 5.3a. Cyclonic circulation is apparent at the grid point (30, 24), where vorticity was noticed in Fig. 5.2. Inflow into the tornadic cyclone is shown at an altitude of 3 km, and divergence and outflow are apparent at 7 km. High-reflectivity factor (60-dBZ) regions are located on the downwind side. These velocity fields are in general agreement with present storm models, particularly in the weak echo region, where both imply a strong updraft northeast of the circulation (Fig. 5.3b; X = 33, Y = 27.0 km). A downdraft (Fig. 5.3b; X = 33, Y = 22.5 km) is found to the southwest of the circulation.

b. Single Doppler radar

Although the Doppler radar measures only the radial wind component, its spatial distribution can signify meteorological events such as tornado cyclones. Moreover, strong straight winds, if not across the beam, can be measured as well as turbulent regions. Thus a single Doppler radar offers

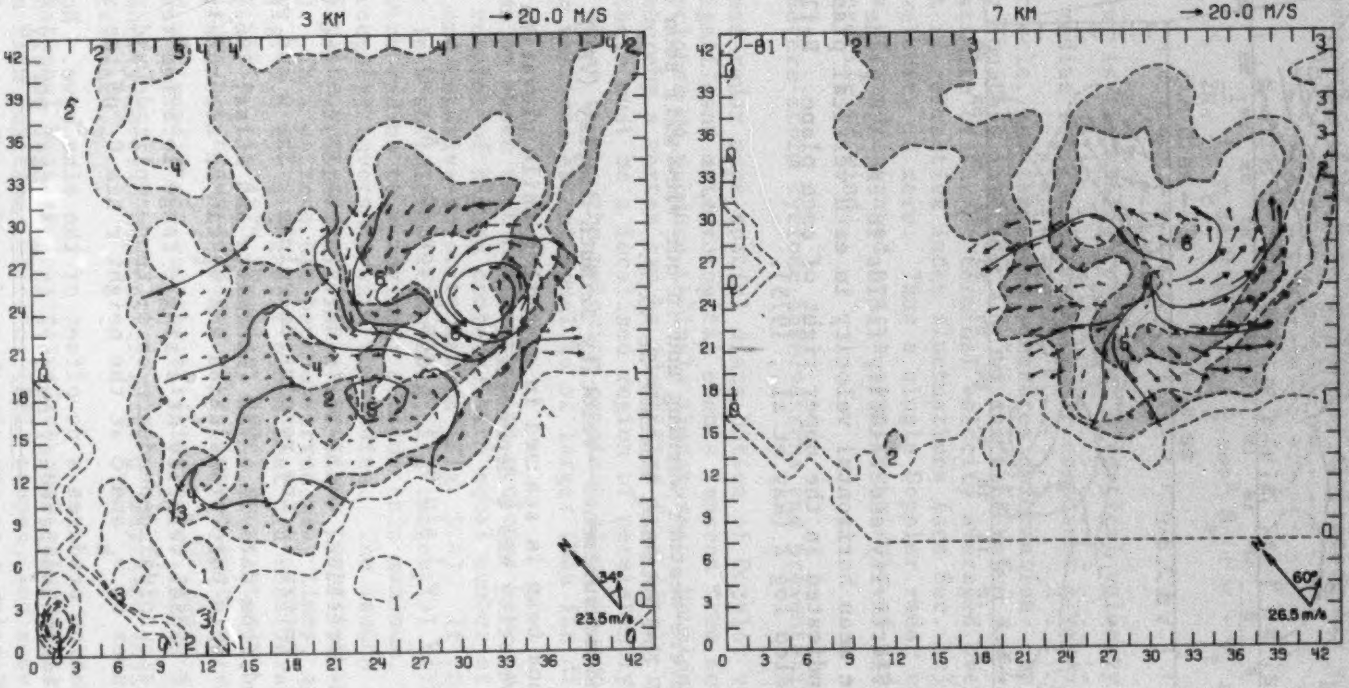

Figure 5.3a.--Perturbation wind and reflectivity factor (log Z) at 3-km and 7-km altitudes. Mean wind at each altitude is given in lower right corner. Velocity scale is above upper right corner. Distances are in kilometers from an origin s = -10, ρ = 15 km (s = 0 is the midpoint of the base line) and abscissa is parallel to $\hat{a}_s$.

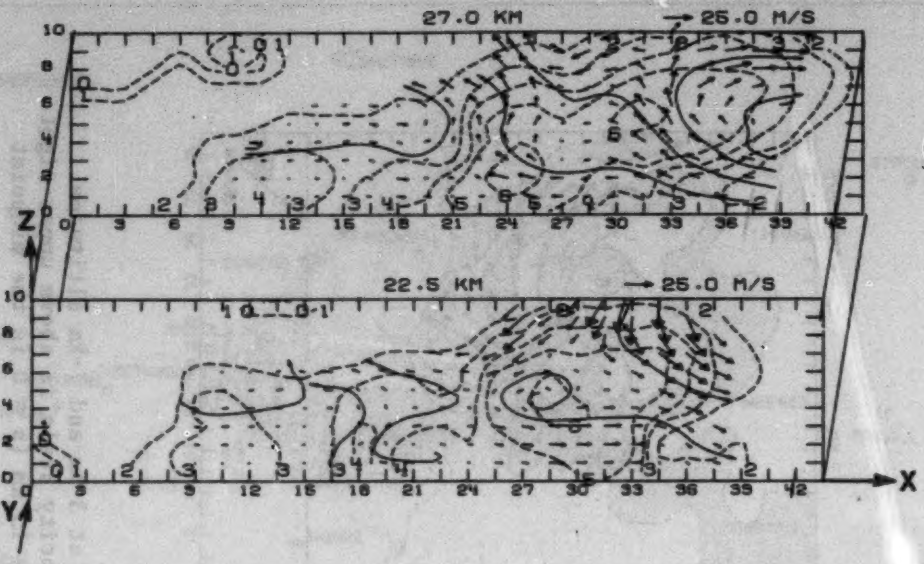

Figure 5.3b.--Reflectivity and velocity fields in the X,Z plane for 27 km and 22.5 km. The mean horizontal velocity in each vertical plane was removed and is indicated in the upper right of each plane. Reflectivity contours are labeled log Z (Ray et al., 1975).

good promise for severe-weather warning and in our view will soon become the operational tool of the National Weather Service.

(1) Linear wind measurements--velocity azimuth display (VAD)

When the antenna beam is scanned in azimuth ϕ while elevation angle θ_e is fixed, the radial velocity has ϕ dependence:

$$v_r = (w - v_t) \sin \theta_e + v_h \cos \theta_e \cos (\phi - \delta - \pi) , \qquad (5.7)$$

where δ is the wind direction, w the air's vertical velocity, and v_h the horizontal speed of tracers in the resolution volume. The w and v_h velocities are readily computed from data in a VAD (Lhermitte and Atlas, 1961) under the assumption that air is in pure translation and v_t can be accurately estimated. (VAD is a display of radial velocity at a single range location versus azimuth.) Then Eq. 5.7 has a sinusoidal dependence on ϕ; thus amplitude and phase of the sine curve are measures of v_h and δ at the height r sin θ_e of the sampling circle. Vertical motion produces a dc offset of the sine wave. However, when wind is not horizontally homogeneous, Eq. 5.7 is no longer purely sinusoidal.

Caton (1963) showed how divergence can be determined from VAD data. Browning and Wexler (1968) carried the analyses even further by assuming the wind field was well represented by a linear velocity field (Hess, 1959, p. 198) over the circle of measurement. With this assumption there are four basic fields of motion that convey air: translational, vortical, divergent, and deformative. Fourier analysis of V_r for linear wind reveals that only the vortical motion cannot be measured by the VAD method. The average component of V_r is proportional to mean horizontal divergence $\overline{\mathrm{DIV}\ v_h}$ plus mean $\overline{w - v_t}$:

$$\frac{1}{2\pi} \int_0^{2\pi} v_r d\phi = (\overline{\mathrm{DIV}\ v_h}) \frac{r}{2} \cos^2 \theta_e + \overline{w - v_t} \sin \theta_e, \qquad (5.8)$$

where $\overline{w - v_t}$ is the average of tracer's vertical velocity on the sampling circle of radius r. The first harmonic component gives $\bar{v}_h$ and $\bar{\delta}$ averaged over the circle, and the second measures deformation. By inserting the mass continuity equation into Eq. 5.8, we can then solve for vertical wind if we have an estimate of target terminal velocity averaged over the circle. If the target is refractive index fluctuations (see Sec. 5c), then clearly terminal velocity is zero. Thus a single Doppler radar can measure the three components of wind averaged over a sampling circle of radius r and produce a vertical profile of wind.

(2) Severe-storm cyclone observations and presentations

Because radar maps spatial distribution of Doppler velocity inside storms, significant meteorological events (unseen from outside) such as tornado cyclones do produce telltale signatures. Donaldson (1970) stipulated criteria whereby a vortex can be identified from single radar observations. Briefly, there must be a localized region of persistently high, $\geq 5 \times 10^{-3}\ s^{-1}$, azimuthal shear (i.e., the velocity gradient along an arc at constant range) that has a vertical extent equal to or larger than its diameter.

It can be shown that nontranslating cyclones have isodops forming a symmetric couplet of closed contours with equal number of isodops encircling positive- and negative-velocity maxima (Fig. 5.4). If the inner portion of the vortex is a solidly rotating core, its tangential velocity increases linearly with radius to a maximum; outside this maximum, the velocity decreases (roughly) inversely with the radius. The isodop contours of such a combined Rankine vortex are circular sections connected with straight lines (Fig. 5.4). This pattern has been observed many times, and an example is shown in Fig. 5.5 for a tornadic storm that did considerable damage to Stillwater, Okla., in 1975 (Burgess, 1976; Brown et al., 1978; Zrnic' et al., 1977). Figure 5.6 shows contours of estimated spectrum width σ_v for the same storm, and we immediately see the striking correlation of σ_v with significant radial velocity shear. Regions of large σ_v may also indicate the presence of strong turbulence.

The National Weather Service radars routinely display reflectivity factors on Plan Position Indicator (PPI) scopes, and some television stations, using their own radar, show the radar images on a color PPI display. The PPI projects any radar data field (but usually reflectivity factor) from the conical surface on which it is acquired onto the plane surface of the indicator. Although target reflectivity cannot be reliably used for tornado detec-

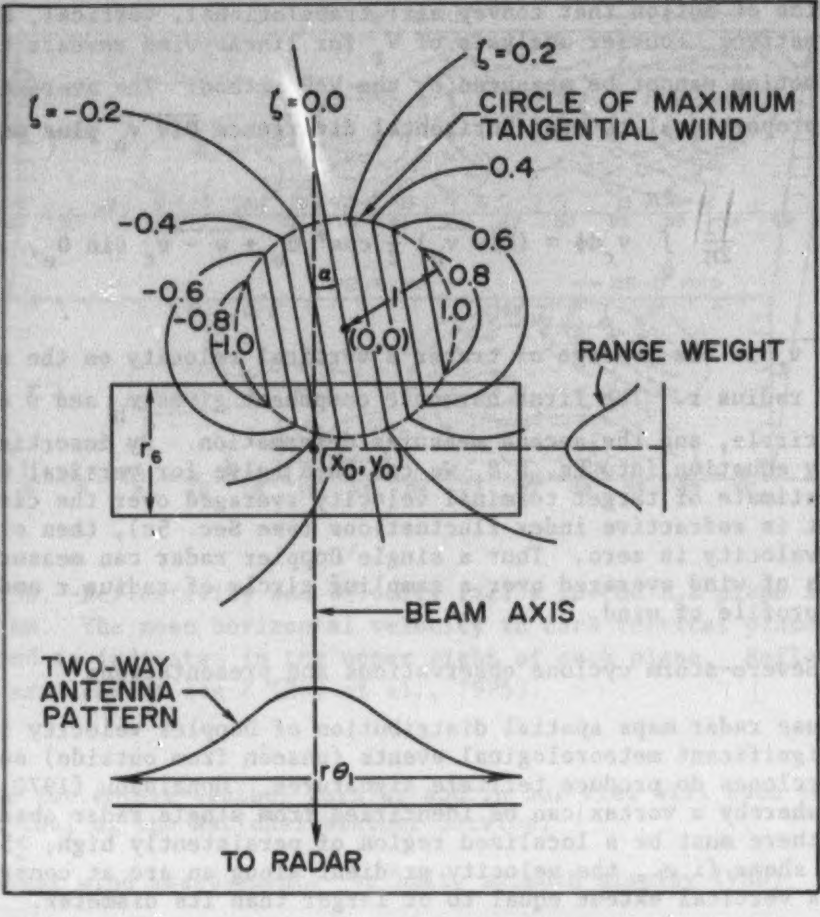
ζ=0.2
ζ=-0.2
ζ=0.0
CIRCLE OF MAXIMUM TANGENTIAL WIND
0.4
-0.4
0.6
α
0.8
-0.6
1.0
-0.8
-1.0
(0,0)
RANGE WEIGHT
r_6
(x_0, y_0)
BEAM AXIS
TWO-WAY ANTENNA PATTERN
$r\theta_1$
TO RADAR

Figure 5.4.--Plan view of idealized isodop pattern for a stationary modified Rankine vortex located at range large compared with vortex diameter. $\zeta = v/v_{max}$ is Doppler velocity normalized to peak tangential wind. Resolution volume, antenna, and range-weighting functions are depicted. The angular tilt α determines radial inflow ($\alpha < 0$) or outflow ($\alpha > 0$).

tion, it has proved valuable for hydrological studies and severe-weather warnings. Those warnings are primarily based on reflectivity values, storm top heights, and sometimes on circulatory features or "hook" echoes. However, PPI displays of Doppler velocity and spectrum width do vividly show signatures of circulations.

Color displays of reflectivity, velocity, and spectrum width allow, in real time, easier quantitative evaluation and better resolution of cyclones. Figure 5.7 is an example of Doppler radar data from a tornadic thunderstorm in central Oklahoma during the evening of 30 April 1978. These data were acquired with NSSL's 10-cm Doppler weather radar, and the pictures depict the fields of the three principal moments of the Doppler spectra.

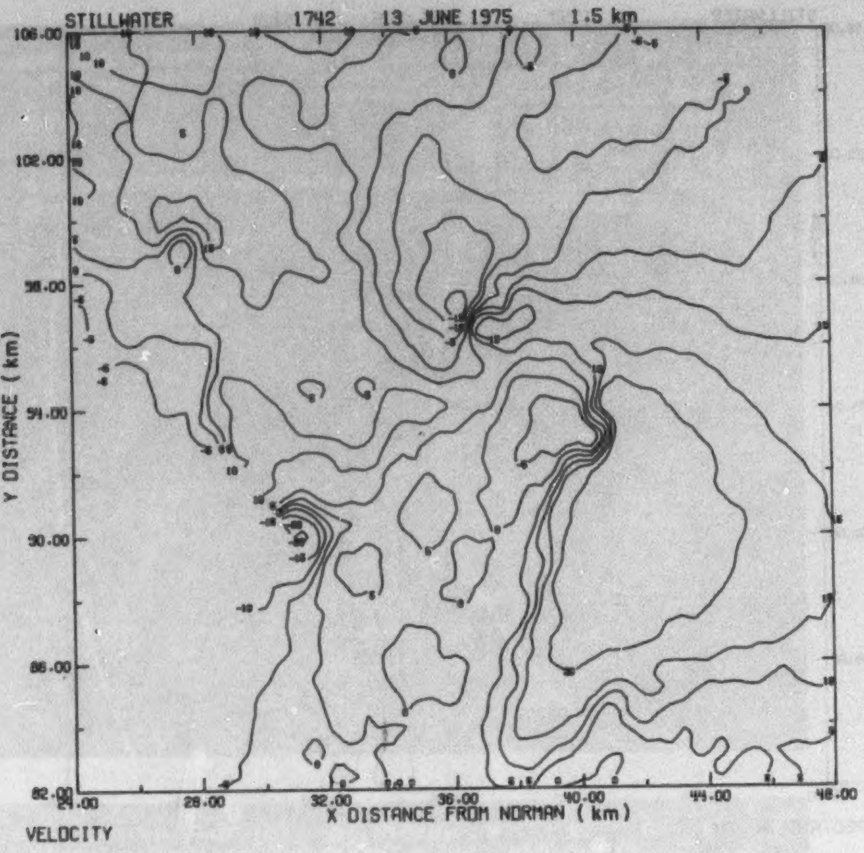

Figure 5.5.--Doppler velocity field for the Stillwater, Okla., storm at 1.5-km height. Velocities are in meters per second; contours (isodops) are in 5-m s^{-1} steps. The mesocyclone is centered at Y = 97 km, X = 36 km. The other shear region from 94 km north, 40 km east to the bottom of the field was identified from dual Doppler data to be the low-level boundary (gust front) between storm inflow to the east of the shear line and outflow to the west.

At the time of the display (1825:32), there was a tornado on the ground at 334° and 50-km range. Although the reflectivity display showed no evidence of a tornado cyclone, the mean Doppler velocity display (b) depicted it remarkably well. The velocity scale is in meters per second with + values (red) indicating motion away from the radar. The signature of a couplet of closed contours of opposing Doppler velocities (bright green next to bright red) indicates presence of the strong circulation associated with the tornado. The display (c) of spectrum width (σ_v) is an indicator of turbulence and shear within the radar's resolution volume. We note high spectrum width values in the vicinity of the circulation and one pinpointing the exact tornado spot.

Figure 5.7d is the multimoment display (MMD) (Burgess et al., 1976); each arrow is a speedometer indicating the Doppler speed at its respective location. Zero Doppler is an arrow pointing at the 3 o'clock position, and positive

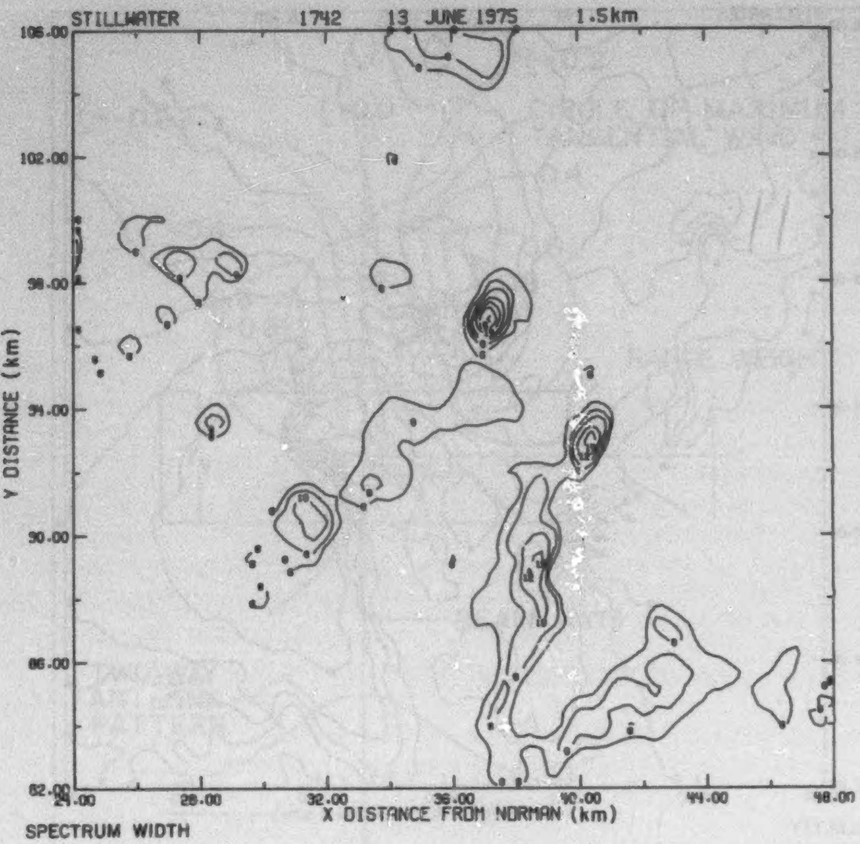

Figure 5.6.--Contours of constant spectrum width for the Stillwater, Okla., storm at 1.5 km above ground. Values equal to or larger than 6 m s^{-1} in steps of 2 m s^{-1} are displayed. Large widths farther north are where the tornado mesocyclone formed; the other region of large width is embedded in the gust front.

velocities (away) cause the vector to rotate counterclockwise (+17 m s^{-1} velocity is at the 12 o'clock position). Negative velocities cause arrows to point toward the bottom of the diagram (i.e., toward the radar). Reflectivity is indicated by arrow length and spectrum width by arrowhead size. The tornado circulation is depicted quite nicely by this graphic display, and the presence of wide spectra is evident by the broad arrowhead width, indicating strong shearing winds or turbulence.

(3) Doppler spectra of tornadoes

In 1961 Smith and Holmes reported a tornado spectrum that was obtained with a CW Doppler radar (Smith and Holmes, 1961); 12 years later a tornado was first observed by a pulsed Doppler radar (Zrnic' and Doviak, 1975).

The Doppler spectrum is principally influenced by the portion of circulation that lies within the resolution volume, so that tracers moving with the

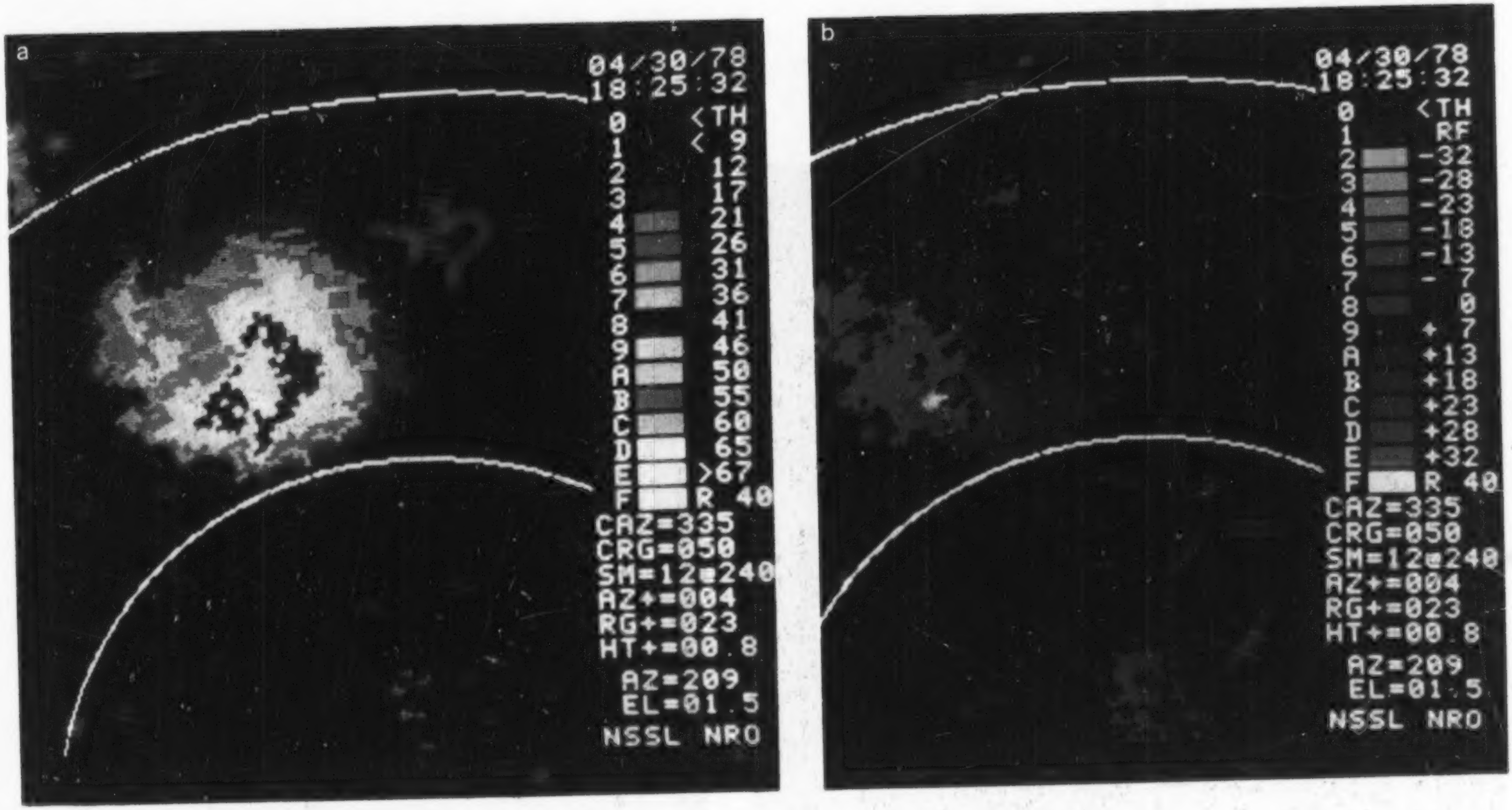
a
04/30/78
18:25:32
0 <TH
1 < 9
2 12
3 17
4 21
5 26
6 31
7 36
8 41
9 46
A 50
B 55
C 60
D 65
E >67
F R 40
CAZ=335
CRG=050
SM=12@240
AZ+=004
RG+=023
HT+=00.8
AZ=209
EL=01.5
NSSL NRO
b
04/30/78
18:25:32
0 <TH
1 RF
2 -32
3 -28
4 -23
5 -18
6 -13
7 - 7
8 0
9 + 7
A +13
B +18
C +23
D +28
E +32
F R 40
CAZ=335
CRG=050
SM=12@240
AZ+=004
RG+=023
HT+=00.8
AZ=209
EL=01.5
NSSL NRO

Figure 5.7.--(a) Display of storm reflectivity factor. Color categories are in dBZ = 10 log Z (mm^6 m^{-3}); range marks are 40 km apart. (b) Doppler velocity. Color categories are in meters per second.

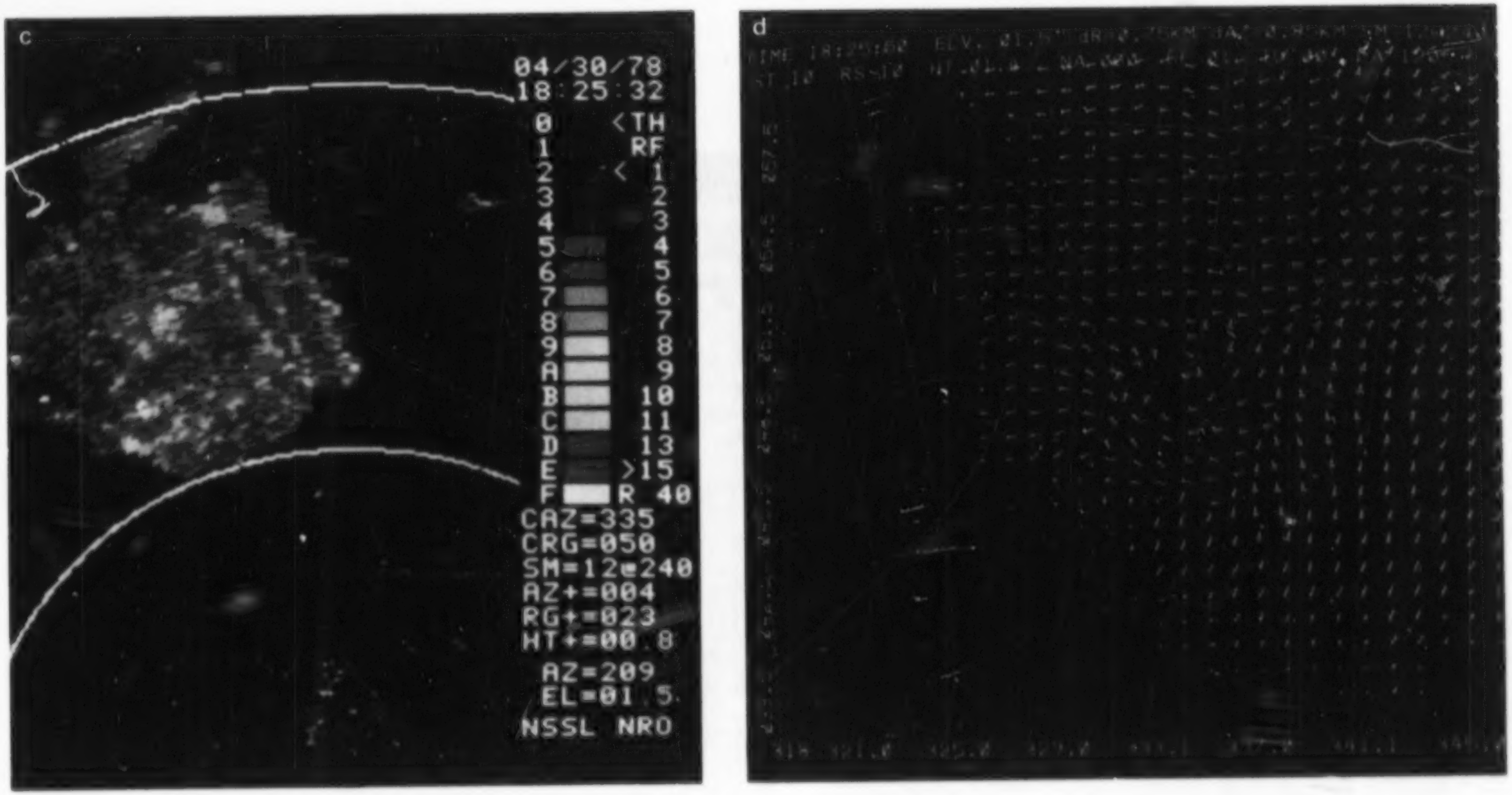
c
04/30/78
18:25:32
0 <TH
1 RF
2 < 1
3 2
4 3
5 4
6 5
7 6
8 7
9 8
A 9
B 10
C 11
D 13
E >15
F R 40
CAZ=335
CRG=050
SM=12@240
AZ+=004
RG+=023
HT+=00.8
AZ=209
EL=01.5
NSSL NRO
d

Figure 5.7. (continued)--(c) Display of spectrum width. Color categories are in meters per second. (d) Multimoment display that uses arrows to show composites of the three principal Doppler spectral moments for each resolution volume. In this B-scan format, azimuthal bearing (deg.) is indicated along the abscissa and range (km) along the ordinate.

same velocities contribute to spectrum components according to their reflectivity, isodop density, and antenna pattern illumination (see Fig. 5.4). Only those targets whose spectral power is above the receiver noise level may be positively identified. However, it has been our experience that tornadoes in a resolution volume offer enough reflectivity, due to debris and hydrometeors, that a large velocity span can be observed. It is not known at this writing whether tracers moving at the peak tornado windspeed can be resolved.

When centered on the beam axis, the Rankine vortex model predicts a bimodal spectrum that was observed experimentally several times (Zrnic' and Doviak, 1975; Zrnic' et al., 1977). Shown in Fig. 5.8 are Rankine model vortex spectra matched to data by a least-squares fit. The spectrum examples are from the Stillwater maxitornado. Maximum velocity of $92\ \mathrm{m\ s^{-1}}$ and tornado diameter of 300 m are deduced from the fitting. The deduced maximum velocity is larger than the radar's unambiguous velocity ($\pm 34.4\ \mathrm{m\ s^{-1}}$); therefore, aliasing has been introduced in the model spectrum and the estimates are indirect.

Two spectra closest to the tornado were simultaneously least-squares fitted. Simulated model vortex spectra and real spectra show very good agreement not only for the two where the fit was made but also for adjacent gate locations (Fig. 5.8). Resolution volumes corresponding to any of these simulated spectra are assumed to have uniform reflectivity within the volume. Differences in echo power from each resolution volume are accounted for by forcing each simulated spectrum to have power equal to its matching data spectrum. Asymmetry of spectral peaks (Az 21.1°; range 104.136 km) about zero velocity suggests that targets were centrifuged outward at a velocity of $13\ \mathrm{m\ s^{-1}}$.

(4) Application of Doppler radar in the National Weather Service

In view of the variety of displays and signatures associated with tornadoes, it is natural to ask which detection technique is most promising. A project involving the Environmental Research Laboratories, National Weather Service, Air Weather Service, and Air Force Geophysical Laboratory was established to conduct experiments that would provide some answers (NSSL, 1979). Operations were conducted during the spring of 1977 and 1978. It became apparent that mesocyclone circulations showed very nicely on the color display of radial velocities. Multimoment display (Burgess et al., 1976) in conjunction with the color display proved most suitable for tornado cyclone recognition. Using criteria discussed in Brown et al. (1978), the project scientists were able to detect all tornadoes that occurred within a range of less than 115 km (Burgess et al., 1978). The average lead time was about 20 minutes. It was established that circulation starts at middle-level altitudes (6-8 km) and works its way toward the ground. At ranges beyond 115 km, signatures of small tornadoes are lost because of poor resolution; however, large, destructive tornadoes were detected up to 240 km away using the 0.8° beam of NSSL's Doppler radar. Spectrum width and shear alone have not been reliable indicators of tornadoes since turbulent areas in storms can be very wide and could be easily mistaken for tornadoes. On the basis of those experiments, it is believed that an operational tornado detection system will involve interaction between human operators and an automated scheme in which the velocity pattern of a tornado cyclone is recognized.

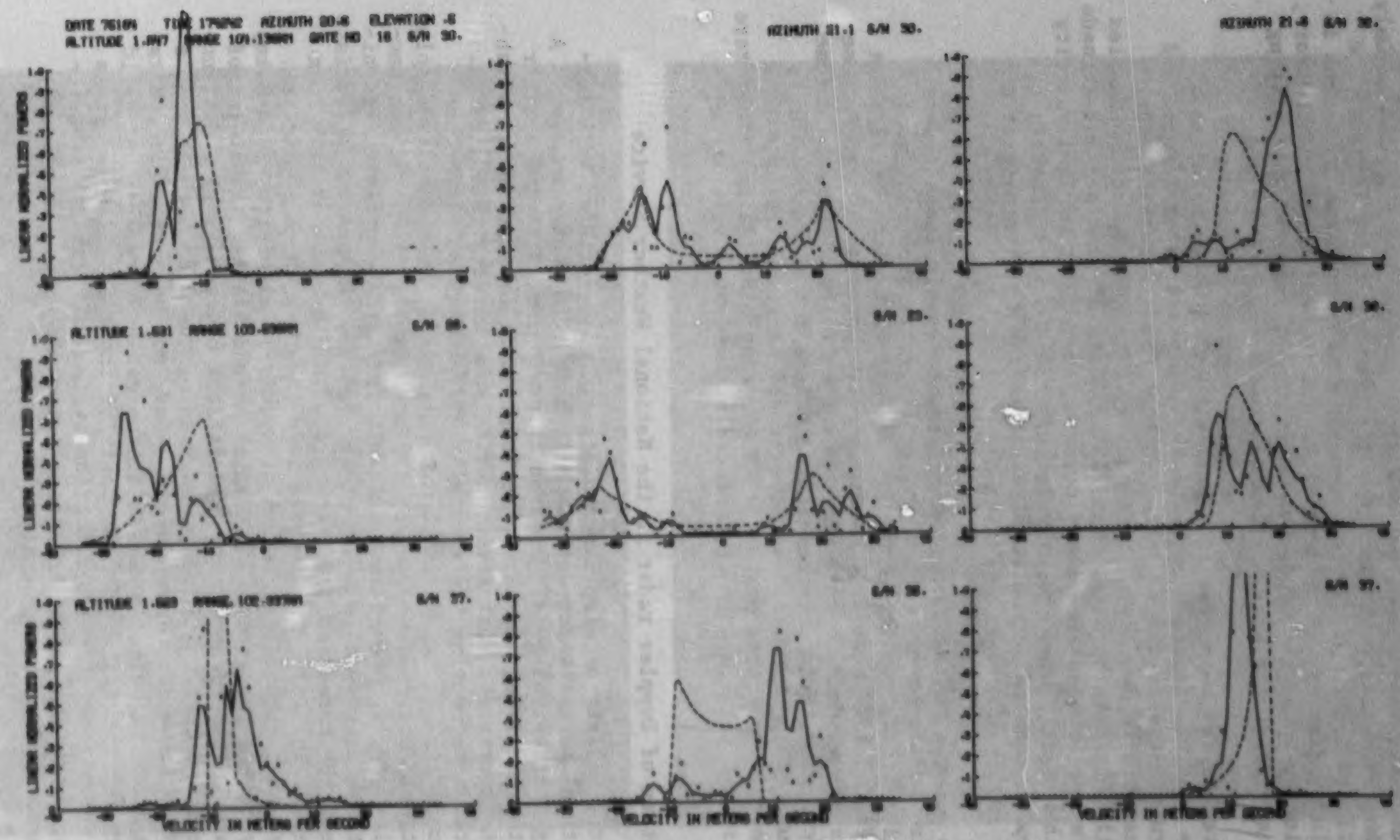

Figure 5.8.--Spectra from three consecutive azimuthal and range locations of Stillwater, Okla., tornado. Dots show spectrum estimates from recorded time series data weighted with a von Hann window. Solid lines are three-point running averages. Dashed lines are simulated spectra. The mean square difference between data and simulated spectra is simultaneously minimized for two spectra (Az = 21.1° and range of 103.5 and 104.1 km). Resolution volume depth is 150 m, range gate spacing 600 m, and antenna beamwidth 0.8°. The tornado is located between the two upper middle gates. Tornado parameters obtained from these two fitted spectra are used to compute the remaining seven simulated spectra. Height above ground for these spectra is 640 m.

c. Pulsed Doppler observation of clear-air wind fields

Whenever turbulence mixes air in which there are gradients of potential temperature and water vapor density, the turbulence causes spatial fluctuations in the refractive index n. The fluctuations are small (e.g., 1 part in 1 million). Nevertheless, sensitive microwave radars detect the very faint echoes returned from these irregularities in what otherwise (without turbulence) would be a smoothly changing n with negligible backscatter.

Echoes from clear air have been seen almost from the inception of radar observations. These "angel echoes" were at first mystifying, but often were associated with birds and insects. Clear-air echoes not related to any visible object in the atmosphere were conclusively proven to emanate from refractive index fluctuations through use of multiwavelength radars at Wallops Island (Hardy et al., 1966). Simultaneous measurements of refractive index fluctuations and reflectivity corroborated this finding (Saxton, 1964). The radar studies were preceded by many measurements using tropospheric-scatter communication links that often depend upon clear-air refractive index fluctuations to provide reliable wideband circuits between distance points (Rice et al., 1967; IEEE, 1955).

In the 1960's ultrasensitive incoherent radars were used to detect remotely and resolve clear-air atmospheric structure, and these studies are well reviewed by Hardy and Katz (1969). The radars showed meteorological phenomena such as convective thermals (Katz, 1966; Konrad, 1970), sea-and-land breezes (Meyer, 1970), and Kelvin-Helmholtz waves (Hicks and Angell, 1968).

Doppler processing of coherent radar echoes can improve target detection by at least an order of magnitude (Hennington et al., 1976), and hence medium-resolution weather radars could have a detection capability often associated with large-aperture (18- to 27-m diameter) antennas used with incoherent radars. Furthermore, a coherent radar provides a way in which ground clutter can be distinguished from moving atmospheric targets and allows data acquisition at closer ranges, thereby taking advantage of the r^{-2} dependence in echo power.

Chadwick et al. (1978) monitored reflectivity values associated with refractive index fluctuations in the planetary boundary layer and concluded after 1 year of observation that winds can always be measured to several hundred meters' height with moderately sensitive radars. Clear-air wind measurement has practical significance because pulsed Doppler radars under development by the FAA also could measure wind shear hazards near airports for all weather conditions (Lee and Goff, 1976).

Harrold and Browning (1971) found that radar can delineate the upper limit of convection before precipitation, showing that it is deeper in some regions than others. Some of these areas of deep convection persist for several hours, and, if showers develop, they occur within, and only within, such regions. Important economic advantage can be achieved if radars can locate aircraft weather hazards and predict the location of incipient showers.

Mapping boundary layer wind over large areas has double significance for severe-storm studies because it allows early observation of thunderstorm development--hence storm genesis can be followed from the very beginning of cumulus development--and the capability of Doppler weather radars to map clear-air wind makes it possible to monitor thunderstorm outflow, which is usually precipitation free.

Strongest fluctuations in refractive index occur where turbulence mixes large gradients of mean potential temperature and specific humidity (Yaglom, 1949). Gage et al. (1973) measured the height distribution of forward scattered signal strength to show good correlation between it and gradients of potential temperature at high altitudes, where water vapor contributions can be ignored. The tropopause is a region where potential temperature always increases with height; it was first detected by radar in 1966 (Atlas et al., 1966). More recently VanZandt et al. (1978), using backscatter results from a vertically pointed VHF radar, obtained consistent agreement between rawinsonde-inferred fluctuations and radar-measured ones for the clear air above the moist boundary layer.

For many years ionospheric scientists have been employing high-power VHF and UHF (Fig. 2.1) radars to observe the ionosphere. Recently these radars at Jicamarca, Peru (Woodman and Guillen, 1974); Arecibo, Puerto Rico; Chatanika, Alaska (Balsley, 1978); and Lindau, Germany (Röttger and Liu, 1978), have lowered their sights to examine echoes in the stratosphere and troposphere. A 6-m VHF ($\lambda = 7$ m) pulsed Doppler radar specifically designed for tropospheric studies was assembled at Sunset, Colo., to make continuous observations of winds in the troposphere (Green et al., 1975). Some advantages of the VHF radar are that it can sometimes differentiate between scatter from hydrometeors and refractive index fluctuations (Green et al., 1978) and that it might be able to detect coherent scatter from mean refractive index gradients at inversion layers (Gage and Green, 1978).

Clear-air winds in the planetary boundary layer (PBL, i.e., surface to heights of about 1.5 km) have been synthesized from dual Doppler radar measurements (Gossard and Frisch, 1976; Kropfli and Kohn, 1978), wherein chaff was dispensed over large areas to provide suitable echo levels for detection and processing. Doviak and Jobson (1979) showed first results of two Doppler radar-synthesized wind fields in the PBL clear air, where only the diffuse and intrinsic scatterers of the medium were used as targets. They observed mean wind fields at low height to have qualitative agreement with mean wind measured (with conventional anemometers) near the surface.

On 27 April 1977, a day marked by strong nondirectional shear and curvature in the wind profile, NSSL's Doppler radar echo power measurements showed evidence of clear-air convective streets (Fig. 5.9), an observation that should signify the presence of roll vortices. First radar detection of clear-air "thermal streets" was reported by Konrad (1968).

Figure 5.10 locates the Cimarron (CIM) and Norman (NRO) radars and a 444-m meteorologically instrumented tower. Reasonably accurate winds can be synthesized from Doppler data in the entire area enclosed by the dashed lines. The winds were fairly uniform from the southwest on this day, but there were small perturbations from the mean wind having a magnitude about one order less than the mean wind itself. The synthesized wind field and its perturbations from the mean are shown in Figs. 5.11a and b.

Berger and Doviak (1979) have examined the spatial spectra of the synthesized winds on this convectively dry day and have compared results with those spectra obtained from anemometers located on the tall tower. The

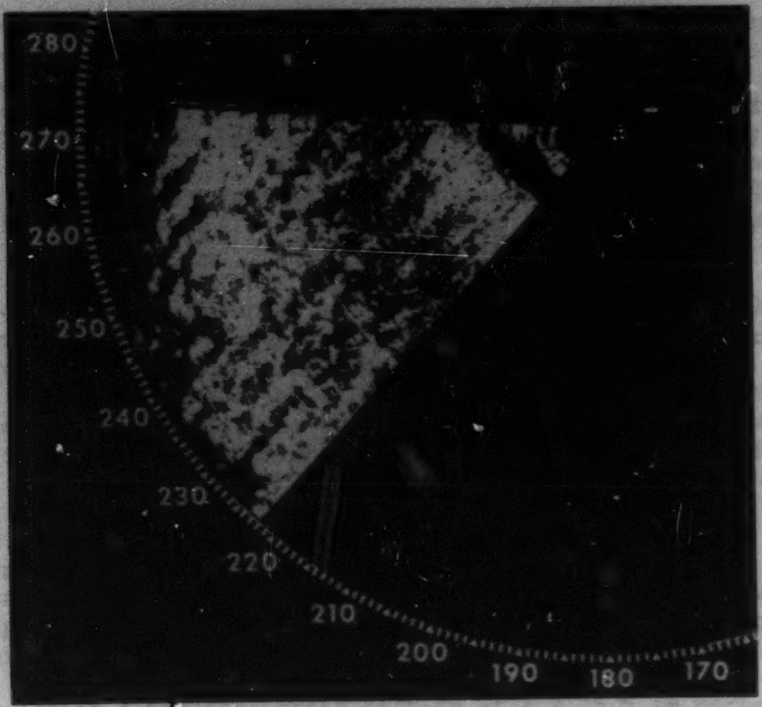

Figure 5.9.--PPI sector scan of echo power from clear air as seen by the NSSL Doppler radar. The bright area of higher power is aligned roughly parallel to mean wind, and the bands are spaced about 4 km apart. Range marks are 20 km apart. EL = 1.6° (27 April 1977, 1447 CST).

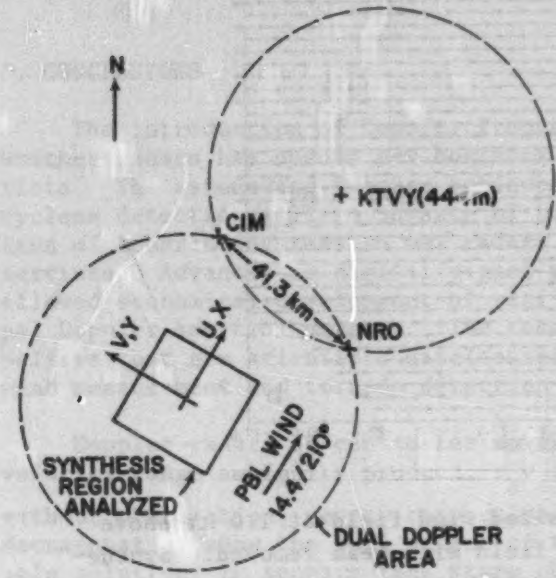
N
+ KTVY(44-.m)
CIM
41.3 km
NRO
V,Y
U,X
PBL WIND
14.4/210°
SYNTHESIS
REGION
ANALYZED
DUAL DOPPLER
AREA

Figure 5.10.--The dual Doppler-radar area (dashed lines) within which the angle subtended by the radials from the Cimarron (CIM) and Norman (NRO) radars lies between 30° and 150°. The outlined box is the region for which the PBL Doppler velocities were synthesized for detailed wind analyses. The windspeed and direction are a mean over 1.25-km depth of the PBL.

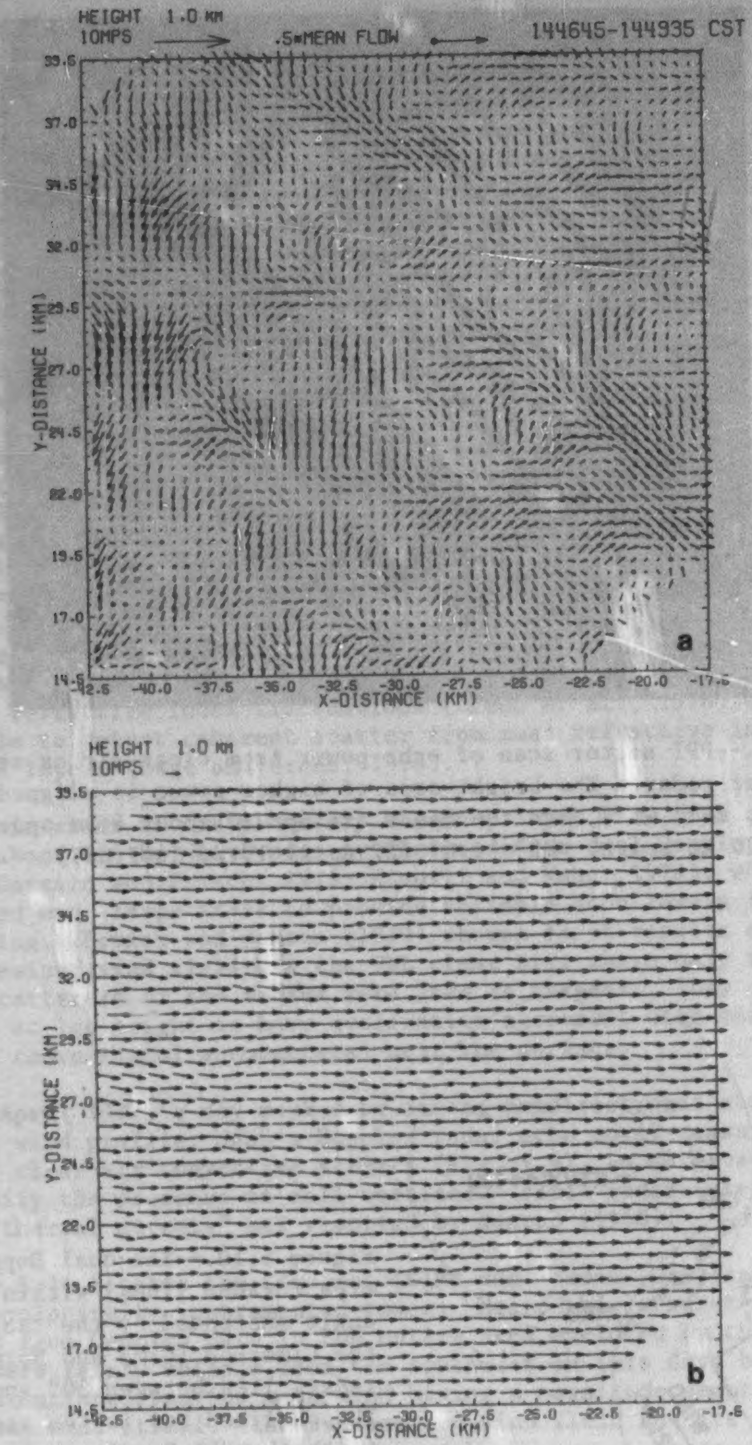

Figure 5.11.--(a) Dual radar synthesized wind field at 1.0 km above ground for 27 April 1977. (b) Wind field with mean removed. Synthesized wind fields were low pass filtered once in X and Y direction with a three-point Shuman (1957) filter.

spectra follow a 5/3 power law in the wavelength range of 1 to 8 km in agreement with spectra of tower winds. The v component spectrum in the y direction (Fig. 5.10) has a peak at 4-km wavelength that persisted over the 1 hour of data collection. Spectral analyses of clear-air longitudinal wind fluctuations using chaff and a single Doppler radar have been reported by Chernikov et al. (1969). Their spectra, extending to 3-km wavelengths, also show a 5/3 power law dependence in agreement with results on this day. However, O'Bannon (1978) shows spectra on another day when such a power dependence is not evident.

Some theories (e.g., Kuettner, 1971; Gossard and Moninger, 1975) suggest that roll vortices tend to form parallel to the mean wind in a strongly heated PBL having a large, unidirectional shear. Keuttner (1971) predicts rolls to have a horizontal spacing of 2.8 times their depth when vertical profiles of horizontal velocity have curvature. The strong 4-km wave in the y direction of the v component might be the convective rolls predicted by theory.

Figure 5.12a depicts perturbation winds observed on 27 April at one of six levels synthesized from a tilt sequence of each Doppler radar. A band pass filter was applied in the y direction to emphasize the 4-km wave feature seen in the spectral displays. A low pass filter was applied in the x direction along which no dominant wavelength was noted.

Figure 5.12b is a vertical cross section at X = 25.5 km perpendicular to the mean wind. Vertical velocities were derived by integrating the mass continuity equation using wind fields from the six horizontal surfaces. Vertical grid spacing is 250 meters. Readily apparent are counterrotating vortices (roll vortices), having approximately 4-km wavelength, whose maximum vertical velocities are approximately 1 m s^{-1}. Furthermore, the ratio of roll spacing to height is 2.6, in good agreement with that predicted by theory. Gilmer et al. (1978) analyzed aircraft gust probe data collected on this day during the time of the radar observation. They too detected a prominent peak in power density at a wavelength of about 4 km in the y direction.

6. CONCLUSIONS

The introduction of Doppler frequency shift measurement capability into weather radars has opened new horizons for exploration by atmospheric scientists. The astounding success achieved with these radars in thunderstorm cyclone detection well in advance of tornado formation should cause incorporation of coherent systems in new radars used for operation by the national services. Advances in digital signal processing and display techniques have allowed economical development of real-time presentation of the three principal Doppler spectral moments. The techniques are constantly improving, and we believe that new scientific disclosures and new operational applications in wind measurement and tornado detection are forthcoming.

Doppler radars at centimeter wavelengths do not have a sufficiently large velocity-range ambiguity product, $r_a v_a$, to match that required to observe, without obscuration, severe convective storms. No comprehensive data and documentation show the full extent of the problem, nor is there any foreseeable solution; it appears that storm observers will have to accept some limitations in Doppler radar weather measurements.

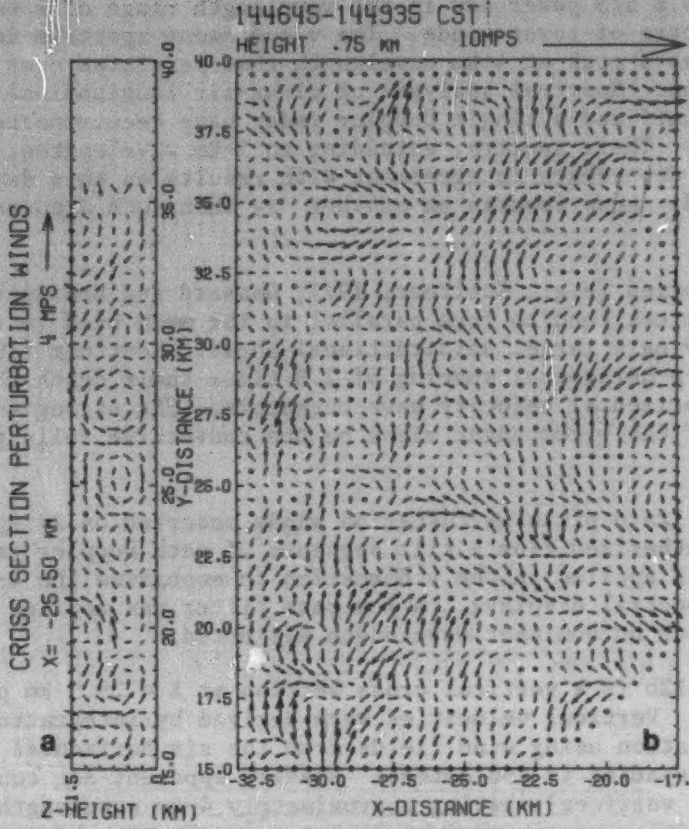

Figure 5.12.--Horizontal (a) and vertical (b) cross sections of band pass filtered wind data that highlight the clear-air roll structure seen in the spectra displays of unfiltered data for 27 April 1977.

Dual Doppler radar observations of the kinematic structure of severe storms and the planetary boundary layer agree with theoretical models, but much investigation is still required. The Doppler weather radar shows promise of greatly increasing our knowledge of thunderstorms and the planetary boundary layer on scales not before possible. Furthermore, we can monitor significant mesoscale phenomena that are of importance to air traffic safety and air pollution control, and we may be able to see the triggering impulses of severe storms that each year cause such destruction. Increased power and sensitivity of weather radars may soon result in meteorologists being able to observe the wind structure and its evolution throughout the troposphere.

The important advances in meteorological observations brought forth by the application of Doppler techniques to weather radars will continue in the future. There is room for further improvement in the radar system to reduce the effect of ambiguities while lessening data acquisition time for observation of severe-storm convection, shear, and turbulence in clear or precipitation-laden air.

Acknowledgments

The authors appreciate the support they have received from their colleagues in the Environmental Research Laboratories, Air Force Geophysics Laboratory, National Weather Service, Energy Research and Development Administration, Nuclear Regulatory Commission, and Federal Aviation Administration, not only in the preparation of this paper, but also for the continuing development of Doppler weather radar technology. We are indebted to Ms. Joy Walton and Ms. Connie Hall for efficient and accurate typing and preliminary editing of the manuscript.

REFERENCES

Abramowitz, M., and I. A. Stegun, 1964. Handbook of mathematical functions. National Bureau of Standards, Appl. Math. Ser. 55, U. S. Government Printing Office, Washington, D.C.

Armijo, L., 1969. A theory for the determination of wind and precipitation velocities with Doppler radars. J. Atmos. Sci. 26:570-573.

Atlas, D., 1964. Advances in radar meteorology. In Advances in Geophysics, Landsberg and Mieghem (eds.), Academic Press, New York, 317-478.

Atlas, D., K. R. Hardy, K. M. Glover, I. Katz, and T. G. Konrad, 1966. Tropopause detected by radar. Science 153:1110-1112.

Atlas, D., R. C. Srivastava, and R. S. Sekhon, 1973. Doppler radar characteristics of precipitation at vertical incidence. Rev. Geophys. Space Phys. 2:1-35.

Balsley, B. B., 1978. The use of sensitive coherent radars to examine atmospheric parameters in the height range 1-100 km. Preprints, Eighteenth Conference on Radar Meteorology. American Meteorological Society, Boston, Mass., 190-193.

Battan, L. J., 1973. Radar Observation of the Atmosphere. University of Chicago Press, Chicago, Ill.

Bean, B. R., and E. J. Dutton, 1966. Radio Meteorology. National Bureau of Standards Monogr. 92, U. S. Government Printing Office, Washington, D.C.

Berger, M. I., and R. J. Doviak, 1979. An analysis of the clear air planetary boundary layer wind synthesized from NSSL's dual Doppler-radar data. Tech. Memo. ERL NSSL-87, NOAA Environmental Research Laboratories, Boulder, Colo.

Blake, L. V., 1970. Prediction of radar range. In Radar Handbook, M. I. Skolnik (ed.), McGraw-Hill Book Co., New York, 2.1-2.73.

Born, M., and E. Wolf, 1964. Principles of Optics. 2nd ed., The Macmillan Co., New York, 808 pp.

Brandes, E. A., 1975. Optimizing rainfall estimates with the aid of radar. J. Appl. Meteorol. 14:1339-1345.

Brown, R. A., L. R. Lemon, and D. W. Burgess, 1978. Tornado detection by pulsed Doppler-radar. Mon. Weather Rev. 106:29-38.

Browning, K. A., and R. Wexler, 1968. The determination of kinematic properties of a wind field using Doppler radar. J. Appl. Meteorol. 7:105-113.

Burgess, D. W., 1976. Single Doppler radar vortex recognition: part I--mesocyclone signatures. Preprints, Seventeenth Conference on Radar Meteorology. American Meteorological Society, Boston, Mass., 97-103.

Burgess, D. W., L. D. Hennington, R. J. Doviak, and P. S. Ray, 1976. Multimoment Doppler display for severe storm identification. J. Appl. Meteorol. 15:1302-1306.

Burgess, D. W., J. D. Bonewitz, and D. R. Devore, 1978. Joint Doppler operational project: results year 1. Preprints, Eighteenth Conference on Radar Meteorology. American Meteorological Society, Boston, Mass., 442-448.

Caton, P. A. F., 1963. Wind measurement by Doppler radar. Meteorol. Mag. 92:213-222.

Chadwick, R. B., K. P. Moran, and G. E. Morrison, 1978. Measurements toward a C_n^2 climatology. Preprints, Eighteenth Conference on Radar Meteorology. American Meteorological Society, Boston, Mass., 100-103.

Chernikov, A. A., Y. V. Mel'nichuk, N. Z. Pinus, S. M. Shmeter, and N. K. Vinnichenko, 1969. Investigations of the turbulence in convective atmosphere using radar and aircraft. Radio Sci. 4:1257-1259.

Crane, R. K., 1979. Automatic cell detection and tracking. IEEE Trans. Geosci. Electron. GE-17(4):250-261.

Crawford, K. C., 1977. The design of a multivariate mesoscale field experiment. Ph.D. dissertation, University of Oklahoma, Norman.

Donaldson, R. J., Jr., 1970. Vortex signature recognition by a Doppler radar. J. Appl. Meteorol. 9:661-670.

Doviak, R. J., and C. T. Jobson, 1979. Dual Doppler radar observations of clear air wind perturbations in the planetary boundary layer. J. Geophys. Res. 84:697-702.

Doviak, R. J., and D. S. Zrnic', 1979. Receiver bandwidth effect on reflectivity and Doppler velocity estimates. J. Appl. Meteorol. 18:69-76.

Doviak, R. J., D. Burgess, L. Lemon, and D. Sirmans, 1974. Doppler velocity and reflectivity structure observed within a tornadic storm. J. Rech. Atmos. 8:235-243.

Doviak, R. J., P. S. Ray, R. G. Strauch, and L. J. Miller, 1976. Error estimation in wind fields derived from dual-Doppler radar measurement. J. Appl. Meteorol. 15:868-878.

Doviak, R. J., D. Sirmans, D. Zrnic', and G. B. Walker, 1978. Considerations for pulse-Doppler radar observations of severe thunderstorms. J. Appl. Meteorol. 17:189-205.

Doviak, R. J., D. S. Zrnic', and D. Sirmans, 1979. Doppler weather radar. Proc. IEEE 67:1522-1553.

Foote, G. B., and P. S. duToit, 1969. Terminal velocity of raindrops aloft. J. Appl. Meteorol. 8:249-253.

Frisch, A. S., and R. G. Strauch, 1976. Doppler radar measurements of turbulent kinetic energy dissipation rates in a northeastern Colorado storm. J. Appl. Meteorol. 15:1012-1017.

Frisch, A. S., L. J. Miller, and R. G. Strauch, 1974. Three-dimensional air motion measured in snow. Geophy. Res. Lett. 1:86-89.

Gage, K. S., and J. L. Green, 1978. Evidence for specular reflection from monostatic VHF radar observations of the stratosphere. Radio Sci. 13:991-1001.

Gage, K. S., W. P. Birkemeyer, and W. H. Jasperson, 1973. Atmospheric stability measurement at tropopause altitudes using forward-scatter CW radar. J. Appl. Meteorol. 12:1205-1212.

Gilmer, R. O., R. E. McGavin, and R. F. Reinking, 1978. A small aircraft gust probe system for studies of boundary layer convection and transport. Preprints, Fourth Symposium on Meteorological Observations and Instruments, 10-14 April. American Meteorological Society, Boston, Mass., 426-432.

Gossard, E. E., and A. S. Frisch, 1976. Kinematic models of a dry convective boundary layer compared with dual Doppler-radar observations of wind fields. Boundary-Layer Meteorol. 10:311-330.

Gossard, E. E., and W. R. Moninger, 1975. The influence of a capping inversion on the dynamic and convective instability of a boundary layer model with shear. J. Atmos. Sci. 32:2111-2124.

Green, J. L., J. M. Warnock, R. H. Winkler, and T. E. VanZandt, 1975. Studies of winds in the upper troposphere with a sensitive VHF radar. Geophys. Res. Lett. 2:19-21.

Green, J. L., R. H. Winkler, J. M. Warnock, W. L. Clark, K. S. Gage, and T. E. VanZandt, 1978. Observations of enhanced clear air reflectivity associated with convective clouds. Preprints, Eighteenth Conference on Radar Meteorology. American Meteorological Society, Boston, Mass., 88-93.

Gunn, K. L. S., and T. W. R. East, 1954. The microwave properties of precipitation particles. Q. J. R. Meteorol. Soc. 80:522-545.

Hardy, K. R., and I. Katz, 1969. Probing the clear atmosphere with high power, high resolution radars. Proc. IEEE 57:468-480.

Hardy, K. R., D. Atlas, and K. M. Glover, 1966. Multiwavelength backscatter from the clear atmosphere. J. Geophys. Res. 71:1537-1552.

Harrold, T. W., and K. A. Browning, 1971. Identification of preferred areas of shower development by means of high power radar. Q. J. R. Meteorol. Soc. 97:330-339.

Hennington, L., R. J. Doviak, D. Sirmans, D. Zrnic', and R. G. Strauch, 1976. Measurements of winds in the optically clear air with microwave pulse-Doppler radar. Preprints, Seventeenth Conference on Radar Meteorology. American Meteorological Society, Boston, Mass., 342-348.

Herman, B. M., S. R. Browning, and L. J. Battan, 1961. Tables of the radar cross sections of water sphere. Tech. Rep. No. 9, Institute of Atmospheric Physics, University of Arizona, Tucson.

Hess, S. L., 1959. Introduction to Theoretical Meteorology. Holt, Rinehart and Winston, New York.

Hicks, J. J., and J. K. Angell, 1968. Radar observations of breaking gravitational waves in the visually clear atmosphere. J. Appl. Meteorol. 7:114-121.

Hitschfeld, W., and A. S. Dennis, 1956. Turbulence in snow generating cells. Sci. Rep. MW-23, McGill University, Montreal, 31 pp.

IEEE (Institute of Electrical and Electronics Engineers), 1955. Scatter propagation issue. Proc. IEEE (formerly IRE) 43:1173-1570.

Jordan, E. C., 1950. Electromagnetic Waves and Radiating Systems. Prentice-Hall, Inc., Englewood Cliffs, N. J.

Katz, I., 1966. Sea breeze structure as seen by radar. Memo. BPD 66U-25, Appl. Phys. Lab., Johns Hopkins University, Baltimore, Md.

Konrad, T. G., 1968. The alignment of clear air convective cells. Preprints, International Conference on Cloud Physics, Toronto, Ontario. American Meteorological Society, Boston, Mass., 539-543.

Konrad, T. G., 1970. The dynamics of the convective process in the clear air as seen by radar. Preprints, Fourteenth Conference on Radar Meteorology, Tucson, Arizona. American Meteorological Society, Boston, Mass., 57-60.

Kraus, J. D., 1966. Radio Astronomy. McGraw-Hill Book Co., New York.

Kropfli, R. A., and N. M. Kohn, 1978. Persistent horizontal rolls in the urban mixed layer as revealed by dual-Doppler radar. J. Appl. Meteorol. 17:669-676.

Kuettner, J. P., 1971. Cloud bands in the Earth's atmosphere. Tellus 23:404-425.

Lee, J. T., 1977. Application of Doppler weather radar to turbulence measurements which affect aircraft. Final Rep. FAA-RD-77-145, Systems Research Development Service, Federal Aviation Administration, Washington, D.C.

Lee, J. T., and C. Goff, 1976. Gust front wind shear and turbulence--concurrent aircraft and surface based observations. Preprints, Seventh Conference on Aerospace and Aeronautical Meteorology and Symposium on Remote Sensing from Satellites, Melbourne, Florida. American Meteorological Society, Boston, Mass., 48-54.

Lhermitte, R. M., 1970. Dual-Doppler radar observations of convective storm circulation. Preprints, Fourteenth Radar Meteorological Conference, Tucson, Arizona. American Meteorological Society, 153-156.

Lhermitte, R. M., and D. Atlas, 1961. Precipitation motion by pulse Doppler radar. Preprints, Ninth Weather Radar Conference, 23-26 October, Kansas City, Missouri. American Meteorological Society, Boston, Mass., 218-223.

Meyer, J. H., 1970. Radar observations of land breeze fronts at Wallops Island, Virginia. Preprints, Fourteenth Conference on Radar Meteorology, Tucson, Arizona. American Meteorological Society, Boston, Mass., 61-67.

Nathanson, F. E., 1969. Radar Design Principles. McGraw-Hill Book Co., New York.

Nathanson, F. E., and P. L. Smith, 1972. A modified coefficient for the weather radar equation. Preprints, Fifteenth Radar Meteorological Conference, Champaign-Urbana, Illinois, 10-12 October. American Meteorological Society, Boston, Mass., 228-230.

NSSL (National Severe Storms Laboratory), 1979. Final report on the Joint Doppler Operational Project (JDOP), 1976-78. Tech. Memo. ERL NSSL-86, NOAA Environmental Research Laboratories, Boulder, Colo., 84 pp.

O'Bannon, T., 1978. A study of dual-Doppler synthesized clear air wind fields. Preprints, Eighteenth Conference on Radar Meteorology. American Meteorological Society, Boston, Mass., 65-69.

Papoulis, A., 1965. Probability Random Variables and Stochastic Processes. McGraw-Hill Co., New York.

Probert-Jones, J. R., 1962. The radar equation in meteorology. Q. J. R. Meteorol. Soc. 88:485-495.

Ray, P. S., R. J. Doviak, G. B. Walker, D. Sirmans, J. Carter, and B. Bumgarner, 1975. Dual-Doppler observation of a tornadic storm. J. Appl. Meteorol. 14:1521-1530.

Rideout, V. C., 1954. Active Networks. Prentice-Hall, Inc., Englewood Cliffs, N. J., 311 pp.

Rice, P. L., A. G. Langley, K. A. Norton, and A. P. Barsis, 1967. Transmission loss predictions for tropospheric communication circuits. National Bureau of Standards Tech. Note 101, vols. 1-2, U. S. Government Printing Office, Washington, D.C.

Röttger, J., and C. H. Liu, 1978. Partial reflection and scattering of VHF radar signals from the clear atmosphere. Geophys. Res. Lett. 5:357-360.

Saxton, A. (ed.), 1964. Advances in Radio Research. Academic Press, New York, 226 pp.

Sherman, J. W., III, 1970. Aperture-antenna analysis. In Radar Handbook, M. I. Skolnik (ed.), McGraw-Hill Book Co., New York, 9.1-9.40.

Shuman, F. G., 1957. Numerical methods and weather predictions, II. Mon. Weather Rev. 85:357-387.

Silver, S., 1949. Microwave Antenna Theory and Design. McGraw-Hill Book Co., New York, 623 pp.

Sirmans, D., and R. J. Doviak, 1973. Meteorological radar signal intensity estimation. Tech. Memo. ERL NSSL-64, NOAA Environmental Laboratories, Boulder, Colo.

Skolnik, M. I., 1970. Radar Handbook. McGraw Hill Book Co., New York.

Smith, R. L., and D. W. Holmes, 1961. Use of Doppler radar in meteorological observations. Mon. Weather Rev. 89:1-7.

Stackpole, J. D., 1961. The effectiveness of raindrops as turbulence sensors. Preprints, Ninth Weather Radar Conference, Kansas City, Missouri. American Meteorological Society, Boston, Mass., 212-217.

Sychra, J., 1972. Relation between real and pulse volume averaged fields of reflectivity and velocity. Canadian Meteorol. Service Res. Report CMRR 5/72.

Taylor, J. W., and J. Mattern, 1970. Receivers. In Radar Handbook, M. I. Skolnik (ed.), McGraw-Hill Book Co., New York, 5.1-5.50.

VanZandt, T. E., J. L. Green, K. S. Gage, and W. L. Clark, 1978. Vertical profiles of refractivity turbulence structure constant: comparison of observations by the sunset radar with new theoretical model. Radio Sci. 13:819-829.

Waldteufel, P., 1976. An analysis of weather spectra variance in a tornadic storm. Tech. Memo. ERL NSSL-76, NOAA Environmental Research Laboratories, Boulder, Colo.

Woodman, R. F., and A. Guillen, 1974. Radar observations of winds and turbulence in the stratosphere and mesosphere. J. Atmos. Sci. 31:493-505.

Yaglom, A. M., 1949. On the local structure of the temperature field in a turbulent flow. Dokl. Akad. Nauk. SSSR 69:743.

Zeoli, G. W., 1971. IF versus video limiting for two-channel coherent signal processors. IEEE Trans. Inform. Theory IT-17:579-587.

Zrnic', D. S., 1975a. Estimated tornado spectra and maximum velocity statistics. NOAA Final Rep. Grant No. 04-5-022-17.

Zrnic', D. S., 1975b. Signal-to-noise ratio in the output of nonlinear devices. IEEE Trans. Inform. Theory IT-21:662-663.

Zrnic', D. S., and B. Bumgarner, 1975. Receiver chain and signal processing effects on the Doppler spectrum. Preprints, Sixteenth Radar Meteorological Conference, Houston, Texas, 22-24 April. American Meteorological Society, Boston, Mass., 163-168.

Zrnic', D. S., and R. J. Doviak, 1975. Velocity spectra of vortices scanned with a pulse Doppler radar. J. Appl. Meteorol. 14:1531-1539.

Zrnic', D. S., and R. J. Doviak, 1978. Matched filter criteria and range weighting for weather radar. IEEE Trans. Aerosp. Electron. Syst. AES-14:925-930.

Zrnic', D. S., R. J. Doviak, and D. W. Burgess, 1977. Probing tornadoes with pulse Doppler radar. Q. J. R. Meteorol. Soc. 103:707-720.

X. MEASURING STORM RAINFALL BY RADAR AND RAIN GAGE

E. A. Brandes and J. W. Wilson

1. INTRODUCTION

The measurement of thunderstorm rainfall has import for hydrology, agriculture, weather modification, climatology, and weather forecasting. Although details of requirements vary, there is always concern for rainfall distribution in space and time. For many agricultural applications and for streamflow in large river basins, rainfall data are needed over large areas for long periods (days or weeks) and a relatively sparse network of rain gages reporting once per day is adequate. In contrast, measurements from many closely spaced stations are required to forecast flash floods on small streams, where data are required for short time intervals (<10 hours) and over small areas (<1000 km^2) or to evaluate weather modification experiments. However, it is difficult and expensive to install and to maintain observation sites sufficiently numerous and capable of transmitting data in a timely manner to a central processing facility. Hence, there has been considerable interest in using weather radar to measure precipitation.

Radar overcomes the primary difficulties associated with rain gages; i.e., the radar measurements are over an area, available in real time, and from a single location. The disadvantage with radar is the lack of a unique relationship between the energy returned to the radar and the precipitation reaching the ground. Although radars are expensive, their cost is similar to that for a dense rain gage network that telemeters data to a central location. Also, when radar is used for other weather surveillance and forecasting activities, the part of the radar cost attributable to the rainfall-reporting function becomes less than the cost of a dense rain gage network.

Figure 1 illustrates the detailed distributions of thunderstorm rainfall that can be obtained by incoherent radar in near real time. The spatial detail in the figure is not defined by the gages, but by the radar analysis. In fact, had there been no Enid observation (near the 400-mm contour), the extreme rainfall would have been virtually unrevealed by gages. The Enid gage measured 398 mm, and the radar estimate for the same location was 374 mm. Such agreement is uncommon, however, and it is not unusual for radar measurements to be in error by more than a factor of 2. Because of this uncertainty, radar cannot replace gages; it can only supplement them.

Several measuring techniques that use various properties of radar signals have been suggested. Because rainfall attenuates microwaves, it has been proposed that rainfall be determined by measuring attenuation (see Atlas, 1964; Battan, 1973) or by comparing measurements obtained at attenuating and nonattenuating wavelengths (Rogers and Wexler, 1963). Ulbrich and Atlas (1975) point out that measurements of both radar reflectivity factor and microwave attenuation yield two parameters of exponential drop size distributions and hence rainfall rate directly. Seliga and Bringi (1976; 1978) propose a technique based on measurements of radar reflectivity factor at horizontal and vertical polarizations. These schemes are in development and will require additional research before they can be considered for operational application.

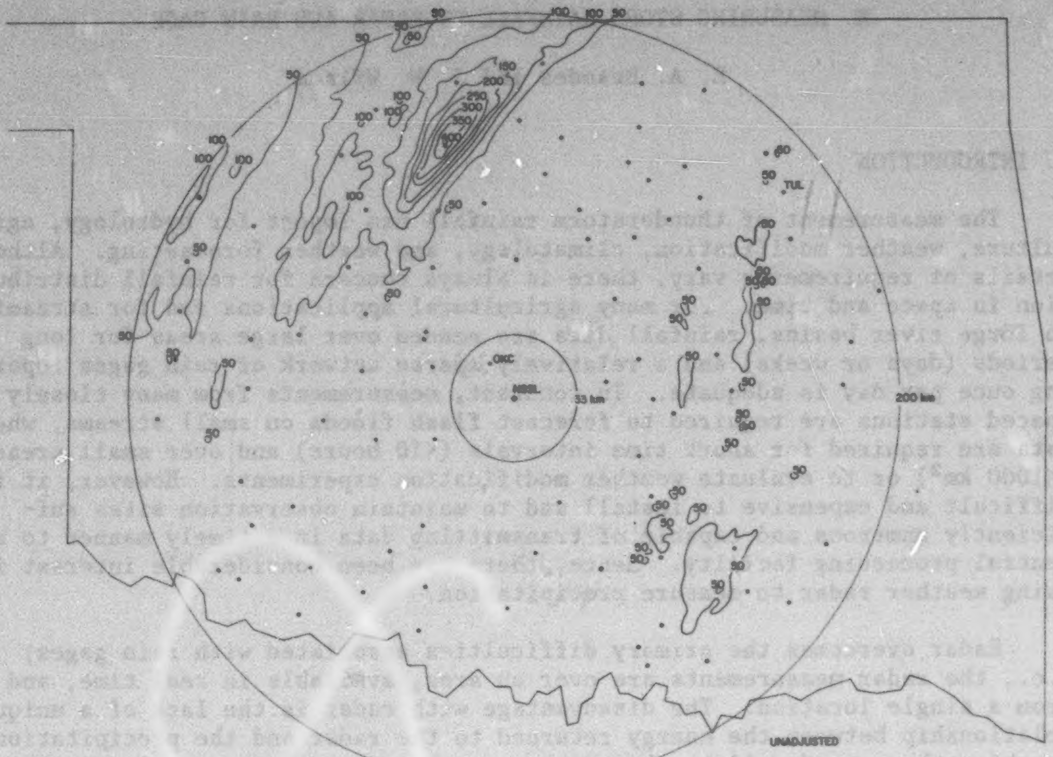

Figure 1.--Radar-measured rainfall totals (in millimeters) for the Enid, Okla., storm of 10-11 October 1973. The rainfall analysis was derived with the National Severe Storms Laboratory (NSSL) WSR-57 radar, without adjustment by gages. The black dots indicate the location of the NWS climatological gages.

Problems in estimating thunderstorm rainfall arise from extreme natural variability associated with these storms. Bias errors (primarily an undercatchment) characterize individual gage measurements, and large spatial variance in depth introduces random errors in areal mean estimates deduced from limited numbers of point observations (Sec. 2). Errors in radar measurements originate with instrumentation, sampling, and meteorological factors such as the absence of a unique relationship for converting radar observations to rainfall measurement (Sec. 3). The accuracy of point and area rainfall measurements by radar is discussed in Sec. 4. Since radar and gage measurements have contrasting strengths and weaknesses, techniques have been developed (Sec. 5) to combine these two observations to produce rainfall estimates superior to those produced by either alone.

2. GAGE MEASUREMENT OF RAINFALL

Rain gages offer a simple, inexpensive method to estimate point or areal rainfall and therefore are extensively used; however, all gage measurements are somewhat erroneous.

a. Instrument error

Numerous papers have been published on gage catch deficiencies in an attempt to quantify the many errors. Annotated bibliographies have been prepared by Kurtyka (1953), Larson (1971), Israelsen (1967), and WMO (1973). Contributing error sources include adhesion or gage wetting, inclination of gage, splash into and out of gage, evaporation, and airflow around the gage. Fortunately, by exercising reasonable precaution, these errors (except perhaps from airflow around the gage) amount to no more than about a 2% deficiency in catch (Dahlström, 1973).

Woodley et al. (1975) compared thunderstorm rainfall measured by gages located within 2 meters of each other. Although the gages were of the same type and had nearly identical exposure, differences averaged 9%. The larger percentage differences were associated with smaller storm totals. For similar comparisons, Huff (1955) found variations of only 2% and Joss et al. (1968) reported a standard relative error of 6% for all rainfall types.

There is general agreement (Larson and Peck, 1974) that much of the total measurement error results from turbulence and increased windspeed in the vicinity of the gage orifice. As the air rises to pass over the gage, precipitation particles that would have passed through the gage orifice instead are deflected and carried farther downwind. A rather wide range of diminished gage catchment versus windspeed is indicated (e.g., Koschmieder, 1934; Dahlström, 1973; Larson and Peck, 1974). Larson and Peck summarize a number of independent studies; they report about a 12% rain deficiency with a 5-m s^{-1} wind and a 19% deficiency at 10 m s^{-1}. Undercatch at higher speeds can be only estimated because of insufficient data; however, it is estimated by extrapolation that a gage may undermeasure rainfall in strong outflow regions of thunderstorms by as much as 20%-40%.

b. Areal estimate error

Gage estimates of area-averaged rainfall reflect both errors inherent in individual measurements and random sampling errors in areas of substantial spatial variation. The sampling errors depend on the number and distribution of gages, area size, length of measurement period, and, most important, spatial rainfall variability.

The common method of estimating sampling error proceeds from a very dense network that is assumed to measure the true areal average rainfall. The difference presented by a subset of the dense network is a measure of the error resulting from sampling at a few points (Linsley and Kohler, 1951; McGuinness, 1963; Nicks, 1966; Huff, 1971; Woodley et al., 1975). In general, error decreases with increasing area size, increasing time period, increasing gage density, and increasing rainfall amount. Figure 2 shows sampling error versus network mean rainfall for various gage densities. Immediately apparent is the much larger error for Florida showers and thunderstorms, because rainfall gradients are considerably larger and storms are smaller in Florida than in Illinois. Huff (1971) showed there is a great variability about the average curves (Fig. 2), making it very difficult to predict the sampling error for a given storm.

Unfortunately, there have been no error studies with gage densities of 10-20 km^2 per gage, which are typically used in comparing radar and gage

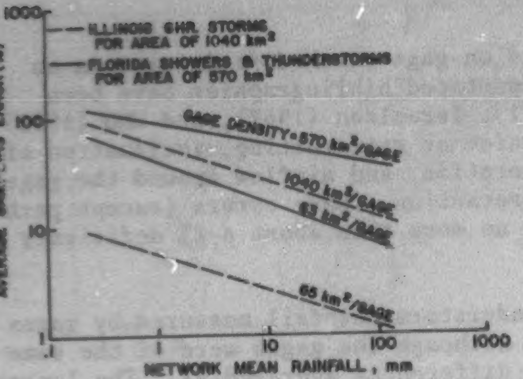

Figure 2.--Average rainfall depth sampling error versus network mean rainfall and gage density for Illinois and Florida summer rainstorms.

rainfall measurements. However, extrapolation of data used in Fig. 2 suggests that for Illinois-type thunderstorms the random sampling error for a watershed of 1,040 km² would be no more than 3% or 4% for rainfall amounts <10 mm and less than 1% for larger amounts. Considerably larger errors are likely for Florida-type storms.

3. RADAR MEASUREMENT OF RAINFALL

Since the late 1940's there have been many radar precipitation measurement studies based upon relationships among radar reflectivity, drop size distribution, and rainfall rate. However, operational implementation of radar has been slow because of difficulties in processing large volumes of data and uncertainties in the accuracy of the measurements. Digital recording and computer technology are solving the former, and substantial progress is being made to quantify the errors.

a. Radar equation and calculation of rainfall rate

A modified version of the Probert-Jones (1962) expression relating reflectivity factor Z to the average power or backscattering energy returned to a radar, $\bar{P}_r$ (in watts), from a target volume (see Ch. IX) is

$$Z = \frac{1024\ C\ \ln 2}{\pi^3}\ \frac{\lambda^2 r^2}{hG\theta\phi}\ \frac{\ell_p^2 \ell_g^2 \ell_c^2 \ell_a}{|K|^2}\ \frac{\bar{P}_r}{P_t}\ \mathrm{mm}^6\ \mathrm{m}^{-3}\ . \qquad (1)$$

The other parameters are these:

λ = radar wavelength (cm)

r = radar slant range (km)

P_t = peak transmitted power (watts)

h = pulse length (m)

G = antenna gain

θ = horizontal one-way 3-dB beamwidth (deg.)

ϕ = vertical one-way 3-dB beamwidth (deg.)

$|K|^2$ = dielectric factor

$C = 3.282 \times 10^{23}$ ($\mathrm{deg^2 mm^6 rad^{-2} cm^{-2} m^{-2} km^{-2}}$)

Implicit in Eq. 1 are the assumptions that particles are significantly smaller than the radar wavelength (Rayleigh approximation) and that they are spherical. The dimensionless loss factors (ℓ_p^2, ℓ_g^2, ℓ_c^2, and ℓ_a) are larger than unity and represent precipitation attenuation (e.g., Burrows and Attwood, 1949), atmospheric gaseous absorption (Blake, 1970), cloud attenuation (Ryde and Ryde, 1945), and space-averaging loss for nonlinear receivers (Rogers, 1971; Sirmans and Doviak, 1973). Details on attenuation losses are presented in the appendix.

The average return power per unit volume ΔV is proportional to the summation of the sixth power of particle diameters (D_i^6, mm) illuminated by the radar beam; hence, the reflectivity factor is also defined by

$$Z = \frac{1}{\Delta V} \sum_{i=1}^{N} D_i^6 \qquad (2)$$

For large scatterers ($D_i \geq \lambda/16$), the above relationships become unsatisfactory approximations to the more general Mie theory, and the meteorologist often defines an equivalent reflectivity factor, Z_e, i.e., the summation of an equivalent distribution of small water droplets that backscatter the same power as that observed.

Except for small diameters, raindrop size distributions have the approximate form (Marshall and Palmer, 1948)

$$N(D) = N_o e^{-\Lambda D} \quad , \qquad (3)$$

where $N(D)$ is the number concentration of size D droplets per size interval ΔD. Of course, there are significant departures from this simple exponential relationship with individual drop size samples and with various types of precipitation. Thus, Marshall and Palmer determined N_o to be 8,000 $\mathrm{m^{-3}\,mm^{-1}}$ and $\Lambda = 4.1\,R^{-.21}$, where R is the rainfall rate ($\mathrm{mm\,h^{-1}}$); other investigations have shown that Λ and N_o vary from storm to storm and that N_o is also a function of rainfall rate; e.g., Sekhon and Srivastava (1971) found $\Lambda = 3.8\ R^{-.14}$ and $N_o = 7{,}000\ R^{.37}$. An illustration of within-storm N_o and Λ variability for stratiform precipitation is presented in Fig. 3.

When the drop size distribution is known, radar reflectivity factor in a unit volume can be calculated from

$$Z = \int_o^\infty D^6\ N(D)dD \quad . \tag{4}$$

Similarly, when the vertical airspeed is zero, rainfall rates are given by

$$R = \frac{\pi\rho}{6} \int_o^\infty D^3 v_t(D) \quad N(D)dD \quad , \tag{5}$$

where ρ is the density of water and $v_t(D)$, the particle terminal velocity, is given approximately by $v_t = 1{,}400\ D^{\frac{1}{2}}$ (in cgs units; Spilhaus, 1948) or more precisely from studies by Gunn and Kinzer (1949) and Best (1950). When N_o is constant, the equations above imply a relationship of the form (Kessler, 1969)

$$Z = AR^b \quad . \tag{6}$$

Some related discussion is given in Vol 2., Ch. XIV. If the drop size distribution were known and if vertical motions were small relative to the drop terminal velocities, there would be no fundamental limitation to the accuracy of the radar rainfall estimates. But variations of drop size distribution are rarely known, and vertical air motions are frequently of the same magnitude as the particle terminal fallspeeds (particularly in thunderstorms). Hence the Z-R relationship is not unique (e.g., Battan, 1973), and there has been much empirical study to seek values of the coefficient and exponent in Eq. 6. The most commonly used relation is

$$Z = 200\ R^{1.6} \quad , \tag{7}$$

following the original work of Marshall and Palmer (1948). Unless otherwise noted, all radar rainfall estimates in this chapter are derived with Eq. 7.

b. Sources of error

The numerous factors causing errors in the radar measurement of rainfall can be grouped into three broad categories: (1) estimating of radar reflectivity factor; (2) time and space averaging of substantial variations in reflectivity; and (3) variations in the Z-R relationship and below-beam effects

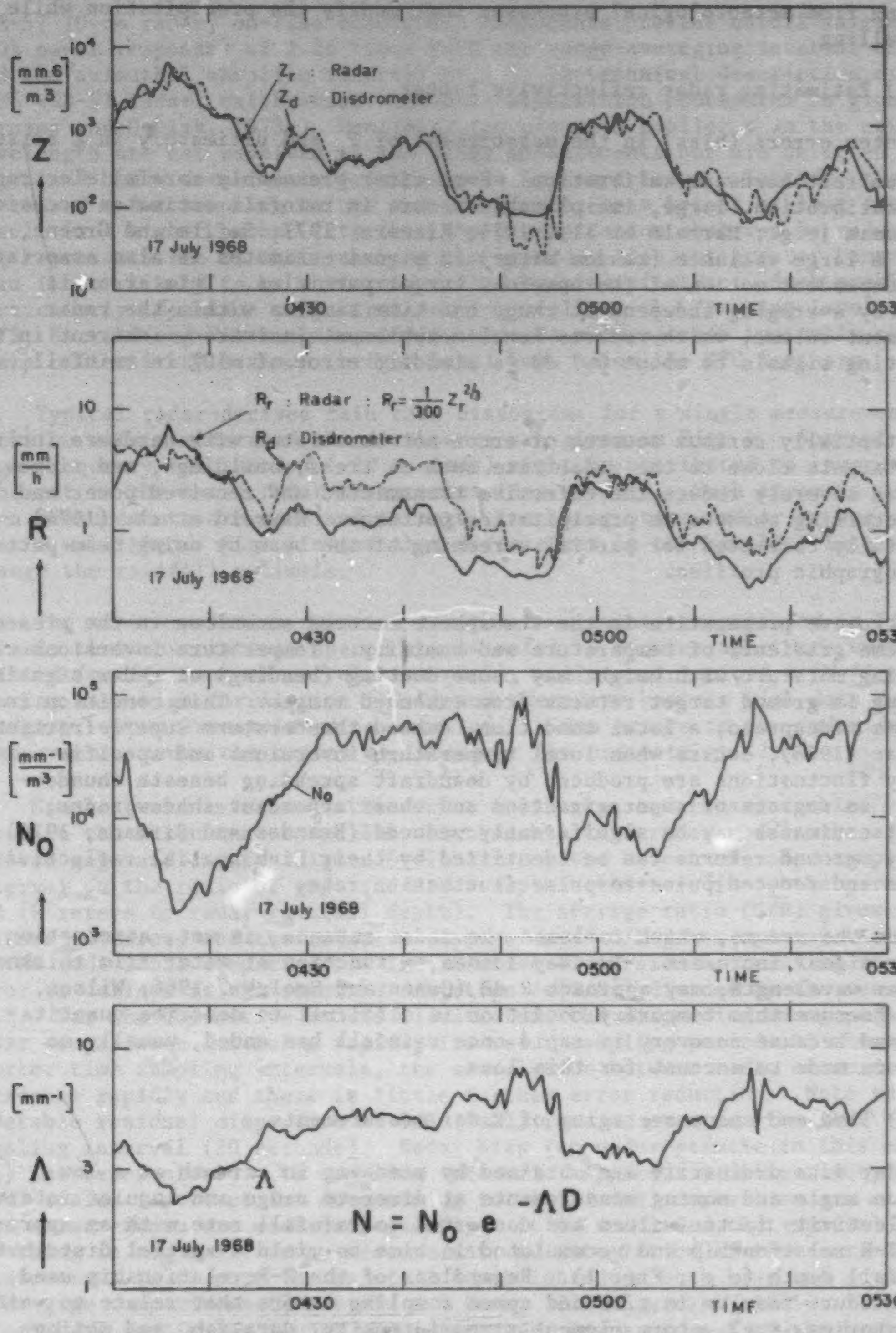

Figure 3.--Time histories of the drop spectra parameters N_0 and Λ. Also given is a comparison of radar reflectivity and rainfall rate measured by a vertically pointing radar sampling 200 m above the ground and by drop size measurements obtained next to the radar (Joss et al., 1970).

resulting from meteorological processes that modify the precipitation while it is falling.

(1) Estimating radar reflectivity factor

System errors (bias) in the measurement of $\bar{P}_r$ and ultimately in Z arise from incorrect hardware calibration. Even after presumably careful electronic system calibration, large, inexplicable errors in rainfall estimates occasionally remain (e.g., Harrold et al., 1974; Klazura, 1977; Saffle and Greene, 1978). A large variance (random error) in signal estimates is also associated with independent motion of the numerous target particles. This error is reduced by averaging independent range and time samples within the radar measurement volume, which reduces local measurement inaccuracy inherent in the fluctuating signals to about 0.7 dB (a standard error of ~10% in rainfall rate).

Potentially serious sources of error not associated with hardware include ground targets close to the radar site such as trees, buildings, and ridges, which can severely reduce the effective transmitted and received power and cause recurring shadows in precipitation patterns. Harrold et al. (1974) successfully corrected for partial screening of the beam by using beam patterns and topographic profiles.

Microwave propagation in the atmosphere becomes anomalous in the presence of extreme gradients of temperature and humidity. Temperature inversions with decreasing moisture with height may cause ducting (bending) of radar signals, resulting in ground target returns from extended ranges. This condition is sometimes widespread; a local condition, dubbed thunderstorm superrefraction by Battan (1973), occurs when local temperature inversions and specific humidity fluctuations are produced by downdraft spreading beneath thunderstorms. In regions of superrefraction and their attendant shadow zones, rainfall estimates may be significantly reduced (Brandes and Sirmans, 1976). Normally, ground returns can be identified by their high spatial reflectivity variance and reduced pulse-to-pulse fluctuation rate.

When the radome, which encloses the radar antenna, is wet, attenuation of radar signal increases. Two-way losses, a function of water film thickness and radar wavelength, may approach 2 dB (Cohen and Smolski, 1966; Wilson, 1978). Because this temporary condition is difficult to describe quantitatively and because recovery is rapid once rainfall has ended, usually no attempt is made to account for this loss.

(2) Time and space averaging of radar measurements

Radar data ordinarily are obtained by scanning in azimuth at a low elevation angle and making measurements at discrete range and angular intervals. The reflectivity factor values are converted to rainfall rate with an appropriate Z-R relationship and accumulated in time to yield a spatial distribution of rainfall depth (e.g., Fig. 1). Regardless of the Z-R relationship used, this procedure results in time and space sampling errors that relate to rain rate histories (i.e., storm element size, intensity, duration, and motion characteristics).

Signal averaging effectively smooths small-scale radial and azimuthal variations. For example, with the National Severe Storms Laboratory (NSSL)

WSR-57 10-cm radar, on-line electronic components provide cutoff wavelengths (50% power response) of 2.26 times both the range-averaging interval of 1 km and the azimuthal sampling interval of 2°. (A technical description of the NSSL WSR-57 radar, calibration, and data acquisition procedures is given by Sirmans and Doviak, 1973.) Precipitation elements smaller than the cutoff wavelength are not resolved in the radar measurements but are detected by gages and hence decorrelate point gage-radar comparisons. Further, the increased radar sampling volume and the greater beam height at long ranges result in a higher probability that the precipitation observed by radar is not representative of that reaching the ground. Also, at greater ranges the beam is not likely to be uniformly filled by precipitation. Such problems are particularly important with stratiform rainfall at the freezing level (Wilson, 1975; Harrold and Kitchingman, 1975), because melting snow typically shows a sharp reflectivity maximum (bright band) just below the 0°C isotherm.

Typical radar-derived rain rate histograms for a single measurement location within moderated thundershowers are given in Fig. 4. Some of the high-frequency fluctuation (~20 seconds) might be attributed to inaccuracies inherent in the basic radar measurement (Sec. 3b[1]). Such error is reduced when measurements are combined through time integration and/or by averaging over a watershed. Fig. 4 shows that differences in the sampling interval can change the rainfall estimate.

The autocorrelation function for the four events represented in Fig. 5 reveals that observations spaced approximately 4 minutes apart are uncorrelated (coefficient of correlation ≤ 0.5), while observations with ≤ 1-min spacing have high correlation (≥ 0.9) and therefore contain high data redundancy. When extrapolated to zero lag, random errors in the individual measurements cause the curves to intercept the ordinate at <1.0.

Sampling and instrumentation error (both gage and radar) combine with error in the selection of the Z-R relationship to further reduce the agreement between gage and radar. Figure 6 illustrates the effect of radar sampling interval on the ratio of gage and radar depth estimates, i.e., the parameter G/R (R refers to radar rainfall depth). The average ratio ($\overline{G/R}$) gives the systematic error, and the relative dispersion of G/R gives spatial variability of the individual comparisons. The relative dispersion or relative standard error is defined as the standard deviation ($\sigma[G/R]$) divided by the mean times 100%. For the convective storms illustrated, the dispersion among point gage-radar comparisons increases rapidly for radar sampling periods >5 minutes. At shorter time sampling intervals, the correlation between radar measurements increases rapidly and there is little further error reduction. Note that considerable residual dispersion of G/R (~22%) remains even for the shortest sampling interval (20 seconds). Radar bias (an underestimate in this example) increases slowly with sampling interval. Apparently reflectivity temporal scales important for determining total rainfall deposition are missed when measurements are made infrequently. It is concluded that spatial smoothing in the basic radar measurement and integration of time-series measurements to compute the rainfall depth introduce both bias and scatter in radar-gage comparisons (Desautels and Gunn, 1970; Zawadzki, 1975). These errors have particular import when gage-radar comparisons form the basis for radar adjustment (Sec. 5).

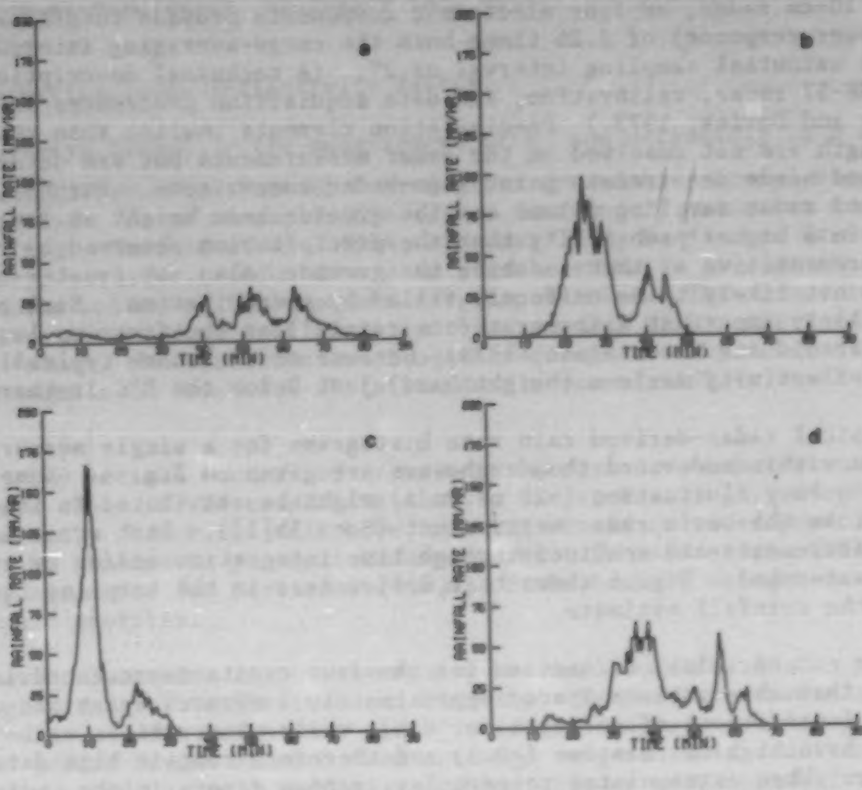

Figure 4.--Representative point rainfall rate versus time traces for Oklahoma thunderstorms. Rainfall rates are derived from the NSSL radar data.

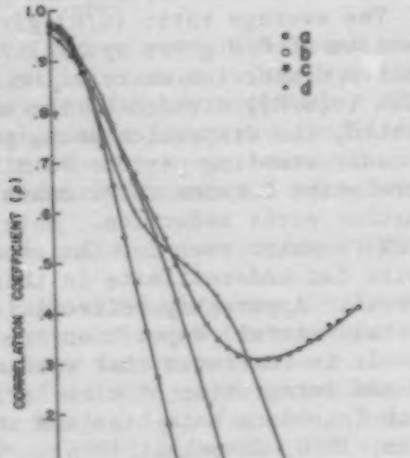

Figure 5.--Autocorrelation function of the four individual rainfall rate traces shown in Fig. 4.

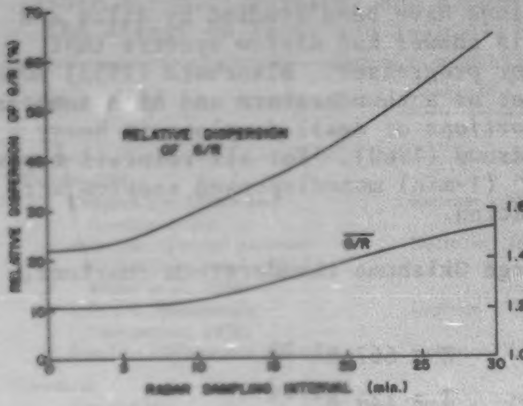

Figure 6.--Effect of radar sampling interval on gage-radar rainfall comparisons. The lower curve illustrates the effect on the average ratio of gage and radar depths ($\overline{G/R}$), and the upper curve illustrates the effect on the relative dispersion of individual G/R ratios. Curves are based on data from 190 gage-radar comparisons of total storm rainfall from Oklahoma thunderstorms observed on 7 April 1975. Radar data obtained from the NSSL WSR-57.

(3) Variations in Z-R relationships and below-beam effects

Drop size distributions have been measured in stratiform rain, showers, and thundershowers, and characteristic Z-R relationships have been reported (Jones, 1955; Imai, 1960; Fujiwara, 1965; Joss et al., 1970; Jatila and Puhakka, 1973a). Ordinarily the coefficient (Eq. 6) increases and the exponent decreases with convection intensity. Although some improvement in radar rainfall estimates may be realized by selecting Z-R relationships based on storm type rather than using a single relationship for all storms, considerable error remains. For example, Jones (1966) reduced radar errors from 62% to 43% by such a technique.

Thunderstorm relationships reported by investigators typically exhibit a wide range (e.g., Fig. 7), comparable with storm variations observed in mean radar precipitation estimate bias (Sec. 4). Instrumental differences among drop size sampling techniques undoubtedly account for some of the total dispersion, but on the whole, the reported variations in thunderstorm Z-R relationships as well as storm type differences are thought to reflect vagaries in microphysical processes.

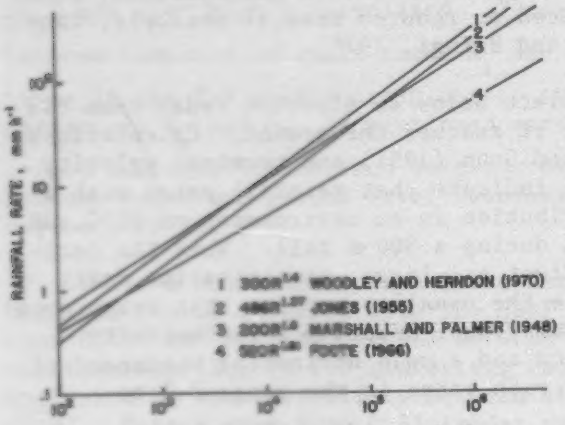

Figure 7.--Plots of various Z-R relationships. Curves 1,2, and 4 were respectively determined for Florida, Illinois, and Arizona thunderstorms. The Marshall and Palmer relation (curve 3) represents a variety of rainfall types and is included for comparison.

Fluctuations in drop size distributions have been studied by Atlas and Plank (1953), who found droplets in a rain shower had narrow spectra that shifted toward smaller sizes as the shower progressed. Blanchard (1953) noted the absence of small droplets at the onset of a thunderstorm and high numbers during heavy rain. Relatively high proportions of small droplets in heavy rains were also reported by Mason and Andrews (1960). For all rainfall types, Joss and Gori (1978) found many "instant" (1-min) monodispersed samples were needed to produce an exponential distribution.

Drop size measurements beneath a large Oklahoma thunderstorm (Martner, 1975) yielded these relationships:

(1) Leading portion $Z = 667\ R^{1.33}$
(2) Central core $Z = 124\ R^{1.64}$
(3) Trailing portion $Z = 436\ R^{1.43}$

Cloudbase spectra from Texas thunderstorms (Carbone and Nelson, 1978) show relatively high number concentrations of large droplets during growth stages, when updrafts dominate, and large total droplet concentrations with smaller median diameters during declining or downdraft stages. The mean relationships were these:

(1) Growth phase $Z = 763\ R^{1.37}$
(2) Decline phase $Z = 400\ R^{1.56}$

Note the similarities with the leading (updraft) and trailing (downdraft) storm regions in Martner's results. Large scatter in drop spectra over short time periods and the wide disparity among Z-R relationships reported by others prompted Twomey (1953) to conclude radar rainfall estimates derived with average Z-R relationships at best were only approximate (a factor of 2 high or low).

Several physical mechanisms that might alter drop size distributions are listed in Table 1, with an indication of their probable influence on the Z-R relationship and of the storm region where the effect is probably a maximum. Such processes may act in combination to modify the drop size distribution to produce a complex net result. Also, droplets lose their sphericity and flatten as their size increases. Depending on the radar polarization, radar reflectivity measurements may be enhanced or reduced several decibels, causing large errors in rainfall rate (Seliga and Bringi, 1976).

Meteorological processes taking place below an elevated radar beam can further alter the precipitation before it reaches the ground. Calculations using the evaporation data of Kinzer and Gunn (1951) and terminal velocity measurements of Gunn and Kinzer (1949) indicate that rainfall rates with a Marshall-Palmer (1948) drop size distribution in an environment of 20°C and 80% relative humidity are reduced ~15% during a 300-m fall. When the horizontal windspeed and reflectivity gradient are large, precipitation drift below an elevated radar beam may negate the usual assumption that measurements are applicable at ground. Simple calculations, assuming a reflectivity gradient of 2 dB km^{-1} at 300-m elevation and a mean horizontal windspeed of 20 m s^{-1}, show droplet drift can alter rain rates in the range 2.5 to 100 mm h^{-1} by 20% to 40%.

Table 1.--Microphysical and kinematic influences on Z-R relationships and the effect on radar and rainfall estimates when no adjustment applied*

Process	Change in $Z = AR^b$		Probable effect on radar rainfall if Z-R is not adjusted	Possible region of maximum influence
	A	b		
Microphysical				
Evaporation (Atlas and Chmela, 1957)	Increase	Decrease	Overestimate	Inflow regions, fringe areas
Accretion of cloud particles (Atlas and Chmela, 1957; Rigby *et al.*, 1954)	Decrease	Increase	Underestimate	Downdraft
Collision, coalescence (Srivastava, 1971)	Increase	Decrease	Overestimate	Reflectivity core
Breakup (Srivastava, 1971)	Decrease	Decrease	Underestimate	Reflectivity core
Kinematic				
Size sorting (Gunn and Marshall, 1955; Atlas and Chmela, 1957)	Increase	Decrease	Tendency to overestimate	Regions of strong inflow and outflow
Vertical Motion				
Updraft	Increase	Decrease	Overestimate	
Downdraft	Decrease	Increase	Underestimate	

*Wilson and Brandes, 1979.

Depending on size and number concentration, hail may enhance reflectivity measurements, or if the hailstones are water coated, significant attenuation may occur (see Battan [1973] for a thorough treatment). Since hail location, composition, shape, and size distribution are rarely known, routine corrections to reflectivity measurements are not possible. Fortunately, hail falls are usually short lived and their effect on storm-accumulated radar rainfall is usually small.

4. RADAR-GAGE COMPARISONS

Radar reflectivity and rainfall rates have been rather precisely related by Joss et al. (1970), who used a raindrop disdrometer and a zenith-pointing radar with a narrow-beam sampling 200 meters above. Results (Fig. 3) show that measurements of the reflectivity factors by radar (Z_r) and disdrometer (Z_d) are very highly correlated. There is substantially less correspondence between computed rainfall rates R_r and R_d. Differences stem from time variations in the Z-R relationship due to changes in the drop size distribution parameters N_o and Λ. As mentioned earlier, at greater radar ranges with larger sampling volumes and with increasing beam height, the correlation between radar and ground level rainfall diminishes (Bruer and Kreuels, 1976; Martner, 1977).

Table 2 summarizes comparisons between radar and gage measurements for 14 Oklahoma storms observed with the NSSL WSR-57 radar. The gages were spread over 8,000 km^2 at radar ranges between 45 and 100 km. The utility of a single relationship (Eq. 7) for converting radar reflectivity to rainfall rate is indicated by the variability between storms in the average gage-to-radar ratio ($\overline{G/R}$). Ratios vary from 0.41 (radar overestimate) to 2.41 (radar underestimate). Storm-to-storm differences in $\overline{G/R}$, exceeding a factor of 2, are

Table 2.--Summary of gage-radar comparisons for 14 Oklahoma thunderstorms (based on 5-min radar samples and $Z = 200R^{1.6}$)*

Date	Number of gages	Storm duration (h)	$\overline{G}$ (mm)	$\overline{G/R}$	Relative[1] dispersion about $\overline{G/R}$ %	Average[2] difference %	Average difference[3] (Storm bias removed) %
28 Apr. 1974	21	7	11	1.62	23	35	16
29 Apr. 1974	20	12	7	0.82	21	30	17
29 Apr. 1974	21	5	22	2.23	31	51	26
1 May 1974	21	9	24	2.41	20	57	13
20 May 1974	12	7	15	0.68	46	75	37
21 May 1974	10	3	5	0.59	36	87	27
23 May 1974	5	2	3	0.64	10	60	8
25 May 1974	22	6	25	0.91	27	30	27
25 May 1974	12	5	23	0.88	32	31	19
30 May 1974	22	7	25	1.09	34	32	33
3 Jun. 1974	15	5	7	0.41	29	160	23
6 Jun. 1974	13	2	16	0.68	43	79	36
8 Jun. 1974	10	5	31	0.49	39	141	42
7 Apr. 1975	19	4	14	1.13	23	17	18
		Average 14 cases:		1.04	30[4]	63	24

[1] Relative dispersion (coefficient of variation) about $\overline{G/R} = 100\%\ \sigma[G/R]/\overline{G/R}$; where $\sigma[G/R]$ is the standard deviation of the gage-radar ratios.

[2] Average difference $= 100\% \sum_{i=1}^{N} \left| \frac{G_i - R_i}{G_i} \right| \Big/ N.$

[3] Average difference (storm bias removed) $= 100\% \sum_{i=1}^{N} \left| \frac{G_i - (\overline{G/R})R_i}{G_i} \right| \Big/ N.$

[4] The relative dispersion among all available gage-radar comparisons (14 storms) is 63%.

---

*Wilson and Brandes, 1979.

frequently observed (see also Joss et al., 1970; Woodley et al., 1974). In view of the observed range in reported Z-R relationships for thunderstorms and aberrant behavior of drop size distributions (Sec. 3b), the wanderings in $\overline{G/R}$ are not suprising and might have been expected a priori. Daily fluctuations in radar hardware calibration account for only a small portion of the total $\overline{G/R}$ variation (about 20% with the NSSL radar). Although most rainfall measurement requirements call for accuracies better than a factor of 2, radar estimates based on a single optimum Z-R relationship can be very useful for identifying, in near real time, regions likely to receive heavy rain and those regions that should be alerted to possible flash flooding.

The average within-storm difference between point radar and gage measurements for the 14 storms in Table 2 is 63%, including biases both storm-to-storm and within individual storms. The latter is disclosed by two statistics, defined in Table 2: the "relative dispersion about $\overline{G/R}$" and the "average difference (storm bias removed)". The average within-storm errors (exclusive of mean bias) vary from 8% to 42%, with an overall mean of 24%. The error reduction, i.e., 63% - 24% or 39%, represents how much of the radar error results from storm differences in the relationship between radar-received power and rainfall rate. A significant reduction in radar error could be achieved if a procedure were found to determine the average storm bias.

As might be expected, the agreement between gage and radar measurements improves when comparisons are made for areas rather than points (Wilson, 1968; Muchnik et al., 1968; Harrold et al., 1974). However, Wilson found significant error reduction with area size was possible only if the mean storm bias (G/R) was removed. The Harrold et al. and Wilson studies also show error decreases as the measurement period lengthens.

Inspection of G/R fields for individual storms reveals that within-storm radar errors are not random but contain scales similar to raincell spacing. For example, Fig. 8a represents the rainfall pattern from two storms passing through a dense network of rain gages (one in the north half and the other in the south half). The G/R pattern in Fig. 8b shows that even contiguous storms exhibit distinctive error relationships (see also Fig. 9). Further, both Figs. 8 and 9 show a correlation between G/R and gage depth; i.e., heavy rainfalls tend to be underestimated by radar (large G/R) and light rainfalls overpredicted (small G/R). This result, mentioned by Woodley and Herndon (1970) and Desautels and Gunn (1970), is attributed to smoothing in the radar observations, variations in the drop size distribution, and vertical and horizontal air motions.

To illustrate how three-dimensional thunderstorm wind flow could create spatial errors in radar rainfall estimates, we examine horizontal wind fields (near ground) synthesized from measurements by two Doppler radars. Wind patterns for the rainfall event in Fig. 8 are shown for early mature (Fig. 10a) and late mature (Fig. 10b) stages. The two northernmost rain cells delineated by 40-dBZ contours in Fig. 10a moved eastward and merged to form the large single storm in Fig. 10b.

Light rainfall during the early mature stage (west side of network in Fig. 8a) and on fringe areas of the storm was overestimated by radar (G/R < 1.0, Fig. 8b). On the other hand, heavy rainfall accompanying storm merger and progression to the fully matured stage was largely underestimated (G/R > 1.0). Converging inflow air in the eastern quadrant of the northernmost storm (Fig. 10a) is characteristic of growth and mature stages and implies upward motion. Precipitation here may be held aloft by updrafts. If the air beneath the storm is unsaturated, evaporation may also occur. Both updrafts and evaporation cause large Z-R relationship coefficients (Table 1); unless the conversion relationship is adjusted accordingly, the actual precipitation, as is the case here, may be overestimated. Large coefficients found for storm growth (Carbone and Nelson, 1978) and for leading storm edge (Martner, 1975), usually an updraft region, are in agreement with these observations (see Sec. 3b).

As storm evolution continues, updrafts and inflow give way to downdrafts and outflow (Fig. 10b). Note the broad divergent area that develops within the storm's reflectivity core. Downdrafts lower actual Z-R relationship coefficients, and rainfall estimated with a fixed relationship would be underestimated (G/R > 1.0). A smaller coefficient like those reported for a rainy storm core by Martner (1975) and for declining storm cells by Carbone and Nelson (1978), would raise the radar rainfall estimates.

Size sorting and droplet drift are possible contributors to radar underestimates beneath the south central storm core (Figs. 8b and 10b). Strong northerly winds, opposite to the reflectivity gradient, may advect significantly higher droplet concentrations downstream below the radar beam than expected from in situ measurements. At the storm's southern boundary, winds

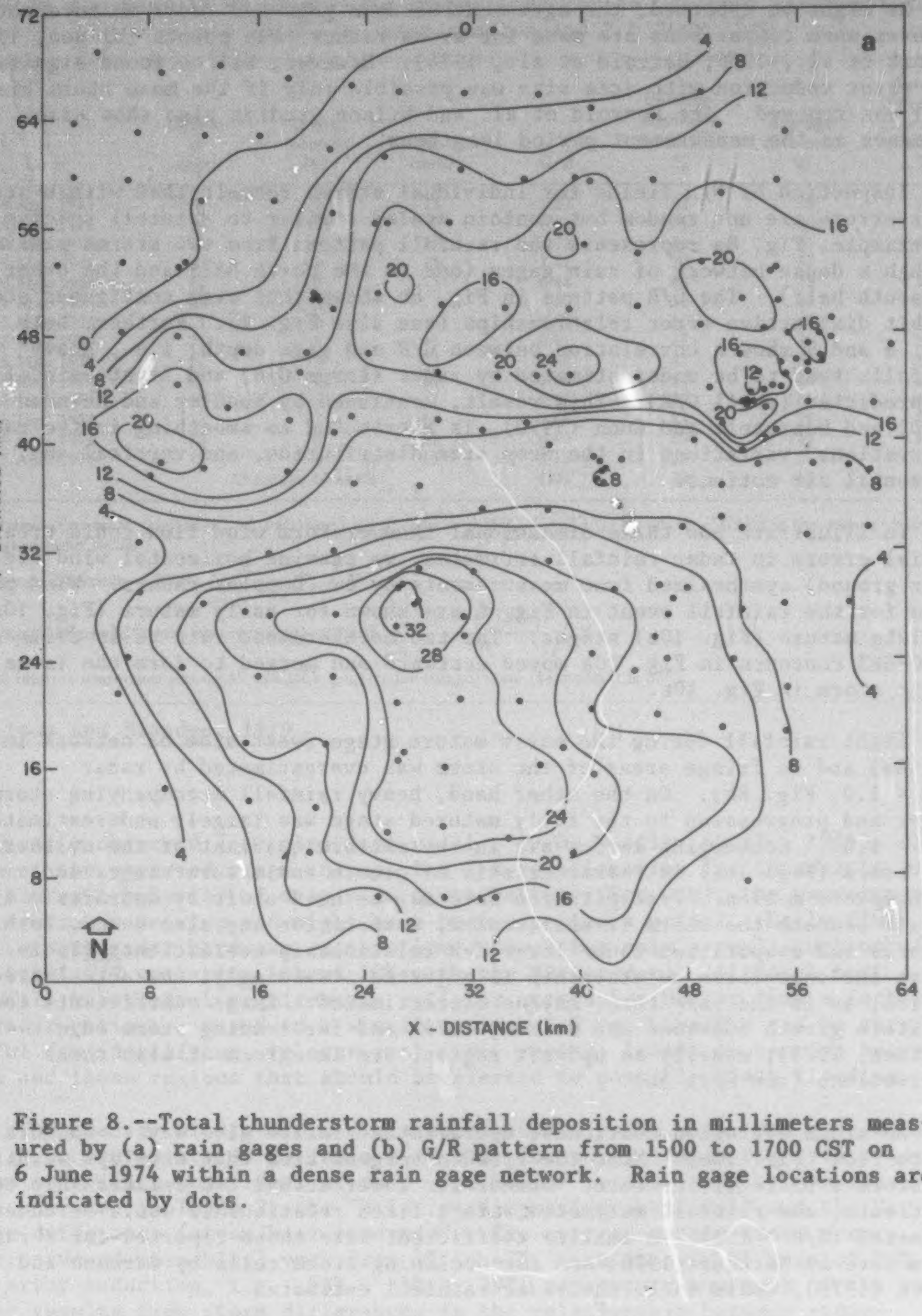
a
Y - DISTANCE (km)
X - DISTANCE (km)
N
0
8
16
24
32
40
48
56
64
72
0
4
8
12
16
20
24
28
32

Figure 8.--Total thunderstorm rainfall deposition in millimeters measured by (a) rain gages and (b) G/R pattern from 1500 to 1700 CST on 6 June 1974 within a dense rain gage network. Rain gage locations are indicated by dots.

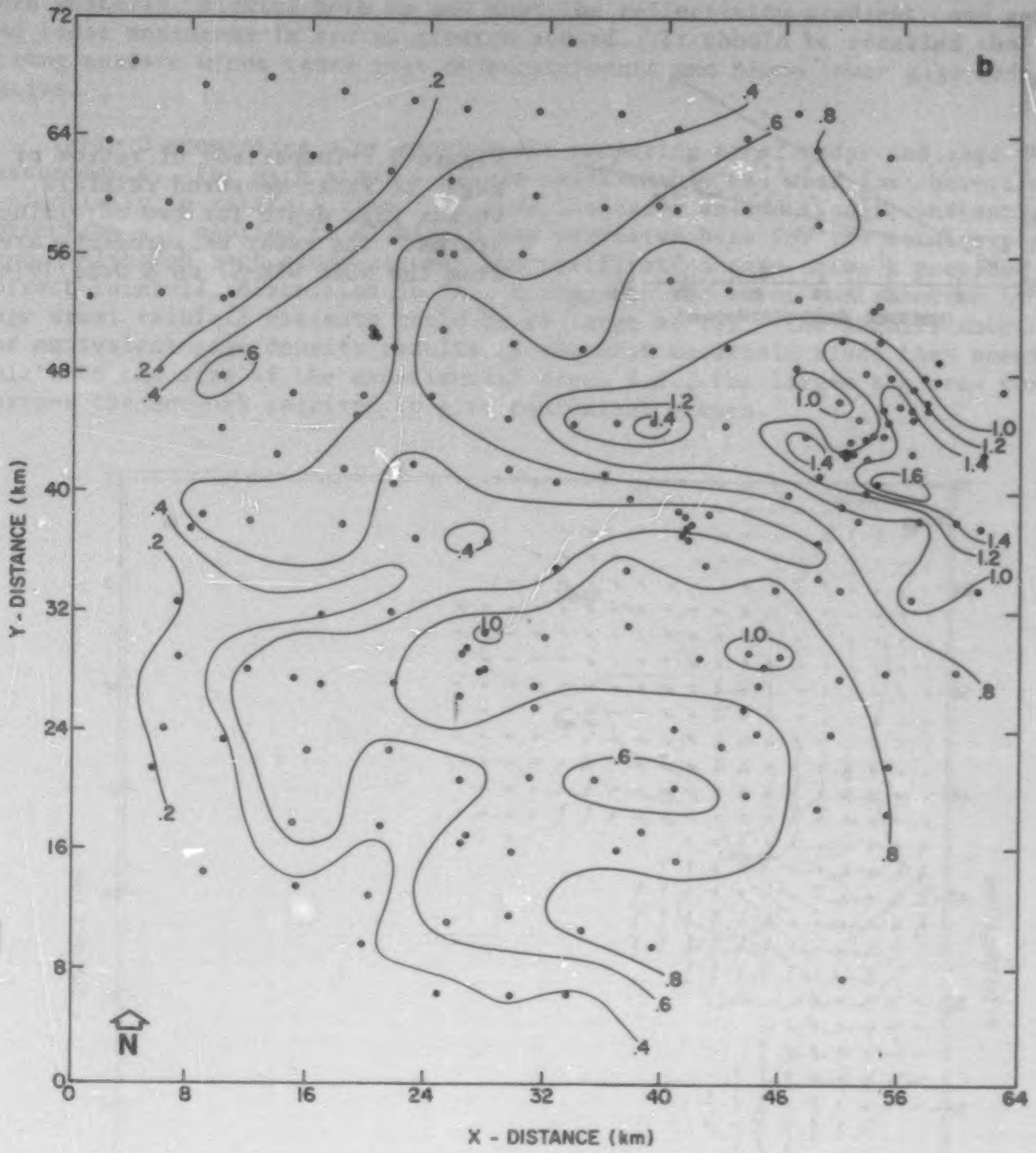
b
Y - DISTANCE (km)
X - DISTANCE (km)
72
64
56
48
40
32
24
16
8
0
0
8
16
24
32
40
46
56
64
N
.2
.4
.6
.8
.6
.8
1.0
1.2
1.4
1.2
1.4
1.0
1.0
1.2
1.4
1.6
1.4
1.2
1.0
.4
.2
.4
1.0
1.0
.8
.6
.8
.8
.6
.4
.2
.2
.4
.6

Figure 8.--Continued.

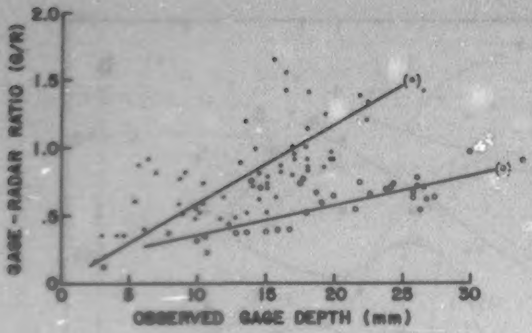

Figure 9.--Comparison of ratios of gage- to radar-measured rainfall versus gage depth for two adjoining storms. The radar measurements are from the NSSL WSR-57 on 6 June 1974.

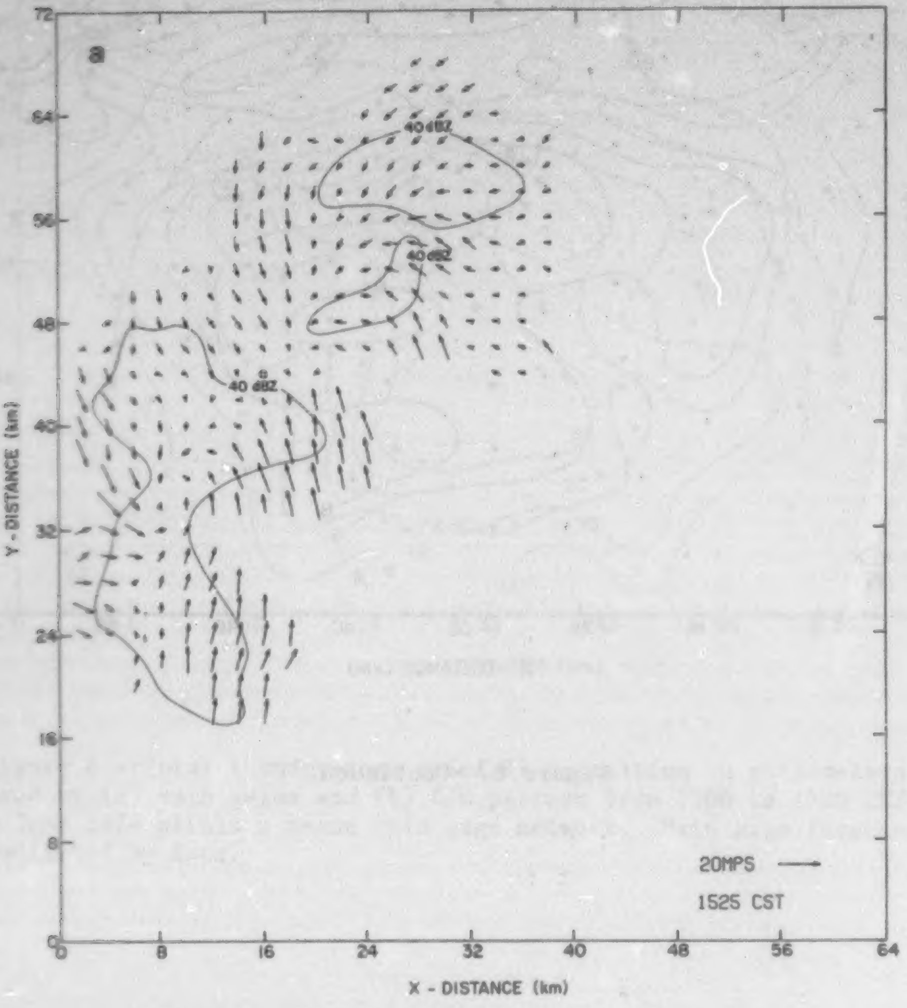

Figure 10.--Ground relative wind fields (0.3-km elevation AGL) and radar reflectivity patterns observed at (a) 1525 CST and (b) 1625 CST on 6 June 1974. Wind fields are derived from measurements obtained with two Doppler radars.

turn westerly, blowing both up and down the reflectivity gradient, and gage and radar measurements are in greater accord. It should be recalled that strong surface winds cause gage undercatchments and hence lower gage-radar ratios.

Table 3 summarizes nine experiments comparing areal radar and gage measurements. For each study a single relationship was used for converting reflectivity to rainfall rate. In some instances an additional constant correction was applied to eliminate any pervasive bias for the total experiment. Although each study assumes the verification gage network provides the correct rainfall, discussion in Sec. 2 suggests the error contribution by the gage areal rainfall estimate could be as large as 10%. The significance of the equivalent gage density results is somewhat uncertain since they seemingly relate to the size of the experimental area; i.e., the larger the area the sparser the network required to give equivalent errors.

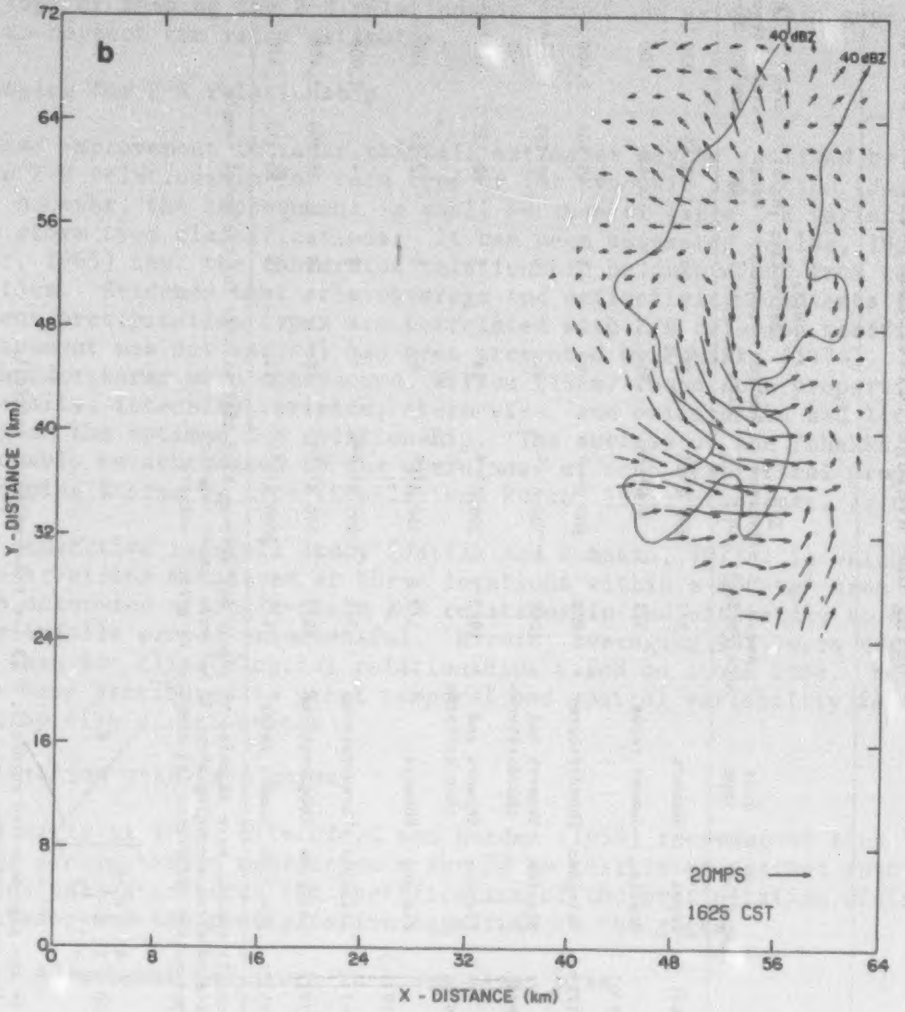

Figure 10.--Continued.

Table 3.--Comparison of radar and gage measurements of area rainfall, using one average relationship for all storms.

Reference	Location	rain type	Radar λ(cm)/θ(deg)	Z-R relationship	Number cases	Radar observation frequency (min)	Radar range (km)	Area size (km^2)	Radar observation duration	Density of verification gages (km^2/gage)	Mean difference† (%)	Gage density required to give accuracy of radar (km^2/gage)
Aoyagi (1964)	Japan	Showers	3/1	200 $R^{1.6}$	5	10	13-45	638	Storm	24	25	200
Borovikov et al. (1970)	Russia	Summer rains	3/1	K $R^{1.5}$*	59	--	60	100	Storm	1	61	400
Brandes (1975)	Oklahoma	Thunderstorms	10/2	200 $R^{1.6}$	9	5	45-100	3,400	Storm	20	52	1,600
Herndon et al. (1973)	Florida	Showers and thunderstorms	10/2	300 $R^{1.6}$*	30	5	90-125	165**	24 h	4	67	57
Woodley et al. (1974)	Florida	Showers and thunderstorms	10/2	300 $R^{1.4}$	39	5	90-125	165**	24 h	4	54	--
Jatila and Puhakka (1973b)	Finland	Showers	3/1.8	360 $R^{1.6}$	6	5	12-28	180	Storm	12	23	26
Jones (1966)	Illinois	Thunderstorms	10/4	435 $R^{1.48}$*	9	2	--	1,000	Storm	20	52	--
Wilson (1970)	Oklahoma	Thunderstorms	10/2	200 $R^{1.6}$*	28	10	35-100	3,400	Storm	20	59	2,000
Wilson (1975)	New York	Summer rains	5/1.7	1000 $R^{1.6}$*	121	10	95-112	170	24 h	10	49	--

*Radar rainfall amounts were adjusted to remove any average bias that existed for the total sample.
**Five scattered areas averaging about 30 km^2 were lumped together.
†Average percentage difference (x) computed by present authors.

$$x = 100 \sum_{i=1}^{N} \left| \frac{G_i - R_i}{G_i} \right| \Big/ N ,$$

where G is the gage-measured rainfall, R is the radar-measured rainfall, and N is the number of cases.

The mean difference between radar and gage measurements (Table 3) varies from 23% to 67%. Excluding the two experiments with the fewest cases, the difference varies only between 49% and 67%. Note the disagreement for areal comparisons in Oklahoma thunderstorms (52% and 59%) is slightly less than the average difference (63%) given in Table 2 for point comparisons in similar thunderstorms. Thus, as stated earlier, measurement accuracy does not significantly improve with increasing area size if adjustments are not made for storm-to-storm variations in $\overline{G/R}$.

5. ADJUSTMENT OF RADAR-DERIVED RAINFALL ESTIMATES

The very large storm-to-storm and within-storm errors in radar rainfall estimates (using a single average Z-R relationship; Tables 2 and 3) dictate that estimates should be adjusted further--preferably on a within-storm basis. Adjustments usually involve either specifying the Z-R relationship by storm type or keeping the Z-R relationship fixed and using rain gage observations to correct the radar estimates.

a. Changing the Z-R relationship

Some improvement in radar rainfall estimates may be realized by adjusting the Z-R relationship for rain type or for synoptic situation (Jones, 1966); however, the improvement is small because of large Z-R variations within storm type classifications. It has been suggested (Atlas, 1964; Kessler, 1965) that the conversion relationship be determined from radar echo statistics. Evidence that echo coverage and reflectivity gradients from different precipitation types are correlated with Z-R relation coefficient (the exponent was not varied) has been presented by Puhakka (1974). When only thunderstorms were considered, Wilson (1966) found echo properties such as intensity, intensity variance, storm size, and orientation had little bearing on the optimum Z-R relationship. The success of the Puhakka study can probably be attributed to the usefulness of echo statistical properties for grouping storms by type (Kessler and Russo, 1963; Schaffner, 1976).

A convective rainfall study (Jatila and Puhakka, 1973a) in which drop size observations monitored at three locations within a 180-km^2 area were used to determine a single-storm Z-R relationship and ultimately to derive radar rainfalls proved unsuccessful. Errors, averaging 98%, were considerably larger than for climatological relationships based on storm type. Negative results were attributed to great temporal and spatial variability in thunderstorm drop size distributions.

b. Calibration with rain gages

As early as 1954, Hitschfeld and Borden (1954) recommended that "radar used for precipitation measurements should be calibrated against rain gages." Their analysis attributes the specification of the precipitation distribution to the radar and the precipitation magnitude to the gages.

(1) Adjustment for storm-to-storm radar bias

In the simplest adjustment procedure, the mean radar bias is determined and a correction applied uniformly to the radar estimates. Ordinarily, a number (N) of gages are used and a multiplicative adjustment factor (F), the ratio of gage-observed (G) and radar-indicated (R) rainfalls, is computed from either

$$F = \sum_{i=1}^{N} G_i \Big/ \sum_{i=1}^{N} R_i \qquad (8)$$

or

$$F = \frac{1}{N} \sum_{i=1}^{N} \frac{G_i}{R_i} \; . \qquad (9)$$

With Eq. 8, observations receive a weight proportionate to depth; with Eq. 9 every comparison has equal weight. (Grayman and Eagleson [1970] and Cain and Smith [1976] note log [G/R] is more normally distributed than G/R; hence, a more appropriate expression of Eq. 8 may be $F = \text{antilog}\,[\overline{\log(G/R)}]$.) Cain and Smith (1976) suggest an alternate method involving sequential analysis in which the logarithm of individual gage-radar ratios is monitored for drifts in the mean. Adjustments based on an accumulated sample mean are applied only when a statistically significant shift is detected. In each case, corrections are applied for systematic bias associated with radar hardware calibration and the Z-R relationship. Indeed the relationship selected to convert reflectivity to rainfall is of little importance and has negligible impact on the final (corrected) radar depth estimate (Brandes, 1974).

The potential of gage-calibrated radar to estimate mean watershed precipitation is elucidated by plotting natural rainfall variability as measured by the relative dispersion of gage observations against the relative dispersion of calibration ratios (G/R) computed at the same gages (Fig. 11). When natural rainfall has high variability, the scatter among gage observations exceeds the deviation among calibration ratios. In such storms, fewer statistically independent gage-radar comparisons are needed to estimate the mean radar bias and consequently to correct the radar depth estimate than to determine the average rain depth from gage observations. For more stratiform rainfalls, at least for this small sample, the advantage of gage-calibrated radar data is less apparent. On the average for individual Oklahoma storms, a single gage-radar comparison determines radar bias with an average expected error of ~30% (Table 2). Because this error is much less than the longer term deviation in G/R of 63% (14 storms), even a single-gage observation can provide useful storm calibration information. If the mean radar bias is estimated from a number of gage-radar comparisons, the expected error will be smaller. Theoretically, using nine independent G/R values reduces the uncertainty in the radar bias estimate to $30/\sqrt{9}$ or 10%.

When Wilson (1970) adjusted radar-derived thunderstorm rainfalls for a 3,500-km^2 watershed measured by a single centrally located gage, the average error was reduced from 51% (unadjusted measurements) to 35%. When the single gage was used to estimate the watershed mean depth, the error was 60%. Single-gage calibration offered no improvement in the Jatila and Puhakka (1973a) study of stratiform rains, but errors in convective rainfalls dropped from 43% to 25%. These and other studies using an average storm adjustment factor are summarized in Table 4. Although procedural and meteorological differences preclude rigorous comparison, the common result is a significant reduction in radar rainfall estimate error when adjustments are made on a

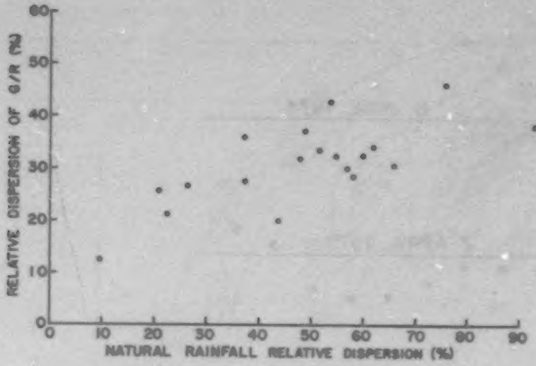

Figure 11.--Comparison of the relative dispersion of gage-measured rainfall with the relative dispersion of the gage-to-radar ratios of measured rainfall. The gage density is 1 per 300-400 km^2. Data were collected with NSSL WSR-57 radar in selected spring Oklahoma thunderstorms from 1973 to 1975.

storm basis. Nevertheless, large spatial errors (e.g., the 30% error in Table 2) remain in the radar precipitation patterns.

(2) Spatial adjustment

Of course, calibration by one nearby gage generally produces rainfall estimates in the neighborhood of that gage site that are superior to estimates adjusted by an ensemble average of all available calibration ratios. For example, in Fig. 12, when point rainfall estimates made on 7 April 1975 were adjusted by a single calibration factor determined at a gage 20 km distant,

Table 4.--Radar areal estimates of rainfall utilizing gages for calibration*

Reference	Location	Rain type	Radar λ(cm)/ θ(deg)	Z-R relation	Number of cases	Radar observation frequency (min)	Radar range (km)	Area size (km²)	Duration	Adjustment type and calibrating gage density (km²/gage) (a)	Error before and after ( ) adjustment (%)	Percent error using calibration gages only
Wilson (1970)	Oklahoma	Thundershowers	10/2	$KR^{1.6}$ (b)	23	5–10	35–100	3500	Storm	A(3500)	51 (35)	60
										A(1200)	(30)	31
										V(1200)	(27)	31
Brandes (1975)	Oklahoma	Thundershowers	10/2	$200R^{1.6}$	9	5	45–100	3000	Storm	V(900)	52 (13)	21
										V(1600)	(14)	24
										A(900)	(18)	21
Woodley *et al.* (1974)	Florida	Showers Thundershowers	10/2	$300R^{1.4}$	39	5	85–115	570	24 hr	A(1600) (c)	43 (30)	—
Harrold *et al.* (1974)	England	Showers Stratiform	10/2	$200R^{1.6}$	27	1	12–48	50–100	1 hr	A(500)	— (19)	40 (d)
Wilson (1975)	New York	Showers Thundershowers Stratiform	5/1.7	$200R^{1.6}$ (e)	41	10	95–112	170	24 hr	V(275)	49 (22)	22
Collier *et al.* (1975)	England	Showers Stratiform	10/1	$200R^{1.6}$	13	1	12–48	700	3 hr	V(233)	— (7)	—
Jatila and Puhakka (1973a,b)	Finland	Showers Thundershowers	3/1.8	$200R^{1.6}$	6	5	18–28	180	Storm	A(180)	43 (23) (f,g)	—
Huff and Towery (1978)	Illinois	Showers Thundershowers	10/1	$300R^{1.35}$	67 (h)	3	20–100	5300	0.5 hr	V(150)	55 (27)	32

Notes:

(a) A: average adjustment; V: variable spatial adjustment.

(b) Radar estimates adjusted to remove average bias for the total experiment.

(c) Density of rain gage clusters is approximately 8 gages per cluster. Clusters outside area of measurement.

(d) Calibrating gage not within boundaries of watersheds, but is 10–20 km distant.

(e) An additional multiplicative factor of 1.7 applied to radar estimates.

(f) Varied *Z–R* coefficient to match point rainfall at central gage.

(g) Error when observed drop-size distribution used is 98%.

(h) Number of 30 min periods in four storms.

*Wilson and Brandes, 1979.

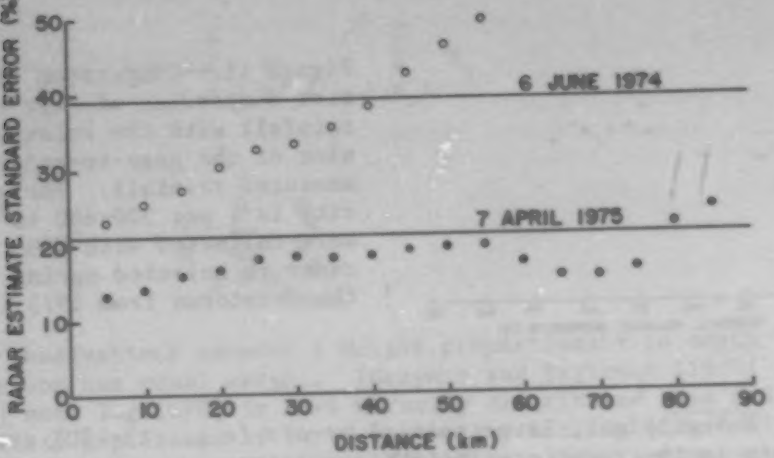

Figure 12.--Standard error of point radar measurements (total storm accumulation) versus the distance of the measurement from the calibrating gage for two thunderstorms. The solid horizontal lines indicate the standard error for each storm after the mean radar bias ($\overline{G/R}$) is used for calibration. The curves represent the error when a single nearby gage-radar ratio is used for calibration. The radar data were collected with the NSSL WSR-57.

errors in the adjusted rainfall were 17% compared with 21% when $\overline{G/R}$ was applied. The maximum useful range of any one calibration factor varies from storm to storm (7 April 1975 and 6 June 1974).

Procedures have been devised (e.g., Brandes, 1975; Collier et al., 1975; Wilson, 1975; Crawford, 1978) to combine routinely radar observations with distributions of calibrating gages. Most often, local adjustments are made by interrogating nearby autoresponsive calibration sites and then assigning weights inversely by distance. (Crawford [1978] describes a refined approach whereby statistical properties of both the radar and gage fields determine the combination procedure.) In essence, the radar observations are molded to the gage observations by a plane-fitting technique while retaining the radar-indicated precipitation variance between gages. Depending upon the calibrating-gage density, potential source error addressed implicitly by this technique includes large-scale error patterns associated with drift in the radar hardware calibration, synoptic influences on the Z-R relationship, small-scale (within-storm) spatial variations in the Z-R relationship, and below-beam changes in the precipitation. Such an analysis for the Enid, Okla., storm appears in Fig. 13 (unadjusted radar estimates for this storm are shown in Fig. 1).

Although the experiments using spatial adjustment techniques (Table 4) differ as to length of the measurement period, area size, radar range, data collection frequency, and density of adjustment gages, the reported error range of 7% to 27% after spatial adjustment is considerably less than unadjusted estimates of 43% to 55% and somewhat less than the 18% to 35% error range for uniform adjustments. Intuitively, we expect the radar, even if

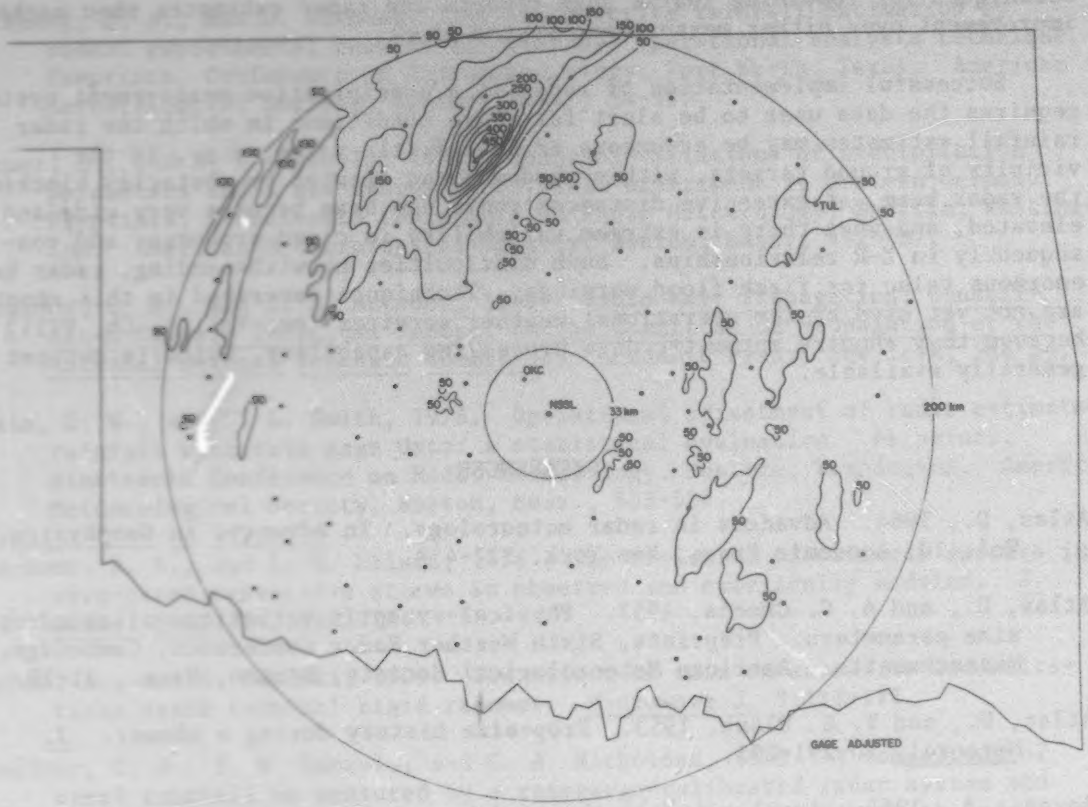

Figure 13.-Radar-measured rainfall for Enid, Okla., storm of 10-11 October 1973, after adjustment with rain gage observations (Brandes and Sirmans, 1976).

only roughly calibrated, to measure the rainfall over the entire area observed by the radar better than a single gage; if the network of calibrating gages were very dense, we would not expect the addition of radar to provide significant improvement. Data in the last three columns in Table 4 confirm this expectation. Results from Illinois convective storms (Hildebrand et al., 1979) indicate that the accuracy of the radar-gage estimates is matched or exceeded by the gage-only estimates when the gage density is 1 or more per 250-300 km^2.

6. CLOSING REMARKS

It has been hypothesized that the primary sources of error in the radar measurements of rainfall result from variations in the Z-R relationship caused by microphysical cloud processes and from smoothing in radar measurements. Radar rainfall error patterns suggest discrepancies occur from storm to storm in a systematic and perhaps predictable manner. Specifically, we noted a tendency for radar to overestimate light rainfall and to underestimate heavy rainfall. The search for systematic error patterns and causes holds promise, but until this knowledge can be applied to radar measurements, we use gage data to calibrate radar data. Indeed even simple adjustment techniques for combining sparse gage reports and radar estimates show marked improvement over either measurement system alone.

Successful implementation of radar in a precipitation measurement system requires the data user to be alert for those conditions in which the radar rainfall estimates may be erroneous or have little value, e.g., in the vicinity of ground targets, within shadow areas created by obstacles blocking the radar beam, at excessive distances where the beam becomes very wide and elevated, and when there is extreme variability in cloud processes and consequently in Z-R relationships. Such difficulties notwithstanding, radar has enormous value for flash flood warnings. Techniques described in this chapter are not yet used by the operational weather services (see Vol. 1, Ch. VIII) because they require automatic data processing capability, which is not yet generally available.

REFERENCES

Atlas, D., 1964. Advances in radar meteorology. In *Advances in Geophysics*, Vol. 10, Academic Press, New York, 317-478.

Atlas, D., and A. C. Chmela, 1957. Physical-synoptic variations of raindrop size parameters. Preprints, Sixth Weather Radar Conference, Cambridge, Massachusetts. American Meteorological Society, Boston, Mass., 21-29.

Atlas, D., and V. G. Plank, 1953. Drop-size history during a shower. *J. Meteorol.* 10:291-295.

Aoyagi, J., 1964. Areal rainfall obtained by a 3.2 cm radar and a raingage network. Preprints, Eleventh Weather Radar Conference, Boulder, Colorado. American Meteorological Society, Boston, Mass., 116-119.

Battan, L. J., 1973. *Radar Observation of the Atmosphere*. University of Chicago Press, Chicago, Ill., 324 pp.

Best, A. C., 1950. Empirical formulae for the terminal velocity of water drops falling through the atmosphere. *Q. J. R. Meteorol. Soc.* 76: 302-311.

Blake, L. V., 1970. Prediction of radar range. In *Radar Handbook*, M. I. Skolnik (ed.), McGraw-Hill, New York, 2-51 to 2-55.

Blanchard, D. C., 1953. Raindrop size-distribution in Hawaiian rains. *J. Meteorol.* 10:457-473.

Borovikov, A. M., V. V. Kostarev, I. P. Mazin, V. I. Smirnov, and A. A. Charnikov, 1970. *Radar Measurements of Precipitation Rate*. Trans. by Israel Program for Scientific Translations (National Technical Information Service, Springfield, Va.).

Brandes, E. A., 1974. Radar rainfall patterns optimizing technique. Tech. Memo. ERL NSSL-67, NOAA Environmental Research Laboratories, Boulder, Colo., 16 pp.

Brandes, E. A., 1975. Optimizing rainfall estimates with the aid of radar. *J. Appl. Meteorol.* 14:1339-1345.

Brandes, E. A., and D. Sirmans, 1976. Convective rainfall estimation by radar: experimental results and proposed operational analysis technique. Preprints, Conference on Hydrometeorology, Fort Worth, Texas. American Meteorological Society, Boston, Mass., 54-59.

Bruer, L., and R. K. Kreuels, 1976. Seasonal variations of precipitation parameters and a new hydrological field experiment in Western Germany. Preprints, Seventeenth Conference on Radar Meteorology, Seattle, Washington. American Meteorological Society, Boston, Mass., 432-437.

Burrows, C. R., and S. S. Attwood, 1949. Radio Wave Propagation: Consolidated Summary Technical Report, of the Committee on Propagation of the National Defense Research Committee. Academic Press, New York, 548 pp.

Cain, D. W., and P. L. Smith, 1976. Operational adjustment of radar estimated rainfall with rain gage data: a statistical evaluation. Preprints, Nineteenth Conference on Radar Meteorology, Seattle, Washington. American Meteorological Society, Boston, Mass., 533-538.

Carbone, R. E., and L. D. Nelson, 1978. The evolution of raindrop spectra in warm-based convective storms as observed and numerically modeled. J. Atmos. Sci. 12:2302-2314.

Cohen, A., and A. Smolski, 1966. The effect of rain on satellite communications earth terminal rigid radomes. Microwave J. 9:111-121.

Collier, C. G., T. W. Harrold, and C. A. Nicholass, 1975. A comparison of areal rainfall as measured by a raingauge-calibrated radar system and raingauge networks of various densities. Preprints, Sixteenth Radar Meteorological Conference, Houston, Texas. American Meteorological Society, Boston, Mass., 467-472.

Crawford, K. C., 1978. On the bivariate objective analysis of surface rainfall using interpolation. Preprints, Eighteenth Conference on Radar Meteorology, Atlanta, Georgia. American Meteorological Society, Boston, Mass., 336-341.

Dahlström, B., 1973. Investigation of errors in rainfall observations: a continued study. Rep. 34, Department of Meteorology, University of Uppsala, Sweden, 31 pp.

Desautels, G., and K. L. S. Gunn, 1970. Comparison of radar with network gauges. Preprints, Fourteenth Radar Meteorology Conference, Tucson, Arizona. American Meteorological Society, Boston, Mass., 239-240.

Doviak, R. J., and D. Sirmans, 1973. Reflectivity equation for NSSL's WDS-71 10-cm Doppler radar. National Severe Storms Lab., Norman, Okla., internal memorandum.

Foote, G. B., 1966. A Z-R relation for mountain thunderstorms. J. Appl. Meteorol. 5:229-231.

Fujiwara, M., 1965. Raindrop-size distribution from individual storms. J. Atmos. Sci. 22:585-591.

Grayman, W. M., and P. S. Eagleson, 1970. A review of the accuracy of radar and raingages for precipitation measurement. M.I.T. Hydrodyn. Lab. Rep. 119, Cambridge, Mass., 103 pp.

Gunn, K. L. S., and J. S. Marshall, 1955. The effect of wind shear on falling precipitation. J. Meteorol. 12:339-349.

Gunn, R., and G. D. Kinzer, 1949. The terminal velocity of fall for water droplets in stagnant air. J. Meteorol. 6:243-248.

Harrold, T. W., and P. G. Kitchingman, 1975. Measurement of surface rainfall using radar when the beam intersects the melting layer. Preprints, Sixteenth Radar Meteorological Conference, Houston, Texas. American Meteorological Society, Boston, Mass., 473-478.

Harrold, T. W., E. J. English, and C. A. Nicholass, 1974. The accuracy of radar-derived rainfall measurements in hilly terrain. Q. J. R. Meteorol. Soc. 100:331-350.

Herndon, A., W. L. Woodley, A. H. Miller, A. Samet, and H. Senn, 1973. Comparison of gage and radar methods of convective precipitation measurement. Tech. Memo. ERL OD-18, NOAA Environmental Research Laboratories, Boulder, Colo., 67 pp.

Hildebrand, P. H., N. Towery, and M. R. Snell, 1979. Measurement of convective mean rainfall over small areas using high density raingages and radar. J. Appl. Meteorol. 18:1316-1326.

Hitschfeld, W., and J. Bordan, 1954. Errors inherent in the radar measurement of rainfall at attenuating wavelengths. J. Appl Meteorol. 11:58-67.

Huff, F. A., 1955. Comparison between standard and small orifice raingages. Trans. Am. Geophys. Union 36:689-694.

Huff, F. A., 1971. Evaluation of precipitation records in weather modification experiments. In Advances in Geophysics, Vol. 15, Adademic Press, New York, 59-134.

Huff, F. A., and N. G. Towery, 1978. Utilization of radar in operation of urban hydrologic systems. Preprints, Eighteenth Conference on Radar Meteorology, Atlanta, Georgia. American Meteorological Society, Boston, Mass., 437-441.

Imai, I., 1960. Raindrop size distributions and Z-R relationships. Preprints, Eighth Weather Radar Conference, San Francisco, California. American Meteorological Society, Boston, Mass., 211-218.

Israelsen C. G., 1967. Reliability of can-type precipitation gage measurements. Tech. Rep. 2, Utah Water Research Laboratory, Utah State University, Logan, 74 pp.

Jatila, E., and T. Puhakka, 1973a. Experiments on the measurement of areal precipitation by radar. Geophysica 12, 23 pp.

Jatila, E., and T. Puhakka, 1973b. On the accuracy of radar rainfall measurements. Geophysica 12, 13 pp.

Jones, D. M. A., 1955. Three-cm and 10-cm wavelength radiation back scatter from rain. Preprints, Fifth Weather Radar Conference, Asbury Park, New Jersey. American Meteorological Society, Boston, Mass., 281-285.

Jones, D. M. A. 1966. The correlation of raingage-network and radar-detected rainfall. Preprints, Twelfth Conference on Radar Meteorology, Norman, Oklahoma. American Meteorological Society, Boston, Mass., 204-207.

Joss, J. K., and E. G. Gori, 1978. Shapes of raindrop size distributions. *J. Appl. Meteorol.* 17:1054-1061.

Joss, J. K., J. C. Thams, and A. Waldvogel, 1968. The accuracy of daily rainfall measurements by radar. Preprints, Thirteenth Radar Meteorological Conference, Montreal. American Meteorological Society, Boston, Mass., 448-451.

Joss, J. K., K. Schram, J. C. Thams, and A. Waldvogel, 1970. On the quantitative determination of precipitation by radar. Wissenschaftliche Mitteilungen Nr. 63, Eidgenössischen Kommission Zum Studium der Hagelbildung und der Hagelawehr, 38 pp.

Kessler, E., 1965. Use of radar measurements for assessment of areal rainfall. Paper presented at 17th Session of the WMO Executive Committee, Geneva, Switzerland, May 1965.

Kessler, E., 1969. *On the Continuity of Water Substance in Atmospheric Circulations*. Meteorol. Monogr. 10, American Meteorological Society, Boston, Mass., 84 pp.

Kessler, E., and J. A. Russo, Jr., 1963. Statistical properties of weather radar echoes. Preprints, Tenth Weather Radar Conference, Washington, D.C. American Meteorological Society, Boston, Mass., 25-33.

Kinzer, G. D., and R. Gunn, 1951. The evaporation, temperature and thermal relaxation-time of freely falling waterdrops. *J. Meteorol.* 8:71-82.

Klazura, G. E., 1977. Changes in gage/radar ratios in high rain rate gradients by varying location and size of radar comparison areas. Preprints, Second Conference on Hydrometeorology, Toronto. American Meteorological Society, Boston, Mass., 376-379.

Koschmieder, H., 1934. Methods and results of definite rain measurements: III. Danzig report (1). *Mon. Weather Rev.* 62:5-7.

Kurtyka, J. C., 1953. Precipitation measurement study. Rep. of Investigation No. 20, Ill. State Water Supv. Div., Urbana, Ill., 178 pp.

Larson, L. W., 1971. Precipitation and its measurement, a state of the art. Water Resour. Ser. 24, Water Resour. Res. Inst., University of Wyoming, Laramie, 74 pp.

Larson, L. W., and E. L. Peck, 1974. Accuracy of precipitation measurements for hydrologic modeling. *Water Resour. Res.* 10:857-863.

Laws, J. O., and D. A. Parsons, 1943. The relation of raindrop-size to intensity. *Trans. Am. Geophys. Union* 24:452-460.

Linsley, R. K., and M. A. Kohler, 1951. Variations in storm rainfall over small areas. Trans. Am. Geophys. Union 32:245-250.

Marshall, J. S., and W. M. Palmer, 1948. The distribution of raindrops with size. J. Meteorol. 5:165-166.

Martner, B. E., 1975. Final report on the University of Wyoming's participation in NSSL Project Storm Intercept, 1975 (data analysis). Department of Atmospheric Science, University of Wyoming, Laramie, 14 pp.

Martner, B. E., 1977. A field experiment on the calibration of radars with raindrop disdrometers. J. Appl. Meteorol. 16:451-454.

Mason, B. J., and J. B. Andrews, 1960. Drop-size distributions from various types of rain. Q. J. R. Meteorol. Soc. 86:346-353.

McGuinness, J. L., 1963. Accuracy of estimating watershed mean rainfall. J. Geophys. Res. 68:4763-4767.

Muchnik, V. M., M. L. Markovich, and L. M. Volynetz, 1968. The results of radar measurements of the areal rainfall. Preprints, Thirteenth Radar Meteorological Conference, Montreal. American Meteorological Society, Boston, Mass., 392-395.

Nicks, A. D., 1966. Field evaluation of rain gage network design principles. Symposium Design of Hydrological Networks, Intl. Assoc. Sci. Hydrol. Pub. 67:82-93.

Probert-Jones, J. R., 1962. The radar equation in meteorology. Q. J. R. Meteorol. Soc. 88:485-495.

Puhakka, T., 1974. On the variability of the Z-R relationship in rainfall related to radar echo pattern. Geophysica 13, 17 pp.

Rigby, E. C., J. S. Marshall, and W. Hitschfeld, 1954. The development of the size distribution of raindrops during their fall. J. Meteorol. 11: 362-372.

Rogers, R. R., 1971. The effect of variable target reflectivity on weather radar measurements. Q. J. R. Meteorol. Soc. 97:154-167.

Rogers, C. W. C., and R. Wexler, 1963. Rainfall determination from 0.86 and 1.82 cm radar measurements. Preprints, Tenth Weather Radar Conference, Washington, D.C. American Meteorological Society, Boston, Mass., 260-270.

Ryde, J. W., and D. Ryde, 1945. Attenuation of centimetre and millimetre waves by rain, hail, fogs, and clouds. General Electric Company Report No. 8670.

Saffle, R. E., and D. R. Greene, 1978. The role of radar in the flash flood watch warning system: Johnstown examined. Preprints, Eighteenth Conference on Radar Meteorology, Atlanta, Georgia. American Meteorological Society, Boston, Mass., 468-473.

Schaffner, M. R., 1976. On the characterization of weather radar echoes, II. Preprints, Eleventh Conference on Radar Meteorology, Seattle, Washington. American Meteorological Society, Boston, Mass., 478-485.

Sekhon, R. S., and R. C. Srivastava, 1971. Doppler radar observations of drop-size distributions in a thunderstorm. J. Atmos. Sci. 28:983-994.

Seliga, T. A., and V. N. Bringi, 1976. Potential use of radar differential reflectivity measurements at orthogonal polarizations for measuring precipitation. J. Appl. Meteorol. 15:69-76.

Seliga, T. A., and V. N. Bringi, 1978. Preliminary results of differential reflectivity measurements in rain. Preprints, Eighteenth Conference on Radar Meteorology, Atlanta, Georgia. American Meteorological Society, Boston, Mass., 134-138.

Sirmans, D., and R. J. Doviak, 1973. Meteorological radar signal intensity estimation. Tech. Memo. ERL-NSSL-64, NOAA Environmental Research Laboratories, Boulder, Colo., 80 pp.

Spilhaus, A. F., 1948. Raindrop size, shape, and falling speed. J. Meteorol. 5:108-110.

Srivastava, R. C., 1971. Size distribution of raindrops generated by their breakup and coalescence. J. Atmos. Sci. 28:410-415.

Twomey, S., 1953. On the measurement of precipitation intensity by radar. J. Meteorol. 10:66-67.

Ulbrich, C. W., and D. Atlas, 1975. The use of radar reflectivity and microwave attenuation to obtain improved measurements of precipitation parameters. Preprints, Sixteenth Radar Meteorology Conference, Houston, Texas. American Meteorological Society, Boston, Mass., 496-503.

Wexler, R., 1947. Radar detection of a frontal storm 18 June 1946. J. Meteorol. 4:38-44.

Wilson, J. W., 1966. Storm-to-storm variability in the radar reflectivity-rainfall rate relationship. Preprints, Twelfth Conference on Radar Meteorology, Norman, Oklahoma. American Meteorological Society, Boston, Mass., 229-233.

Wilson, J. W., 1968. Factors affecting the accuracy of radar rainfall measurement. Final Rep. 7488-331 to the National Severe Storms Laboratory, The Travelers Research Center, Inc., Hartford, Conn., 33 pp.

Wilson, J. W. 1970. Integration of radar and raingage data for improved rainfall measurement. J. Appl. Meteorol. 9:489-497.

Wilson, J. W., 1975. Radar-gage precipitation measurements during the IFYGL. CEM Rep. 4177-4546, The Center for the Environment and Man, Hartford, Conn., 121 pp.

Wilson, J. W., 1978. Observations of radome transmission losses at 5 cm wavelengths. Preprints, Eighteenth Conference on Radar Meteorology, Atlanta, Georgia. American Meteorological Society, Boston, Mass., 288-291.

Wilson, J. W., and E. A. Brandes, 1979. Radar measurement of rainfall--a summary. Bull. Am. Meteorol. Soc. 60:1048-1058.

WMO (World Meteorological Organization), 1973. Annotated Bibliography on Precipitation Measurement Instruments. Rep. 17, WMO-343, Geneva, 278 pp.

Woodley, W., and A. Herndon, 1970. A raingage evaluation of the Miami reflectivity-rainfall rate relation. J. Appl. Meteorol. 9:258-263.

Woodley, W., A. Olsen, A. Herndon, and V. Wiggert, 1974. Optimizing the measurement of convective rainfall in Florida. Tech Memo ERL-WMPO-18, NOAA Environmental Research Laboratories, Boulder, Colo., 99 pp.

Woodley, W., A. Olsen, A. Herndon, and V. Wiggert, 1975. Comparison of gage and radar methods of convective rain measurement. J. Appl. Meteorol. 14:909-928.

Zawadski, I. I., 1975. On radar-raingage comparison. J. Appl. Meteorol. 14:1430-1436.

Appendix:

ADJUSTMENTS TO THE RADAR MEASUREMENT

Edward A. Brandes and Dale Sirmans

A.1. ATTENUATION BY RAINFALL

When radar path lengths are long and precipitation echoes are highly reflective (e.g., along radially oriented squall lines), radar signals are significantly attenuated by rainfall even at 10-cm wavelengths. Thus, attenuation can approach 1 dB corresponding to a diminution in rainfall estimates of about 20%. Attenuation losses, an inverse function of wavelength λ, have been calculated by Burrows and Attwood (1949) for the raindrop size distribution observed by Laws and Parsons (1943). A least-squares fit applied to the logarithms of the Burrows and Attwood data yields the following two-way loss relationships:

$$L_p = .000687\ R^{.97}\ \mathrm{dB\ km^{-1}} \qquad (\lambda = 10\ \mathrm{cm})$$

and

$$L_p = .0251\ R^{1.21}\ \mathrm{dB\ km^{-1}} \qquad (\lambda = 3\ \mathrm{cm})\ ,$$

where R is the rainfall rate in millimeters per hour (Fig. A.1), and $L_p = 10 \log \ell_p^2$, as presented in Eq. (1).

It is convenient to express attenuation in terms of reflectivity factor Z ($\mathrm{mm^6\ m^{-3}}$). Assuming $Z = 320\ R^{1.44}$, a relationship derived by Wexler (1947) for the Laws and Parsons drop size distribution, we obtain the two-way losses

$$L_p = 1.41(10^{-5})Z^{.67}\ \mathrm{dB\ km^{-1}} \qquad (\lambda = 10\ \mathrm{cm})$$

and

$$L_p = 1.98(10^{-4})Z^{.84}\ \mathrm{dB\ km^{-1}} \qquad (\lambda = 3\ \mathrm{cm})$$

Rainfall attenuation has the temperature dependency given in Table A.1.

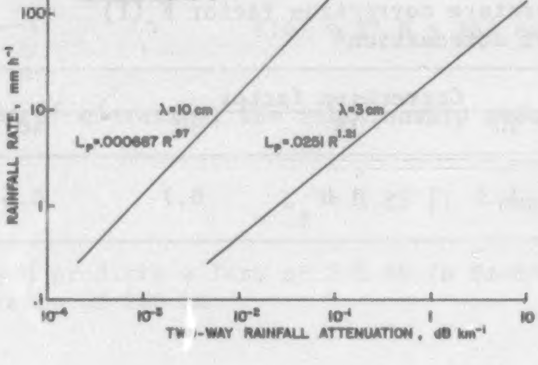

Figure A.1.--Two-way attenuation by rainfall at 18°C (Burrows and Attwood, 1949).

Table A.1.--Multiplicative temperature correction factor $K_p(T)$ for rainfall attenuation*

λ (cm) \ T(°C)	0	10	18	30	40
10 (all rainfall rates)	2.0	1.4	1.0	0.7	0.6
3 ($R = 2.5$ mm h^{-1})	0.8	1.0	1.0	0.8	0.6
3 ($R = 50$ mm h^{-1})	0.6	0.9	1.0	1.0	0.8

Note: $L_p(T) = L_p(18°C)K_p(T)$

*After Burrows and Attwood (1949).

A.2. ATTENUATION BY CLOUDS

Cloud and fog particles (liquid and ice) with diameters $D \lesssim .01$ cm generally are not detected with conventional radars, but nevertheless can cause significant attenuation of radar signals. Losses, $L_c (\equiv 10 \log \ell_c^2)$, are primarily by signal absorption and are proportional to D^3. Total loss is proportional to liquid water content M (g m^{-3}) within the radar beam.

Ryde and Ryde (1945) determined two-way losses at T = 18°C to be

$$L_c = 0.009 \text{ dB km}^{-1} M^{-1} \quad (\lambda = 10 \text{ cm})$$

and

$$L_c = 0.100 \text{ dB km}^{-1} M^{-1} \quad (\lambda = 3 \text{ cm})$$

Attenuation by cloud is also temperature dependent (Table A.2).

Table A.2.--Multiplicative temperature correction factor $K_c(T)$ for cloud droplet attenuation*

λ (cm)	T(°C)	0	10	18	30	40
		Correction factor				
≥ 3		2.0	1.3	1.0	0.7	0.6

Note: $L_c(T) = L_c(18°C)K_c(T)$

*After Ryde and Ryde (1945).

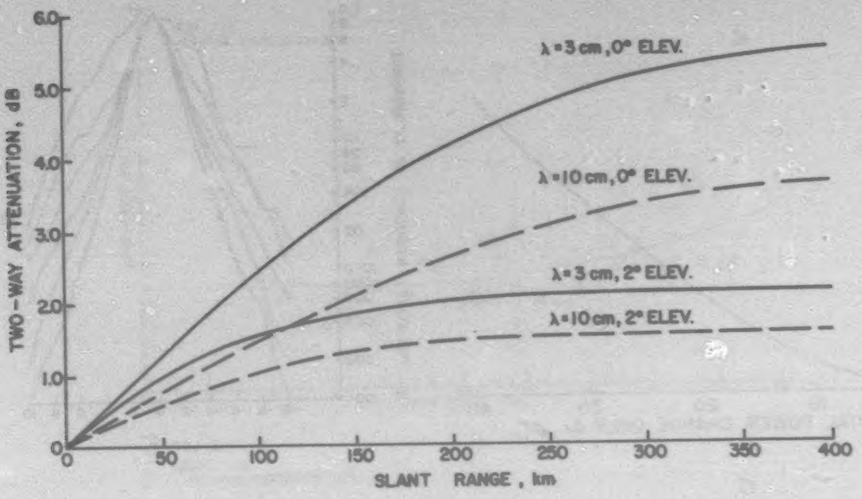

Figure A.2.--Two-way attenuation by water vapor and oxygen. (From Radar Handbook, M. I. Skolnik [ed.], Ch. II, by L. V. Blake. Copyright © 1970 by McGraw-Hill, Inc. Used with the permission of McGraw-Hill Book Company.)

A.3. ABSORPTION BY ATMOSPHERIC GASES

Oxygen and water vapor are the principal gaseous absorbers of microwave radiation. Losses are a function of the radar wavelength and the region of the atmosphere penetrated. Total two-way absorption by both gases L_g ($\equiv 10 \log \ell_g^2$) for the ICAO standard atmosphere has been computed by Blake (1970) (Fig. A.2). A formula that approximates Blake's two-way theoretical losses at λ = 10 cm for elevation angles (ϕ) less than 10° and slant ranges (r) less than 200 km is

$$L_g = L(\phi)\left[1 - \exp\frac{-r}{K(\phi)}\right]\text{dB} ,$$

where

$$L(\phi) = 0.4 + 3.45 \exp(-\phi/1.8)$$

and

$$K(\phi) = 27.8 + 154 \exp(-\phi/2.2)$$

At 0° elevation, the relationship reduces to

$$L_g = 3.85\,[1 - \exp(-r/182)]$$

and predicts a loss of 2.6 dB (a factor of 1.45 in rainfall rate) at a range of 200 km.

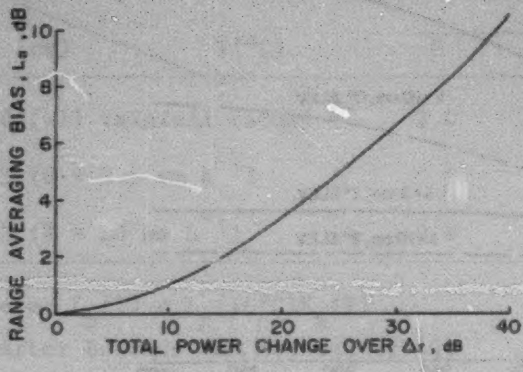

Figure A.3.--Range-averaging bias for an exponential power distribution.

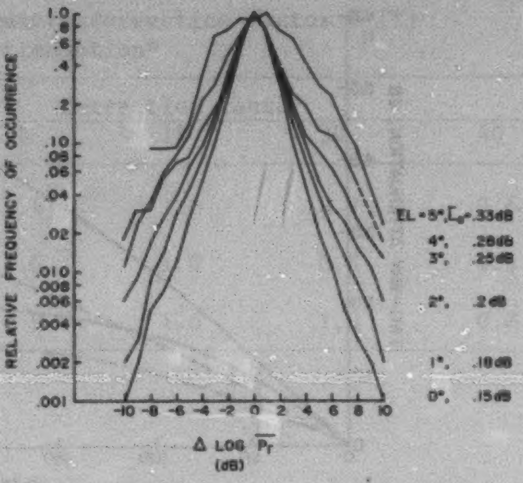

Figure A.4.--Frequency distribution of reflectivity gradients between adjacent range measurements and average bias ($\overline{L_a}$) for tilt sequence of 24 May 1973.

A.4. RANGE-AVERAGING BIAS FOR LOGARITHMIC RECEIVERS

The radar digital integrator produces return power estimates (measurements) by averaging time and range samples. Range averaging of a logarithmic receiver output in regions of reflectivity gradient results in a bias, L_a ($\equiv 10 \log \ell_a$), due to the difference between the logarithm of the spatial average of mean power ($\log \bar{P}_r$) and the spatial average of the logarithm of mean power ($\overline{\log P_r}$).

If the reflectivity distribution across the measurement interval (Δr) is exponential (i.e., $b = 10\ \Delta\log \bar{P}_r/\Delta r$ is constant, where b is the power gradient in dB), the measurement bias is

$$L_g = 10 \left[1 - b\Delta r/20 + \log \left(\frac{10^{b\Delta r/10} - 1}{b\Delta r\ \ln\ 10} \right) \right] \quad \text{dB}$$

(Rogers, 1971; Sirmans and Doviak, 1973). The bias is always positive (Fig. A.3); i.e., estimates of the mean power returned from an averaging volume are less than the true mean.

The distribution of echo reflectivity gradients between adjacent radial measurements 1 km long for a large thunderstorm is given in Fig. A.4. Increased distribution width with elevation angle reflects the reflectivity gradient increase with height. For radar point measurements, gradient bias errors can be very large compared with other errors in the reflectivity measurement.

best copy available

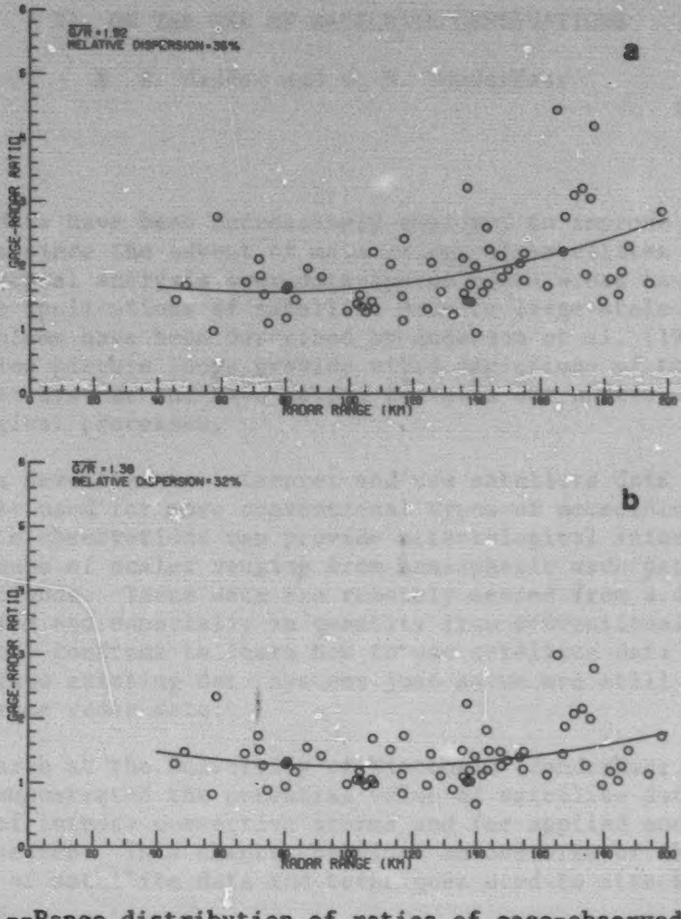

Figure A.5.--Range distribution of ratios of gage-observed and radar-estimated rainfall G/R from 10-11 October 1973 computed with radar measurements (a) unadjusted and (b) adjusted for attenuation by rainfall, attenuation by cloud, atmospheric adsorption, and signal range-averaging loss (after Brandes and Sirmans, 1976).

A.5. CONCLUDING REMARKS

Because the spatial distribution of temperature, water vapor, cloud water, and rainfall is not measured directly and must be estimated, corrections are only approximate. The comparative parameter of importance for hydrological measurements is the ratio of gage-observed and radar-estimated rainfall depth (G/R) and the mean ratio $(\overline{G/R})$; range dependency of G/R and the dispersion among ratios are all reduced if return power is adjusted for the above losses (compare Figs. A.5a and A.5b).

XI. ON THE USE OF SATELLITE OBSERVATIONS

R. A. Maddox and T. H. VonderHaar

1. INTRODUCTION

Satellite data have been increasingly employed to improve large-scale weather analyses since the advent of meteorological satellites in 1960. Improvements in frontal analysis over data-sparse ocean areas have been dramatic; many of the applications of satellite data to large-scale analysis and forecasting problems have been described by Anderson et al. (1974). Visual imagery and motion picture loops provide vivid depictions of the life cycles of entire weather systems and have helped increase our understanding of large-scale meteorological processes.

The methods developed to interpret and use satellite data differ considerably from those used for more conventional types of meteorological observations. Satellite observations can provide meteorological information that bridges a continuum of scales ranging from hemispheric wave patterns to individual cumulus clouds. These data are remotely sensed from a space platform and differ in kind and especially in quantity from conventional in situ data. Therefore, we must continue to learn how to use satellite data and how to incorporate them into existing data systems just as we are still learning to use and incorporate radar data.

Early research at the University of Wisconsin (VonderHaar, 1969; Sikdar et al., 1970) demonstrated the potential value of satellite data for detection and monitoring of intense convective storms and for applied and theoretical thunderstorm research. This chapter provides an overview of the many types of applications of satellite data and techniques used to attack thunderstorm-related problems.

2. SATELLITE TECHNOLOGY

The National Oceanic and Atmospheric Administration (NOAA) and its National Earth Satellite Services (NESS), in cooperation with the National Aeronautics and Space Administration (NASA), have established and operated a system of polar-orbiting and geostationary operational environmental satellites. Although the first satellites were rather crude and carried low-resolution imaging devices, the current generation ITOS/NOAA and SMS/GOES satellites carry sophisticated, high-resolution sensors that provide quantitative data in the infrared and visible spectra. (The above acronyms stand for Improved TIROS Operational Satellite [ITOS], Synchronous Meteorological Satellite [SMS], and Geostationary Operational Environmental Satellite [GOES].) See Ludwig (1974) and Fordyce et al. (1974) for more details of the environmental satellite program.

Visible channel data from GOES East and West provide routine operational coverage of the United States during daylight hours. Infrared (IR) data are available around the clock, and these data are computer processed to produce enhanced displays that quantitatively depict cloudtop temperature. These satellite products are routinely used in operations of the six Satellite Field Service Stations (Washington, D.C.; Miami, Fla.; Kansas City, Mo.; Anchorage, Alaska; San Francisco, Calif.; and Honolulu, Hawaii) and are transmitted via telephone lines to all of the National Weather Service's (NWS) Weather Service Forecast Offices (WSFO's) and other users (universities, private sector forecasters, etc.). These data are routinely used to monitor thunderstorm development, intensity, and movement and are also used to refine regional-scale analyses of meteorological conditions.

The GOES data are routinely available at 30-min intervals; occasionally, however, more frequent collections support field projects or special research efforts. Krietzberg (1977) described the special satellite data taken during 1977 Research Rapid Scan Days to provide special severe-storm and mesoscale numerical-modeling data, and Reynolds and Matthews (1976) reported on the use of satellite imagery by forecasters involved in the Bureau of Reclamation's High Plains Experiment, HIPLEX. HIPLEX involved a study of the feasibility of enhancing convective precipitation over the High Plains.

Multiple-channel radiometric measurements may be used to remotely sound atmospheric profiles of temperature and water vapor (McMillin et al., 1973; Weinreb and Crosby, 1973). Such soundings will play an increasingly important role for forecasting thunderstorm potential and intensity, for studying prestorm and near-storm environment, and for initialization of regional, or mesoscale, numerical models. The role of satellite observations in numerical modeling has been reviewed by Krietzberg (1976). Remotely sensed atmospheric profiles may be important for future field programs designed to study thunderstorm environments and interactions (see Lilly, 1977). Several important radiation sensors are discussed in more detail in the following sections.

a. Vertical-temperature profile radiometer (VTPR)

The VTPR was flown on the NOAA 2 and 3 satellites and was designed to obtain measurements of atmospheric vertical-temperature structure. Radiant energy is measured in six discrete intervals within the 15-μm CO_2 region, at an interval in the 11-μm atmospheric window, and at an interval in the 18-μm water vapor region. The data may be used to infer vertical-temperature profiles and to compute integrated water vapor content.

The VTPR is equipped with a detector that is sensitive to radiant energy. Eight filters that define the wavelength intervals are located on a wheel in front of the detector, and each one rotates into the field of view every 62.5 milliseconds. A schematic drawing of the VTPR radiometer is shown in Fig. 1. The instrument scans 31.45° to either side of the orbit track in 23 equal steps. Coverage along the track results from the movement of the satellite. Global coverage is obtained; however, since the satellite orbits are Sun synchronous, coverage for any particular geographic area is available only twice per day.

b. Visible and infrared spin scan radiometer (VISSR)

The VISSR is the principal instrument on the SMS/GOES satellites (see Fig. 2) and is basically a telescope with a precision latitude-stepping mechanism. The instrument scans west to east with each revolution of the satellite, and a latitude step between each rotation produces a scan of the full Earth disk. A visible channel (0.55-0.75 μm) and an infrared channel (10.5-12.6 μm) are observed. The IR channel scans one line each rotation, which provides approximately 8-km resolution at the subpoint (point on

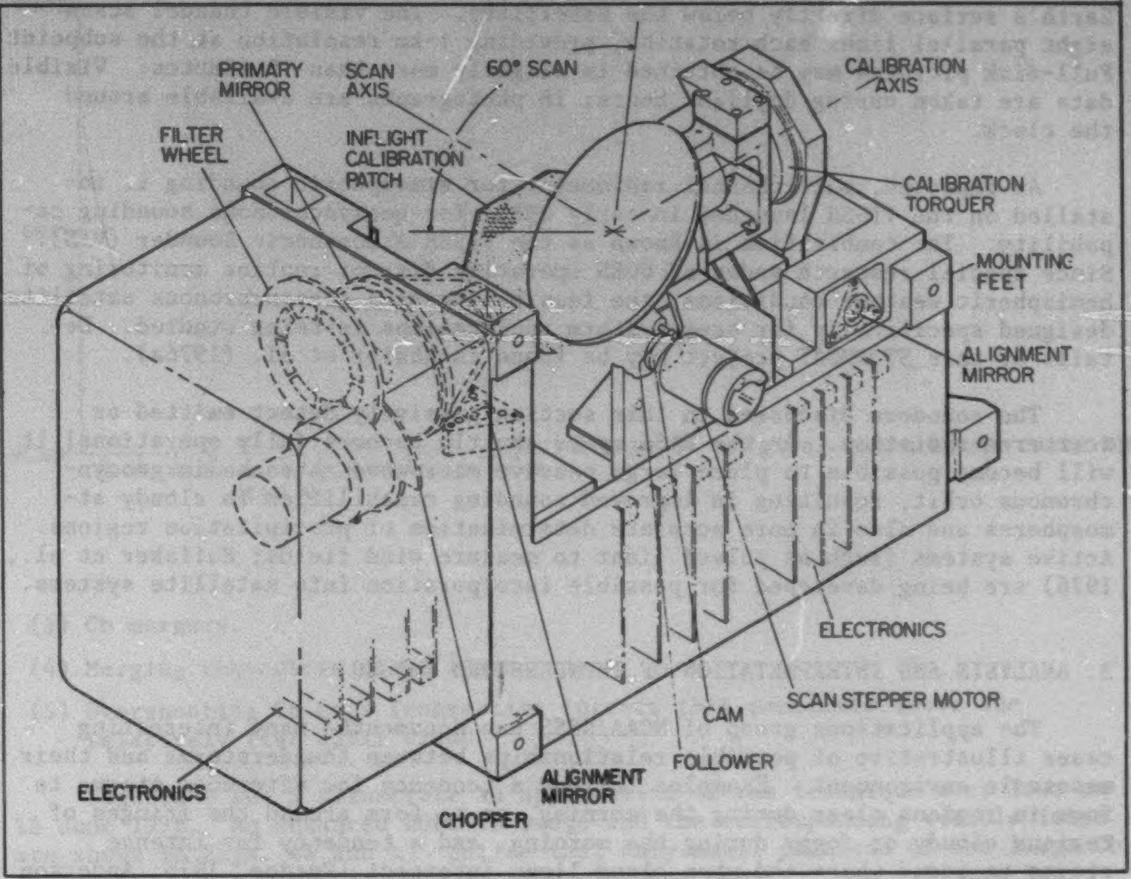
PRIMARY MIRROR
SCAN AXIS
60° SCAN
CALIBRATION AXIS
FILTER WHEEL
INFLIGHT CALIBRATION PATCH
CALIBRATION TORQUER
MOUNTING FEET
ALIGNMENT MIRROR
ELECTRONICS
SCAN STEPPER MOTOR
CAM
FOLLOWER
ALIGNMENT MIRROR
ELECTRONICS
CHOPPER

Figure 1.--Isometric view of the Vertical Temperature Profile Radiometer (cover removed) (McMillin et al., 1973).

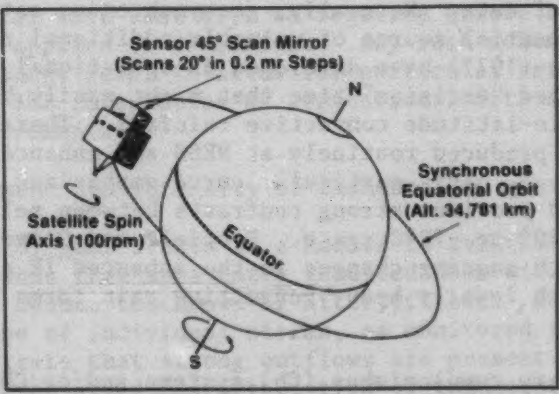
Sensor 45° Scan Mirror (Scans 20° in 0.2 mr Steps)
N
Synchronous Equatorial Orbit (Alt. 34,781 km)
Satellite Spin Axis (100rpm)
Equator
S

Figure 2.--GOES/VISSR configuration (after Fordyce et al., 1974).

Earth's surface directly below the satellite). The visible channel scans eight parallel lines each rotation, providing 1-km resolution at the subpoint. Full-disk pictures may be obtained in slightly more than 15 minutes. Visible data are taken during daylight hours; IR photographs are available around the clock.

An improved, multichannel radiometer for atmospheric sounding is installed on the VISSR launched in early 1981, for geosynchronous sounding capability. The combination is known as the VISSR Atmospheric Sounder (VAS). Since special research modes of GOES operation disrupt routine monitoring of hemispheric weather conditions, the feasibility of a geosynchronous satellite designed specifically for severe-storm applications is being studied. Details of this STORMSAT project may be found in Hasler et al. (1976a).

The sounders discussed in this section passively detect emitted or scattered radiation. As the NASA space shuttle becomes fully operational it will become possible to place large passive microwave antennae in geosynchronous orbit, resulting in improved sounding capabilities in cloudy atmospheres and also in more accurate determination of precipitation regions. Active systems (such as pulsed lidar to measure wind fields; Huffaker et al., 1976) are being developed for possible incorporation into satellite systems.

3. ANALYSIS AND INTERPRETATION OF THUNDERSTORM IMAGES

The applications group of NOAA/NESS has documented many interesting cases illustrative of possible relationships between thunderstorms and their mesoscale environment. Examples include a tendency for afternoon storms to form in regions clear during the morning, or to form around the fringes of regions cloudy or foggy during the morning, and a tendency for intense storms to occur where and when cloud lines intersect (Purdom, 1976; Anderson et al., 1974; Scofield and Weiss, 1976). Specific cases demonstrating the use of satellite imagery in thunderstorm detection, monitoring, and forecasting are presented in the following sections.

a. Determination of convective rainfall

Meteorologists and hydrologists must often issue river forecasts and/or flood warnings when important precipitation events are occurring over regions relatively devoid of data. Naturally, geosynchronous satellite data have been considered as a potential source of valuable additional rainfall information. Scofield and Oliver (1977) have developed an operational, quantitative scheme (involving a detailed "decision" tree that might easily be automated) for use in estimating middle-latitude convective rainfall. Their technique employs IR images that are produced routinely at NESS and enhanced according to the curve shown in Fig. 3. This particular curve emphasizes cold cloudtop temperatures ($\leq -30°C$) and provides strong contrasts between selected temperature intervals in the -30° to -70°C range. Scofield and Oliver noted that certain patterns, along with ongoing changes in the enhanced IR and visible imagery, were associated with locally heavy convective rainstorms. The features were these:

(1) Quasi-stationary cumulonimbus (Cb) systems and/or Cb systems regenerating over the same location.

(2) Cold, rapidly expanding Cb anvils.

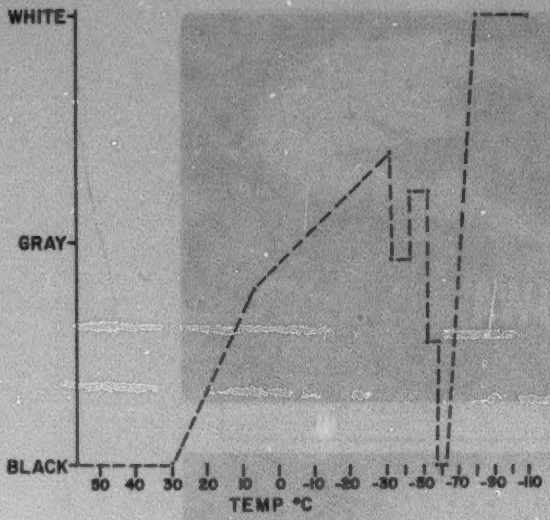

Figure 3.--Digital enhancement curve MB.

(3) Cb mergers.

(4) Merging convective cloud lines.

(5) Overshooting Cb tops (convective turrets that penetrate above the relatively flat anvil cloud).

Figures 4 and 5 illustrate an application of the technique over Iowa on 13 June 1976. An enhanced GOES IR image and the corresponding visible image are shown in Figs. 4a and b. Notice that only small portions of the large Cb systems are characterized by very cold cloudtop temperatures. Figure 5a presents the 24-h accumulated rainfall estimate derived from satellite data for 1200 GMT 13 June to 1200 GMT 14 June. The observed 24-h rainfall (Fig. 5b) indicates that the technique defined areal rainfall patterns reasonably well; however, small-scale variations were not resolved (see regions designated A) and nighttime rains (with no visible data available) were underestimated in the regions designated B.

This particular method of rainfall estimation represents an initial phase of developmental work that will be required before a scheme that can be more universally applied is determined. Any such scheme will require fine tuning at the local level to allow for particular terrain and climate variations and also for integration of conventional data such as surface and radar rainfall measurements.

b. Monitoring movement and intensity of thunderstorm gust fronts

The importance of gust fronts as a hazard to aviation has been emphasized by recent crashes that apparently resulted when aircraft penetrated gust fronts shortly before touchdown or after liftoff. Fujita (1978) believes that the shape of individual storms, as monitored in satellite and radar data, may indicate that strong outflows are present. Gurka (1976) has correlated satellite-observed characteristics of thunderstorm cloud arcs with concurrent surface wind observations. Figures 6a and b show the southward progression of a cloud arc across the Baltimore/Washington, D.C., area from

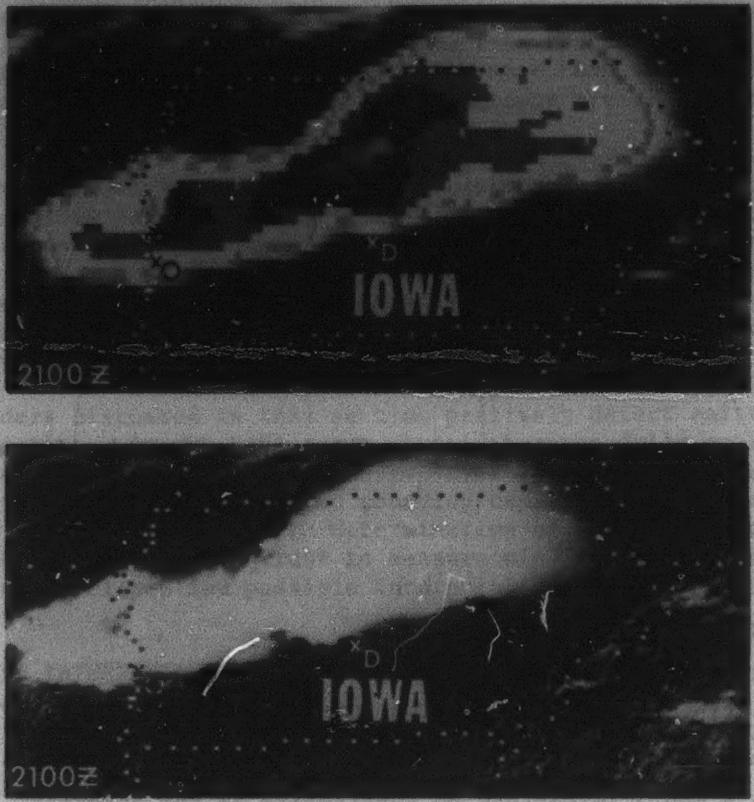

Figure 4.--Enlarged area from (above) 2-km equivalent IR produced using digital enhancement (MB curve) and (below) 2-km visible imagery for 2100 GMT, 13 June 1976 (Scofield and Oliver, 1977).

2100 to 2200 GMT on 3 July 1975. Selected surface wind observations have been superposed on the images.

Gurka lists the following characteristics of thunderstorm gust fronts that can be identified using satellite imagery:

(1) Wind gusts and wind shear occur very near to or at the leading edge of the cloud arc.

(2) Strongest winds occur beneath the portion of the arc nearest to the most vigorous convection.

(3) The regions of vigorous convection are pinpointed by the cloud edge brightness gradients on enhanced IR imagery.

(4) Cloud arcs bounding mesohighs associated with a cloudy area and active convection are characterized by stronger gusts than are narrow cloud arcs that are trailed by clear skies.

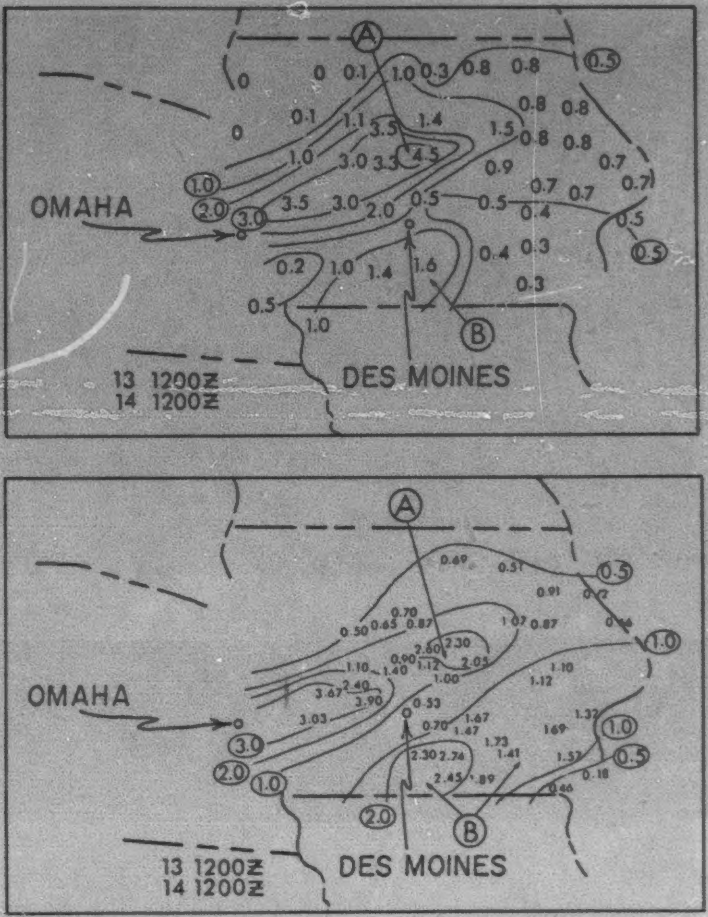

Figure 5.--1200 GMT, 13 June-1200 GMT, 14 June 1976: (above) satellite-derived rainfall estimate in inches; (below) observed rainfall in inches (Scofield and Oliver, 1977).

(5) Rapidly moving cloud arcs are generally associated with strong low-level winds.

c. Severe-thunderstorm/jetstream relationship

Many researchers have presented both observational and theoretical studies that relate positions of jetstreams, or bands of maximum windspeeds, with the development, location, and orientation of severe thunderstorms. Whitney (1977), studying severe-storm occurrences on 16 active days, found that severe activity rarely developed south of the subtropical jetstream. The positions of jetstream features were determined using both satellite photographs and conventional upper-air sounding data..

Figure 7 shows Whitney's analysis of the 30 April 1975 severe-thunderstorm situation. The subtropical jetstream sharply delineates the southern

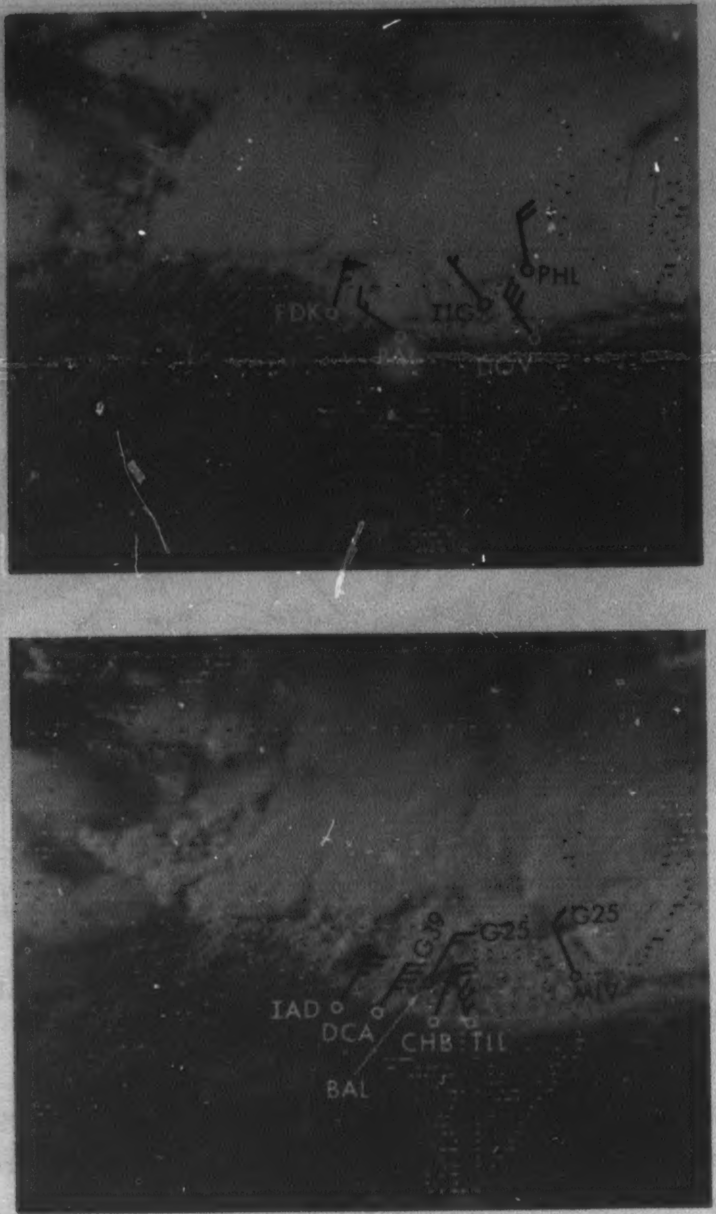
FDK
IIG
PHL
BAL
DOV
G30
G25
G25
IAD
DCA
CHB
TII
BAL
MIV

Figure 6.--SMS-1 visible 1-km data showing surface wind observations for 2100 GMT, 3 July 1975 (above); 2200 GMT, 3 July 1975 (below) (Gurka, 1976).

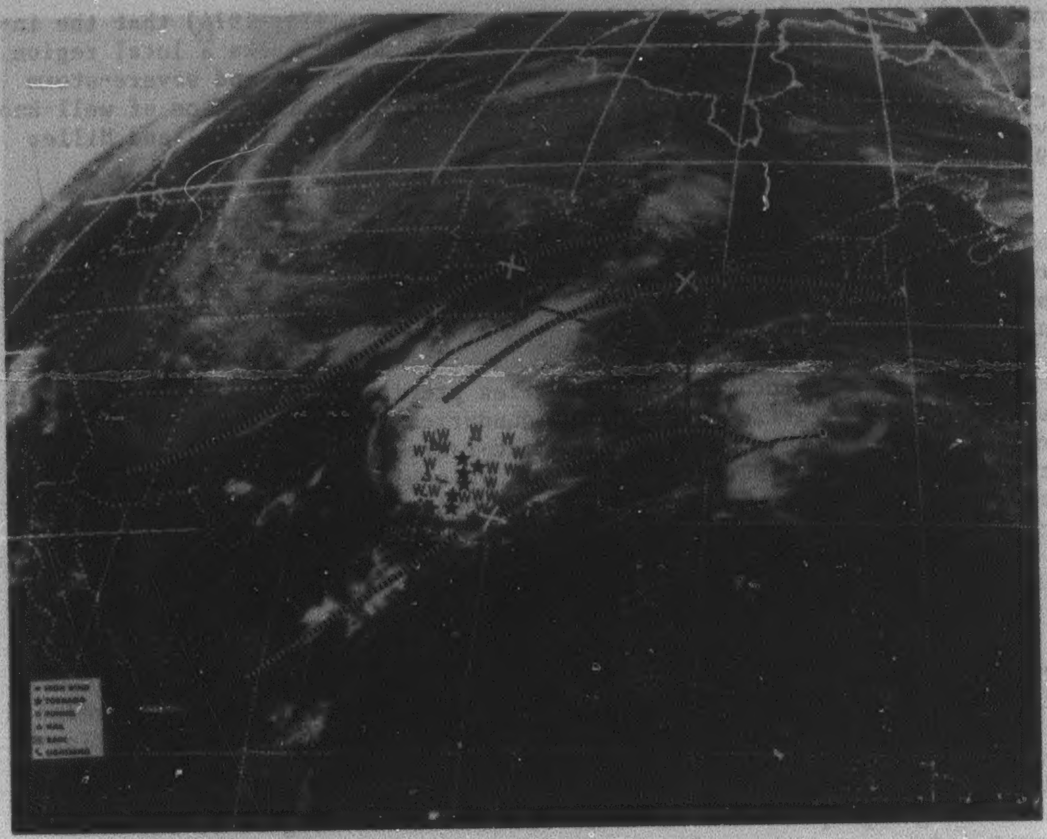

Figure 7.--SMS infrared picture at 0000 CST, 30 April 1975 showing concurrent severe storms and the synoptic features of jetstreams and surface fronts. Bold dashed lines are the axes of the jetstreams. Heavy ×'s are positions of wind maxima. Subtropical windspeed maximum is >100 knots. Thin, candy-striped lines are surface fronts. Dotted lines are geographical and political grid overlay (Whitney, 1977).

boundary of the large area of severe-storm occurrences. He found that severe thunderstorms usually develop first along the surface front very near to the polar jetstream (note that a double polar jet structure was analyzed in Fig. 7). Activity then moves eastward ahead of the surface front while developing southward across the zone between the diverging jetstreams. Miller and McGinley (1978) have recently developed a technique for forecasting severe thunderstorms that integrates conventional upper-air data, surface analyses, and satellite imagery to identify zones or areas having storm potential. The detection and tracking of various jetstreams and jetstream branches (using both satellite imagery and upper-air reports) play a crucial role in this innovative forecast scheme, and the interested reader should refer to their extensive report for specifics.

d. Thunderstorm boundaries and intersections

Making use of satellite imagery, Purdom (1976) shows that the leading boundary of a thunderstorm-associated mesohigh often appears as an arc-shaped line of convective clouds. He also shows (Purdom, 1973; 1974) that the intersection of such an arc cloud with another boundary marks a local region with a high potential for intense convective development and severe-storm occurrence. These findings provide "photographic" verification of well-known severe-storm characteristics presented earlier by Magor (1959) and Miller (1972).

Such a convective development is presented in Figs. 8a, b, and c, which show the 2100 GMT GOES-1 photograph on 26 May 1975, a corresponding mesoscale surface analysis, and a subsequent photograph for 2230 GMT. The impressive convective development in south central Oklahoma occurred in the favored arc line/boundary intersection zone at point A.

The ability to locate such boundaries precisely in GOES imagery and to observe their interaction with other boundaries provides the forecaster information that can be of use in the short-range prediction of intense convective development. Such data are also valuable for studies of the climatology of such boundary effects and the dynamical reasons for their occurrences.

e. Cloudtop tornadic signatures

Fujita and his colleagues have tried to relate cloudtop features to severe-weather occurrences at the surface (Fujita 1973; Shenk, 1974). Fujita has proposed that the decay of overshooting cloudtops may be related to tornado development. Figure 9 presents a correlation of overshooting cloudtops with the occurrence of several intense tornadoes in Illinois and Indiana on the afternoon of 20 March 1976. The storm was characterized by overshooting tops prior to and after the tornadoes. Figure 10 shows concurrent radarscope and satellite photographs at the time when the large Sadorus tornado was known to be on the ground at point A, where the satellite photograph shows a swirl in the relatively flat anvil top. Temporal and spatial satellite data of very high resolution are required if such features are to be closely monitored, and many more case studies are needed before reliable forecast techniques can be developed.

f. Mesoscale convective weather systems

The identification of large, long-lived convective weather systems (called Mesoscale Convective Complexes [MCCs] by Maddox [1980]) was made possible by the operational availability of enhanced IR satellite images (see Figs. 3 and 4) at half-hourly intervals. The life cycle of a typical MCC is illustrated in Fig. 11. These systems produce a wide variety of significant convective weather phenomena including tornadoes, hail, wind, flash floods, and intense electrical storms, in addition to widespread beneficial rains. Substantial research efforts are required before we will understand the physical mechanisms that produce MCCs; however, satellite imagery has already proved useful in helping forecasters recognize and track MCCs and thereby improve local weather forecasts.

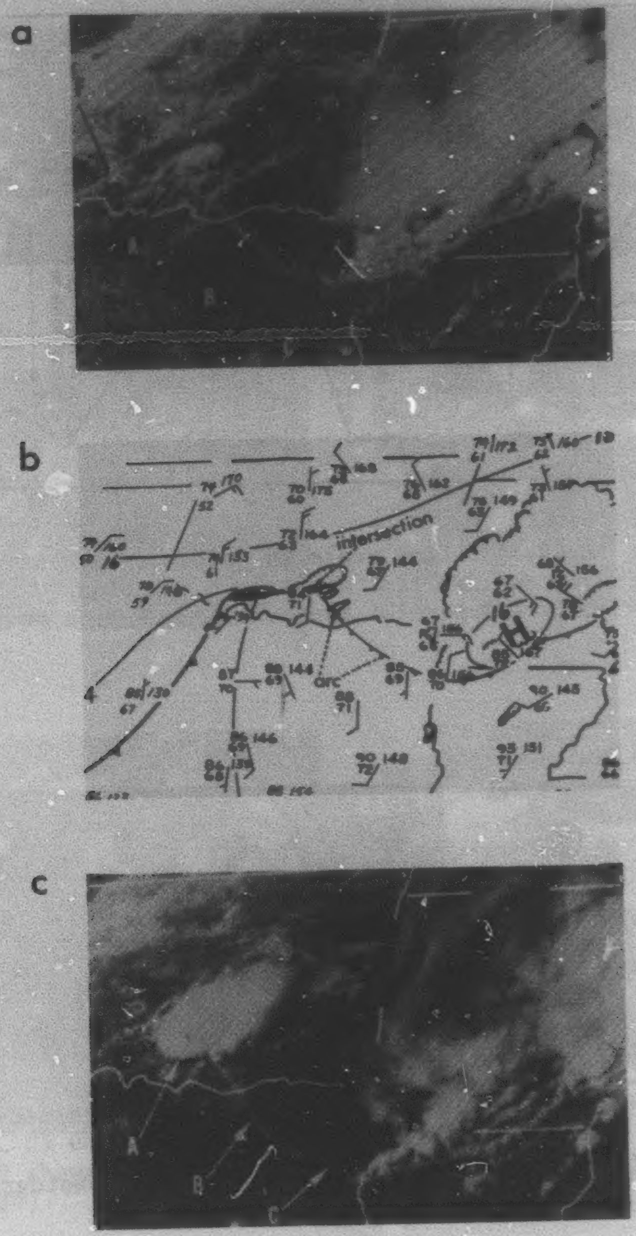

Figure 8.--(a) GOES-1 1-km visible imagery for 2100 GMT, 26 May 1975. A cloud arc, produced by the storms over Arkansas, stretches from A to B to C. A second arc line is indicated at F. (b) Surface analysis for 2100 GMT, 26 May 1975, showing selected clouds and cloud boundaries. (c) GOES-1 1-km visible imagery for 2230 GMT, 26 May 1975 (Purdom, 1976).

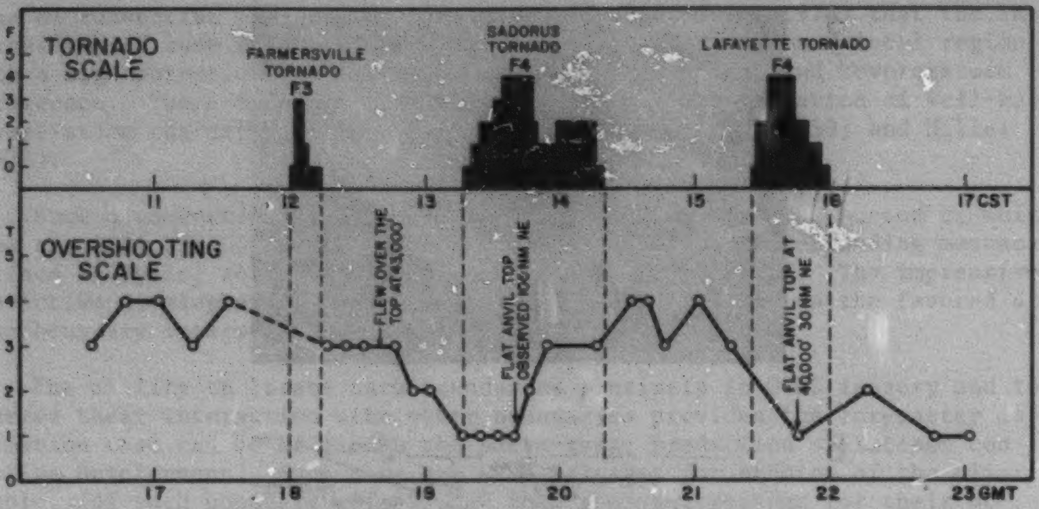

Figure 9.--Change in overshooting scale (5 indicates intense overshooting top activity; 1 indicates very flat anvils) in relation to the intensity of tornadoes spawned by a supercell thunderstorm (Fujita et al., 1976).

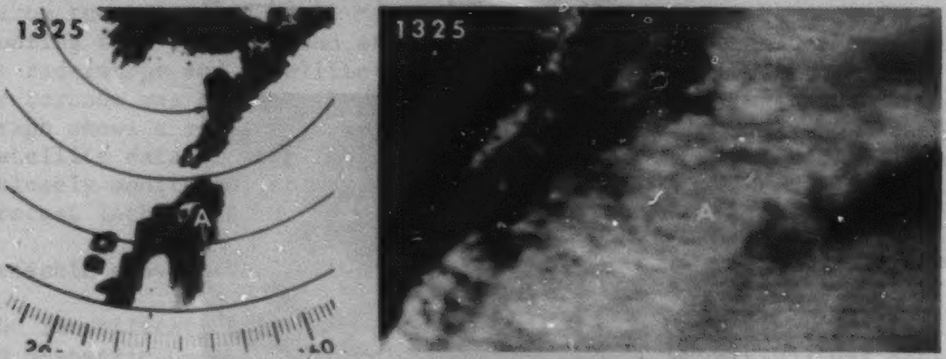

Figure 10.--Concurrent radar PPI scope and satellite photographs of the tornadic thunderstorm (Fujita et al., 1976).

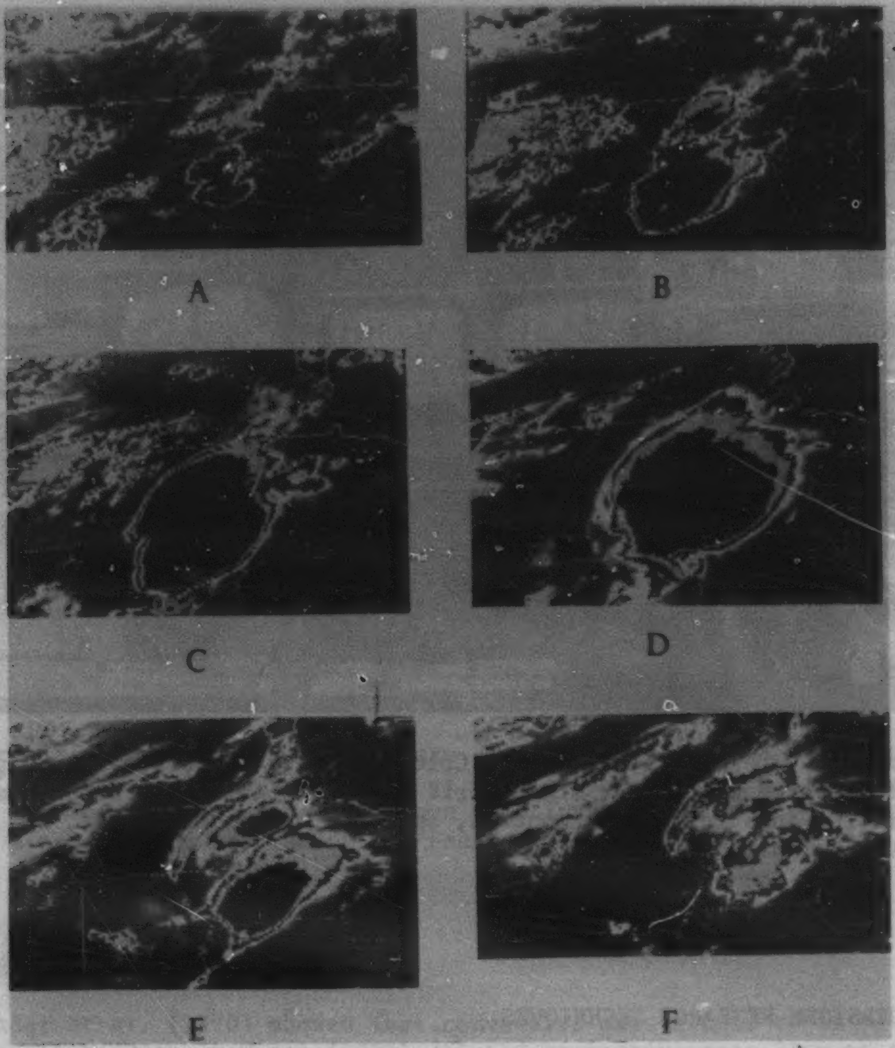

Figure 11.--Series of enhanced infrared satellite images for A) 0030 GMT, B) 0300 GMT, C) 0600 GMT, D) 0900 GMT, E) 1430 GMT, and F) 1630 GMT on 12 July 1979 showing the life cycle of a Mesoscale Convective Complex (Maddox, 1980).

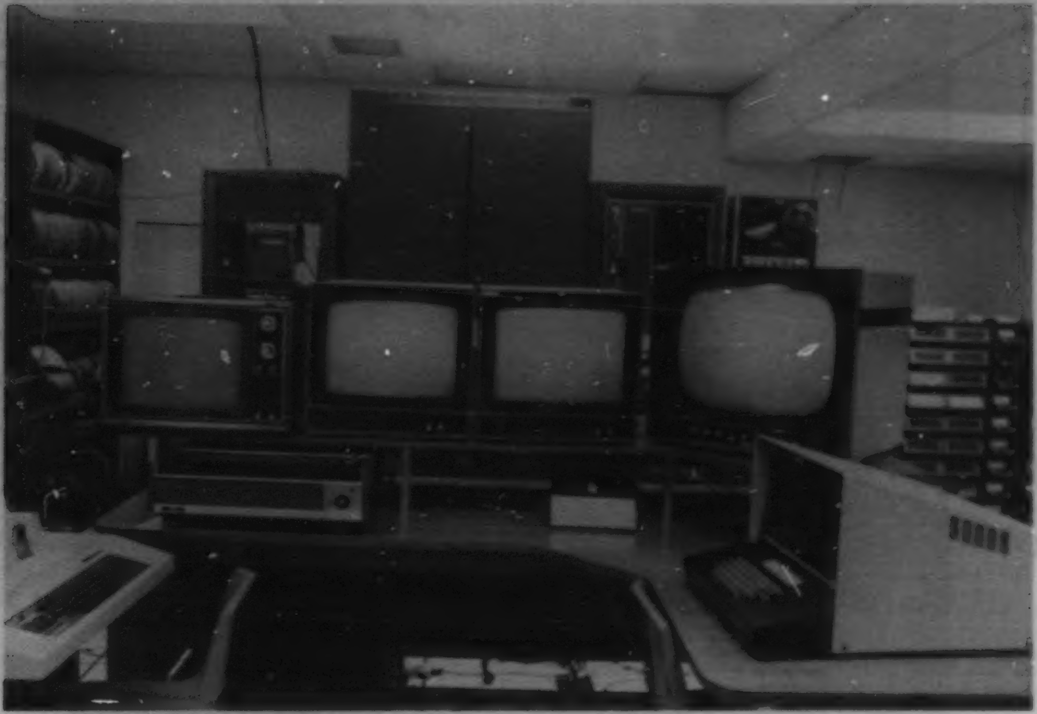

Figure 12.--Design layout of the Colorado State University All Digital Video Imaging System for Atmospheric Research (ADVISAR): color display monitors, joystick cursor control, operator CRT and keyboard, and the system teleprinter and keyboard.

4. THUNDERSTORM RESEARCH TECHNIQUES

The recent development of interactive human/machine computer systems specifically designed for processing and analyzing satellite data has encouraged more quantitative thunderstorm research. Use of digital data transmitted from the satellite and stored on magnetic tape is possible in these systems. Different applications, ranging from sequential looping and cloud tracking to produce a wind field, to color enhancements of specific features, to superposed displays of differing data types, are available. Navigation (Earth coordinate location of features) accuracy to within a single data element (pixel) is possible on these systems. Interactive satellite data-processing systems have been developed by Goddard Space Flight Center (NASA), the University of Wisconsin, and Colorado State University. (See, for example, Billingsley's [1976] description of the NASA/AOIPS [Atmospheric and Oceanic Information Processing System] and Anthony and Bristor's [1978] article on interactive systems and storm prediction.) Specifications and details of the different systems vary, but they allow the researcher to get at the data in varying ways and process them accurately, pixel by pixel if required. Figure 12 shows the physical setup of the CSU ADVISAR (All Digital Video Imaging System for Atmospheric Research).

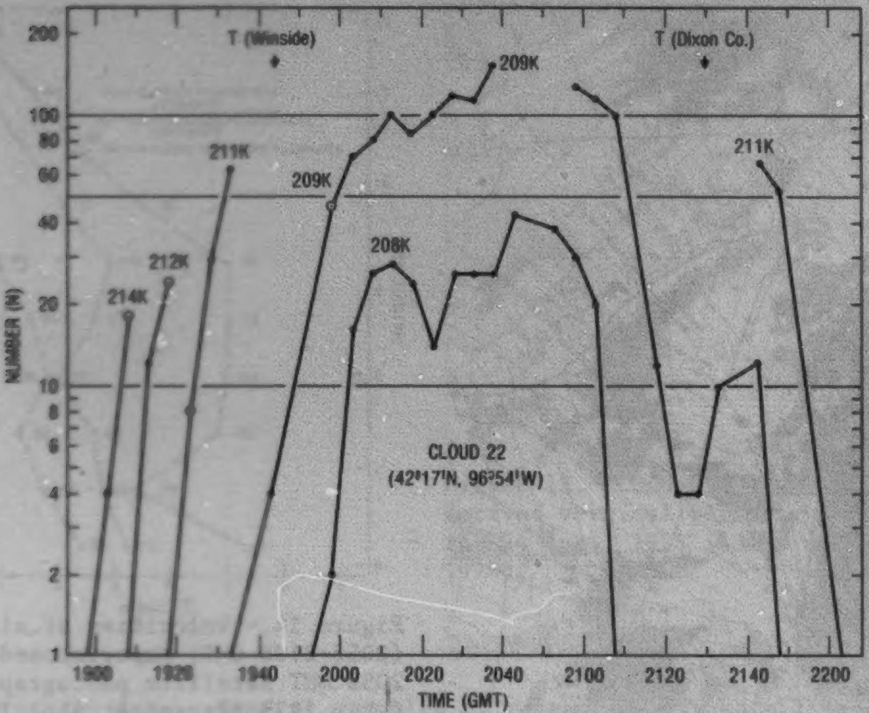

Figure 13.--Thunderstorm growth rate diagram for a tornado over South Dakota on 6 May 1975. The number of pixels (i.e., area) having specific cold radiative temperatures is shown as a function of time. T's indicate time of tornadoes (Adler and Fenn, 1977).

a. Cloudtop temperature fields

Sikdar et al. (1970) showed that convective mass fluxes could be estimated using satellite data, and Arn (1975) related convective mass flux to severity for several storms. Adler and Fenn (1977) used infrared data and an interactive system to compute cold cloudtop areas as a function of time for many cloud systems that included several significant severe thunderstorms. They also used the rate of increase of cloudtop area to estimate anvil divergence. Figure 13 shows a plot of cold cloudtop area with time for a tornadic cloud system over South Dakota on 6 May 1975.

Adler and Fenn found that the first report of tornadic activity took place during, or just after, the rapid expansion of cold cloud area, indicating rapid ascent and growth of thunderstorm tops on the scale observed by the satellite. These findings are different from the results presented in Fig. 9. This discrepancy may be due to the difference in resolution of the IR and visible sensors (overshooting tops must be quite large to be detected in the IR), and the need for further studies of cloudtop activity as a signature of storm severity is apparent. It is possible that such studies may lead not only to improved detection and warning of tornadic storms but also to better understanding of the dynamics and thermodynamics of tornado development.

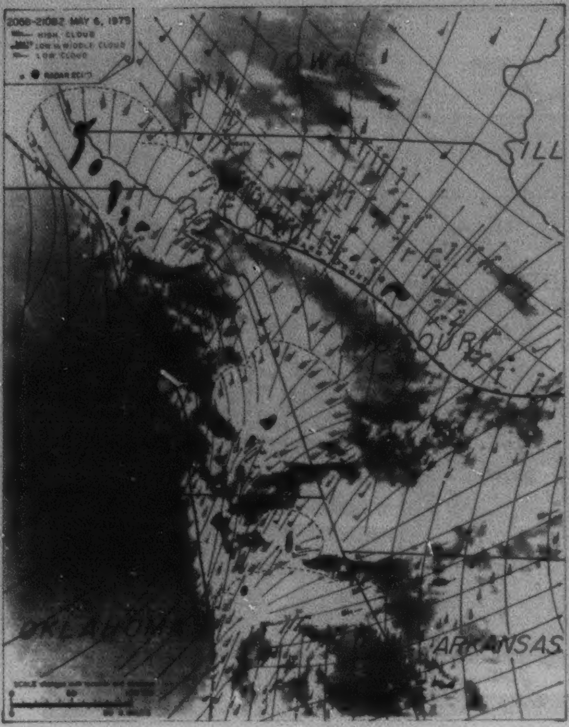

Figure 14.--Velocities of all clouds (2058-2108 GMT) superimposed on the 2058 GMT satellite photograph for 6 May 1975 (Tecson et al., 1977).

Reynolds (1980) studied the IR cloudtop temperature fields associated with a number of damaging hailstorms. In all but one case, he found that the coldest temperatures were located near the hailfall. The cloudtop temperatures were also noted to be 1° to 8°C colder than the environmental tropopause temperature. He thus identified a potential technique for identifying damaging hailstorms through enhancement of digital GOES infrared imagery. However, since all of his cases occurred over the High Plains, further study is required to determine if this technique is applicable to storms over other regions.

b. Cloud motions and wind fields

Animated film loops dramatically show cloud motion fields, and interactive computer systems allow tracking of individual clouds and derivation of associated environmental wind fields. A composite flow field obtained by Tecson et al. (1977) by tracking low, middle, and high clouds on 6 May 1975 is shown in Fig. 14. Since many of the important cloud features associated with thunderstorm developments are convective and have relatively short lifetimes, it is important that the time interval between successive photographs in the data loop be as short as possible. Special projects and research efforts have been set up, and a considerable base of GOES data at intervals of 3 to 15 minutes has been gathered. (Details of several such special projects may be found in Hill and Turner [1977].)

Fujita et al. (1975) and Hasler et al. (1976b) have examined cumulus-cloud motion in relation to the environmental wind field. Although low-level clouds are not perfect tracers, the uncertainty seems similar to that

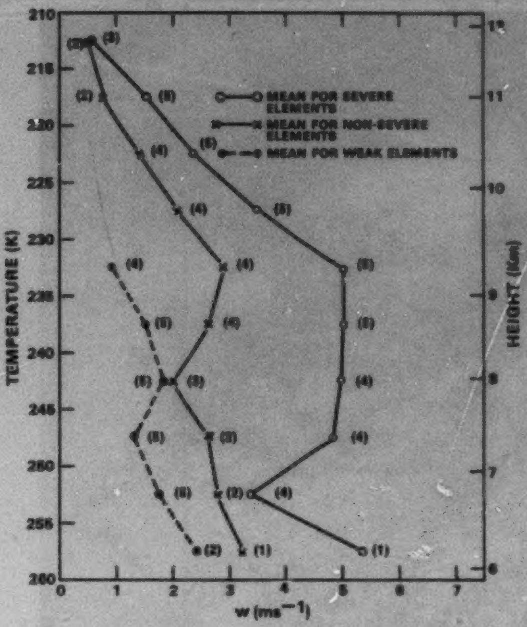

Figure 15.--Composite satellite-derived vertical velocity profiles for 24 April 1975 (Adler and Fenn, 1979).

for rawinsonde data. Several examples of research using satellite-derived wind fields from intense convective storm situations are included below.

(1) Vertical motion

Investigators at the University of Wisconsin have tracked clouds at all available levels within the troposphere and then used the derived winds in a simple, multilayered, diagnostic numerical model. (Details of this work may be examined in Houghton and Lee [1977].) Diagnosed vertical motion corresponded roughly with ongoing convective activity and with vertical motion fields generated by a prognostic numerical model.

The Wisconsin investigators believed that it was possible to obtain a sufficient number of horizontal motion vectors from the clouds to describe the three-dimensional structure of the atmospheric wind field. Mesoscale horizontal divergence and vertical motion fields related in a consistent manner to observed clouds and to the area of subsequent severe-storm occurrence. They believe that satellite data can be used to enhance the descriptions of atmospheric velocity fields obtained by more conventional means.

On a much smaller scale, Adler and Fenn (1979) used infrared geosynchronous satellite data with an interval of 5 minutes between images to estimate thunderstorm top ascent rates. They found a significant difference in the mean calculated vertical velocity between elements associated with severe-weather reports and those with no such reports (see Fig. 15 for an example of their results). Their study provides an important starting point for quantitative use of satellite data in the study of individual thunderstorms and their intensity.

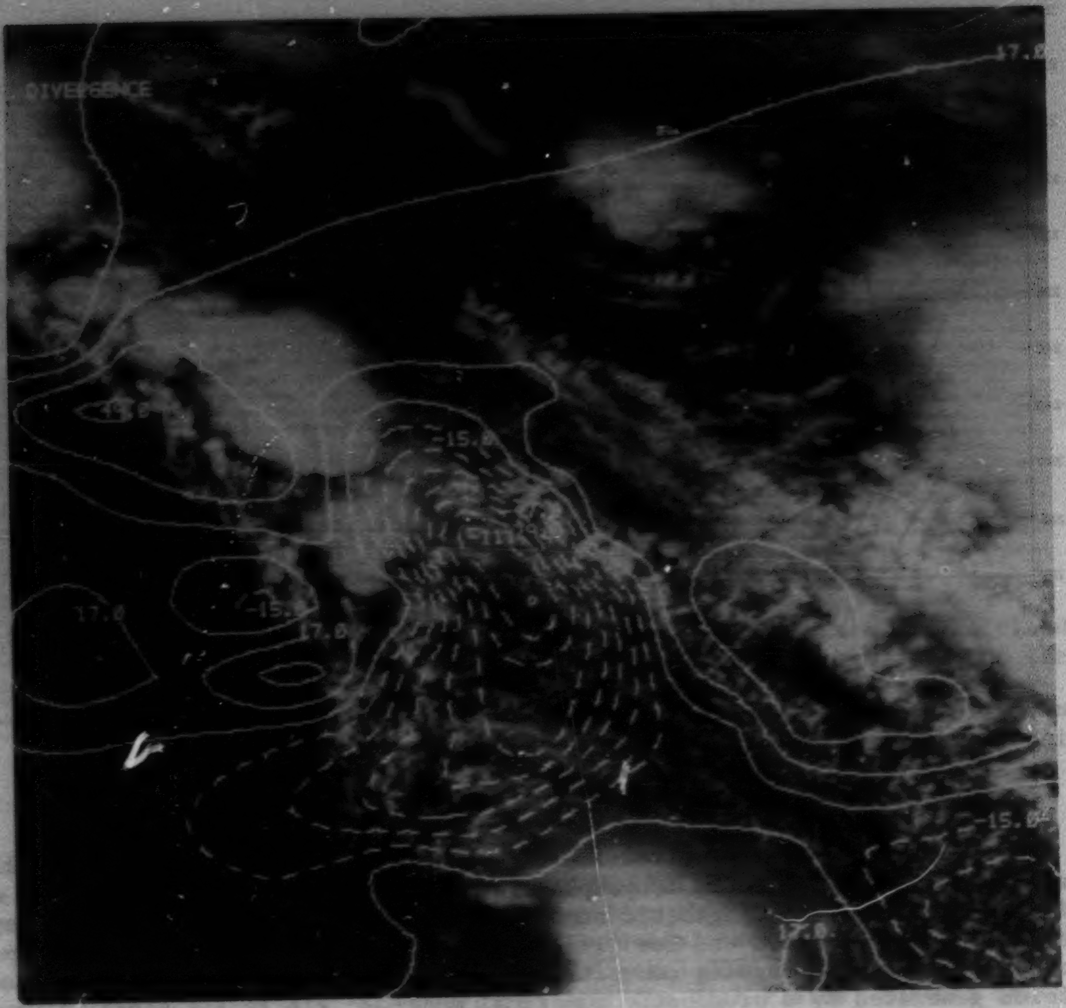

Figure 16.--Divergence (× 10^{-6} s^{-1}) calculated from satellite-derived low-level cloud motion vectors for 1918-1928 GMT on 6 May 1976 (Peslen, 1977).

(2) Divergence fields

Researchers at Goddard Space Flight Center have used the NASA/AOIPS system to develop many sets of low-level wind data. Examples of divergence fields computed using these wind data were presented by Peslen (1977). The computed divergence for 1918-1928 GMT on 6 May 1975 superimposed on the visible GOES image is shown in Fig. 16. The most intense convective developments occur near the region of diagnosed strong convergence. The availability and distribution of small cumulus-cloud tracers near large storms affects such computations.

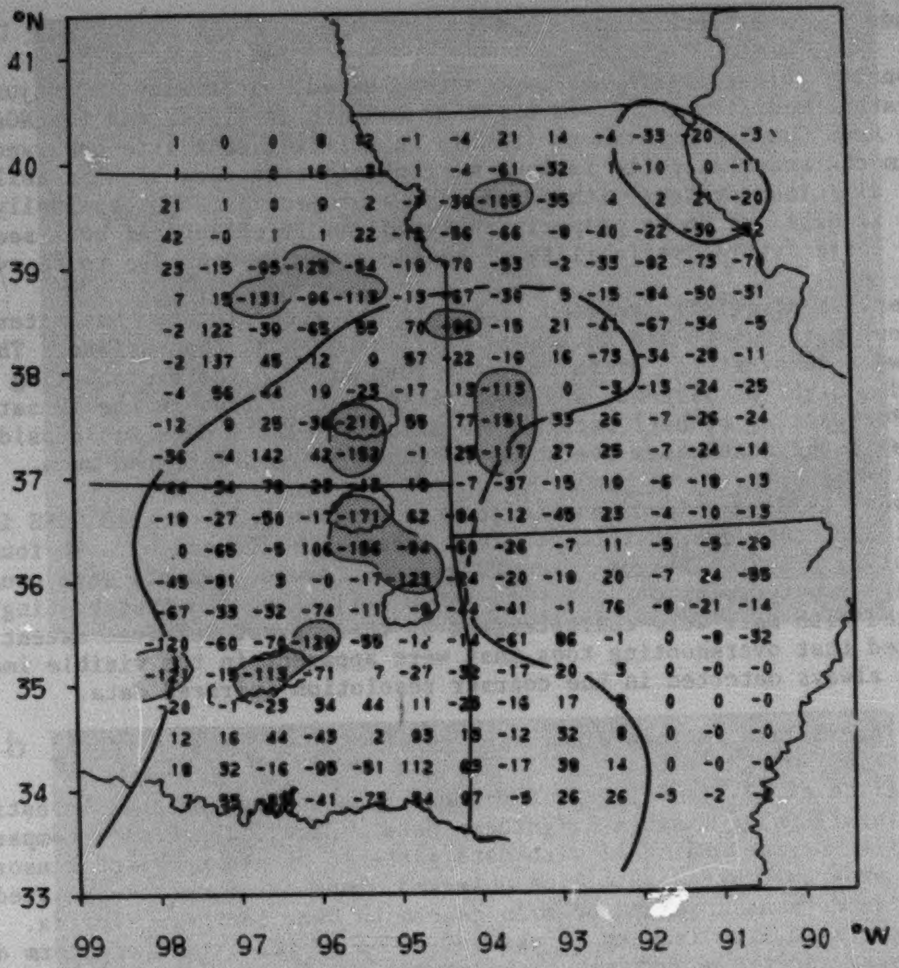

Figure 17.--Moisture divergence field. Units are 10^{-5} g kg^{-1} s^{-1} and values of convergence $>10^{-3}$ are stippled. In the x direction, only alternate grid point values have been plotted. Cloud outlines indicate severe-storm genesis areas, and the zone of confidence is enclosed by the solid lines (Negri and VonderHaar, 1980).

(3) Moisture divergence

Negri and VonderHaar (1980) combined low-level, satellite-derived wind data with an analysis of conventionally determined surface mixing ratios. The computed regions of strong moisture convergence (see Fig. 17) were characterized by subsequent (1-2 hours later) development of severe thunderstorms. Their work indicates that operational applications making use of real-time satellite wind data may eventually play an important role in future severe-storm prediction techniques, especially if extensive cumulus-cloud fields are present within the precursor storm environment.

c. Thunderstorm microphysics

Considerable research has been accomplished, especially in conjunction with weather modification field experiments such as HIPLEX and the NOAA Florida Area Cumulus Experiment (FACE), in relating satellite-observed thunderstorm characteristics to incloud microphysical processes. The ability to monitor all cloud systems within and near a project area is especially important if data are to be properly analyzed and if effects of both seeding and the large natural variability of thunderstorm systems are to be evaluated.

Pearl et al. (1975) related satellite-observed cloudtop characteristics to incloud hail growth and subsequent hail reports at the surface. The hail storms were quasi-steady state and also long lived. The overshooting tops were wide, high, persistent, and detectable as cold tops in the IR satellite data. Forecasting of hail occurrences using satellite data was considered possible if the continuous overshooting tops were concentrated upon.

Pryor (1978) examined many collocated visible and infrared GOES images for a significant severe-storm outbreak (see Figs. 18a and b). He found that overshooting cloudtop heights associated with tornado reports were considerbly lower than those associated with large hailfalls, and overshooting tops associated with hail were characterized by their great vertical extent. He also noted that overshooting tops that were apparent in the visible imagery were not always detected in the coarser resolution infrared data.

(1) Areal rain estimates

Griffith et al. (1976) have developed quantitative methods to estimate areal rainfall using visible brightness data. Figure 19 shows a comparison of satellite-derived rainfall with data gathered by ground-based sensors in the FACE program. Here, satellite-observed cloud brightness is related to 10-cm radar data as adjusted by rain gage data over southern Florida. Brightness in the satellite imagery is assumed to be an indication of storm deepness and wetness, and the adjustment of radar data with rain gages is explained in Ch. IX. Work is under way to determine the transferability of the procedure and also to use digital data in place of digitized negatives.

A recently developed technique (Bielicki, 1978) allows stream drainage basin boundaries to be superposed on digitized satellite data. This procedure provides areal rainfall estimations for specific basins and allows a quantitative determination of flash flood potential. A case study of the 1976 Big Thompson flash flood in Colorado, using digital infrared data, produced accurate apportionments of precipitation over the various drainages along the Colorado Front Range. This type of dual meteorological/hydrological application of satellite data is illustrated in Fig. 20.

(2) HIPLEX cloud studies

Reynolds (1977) has reported HIPLEX cloud case studies where the emphasis is on comparison of radar and satellite characteristics. He found that brightness centers corresponded well with locations of active radar return but not particularly well with radar intensity. With some clouds, satellite- and radar-measured tops agreed well, but in other cases they did not. This was apparently caused by the variability of the horizontal extent of the overshooting tops of individual clouds. Negri et al. (1976) noted a relation

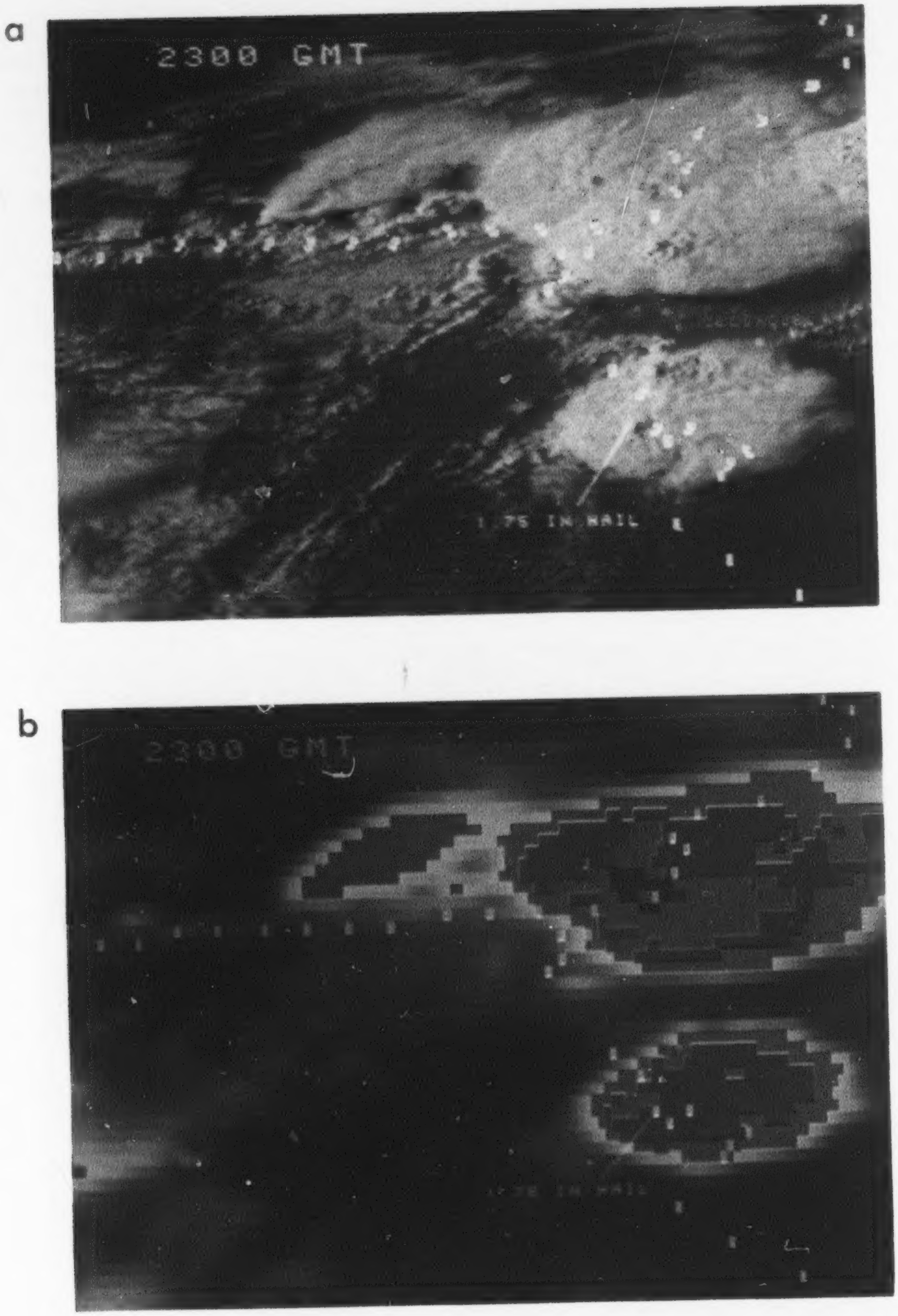

Figure 18.--(Above) GOES-1 visible image (resolution ~1.3 km) at 2300 GMT, 5 May 1977. Large hail was reported at 2300 GMT; the hailfall location is indicated. (Below) GOES-1 infrared image (resolution ~11.6 km) at 2300 GMT, 5 May 1977. The image was color enhanced (red, $\leq$205 K; green, 206-208 K; blue, 209-211 K; yellow, 212-224 K; and gray, $\geq$225 K) on the Colorado State University interactive data processing system (ADVISAR). The hailfall location is indicated (Pryor, 1978).

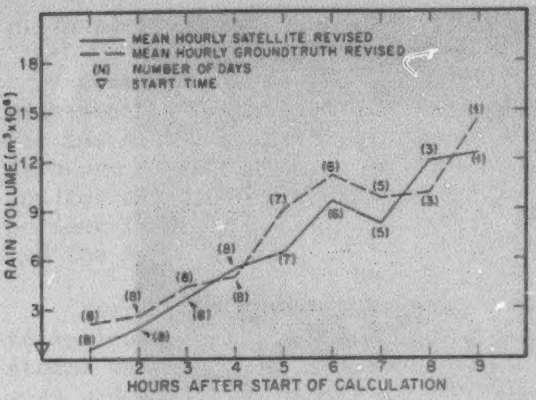

Figure 19.--Mean hourly satellite target rain volumes compared with mean hourly ground truth (Griffith et al., 1976).

BIG THOMPSON
0330 GMT

Figure 20.--Digitized GOES-1 infrared image (black <198 K, red 199-200 K, green 201-202 K, blue 203-206 K, yellow 207-210 K, and gray shades ≥211 K) for 0330 GMT, 1 August 1976, showing the location of cold cloudtops over the Colorado front-range drainage basins. The dashed line indicates the Big Thompson drainage basin (Bielicki, 1978).

between the time that a particular cloud reached a brightness threshold and the time that the first radar echo return was detectable. This study also found that the IR sensor may not accurately respond to isolated small clouds and caution is required in interpreting research results.

5. REMOTE SOUNDING OF THE THUNDERSTORM ENVIRONMENT

The multichannel radiation data gathered by an instrument such as the VTPR described in Sec. 2a can be used to infer the vertical temperature structure of the atmosphere. The radiative transfer equation (McMillin et al., 1973; Fritz et al., 1972) may be inverted for each radiance channel to obtain the vertical blackbody radiance, or temperature, profile of the atmosphere.

Since the mixing ratio of CO_2 in the atmosphere is nearly constant, it can be assumed that changes in radiance sensed at a satellite for a given CO_2 channel are due to atmospheric temperature and moisture changes. The transmission of the atmosphere due to CO_2 is also slightly dependent on temperature, but this dependence is of lesser magnitude and can be accounted for with temperature-dependent CO_2 transmittances (Smith, 1969). The effects of varying amounts of water vapor on the CO_2 transmission functions are more significant than those of temperature variations, but until recently they were neglected.

Cloudy situations represent a particularly difficult problem, since the infrared transmission from below clouds is highly variable and depends upon their opacity, and since clouds may obscure only a portion of the field of view. Cloudy column radiances may be eliminated from the data sample or an attempt can be made to account for the clouds (Hillger and VonderHaar, 1977).

Hillger and VonderHaar used VTPR data to retrieve soundings having a horizontal resolution much finer than that of the standard rawinsonde network. Resultant mesoscale analyses of the 500-mb temperature field and of integrated atmospheric water content are shown in Figs. 21 and 22. Satellite-derived resolution of small-scale thermal waves and of the dryline could be used to determine areas having a high convective potential. The uncertainties involved in using satellite soundings on the mesoscale (i.e., how accurately are important atmospheric features detected and resolved) will be evaluated as the VAS sounding data become available.

Fritz (1977) has presented an empirical method for retrieving temperature profiles. In his procedure, known profiles (from sounding data) are used as benchmark data to improve the absolute accuracy of retrievals at points between the benchmark locations. He applied the technique to simulated VTPR data for an actual severe-thunderstorm situation and found a significant increase in the accuracy of the retrieved profiles.

Weinreb (1977) has shown that transmittance changes caused by varying water vapor content may significantly affect the accuracy of retrieved temperature profiles. Instruments in the advanced satellites such as the VAS allow more accurate determination of water vapor vertical profiles and should increase the representativeness of the corresponding temperature profiles, and perhaps eventually allow four-dimensional monitoring of atmospheric stability from geosynchronous platforms.

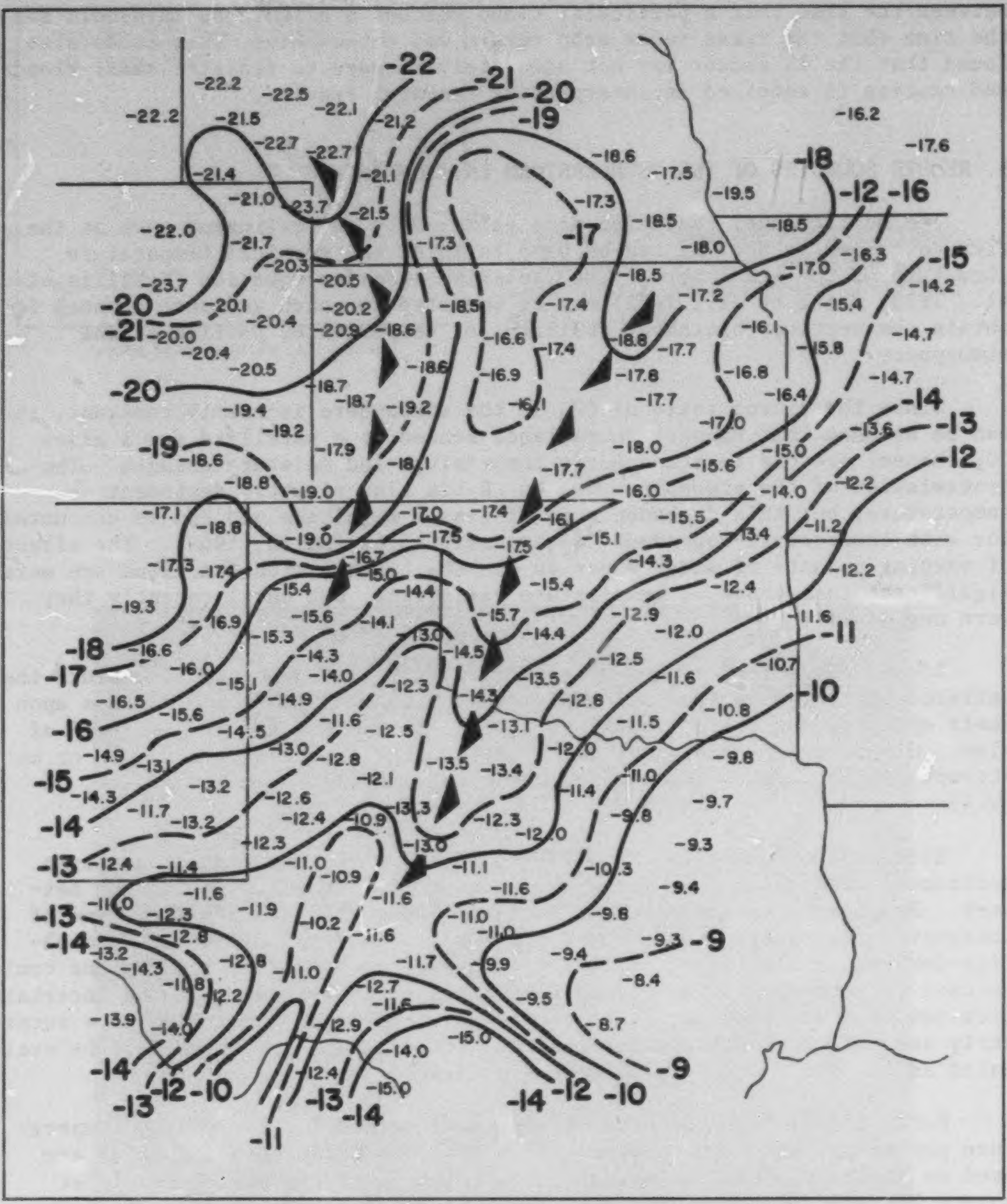
-22
-21
-20
-19
-22.2
-22.5
-22.2
-21.5
-22.1
-21.2
-22.7
-22.7
-21.4
-21.1
-21.0
23.7
-21.5
-22.0
-21.7
-20.3
-20.5
-17.3
-23.7
-20
-20.1
-20.2
-20.4
-18.5
-21
-20.0
-20.9
-18.6
-20.4
-20.5
-18.6
-20
-18.7
-18.7
-19.2
-19.4
-19.2
-17.9
-19
-18.6
-18.1
-18.8
-19.0
-17.1
-18.8
-19.0
-17.0
-17.5
-16.7
-17.3
-17.4
-15.4
-15.0
-19.3
-16.9
-15.6
-14.1
-14.4
-15.3
-18
-16.6
-14.3
-13.0
-17
-16.0
-14.0
-12.3
-16.5
-15.1
-14.9
-15.6
-14.5
-11.6
-12.5
-16
-13.0
-14.9
-12.8
-13.1
-12.1
-15
-13.2
-14.3
-12.6
-14
-11.7
-13.2
-12.4
-10.9
-13.3
-12.3
-13
-12.4
-11.4
-11.0
-13.0
-11.6
-10.9
-11.6
-11.9
-11.0
-13
-12.3
-10.2
-11.6
-12.8
-14
-13.2
-12.8
-11.0
-14.3
-11.8
-12.2
-12.7
-11.6
-13.9
-14.0
-12.9
-14.0
-14
-12.4
-15.0
-13
-12
-10
-13
-14
-11
-18.6
-17.5
-17.3
-17
-18.5
-18.0
-18.5
-17.4
-16.6
-17.4
-18.8
-17.7
-16.9
-17.8
-16.1
-17.7
-18.0
-17.7
-16.0
-17.4
-16.1
-17.5
-15.1
-15.4
-15.7
-14.4
-14.5
-13.5
-14.3
-13.1
-13.5
-13.4
-11.1
-11.6
-11.0
-11.0
-11.7
-9.9
-9.5
-15.0
-14
-12
-10
-16.2
-17.6
-19.5
-18
-12
-16
-18.5
-15
-17.2
-17.0
-16.3
-14.2
-16.1
-15.4
-14.7
-15.8
-16.8
-16.4
-14.7
-17.0
-14
-13.6
-13
-15.6
-15.0
-12
-14.0
-12.2
-15.5
-13.4
-11.2
-14.3
-12.4
-12.2
-12.9
-12.0
-11.6
-11
-12.5
-10.7
-11.6
-10
-12.8
-10.8
-11.5
-12.0
-9.8
-11.0
-11.4
-9.7
-9.8
-12.0
-9.3
-10.3
-9.4
-9.8
-9.3
-9
-9.4
-8.4
-8.7
-9

Figure 21.--Mesoanalysis (in °C) of a satellite-derived 500-mb temperature field obtained using an iterative retrieval algorithm with an initial-guess vertical temperature profile (Hillger and VonderHaar, 1977).

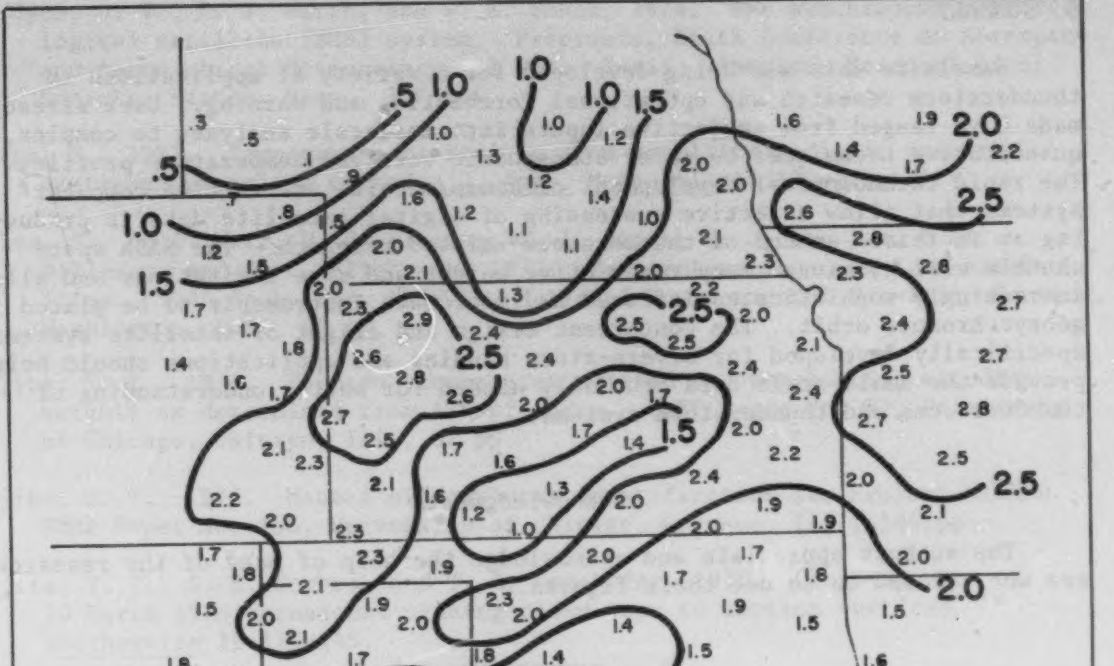
.5
1.0
1.0
1.0
1.5
2.0
.5
2.5
1.0
1.5
2.5
2.5
1.5
2.5
2.0
1.5
1.0
.5
2.0
.5
2.5
1.0
2.0

Figure 22.--Mesoanalysis (in cm) of a satellite-derived precipitable water field obtained using a least-squares linear regression of radiosonde values against H_2O channel radiance residuals (Hillger and VonderHaar, 1977).

6. SUMMARY

Satellite data are being developed for a variety of applications to thunderstorm research and operational forecasting and warning. Uses already made have ranged from subjective inputs into mesoscale analyses to complex, quantitative techniques to infer atmospheric vertical temperature profiles. The rapid technological development of human/machine interactive computer systems that allow selective processing of digital satellite data is producing an increased amount of thunderstorm-related research. The NASA space shuttle will eliminate many restrictive weight and size limitations and allow increasingly sophisticated infrared and microwave instruments to be placed in geosynchronous orbit. The concurrent design and flight of satellite systems specifically developed for severe-storm studies and applications should help provide the small-scale data crucially needed for better understanding of thunderstorms and thunderstorm systems.

Acknowledgments

The authors appreciate and acknowledge the help of many of the researchers who allowed us to use their figures.

REFERENCES

Adler, R. F., and D. D. Fenn, 1977. Satellite-based thunderstorm intensity parameters. Preprints, Tenth Conference on Severe Local Storms, 18-21 October, Omaha, Nebraska. America Meteorological Society, Boston, Mass., 8-15.

Adler, R. F., and D. D. Fenn, 1979. Thunderstorm vertical velocities estimated from satellite data. J. Atmos. Sci. 36:1747-1754.

Anderson, R. K., et al., 1974. Application of meteorological satellite data in analysis and forecasting. ESSA Tech. Rep. NESC 51, 250 pp.

Anthony, R. W., and C. L. Bristor, 1978. Interactive system requirements for the realtime demonstration of mesoscale weather detection and prediction. Preprints, Conference on Weather Forecasting and Analysis and Aviation Meteorology, Silver Springs, Maryland. American Meteorological Society, Boston, Mass., 219-227.

Arn, R. M., 1975. Anvil area and brightness characteristics as seen from geosynchronous satellites. Master's thesis, Colorado State University, Fort Collins, 88 pp.

Bielicki, D. E., 1978. Estimation of Big Thompson flood rainfall using infrared satellite imagery. Atm. Sci. Paper (unnumbered), Colorado State University, Ft. Collins, 60 pp.

Billingsley, J. B., 1976. Interactive image processing for meteorological applications at NASA/Goddard Space Flight Center. Preprints, Seventh Conference on Aerospace and Aeronautical Meteorology and Symposium on Remote Sensing from Satellites, Melbourne, Florida. American Meteorological Society, Boston, Mass., 268-275.

Fordyce, D. V., R. J. Wirth, and W. E. Shenk, 1974. The synchronous meteorological satellite (SMS) system. Preprints, Sixth Conference on Aerospace and Aeronautical Meteorology, El Paso, Texas. American Meteorological Society, Boston, Mass., 158-164.

Fritz, S., 1977. Temperature retrievals from satellite radiance measurements--an empirical method. J. Appl. Meteorol. 16:172-176.

Fritz, S., D. Q. Wark, H. E. Fleming, W. L. Smith, H. Jacobowitz, D. T. Hilleary, and J. C. Alishouse, 1972. Temperature sounding from satellites. NOAA Tech. Rep. NESS 59, National Environmental Satellite Service, Washington, D.C., 49 pp.

Fujita, T. T., 1973. Tornado occurrences related to overshooting cloudtop heights as determined from ATS pictures. SMRP Paper No. 97, University of Chicago, Chicago, Ill., 32 pp.

Fujita, T. T., 1978. Manual of downburst identification for Project NIMROD. SMRP Paper No. 156, University of Chicago, Chicago, Ill., 104 pp.

Fujita, T. T., G. S. Forbes, and T. A. Umenhofer, 1976. Close-up view of 20 March 1976 tornadoes: sinking cloud tops to suction vortices. Weatherwise 29:116-145.

Fujita, T. T., E. W. Pearl, and W. E. Shenk, 1975. Satellite-tracked cumulus velocities. J. Appl. Meteorol. 14:407-413.

Griffith, C. G., et al., 1976. Rainfall estimation from geosynchronous satellite imagery during daylight hours. Tech. Rep. ERL 356-WMPO 7, NOAA Environmental Research Laboratories, Boulder, Colo., 106 pp.

Gurka, J. J., 1976. Satellite and surface observations of strong wind zones accompanying thunderstorms. Mon. Weather Rev. 104:1484-1493.

Hasler, A. F., W. E. Shenk, J. P. Gary, and H. W. Robinson, 1976a. A study of STORMSAT interactive data analysis facility. Preprints, Seventh Conference on Aerospace and Aeronautical Meteorology and Symposium on Remote Sensing from Satellites, Melbourne, Florida. American Meteorological Society, Boston, Mass., 284-290.

Hasler, A. F., W. E. Shenk, and W. C. Skillman, 1976b. Wind estimates from cloud motions: phase 1 of an in situ aircraft verification experiment. J. Appl. Meteorol. 15:10-15.

Hill, K., and R. E. Turner, 1977. NASA's atmospheric variability experiments (AVE). Bull. Am. Meteorol. Soc. 58:170-172.

Hillger, D. W., and T. H. VonderHaar, 1977. Deriving mesoscale temperature and moisture fields from satellite radiance measurements over the United States. J. Appl. Meteorol. 16:715-726.

Houghton, D. D., and D. K. Lee, 1977. Mesoscale wind fields for the May 6, 1975 Omaha tornado situation derived from SMS cloud observations. Preprints, Tenth Conference on Severe Local Storms, Omaha, Nebraska. American Meteorological Society, Boston, Mass., 16-21.

Huffaker, R. M., D. W. Beran, and C. G. Little, 1976. Pulsed coherent lidar systems for airborne and satellite based wind field measurements. Preprints, Seventh Conference on Aerospace and Aeronautical Meteorology and Symposium on Remote Sensing from Satellites, Melbourne, Florida. American Meteorological Society, Boston, Mass., 318-324.

Krietzberg, C. W., 1976. Interactive applications of satellite observations and mesoscale numerical models. Bull. Am. Meteorol. Soc. 57:679-685.

Krietzberg, C. W., 1977. SESAME '77 experiments and data availability. Bull. Am. Meteorol. Soc. 58:1299-1301.

Lilly, D. K. (ed.), 1977. Project Severe Environmental Storms and Mesoscale Experiment. Planning documentation volume, NOAA Environmental Research Laboratories, Boulder, Colo., 308 pp.

Ludwig, G. H., 1974. The NOAA operational environmental satellite system--status and plans. Preprints, Sixth Conference on Aerospace and Aeronautical Meteorology, El Paso, Texas. American Meteorological Society, Boston, Mass., 137-145.

Maddox, R. A., 1980. Mesoscale convective complexes. Bull. Am. Meteorol. Soc. 61:1374-1387.

Magor, B. W., 1969. Mesoanalysis: some operational analysis techniques utilized in tornado forecasting. Bull. Am. Meteorol. Soc. 40:499-511.

McMillin, L. M., et al., 1973. Satellite infrared soundings from NOAA spacecraft. NOAA Tech. Rep. NESS 65, National Environmental Satellite Service, Washington, D.C., 121 pp.

Miller, R. C., 1972. Notes on analysis and severe storm forecasting procedures of the Air Force Global Weather Central. Air Weather Service TR 200 (Rev.), 102 pp.

Miller, R. C, and J. A. McGinley, 1978. Using satellite imagery to detect and track comma clouds and the application of the zone technique in forecasting severe storms. Project Report, GE/Management and Technical Services Company, Beltsville, Md., 100 pp.

Negri, A. J., and T. H. VonderHaar, 1980. Moisture convergence using satellite-derived wind fields: a severe local storm case study. Mon. Weather Rev. 108:1170-1182.

Negri, A. J., D. W. Reynolds, and R. A. Maddox, 1976. Measurements of cumulonimbus clouds using quantitative satellite and radar data. Preprints, Seventh Conference on Aerospace and Aeronautical Meteorology and Symposium on Remote Sensing from Satellites, Melbourne, Florida. American Meteorological Society, Boston, Mass., 119-124.

Pearl, E. W., W. E. Shenk, and W. Skillman, 1975. Cloud-top parameters--a hail indicator. Preprints, Ninth Conference on Severe Local Storms, Norman, Oklahoma. American Meteorological Society, Boston, Mass., 464-467.

Peslen, C. A., 1977. A satellite interpretation of the dynamics of a severe local storm area using 5 minute interval SMS data. Preprints, Tenth Conference on Severe Local Storms, Omaha, Nebraska. American Meteorological Society, Boston, Mass., 1-7.

Pryor, S. P., 1978. Measurement of thunderstorm cloud-top parameters using high-frequency satellite imagery. Atm. Sci. Paper (unnumbered), Colorado State University, Fort Collins, 101 pp.

Purdom, J. F. W., 1973. Meso-highs and satellite imagery. Mon. Weather Rev. 101:180-181.

Purdom, J. F. W., 1974. Satellite imagery applied to the mesoscale surface analysis and forecast. Preprints, Fifth Conference on Weather Forecasting and Analysis, St. Louis, Missouri. American Meteorological Society, Boston, Mass., 63-68.

Purdom, J. F. W., 1976. Some uses of high-resolution GOES imagery in the mesoscale forecasting of convection and its behavior. Mon. Weather Rev. 104:1474-1483.

Reynolds, D. W., 1977. Intensive case study analysis of 3 and 5 June 1976 using geosynchronous digital satellite data. Special report, Bureau of Reclamation Contract No. 6-07-DR-20020, 44 pp.

Reynolds, D. W., 1980. Observations of damaging hailstorms from geosynchronous satellite digital data. Mon. Weather Rev. 108:337-348.

Reynolds, D. W., and D. A. Matthews, 1976. Real-time satellite support for the high plains cooperative experiment. Preprints, Second WMO Scientific Conference on Weather Modification, Boulder, Colorado. WMO No. 43, 497-502.

Scofield, R. A., and V. J. Oliver, 1977. A scheme for estimating convective rainfall from satellite imagery. Tech. Memo. NESS 86, NOAA Environmental Laboratories, Boulder, Colo., 41 pp.

Scofield, R. A., and C. E. Weiss, 1976. Application of synchronous meteorological satellite products and other data for short range forecasting in the Chesapeake Bay region. Preprints, Sixth Conference on Weather Forecasting and Analysis, Albany, New York. American Meteorological Society, Boston, Mass., 67-73.

Shenk, W. E., 1974. Cloud top height variability of strong convective cells. J. Appl. Meteorol. 13:917-922.

Sikdar, D. N., V. E. Suomi, and C. E. Anderson, 1970. Convective transports of mass and energy in severe storms over the United States--an estimate from a geostationary altitude. Tellus 22:521-532.

Smith, W. L., 1969. A polynomial representation of carbon dioxide and water vapor transmission. ESSA Tech. Memo. NESC 647.

Tecson, J. J., T. A. Umenhofer, and T. T. Fujita, 1977. Thunderstorm-associated cloud motions as computed from 5-minute SMS pictures. Preprints, Tenth Conference on Severe Local Storms, Omaha, Nebraska. American Meteorological Society, Boston, Mass., 22-29.

VonderHaar, T. H., 1969. Meteorological applications of reflected radiance measurements from ATS 1 and ATS 3. J. Geophys. Res. 74:5404-5412.

Weinreb, M. P., 1977. Practical problems in meteorological soundings from satellites. Paper presented at AAAS 1977 Annual Meeting, Denver, Colo., 20-25 February, 15 pp.

Weinreb, M. P., and D. S. Crosby, 1973. Estimation of atmospheric moisture profiles from satellite measurements by a combination of linear and non-linear methods. Preprints, Third Conference on Probability and Statistics in Atmospheric Science, Boulder, Colorado. American Meteorological Society, Boston, Mass., 231-235.

Whitney, L. F., 1977. Relationship of the sub-tropical jet stream to severe local storms. Mon. Weather Rev. 105:398-412.

BIOGRAPHIES

ROY T. ARNOLD, a native of Jackson, Miss., was born on 27 March 1933. He studied physics at both the undergraduate and graduate levels and received the B.S. degree from Millsaps College in 1954. The M.S. degree was awarded in 1956 and the Ph.D. degree in 1960, both from Vanderbilt University. After 4 years as a research scientist at the Sperry Microwave Electronics Company in Clearwater, Fla., he joined the physics faculty at the University of Mississippi in 1963 and is now a professor of physics there. His research interests have been diversified, but in the past 12 years he has worked principally in physical acoustics. Since the 3-4 April 1974 tornado outbreak, he has been engaged in storm acoustic research, with a particular interest in tornadic sounds, and has participated extensively and successfully with his students in the storm intercept program headquartered at the National Severe Storms Laboratory.

STANLEY L. BARNES is Program Manager for the Mesometeorology Division of the Office of Weather Research and Modification, Environmental Research Laboratories, National Oceanic and Atmospheric Administration, in Boulder, Colo. After 4 years as a naval weather observer, he studied meteorology at Oklahoma State University and Texas A & M University, receiving the B.S. and M.S. degrees from the latter. His Ph.D. degree is from the University of Oklahoma. During the late 1960's he was Chief of the Severe Storm Morphology and Dynamics Project at the National Severe Storms Laboratory. He has published several papers dealing with mesoscale objective analysis techniques and the description of severe thunderstorm phenomena synthesized from surface, upper-air, and radar data. From 1974 until 1981 he served as meteorologist and office manager for the Severe Environmental Storms and Mesoscale Experiment Program (Project SESAME), and as Deputy Director of Operations during its 1979 field program. The division he now heads is engaged in mesoscale numerical weather simulation model development and in a variety of studies from which are developing diagnostic techniques and forecasting aids for significant precipitation events produced by convective storms.

EDWARD A. BRANDES is a research meteorologist at the National Severe Storms Laboratory in Norman, Okla., a component of the NOAA Environmental Research Laboratories. He holds a B.S. degree in Mechanical Engineering from the Newark College of Engineering and obtained his M.S. degree in meteorology from New York University. During service with the U.S. Air Force, he provided weather forecasts from Shaw Air Force Base, South Carolina; Thule Air Force Base, Greenland; and Egland Air Force Base, Louisiana. His interests are in the application of weather radar for the detection, prediction, and study of severe thunderstorms, and for estimating point and areal rainfall.

ROBERT DAVIES-JONES completed undergraduate work in physics at Birmingham University, England, received the Ph.D. in astrogeophysics from the University of Colorado, and during 1969-1970 held a postdoctoral research appointment at the National Center for Atmospheric Research. His specialties are the fluid dynamics of tornadoes and severe thunderstorms. Now at the National Severe Storms Laboratory, he directs work of the Tornado Dynamics Unit and of the Tornado Intercept Project to observe severe storms in the field. He also holds an adjunct appointment at the University of Oklahoma and is a consultant on tornadoes to the Nuclear Regulatory Commission and other agencies.

RICHARD J. DOVIAK is Chief of the Advanced Techniques Project at the National Severe Storms Laboratory in Norman, Okla., and Adjunct Professor of Electrical Engineering at the University of Oklahoma. Prior to his present position he was Assistant Professor of Electrical Engineering and lecturer (1965-1971) at the University of Pennsylvania in Philadelphia, where he taught subjects related to electromagnetic theory and was Supervisor of Academic Laboratories (1967-1971). Dr. Doviak received his M.S.E.E. (1959) and Ph.D. (1963) degrees from this university and his B.S.E.E. from Rensselaer Polytechnic Institute (1956). His specialties include remote sensing of the atmosphere with Doppler radar, with emphasis on Doppler radar studies of weather.

THOMAS H. GEORGES received a B.S. degree in engineering from Loyola University of Los Angeles in 1961 and an M.S. from U.C.L.A. in 1963, also in engineering. Since 1963 he has worked with the Boulder Laboratories of the U.S. Department of Commerce, first with the National Bureau of Standards, now with NOAA's Wave Propagation Laboratory. In 1967, he received a Ph.D. in engineering from the University of Colorado. He is the author or coauthor of more than 30 publications on radio and acoustic gravity wave propagation, ionospheric dynamics, meteorology, and acoustics. He now works in WPL's Sea State Studies perfecting ways to use over-the-horizon radar for measuring ocean wave heights.

RONALD L. HOLLE is a meteorologist with the Cumulus Dynamics and Microphysics Program Office of the Office of Weather Research and Modification in Boulder, Colo., a component of the NOAA Environmental Research Laboratories. He obtained B.S. and M.S. degrees in meteorology from Florida State University, and took additional coursework at the University of Miami. Principal areas of research have emphasized cloud photogrammetry for study of populations of convective clouds in the tropics and mesoscale cloud organization and interaction. Mr. Holle has participated in all FACE projects, as well as field programs in Barbados, the Bahamas, and the GATE project. He has conducted research on GATE photos in conjunction with the University of Virginia, and has been rapporteur to the World Meteorological Organization (WMO) on tropical cloud codes and photographs, and the revision of the WMO International Cloud Atlas.

ROBERT A. MADDOX is a research scientist with the Office of Weather Research and Modification in Boulder, Colo., a component of NOAA Environmental Research Laboratories. He holds a B.S. degree in meteorology from Texas A & M University and M.S. and Ph.D. degrees in atmospheric science from Colorado State University. Dr. Maddox spent 8 years as an Air Force meteorologist, working primarily as a lead forecaster in the Military Severe Weather Warning Center, before joining the research component of NOAA. His special research interests include mesometeorology and satellite applications with emphasis on convective storms and flash floods.

JOHN McCARTHY is a Staff Scientist with the Field Observing Facility, National Center for Atmospheric Research. Formerly he was Associate Professor of Meteorology at the University of Oklahoma. His chief interests have been in aviation meteorology, dynamics and morphology of severe local storms, and policy aspects of weather modification. He received the A.B. in physics from Grinnell College, the M.S. in meteorology from the University of Oklahoma, and in 1973, the Ph.D. in geophysical sciences from the University of Chicago. Dr. McCarthy was a visiting professor of meteorology at the University of Washington, Seattle, during summer 1977.

GRIFFITH M. MORGAN, JR. is head of the Design and Evaluation Group of the Convective Storms Division at the National Center for Atmospheric Research in Boulder, Colo. He came to NCAR following 6 years as Senior Meteorologist at the Illinois State Water Survey; prior to that, he was Director of the Observatory for Hailstorm Research in Verona, Italy. He is author of more than 60 papers and reports, mainly on hailstorms, cloud physics, and synoptic meteorology. Mr. Morgan received a B.A. degree in physics from Northwestern University in 1955 and an M.S. degree in meteorology from New York University in 1961. On graduation from Northwestern he received a commission in the U.S. Air Force and served as a weather forecaster in Europe and North Africa. He received a Fulbright Study Grant in 1962 to study hailstorms in Italy.

EDWARD T. PIERCE graduated from the University of Wales and received the doctorate in atmospheric physics from Cambridge University, England, in 1951. After more than a decade of teaching and research at Cambridge in solar and meteorological research, he was employed for high-voltage research by Vickers, Ltd., and for research in geophysics by AVCO Corporation. During 1960-1976, he was employed at Stanford Research Institute and became widely known as an authority on atmospheric electricity and the hazardous effects of electric fields and lightning on aircraft, supertankers, and rockets. During 1976-1977, Dr. Pierce worked at NOAA's National Severe Storms Laboratory in Norman, Okla. In his professional career he produced more than 150 reports and publications. Dr. Pierce was honorary president of the International Commission on Atmospheric Electricity from 1975 until his untimely death in 1978.

DALE SIRMANS is Chief Engineer at the National Severe Storms Laboratory. He studied at the Georgia Institute of Technology and holds a B.S. in electrical engineering from the University of Oklahoma. Prior to joining the National Severe Storms Project in 1962, Mr. Sirmans worked in aviation electronics with both military and commercial carriers and with manufacturers. Mr. Sirmans' chief activities are in design and development of meteorological radar systems and signal-processing techniques.

DONALD L. VEAL is President of the University of Wyoming, Laramie. He completed undergraduate work at South Dakota State University and received M.S. and Ph.D. degrees in civil engineering from the University of Wyoming. He was a pilot and instructor in the Air Force, and held various academic posts before becoming head of the Department of Atmospheric Science in the University of Wyoming's College of Engineering in 1971. During 1976 he was on leave from the University of Wyoming to be director of the National Hail Research Experiment of the National Center for Atmospheric Research, Boulder, Colo. His contributions to the professional literature emphasize instrumentation and use of aircraft in meteorological investigations.

THOMAS H. VONDERHAAR attended Parks College, St. Louis, Mo., and the University of Wisconsin, Madison, where he earned his doctoral degree in 1968. In 1970 he joined the Department of Atmospheric Science at Colorado State University, where he is now a professor and the head of the department. Dr. VonderHaar and his students have published extensively on the meteorological applications of satellite data and have contributed substantially to the development and use of satellite-borne radiation sensors. He is a member of several learned societies and scientific commissions.

KENNETH E. WILK is head of the Interim Operational Test Facility of the Joint Systems Program Office, National Weather Service; he holds key responsibilities for development of radar methodologies to be applied in a new national network of Doppler weather radars. He has B.A. and B.S. degrees in physics and meteorology from the University of Illinois and Pennsylvania State University, respectively. During 1952-1956, Mr. Wilk provided weather forecasts for U.S. Air Force units in England and Germany. In 1962, he joined the U.S. Weather Bureau's National Severe Storms Project to establish its Weather Radar Laboratory at Norman. After 1964, when the Norman group became the nucleus of NSSL, he led the operation of many of NSSL's observational facilities, which have provided basic data for numerous studies during the past decade. He was manager of the Joint Doppler Operational Project, which demonstrated Doppler radar capabilities and thereby established the basis for use of Doppler radars throughout the United States.

JAMES W. WILSON is a staff scientist at the National Center for Atmospheric Research (NCAR) in Boulder, Colo. He obtained a B.S. degree in physics from the University of North Carolina in 1959 and an M.S. degree in meteorology from the University of Washington in 1961. From 1961 until 1978, when he joined NCAR, he worked for The Travelers Research Center in Hartford, Conn. (renamed the Center for the Environment and Man in 1970) as a research scientist. His research specialties are the use of Doppler radar and mesometeorological observation networks to study air motions and precipitation structure of convective and stratiform storms, with a special emphasis on research applied to operational problems. He has played a leading role in the development of radar techniques to measure precipitation.

DUSAN S. ZRNIC' is leader of Doppler radar research and development in the Advanced Techniques Group at the National Severe Storms Laboratory. He graduated from the University of Belgrade, Yugoslavia, with a B.S. degree in electrical engineering in 1965, and he obtained M.S. and Ph.D. degrees in electrical engineering at the University of Illinois, Urbana. Following employment as a research and teaching assistant with the Charged Particle Research Laboratory at the University of Illinois, he joined the Electrical Engineering Department of California State University, Northridge. He became Associate Professor in 1974, and Professor in 1978. During the 1973-1974 academic year, Dr. Zrnic' was a National Research Council Post-Doctoral Fellow at NSSL, and in 1975-1976 he was on sabbatical leave at the same laboratory. His research experience includes circuit design, applied mathematics, magnetohydrodynamics, and signal-processing and radar systems; his most recent work, performed for various private firms and government organizations, is in radar meteorology, random processes, and signal parameter estimation.

☆ U.S. GOVERNMENT PRINTING OFFICE: 1982-0-578-647